SAKARYA ÜNİVERSİTESİ

FEN BİLİMLERİ ENSTİTÜSÜ DERGİSİ

Sakarya University Journal of Science (SAUJS)

SAKARYA ÜNİVERSİTESİ

e-issn: 2147-835X

SAÜ Fen Bil Der/SAUJS

Cilt/Volume: 25

Sayı/Issue: 4

Ağustos/August 2021

Sakarya Üniversitesi Fen Bilimleri Enstitüsü Dergisi
(Sakarya University Journal of Science)
Cilt/Volume: 25 No/ Issue:4 Ağustos/August 2021
Editör Kurulu/Editorial Boards

Editor-in-Chief

Editors

Editorial Board

English Language Editor

SAKARYA ÜNİVERSİTESİ FEN BİLİMLERİ ENSTİTÜSÜ DERGİSİ
(SAKARYA UNIVERSITY JOURNAL OF SCIENCE)
İÇİNDEKİLER/CONTENTS
Cilt/Volume: 25 – No/Issue4: (AĞUSTOS/AUGUST-2021)

RESEARCH ARTICLES

SAKARYA ÜNİVERSİTESİ
FEN BİLİMLERİ ENSTİTÜSÜ DERGİSİ

Sakarya University Journal of Science
SAUJS

ISSN 1301-4048 | e-ISSN 2147-835X | Period Bimonthly | Founded: 1997 | Publisher Sakarya University | http://www.saujs.sakarya.edu.tr/

Title: Corrosion Effects on Fatigue Behavior of Zn-Cr+3 and Zn Flake Coated M8 DIN 933 Bolts

Authors: Sezgin YURTDAŞ, Umut İNCE, Barış TANRIKULU, Cenk KILIÇASLAN, Muhammed Burak TOPARLI

Recieved: 2020-09-18 16:30:06

Accepted: 2021-05-18 11:47:58

Article Type: Research Article

Volume: 25
Issue: 4
Month: August
Year: 2021
Pages: 867-874

How to cite
Sezgin YURTDAŞ, Umut İNCE, Barış TANRIKULU, Cenk KILIÇASLAN, Muhammed Burak TOPARLI; (2021), Corrosion Effects on Fatigue Behavior of Zn-Cr+3 and Zn Flake Coated M8 DIN 933 Bolts. Sakarya University Journal of Science, 25(4), 867-874,
DOI: 10.16984/saufenbilder.796745
Access link
http://www.saujs.sakarya.edu.tr/en/pub/issue/64755/796745

Sakarya University Journal of Science 25(4), 867-874, 2021

Corrosion Effects on Fatigue Behavior of Zn-Cr+3 and Zn Flake Coated M8 DIN 933 Bolts

Sezgin YURTDAŞ[1], Umut İNCE[1], Barış TANRIKULU[1], Cenk KILIÇASLAN[1*], Muhammed Burak TOPARLI[1]

Abstract

In this study, fatigue behavior of Zn-Cr+3 and zinc flake coated bolts was investigated experimentally by considering corrosion effects. Fatigue tests were conducted on M8x50x1.25 8.8 DIN 933 bolts at normal and corroded conditions at force amplitudes between 2.35 and 5.36 kN at test frequency of 75 Hz. A part of bolts was subjected to salt atmosphere for corrosion. According to the Wöhler curves obtained from fatigue tests before corrosion, zinc flake coated bolts showed 1.55 times higher fatigue life compared to Zn-Cr+3. After corrosion, fatigue tests showed that the fatigue life difference increased to 2.10 times for the zinc flake coating. Moreover, corrosion was found to be ineffective on crack initiation region. For both coatings and corrosion conditions, fatigue cracks were seen to initiate from the thread roots.

Keywords: Bolt, fatigue life, coating, corrosion

1. INTRODUCTION

Fasteners are one of the most widely used machine elements in engineering world. They are exposed to various types of external loads and environments. Fatigue under cyclic loading can be considered as the major reason on failure of engineering components. It is estimated that 90% of the mechanical service failures are caused by fatigue [1]. Fatigue life of fasteners depends on many factors such as production method, microstructure, geometry, surface conditions, and coating type. It was shown that inadequate tension and clamping force, fasteners are highly susceptible to fatigue failures [2]. In addition to that, inter-granular cracks in the structure of material was also found to cause fatigue fracture. In another study, the fatigue behavior of the fasteners resulting from corrosion was investigated [3]. According to the experimental results, it was determined that there was a significant fatigue life loss compared to the parts that were not corroded. The previous studies showed that smooth surface conditions in the threads of fasteners and more compressive residual stresses on the surface lead to increase in fatigue strength of the parts [4]. One of the ways to achieve these conditions is to make the threading of the fasteners after the heat treatment process [5-6]. Fatigue tests revealed that fasteners which are threaded after heat treatment showed increased the fatigue life. It was also discussed

* Corresponding author: cenk.kilicaslan@norm-fasteners.com.tr
[1] Norm Cıvata San. ve Tic. A.Ş., AOSB, Çiğli, İzmir, Turkey.
E-mail: sezgin.yurtdas@norm-fasteners.com.tr; umut.ince@norm-fasteners.com.tr; baris.tanrikulu@norm-fasteners.com.tr; burak.toparli@norm-fasteners.com.tr.
ORCID: https://orcid.org/0000-0002-4120-8882; https://orcid.org/0000-0002-3118-3060; https://orcid.org/0000-0001-5441-0118; https://orcid.org/0000-0002-5787-9891; https://orcid.org/0000-0002-5203-5171.

that the type and angle of the thread of the bolts were very important for the fatigue life [7-8]. Specimens with 60° flank angle were found to have higher fatigue life about 20% than those with 90° flank angle. It was also found that the fatigue life of coarse threaded fasteners is higher than that of fine threaded fasteners for bolt sizes of M10 and M24. In another study, bolt length effect was evaluated on the fatigue behavior of joints [9]. Two different bolt lengths were examined and it was shown that increasing bolt length for the same tightening torque increases the joint fatigue strength. The effect of the eccentric cyclic loading on the bolt fatigue life was investigated [10]. It was found that the eccentric load reduced the fatigue life of the bolts and eccentricity did not significantly affect the shape of the cracks. However, a higher mean stress resulted in cracks with a more crescent shape. Considering the fatigue and corrosion behavior of bolts, the effects of corrosion on different threaded elements to investigate bolted joints working in a saline environment was studied [11]. FEM analysis was also carried out to evaluate the stress intensity factor and the change in applied corrosion rate. It was shown that corrosion caused a variation on the surface geometry of the threaded part, leading to a diversity of stress distribution. Corrosion fatigue performance of the high strength bolts were investigated [12]. The crack depth and fatigue life in the corrosion environment of high strength bolts were quantitatively analyzed. The fatigue life of the corroded high strength bolts was reduced by increasing material yield strength, applied tensile and stress amplitude. Stress amplitude had a crucial effect on the fatigue life. As a conclusion, it was shown that the stress amplitude should be controlled at a low level.

Despite there are many investigations on fatigue behavior of fasteners, limited studies concentrating on the corrosion effect of different coating types of fasteners are present in the literature. In this study, M8x50x1.25 8.8 DIN 933 bolts having two different coating types, Zn-Cr+3 and zinc flake, were fatigue tested. Zn-Cr+3 and Zinc flake coated bolts were subjected to salt spray test for 144 and 600 hours respectively until the red corrosion was seen, according to ISO 9227. Then, the effect of coating and corrosion to fatigue life were studied in details.

2. MATERIALS AND METHODS

M8x50x1.25 8.8 DIN 933 bolts used in this study were cold-forged in NORM Cıvata, Turkey. The chemical composition of the bolt material, 23MnB4, was given in Table 1. After cold forging, bolts were threaded using flat rolling process. Heat treatment process according to ISO 898-1 "Mechanical properties of fasteners made of carbon steel and alloy steel - Part 1: Bolts, screws and studs with specified property classes - Coarse thread and fine pitch thread" was carried out to obtain 8.8 grade.

Table 1 23MnB4 Chemical Analysis (%Weight).

C	**Mn**	**Si**	**P**	**S**	**Cr**	**Ni**
0.224	0.941	0.095	0.003	0.011	0.24	0.043
Mo	**Cu**	**Sn**	**Al**	**B**	**Ti**	
0.006	0.039	0.007	0.029	0.003	0.034	

The bolts, obtained from the same batch, are randomly divided into two groups and coated with two different types of coating as Zn-Cr+3 and Zinc flake. Electrolytic zinc plating is one of the most traditional and low-cost coating type for the protection of steel and ferrous metals against corrosion; a thin film layer is formed on the base metal by electrolysis to protect the base metal from corrosion. On the other hand, Zinc flake coatings are cured at comparatively low temperatures, and this type of coating does not contain Cr+6 and therefore, it does not cause hydrogen embrittlement. Contrary to Zn-Cr+3 coating, zinc flake coating process takes place with a binder system. This chemical process requires a firing process. For this reason, the strength of the salt spray test in Zinc flake coating is higher than the zinc coating in the same thickness, according to ISO 9227. Zn-Cr+3 and Zinc flake coated specimens are shown in Figure 1.

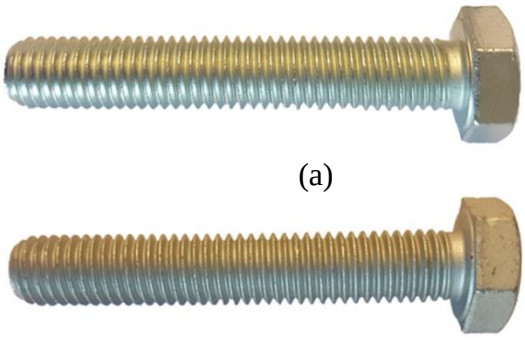

(a)

(b)

Figure 1 Specimens; a) Zn-Cr+3 b) Zinc flake.

Fatigue tests were performed according to ISO 3800 "Threaded fasteners-Axial load fatigue testing-Test methods and evaluation of results" standard using Zwick/Roell high frequency fatigue tester. Testing equipment is shown in Figure 2(a). In order to determine the mean force to be applied, 75% of the proof load specified in ISO 898-1 (Mechanical properties of fasteners) was taken as 21.1 kN. Test frequency in all fatigue test, 75 Hz was kept constant. The Wöhler curves for each coating type were determined by means of 36 tests with 6 different applied stress amplitudes. Salt spray test system is shown in Figure 2(b). In this tests, bolts are placed in chamber. NaCl solution is sprayed constantly in the chamber and the atmosphere is controlled by pressured air cycle. The salt spray tests were conducted according to ISO 9227 “Corrosion tests in artificial atmospheres - Salt spray tests” standard.

The macro optical investigations were carried out by employing Zeiss Stemi 508 Streezoom microscope. Images were obtained focusing on the thread root morphology of the bolts to reveal differences between Zn-Cr+3 and Zinc flake coatings. In addition, SEM images were taken by using Carl Zeiss 300 VP to examine fracture surfaces of the bolts after fatigue testing.

(a)

(b)

Figure 2 Test equipments; (a) Axial load fatigue and (b) salt spray testing chamber.

3. RESULTS AND DISCUSSIONS

After coating operations, bolt threads were examined under microscope since these regions were the most susceptible crack initiation locations. Figure 3(a) and (b) shows Zn-Cr+3 and Zinc flake coated threads, respectively [13]. As seen in the figure, thread roots (depicted with red arrow in the figure) were more homogenously coated in Zinc flake while Zn-Cr+3 coating was seen to have rougher surface.

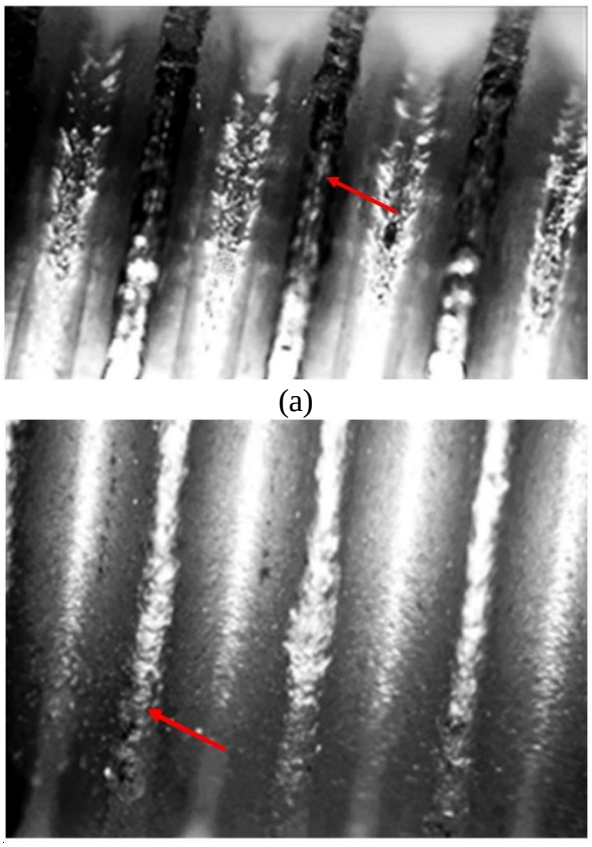

(a)

(b)

Figure 3 Pictures of thread roots; a) Zn-Cr+3, b) Zinc flake [13].

Bolts subjected to salt spray test are shown in Figure 4. As seen in the figure, red corrosion occurred on the bolt surface. Bolt head region was seen to be heavily corroded for Zn-Cr+3 coating while level of red corrosion was more less and uniformly distributed to the shaft region for Zinc flake coating.

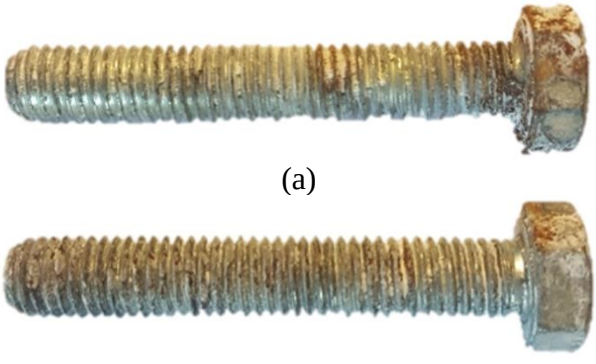

(a)

(b)

Figure 4 Bolts after salt spray test; a) Zn-Cr+3 b) Zinc flake. The length of the bolts is 50 mm.

Fatigue tests were carried out before and after salt spray test for both coatings. In all specimens, fatigue cracks occurred at the roots of the threads as seen in Figure 5. Typical fatigue fracture surface of the tested specimens coated with Zn-Cr+3 are given in Figure 5. The failure pattern was very similar for the samples coated with Zinc-flake. A representative SEM image from the fracture surface of the samples can be seen in Figure 6. Considering the geometry of the fatigue zone and instantaneous fracture zone, it was inferred that the applied nominal stress during fatigue testing was low enough for fatigue cracks to initiate and propagate. In addition, based on the morphology of the fatigue zone and instantaneous fracture zone, it was observed that the thread roots acted as stress concentration leading to the fracture surface as given in Figure 5 and Figure 6. Considering the fatigue zone, no clear fatigue striations were observed. For the instantaneous fracture zone, "woody" like morphology, i.e. elongated dimple rupture, was seen.

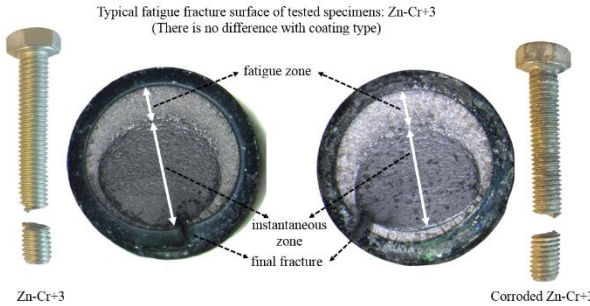

Figure 5 Fatigue fracture surface of the tested specimen; Zn-Cr+3 vs corroded Zn-Cr+3.

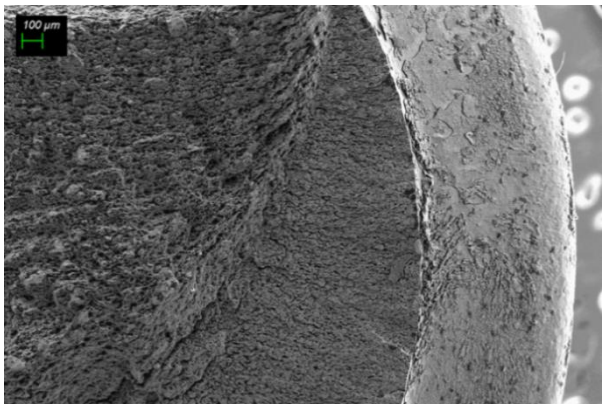

Figure 6 SEM image of fracture surface of the tested specimen.

In Figure 7(a), fatigue life of Zn-Cr+3 coated bolts tested at force amplitudes of 5.36, 3.50 and 2.50 kN were presented. Significant fatigue life reduction was observed after salt spray tests. For force amplitudes of 5.36 kN and 3.50 kN, percent

reductions in fatigue life were 23% and 28%, respectively. However, when force amplitude was 2.50 kN, the decrease in fatigue life was 45%. Considering the S-N curves for the Zn-Cr+3 bolts before and after salt spray test, fatigue performance was adversely affected from corrosion (Figure 7(b)). Zn-Cr+3 coated bolts exhibits 1.30 to 1.82 times higher fatigue resistance than 144 hours salt spray tested Zn-Cr+3 coated bolts.

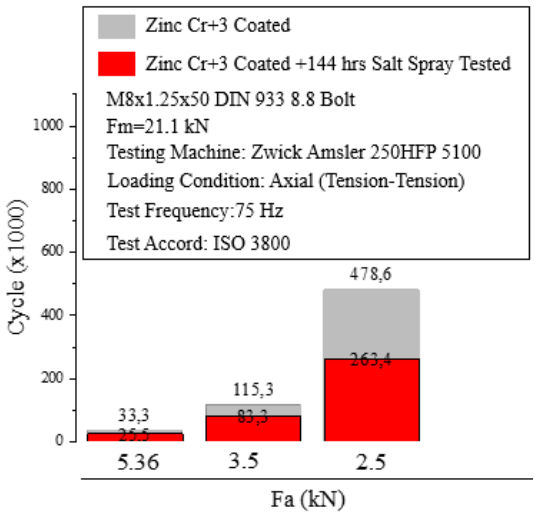

(a)

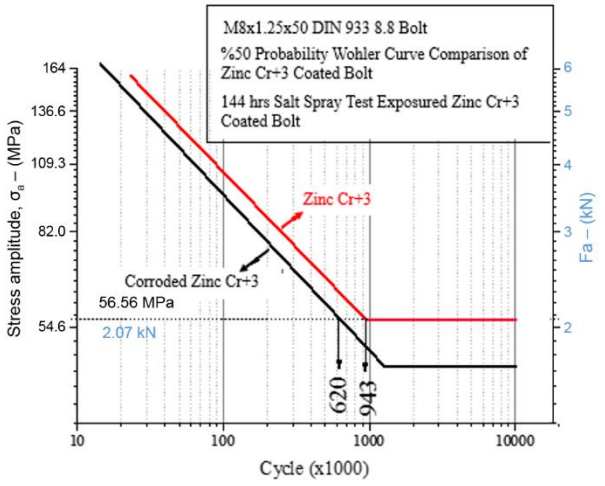

(b)

Figure 7 (a) Fatigue tests results and (b) Wöhler curves of Zn-Cr+3 coated bolts before and after salt spray tests.

In Figure 8(a), fatigue life of Zinc flake coated bolts tested at force amplitudes of 5.36, 3.50, 2.50 and 2.35 kN were introduced. As for Zn-Cr+3, remarkable fatigue life degradation was find after salt spray tests. For force amplitudes of 5.36 and 3.50 kN, decrease in fatigue life was found as 23%. When force amplitude was decreased to 2.50 and 2.35 kN, decrease in fatigue life was 9% and 16%, respectively. Considering the S-N curves for the Zinc flake bolts before and after salt spray test, fatigue performance was adversely affected from corrosion (Figure 8(b)). Zinc flake coated bolts exhibits 1.09 to 1.29 times higher fatigue resistance than 600 hours salt spray tested Zinc flake coated bolts.

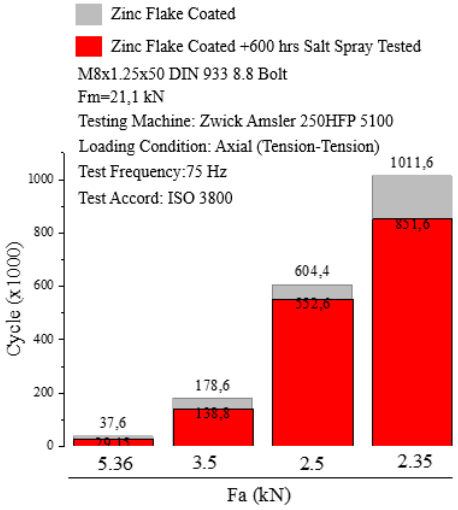

(a)

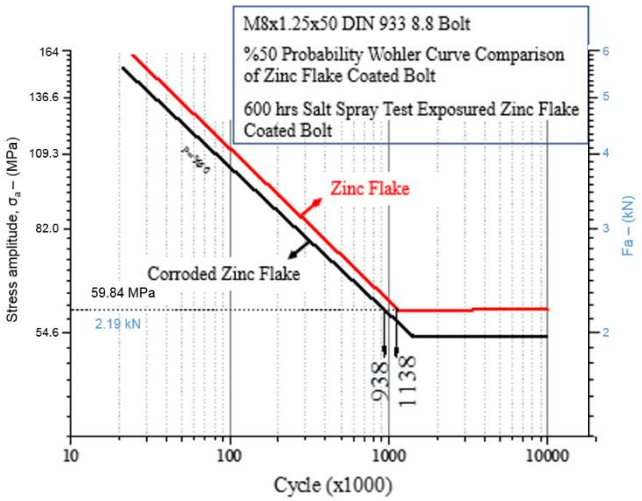

(b)

Figure 8 (a) Fatigue tests results and (b) Wöhler curves of Zinc flake coated bolts before and after salt spray tests.

Considering fatigue life of coated bolts before and after salt spray tests, Zinc flake coated bolts showed higher number of cycles compared to Zn-Cr+3 (Figure 9) though salt spray testing was conducted for 144 and 600 hours for Zn-Cr+3 and zinc flake, respectively. The difference was more significant as the force amplitude of fatigue tests were increased; i.e. Zinc flake bolts showed 1.1,

1.7 and 2.1 times higher fatigue performance for the force amplitude of 5.36, 3.50 and 2.50 kN, respectively.

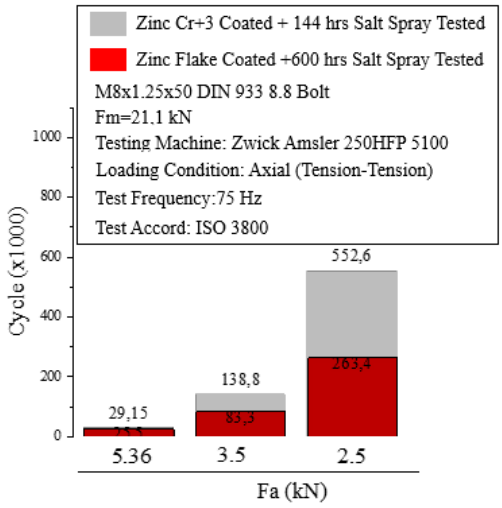

(a)

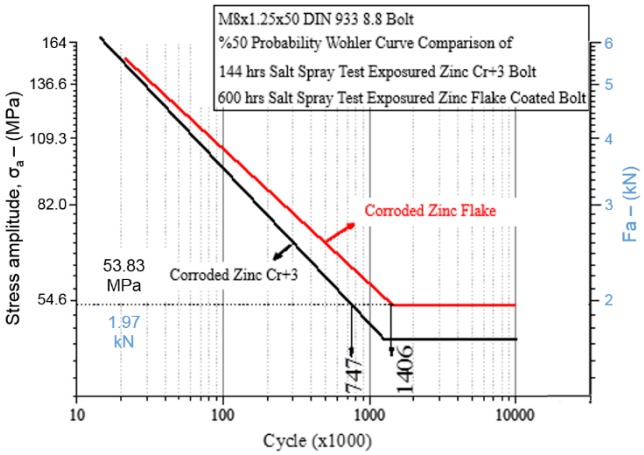

(b)

Figure 9 Comparison of (a) Fatigue tests results and (b) Wöhler curves of Zinc flake and Zn-Cr+3 coated bolts after salt spray tests.

Fatigue life of corroded Zinc flake coated bolts were compared to plain Zn-Cr+3 coated bolts in Figure 10. As depicted in the figure, fatigue life of both bolts were found to be similar. Main reason of that can be attributed to the difference in coating process of Zn-Cr+3 and zinc flake. Zn-Cr+3 coating is based on electrolytic bonding between the coating and the substrate. However, zinc flake coating is non-electrolytically applied. Since, zinc plating is an electrolytic proses, surface roughness is higher compared to zinc flake coating. As discussed in the literature [14-17] depending on the conditions, surface roughness can act as a stress concentrator and lead to premature crack initiation leading fractures due to fatigue. Therefore, fatigue performance was higher for zinc flake coating having better surface finish compared to Zn-Cr+3 plating.

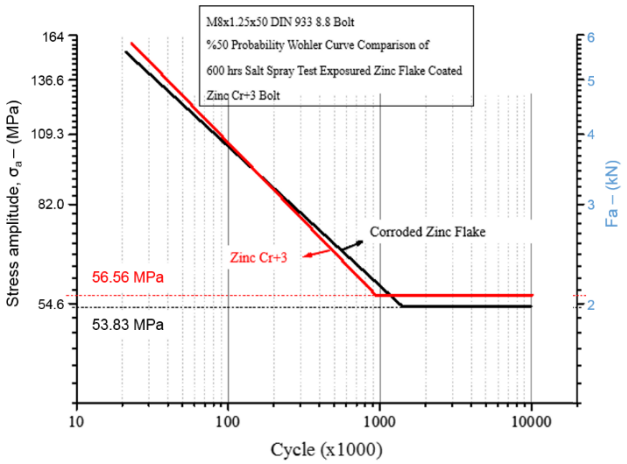

Figure 10 Fatigue life comparison of Zinc flake bolts after corrosion test and Zn-Cr+3 coated bolts.

4. CONCLUSIONS

In this study, fatigue behavior of Zn-Cr+3 and zinc flake coated bolts was investigated experimentally by considering corrosion effects. Based on the results, following conclusions can be drawn:

- Zinc flake coated bolts showed higher fatigue resistance compared to Zn-Cr+3 coated bolts. This phenomenon can be explained by effect of porous morphology of thread roots of Zn-Cr+3 coated bolts. This porous morphology can act as a trigger for crack initiation leading to lower fatigue resistance. Another factor contributing to fatigue performance difference can be incorporated with the higher coating thickness of zinc flake leading to higher radius on thread root and decrease in stress concentration at possible crack tips.
- As a result of comparison of Wöhler curves of corroded bolts, corrosion lowers the fatigue resistance of both coating type. However, negative effect of corrosion on fatigue life of Zn-Cr+3 coated bolts was higher than Zinc flake coated bolts.
- 600 hours salt spray tested Zinc flake coated bolts and non-salt spray tested Zn-Cr+3 coated bolts exhibit similar fatigue

resistance. Therefore, it can be concluded that zinc flake coated bolts have significantly higher resistance to corrosion fatigue compared to Zn-Cr+3 coated bolts.

Acknowledgements

Authors would like to thank to Uysal Makina, İzmir, Turkey for their support.

Funding

The authors received no financial support for the research, authorship or publication of this work.

The Declaration of Conflict of Interest/ Common Interest

No conflict of interest or common interest has been declared by the authors.

Authors' Contribution

Sezgin YURTDAŞ and Umut İNCE designed the research idea and carried out the experimental work. Barış TANRIKULU, Cenk KILIÇASLAN and M. Burak TOPARLI conducted literature survey and contributed to experimental work and data analyses. All authors participated in discussions of results and manuscript preparation.

The Declaration of Ethics Committee Approval

The authors declare that this document does not require an ethics committee approval or any special permission.

The Declaration of Research and Publication Ethics

The authors of the paper declare that they comply with the scientific, ethical and quotation rules of SAUJS in all processes of the article and that they do not make any falsification on the data collected. In addition, they declare that Sakarya University Journal of Science and its editorial board have no responsibility for any ethical violations that may be encountered, and that this study has not been evaluated in any academic publication environment other than Sakarya University Journal of Science.

REFERENCES

[1] F. C. Campbell, "Elements of Metallurgy and Engineering Alloys", *Publisher: ASM International*, 2008

[2] A. Hudgins and B. James, “Fatigue of threaded fasteners,” *Adv. Mater. Process.*, vol. 172, no. 8, pp. 18–22, 2014.

[3] P. Zampieri, A. Curtarello, C. Pellegrino, and E. Maiorana, “Fatigue strength of corroded bolted connection,” *Frat. ed Integrita Strutt.*, vol. 12, no. 43, pp. 90–96, 2018, doi: 10.3221/IGF-ESIS.43.06.

[4] L. Mordfin, “Some Problems of Fatigue of Bolts and Bolted Joints in Aircraft Applications”, *U. S. Dep. Commer. Natl. Bur. Stand.*, 1962.

[5] S. Ifergane, N. Eliaz, N. Stern, E. Kogan, G. Shemesh, H. Sheinkopf and D. Eliezer, “The effect of manufacturing processes on the fatique lifetime of aeronautical bolts,” *Eng. Fail. Anal.*, vol. 8, no. 3, pp. 227–235, 2001, doi: 10.1016/S1350-6307(00)00013-3.

[6] A. L. Marcelo, A. Y. Uehara, R. M. Utiyama, and A. I. Ferreira, “Fatigue properties of high strength bolts,” *Procedia Eng.*, vol. 10, pp. 1297–1302, 2011, doi: 10.1016/j.proeng.2011.04.216.

[7] S. Mushtaq, N. A. Sheikh, “Experimental evaluation of the effect of thread angle on the fatigue life of bolts,” *Int. J. Fatigue*, vol. 7, no. 1, pp. 12–19, doi: 10.1016/j.ijfatigue.2004.06.011.

[8] G. H. Majzoobi, G. H. Farrahi, and N. Habibi, “Experimental evaluation of the effect of thread pitch on fatigue life of bolts,” *Int. J. Fatigue*, vol. 27, no. 2, pp. 189–196, 2005, doi: 10.1016/j.ijfatigue.2004.06.011.

[9] S. Griza, M. E. G. da Silva, S. V. dos Santos, E. Pizzio, and T. R. Strohaecker, “The effect of bolt length in the fatigue

strength of M24×3 bolt studs," *Eng. Fail. Anal.*, vol. 34, pp. 397–406, Dec. 2013, doi: 10.1016/j.engfailanal.2013.09.010.

[10] J. W. Hobbs, R. L. Burguete, P. F. Heyes and E. A. Patterson, "The effect of eccentric loading on the fatigue performance of high-tensile bolts," *Int. J. Fatigue*, vol. 22, no. 6, pp. 531–538, Jul. 2000, doi: 10.1016/S0142-1123(00)00004-9.

[11] L. Solazzi, R. Scalmana, M. Gelfi, and G. M. L. Vecchia, "Effect of different corrosion levels on the mechanical behavior and failure of threaded elements," *J. Fail. Anal*. Prev., vol. 12, no. 5, pp. 541–549, 2012, doi: 10.1007/s11668-012-9593-x.

[12] H. L. Wang, J. G. Xia, and S. F. Qin, "High-strength bolt corrosion fatigue life estimate model and its application," *Dalian Haishi Daxue Xuebao/Journal Dalian Marit. Univ.*, vol. 40, no. 3, 2014.

[13] U. İnce, B. Güler, N. E. Kılınçdemir and M. Güden, "The effect of coating type on bolt fatigue life" 2. International Iron&Steel Symposium, Karabük, 2015.

[14] N. Sanaei and A. Fatemi, "Analysis of the effect of surface roughness on fatigue performance of powder bed fusion additive manufactured metals," *Theor. Appl. Fract. Mech.*, vol. 108, no. March, p. 102638, 2020, doi: 10.1016/j.tafmec.2020.102638.

[15] B. Vayssette, N. Saintier, C. Brugger, and M. El May, "Surface roughness effect of SLM and EBM Ti-6Al-4V on multiaxial high cycle fatigue," *Theor. Appl. Fract. Mech.*, vol. 108, no. March, p. 102581, 2020, doi: 10.1016/j.tafmec.2020.102581.

[16] V. Martín, J. Vázquez, C. Navarro, and J. Domínguez, "Effect of shot peening residual stresses and surface roughness on fretting fatigue strength of Al 7075-T651," *Tribol. Int.*, vol. 142, no. October 2019, 2020, doi: 10.1016/j.triboint.2019.106004.

[17] A. du Plessis and S. Beretta, "Killer notches: The effect of as-built surface roughness on fatigue failure in AlSi10Mg produced by laser powder bed fusion," *Addit. Manuf.*, vol. 35, no. March, p. 101424, 2020, doi: 10.1016/j.addma.2020.101424.

SAKARYA ÜNİVERSİTESİ
FEN BİLİMLERİ ENSTİTÜSÜ DERGİSİ

Sakarya University Journal of Science
SAUJS

e-ISSN: 2147-835X | Founded: 1997 | Period: Bimonthly | Publisher: Sakarya University
http://www.saujs.sakarya.edu.tr/en/

Title: Sound Level Measurement and Spectrum Analysis in Full and Empty Various Social Spaces

Authors: Serden BAŞAK, Kazim Onur DEMİRARSLAN

Recieved: 2020-12-10 13:07:55

Accepted: 2021-06-02 13:07:12

Article Type: Research Article

Volume: 25
Issue: 4
Month: August
Year: 2021
Pages: 875-884

How to cite
Serden BAŞAK, Kazim Onur DEMİRARSLAN; (2021), Sound Level Measurement and Spectrum Analysis in Full and Empty Various Social Spaces. Sakarya University Journal of Science, 25(4), 875-884, DOI:
https://doi.org/10.16984/saufenbilder.838589
Access link
http://www.saujs.sakarya.edu.tr/en/pub/issue/64755/838589

Sakarya University Journal of Science 25(4), 875-884, 2021

Sound Level Measurement and Spectrum Analysis in Full and Empty Various Social Spaces

Serden BAŞAK[1], Kazim Onur DEMİRARSLAN[*2]

Abstract

The noise seen in different areas throughout human history has turned into a frequently complained problem with the increasing industry and technology. Unfortunately, the problem of noise has become a part of social life today. Noise pollution, which is a side effect of urbanization and industrialization, threatens society's mental and physical health. However, knowing the noise level makes it possible to take precautions. In some cases where the sound limit levels set by laws and/or regulations of many countries are not exceeded, people may complain about the noise. Noises that occur in different places in educational institutions such as universities can cause adverse effects on both students and the administrative and academic staff working there. The noise in the places where the staff and students spend their time both for relieving their hunger and resting and socializing during their rest periods prevents people from relaxing. This situation causes people not to feel rested when returning to their lessons or work. In this analysis, the Artvin Coruh University staff dining hall's sound levels, the student dining hall, and the cafeteria/bowling alley spaces used by the students were measured when they were empty and full. Besides, the bandgap of the sounds complained about by the users was determined by spectrum analysis. As a result of the study, noise levels of 29.43 dB(A), 30.75 dB(A), and 32.94 dB(A) were obtained in the measurements made in empty spaces, and 56.10 dB(A), 57.56 dB(A)and 69.76 dB(A) in the measurements made in filled areas.

Keywords: Dining hall-cafeteria, noise, sound level measurement, spectrum analysis, social space

1. INTRODUCTION

Sound has guided humanity since its early ages and is now an indispensable part of our daily life. Considering the definition of sound, it is seen that it is made in two ways, physical and physiological. Physically sound; is a change in the balance pressure of the environment by a source that causes periodic vibrations in a flexible environment.

These pressure changes are conveyed to the environment's distant points with a constant velocity and a particular phase difference.

Physiologically sound is the perception that results from the transmission of pressure changes to the brain through the communication mechanism in the ear [1]. The lowest pressure

* Corresponding author: onurdemirarslan@artvin.edu.tr
[1] Artvin Çoruh University, Faculty of Health Sciences, Occupational Health and Safety Department, Artvin.
E-Mail: serdenbasak@ gmail.com
[2] Artvin Çoruh University, Faculty of Engineering, Environmental Engineering Department, Artvin
ORCID: https://orcid.org/0000-0002-5403-1609, https://orcid.org/0000-0002-1023-7584

variation perceived by humans is $2x10^{-5}$ Pascal (Pa) or 0 decibel (dB) [2, 3]. Noise, a different type of sound, started to be a social problem, especially after the industrial revolution [1]. Noise can simply be defined as unwanted sound. It is also a physical hazard and an environmental risk that poses a threat. There are various types of noise, such as transport noise emanating from roads, rail, air traffic, the noise created by human activity from industrial facilities, workplace noise produced by unwanted noise in the working environment [4]. More than 30% of Europe's population are exposed to noise levels higher than 55 dB(A) [5]. Noise exposure; varies depending on the source that emits the sound, how it is received by the human, the environment required for its propagation and perception [6].

According to the "Regulation on the Protection of Employees from Noise Related Risks" published in the Official Gazette dated 2013 and numbered 28721 (Republic of Turkey), the lowest exposure action values (L_{EX}, 8 hours) 80 dB(A), the highest exposure action values (L_{EX}, 8 hours) 85 dB(A) and exposure limit values (L_{EX}, 8 hours) are determined as 87 dB(A) [7]. These values indicate the amount of noise that the employee may be exposed to during work. However, the dosimeter is used to take these measurements during working hours.

The undesired and undesirable state of noise can vary from person to person due to different effects on people's psychology, nervous systems, and performances. However, its impact, which does not usually differ, is its effect on hearing. The effects of noise are analyzed in four categories: physical effects, physiological effects, psychological effects, and performance effects [1].

Prolonged exposure to noise increases the risk of coronary heart disease as well as psychological effects such as attention deficit. Besides diabetes, myocardial infarction, and hypertension, a series of predictable and short-term physiological responses through the autonomic nervous system, increased blood pressure, and peripheral vasoconstriction can also be seen. Other factors, both physical and psychosocial, associated with high blood pressure are also indicators of noise exposure [4, 5, 8, 9]. Continuous exposure to noise of 85-90 dB(A), especially in industrial environments, can lead to hearing loss in the future, increasing the threshold of hearing sensitivity [8]. As an element of stress, noise can also cause public health problems such as tension, nervousness, and difficulty sleeping [10].

Environmental noise is the unwanted noise in the environment and open-air arising from vehicles, road traffic, railway traffic, airway traffic, sea road traffic, construction sites, equipment used in open areas, industrial facilities, manufacturing plants, workplaces, and similar places and recreation areas. Besides, noise refers to the internal noise arising from the mechanical systems and other building sources and negatively affecting people in another space [11].

Unlike standard noise measurements, which measure noise intensity in decibels (dB), octave band analysis measures both the volume of noise in an area and the frequencies at which the noise occurs. The test is known as the "octave band analysis" because it relies on categorizing sounds into separate categories called "bands." Each band's frequency spectrum is referred to as an "octave," as the name implies. Octave band analysis allows noises with similar physical properties to be grouped so that environmental noise can be understood in terms of the cumulative volume of all the sounds within a particular band [12].

According to some literature, people feel some voices as noise with characteristic features. For example, if the sound is stuck in the narrowband range, it is perceived as louder than the same energy's broadband sound. Another example is related to the sound's rising period, and a sound that rises faster than two sounds of the same point is perceived as louder. An irregular, variable sound can be perceived as more audible than a stable sound [11]. The frequency spectrum of complex sounds, which do not consist of a single frequency, is a crucial definition of noise, which physically indicates the wave frequency and tonal property in perception. The noise's frequency content also affects the perception and the degree

of disturbance [1]. According to the frequencies, the sounds are classified into three as low frequency (25-125 Hz), medium frequency (160-400 Hz), and high frequency (500-10000 Hz) sounds [11].

Noise is an environmental problem that can directly affect people's attention and work performance. Thus, the workplace's noise affects the employees' physical and mental health, and this situation may cause performance issues. The effects of noise in schools and universities where education is offered have the same effect on individuals. People are exposed to noise, particularly in places for dining, resting, and leisure. This situation creates a variety of different issues.

While the recommended noise level in restaurants is in the range of 50-55 dB(A), the noise level is specified as 45-50 dB(A) for fair listening conditions desired [13, 14].

According to the "Regulation on the Assessment and Management of Environmental Noise (RAMEN)," which was first published in the Official Gazette in 2010 and later changed its current form in 2011 and 2015 (Rebuplic of Turkey), the required noise level in dining halls is also 45 dB(A) when the windows are closed, and there is no activity in the dining hall [15]. Later, with the Environmental Noise Assessment and Management Regulation (2002/49/EC) made in the EU harmonization process, this value was revised to be 55 dB(A) during the activity [16].

In studies available in the literature, noise levels in restaurants were measured and reported. In this study, on the other hand, octave band analyzes were also made and evaluated. This situation reveals its difference from other articles.

People using the Artvin Coruh University dining hall verbally stated that specific voices, such as forks and knives, disturbed them at a busy period. In this study, sound levels were measured in the staff dining hall, student dining hall, and cafeteria/bowling alley. Also, the bandgap of disturbing sounds was determined by spectrum analysis.

2. MATERIAL AND METHOD

This study was carried out using the pathway in Figure 1. The measurements were carried out in the middle of Artvin Çoruh University staff and student dining halls and cafeteria/bowling alley, according to ISO 1966-I and 1996-II standards, on a tripod with a CESVA brand and SC310SB model (Class 1, Spain) which had valid calibration (Figure 2). The measurements made before the Covid-19 pandemic shows the situation in which the dining hall did not start service and the staff on duty prepared the food stalls (empty state). The other measurement belongs to when the dining hall is most used and demonstrates the noise condition of certain employees in the queue of the table d'hote as some employees eat at the tables (full state). The measurements made were analyzed with the program called CESVA Capture Studio (ver.9.13.0). There are 38 tables in the staff dining hall where 152 people can eat simultaneously, and it has been found from plans and projects that the area of this space is 492 m^2, and its volume is 1771 m^3. The student dining hall dimensions and the cafeteria/bowling alley located on the ground floor are 503 m^2 and 1630 m^3 for each space. The graphical representation of the measured places is given in Figure 3 without scale.

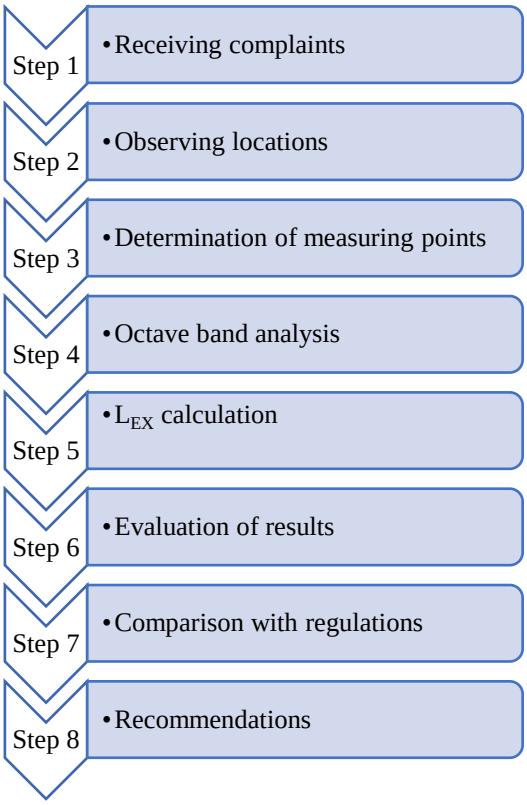

Figure 1 Pathway of the study

(A) (B)

Figure 2 (A) Staff dining hall empty measurement, (B) Full cafeteria/bowling alley measurement

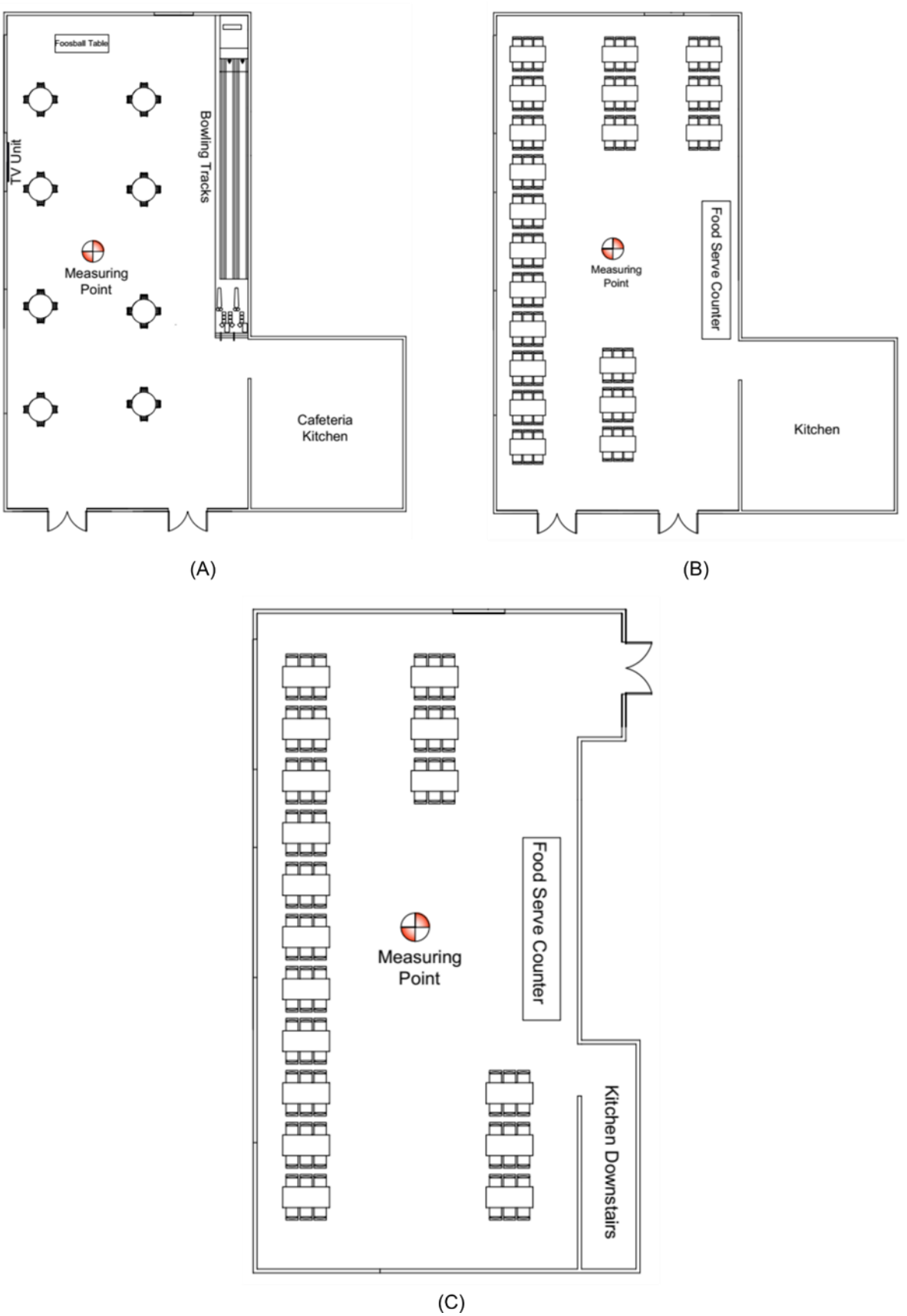

Figure 3 Measuring points (A) cafeteria/bowling alley, (B) student dining hall, (C) staff dining hall

3. RESULTS

The dB values obtained from the noise measurements made in the empty and full times of the dining hall and cafeterias are shown in Table 1. During the measurements, there were four staff members in the staff dining hall, while there were 120 people in the hall that were full. The student dining hall was empty while measurement was taken, and 170 students were eating that was full. The cafeteria/bowling alley is located in the same place. Six students watched TV during the measurements, unlike the dining halls. Throughout the midday measurement, only one of the bowling tracks remained in use for half of the measurement period. The frequency comparison of the two measurements for the staff dining hall is given in Figure 4.

Table 1 Sound level measurement results of the spaces

Measurement location	Measurement Results (dBA)	RAMEN (2015)	2002/49/EC
The staff dining hall is empty	30.75	-	-
The staff dining hall is full	56.10	45	55
The student dining hall is empty	29.43	-	-
The student dining hall is full	57.56	45	55
The cafeteria/bowling alley is empty	32.94	-	-
The cafeteria/bowling alley is full	69.76	45	55

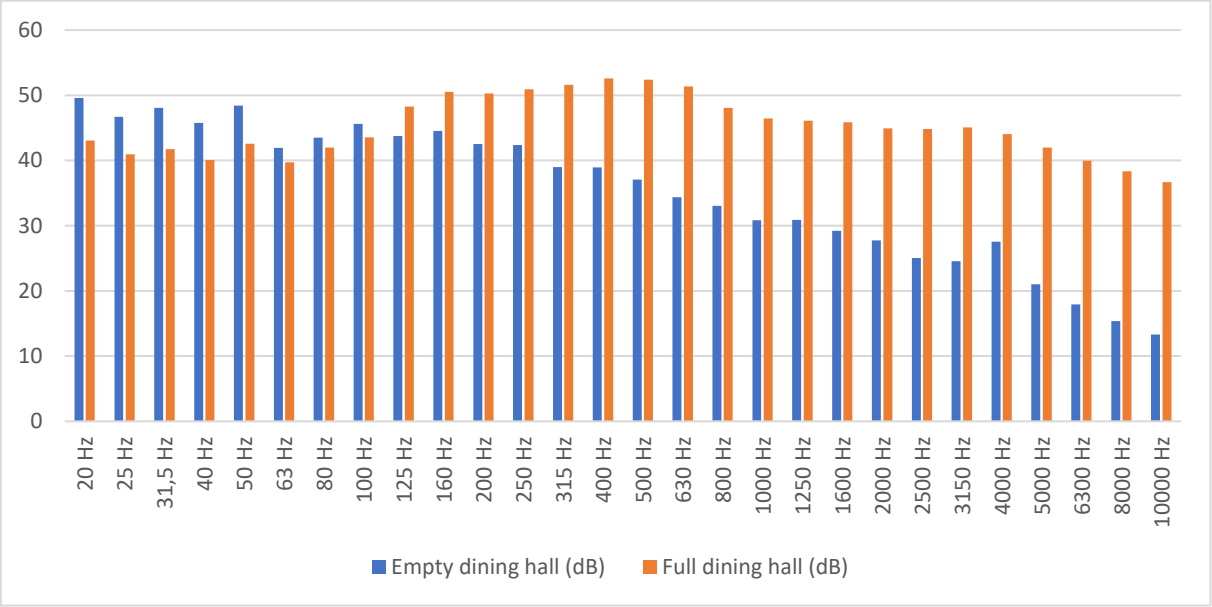

Figure 4 Staff dining hall frequency distribution comparison

The low-frequency distribution was higher when the staff dining hall was empty. This can be said to be the noises the staff made during the measurement while placing the heavy food containers on the presentation counter. After the dining hall was full, a significant increase was measured at 250 Hz and upper frequencies. The cause of the above condition is fork-knife noises and the employees' sounds when communicating among themselves. Comparing the frequency distribution of the full and empty student dining hall is given in Figure 5.

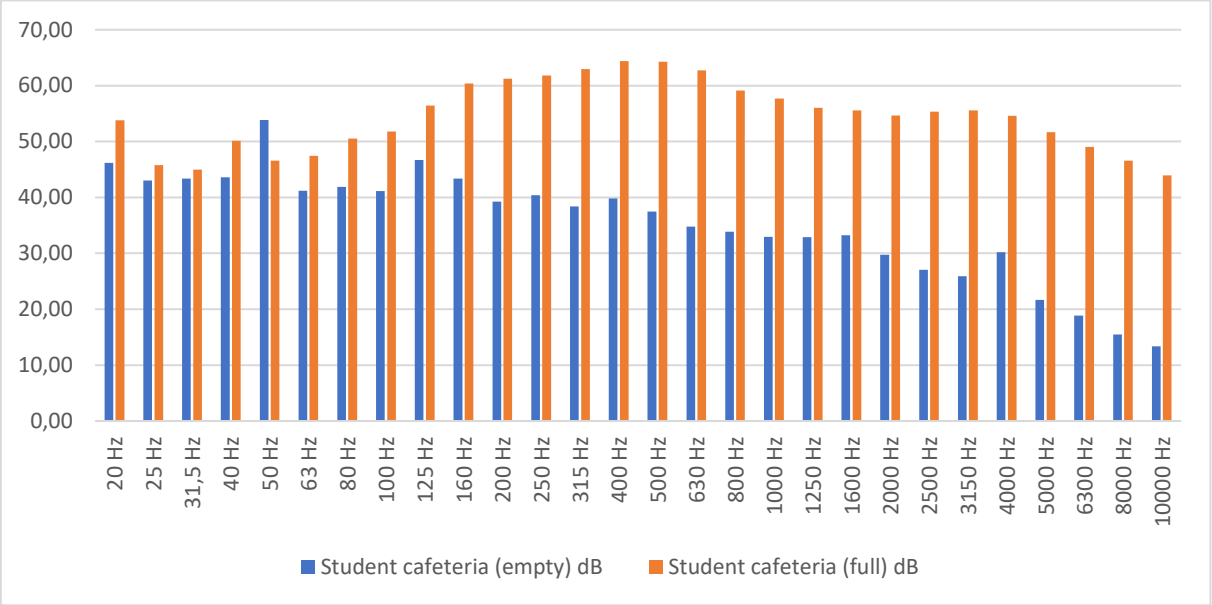

Figure 5 Student dining hall frequency distribution comparison

The full and empty student dining hall results are similar since the sound sources have been equivalent to the staff dining hall's sound sources. Since the student dining hall was more crowded than the staff dining hall and space's volumetric differences, the average noise was higher than the staff dining hall. Comparing the frequency distribution of full and empty cafeteria/bowling alley is given in Figure 6.

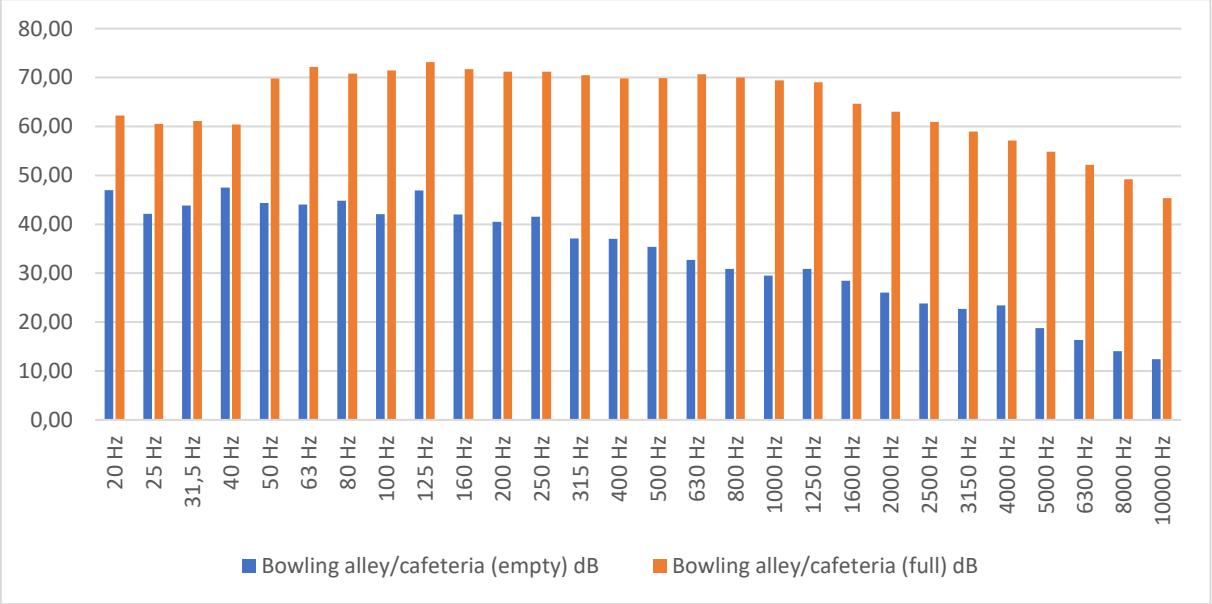

Figure 6 Cafeteria/bowling alley frequency distribution comparison

Figure 6 indicates a different distribution than the dining hall and student dining hall when the cafeteria/bowling alley is full, and the octave band analysis is studied. While fast food items are consumed in the cafeteria/bowling hall, there is not much cutlery use. Moreover, considering the limited number of students, the bowling game played during the full hall measurement, the bowling ball's sounds striking the ground, and bowling pins caused the low frequency sounds to be more in the full hall than in the empty hall. Simultaneously, foosball and the switched-on

television raised the overall average, and significantly higher sound levels were measured at 50 Hz and upper frequencies.

4. DISCUSSION

In this study, the L_{EX} values obtained for the staff and student dining halls and cafeteria/bowling alley in the measurements made with the windows closed and without activity are well below the 45 dB(A) values specified in the standard, respectively 30.75, 29.43 and 32.94 dB(A). One of the most important reasons for this is that these places in the same building are located in an area where traffic and human circulation are not heavy. However, when the units are in service, the calculated values are L_{EX} 56.10, 57.26, and 69.76 dB(A) for the staff and student dining halls and cafeteria/bowling alley, respectively, and this value is above 55 dB(A) as stated in the standard. From the staff working in the cafeterias and dining hall, the measurements made even when the cafeteria is full are well below the lowest exposure action value. Besides, while the average of 8 hours is taken in the regulation, the time spent fully in the dining hall is a maximum of 1 hour. Therefore, from the regulation perspective, there is no need for any action planning for the employees.

In a similar analysis conducted in the cafeteria of the Rector building, 80.5 dB(A) values were calculated at Ege University (Izmir/Turkey) [17]. The average work conducted in the cafeteria of the 10 pre-primary schools in the province of Usak (Turkey) is 81.18 dB(A) [18]. In another study conducted in Germany, school cafeterias' average noise was reported as 75 dB(A) [19]. In the mentioned studies, the noise levels before cafeterias' activities and the number of people using the cafeteria were not reported. Therefore, it is not possible to make a complete comparison. However, the potential reasons that when the cafeteria is in service, the findings found in this analysis are smaller than those in the literature are that the amount of outside noise is very low and the cafeteria's capacity is lower than the other dining halls.

5. CONCLUSIONS

In this study, noise levels of 29.43 dB(A), 30.75 dB(A), and 32.94 dB(A) were obtained in the measurements made in empty spaces, and 56.10 dB(A), 57.56 dB(A), and 69.76 dB (A) in the measurements made in filled areas. The reason for the users' complaints at the staff dining hall noise level, which is 1.10 dB(A) above the limit value, is the humming of people during their conversation and the service teams' sounds, rather than this value difference. Since it is not possible to detect this only by noise measurement, spectrum analysis has been performed. Although the results show an increase in the noise level in general, high-pitched sounds (high frequencies) are more. Metallic noise emanating from the service sets explains this phenomenon. Similar spectrum changes were also recorded in the student dining hall. However, as the cafeteria and bowling alley are together and bowling was played during the measurement, spectrum analysis observed a significant rise in the low-frequency bands, indicating the bowling ball's sound is hitting the track.

To reduce the noise level in the environment in restaurants, panels can be placed on the walls to absorb high-pitched sounds. However, in normal restaurants, the walls may be less than the space's square meter or can be used as interior design. For these reasons, restaurant owners may not want such panels on the walls. For such cases, the tables are positioned in clusters and the panels suspended from the ceiling can reduce the time of ringing and therefore the sounds of forks, knives, and plates. Another element is furnishing details such as thick carpets and curtains.

Although it is not possible to use the furnishing details in the dining hall and the cafeteria/bowling hall where the measurement is made, it is possible that the walls are covered with sound-absorbing materials, unlike normal restaurants. According to octave band analysis, open foams may be preferred because they are predominantly high-pitched in cafeterias. It would be appropriate for the cafeteria/bowling hall to choose composite materials as there are both TV and bowling balls.

The results of many studies in the literature belong only to situations when space is full or in use. Therefore, it is not possible to calculate the net noise level of the activities. Besides, no sound sources were detected by octave band analysis in the measurements mentioned above. The most important difference of this study from other studies is that the empty and full sound levels of the spaces are measured, and octave band analysis is made in these environments. The study once again proved that the concept of noise is subjective as the units' levels were compared, while the users with the lowest noise level complained about the noise in the staff dining hall, the students who used the cafeteria/bowling alley with a noise rating of approximately 100 times that noise value did not complain. The purposes and duration of stay of the people in the cafeteria/bowling hall and dining halls are different. The main reason for not complaining from those in the cafeteria/bowling hall is that they do not notice the noise, but probably because they are satisfied with the activity and the environment.

Since the sound/noise level measurement alone may not exceed the limit value or be just above the limit value, as in this study, it may prevent any measures from being taken in the places where noise complains. For this reason, the primary source of the noise should be determined by performing spectrum analysis as well as sound level measurement in areas where noise complains. After this determination, damping the disturbing frequency can be achieved using an acoustic isolator for that frequency range.

Because the noise level that employees may encounter is below the limit values specified in the Official Gazette, there is no need to measure with a dosimeter during working hours. However, by taking the precautions above for the environment, people can socialize by talking while eating.

Funding

This study is supported by Artvin University Scientific Research Projects Coordination Unit. Project Number: ACU BAP 2017.M82.02.01."

The Declaration of Conflict of Interest/ Common Interest

No conflict of interest or common interest has been declared by the authors.

Authors' Contribution

The authors contributed equally to the study.

The Declaration of Ethics Committee Approval

This study does not require ethics committee permission or any special permission.

The Declaration of Research and Publication Ethics

The authors of the paper declare that they comply with the scientific, ethical and quotation rules of SAUJS in all processes of the paper and that they do not make any falsification on the data collected. In addition, they declare that Sakarya University Journal of Science and its editorial board have no responsibility for any ethical violations that may be encountered, and that this study has not been evaluated in any academic publication environment other than Sakarya University Journal of Science.

REFERENCES

[1] S. Kurra, “Çevre Gürültüsü ve Yönetimi”, Cilt 1, Bahçeşehir Üniversitesi Yayınları, 2009, İstanbul, Turkey.

[2] S. Basak and K.O. Demirarslan, "Determination of noise exposure values at three different offices in Artvin/Turkey," International Research Journal of Advanced Engineering and Science, Vol. 3, no. 1, pp. 156-159, 2018.

[3] FMO, Chamber of Physical Engineers, “A-2 Tip Mühendislik Akustiği ders notları,” Ankara/Turkey, 2016.

[4] O.A., Al-Arja, and T.S., Awadallah, "Assessment of occupational noise exposure in coffee grinding shops," Appl. Acoust. Vol. 158, 107047, 2020.

[5] L., Chen, B., Sun, H., Wang, Q., Li, L., Hu, Z., Chen, "Forecast and control of traffic noise based on improved UE model during road network design", Appl. Acoust. Vol. 170, 2020.

[6] M.L., Bistrup, S., Hygge, L., Keiding, W., Passchier-Vermeer, "Health effects of noise on children and perception of the risk of noise," National Institute of Public Health, Denmark, Copenhagen, 2001.

[7] ÇGİRKDY 2013, Çalışanların Gürültü ile İlgili Risklerden Korunmalarına Dair Yönetmelik, 28 Temmuz 2013, 28721, https://www.resmigazete.gov.tr/eskiler/2013/07/20130728-11.htm

[8] S.A., Stansfeld, and M.P., Matheson, "Noise pollution: Non-auditory effects on health," Br. Med. Bull. Vol. 68, pp. 243–257, 2003.

[9] H., Kolya and C.W., Kang, "High acoustic absorption properties of hackberry compared to nine different hardwood species: A novel finding for acoustical engineers," Appl. Acoust. Vol. 169, 107475, 2020.

[10] LC., Erickson, RS., Newman, "Influences of Background Noise on Infants and Children," 2017. Curr Dir Psychol Sci. vol. 26, no. 5, pp. 451-457, 2017.

[11] TR Ministry of Environment and Forestry, General Directorate of Environmental Management, Environmental Noise Measurement and Assessment Guide, 2011, Ankara/Turkey.

[12] Octave Band Analysis, https://www.safeopedia.com/definition/7628/octave-band-analysis

[13] Engineering ToolBox, NC - Noise Criterion https://www.engineeringtoolbox.com/nc-noise-criterion-d_725.html

[14] Fundamentals of Sound, Baltimore Aircoil Company https://www.baltimoreaircoil.eu/en/downloads/pdf-fundamentals-of-sound

[15] ÇGDYY, 2010, Çevresel Gürültünün Değerlendirilmesi ve Yönetimi Yönetmeliği, 04 Haziran 2010, 27601, https://www.mevzuat.gov.tr/mevzuat?MevzuatNo=14012&MevzuatTur=7&MevzuatTertip=5

[16] ÇGDYY, 2005, Çevresel Gürültünün Değerlendirilmesi ve Yönetimi Yönetmeliği https://www.resmigazete.gov.tr/eskiler/2005/07/20050701-7.htm

[17] A., Özdamar, A., Baltacı, "Ege Üniversitesi kampüsünün gürültü profile", Mühendis ve Makine Dergisi, Mayıs, 2001.

[18] F., Çetinkaya, İ., Bulduk, D., İşçi, A., Demir, "Okul Öncesi Öğretmenlerin Gürültü Maruziyeti," Uşak Üniversitesi Eğitim Araştırmaları Dergisi, Vol. 3, no. 2, pp. 1-14, 2017.

[19] R., Braun, S., Brutscher, G., Winkler, "Are school cafeterias really so loud? Noise measurements in school canteens", Ernährungs Umschau, vol. 58, no. 8, pp. 410-415, 2011.

SAKARYA ÜNİVERSİTESİ
FEN BİLİMLERİ ENSTİTÜSÜ DERGİSİ

Sakarya University Journal of Science
SAUJS

ISSN 1301-4048 | e-ISSN 2147-835X | Period Bimonthly | Founded: 1997 | Publisher Sakarya University | http://www.saujs.sakarya.edu.tr/

Title: Green Supplier Selection Using Game Theory Based on Fuzzy SWARA

Authors: Mehmet Ali TAŞ, Esra ÇAKIR

Recieved: 2021-02-10 05:32:21

Accepted: 2021-06-08 12:02:06

Article Type: Research Article

Volume: 25
Issue: 4
Month: August
Year: 2021
Pages: 885-897

How to cite
Mehmet Ali TAŞ, Esra ÇAKIR; (2021), Green Supplier Selection Using Game Theory Based on Fuzzy SWARA. Sakarya University Journal of Science, 25(4), 885-897, DOI: 10.16984/saufenbilder.877919
Access link
http://www.saujs.sakarya.edu.tr/en/pub/issue/64755/877919

Sakarya University Journal of Science 25(4), 885-897, 2021

Green Supplier Selection Using Game Theory Based on Fuzzy SWARA

Mehmet Ali TAŞ[1], Esra ÇAKIR[*2]

Abstract

Green supply chains are supply chains that prioritize nature in every activity and aim to minimize the damage to the environment. Finding suppliers that meet the desired criteria and meet the company's environmental objectives in establishing the green supply chain is a difficult process. The selection problem becomes more complicated when some criteria conflict with each other. It is also critical to consider the strategies that alternative suppliers can implement. Therefore, multi-criteria decision making methods and game theory approaches are suitable to overcome these difficulties. This study proposes a new integrated fuzzy SWARA, which is a multi-criteria decision making method using fuzzy numbers to express uncertainty, and game theory approach to compare green supplier alternatives. The proposed approach is carried out in a chemical company that produces cleaning products in Turkey. The manufacturer company wants to compare two alternative green suppliers. Green strategies of alternative suppliers are weighted via fuzzy SWARA method. Then, the game theory payoff matrix and the iterated elimination of strictly dominated strategies are applied to compare two alternative suppliers. The proposed methodology gets a compromise solution. These results are intended to contribute to green supplier evaluation practices.

Keywords: Green supplier selection, sustainable environment, game theory, fuzzy SWARA, multi-criteria decision making

1. INTRODUCTION

The concept of sustainable environment has become one of the most important and controversial issues of recent years with global warming, carbon footprint and ecological balance [1]. Increasing production and consumption activities cause an increase in greenhouse gas emissions in the atmosphere, which is one of the most important causes of global warming [2]. All living creatures in the ecosystem are under risk due to the effects of global warming and deteriorating ecological balance [3]. Compared to the pre-industrial revolution, it is thought that the temperature increased by 1 ° C only because of the human activities [4]. For this reason, organizations should design their operations to be environmentally accountable [5]. One of these operation areas is supply chain management. The supply chains are anticipated to be environmentally friendly due to the increasing environmental worries and the sanctions that may

* Corresponding author: ecakir@gsu.edu.tr
[1] Turkish-German University, Department of Industrial Engineering, İstanbul, Turkey.
E-Mail: mehmetali.tas@tau.edu.tr
ORCID: https://orcid.org/0000-0003-3333-7972.
[2] Galatasaray University, Department of Industrial Engineering, İstanbul, Turkey.
ORCID: https://orcid.org/0000-0003-4134-7679.

arise as a result of the legal regulations to comply [6].

The green supplier selection problem is investigated as an application of multi-criteria decision making methods in many researches. In the literature, many studies have proven that multi-criteria decision making methods can be used for this problem [7]. In addition to the methods applied alone, there are also combined MCDM studies such as goal programming, linear programming, fuzzy logic etc. [8]. The game theory approaches can also be added to these combinations. Game theory can be used to determine the highest payoff of alternatives as a result of the competition that a number of opponents show according to the strategies [9]. This article proposes a new integrated fuzzy SWARA and game theory approach in the selection of green supplier in chemical industry.

In the last decade, the fuzzy SWARA technique has been highly researched. Mavi et al. [10] used fuzzy SWARA and fuzzy MOORA method to rank nine alternative 3rd-party reverse logistics providers for the plastics industry. Tadić et al. [11] employed an integrated Delphi, AHP, and fuzzy SWARA methods in city logistics initiatives. Zarbakhshnia et al. [12] evaluated sustainable third party reverse logistics providers for an automobile business using fuzzy SWARA and fuzzy COPRAS. Ansari et al. [13] used fuzzy SWARA and fuzzy COPRAS to assess the sustainable supply chains of a business in India. Kaya and Erginel [14] made the sustainable design for an airport in Turkey using hesitant fuzzy sustainable Quality Function Deployment as well as hesitant fuzzy SWARA. Ulutas [15] used hybrid fuzzy SWARA and fuzzy ARAS methods in supplier selection. Rani et al. [16] used Pythagorean fuzzy numbers on SWARA and VIKOR methods in solar panel selection. Moniri et al. [17] selected fuzzy SWARA and fuzzy EDAS methods in order to risk assessment in the oil processing industry.

In the literature, the game theory has been examined in numerous application researches. Hu and Rao [18] sought an answer to the optimization problem by using a game theory for optimum design. Tan et al. [19] investigated the competition in the software market in South Korea with a game theory approach. Peldschus et al. [20] discussed the site assessment using the theory of the two-person zero-sum game. Madani and Lund [21] used the Monte-carlo game theory approach to solve the California's Sacramento-San Joaquin Delta problem.

A number of combined approaches with game theory have also appeared in the literature. Medineckiene et al. [22] practiced choosing the best alternative between eight houses (two houses and four different heating combinations of them). They combined fuzzy sets and game theory. Kermani et al. [9] evaluated two alternatives by considering three criteria using ordinal game theory and TOPSIS, which is a multi-criteria decision making method. Zolfani and Banihashemi [23] solved the problem of choosing CEO among two candidates of GATA company in Iran by SWARA integrated game theory approach. Hindia et al. [24] implemented the planning scheme in LTE high speed wireless data transmission network with cooperative game theory (bankruptcy and shapely) and TOPSIS. Hashemkhani Zolfani et al. [25] examined supplier cooperation strategies using game theory, SWARA and WASPAS. Moradi et al. [26] evaluated the seismic vulnerability of Tehran city in Iran using a combination of methods including game theory and Choquet Integral. Debnath et al. [27] discussed strategies between the tea industry and the government tea board in India with Dempster-Shafer belief structure and evolutionary game. Liu et al. [28] investigated the Salzer manufacturing company's selection among four evidential suppliers as a case study. They determined the subjective criteria weights by ANP, the objective criteria weights by Entropy, and the comprehensive weights combined by DEMATEL-game theory methods. Dempster-Shafer evidence theory was discussed to remove uncertainty and order alternatives. Najafi et al. [29] selected best alternative among four suppliers for the casting plant. The criteria weights are calculated via BWM and SWARA. DEMATEL and game theory were used together to calculate comprehensive weights. Alternatives are evaluated by Dempster-Shafer evidence theory.

In this study, SWARA method and game theory approach are integrated. Since the SWARA method depends on pairwise comparisons within the order, it contains fewer computation processes than the most frequently used multi-criteria decision making methods. Therefore, the SWARA method was chosen to progress in a shorter time. Subsequently, the game theory approach is used in the selection of two alternatives. The technique of iterated elimination of strictly dominated strategies is used to properly observe the situation between the strategies of the players competing with each other and to select the most suitable green supplier.

This article contributes to the literature by proposing a new integration of game theory and fuzzy SWARA approaches. Also, the proposed methodology is a pioneering work on the green supplier selection problem.

The rest of the article is organized as follows. The introduction section is followed by the Section 2 which introduces the fuzzy SWARA and the game theory approaches. The steps of the new integrated methodology is detailed in this section. The proposed approch is applied on the selection of best option for chemical company case study in Section 3. Finally, the article ends with the conclusions in Section 4 that contains results, limitations, theoretical and managerial implications, and future directions.

2. METHODOLOGY

2.1. Fuzzy SWARA

The Step-wise Weight Assessment Ratio Analysis (SWARA) method is a multi-criteria decision making method introduced in 2010 by Keršuliene et al. [30]. Although relatively being a novel method, it is frequently employed due to its simple utilization and ability to reach results rapidly [31].

Fuzzy set is to express the uncertainties that occurs in decision makers' evaluations. In this study, triangular fuzzy numbers are used to include the uncertainty opinions in the calculation steps. A triangle fuzzy number is presented by (l,m,u). The membership function μ, where $\tilde{A}$ is a triangular fuzzy number is described as follows (Eq. 1) [32]:

$$\mu_{\tilde{A}}(x) = \begin{cases} 0, & x < l, \\ \frac{x-l}{m-l}, & l \le x \le m, \\ \frac{u-x}{u-m}, & m \le x \le u, \\ 0, & x > u. \end{cases} \quad (1)$$

Let $A_1 = (l_1, m_1, u_1)$ and $B_1 = (l_2, m_2, u_2)$ are two triangular fuzzy numbers and the arithmetic operations (addition, subtraction, multiplication, and division) on fuzzy numbers are formulated as follows (Eq. 2-5):

$$A_1 \oplus B_1 = (\mathrm{l}_1 + \mathrm{l}_2, m_1 + m_2, u_1 + u_2) \quad (2)$$
$$A_1 \ominus B_1 = (\mathrm{l}_1 - u_2, m_1 - m_2, u_1 - l_2) \quad (3)$$
$$A_1 \otimes B_1 = (\mathrm{l}_1\mathrm{l}_2, m_1 m_2, u_1 u_2) \quad (4)$$
$$A_1 \oslash B_1 = \left({}^{l_1}/_{u_2}, {}^{m_1}/_{m_2}, {}^{u_1}/_{l_2}\right) \quad (5)$$

The steps of the triangular fuzzy SWARA method are as follows [10]:

Step 1. Ranking of alternatives from the most to the least important according to the evaluations of decision makers.

Step 2. Starting from the first row, determining the differences in importances of two successive criteria in order of importance. The difference in importances of the two alternatives compared is called "comparative importance of average value" [30] and it is represented by $\tilde{s}_j$.

Step 3. Determination of $\tilde{k}_j$ coefficient. The $\tilde{k}_j$ coefficient is calculated as follows (Eq. 6):

$$\begin{cases} \tilde{1} & \mathrm{j} = 1 \\ \tilde{\mathrm{s}}_{\mathrm{j}} + \tilde{1} & \mathrm{j} > 1 \end{cases} \quad (6)$$

Step 4. Calculation of fuzzy weight $\tilde{q}_j$ (Eq. 7):

$$\begin{cases} \tilde{1} & j = 1 \\ \frac{\tilde{x}_{j-1}}{\tilde{k}_j} & j > 1 \end{cases} \quad (7)$$

Step 5. Calculation of final fuzzy weight by normalizing (Eq. 8):

$$\widetilde{w}_j = \frac{\tilde{q}_j}{\sum_{k=1}^{n} \tilde{q}_k} \quad (8)$$

The fuzzy weights calculated by fuzzy SWARA must be converted into crisp numbers via defuzzification process. The following formula of the Best Nonfuzzy Performance Value (BNP) [33] is used for defuzzification of trianguler fuzzy numbers (Eq. 9):

$$BNP = \frac{[(u-l)+(m-l)]}{3} + l \quad (9)$$

2.2. Game Theory

Mathematical interpretations that occur in interactive situations are called game theory. The theory was developed and implemented by Nash [34]. In game theory, the strategies that the players implement are not only relevant to themselves, but also to the strategy of the opponents [9]. The result of the payoff function shows the returns of the decisions made by the players, and this is shown in the payoff matrix, also called normal-form game representation.

The concept of the game theory in which no player in a game changes her/his strategy after evaluating her/his opponent's choice is Nash Equilibrium [34]. In a Nash Equilibrium game, when the strategies of other players remain the same, no player benefits from the strategies that are changed [28].

The assumptions for the game theory about human behavior can be listed as follows [35]: players in the game are rational, players in the game have expectations of other players and think everyone will play the rational, players' priorities are common and all players know the rules of the game, the terms of winning and losing.

In fact, since it is accepted that all events are games, everything becomes the subject of game theory [23]. Although game theory first appeared in the field of economics, it is frequently used in many areas such as politics, management, marketing, chemistry, an so on [36, 37]. Game theory can be considered as an important tool used in supply chain studies [38].

2.3. A new integrated game theory and fuzzy SWARA methodology

Game theory is a concept that can be used in decision making [21]. There is a relationship between the games and multi-criteria decision making outcomes. In this paper, the game theory approach is combined with multi-criteria decision making methods. The strategies of alternative suppliers are set as the criteria in the fuzzy SWARA method (Figure 1).

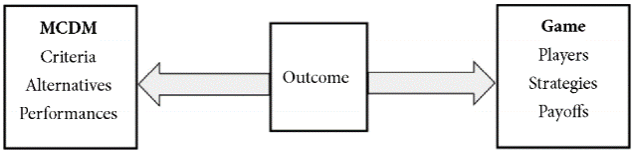

Figure 1 The relationship between multi-criteria decision making and game theory [21]

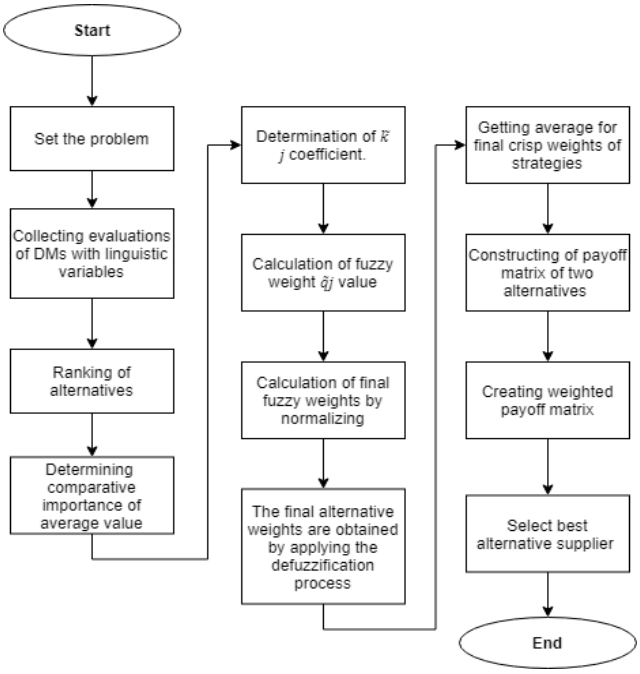

Figure 2 Flowchart of the proposed methodology

In the game theory part, the strategies of two alternatives are solved with the superiority they establish over each other. This technique is called iterated elimination of strictly dominated strategies [39]. The normal-form game representation of an n-player game shows the strategy space of players $S_1,\ldots,S_n$. The payoff functions of these players are $u_1,\ldots,u_n$ and the game can be shown as $G=\{S_1,\ldots,S_n;u_1,\ldots,u_n\}$. Let s_i' and s_i'' are the feasible strategies of each

players, all strategies are from S_1,…,S_n strategy space, then :

$$u_i(s_1, s_2, \dots, s_i'', s_{i+1}, \dots, s_n) > u_i(s_1, s_2, \dots, s_i', s_{i+1}, \dots, s_n) \quad (10)$$

Therefore, s_i' strategy is strictly dominated by s_i'', which means that the player prefers strategy s_i'' to s_i' under all circumstances assuming all players are rational [40].

The flowchart of the new integrated methodology of two approaches described above is shown in Figure 2.

3. CASE STUDY

The manufacturers in the chemical industry have expansively negative impacts on the environment due to the essence of the raw materials and products. Measures should be taken for the chemical raw materials and products used in the industry to cause the least harm to nature. International environmental norms must be strictly followed and obligations must be fulfilled. In this manner, the proposed approach is applied to a chemical company that wants to choose the supplier that offers the best environmental strategy.

The case company is a chemical cleaning product manufacturer located in Turkey's southern region. In the sector of the chemical products used for cleaning industry, it is one of Turkey's leader company. In addition, it has become one of the big exporters of the region with its numerous brands by exporting to more than 40 countries in five continents.

The company wants to choose an environmentally friendly supplier for the chemical raw materials used in processes. At first, the purchasing department of the company evaluates a number of alternative suppliers in the market. As a result of market research, the best two suppliers that performed very close to each other are presented to the management. These alternative suppliers are named as S_1 and S_2. Seven experts working within the company are identified, and the information of these experts is displayed in Table 1.

Table 1 The information of experts

Experts	Titles	Experiences in the industry (years)	Academic degrees
E_1	Project engineer	5	Bachelor's degree in engineering
E_2	Supply chain manager	12	Bachelor's degree in engineering
E_3	Project manager	14	Master's degree in engineering
E_4	Project engineer	8	Master's degree in engineering
E_5	Assisstant project manager	6	Bachelor's degree in economics
E_6	Purchasing engineer	9	Master's degree in engineering
E_7	Production chief	11	Master's degree in engineering

The strategies that these suppliers can implement in order to contribute to the company's green objectives are shown in Table 2 and Table 3.

Table 2 Strategies of S_1

Code	Strategy	Definition	Reference
S_{11}	Investing in ecological packing activities	Increasing the green material and technology investment in the enfoldment used to reduce the harmful effect on nature [41].	[41], [42], [43]
S_{12}	Promoting scientific studies on ecological shipping	It refers to supporting studies examining the reduction of environmentally harmful effects in shipping and storage processes by various methods.	[41], [44]
S_{13}	Focusing on energy usage level	It expresses the amount of energy consumption during the processes [45].	[45], [46], [47]

Table 3 Strategies of S_2

Code	Strategy	Definition	Reference

S_{21}	Making more efforts to apply pollution-reducing techniques	It shows the tendency and focus on pollution reduction techniques.	[47], [48], [49]	
S_{22}	Increasing level on green instructions	It specifies to provide environmental practices to all employees of enterprises in the supply chain.	[50], [51], [52]	
S_{23}	Increasing green perception activities	It describes advertising for the elements in the supply chain and for the consumer in order to increase the perception of green image.	[52], [53], [54]	

Table 4 Linguistic variables and fuzzy numbers equivalents [55]

Code	Linguistic variable	Fuzzy number
EI	Equally Important	(1.0000, 1.0000, 1.0000)
MI	Moderately Less Important	(0.6667, 1.0000, 1.5000)
LI	Less Important	(0.4000, 0.5000, 0.6667)
VI	Very Less Important	(0.2857, 0.3333, 0.4000)
ML	Much Less Important	(0.2222, 0.2500, 0.2857)

To handle with uncertainty, linguistic variables are used for the experts evaluations. The description of the linguistic variables are given as triangular fuzzy numbers. Because they allow the effortless conversion of linguistic variables in evaluations into numerical form, triangular fuzzy numbers have opted. The scales of the triangular fuzzy number are represented in Table 4.

The steps of the fuzzy SWARA method are applied sequentially.

Step 1. The importance orders given by E_1 is included in the second column of Table 5. According to E_1, the most important strategy is S_{12} (promoting scientific studies on ecological shipping) while the least important is S_{23} (increasing green perception activities).

Step 2. According to E_1's evaluations, the linguistic variable codes given by the pairwise comparisons of the sequential strategies at the order of importance and their fuzzy number equivalents are determined according to Table 4.

Step 3. The $\tilde{k}_j$ coefficient is determined using Eq. (6).

Step 4. The fuzzy weights $\tilde{q}_j$ are calculated using Eq. (7).

Step 5. The final fuzzy weights of the strategies by using Eq. (8) and the results of all other steps are given in Table 5.

Table 5 The steps of fuzzy SWARA for E_1

No	Strategy	Code	$\tilde{s}_j$	$\tilde{k}_j$	$\tilde{q}_j$	$\tilde{w}_j$
1	S_{12}	-	-	(1.0000, 1.0000, 1.0000, 1.0000)	(1.0000, 1.0000, 1.0000)	(0.3172, 0.3484, 0.3949)
2	S_{11}	LI	(0.4000, 0.5000, 0.6667)	(1.4000, 1.5000, 1.6667)	(0.60000, 0.6667, 0.7143)	(0.1903, 0.2323, 0.2820)
3	S_{13}	VI	(0.2857, 0.3333, 0.4000)	(1.2857, 1.3333, 1.4000)	(0.4286, 0.5000, 0.5556)	(0.1359, 0.1742, 0.2194)
4	S_{21}	LI	(0.4000, 0.5000, 0.6667)	(1.4000, 1.5000, 1.6667)	(0.2571, 0.3333, 0.3968)	(0.0816, 0..1161, 0.1567)
5	S_{22}	LI	(0.4000, 0.5000, 0.6667)	(1.4000, 1.5000, 1.6667)	(0.1543, 0.2222, 0.2834)	(0.0489, 0.0774, 0.1119)
6	S_{23}	LI	(0.4000, 0.5000, 0.6667)	(1.4000, 1.5000, 1.6667)	(0.0926, 0.1481, 0.2025)	(0.0294, 0.0516, 0.0799)

For each experts' evaluations, the steps of the fuzzy SWARA method are applied step by step. The fuzzy weights are defuzzified using the BNP method (Eq. (9)). For example, the $\tilde{w}_j$ value of S_{22} (increasing level on green instructions) is calculated as $(0.0446, 0.0882, 0.1582)$ by fuzzy SWARA according to the evaluations of E_3.

$$BNP = \frac{[(0.1582 - 0.0446) + (0.0882 - 0.0446)]}{3} + 0.0446 = 0.0970$$

Since the sum of the weights should be 1, it is necessary to normalize the defuzzified values. The normalized crisp weights of the strategies are determined and shown in Table 6.

In order to calculate the final criteria weights, the local criteria weights should be aggregated as in Table 6. The arithmetic mean is used to aggregate the weights of strategies. It is considered appropriate to use the arithmetic mean, as each

expert's evaluations are assumed to be weighted equally. Taking the S_{22} strategy as an example to illustrate the use of arithmetic mean, and the weight of the strategy can be calculated as follows:

$$w_{S_{22}} = \frac{0.0782 + 0.2322 + 0.0928 + 0.0466 + 0.1151 + 0.0717 + 0.1918}{7} = 0.1183$$

Subsequently, the final weights in Figure 3 are calculated by using arithmetic averages for other strategies.

Table 6 The results of the fuzzy SWARA method according to experts

	S_{11}	S_{12}	S_{13}	S_{21}	S_{22}	S_{23}	Tot.
E_1	0,2312	0,3479	0,1737	0,1163	0,0782	0,0528	1
E_2	0,1307	0,1741	0,0658	0,3100	0,2322	0,0873	1
E_3	0,4545	0,0344	0,0633	0,1222	0,0928	0,2328	1
E_4	0,3902	0,0685	0,2597	0,1338	0,0466	0,1011	1
E_5	0,3241	0,2592	0,1723	0,0520	0,1151	0,0772	1
E_6	0,0948	0,3674	0,2443	0,1836	0,0717	0,0381	1
E_7	0,0982	0,0391	0,3411	0,2556	0,1918	0,0742	1

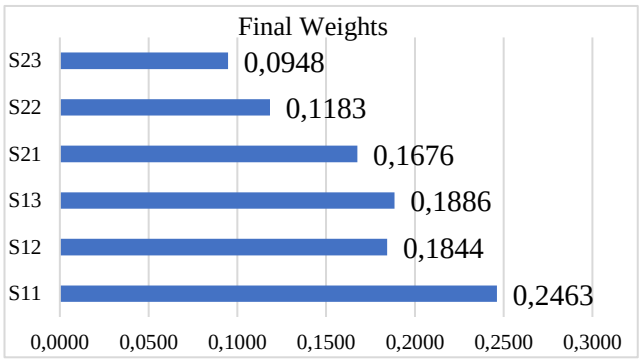

Figure 3 Final weights of strategies

According to the result of the fuzzy SWARA method, the most important strategy is S_{11} (investing in ecological packing activities). This strategy is followed by S_{13} (focusing on energy usage level) and S_{12} (promoting scientific studies on ecological shipping), respectively. S_{23} (increasing green perception activities) is emerged as the strategy with the fewest weight.

The second part of the proposed methodology, which includes a game theory approach, is applied. Representatives of two alternative green suppliers are brought together by the company's experts to ask questions about their green strategy. The aim is to establish a payoff matrix where the payoffs of two alternative suppliers are combined based on their information.

The method of constructing the payoff matrix is based on the study of Zolfani and Banihashemi [23]. According to the method, the values in the payoff matrix express the probability of success of alternative suppliers. The representation of the payoff matrix is given in Table 7, which is created by project manager (E_3), who evaluated the strategies of two alternative suppliers in company. The success probability percentages of the S_1 and S_2 alternatives are used. The success percentages are expressed in the scale of 0-10. In other words, the percentages are added to the table as discrete numbers.

Table 7 The payoff matrix

S_1, S_2	S_{21}	S_{22}	S_{23}
S_{11}	(8, 9)	(6, 7)	(9,8)
S_{12}	(5, 6)	(8, 5)	(6, 7)
S_{13}	(6, 5)	(5, 8)	(4, 4)

By applying the iterated elimination of strictly dominated strategies technique, the strategies in the payoff matrix are evaluated. It first starts with the strategies that the S_1 alternative can play. In the strategies of the S_1 alternative, it is clear that the strategy S_{13} is strictly dominated by S_{11} using Eq. (10), which means that the S_1 player never plays S_{13}. Therefore, S_{13} strategy is removed from the matrix and operations are continued. Since the strategies S_{11} and S_{12} do not dominate each other, S_2 players' strategies are followed. Strategy S_{22} is strictly dominated by strategy S_{23}. Because player S_2 never plays the S_{22} strategy, this strategy is removed from the matrix. In the resulting 2*2 matrix, since strategy S_{12} is dominated by S_{11}, it is concluded that S_{11} is the only strategy that can be played for alternative S_1. When S_1 plays strategy S_{11}, S_2 has chance to play strategies S_{21} and S_{23}. If these strategies are played out, it is seen that the payoffs of the two alternatives are (8, 9) and (9, 8), respectively. As the highest payoff of both alternatives is 9 and the company wants to

choose the highest one, there is an impasse for the company. In the case of equality, it is necessary to examine the weighted payoff matrix.

The weighted payoff matrix is established in Table 8 by multiplying the weights calculated via fuzzy SWARA method by the values in the payoff matrix.

Table 8 The payoff matrix with weights

Weight	S_2	**0,1676**	**0,1183**	**0,0948**
S_1	S_1, S_2	S_{21}	S_{22}	S_{23}
0,2463	S_{11}	(1.9704, 1.5084)	(1.4778, 0.8281)	(2.2167, 0.7584)
0,1844	S_{12}	(0.922, 1.0056)	(1.4752, 0.5915)	(1.1064, 0.6636)
0,1886	S_{13}	(1.1316, 0.838)	(0.943, 0.9464)	(0.7544, 0.3792)

The game is replayed with the same approach based on the weighted payoff matrix. As an outcome of the game, it is seen that the strategies are the same. S_1 has strategy S_{11} against S_2's S_{21} and S_{23} strategies. The payoffs of these strategies are (1.9704, 1.5084) and (2.2167, 0.7584), respectively. In the new case, the strategy that offers the highest payoff for the company is for S_2 alternative to play S_{23}. Thus, S_1 alternative becomes the most suitable supplier by playing the S_{11} (investing in ecological packing activities) strategy. Offering the highest payoff in this weighted game, S_1 is the most suitable alternative for the chemical company. Thus, it is clear that the weight of strategies can affect the outcome of the games.

4. CONCLUSION

Due to conflict relations between criteria, green supplier selection is a complex task. Numerous multi criteria decision making tools applied on the decision-making process in supplier selection practices. Furthermore, the strategies of alternatives that can be managed by game theory approaches should be considered. In this paper, a new integrated multi-criteria decision-making method and game theory approach is proposed for green supplier selection problem. Triangular fuzzy numbers are used in SWARA, which is determined as a multi-criteria decision-making method to handle uncertainties in evaluations of experts. This method is used to weight the strategies of alternative green suppliers. Then, a payoff matrix is created, and a best alternative is selected between two alternative green suppliers. Thanks to the new integrated approach, decision making processes is dynamically managed. When the game is solved with dominance, two strategies with the highest payoffs are emerged. Considering the weights calculated by the fuzzy SWARA, the S_1 alternative green supplier that offers the highest payoff to the company is selected as the most suitable supplier for company's green goals. With regard to unweighted strategies, the game has different consequences. Therefore, weighting the strategies with fuzzy SWARA affects the outcome of the game.

To compare this study with the existing literature, the research of Zolfani and Banihashemi [23] proposed an approach involving multi-criteria decision making and game theory. They applied SWARA and game theory methodology on human resource assessment. In the study of the Taş et al. [56], a hybrid fuzzy SWARA method is examined to select green suppliers. Therefore, it is inferred that multi-criteria decision making and game theory approaches can also be used in green supplier selection problems.

Working with the suitable green supplier increases the green supply chain performance of companies.This methodology benefits industry in developing strategies for green supply chains and selecting the best supplier.

Besides the benefits, this study has some limitations such as the combined fuzzy SWARA and game theory approach is performed according to the subjective evaluations of the experts. Therefore, the group decision, which is the aggregated opinions, may vary due to their different education level or experience. Moreover, selecting a chemical manufacturer as a case study creates a limitation in determining the strategies of green suppliers. For different sectors, new green strategies should be considered with new weights. Also, as the priorities of green

targets of countries may change, the results may vary.

For further research, the proposed methodology can be adapted for businesses in other sectors. Different types of fuzzy numbers (neutrosophic, Pythagorean, etc.) can be used to develop the new integrated approach. By increasing the number of players and the number of strategies, large-scale problems for real-life problems can be examined. In addition, other multi-criteria decision-making methods can be combined with game theory to contribute to the literature.

Funding

This study has not received any financial support for the research, authorship, or publication.

The Declaration of Conflict of Interest

No conflict of interest or common interest has been declared by the authors.

Authors' Contribution

All authors have contributed in experimental study and writing of the manuscript equally.

Ethics Committee Approval Notice

This study does not require ethics committee approval or any special permission.

The Declaration of Research and Publication Ethics

"The authors of the paper declare that they comply with the scientific, ethical and quotation rules of SAUJS in all processes of the paper and that they do not make any falsification on the data collected. In addition, they declare that Sakarya University Journal of Science and its editorial board have no responsibility for any ethical violations that may be encountered, and that this study has not been evaluated in any academic publication environment other than Sakarya University Journal of Science."

REFERENCES

[1] A. L. Radu, M. A. Scrieciu and D. M. Caracota, "Carbon Footprint Analysis: Towards a Projects Evaluation Model for Promoting Sustainable Development," Procedia Economics and Finance, vol. 6, pp. 353-363, Jan. 2013.

[2] H. O. Arslan, C. Cigdemoglu, and C. Moseley, "A three-tier diagnostic test to assess pre-service teachers' misconceptions about global warming, greenhouse effect, ozone layer depletion, and acid rain," International Journal of Science Education, vol. 34, no. 11, pp. 1667-1686, 2012.

[3] J. Houghton, "Global warming," Reports on Progress in Physics, vol. 68, no. 6, pp. 1343–1403, Jun. 2005.

[4] Intergovernmental panel on climate change (IPCC) Global warming of 1.5 °C [Data accessed: Jul. 2020]. Available: https://www.ipcc.ch/sr15/chapter/spm/

[5] J. A. Dearing, R. W. Battarbee, R. Dikau, I. Larocque, and F. Oldfield, "Human–environment interactions: learning from the past," Regional Environmental Change, vol. 6, pp. 1-16, 2006.

[6] A. Zakeri, F. Dehghanian, B. Fahimnia, and J. Sarkis, "Carbon pricing versus emissions trading: A supply chain planning perspective," International Journal of Production Economics, vol. 164, pp. 197–205, 2015.

[7] S. Onut, S. S. Kara, E. Isik, "Long term supplier selection using a combined fuzzy MCDM approach: A case study for a telecommunication company," Expert Systems with Applications, vol. 36, 2009, pp. 3887-3895.

[8] M. Stojčić, E. K. Zavadskas, D. Pamučar, Ž. Stević, and A. Mardani, "Application of MCDM methods in sustainability engineering: A literature review 2008–

2018," Symmetry, vol. 11, no. 3, pp. 350, 2019.

[9] M. A. M. A. Kermani, H. Navidi, and F. Alborzi, "A novel method for supplier selection by two competitors, including multiple criteria," International Journal of Computer Integrated Manufacturing, vol. 25, no. 6, pp. 527-535, 2012.

[10] R. K. Mavi, M. Goh, and N. Zarbakhshnia, "Sustainable third-party reverse logistic provider selection with fuzzy SWARA and fuzzy MOORA in plastic industry," The International Journal of Advanced Manufacturing Technology, vol. 91, no. 5, pp. 2401-2418, 2017.

[11] S. Tadić, S. Zečević, and M. Krstić, "Assessment of the political city logistics initiatives sustainability," Transportation research procedia, vol. 30, pp. 285-294, 2018.

[12] N. Zarbakhshnia, H. Soleimani, and H. Ghaderi, "Sustainable third-party reverse logistics provider evaluation and selection using fuzzy SWARA and developed fuzzy COPRAS in the presence of risk criteria," Applied Soft Computing, vol. 65, pp. 307-319, 2018.

[13] Z. N. Ansari, R. Kant, and R. Shankar, "Evaluation and ranking of solutions to mitigate sustainable remanufacturing supply chain risks: a hybrid fuzzy SWARA-fuzzy COPRAS framework approach," International Journal of Sustainable Engineering, vol. 13, no. 6, pp. 473-494, 2020.

[14] S. K. Kaya and N. Erginel, "Futuristic airport: A sustainable airport design by integrating hesitant fuzzy SWARA and hesitant fuzzy sustainable quality function deployment," Journal of Cleaner Production, vol. 275, 123880, 2020.

[15] A. Ulutas, "Using of Fuzzy SWARA and Fuzzy ARAS Methods to Solve Supplier Selection Problem," Theoretical and Applied Mathematics in International Business, pp. 136-148, 2020.

[16] P. Rani, A. R. Mishra, A. Mardani, F. Cavallaro, D. Štreimikienė, and S. A. R. Khan, "Pythagorean Fuzzy SWARA–VIKOR Framework for Performance Evaluation of Solar Panel Selection," Sustainability, vol. 12, no. 10, pp. 4278, 2020.

[17] M. R. Moniri, A. A. Tabriz, A. Ayough, and M. Zandieh, "Turnaround project risk assessment using hybrid fuzzy SWARA and EDAS method: case of upstream oil process industries in Iran," Journal of Engineering, Design and Technology, 2020.

[18] Y. Hu and S. S. Rao, "Game-theory approach for multi-objective optimal design of stationary flat-plate solar collectors," Engineering Optimization, vol. 41, no. 11, pp. 1017-1035, 2009.

[19] C. H. Tan, X. Yang, and H. Xu, "An investigation of the word-processing software market war in South Korea: A game-theoretic approach," Information & Management, vol. 47, no. 2, pp. 96-101, 2010.

[20] F. Peldschus, E. K. Zavadskas, Z. Turskis, and J. Tamosaitiene, "Sustainable Assessment of Construction Site by Applying Game Theory," Engineering Economics, vol. 21, no. 3, pp. 223-237, 2010.

[21] K. Madani and J. R. Lund, "A Monte-Carlo game theoretic approach for multi-criteria decision making under uncertainty," Advances in water resources, vol. 34, no. 5, pp. 607-616, 2011.

[22] M. Medineckiene, E. K. Zavadskas, and Z. Turskis, "Dwelling selection by applying fuzzy game theory," Archives of civil and mechanical engineering, vol. 11, no. 3, pp. 681-697, 2011.

[23] S. H. Zolfani and S. S. A. Banihashemi, "Personnel selection based on a novel model of game theory and MCDM approaches," Proceeding of 8th International Scientific Conference" Business and Management, pp. 15-16, 2014.

[24] M. N. Hindia, A. W. Reza, and K. A. Noordin, "A novel scheduling algorithm based on game theory and multicriteria decision making in LTE network," International Journal of Distributed Sensor Networks, vol. 11, no. 3, 604752, 2015.

[25] S. Hashemkhani Zolfani, R. Maknoon, and E. K. Zavadskas, "Multiple nash equilibriums and evaluation of strategies. New application of MCDM methods," Journal of Business Economics and Management, vol. 16, no. 2, pp. 290-306, 2015.

[26] M. Moradi, M. R. Delavar, and B. Moshiri, "A GIS-based multi-criteria analysis model for earthquake vulnerability assessment using Choquet integral and game theory," Natural hazards, vol. 87, no. 3, pp. 1377-1398, 2017.

[27] A. Debnath, A. Bandyopadhyay, J. Roy, and S. Kar, "Game theory based multi criteria decision making problem under uncertainty: a case study on Indian tea industry," Journal of Business Economics and Management, vol. 19, no. 1, pp. 154-175, 2018.

[28] T. Liu, Y. Deng, and F. Chan, "Evidential supplier selection based on DEMATEL and game theory," International Journal of Fuzzy Systems, vol. 20, no. 4, pp. 1321-1333, 2018.

[29] N. V. Najafi, A. A. Khamseh, and A. Mirzazadeh, "An integrated sustainable and flexible supplier evaluation model under uncertainty by game theory and subjective/objective data: Iranian casting industry," Global Journal of Flexible Systems Management, vol. 21, no. 4, pp. 309-322, 2020.

[30] V. Keršuliene, E. K. Zavadskas, and Z. Turskis, "Selection of Rational Dispute Resolution Method by Applying New Step-Wise Weight Assessment Ratio Analysis (SWARA)," Journal of Business Economics and Management, vol. 11, no. 2, pp. 243-258, 2010.

[31] S. H. Zolfani and J. Saparauskas, "New application of SWARA method in prioritizing sustainability assessment indicators of energy system," Engineering Economics, vol. 24, no. 5, pp. 408-414, 2013.

[32] C. Kahraman, U. Cebeci, and Z. Ulukan, "Multi-criteria supplier selection using fuzzy AHP," Logistics information management, vol. 16, no. 6, pp. 382-394, 2003.

[33] H. Y. Wu, G. H. Tzeng, Y. H. Chen, "A fuzzy MCDM approach for evaluating banking performance based on Balanced Scorecard," Expert systems with applications, vol. 36, no. 6, pp. 10135-10147, 2009.

[34] J. F. Nash, "Equilibrium points in n-person games," Proceedings of the national academy of sciences, vol. 36, no. 1, pp. 48-49, 1950.

[35] S. P. H. Heap and Y. Varoufakis, Game Theory: A Critical Text. Routledge, London; New York, 2004.

[36] R. Li, H. Ma, F. Wang, Y. Wang, Y. Liu, and Z. Li, "Game optimization theory and application in distribution system expansion planning, including distributed generation," Energies, vol. 6, no. 2, pp. 1101-1124, 2013.

[37] D. Velegol, P. Suhey, J. Connolly, N. Morrissey, and L. Cook, "Chemical game theory," Industrial & Engineering

Chemistry Research, vol. 57, no. 41, pp. 13593-13607, 2018.

[38] G. P. Cachon and S. Netessine, "Game theory in supply chain analysis," Models, methods, and applications for innovative decision making, pp. 200-233, 2006.

[39] T. Börgers, "Iterated elimination of dominated strategies in a Bertrand-Edgeworth model," The Review of Economic Studies, vol. 59, no. 1, pp. 163-176, 1992.

[40] R. Gibbons, A primer in game theory. Harvester Wheatsheaf New York, 1992.

[41] A. Fallahpour, E. U. Olugu, S. N. Musa, K. Y. Wong, and S. Noori, "A decision support model for sustainable supplier selection in sustainable supply chain management," Computers & Industrial Engineering, vol. 105, pp. 391-410, 2017.

[42] S. B. Tsai, Y. M. Wei, K. Y. Chen, L. Xu, P. Du, and H. C. Lee, "Evaluating green suppliers from a green environmental perspective," Environment and Planning B: Planning and Design, vol. 43, no. 5, pp. 941-959, 2016.

[43] A. Liu, Y. Xiao, H. Lu, S. B. Tsai, and W. Song, "A fuzzy three-stage multi-attribute decision-making approach based on customer needs for sustainable supplier selection," Journal of Cleaner Production, vol. 239, 118043, 2019.

[44] A. Ulutaş, A. Topal, A., and R. Bakhat, "An application of fuzzy integrated model in green supplier selection," Mathematical Problems in Engineering, 2019, 2019.

[45] J. Qin, X. Liu, X., and W. Pedrycz, "An extended TODIM multi-criteria group decision making method for green supplier selection in interval type-2 fuzzy environment," European Journal of Operational Research, vol. 258, no. 2, pp. 626-638, 2017.

[46] C. Bai and J. Sarkis, "Integrating sustainability into supplier selection with grey system and rough set methodologies," International Journal of Production Economics, vol. 124, no. 1, pp. 252-264, 2010.

[47] K. Govindan, R. Khodaverdi, and A. Jafarian, "A fuzzy multi criteria approach for measuring sustainability performance of a supplier based on triple bottom line approach," Journal of Cleaner Production, vol. 47, pp. 345-354, 2013.

[48] F. Vahidi, S. A. Torabi, and M. J. Ramezankhani, "Sustainable supplier selection and order allocation under operational and disruption risks," Journal of Cleaner Production, vol. 174, pp. 1351-1365, 2018.

[49] S. A. S. and J. Rezaei, "A grey-based green supplier selection model for uncertain environments," Journal of cleaner production, vol. 221, pp. 768-784, 2019.

[50] A. Awasthi, S. S. Chauhan, and S. K. Goyal, "A fuzzy multicriteria approach for evaluating environmental performance of suppliers," International Journal of Production Economics, vol. 126, no. 2, pp. 370-378, 2010.

[51] L. Shen, L. Olfat, K. Govindan, R. Khodaverdi, and A. Diabat, "A fuzzy multi criteria approach for evaluating green supplier's performance in green supply chain with linguistic preferences," Resources, Conservation and Recycling, vol. 74, pp. 170-179, 2013.

[52] R. Liang and H. Y. Chong, "A hybrid group decision model for green supplier selection: A case study of megaprojects," Engineering, Construction and Architectural Management, vol. 26, no. 8, pp. 1712-1734, 2019.

[53] A. H. Lee, H. Y. Kang, C. F. Hsu, and H. C. Hung, "A green supplier selection model for high-tech industry," Expert systems

with applications, vol. 36, no. 4, pp. 7917-7927, 2009.

[54] T. Lee, T. P. N. Le, A. Genovese, and L. S. Koh, "Using FAHP to determine the criteria for partner's selection within a green supply chain," Journal of Manufacturing Technology Management, vol. 23, no. 1, 25-55, 2012.

[55] D. Y. Chang, "Applications of the extent analysis method on fuzzy AHP," European journal of operational research, vol. 95, no. 3, pp. 649-655, 1996.

[56] M. A. Taş, E. Çakır, and Z. Ulukan, "Spherical Fuzzy SWARA-MARCOS Approach For Green Supplier Selection," 3C Tecnologia, vol. 10, pp. 115-133, 2021.

SAKARYA ÜNİVERSİTESİ
FEN BİLİMLERİ ENSTİTÜSÜ DERGİSİ

Sakarya University Journal of Science
SAUJS

e-ISSN: 2147-835X | Founded: 1997 | Period: Bimonthly | Publisher: Sakarya University
http://www.saujs.sakarya.edu.tr/en/

Title: Catalytic Effect of Ni and Cu Embedded Graphene Surface on Sulfur Dioxide (SO_2) Decomposition Reaction

Authors: Aykan AKÇA

Recieved: 2021-02-23 15:42:29

Accepted: 2021-06-10 23:30:52

Article Type: Research Article

Volume: 25
Issue: 4
Month: August
Year: 2021
Pages: 898-905

How to cite
Aykan AKÇA; (2021), Catalytic Effect of Ni and Cu Embedded Graphene Surface on Sulfur Dioxide (SO_2) Decomposition Reaction. Sakarya University Journal of Science, 25(4), 898-905, DOI: https://doi.org/10.16984/saufenbilder.885501
Access link
http://www.saujs.sakarya.edu.tr/en/pub/issue/64755/885501

Sakarya University Journal of Science 25(4), 898-905, 2021

Catalytic Effect of Ni and Cu Embedded Graphene Surface on Sulfur Dioxide (SO_2) Decomposition Reaction

Aykan AKÇA*[1]

Abstract

Sulfur dioxide (SO_2) decomposition reaction on Ni and Cu embedded graphene surfaces were investigated using density functional theory. Grimme-D2 correction was used for Van der Waals interactions that could be induced by the interactions between adsorbed structures and surface. Metal-embedded graphene surfaces are expected to be much cheaper than bulk system because they only use a few metal atoms contrary to bulk. Firstly, the charge density on metal embedded systems and SO_2 adsorbed on both surface was displayed with the electron density difference map and investigated with the Bader charge analysis. Then, the sequential dissociation of SO_2 were systematically investigated. Finally, SO_x molecules and their decomposed geometries were obtained and CI-NEB calculation was performed to find activation barriers related to SO_x+yO. It is concluded that Cu embedded graphene surface is more favorable than Ni embedded graphene surface in terms of activation energetics. Cu-based graphene materials can be used as catalyst an efficient and cheap in SO_2 decomposition.

Keywords: Nickel-embedded graphene, copper-embedded graphene, SO_2 decomposition, single-atom catalysis

1. INTRODUCTION

A significant part of energy needs in transportation, power plants, factories and houses is supplied by fossil fuels [1,2]. Sulfur dioxide (SO_2), which is an important air pollutant formed during the combustion reactions of fossil fuels, causes negative health and environmental effects known as acid rain by releasing into the atmosphere. Moreover, sulfur dioxide is an important environmental pollutant containing sulfur in its molecular structure. Environmental regulations emphasize the development of highly efficient catalysts to reduce SO_2 emissions, control automobile emissions, remove sulfur from fossil fuels, and reduce the SO_2 ratio generated during combustion reactions [3]. Adsorption and decomposition of SO_2 have been extensively studied before experimentally and theoretically on various metal surfaces including Ni [4,5]Cu [5,6], Pt [7,8], Pd [9], Rh [10]. Yokoyama et al. observed the adsorption mechanism of SO_2 on Ni (111) and Ni (100) surfaces by using near-edge-adsorption fine structure (NEXAFS) and X-ray photoelectron spectroscopy (XPS) [11]. They found that SO_2 bound to both surfaces molecularly and S-O intramolecular bonds elongated. Wilde et al. investigated the SO_2 decomposition depending on the temperature on the Ni (110) surface and they observed that SO_2 lost its molecular structure under 160 K temperature and SO_3 and S structures occurred on both surfaces [12]. Moreover, they found the average bond length of all S containing species

* Corresponding author: aykanakca@aksaray.edu.tr
[1] Aksaray University, Department of Physics, Aksaray, Turkey
ORCID: https://orcid.org/ 0000-0002-2517-765X

(S-Ni) as 2.30 Å Yokoyama et al. studied the adsorption mechanism of the SO_2 molecule on the Ni (110) surface and they reported that the S-O bond lengths elongated compared to the gas phase [13]. In another study by Jackson et al., the adsorption mechanism of SO_2 molecule on Cu (111) surface was investigated by using Chemical-shift normal-incidence X-ray standing waves (CS-NIXSW) technique [14].At that study, it was found that while SO_2 bound to the surface molecularly at low temperatures, it disintegrated as it approached to room temperature Terada et al. examined the adsorption mechanism of the SO_2 molecule on the Pd (111) surface using X-ray absorption fine structure measurements [15]. In the study, it was reported that the asymmetrical structure of SO_2 bonds played an important role in the elongation of S-O bonds Ungerer et al. investigated Platinum surface morphology and SO_2 decomposition reaction on different surfaces depending on the temperature parameter, and they stated that the percentage surface ratios expressed in Pt surface morphology changed depending on the temperature [16]. Moreover, they stated that while two surfaces ((001) and (111)) were dominant at 0 and 800 K, three surfaces ((001), (011) and (111)) were dominant at 298 and 400 K. Besides, they indicated that the Pt (111) surface was more active than other surfaces on the reaction Rodriguez et al. studied SO_2 decomposition on the surface of TiC (001) experimentally and theoretically. In their study, the adsorption heat of SO_2 was determined as 13-16 kcal/mol. Furthermore, they reported that while a significant part of the molecular structures was moving away from the surface below room temperature, some of them underwent complete decomposition into S-O atoms [17]. Rodriguez et al. investigated the catalytic activity of the Au/TiO_2 (110) surface, which was doped with metal to the metal oxide surface, on the SO_2 decomposition reaction [18]. Moreover, they reported that the Au/TiO_2 surface was more active compared to stoichiometric gold Graphene-based materials have highly superior mechanical and electrical capabilities. Because of these properties, they are used extensively in chemical sensors and catalyst researches [19-22].

To date, a few studies were available studying SO_2 decomposition on cost effective systems instead of expensive transition metals. In this study, the catalytic activities of single atom Ni and Cu elements on defective graphene substrate were theoretically investigated for SO_2 decomposition reaction.

2. COMPUTATIONAL METHODS

All calculations are by Quantum Espresso package (version 6.3, [23]) based on performed based on density functional theory GGA-PBE was selected as an exchange-correlation functional [24]. PAW (the projector augmented wave) potential was used to analyze the electronic structure [25]. 80 Ry and 800 Ry were considered for kinetic energy cutoff for wavefunctions and kinetic energy cutoff for charge density and potential, respectively during all geometric calculations. Grimme-D2 term was embedded in the system to observe the weak and van der Waals interactions [26]. $1x10^{-5}$ Ry/atom and $1x10^{-6}$ Ry/atom were used as criteria for force and energy converging during geometric optimization, respectively. Spin-polarization effect is considered for all calculations. Brillouin zone samplings of 14x14x1 for the electronic structure interactions and 4x4x1 Monkhorst-Pack k-point for geometric optimizations were used. Gas calculations were made in a 15 $Å^3$ length of three-dimensional box. Partial atomic charges were calculated by using Bader charge analysis.

The adsorption energy of atomic and molecular structures (adsorbate) on the graphene surfaces are calculated by using the following, $E_{ads,}$ equation:

$$E_{ads}=E_{adsorbates/surface}-(E_{surface+}\ E_{adsorbate}) \quad (1)$$

where $E_{adsorbates/surface}$ is the total energy of atomic and molecular system on the graphene surface; $E_{surface}$ is the total energy of the optimized graphene layer and $E_{adsorbate}$ is the total energy of the optimized atomic and molecular structures in gas phase.

Transition geometry and the energy that is needed was calculated with CI-NEB (climbing image-nudged elastic band) [27,28]. In this study, the

reaction and activation energies were calculated using the equation (2) and equation (3), respectively.

$$E_r=E_{IS}-E_{FS} \quad (2)$$

$$E_a=E_{TS}-E_{IS} \quad (3)$$

E_{IS} and E_{FS} represent the initial energy and final energy, respectively. E_{TS} is the transition energy between E_{IS} and E_{FS}. Avogadro [29] and Burai software [35] were used to visualize for all geometric configuration and the bond lengths.

3. RESULTS AND DISCUSSION

3.1. Modeling of Ni and Cu Embedded Graphene Surfaces

To ensure sufficient accuracy of our calculations, some important parameters obtained for Ni-embedded graphene (NiG) and Cu-embedded graphene (CuG) surfaces are given in Table 1. For modeling graphene systems, a 4 × 4 single-graphene layer consisting of 32 carbon atoms was constructed. The distance between the nearest C-C on the optimized graphene sheet was obtained by 1.42 Å. This value is consistent with other studies in the literature [30]. Then, the carbon at the center of graphene nanosheet were substituted with Ni or Cu. These systems are shown in Figure 1.

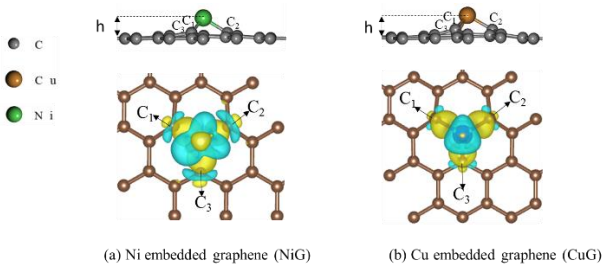

Figure 1 The electron density difference (EDD) maps (±0.006 au) of (a) Ni and (b) Cu embedded graphene systems

The binding energy of the Ni and Cu atoms to the defective graphene surface were -6.77 eV and -3.92 eV. Moreover, the bond lengths between the closest carbon atoms and Cu and Ni were 1.87 Å and 1.88 Å, respectively.

All values obtained in Table1 are consistent with the study reported by Krasheninnikov et. [31]. According to Bader charge analysis, electron transfer occurs from metal atoms to neighboring carbon atoms. After this charge transfer, positive charge accumulation is +0.67|e| and +0.65|e| at Ni and Cu atoms, respectively.

Table 1 Physical parameters obtained for the Ni and Cu embedded graphene surfaces

Parameters	NiG	CuG
Elevation-h (Å)	1.4	1.51
Bond Lengths (Å) (Ni-C), Cu-C)	1.87	1.88
Magnetic Moment (μ_B)	0	1
Binding Energy (E_B) (eV)	-6.77	-3.92
Metal (Ni, Cu), C_1, C_2, C_3 charges, |e|	+0.67,0.27,-0.22,-0.27	+0.65,0.25,-0.24,-0.20

The electron density difference (EDD) maps is plotted, where the electron density accumulation and depletion sites are displayed in yellow and blue, respectively. According to EDD, electron density accumulation was occurred around Ni-C and Cu-C bonds, which verifies strong binding between metal atom and neighboring carbon atoms. Moreover, the blue regions are showed the positive charge density around both Ni and Cu. Positive charge centers create a strong potential attraction region. Therefore, SO_2 and other intermediate state are expected to interact on these regions

3.2. The Adsorption of SO_2 on The Ni and Cu Embedded Graphene Surfaces

Two different adsorption geometry were considered for SO_2 molecule on the Cu and Ni embedded graphene surfaces. SO_2 can adsorb to graphene surfaces by both sulfur and oxygen, namely through its S-end or O-end. These configurations were showed in Figure 2 and the results obtained were given in Table 2.

In the complex_1, the adsorption energy of SO_2 was -0.9 eV on NiG surface. The bond lengths between S and O atoms were calculated to be 1.47 Å. Also, the Bader analysis reveals that about 0.34 |e| are transferred from the surface to the SO_2

molecule. According to EDD maps, a great electron density accumulation is found around the Ni-O bond, which confirms the chemical binding between the O atom and Ni. Therefore, the total electron density around the Ni Atom has been seen to decrease. In other words, very low a charge transfer takes place from the surface to the S-O bonds. This implies that the surface has low activity over the S-O bond lengths.

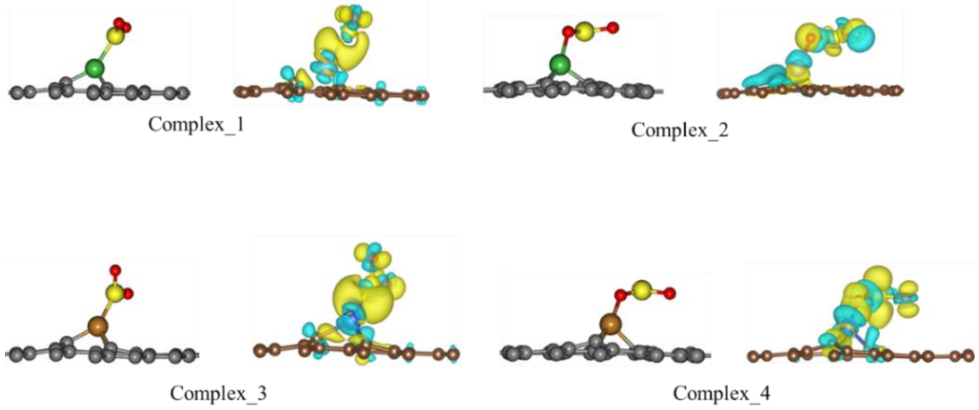

Figure 2 The different adsorption geometries of SO_2 molecules on both surface and EDD maps (±0.003 au)

Table 2 The adsorption energies and the bond lengths of SO_2 on both graphene surface and in gas phase

Bond type	NiG (Å)		CuG(Å)		Gas phase (Å)
	Complex_1	Complex_2	Complex_3	Complex_4	
S-O1	1.47	1.54	1.47	1.55	1.45
S-O2	1.47	1.48	1.47	1.49	1.45
	Eads(eV)		Eads (eV)		-
	-0.9	-1.17	-1.02	-1.36	-

In the Complex 2, the adsorption energy of the molecule SO_2, which binds to the surface by oxygen-end, is calculated as -1.17 eV. The bond lengths between S and O atoms were calculated to be 1.48 Å and 1.54 Å. Bader analysis results of these geometry showed that 0.43|e| was transferred from the surface to the SO_2 molecule. Moreover, the adsorption of the SO_2 molecule by O-end tends to cause a significant electron density on molecule, which shows elongation in the S-O bonds of the molecule.

In the Complex 3, the adsorption energy of SO_2 molecule was determined to be of -1.02 eV. Bader analysis results 0.35 |e| charge transfer was realized from the surface to the SO_2 molecule. Similar to the Bader analysis results of the "Complex 1", a great amount of electron density on Cu atom was observed to be consumed and this density was accumulated on between Cu and S. The surface had a low effect on the S-O bond length.

In the complex 4, the adsorption energy of SO_2, which is adsorbed to the surface by the O-end, is -1.36 eV. From Bader charge analysis results, a transfer of 0.47|e| from surface to SO_2 molecule was found. Most of the transferred electron was observed to accumulated on the S-O bonds. This result could be the reason for the elongation in S-O bonds that was given in Table 2.

It is found that, the adsorption geometries of SO_2, which is adsorbed to the surface by the O-end have significant catalytic activity in the elongation of S-O bonds.

3.3. Decomposition Mechanism of $SO_2 \rightarrow SO+O$ on Ni and Cu Embedded Graphene

The reaction pathway for the sequential decomposition of SO_2 to S and O on Ni and Cu embedded graphene have been systematically studied using density functional theory. The adsorption geometries of SO_2, which binds with

oxygen-end to the surfaces were considered as initial state. SO+O geometry obtained by breaking down one of the S-O bonds was considered the final geometry of first step. The transition states have been investigated using the CI-NEB method. CI-NEB method allows to calculate the energy barrier needed between the initial and final state.

For the initial state, the distance between S and O bonds was 1.48 Å, 1.54 Å and 1.49 Å, 1.55 Å on NiG and CuG, respectively. In the transition state, SO_2 molecule loses one of its oxygen bound to the sulfur atom. The oxygen atom dissociated in the TS is at distances of 2.34 Å and 1.99 Å from Sulfur atom on NiG and CuG, respectively. According to our calculations, the energy barriers required for breaking the S-O bond was 0.86 eV and 1.58 eV on NiG and CuG, respectively. The positive reaction energy values, which was found as +0.53 eV and +0.73 eV on NiG and CuG, respectively, indicates that the reaction occurred as endothermic.

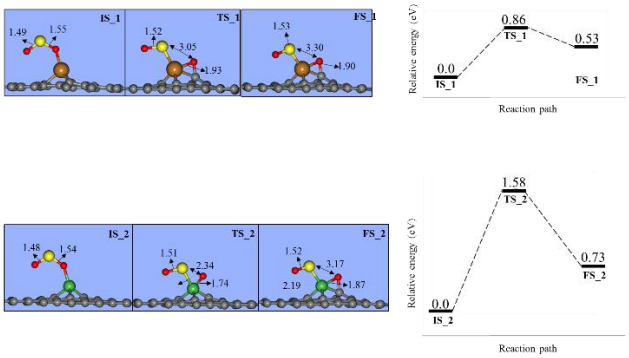

Figure 3 Side view of the initial, final, and transition states for $SO_2 \rightarrow SO+O$ on CuG ve NiG surfaces

3.4. Adsorption and Decomposition of SO molecules Ni and Cu embedded graphene surfaces

The adsorption geometry optimized of the SO molecule on both graphene surfaces was shown in Figure 4. Our calculations show that the adsorption energies of SO molecules on the Ni and Cu graphene surface were determined to be of -1.80 eV and -1.84 eV, respectively.

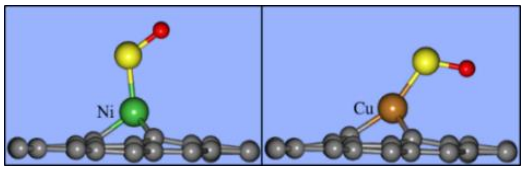

Figure 4 Side view of optimized adsorption geometries of SO molecule on CuG and NiG surfaces

The most stable adsorption geometries of the SO molecule on surfaces were considered to be the initial state of the second reaction step. The S+O configuration, which was obtained through the transition state, was considered as the final stage of the reaction. The initial, final and transition state geometries for the decomposition of SO → S+O are shown in Figure 5.

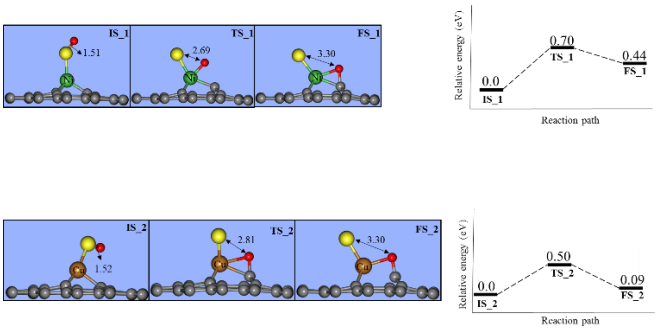

Figure 5 Side view of the initial, final and transition states for SO → S+O on CuG ve NiG surfaces.

For the initial state, the bond distances between S and O on the Ni and Cu surface was 1.51 Å and 1.52 Å. In transition state (TS), the oxygen passing over the activation energies were at distances of 2.69 Å and 2.81 Å from the sulfur atom on NiG and CuG surfaces, respectively. Moreover, the values of activation energies for NiG and CuG surfaces were calculated to be 0.70 eV and 0.50 eV, respectively. The reaction energies of SO→S+O were 0.44 eV and 0.09 eV on NiG and CuG, respectively. This reaction step occurs endothermically on both graphene surface. It also appears that the transition state geometry on the NiG surface exhibit behavior close to the IS geometry, while it was close to the FS geometry on CuG surface. This result may explain the low activation energy calculated on the CuG surface.

4. CONCLUSION

In this article, SO_2 decomposition studied on Ni and Cu embedded graphene surfaces through density functional theory. Bader charge analysis of the graphene surface was calculated and the map of electron density difference (EDD) was obtained. The charge analysis results show that a positive charge density region on the Ni and Cu atoms played an important role in detecting catalytic activity. The adsorption energies of SO_x (x= 1,2) were calculated. It was observed that SO_x structures bound to the surface through chemical interaction. The activation energies needed for the $SO_2 \rightarrow$ SO+O reaction on NiG and CuG surfaces were found as 1.58 eV and 0.86 eV, respectively. The required activation energies SO→ S+O reaction were calculated as 0.70 eV for NiG and 0.50 eV for CuG. The results show that CuG surface are the more active than NiG surface. The results of the CuG surface have comparable activation barriers in all steps for other transition metals [32-34].

Acknowledgments

The numerical calculations reported in this paper were fully performed at TUBITAK ULAKBIM, High Performance and Grid Computing Center (TRUBA resources).

Funding

The author received no financial support for this work.

The Declaration of Conflict of Interest/ Common Interest

No conflict of interest or common interest has been declared by the author.

The Declaration of Ethics Committee Approval

This work does not require ethics committee permission or any special permission.

The Declaration of Research and Publicatıon Ethics

The author of the paper declares that he complies with the scientific, ethical and quotation rules of SAUJS in all processes of the article and that he does not make any falsification on the data collected. In addition, he declares that Sakarya University Journal of Science and its editorial board have no responsibility for any ethical violations that may be encountered, and that this study has not been evaluated in any academic publication environment other than Sakarya University Journal of Science.

REFERENCES

[1] T. Wei and B. Khoshnevis, “Integration of process planning and scheduling: a review,” Journal of Intelligent Manufacturing, vol. 24, no. 6, pp. 51–63, 2000.

[2] P. R. Buseck, and M. Pósfai, “Airborne minerals and related aerosol particles: Effects on climate and the environment,” Proceedings of the National Academy of Sciences, vol. 96, no. 7, pp. 3372-3379, 1999.

[3] A. Piéplu, O. Saur, J. C. Lavalley, O. Legendre, and C. Nédez, “Claus catalysis and H2S selective oxidation,” Catalysis Reviews, vol. 40, no. 4, pp. 409-450, 1998.

[4] X. Wei, C. Dong, Z. Chen, K. Xiao, X. Li, “Density functional theory study of SO2-adsorbed Ni (1 1 1) and hydroxylated NiO (111) surface,” Applied Surface Science, vol. 355, pp. 429-435, 2015.

[5] Y. Sakai, M. Koyanagi, K. Mogi, and E. Miyoshi, “Theoretical study of adsorption of SO2 on Ni (111) and Cu (111) surfaces,” Surface Science, vol. 513, no. 2, pp. 272-282, 2002.

[6] T. Nakahashi, S. Terada, T. Yokoyama, H. Hamamatsu, Y. Kitajima, M. Sakano, T. Ohta, “Adsorption of SO2 on Cu (100) studied by X-ray absorption fine structure spectroscopy and scanning tunneling

microscopy," Surface Science, vol. 373, no. 1, pp. 1-10, 1997.

[7] R. Streber, C. Papp, M. P. A. Lorenz, O. Höfert, E. Darlatt, A. Bayer, H. P. Steinrück, "SO2 adsorption and thermal evolution on clean and oxygen precovered Pt(111)," Chemical Physics Letters,vol. 494 no. 4-6, pp. 188-192, 2010.

[8] M. Xia, R. Yue, P. Chen, M. Wang, T. Jiao, L. Zhang, L. Li, "Density functional theory investigation of the adsorption behaviors of SO2 and NO2 on a Pt (111) surface," Colloids and Surfaces A: Physicochemical and Engineering Aspects, vol. 568, pp. 266-270, 2019.

[9] M. S. Wilburn, W. S. Epling, "SO2 adsorption and desorption characteristics of Pd and Pt catalysts: Precious metal crystallite size dependence," Applied Catalysis A: General, vol. 534, pp. 85-93, 2017.

[10] D. Fu, W. Guo, M. Li, H. Zhu, Y. Liu, "Adsorption and reaction mechanisms of SO2 on Rh (111) surface: A first-principle study," Journal of Molecular Structure, vol. 1062, pp. 68-76, 2014.

[11] T. Yokoyama, S. Terada, S. Yagi, A. Imanishi, S. Takenaka, Y. Kitajima, T. Ohta, "Surface structures and electronic properties of SO2 adsorbed on Ni (111) and Ni (100) studied by S K-edge X-ray absorption fine structure spectroscopy," Surface Science, vol. 324, no. 1, pp. 25-34, 1995.

[12] L. Wilde, M. Polcik, J. Haase, B. Brena, D. Cocco, G. Comelli, G. Paolucci "Adsorption and temperature-dependent decomposition of SO2 on Ni (110): an XPS and XAFS study," Surface Science, vol. 405, no. 2-3, pp. 215-227, 1995.

[13] T. Yokoyama, A. Imanishi, S. Terada, H. Namba, Y. Kitajima, T. Ohta, "Electronic properties of SO2 adsorbed on Ni (100) studied by UPS and O K-edge NEXAFS," Surface science, vol. 334, no. 1-3, pp. 88-94,1995.

[14] G. J. Jackson, S. M. Driver, D. P. Woodruff, N. Abrams, R. G. Jones, M. T. Butterfield, V. Formoso, "A structural study of the interaction of SO2 with Cu (111)," Surface Science, vol. 459 no. 3, pp. 231-244, 2000.

[15] S. Terada, T. Yokoyama, M. Sakano, M. Kiguchi, Y. Kitajima, T. Ohta, "Asymmetric surface structure of SO2 on Pd (111) studied by total-reflection X-ray absorption fine structure spectroscopy," Chemical physics letters, vol. 300, no. 5-6, pp. 645-650, 1999.

[16] M. J. Ungerer, D. Santos-Carballal,A. Cadi-Essadek, C. G. Van Sittert, N. H. De Leeuw, "Interaction of SO2 with the Platinum (001), (011), and (111) Surfaces: A DFT Study," Catalysts, vol. 10, no. 5, pp. 558, 2020.

[17] J. A. Rodriguez, P. Liu, J. Dvorak, T. Jirsak, J. Gomes, Y. Takahashi, K. Nakamura, "Adsorption and decomposition of SO2 on TiC (0 0 1): An experimental and theoretical study," Surface Science, vol. 543, no. 1-3, pp. 675-682, 2003.

[18] J. A. Rodriguez, G. Liu, T. Jirsak,J. Hrbek, Z. Chang, J. Dvorak, A. Maiti, " Activation of gold on titania: Adsorption and reaction of SO2 on Au/TiO2 (110)," Journal of the American Chemical Society, vol. 124, no. 18, pp. 5242-5250, 2002.

[19] L. Wang, Q. Luo, W. Zhang, J. Yang, "Transition metal atom embedded graphene for capturing CO: a first-principles study," International Journal of Hydrogen Energy, vol. 39, no. 35, pp. 20190-20196, 2014.

[20] V. Singh, D. Joung, L. Zhai, S. Das, S. I. Khondaker, S. Seal, "Graphene based materials: past, present and future" Progress in Materials Science, vol. 56, no. 8, pp. 1178-1271, 2011.

[21] N.O. Weiss, H. Zhou, L. Liao, Y. Liu, S. Jiang, Y. Huang, "Graphene: an emerging electronic material" Advanced Materials, vol. 24, no. 43, pp. 5782-5825, 2012.

[22] M.R. Islam, K. Liu, Z. Wang, S. Qu, C. Zhao, X. Wang, Z. Wang, "Impact of defect and doping on the structural and electronic properties of monolayer boron phosphide," Chemical Physics, vol. 542, pp. 111054, 2021.

[23] Giannozzi P, et al. "Quantum espresso: a modular and open source software project for quantum simulations of materials," Journal of Physics: Condensed Matter, vol. 21, no. 39, pp. 395502, 2009.

[24] H. J. Monkhorst, J. D. Pack, "Special points for Brillouin-zone integrations," Physical Review B, vol. 13, no. 12, pp. 5188, 1976.

[25] G. Kresse, D. Joubert "From ultrasoft pseudopotentials to the projector augmented-wave method," Physical Review B, vol. 59, no. 3, pp. 1758, 1999.

[26] Grime S, et al. "A consistent and accurate ab initio parametrization of density functional dispersion correction (DFT-D) for the 94 elements H-Pu," The Journal of Chemical Physics, vol. 132, no. 15, pp. 154104, 2010.

[27] H. Jonsson, G. Mills, K. W. Jónsson, H. Jacobsen, W. Karsten, "Nudged elastic band method for finding minimum energy paths of transitions," 1998.

[28] G. Henkelman, B. P. Uberuaga, H. Jónsson, "A climbing image nudged elastic band method for finding saddle points and minimum energy paths," The Journal of Chemical Physics, vol. 113, no. 22, pp. 9901-9904, 2000.

[29] M. D. Hanwell, D. E. Curtis, D. C. Lonie, T. Vandermeersch, E. Zurek, G. R. Hutchison, "Avogadro: an advanced semantic chemical editor, visualization, and analysis platform," Journal of Cheminformatics, vol. 4, no. 1, pp. 1-17, 2012.

[30] O. I. Malyi, K. Sopiha, V. V. Kulish, T. L. Tan, S. Manzhos, C. Persson, "A computational study of Na behavior on graphene," Applied Surface Science, vol. 333, pp. 235-243, 2015.

[31] A. V. Krasheninnikov, P. O. Lehtinen, A. S. Foster, P. Pyykkö, R. M. Nieminen, "Embedding transition-metal atoms in graphene: structure, bonding, and magnetism," Physical review letters, vol. 102, no. 12, pp. 126807, 2009.

[32] R. Jiang, W. Guo, M. Li, H. Zhu, J. Li, L. Zhao, H. Shan, "Density functional study of the reaction of SO2 on Ir (111)," The Journal of Physical Chemistry C, vol. 113, no. 42, 18223-18232, 2009.

[33] D. Fu, W. Guo, M. Li, H. Zhu, Y. Liu, "Adsorption and reaction mechanisms of SO2 on Rh (111) surface: A first-principle study," Journal of Molecular Structure, vol. 1062, pp. 68-76, 2014.

[34] J. A. Rodriguez, J. M. Ricart, A. Clotet, F. Illas, "Density functional studies on the adsorption and decomposition of SO2 on Cu (100)," The Journal of Chemical Physics, vol. 115, no. 1, pp. 454-465, 2001.

[35] G. E. Pitti, Estudio de propiedades estructurales y electrónicas del hierro, silicio y aluminio utilizando el Software Burai (GUI de Quantum Espresso).

SAKARYA ÜNİVERSİTESİ
FEN BİLİMLERİ ENSTİTÜSÜ DERGİSİ

Sakarya University Journal of Science
SAUJS

e-ISSN: 2147-835X | Founded: 1997 | Period: Bimonthly | Publisher: Sakarya University
http://www.saujs.sakarya.edu.tr/en/

Title: Microencapsulation of vitamin E: Characterization of Complex Coacervation Conditions Using Response Surface Methodology

Authors: Elif KÖKSAL, Okan BAYRAM, Fethiye GÖDE, Ahmet Hakan AKTAŞ

Recieved: 2020-03-10 14:22:07

Accepted: 2021-06-15 22:53:41

Article Type: Research Article

Volume: 25
Issue: 4
Month: August
Year: 2021
Pages: 906-913

How to cite
Elif KÖKSAL, Okan BAYRAM, Fethiye GÖDE, Ahmet Hakan AKTAŞ; (2021), Microencapsulation of vitamin E: Characterization of Complex Coacervation Conditions Using Response Surface Methodology . Sakarya University Journal of Science, 25(4), 906-913, DOI: https://doi.org/10.16984/saufenbilder.701570
Access link
http://www.saujs.sakarya.edu.tr/en/pub/issue/64755/701570

Sakarya University Journal of Science 25(4), 906-913, 2021

Microencapsulation of vitamin E: Characterization of Complex Coacervation Conditions Using Response Surface Methodology

Elif KÖKSAL*[1], Okan BAYRAM[1], Fethiye GÖDE[1], Ahmet Hakan AKTAŞ[1]

Abstract

In this study, high efficiency vitamin E microencapsulation was aimed with the complex coacervation method. Response surface methodology (RSM) was used to optimize the microencapsulation efficiency of vitamin E. The microencapsulation efficiency of microencapsulated vitamin E was investigated in terms of two variables, including the amount of core material and surfactant concentration (SDS). According to the RSM results, the experimental condition with the highest efficiency (93.42%) was found in 4.00 g of core material and 0.50% surfactant in the experiment set. Morphological and chemical analyzes of microcapsules were characterized by optical microscopy and scanning electron microscopy (SEM) and Fourier transformation infrared spectroscopy (FT-IR).

Keywords: Vitamin E, microencapsulation efficiency, response surface methodology, complex coacervation, micro technology.

1. INTRODUCTION

Vitamin E is a member of fat-soluble vitamins and its chemical term is alpha-tocopherol [1-5]. Vitamin E has a significant role in the protection of fatty molecules in cell membranes and blood. It is referred to as an antioxidant because of its ability to quench or stabilize time-saving free radicals in degenerative diseases. Vitamin E can rapidly break down in the presence of free radical and oxygen induced oxidative processes [2-7]. It is suggested that it must be protected from its close surroundings before its application. The most commonly used technology to develop durability and safety of functional materials is microencapsulation [8]. Microencapsulation is a technique which is particles of liquid or solid materials or droplets are covered in a film of polymeric material [9-12]. Encapsulation preserves the secured active ingredient from the outer surrounding, then releases active material, as soon as interacting with exact stimulus, at a point when its functional features are required [13]. Encapsulation can also be described as the process of storing active ingredients in a carrier material to increase the distributing of active compounds to sustenance products. Various nutrient compounds, like enzymes, polyphenols, vitamins, essential oils and carotenoids are held into biopolymer micro particles and nanoparticles for retain their basic properties without changing them [14]. Microencapsulation is used for other several aims such as increasing the shelf life of

* Corresponding author: elfkoksall@hotmail.com
[1] Süleyman Demirel University, Isparta, Turkey.
E-Mail: okan.bayram.32@gmail.com, fethiyegode@sdu.edu.tr, hakanaktas@sdu.edu.tr.
ORCID: https://orcid.org/0000-0001-5131-3531; https://orcid.org/0000-0002-1748-9354, https://orcid.org/0000-0002-3008-1353, https://orcid.org/0000-0003-2327-4031.

foods, in particular, raising the nutritional value, providing digestibility, and shortening the duration of ripening [15,16]. In addition, microencapsulation has various implementation in cosmetics, pharmaceutical, pesticides and medical applications, catalysis, biology and many other fields [17]. Various techniques are available for encapsulating core materials [18]. In general, spray drying or solvent evaporation techniques have been observed in the literature as microencapsulation of vitamins. Unlike in the study, vitamin E containing microcapsules were developed using complex coacervation (physicochemical method). It has been reported that complex coacervation is based primarily on pH and occurs in systems including two dispersed colloids of the opposite electric charge. Optimum circumstances for complex coacervation are obtained when the pH is arranged to a point where two colloids are present [19, 20]. Microencapsulation with complex coacervation has many advantages. Complex coacervation is known for its simplicity, low cost, reproducibility and scalability, which provides high encapsulation efficiency even at very high transport loads [19]. The wall of the microcapsules does not dissolve in water when the cross-linked chemical is present. This is an important advantage over microcapsules such as spray drying or solvent evaporation. Microcapsules prepared with complex coacervation which has excellent oxidation stability and low moisture content such as pH change, diffusion, temperature, osmotic pressure, dissolution and wall deterioration [19-21]. Complex coacervation in active ingredient encapsulation basically involves the use of two mutually loaded biopolymers which can form complex shell surrounding the core material [19]. Present study, gelatin and gum Arabic with biocompatible properties were used as coating materials to produce microcapsules. Despite the protective effect of microencapsulation, serious oxidation may occur on the top of microcapsules because of high temperature exposure during the process. Residues on the top of microcapsules will have a damaging effect on the oxidation of microencapsulated active component. In the context, microencapsulation efficiency was used as a significant parameter to evaluate the quality of microencapsulated active components [22]. The purpose of the study is to research the effect of two different variables on microencapsulation efficiency using RSM, to prepare microcapsules and to perform the characterization of the microcapsules obtained.

2. MATERIAL AND METHODS

2.1. Materials

Vitamin E was purchased from medicine in Isparta/Turkey. Gelatin and gum Arabic (Merck), sodium dodecyl sulfate (Merck), sodium hydroxide (Merck), n-hexane (Merck), acetic acid (Merck) and glutaraldehyde (Merck) were used during all experiments.

2.2. Experimental design

The optimization of vitamin E encapsulation was planned with central composite design (CCD). CCD is a 2^k factorial design with central point and star points [23]. The response surface methodology (RSM) was performed to optimize the microencapsulation efficiency of vitamin E through two independent variables; amount of core material (g) and surfactant concentration (%w/v). To facilitate multiple regression analysis, independent variables are encoded (Table 1). The experimental design was generated using MINITAB 16 (Licensing: lifetime) software. The square polynomial regression model was presumed to predict the *Y* variable (microencapsulation efficiency). The model aimed to the response of *Y* fitted Eq. (1) as follows [22-25]:

$$Y = \beta_0 + \beta_1 X_1 + \beta_2 X_2 + \beta_{11} X_1^2 + \beta_{22} X_2^2 + \beta_{12} X_1 X_2 + \varepsilon \quad (1)$$

Where *Y* is response (efficiency of microencapsulated vitamin E, %). β_0, β_1, β_2, β_{11} and β_{12} are coefficients of intercept, linear, square and interaction terms, respectively. X_1 and X_2 are uncoded independent variables (amount of core material and concentration of surfactant).

Table 1 It is used to show coded levels for independent variables in experimental design for microencapsulation of vitamin E

Variables	Coaded level	
	-1	+1
Amount of core material (g)	2.00	6.00
Concentration of surfactant (w/v%)	0.30	0.70

2.3. Preparation of microcapsules

Vitamin E particles covered by gelatin (GE) and gum Arabic (GA) have been prepared with complex coacervation method. Wall materials, aqueous solutions of GE and GA (2%, w/v) solutions were prepared separately. Then, 100 mL of an aqueous gelatin solution was warmed at 50 °C – 55 °C with stirring for vitamin E (2.00 g – 6.00 g) 15 min. For providing emulsifying, SDS solution (0.30% w/v – 0.70% w/v) was prepared and added. Finally, 100 mL of gum Arabic solution (2%, w/v) were added to the material and stirred for 30 min. Next, pH value of emulsion was adjusted to 4-4.5 with acetic acid (10%, v/v) which is the isoelectric point of gelatin and gum Arabic (at 1500 rpm, 45 °C, 90 min.). This mixture was transferred into 300 mL cooled deionized water. The temperature of the system was progresively decrease to 10 °C in an ice bath during the coacervation process. Glutaraldehyde solution was slowly added drop wise for cross-linking the microcapsules and was stirred 2.5 hours. Then pH system was adjusted to 9-9.5 with sodium hydroxide (10%, v/v). The mixture was allowed to stand for 1 day. The next day, the retiform microcapsules were splited by centrifugation for 5 mins at 1500 rpm and 25 °C, washed two times with deionized water and oven dried at 40 °C [26].

2.4. Microencapsulation efficiency

Microencapsulation efficiency was calculated from the next equation based on similar studies Eq. (2) [22, 27, 28].

$$MEE\% = \frac{Total\ amount\ vit.E - surface\ vit.E\ amount}{\text{Total amount vit. E}}\ x100 \quad (2)$$

The total vitamin E amount in this equation represents the amount of vitamin E that is known to be used based on the experimental set, while the surface extract amount represents the amount of non-encapsulated extract that remains between the products and the surface. Capsule sample was put in an erlenmeyer flask containing 50 mL of n-hexane and gently shaken for 5.00 minutes without capsule destruction while measuring the volume of surface extract. The solution was then filtered onto filter paper. A rotary evaporator was used to evaporate the n-hexane in the solution. After removing the n-hexane, the amount of vitamin E left was weighed and recorded [22, 27, 28].

2.5. Characterization of microcapsules

Morphological structure of the prepared microcapsules was examined by optical microscopy and scanning electron microscope (SEM). Optical images were taken with device of Boeco brand microscope. Microcapsules shape and morphology were measured from SEM images using Quanta FEG250 (Thermo Fisher Scientific). The chemical structures of samples were analyzed by a fourier-transform spectrometer. Samples were ground and mixed with KBr to make pellets, and FT-IR studies were performed on a Perkin Elmer Spectrum BX device.

3. RESULTS AND DISCUSSIONS

3.1. Experimental design and ANOVA results

The experimental studies for optimization of microencapsulation conditions of vitamin E, a two factor CCD was adjusted on the principle of coded from two independent variables (Table 1) and thirteen simplified experimental sets were obtained (Table 2). The amount of core material vitamin E and surfactant concentration were researched in the ranges of 2.00 g – 6.00 g and 0.30% w/v – 0.70% w/v, respectively.

Table 2 Central composite design for the optimization of vitamin E microencapsulation

NO	Core Material (A)	Concentration of Surfactant (B)	Experimental Efficiency (%EE)	Predicted Efficiency (%)
1	4.00	0.50	89.75	91.40
2	4.00	0.50	90.12	91.40
3	4.00	0.50	91.38	91.40
4	1.17	0.50	68.20	69.99
5	2.00	0.70	69.27	68.65
6	6.83	0.50	67.29	67.58
7	4.00	0.50	93.42	91.40
8	6.00	0.30	68.18	66.68
9	2.00	0.30	72.28	69.76
10	4.00	0.78	68.40	68.12
11	4.00	0.50	90.57	91.40
12	6.00	0.70	67.92	68.33
13	4.00	0.22	65.37	67.73

The response surface graphs for microencapsulation efficiency as a function of two selected parameters using important factors for microencapsulation efficiency are demonstrated in Fig.1. Each of the two parameters was observed to be effective on efficiency. Microencapsulation of vitamin E with the amount of core material concentration of 4.00 g and surfactant concentration 0.50% gave rise to the highest microencapsulation efficiency (93.42%) (Fig.1).

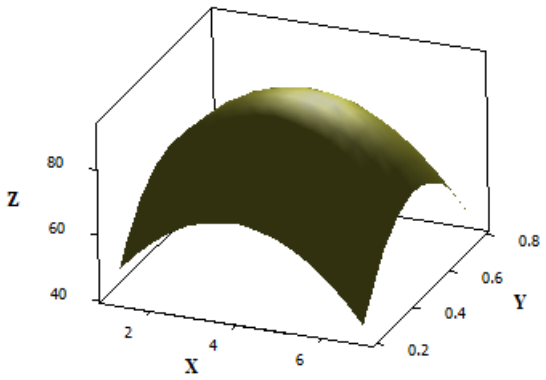

Figure 1 Microencapsulation efficiency (Z), amount of core material (X), surfactant concentration (Y).

According to RSM results, the ideal circumstances for microencapsulation of vitamin E aimed to be 4.00 g core material and 0.50% surfactant concentration where the microencapsulation efficiency was 91.38%. Response efficiency was determined under thirteen experimental circumstances; the regression coefficients were calculated. The model equation is shown in next Eq. (3):

$$\textbf{MEE\%} = -20.89 + 20.97*A + 282.69*B - 2.78*A*A - 288.92*B*B + 1.72*A*B \quad (3)$$

To determine the optimal state of microencapsulated vitamin E and the important variables, statistical analysis of ANOVA was carried out by the common test of two parameters (Table 3).

Table 3 Regression coefficient values are calculated for the microencapsulation of vitamin E

	DF	Adj SS	Adj MS	F-Value	P-Value
Model	5	1591.74	318.348	83.74	0.000
Linear	2	5.80	2.901	0.76	0.501
A	1	5.67	5.673	1.49	0.261
B	1	0.13	0.129	0.03	0.859
Square	2	1584.05	792.024	208.34	0.000
A*A	1	861.31	861.307	226.56	0.000
B*B	1	929.16	929.163	244.41	0.000
2-Way Interaction	1	1.89	1.891	0.50	0.503
A*B	1	1.89	1.891	0.50	0.503
Error	7	26.61	3.802		
Lack-of-Fit	3	18.10	6.033	2.84	0.170
Pure Error	4	8.51	2.128		
Total	12	1618.35			

R^2	R^2(adj)	R^2(pred)
98.36	97.18	91.22

The model is significant ($p<0.05$). The model does not show linearity ($p>0.05$). Quadratic part of model is significant ($p<0.05$). Two-way interaction is not significant in the model ($p> 0.05$). Lack-of-fit p value was found as 0.170. Hence the model matches the data. R^2 value was found 98.36. The probability plot of residuals chart is given in Figure 2.

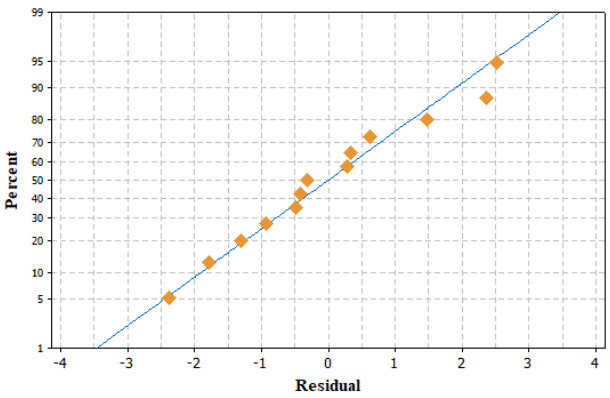

Figure 2 Probability plot of residuals graph

In the analysis of the graph, the mean and standard deviation of the residuals were 0.0±1.489 (n = 13). According to normality AD test, p=0.838. Residuals show normality (p=0.838).

3.2. Morphological analysis of microcapsules

The morphological characterizations of the microcapsules produced by considering the optimum conditions by RSM were performed with optic microscope and SEM images. Images of SEM analysis and optical microscopy showed that the microcapsules have a smooth shape and a flat shell structure. The optic microscope image which is taken from the highly efficient sample is shown in Fig.3.

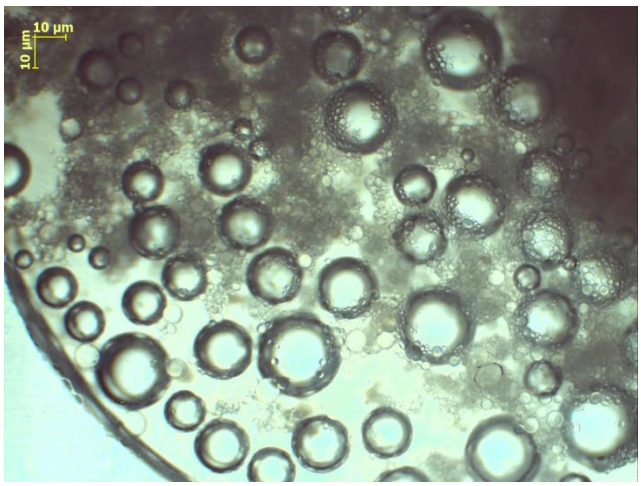

Figure 3 Optical microscope image of microencapsulated vitamin E

The SEM image which is taken from the highly efficient sample is shown in Fig.4.

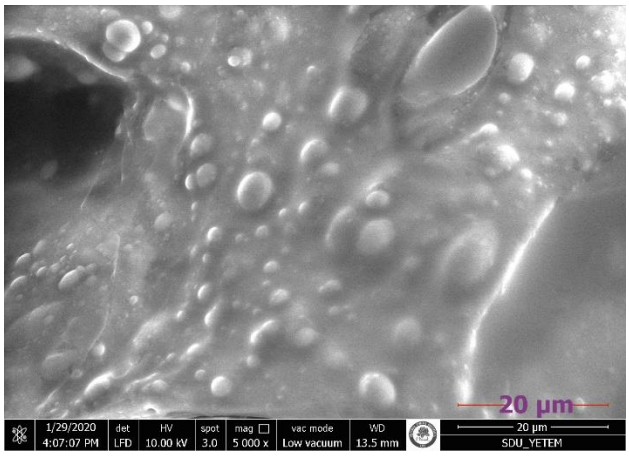

Figure 4 SEM images of microencapsulated vitamin E

The sphericity of the vitamin E microcapsules prepared by complex coacervation was good, and the particle size ranged from ~4 to ~80 µm.

3.3. FT-IR analysis of microcapsules

FT-IR spectrum of microcapsule produced was obtained. The comments were inferred utilizing the FT-IR analysis results of similar studies [29-31]. Specific bands of core material and polymers (vitamin E) used in microencapsulation were observed in the FT-IR spectrum of microcapsules also (Fig.5). FT-IR results show that the values of some groups deviate when complex is formed. When the FT-IR spectra of gelatin and gum Arabic are examined, it is seen that some bands in these spectra form a are lost complexes. Esterification was formed as a result of the reaction of alcohol in the functional group of gelatin with the acid in the medium. This peak is seen in the FT-IR spectrum of the microcapsule at 1600 cm^{-1}. The peak between 2340 cm^{-1} and 2300 cm^{-1} in the spectrum of microcapsules is the combination of C-N (amide I) stress peaks in gelatin and O-H stress peaks in gum Arabic. As seen from the microcapsule spectrum, ~1028 cm^{-1} band is the characteristic band of Arabic gum. This shows that the gum Arabic was successfully put into the structure of microcapsule. The notable FT-IR bands for gelatin came out at 3001.2 cm^{-1}, 2340 cm^{-1}, 1530 cm^{-1}, and 1480 cm^{-1}. From the spectrum of gum Arabic, OH stretching at ~2900 cm^{-1}, C-H stretching at ~2350 cm^{-1}, and C=O stretching at ~1665 cm^{-1} were observed (Fig.5). From the spectrum of gelatin, O-H bonds at

~3500 cm^{-1}, and C=O bonds at ~1678 cm^{-1} were observed. In the spectra, we confirmed the presence of -OH and -C-O-C- functional groups in the chromane ring of vitamin E at 1300-1750 cm^{-1}. FT-IR spectrum showed C=O streching vibration at around 700-1100 cm^{-1}, C-O formation at 1220 cm^{-1}, C=C formation at 1780 cm^{-1} and C-H alkanes group at 2945 cm^{-1} [31]. According to FT-IR spectrum results, there were electrostatic interactions between gelatin and gum Arabic, and the vitamin E was in the microcapsule.

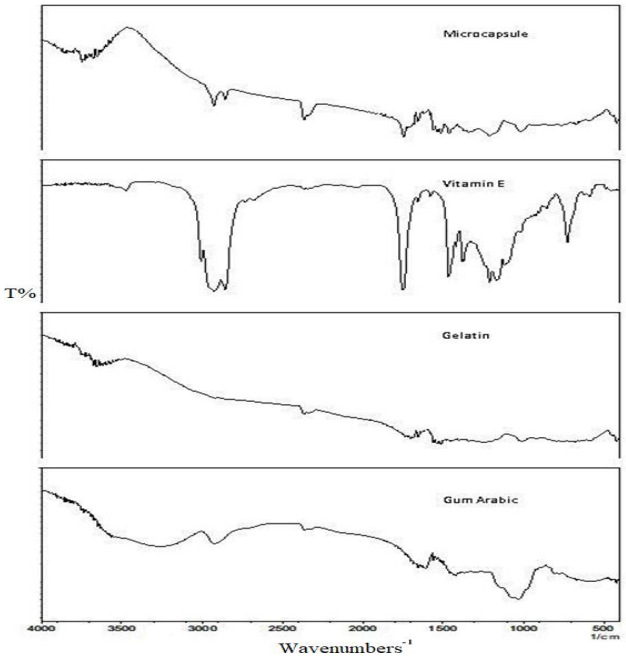

Figure 5 Results of FT-IR spectrum analysis (spectrum of microcapsule; spectrum of vitamin E; spectrum of gelatin, spectrum of gum Arabic).

4. CONCLUSION

In this study, we have aimed at optimizing microencapsulation conditions for vitamin E by using response surface methodology (RSM). The efficiency of microencapsulated vitamin E was remarkably affected by amount of core material surfactant concentration. As a result of RSM, the best conditions for this experiment set, microencapsulation of vitamin E were found to be 4.00 g core material and 0.50% surfactant concentration (%w/v). Microencapsulated vitamin E under optimized conditions showed 93.42% efficiency. The microcapsules were prepared at the optimum conditions in RSM. It was found from the morphological analysis of microcapsules with optical microscope and SEM that microcapsules generally have a regular and similar size structure. The FT-IR spectrum showed that there were electrostatic interactions between gelatin and gum Arabic and that vitamin E was in microcapsules. In a similar different study [32], α-TP was encapsulated in gelatin/pectin wall material using tween 80 as surfactant. In the study, nano-sized capsules were produced with the help of an experimental set created by RSM and capsule size was used as response to response. In our previous study, we encapsulated vitamin E in micro size with the help of different variables. In this study, with the help of RSM, it is investigated the effect of core matter amount and surfactant substance concentration on the efficient obtained at the end of the experiment. The FT-IR results show similarity to our previous study [33]. With this study, vitamin E was successfully microencapsulated with complex coacervation method in an experiment set with RSM.

5. REFERENCES

[1] Shabbar, D. W. Chang, H. Khizar and X. Zhang, "Ascorbic Acid: Microencapsulation techniques and trends—A Review," Food Reviews International, 28(4), pp 343-374, 2012.

[2] J. Singh, K. Kaur and P. Kumar, "Optimizing microencapsulation of α-tocopherol with pectin and sodium alginate," J Food Sci Technology. 55(9), pp 3625-363, 2018.

[3] M. Otadi and H. Zahibi, "Vitamin E microcapsulation by ethylcellulose through emulsion solvent evaporation technique; An operational condition study," World Applied Sciences Journal, 14 (Special Issue of Food and Environment), 20-25, 2011.

[4] Anandharamakrishnan, "Spray drying techniques for food ingredient encapsulation," John Wiley & Sons, 2015.

[5] K. Son, D. I. Yoo and Y. Shin, "Fixation of vitamin E microcapsules on dyed cotton fabrics," Chemical Engineering Journal, pp 284-289, 2014.

[6] P. Chaiyasat, P. Teeka, S. Noppalit, U. Srinorachun, "Preparation of poly (l-lactic acid) microencapsulated vitamin E," 10th Eco-Energy and Materials Science and Engineering, pp 656–663, 2012.

[7] Y. Byun, J. B. Hwang, S. H. Bang, D. Darby, K. Cooksey, P. L. Dawson and S. Whiteside, Formulation and characterization of α-tocopherol loaded poly 3-caprolactone (PCL) nanoparticles, Lwt-Food Science and Technology, 44(1), pp 24-28, 2011.

[8] M. X. Quintanilla-Carvajal, H. Hernández-Sánchez and L. Alamilla-Beltrán, "Effects of microfluidisation process on the amounts and distribution of encapsulated and nonencapsulated α-tocopherol microcapsules obtained by spray drying," Food Research International. 63, 2–8, 2014.

[9] Butstraen and F. Salaün, "Preparation of microcapsules by complex coacervation of gum Arabic and chitosan," Carbohydrate polymers, 99, 608-616, 2013.

[10] R. Dubey, T. C. Shami and K. U. Bhasker Rao, "Microencapsulation Technology and Applications," Defence Science Journal. 59(1), pp 82-95, 2009.

[11] N. V. N. Jyothi, P. M. Prasanna, S. N. Sakarkar, K. S. Prabha, P. S. Ramaiah and G. Y. Srawan, "Microencapsulation techniques, factors influencing encapsulation efficiency," Journal of microencapsulation, 27(3), 187-197, 2010.

[12] H. Umer, H. Nigam, A. M. Tamboli and M.S. Nainar, "Microencapsulation: Process, techniques and applications," International Journal of Research in Pharmaceutical and Biomedical Sciences, pp 2229-3701, 2011.

[13] G. Başal and S. Karagönlü, "Preparation of antimicrobial agent loaded microcapsules for medical textiles," Pamukkale University Journal of Engineering Sciences. 19(4), pp 174-178, 2012.

[14] N. Eghbal and R. Choudhary, "Complex coacervation: Encapsulation and controlled release of active agents in food systems," Lwt-Food Science and Technology. 90, pp 254-264, 2018.

[15] N. Wilson and N.P. Shah, "Microencapsulation of vitamins," ASEAN Food Journal, 14(1), 2017.

[16] S. Yıkmış, H. Aksu, M. Alpaslan and O. Şimşek, "Probiotic Microorganisms and Encapsulation Method Approaches," In Microbial Cultures and Enzymes in Dairy Technology, pp. 132-151, IGI Global, 2018.

[17] W. Li, G. Wu, H. Chen and M. Wang, "Preparation and characterization of gelatin/SDS/NaCMC microcapsules with compact wall structure by complex coacervation," Colloids and Surfaces A: Physicochemical and Engineering Aspects. 333(1-3), pp 133-137, 2009.

[18] S. Gökmen, R. Palamutoğlu and C. Sarıçoban, "Application of encapsulation food industry," Electronic Journal of Food Technologies, 36-50, 2012.

[19] Y.P. Timilsena, O. Akanbi, N. Khalid, B. Adhikari and C.J. Barrow, "Complex coacervation: Principles, mechanisms and applications in microencapsulation," International Journal of Biological Macromolecules, 121, pp 1276-1286, 2019.

[20] H. Epinosa-Andrews, J.G. Baez-Gonzales, F. Cruz-Sosa and E.J. Vernon-Carter, "Gum Arabic-Chitosan Complex Coacervation," Biomacromolecules. 8, 1313-1318, 2007.

[21] M. Yan, "Handbook of Encapsulation and Controlled Release," Taylor&Francis Group, New York, 2015.

[22] J. H. Ahn, Y. P. Kim and Y. M. Lee, "Optimization of microencapsulation of seed oil by response surface methodology," Food Chemistry, 107, pp 98–105, 2008.

[23] S. H. Yoo, Y. B. Song, P. S. Chang, H. Lee, "Microencapsulation of α-tocopherol using sodium alginate and its controlled release properties," International Journal of Biological Macromolecules, 38, 25-30, 2006.

[24] I. Khuri and S. Mukhopadhyay, "Response surface methodology," Wiley Interdisciplinary Reviews: Computational Statistics, 2(2), pp 128-149, 2010.

[25] Baş and I. H. Boyacı, "Modeling and optimization I: Usability of response surface methodology," Journal of food engineering, 78(3), pp 836-845, 2007.

[26] Köksal, "Production of Microcapsule Containing Vitamin E By Complex Coacervation Method," Süleyman Demirel University, Graduate School of Natural And Applied Sciences, M. Sc. Thesis, 2016.

[27] L. Hu, J. Zhang, Q. Hu and N. Gao, "Microencapsulation of brucea javanica oil: Characterization, stability and optimization of spray drying conditions," Journal of Drug Delivery Science and Technology, 36, pp 46-54, 2018.

[28] B. Ocak, "Complex coacervation of collagen hydrolysate extracted from leather solid wastes and chitosan for controlled release of lavender oil." Journal of environmental management, 100, pp 22-28, 2012.

[29] S. Demirbağ, "Production of flame retardant microcapsules with heat storage property by complex coacervation and textile applications," Süleyman Demirel University Department of Textile Engineering, M. Sc. Thesis, 2014.

[30] K. Kebapçı, "Flavor microcapsules," Süleyman Demirel University Department of Chemistry, M. Sc. Thesis, 2012.

[31] M. Fathi, M. N. Nasrabadi and J. Varshosaz, "Characteristics of vitamin E-loaded nanofibres from dextran,". International Journal of Food Properties, 20(11), pp 2665-2674, 2017.

[32] Sharifi, F. Hadizadeh, F. Sadeghi, M. T. Hamed Mosavian and C. Zarei, "Process Optimization, Physical Properties, and Environmental Stability of an α-Tocopherol Nanocapsule Preparation Using Complex Coacervation Method and Full Factorial Design," Chemical Engineering Communications, 203 (1), pp 64-74, 2016.

[33] E. Köksal and F. Göde, "Production of microcapsules containing vitamin E with complex coacervation method," Süleyman Demirel University Faculty of Arts and Sciences Journal of Science, 12(1), pp 1-14, 2017.

SAKARYA ÜNİVERSİTESİ
FEN BİLİMLERİ ENSTİTÜSÜ DERGİSİ

Sakarya University Journal of Science
SAUJS

ISSN 1301-4048 | e-ISSN 2147-835X | Period Bimonthly | Founded: 1997 | Publisher Sakarya University | http://www.saujs.sakarya.edu.tr/

Title: Voltage Stability Analysis of a Large Scale PV Plant for Different Control Options

Authors: Bora ÇAVDAR, Ömür AKYAZI, Erdinc SAHIN, Fatih NUROGLU

Recieved: 2020-10-09 15:32:06

Accepted: 2021-06-16 12:33:05

Article Type: Research Article

Volume: 25
Issue: 4
Month: August
Year: 2021
Pages: 914-925

How to cite
Bora ÇAVDAR, Ömür AKYAZI, Erdinc SAHIN, Fatih NUROGLU; (2021), Voltage Stability Analysis of a Large Scale PV Plant for Different Control Options. Sakarya University Journal of Science, 25(4), 914-925, DOI: 10.16984/saufenbilder.808343
Access link
http://www.saujs.sakarya.edu.tr/en/pub/issue/64755/808343

Sakarya University Journal of Science 25(4), 914-925, 2021

Voltage Stability Analysis of a Large Scale PV Plant for Different Control Options

Bora ÇAVDAR[1], Ömür AKYAZI[1], Erdinc SAHIN*[1], Fatih NUROGLU[1]

Abstract

The increasing integration of photovoltaic (PV) plants into conventional power systems has led to the need to examine the effects of these plants on the system dynamics. By considering this increasing integration rate, in this study, a well-known IEEE-9 bus power system is modified by adding a PV plant in DigSilent Powerfactory environment. Three different transient cases are tested by using PV plant control units designed by Western Electricity Coordinating Council (WECC). The effect of the load and line transient disconnections and 3-phase short circuit fault on modified power system are investigated as case-I, case-II, and case-III, respectively. In all cases, two sub-cases are considered according to the location as a distance factor. As a result, comparison of PV different control options (DCO) is done in terms of voltage stability for these 3 cases and the obtained results are discussed in detail.

Keywords: Reactive power control methods, IEEE-9 bus power system with large scale PV integration, voltage stability, 3-phase short circuit fault, transient line and load disconnection, distance factor

1. INTRODUCTION

Due to the developing technology, increasing demand in energy consumption and the necessity of the clean energy of future, renewable energy sources expands their energy generation area day by day. Considering the part of energy production among the renewable energy sources, it can be definitely said that the PV power plants are one of the most popular source [1].

Some differences between the PV plants and conventional energy sources in terms of energy generation methods occurs. There are some disadvantages of PV plants in energy generation such as the effect of reducing the total moment of inertia of the power system and being affected by weather conditions directly [2, 3]. On the other hand, their ability of distribute generation and voltage and frequency control through power electronic control units reveals the advantages of the PV plants. Therefore, it is important to examine the PV plant effects on the power system dynamics based on stability and sustainability.

It is seen from the literature that there are stability studies containing the effect of the PV plants on the power systems for various type of situations. Generally, it is possible to classify these studies as frequency stability, rotor angle stability, and voltage stability [4, 5].

* Corresponding author: esahin@ktu.edu.tr
[1] Karadeniz Technical University, University Mah., National Sovereignty Cad., Ortahisar, Trabzon, Turkey
E-Mail: boracavdar@ktu.edu.tr, oakyazi@ktu.edu.tr, fmn@ktu.edu.tr.
ORCID: https://orcid.org/0000-0002-0545-2925; https://orcid.org/0000-0001-6266-2323; https://orcid.org/0000-0002-9740-599X; https://orcid.org/0000-0003-2530-8901.

In the investigation of the voltage stability of PV plants, it is generally studied that PV plants are integrated to traditional power systems [6-10]. On the other hand, integration of PV plant with wind power systems are also available [11-13]. Voltage stability studies of PV plant integrated power systems contain consideration of different reactive power support methods [8], solar radiation, temperature and load changes [9], conventional and developed dynamic voltage support (DVS) [10], low voltage ride through (LVRT) [14], different penetration levels [15, 16], central and distributed generation [16], different constant power factors and automatic voltage control [17], one or more PV plant with connected to the same bus [18], reactive power compensation system [19] and so on. Stability studies by comparing the DCO of the PV power plants designed by WECC is rarely analyzed in literature [7, 20]. In these studies, voltage stability in short circuit fault and small signal stability are investigated, respectively.

The PV plants can be integrated to the power systems through WECC PV plant model [21]. It has been observed from the reported studies in the literature that there are limited studies to compare the DCO modeled by WECC. In the light of this motivation, the effect of DCO are need to be investigated in terms of voltage stability by considering different cases.

In this study, the effects of PV plants on voltage stability for different control options have been analyzed in detail by considering different conditions such as transient disconnection of the load, transient disconnection of the line, and 3-phase short circuit fault. In addition, the location of the fault with respect to the PV plant is also studied in this paper. In this manner, a well-known IEEE 9-bus power system has been modified by connecting a PV plant instead of G3 generator for the Bus-3. The whole power system is simulated in DigSilent Powerfactory program and the obtained results are discussed in detail in Section III and IV, respectively.

The organization of this study is given as follows. Voltage stability analysis and modelling of the modified power system are presented in Section II. Considered cases and simulation results with comparative analysis are illustrated in Section III. Finally, conclusion is stated in Section IV.

2. VOLTAGE STABILITY AND POWER SYSTEM MODELLING

2.1. Voltage stability

Voltage stability generally can be expressed as the ability of the power system to maintain the scheduled voltages of all buses in case of disturbance [5]. It depends on keeping the equilibrium between load demand and supply. The voltage stability criterion can be demonstrated as shown in Fig. 1 by separating active power and reactive power demands. In Fig. 1, $[P_L(V)\ ,Q_L(V)]$ and $[P_S(V),\ Q_S(V)]$ are the active and reactive power of the load and supply, respectively [22].

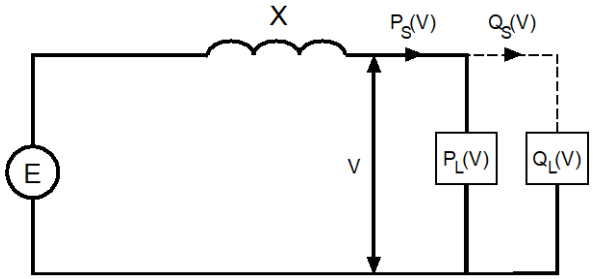

Figure 1 Equivalent circuit of the separated presentation of active and reactive power [22]

In normal operating conditions, $P_L(V)$ is equal to $P_S(V)$ and $Q_L(V)$ is equal to $Q_S(V)$. However, the relationship between the reactive power of the load and supply can be considered separately for voltage stability analysis. It is also assumed that the load is not determined by the reactive power demand. The active and reactive power equations are given below.

$$P_L(V) = P_S(V) = \frac{EV}{X}\sin\delta \quad (1)$$

$$Q_S(V) = \frac{EV}{X}\cos\delta - \frac{V^2}{X} \quad (2)$$

where E is the voltage of the supply, V is the voltage of the load, and X and δ are the total reactance and angle between the supply and load voltages, respectively. By considering $(sin^2\delta + cos^2\delta = 1)$, (3) can be written by using (1) and (2).

$$\left(\frac{EV}{X}\right)^2 = {P_L}^2(V) + [Q_S(V) + \frac{V^2}{X}]^2 \quad (3)$$

The final equation (4) which defines the reactive power-voltage characteristic can be obtained from (3) as follow [22].

$$Q_S(V) = \sqrt{[\frac{EV}{X}]^2 - [P_L(V)]^2} - \frac{V^2}{X} \quad (4)$$

2.2. Power system modelling

In this study, the IEEE 9-bus power system has been modified by integrating a PV plant to the Bus-3 in DigSilent Powerfactory simulation environment. The modeled power system schematic is shown in Fig. 2. In the modified model, G1 and G2 generators have a governor and automatic voltage regulator (AVR). The considered governor and AVR types are HYGOV and AVR EXAC1 for G1 generator, GAST and AVR IEEET1 for G2 generator, respectively. A detailed system model can be accessed in [23].

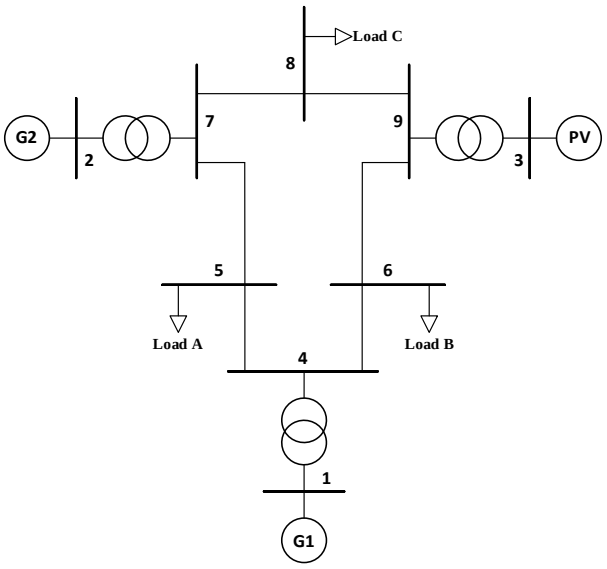

Figure 2 The modified IEEE 9-bus power system

In the studied model, generator power and voltage values are given in Table 1 and load values are given in Table 2. The bus connected to the G1 generator is selected as the slack bus, and the angle of the voltage of this bus is set to 0º.

Table 1 Power and voltage values of the sources

Sources	Bus no	Operating power (MW)	Nominal power (MVA)	Voltage (pu)
G1	Bus 1	-	260	1.040
G2	Bus 2	90	150	1.025
PV	Bus 3	140	150	1.000

Table 2 Power values of the loads

Load types	Bus no	Active power (MW)	Reactive power (MVA)
Load A	Bus 5	160	260
Load B	Bus 6	80	150
Load C	Bus 8	140	150

2.3. PV plant modelling for DCO

The integration of PV power plants into the power systems is accomplished via control units. In the integration, the power capacity of the PV plant is an important issue for the control. Considering the capacities of the PV plants, three different types can be categorized as small scale, medium scale and large scale [24]. Large scale PV plants can produce more than 20 MW active power [24]. In this study, a large scale PV plant has been modeled using WECC control modules. The WECC control modules used in this study are Renewable Energy Generator Convertor (REGC_A), Renewable Energy Electrical Control (REEC_B), Renewable Energy Plant Controller (REPC_A) [25]. The structure of the control block diagrams with sub-control units are presented in detail in Fig. 3.

There are different type DCO that can be applied by setting the flags on the WECC control modules. In order to set DCO, *pfflag*, *vflag* and *qflag* flags are arranged in REEC_B module, while *refflag* flag is set in REPC_A module. The most used DCO are tabulated in Table 3 [4] and the parameter and flag values of the REGC_A, REEC_B and REPC_A modules used in this paper are given in [26]. Also, LVRT is used in the PV plant model to ensure the connection of the power in case of a voltage drop [27]. In addition, the PV plant restores its active power at a rate of 100% of its nominal active power per second after the fault is clear. To use this feature, the parameter *rrpwr* in the REGC_A module is set to 1.

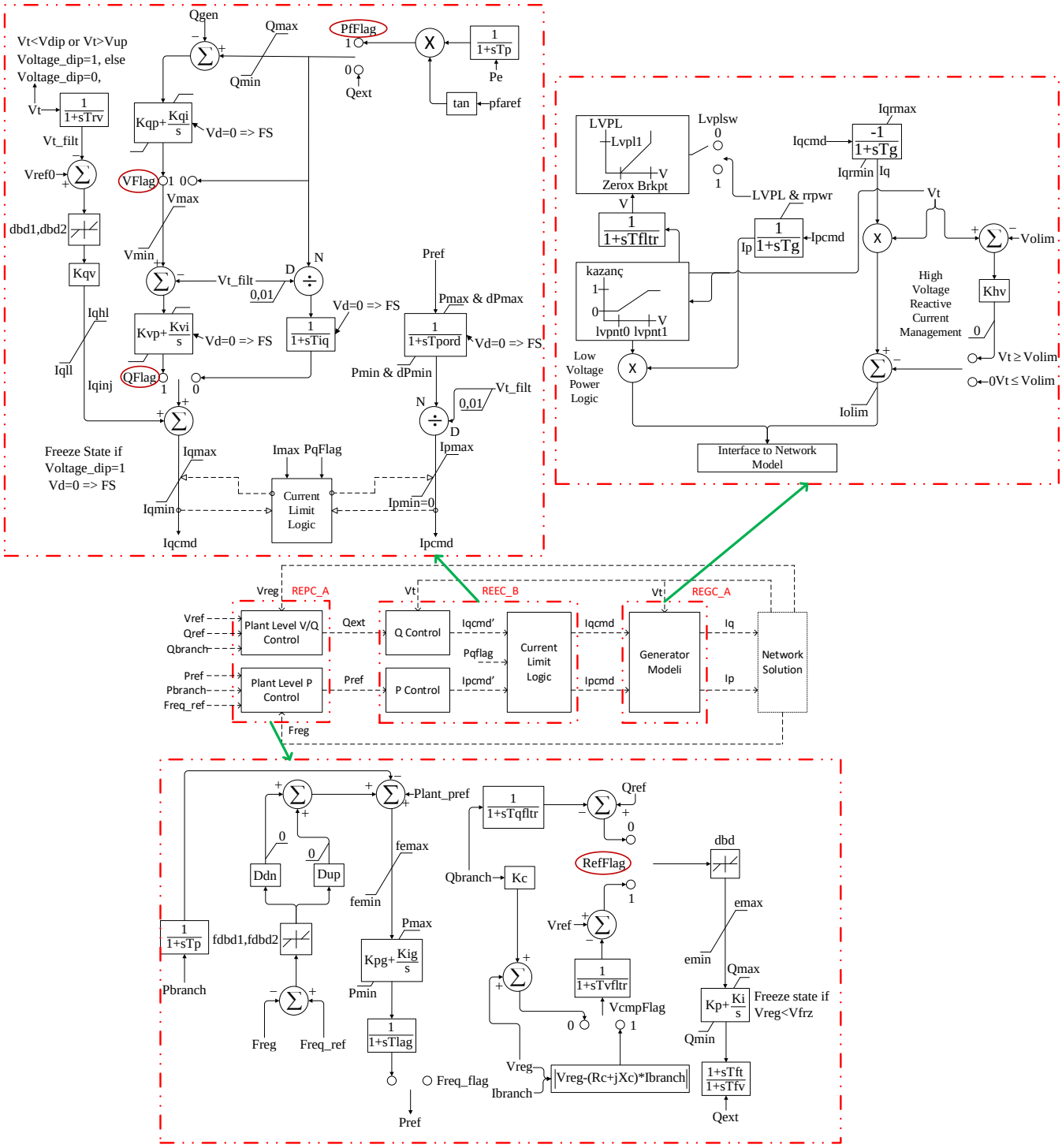

Figure 3 Control block diagram of the WECC generic central station PV system model [25].

Table 3 Type of the DCO.

Required Models	**(CLPFC)**	**(CLQC)**	**(LVC)**	**(LCQ/VC)**	**(PLQC)**	**(PLVC)**	**(PLQC& LCQ/VC)**	**(PLVC& LCQ/VC)**
Required Models	REEC_B	REEC_B	REEC_B	REEC_B	REEC_B + REPC_A	REEC_B + REPC_A	REEC_B + REPC_A	REEC_B + REPC_A
pfflag	1	0	0	0	0	0	0	0
vflag	1	1	0	1	1	1	1	1
qflag	0	0	1	1	0	0	1	1
refflag	N/A	N/A	N/A	N/A	0	1	0	1

CLPFC: Constant local power factor control, *CLQC*: Constant local Q control, *LVC*: Local V control, *LCQ/VC*: Local coordinated Q/V control, *PLQC*: Plant level Q control, *PLVC*: Plant level V control, *PLQC & LCQ/VC*: Plant level Q control & Local coordinated Q/V control, *PLVC & LCQ/VC*: Plant level V control & Local coordinated Q/V control. (More detailed explanations are available in [25, 26, 28]

PV plants can inject reactive power to the system to prevent deterioration in short-term voltage stability [10]. This feature is defined as DVS. If the voltage values specified in the REEC_B module exceeds to its nominal value, DVS is activated. The *kqv* parameter should be adjusted to activate this feature. It is recommended to select *kqv* value between 0 and 10 in the module [29]. If *kqv* parameter is set to 0, the DVS is disabled. Higher selection of the *kqv* value results to decrease the voltage drop and to increase the overshoot value because of reactive power transfer during the transient event. Therefore, the *kqv* value is set to 2 in this study. In addition, over voltage (V_{up}) and under voltage (V_{dip}) points in this study are determined as 1.1 pu and 0.9 pu, respectively. The DVS is activated for all cases in this study.

3. SIMULATION RESULTS

While analyzing the effects of the power system components on the system dynamic, it is important to consider different type unexpected cases. In this manner, the effect of DCO of the PV plant for different cases have been observed in this study. In all cases, considered transient events are applied at t=1 s and ended at t=1.1 s. The investigated voltage stability for all cases are achieved with the voltage measurement on Bus-9 which connected to PV plant via station transformer. The considered cases are given in Table 4.

Table 4 The all cases on modified power system

Case	**Transient event**	**Location of the transient event**
I	Disconnection of the load	Load A
		Load B
II	Disconnection of the line	Line 5-7
		Line 6-9
III	3-Phase short circuit fault	Bus 5
		Bus 6

In the cases given in Table 4, 2 sub-cases of 3 cases are investigated to observe the effect of the distance factor from the PV plant. The sub-cases are separately considered as given below.

3.1. Case I: transient disconnection of the load

In this case, the transient disconnection of the Load A and Load B shown in Fig. 2 has been analyzed. While Load A is located far away from the PV plant, Load B is located close to the PV plant. The reactive power demand of the Load A is twice of the Load B. In Fig. 4-5 and Fig. 6-7, voltage and reactive power with the transient disconnection of Load A and Load B are illustrated, respectively.

It can be concluded from the Fig. 4-6 that the highest voltage is obtained in the order of PLQC, CLQC, CLPFC and PLVC control modes. The control modes with the lowest voltage are LVC, PLVC&LCQ/VC, LCQ/VC and PLQC&LCQ/VC, respectively. The control modes with the least voltage deviation are LVC, PLVC&LCQ/VC, LCQ/VC and PLQC&LCQ/VC, respectively.

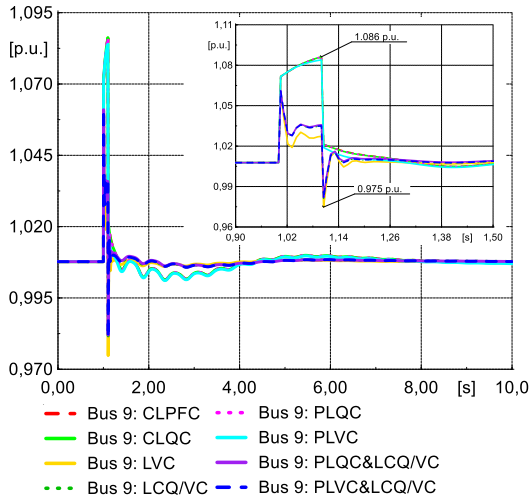

Figure 4 Voltage of the Bus-9 under transient disconnection of the Load A

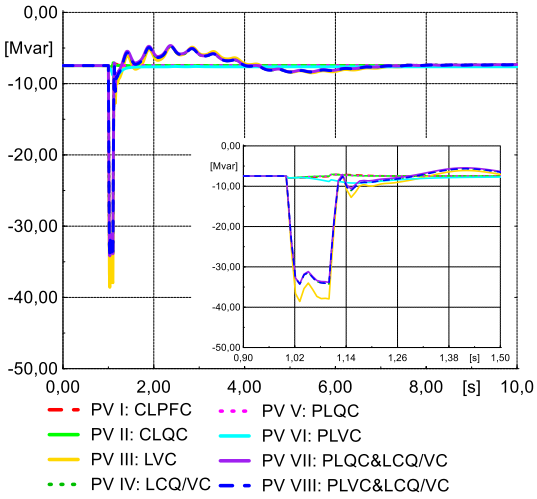

Figure 5 Reactive Power of the PV Plant under transient disconnection of the Load A

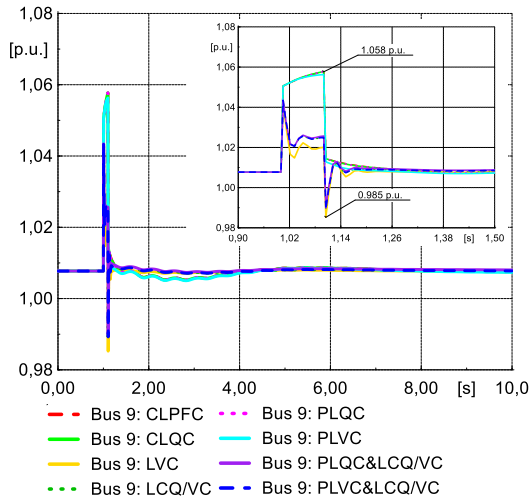

Figure 6 Voltage of the Bus-9 under transient disconnection of the Load B

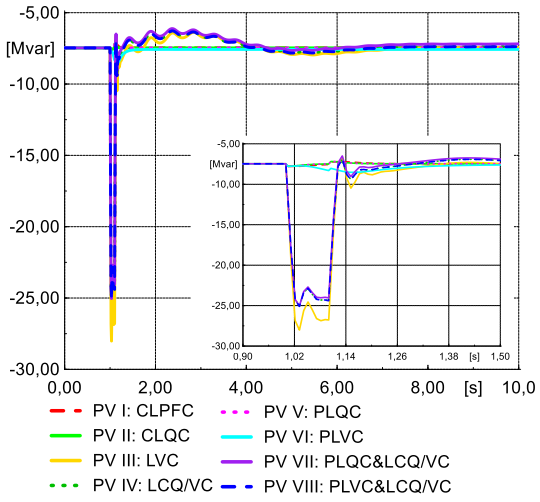

Figure 7 Reactive Power of the PV Plant under transient disconnection of the Load B

The voltage response shown in Fig. 4-6 are provided by the reactive power response of the PV plant in Fig. 5-7 to control the voltage. It is clear from the figures that reactive power response of the PV plant deviates the most in the modes with the least deviation in voltage.

As a result, the responses of the control modules in both load locations seem similar. However, the reactive power demanded by the loads is not equal and the maximum and minimum peak values are different from each other.

3.2. Case II: transient disconnection of the line

In this case, the transient disconnection of Line 5-7 and Line 6-9 seen in Fig. 2 has been analyzed. While line 5-7 is far away from the PV plant, Line 6-9 is located close to it. Voltage and reactive power responses under the transient disconnection of Line 5-7 is shown in Fig. 8 and 9, respectively.

In case of the disconnection of the Line 5-7, the reactive power supplied by G2 generator to Load A has been eliminated. As a result, the total reactive power supplied by the G2 generator during the transient event is dropped to 97.6% for the PV central reactive power control modes CLPFC, CLQC, PLQC and PLVC; 91.1% for LCQ/VC, PLQC&LVQ/VC and PLVC&LVQ/VC; 90.2% for LVC. On the other hand, G1 generator increases reactive power

generation to compensate the elimination of reactive power from Line 5-7.

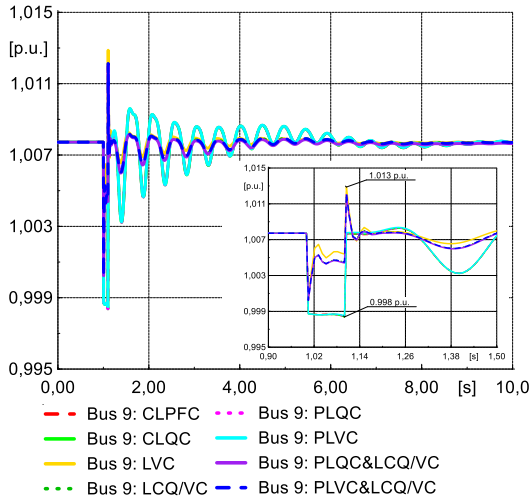

Figure 8 Voltage of the Bus-9 with the deactivation of Line 5-7

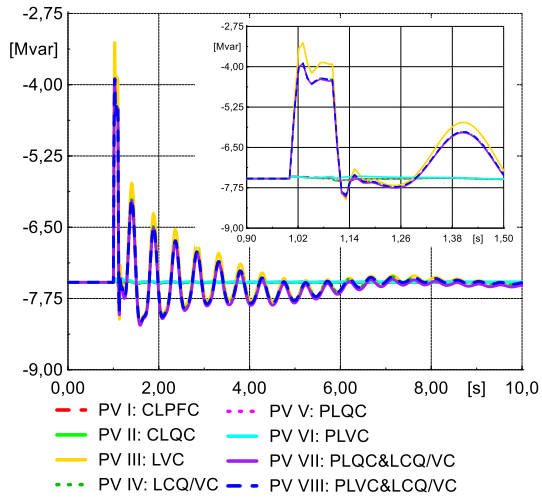

Figure 9 Reactive power of the PV plant with the deactivation of Line 5-7

In Fig. 8, the oscillation in the voltage response after the line disconnection is occurred due to the oscillation in the reactive power generation of the G2 generator. However, there is not much reactive power oscillation in the G1 generator. The effect of reactive power oscillation in the G2 generator on the Bus-9 is responded by the reactive power modes LVC, LCQ/VC, PLQC&LVQ/VC and PLVC&LVQ/VC. It results that the voltage oscillation is reduced. In the other modes, more oscillation is observed as seen from the Fig. 8 and 9.

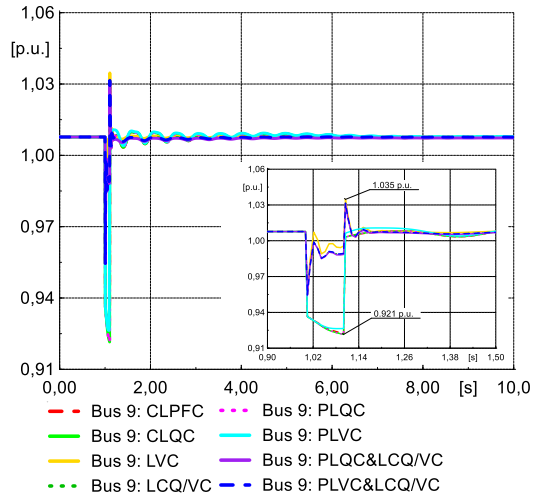

Figure 10 Voltage of the Bus-9 with the deactivation of Line 6-9

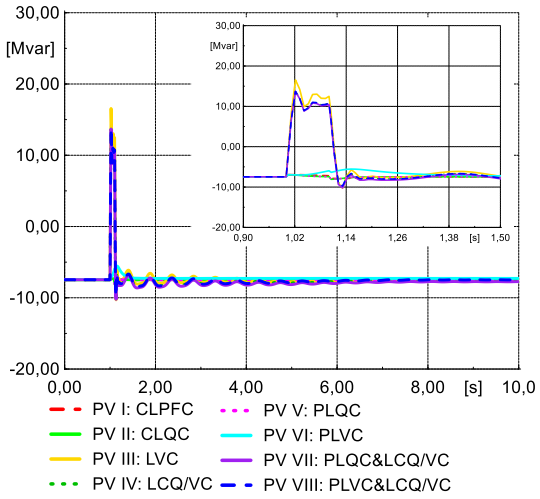

Figure 11 Reactive power of the PV plant with the deactivation of Line 6-9

In Fig. 10 and 11, the voltage and reactive power in case of transient disconnection of the Line 6-9 are given. With the disconnection of the Line 6-9, the reactive power supplied to Load B is eliminated. The G1 and G2 generators have performed more to balance the reactive power demand. After the transient event, there is not much oscillation in reactive power of the G1 and G2 generators. DCO of PV plant; LVC, LCQ/VC, PLQC&LVQ/VC and PLVC&LVQ/VC reacts against the decrease in the voltage response shown in Fig. 10 in order not to deviate the voltage from the nominal value.

In Fig. 8 and 10, the control modes of which the voltage has the highest values are LVC,

PLVC&LCQ/VC, LCQ/VC and PLQC&LCQ/VC, respectively. The control modes with the lowest voltage value are PLQC, CLQC, CLPFC and PLVC, respectively. In addition, the control modes LVC, PLVC&LCQ/VC, LCQ/VC and PLQC&LCQ/VC provides the least voltage deviation.

As a result, it has been observed that the response of the control modules with the disconnection of the close (Line 6-9) or remote (Line 5-7) lines to the PV plant under the fault seems similar.

The disconnection of the remote line after the transient event causes oscillation in the voltage response. However, the close line almost causes any oscillation.

In this sub-case, LVC, PLVC&LCQ/VC, LCQ/VC, and PLQC&LCQ/VC are performed more to balance the oscillation in voltage response. Because of the differences in the power flows and locations of the lines, it results to differ peak and deep values in the responses.

3.3. Case III: 3-phase short circuit fault

In this case, 3-phase short circuit fault in Bus-5 and 6 shown in Figure 2 has been analyzed. The Bus-6 is located close to PV plant while the Bus-5 is far from the PV plant. The voltage and reactive power responses with the considered fault in Bus-5 and Bus-6 are indicated in Fig. 12-13 and Fig. 14-15, respectively.

In Fig. 12 and 14, the control modes with the highest voltage value are obtained by LVC, PLVC&LCQ/VC, LCQ/VC and PLQC&LCQ/VC, respectively. On the other hand, the lowest voltage values are provided by PLQC, CLQC, CLPFC and PLVC, respectively.

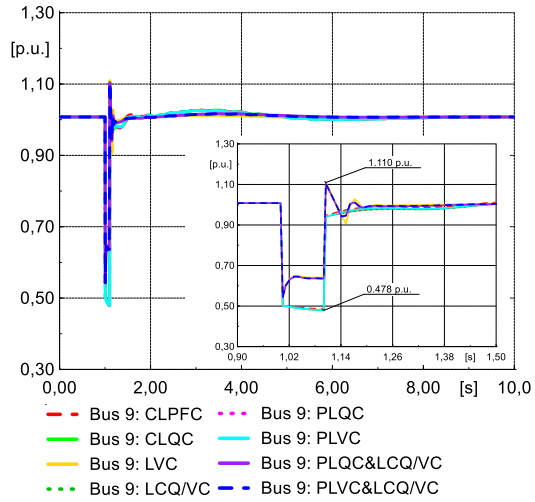

Figure 12 Voltage of the Bus-9 under the 3-phase short circuit failure in Bus-5

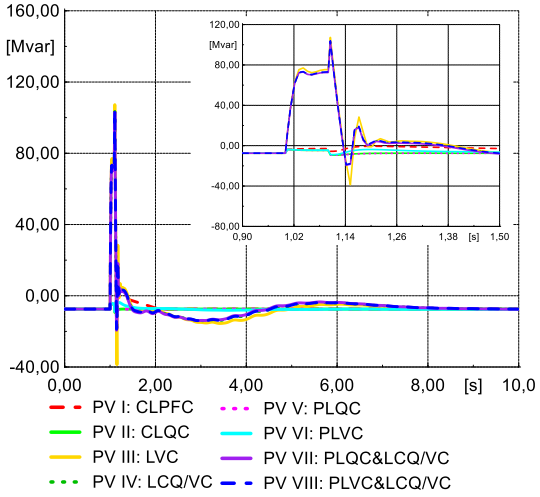

Figure 13 Reactive power of the PV plant under the 3-phase short circuit failure in Bus-5

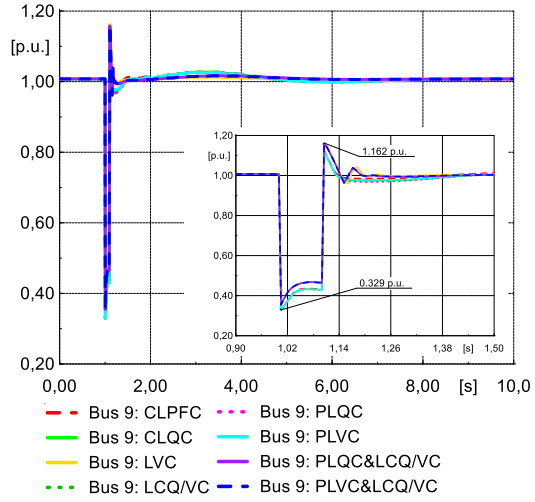

Figure 14 Voltage of the Bus-9 under the 3-phase short circuit failure in Bus-6

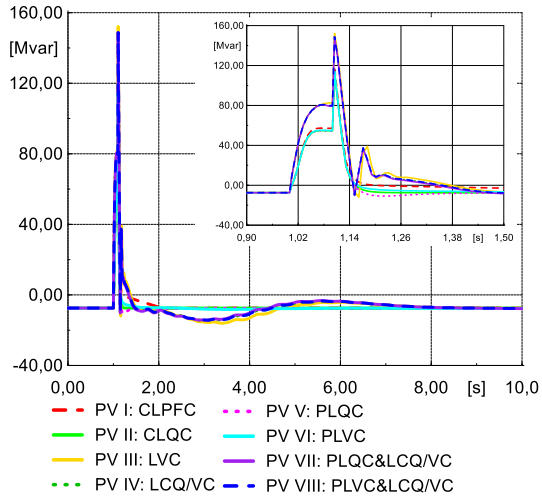

Figure 15 Reactive power of the PV plant under the 3-phase short circuit failure in Bus-6

It is known that the voltage value of the bus where 3-phase short circuit fault occurs can drop to zero. Therefore, the fault in close bus (Bus-6) to the PV plant results further decrease in the voltage of the Bus-9. At this point, the PV plant provides more reactive power to the 3-phase short circuit fault in Bus-6. It causes the voltage value of the Bus-6 is higher than Bus-5 after the fault.

In both short circuit faults on Bus-5 and Bus-6, since the voltage limit of DVS exceeds, DVS is activated. Therefore, the dynamic responses seem similar in all control modes.

4. RESULTS

Because of the increasing integration of the PV power plants into the conventional power systems, it becomes more important to analyze the effect of these plants on power systems. In this study, the effect of the DCO of the PV plant in terms of the voltage stability are investigated in IEEE 9-bus power system. Three cases with their two sub-cases are considered for the test system. The sub-cases are considered for the distance factor (close or remote to the PV plant). The obtained results of the studied cases are summarized below.

- In case I, it is observed that the responses of the DCO according to the position of the load is similar. But the magnitude of the response changes with the size of the load.
- In case II, it is seen that DCO show similar dynamic responses according to the position of the line during the considered transient event. After the transient event, the deviations in voltage are observed in remote location. Therefore, DCO incorporating local voltage control performs more to compensate the oscillation in the remote event. In addition, the difference in position has affected the maximum and minimum values of the voltage.
- In case III, it is again observed that DCO show similar responses according to the location of the fault considered in this case. However, if the fault location is close to the PV plant, the voltage on Bus-9 drops more. It results that the reactive power generation of the PV plant is increased more in remote fault (Bus-5).

In addition, two highlighted results of this study are given as follows.

- It is determined that DCO with local voltage control have more effective responses on voltage.
- When the DVS is activated, all reactive power control modes behave similarly in dynamic response.

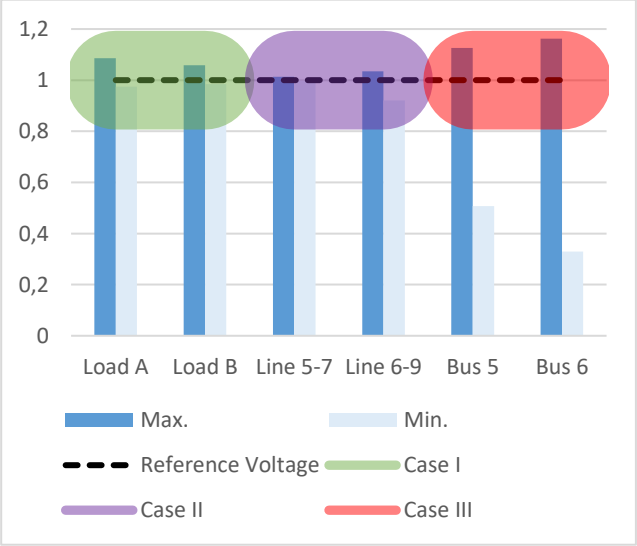

Figure 16 The obtained peak and deep voltages in cases

Finally, the peak and deep voltage values of the considered cases are shown in Fig. 16. In Fig. 16, the minimum and maximum points do not deviate in Case I and II. However, in Case III, the voltage deviation is higher than the nominal value.

Acknowledgments

The authors would like to acknowledge the reviwers and editors of Sakarya University Journal of Science.

Funding

The author (s) has no received any financial support for the research, authorship or publication of this study.

The Declaration of Conflict of Interest/ Common Interest

No conflict of interest or common interest has been declared by the authors.

The Declaration of Ethics Committee Approval

This study does not require ethics committee permission or any special permission.

The Declaration of Research and Publication Ethics

The authors of the paper declare that they comply with the scientific, ethical and quotation rules of SAUJS in all processes of the paper and that they do not make any falsification on the data collected. In addition, they declare that Sakarya University Journal of Science and its editorial board have no responsibility for any ethical violations that may be encountered, and that this study has not been evaluated in any academic publication environment other than Sakarya University Journal of Science.

REFERENCES

[1] M. Dreidy, H. Mokhlis and Saad Mekhilef, "Inertia response and frequency control techniques for renewable energy sources: A review." Renewable and Sustainable Energy Reviews, vol 69, pp. 144-155, March 2017, doi: 10.1016/j.rser.2016.11.170

[2] S. You et al., "Impact of high PV penetration on U.S. eastern interconnection frequency response," 2017 IEEE Power & Energy Society General Meeting, Chicago, IL, 2017, pp. 1-5, doi: 10.1109/PESGM.2017.8273793.

[3] H. Patel and V. Agarwal, "MATLAB-Based Modeling to Study the Effects of Partial Shading on PV Array Characteristics," in IEEE Transactions on Energy Conversion, vol. 23, no. 1, pp. 302-310, March 2008, doi: 10.1109/TEC.2007.914308.

[4] R. Shah, N. Mithulananthan, R. C. Bansal and V. K. Ramachandaramurthy, "A review of key power system stability challenges for large-scale PV integration." Renewable and Sustainable Energy Reviews, vol 41, pp. 1423-1436, January 2015, doi: 10.1016/j.rser.2014.09.027.

[5] P. Kundur et al., "Definition and classification of power system stability IEEE/CIGRE joint task force on stability terms and definitions," in IEEE Transactions on Power Systems, vol. 19, no. 3, pp. 1387-1401, Aug. 2004, doi: 10.1109/TPWRS.2004.825981.

[6] Z. Conka, V. Kohan and M. Kolcun, "Impact of photovoltaic power plants on voltage stability of power system," 2019 International IEEE Conference and Workshop in Óbuda on Electrical and Power Engineering (CANDO-EPE), Budapest, Hungary, 2019, pp. 79-84, doi: 10.1109/CANDO-EPE47959.2019.9111014.

[7] G. Lammert, D. Premm, L. D. P. Ospina, J. C. Boemer, M. Braun and T. Van Cutsem, "Control of Photovoltaic Systems for Enhanced Short-Term Voltage Stability and Recovery," in IEEE Transactions on Energy

Conversion, vol. 34, no. 1, pp. 243-254, March 2019, doi: 10.1109/TEC.2018.2875303.

[8] G. Lammert et al., "Impact of fault ride-through and dynamic reactive power support of photovoltaic systems on short-term voltage stability," 2017 IEEE Manchester PowerTech, Manchester, 2017, pp. 1-6, doi: 10.1109/PTC.2017.7980926.

[9] Y. Xue, M. Manjrekar, C. Lin, M. Tamayo and J. N. Jiang, "Voltage stability and sensitivity analysis of grid-connected photovoltaic systems," 2011 IEEE Power and Energy Society General Meeting, Detroit, MI, USA, 2011, pp. 1-7, doi: 10.1109/PES.2011.6039649.

[10] K. Kawabe, Y. Ota, A. Yokoyama and K. Tanaka, "Short-term voltage stability improvement by active and reactive power control using advanced fault ride-through capability of photovoltaic systems," 2016 Power Systems Computation Conference (PSCC), Genoa, 2016, pp. 1-8, doi: 10.1109/PSCC.2016.7540842.

[11] E. Youssef, R. M. El Azab and A. M. Amin, "Comparative study of voltage stability analysis for renewable energy grid-connected systems using PSS/E," SoutheastCon 2015, Fort Lauderdale, FL, 2015, pp. 1-6, doi: 10.1109/SECON.2015.7133012.

[12] Y. Liu, W. Qin, X. Han and P. Wang, "Modelling of large-scale wind/solar hybrid system and influence analysis on power system transient voltage stability," 2017 12th IEEE Conference on Industrial Electronics and Applications (ICIEA), Siem Reap, 2017, pp. 477-482, doi: 10.1109/ICIEA.2017.8282892.

[13] P. Kayal and C. K. Chanda, "Placement of wind and solar based DGs in distribution system for power loss minimization and voltage stability improvement." International Journal of Electrical Power & Energy Systems, vol 53, pp. 795-809, December 2013, doi: 10.1016/j.ijepes.2013.05.047

[14] X. Chen, Y. Cui, X. Wang and S. Li, "Research of low voltage ride through control strategy in photovoltaic(PV) grid," 2017 Chinese Automation Congress (CAC), Jinan, 2017, pp. 5146-5150, doi: 10.1109/CAC.2017.8243693.

[15] S. Eftekharnejad, V. Vittal, G. T. Heydt, B. Keel and J. Loehr, "Impact of increased penetration of photovoltaic generation on power systems," in IEEE Transactions on Power Systems, vol. 28, no. 2, pp. 893-901, May 2013, doi: 10.1109/TPWRS.2012.2216294.

[16] B. Tamimi, C. Cañizares and K. Bhattacharya, "System Stability Impact of Large-Scale and Distributed Solar Photovoltaic Generation: The Case of Ontario, Canada," in IEEE Transactions on Sustainable Energy, vol. 4, no. 3, pp. 680-688, July 2013, doi: 10.1109/TSTE.2012.2235151.

[17] Y. T. Tan and D. S. Kirschen, "Impact on the Power System of a Large Penetration of Photovoltaic Generation," 2007 IEEE Power Engineering Society General Meeting, Tampa, FL, 2007, pp. 1-8, doi: 10.1109/PES.2007.385563.

[18] S. Soni, G. G. Karady, M. Morjaria and V. Chadliev, "Comparison of full and reduced scale solar PV plant models in multi-machine power systems," 2014 IEEE PES T&D Conference and Exposition, Chicago, IL, 2014, pp. 1-5, doi: 10.1109/TDC.2014.6863299.

[19] J. Dai, Y. Tang, Y. Xu and Q. Yan, "Reactive Power Optimization Coordinated Control Strategy of the Large-Scale PV Power Station," 2018 International Conference on Power System Technology (POWERCON), Guangzhou, 2018, pp. 1632-1637, doi: 10.1109/POWERCON.2018.8602233.

[20] Y. Zhou, Y. Li, D. Yu and J. Liu, "MPPT-considered detailed models of large-scale photovoltaic plants and its application in power system small-signal stability analysis," 2016 19th International Conference on Electrical Machines and Systems (ICEMS), Chiba, 2016, pp. 1-6.

[21] WECC Renewable Energy Modeling Task Force, "Central station photovoltaic power plant model balidation guideline" March 2015. [Online]. Available: https://www.wecc.org/Reliability/150318 WECC Pv Plant Model Val Guide Rev2.pdf

[22] J. Machowski, Z. Lubosny, J. W. Bialek and J. R. Bumby, "Voltage Stability" in Power System Dynamics: Stability and Control, John Wiley & Sons, 2020.

[23] DigSILENT, "Digsilent Powerfactory," 2020.

[24] M. Ding, Z. Xu, W. Wang, X. Wang, Y. Song and D. Chen, "A review on China′ s large-scale PV integration: Progress, challenges and recommendations." Renewable and Sustainable Energy Reviews, vol 53, pp. 639-652, January 2016, doi: 10.1016/j.rser.2015.09.009

[25] WECC Renewable Energy Modeling Task Force, "WECC solar plant dynamic modeling guidelines," April 2014. [Online]. Available: https://www.wecc.org/Reliability/WECC Solar Plant Dynamic Modeling Guidelines.pdf

[26] G. Lammert, Modelling, "Control and Stability Analysis of Photovoltaic Systems in Power System Dynamic Studies" Energy Management and Power System Operation vol. 9. Kassel Univ. Press GmbH, 2019.

[27] J. Keller and B. Kroposki, "Understanding fault characteristics of inverter-based distributed energy resources" No. NREL/TP-550-46698. National Renewable Energy Lab.(NREL), Golden, CO (United States), January 2010.

[28] WECC Renewable Energy Modeling Task Force, "WECC PV plant power flow modeling guidelines," August 2010. [Online.] Available: https://www.wecc.org/Reliability/WECC PV Plant Power Flow Modeling Guidelines - August 2010.pdf

[29] WECC Renewable Energy Modeling Task Force, "WECC solar PV dynamic model specification" September 2012. [Online]. Available: https://www.wecc.org/Reliability/WECC Solar PV Dynamic Model Specification - September 2012.pdf

SAKARYA ÜNİVERSİTESİ
FEN BİLİMLERİ ENSTİTÜSÜ DERGİSİ

Sakarya University Journal of Science
SAUJS

e-ISSN: 2147-835X | Founded: 1997 | Period: Bimonthly | Publisher: Sakarya University
http://www.saujs.sakarya.edu.tr/en/

Title: Buck-type Single-phase AC-AC Active Tracking Voltage Regulator Controlled by an Enhanced Hybrid Control Method

Authors: Faruk YALÇIN, Felix HIMMELSTOSS

Recieved: 2021-05-07 21:40:55

Accepted: 2021-06-17 15:11:33

Article Type: Research Article

Volume: 25
Issue: 4
Month: August
Year: 2021
Pages: 926-937

How to cite
Faruk YALÇIN, Felix HIMMELSTOSS; (2021), Buck-type Single-phase AC-AC Active Tracking Voltage Regulator Controlled by an Enhanced Hybrid Control Method. Sakarya University Journal of Science, 25(4), 926-937, DOI: https://doi.org/10.16984/saufenbilder.900419
Access link
http://www.saujs.sakarya.edu.tr/en/pub/issue/64755/900419

Sakarya University Journal of Science 25(4), 926-937, 2021

Buck-type Single-phase AC-AC Active Tracking Voltage Regulator Controlled by an Enhanced Hybrid Control Method

Faruk YALÇIN*[1], Felix HIMMELSTOSS[2]

Abstract

In this paper, a single-phase switch-mode buck-type AC-AC voltage regulator is presented with reduced numbers of elements which are used in the topology. Apart from similar studies in the literature, a new hybrid control method which is structured by the closed-loop PID controller and a new enhanced feedforward controller is used for the control of the regulator. The hybrid controller improves the active tracking capability of the reference to achieve an output voltage as close to the sine-wave with high quality. The input AC voltage may be an ideal sine wave or it may include harmonics. Both simulation and experimental tests are applied for the proposed regulator controlled by this control method. The experimental set-up for the regulator is designed for 0-200 Vp input voltage (50 Hz), 0-100 Vp output voltage, and 0.6 kW output power. The results proved the capability of the proposed buck-type switch-mode regulator to achieve the requested output voltage as near as possible to sine wave. The obtained output voltages for different load conditions and input-output parameters have less than 5% THD (total harmonic distortion) and high quality.

Keywords: AC-AC regulator, active tracking, buck converter, single-phase, harmonics

1. INTRODUCTION

Increasing demand for electrical power causes many problems in power systems such as decreasing power quality for the AC consumers. AC devices must be supplied by an alternating supply voltage between a magnitude band that is generally very narrow for most of the sensitive devices. Various loadings in the distribution systems effect voltage sags/swells which are the main quality problem for the AC consumers. Also in some specific applications, some AC consumers require adjustable voltage magnitudes different to the network voltage levels. Thus, AC voltage regulation becomes so important, that studies are published in increasing number.

The regulation of voltage variations can be provided by the FACTS devices, such as voltage sag supporters [1,2], DVRs (dynamic voltage restorers) [3,4], voltage sag/swell compensators [5,6], and voltage conditioners [7,8] in distribution systems. The mentioned devices provide voltage regulation of the distribution line

* Corresponding author: farukyalcin@sakarya.edu.tr
[1] Sakarya University Of Applied Sciences, Faculty Of Technology, Department Of Mechatronics Engineering, Sakarya, Turkey.
ORCID: https://orcid.org/0000-0003-2672-216X
[2] Fachhochschule Technikum Wien, Höchstädtplatz 6, 1200 Wien.
E-Mail: felix.himmelstoss@technikum-wien.at
ORCID: https://orcid.org/0000-0001-8482-2295

to reach the desired network voltage levels. In this way, supply of the AC consumers which are connected to the distribution buses by the determined network voltages is provided. Thus, individual voltage regulation of each independent AC consumer cannot be possible in this way. On the other hand, these regulators based on FACTS devices require a coupling transformer in addition to a VSI (voltage source inverter). The VSIs, which are incorporated into the mentioned FACTS devices-based regulators, can be structured by either an AC-DC-AC converter or a DC-AC converter. VSIs based on a DC-AC converter demand capacitors and batteries which are independent external DC storage systems. Thus, robust compensation of voltage sags/swells cannot be provided by VSIs based on a DC-AC converter for long terms. Besides, the capabilities of the compensation are limited because of the external storage unit capacities. AC-DC-AC converter-based VSIs do not require any external storage systems, because these converters include an AC-DC structure in the converter topologies. Despite the mentioned advantage of AC-DC-AC converters, additional AC-DC sub-units cause increased losses of the FACTS devices.

Voltage regulation of AC consumers can be provided by standalone AC-DC-AC based VSIs mentioned above instead of using the FACTS-based voltage regulators [9,10]. On the other hand, individual voltage regulation of each AC consumer can be achieved from the constant distribution voltage level in this way. But, the AC-DC stage of these VSIs causes loss increase of the complete AC-AC conversion.

As mentioned above, direct VSI applications and the FACTS devices-based regulators have disadvantages and complexity problems. So, the direct AC-AC conversion method becomes the best solution. For this aim, various kinds of direct AC-AC regulators are studied in the literature. PWM-based traditional AC-AC choppers emerge as the simple and basic solution for the AC-AC regulation [11]. But these AC regulators cause high-level harmonics at the output, because of the chopping structure of the input sine-wave. Thus, these chopper regulators require additional filtering units, such as coupling transformers or passive filters. Buck [12-14], boost [15,16], and buck-boost [17,18] type switch-mode AC-AC regulators are studied increasingly for AC regulation in the literature in recent years. These switch-mode regulators do not need additional filtering units as in PWM AC choppers because of the switch-mode operation. Thus, obtaining close to sine wave output voltages with low THD can be achieved. These regulators have also a lower complex topology. The mentioned switch-mode AC-AC regulators are applied successfully to the AC regulation applications in the literature. But these studies have the lack that applying input AC voltages including harmonics is absent in these studies. In the literature, the existing similar studies consider pure sine-wave input AC voltages. But, many AC consumers may be supplied with non-sinusoidal voltages with different harmonics because of various distortions in application and in the mains. So, harmonic elimination capability of an AC-AC regulator is required in addition to the AC voltage regulation capability. According to the standards, supplying of the AC customers through high-quality AC voltages with THD less than 5% is so important [19].

In this study, a single-phase buck-type active tracking AC-AC voltage regulator is presented. Also, an improved control method is proposed for the active tracking of the desired reference output sine-wave. The presented topology (and other ones) of the regulator and the control method are patented by the co-author of this study [20]. The presented topology of the regulator incorporates moderate numbers of components, just one inductor, one capacitor, and four active switches. The buck-type structure of the presented regulator enables the achievement of a wide range of output voltage amplitude lower than the input voltage amplitude. Apart from similar studies in the literature, the proposed control method is a novel hybrid control method composed of a closed-loop PID controller and a new feedforward controller. By this way, active tracking of the reference sine-wave output voltage is improved to achieve nearly close to sine-wave output voltage in the case that the input voltage is a pure sine or not. The presented regulator and control method is tested by both simulation and experimental studies. The

obtained results demonstrate that the proposed buck type switch-mode regulator has the ability of achieving the requested output voltage with reduced harmonics under 5% THD for different load conditions and input-output parameters.

2. THE PROPOSED SINGLE-PHASE BUCK AC-AC REGULATOR

This section describes the proposed buck-type single-phase AC-AC regulator topology, as well as the regulator's operation procedure and dynamic analysis.

2.1. The Regulator Topology

Figure 1 depicts the main circuit of the proposed buck-type single-phase AC-AC regulator [20].

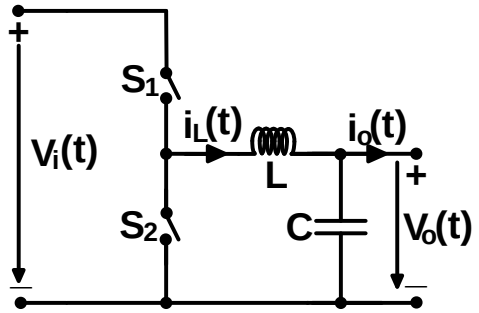

Figure 1 General topology of the proposed buck-type single-phase AC-AC regulator

V_i, V_o, L, and C represent input AC voltage, output AC voltage, inductor and capacitor, respectively in Figure 1. S_1 and S_2 are the bidirectional active switches. These bidirectional active switches are realized by MOSFETs in this study. Thus, the proposed regulator circuit with MOSFETs can be shown in Figure 2.

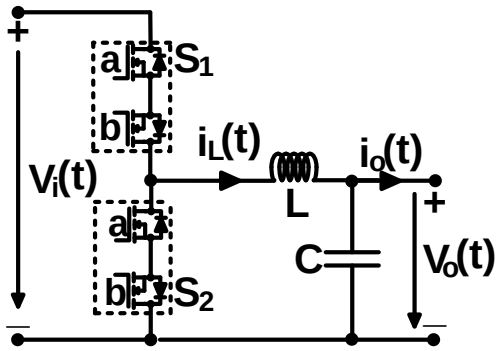

Figure 2 The proposed buck-type single-phase AC-AC regulator with MOSFETs

2.2. The Regulator Operation Procedure

The proposed single-phase AC-AC regulator's operation is based on the well-known conventional buck converter. Instant input voltage $V_i(t)$ is bucked as $V_o(t)$ at the output depending on the control of PWM duty ratio (d) for S_1. Thus, the output voltage is obtained as an AC voltage with the same polarity as the input voltage, but with lower amplitude value than at the input. S_2 acts as supplementary switch of S_1. S_2 is turned off when S_1 is turned on. In this stage, V_i supplies the inductor, the capacitor and the output load. S_2 is turned on when S_1 is turned off. In this stage, the pre-energized inductor supplies both the capacitor and the output load.

The polarity of V_i changes in each half period, because the input voltage V_i is an alternating voltage. So, the on-off states of the sub-active switches of the bidirectional active switches S_1 and S_2 change for each half-period of the input voltage depending on the polarity. The control of the active switches S_1 and S_2 is summarized in Table 1.

Table 1 Control signal of MOSFETs used in Figure 2 as part of the bidirectional active switches S_1 and S_2

State	S_1				S_2			
	Positive Half-Wave Stage		Negative Half-Wave Stage		Positive Half-Wave Stage		Negative Half-Wave Stage	
	S_{1a}	S_{1b}	S_{1a}	S_{1b}	S_{2a}	S_{2b}	S_{2a}	S_{2b}
ON	on	off	off	on	off	on	on	off
OFF	off	off	off	off	off	off	off	off

The MOSFETs' switching pattern can be seen in Figure 3.

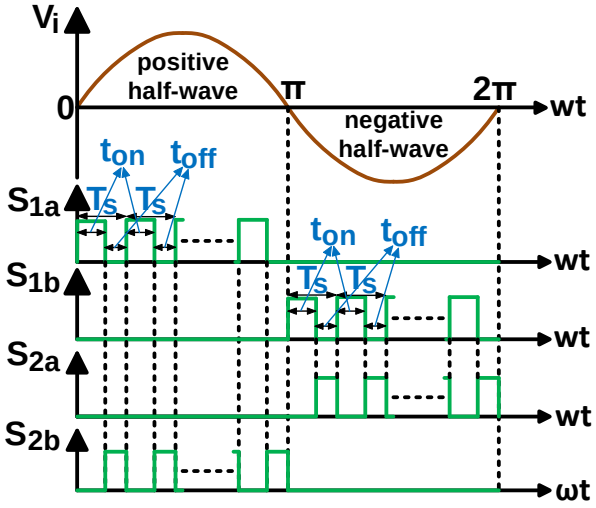

Figure 3 The switching pattern of the MOSFETs

In Figure 4, the equivalent sub-circuits of the proposed regulator topology, which is shown in Figure 2, are given according to the proper control of the mentioned active switches for one cycle sine-wave input voltage.

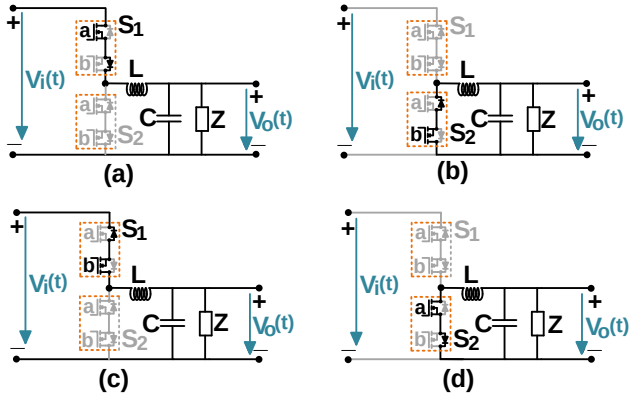

Figure 4 The equivalent sub-circuits of the proposed buck-type regulator *(a) Positive half-wave output stage, on mode (S_1 is on, S_2 is off), (b) Positive half-wave output stage, off mode (S_1 is off, S_2 is on), (c) Negative half-wave output stage, on mode (S_1 is on, S_2 is off), (d) Negative half-wave output stage, off mode (S_1 is off, S_2 is on)*

Thus, producing of the output voltage for one cycle in the proposed regulator operation can be summarized in two main stages by Figure 3 and Figure 4 as follows.

Stage 1 ($0 \le wt < \pi$): Input AC voltage is in the positive half-wave in this stage. While the PWM on-stage of S_1 (S_2 is off), S_{1a} is turned on, S_{1b} is turned off and both S_{2a} and S_{2b} are turned off. While the PWM off-stage of S_1 (S_2 is on), both S_{1a} and S_{1b} are turned off, S_{2a} is turned off, and S_{2b} is turned on. The desired positive half sine-wave output voltage is produced by the input voltage based on the continuous proper control of d, which is the PWM duty ratio of S_1.

Stage 2 ($\pi \le wt < 2\pi$): Input AC voltage is in the negative half-wave in this stage. While the PWM on-stage of S_1 (S_2 is off), S_{1b} is turned on, S_{1a} is turned off and both S_{2a} and S_{2b} are turned off. While the PWM off-stage of S_1 (S_2 is on), both S_{1a} and S_{1b} are turned off, S_{2a} is turned on, and S_{2b} is turned off. The desired negative half sine-wave output voltage is produced from the input voltage based on the continuous proper control of d, which is the PWM duty ratio of S_1.

2.3. The Regulator's Dynamic Analysis

In this section, the detailed dynamic analysis of the proposed buck-type single-phase AC-AC regulator is presented. In order to provide reliable analysis for real-time applications, real parasitic effects of the elements used in the topology are taken into account in the analysis.

In Figure 5, the equivalent circuits of the proposed regulator for the positive half-wave input stage are demonstrated. In the given equivalent circuit the selected MOSFETs are identical.

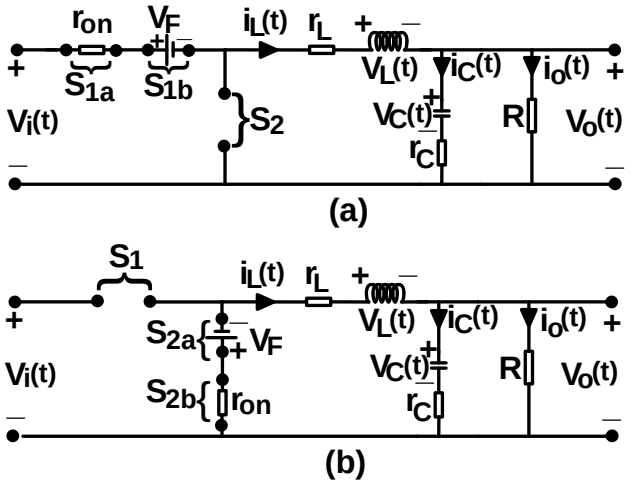

Figure 5 The positive half-wave stage equivalent circuits of the regulator *(a) on-mode – S_1 is turned on and S_2 is turned off, (b) off-mode – S_1 is turned off and S_2 is turned on*

The symbols i_o, i_L, i_C, V_L, V_C, V_F, r_{on}, r_L, r_C, and R represent the output current, inductor current, capacitor current, inductor voltage, capacitor

voltage, forward biasing voltage of the MOSFET's anti-parallel diode, on-resistance of the MOSFET, equivalent series resistance (ESR) of the inductor, ESR of the capacitor, and output load resistance, respectively in Figure 5.

The dynamic analysis of the regulator can be obtained for the positive half-wave input stage from Figure 5. As seen in Figure 5, the dynamic equations for the state variables inductor current and output voltage are obtained for the two modes: on-mode and off-mode.

On-mode (S_1 is on and S_2 is off): For this mode, the state equations for the inductor current and the output voltage can be determined by Figure 5*a*, respectively as below.

$$\frac{di_L(t)}{dt} = -\frac{1}{L}\left(r_L + r_{on}\right)i_L(t) - \frac{1}{L}V_o(t) + \frac{1}{L}\left[V_i(t) - V_F\right] \tag{1}$$

$$\frac{dV_o(t)}{dt} = \frac{R}{R+r_C}\left[\frac{1}{C} - \frac{r_C}{L}\left(r_L + r_{on}\right)\right]i_L(t) - \frac{R}{R+r_C}\left[\frac{r_C}{L} + \frac{1}{RC}\right]V_o(t) + \frac{r_C R}{\left(R+r_C\right)L}\left[V_i(t) - V_F\right] \tag{2}$$

Off-mode (S_1 is off and S_2 is on): For this mode, the state equations for the inductor current and the output voltage can be determined by Figure 5*b*, respectively as below.

$$\frac{di_L(t)}{dt} = -\frac{1}{L}\left(r_L + r_{on}\right)i_L(t) - \frac{1}{L}V_o(t) - \frac{1}{L}V_F \tag{3}$$

$$\frac{dV_o(t)}{dt} = \left(\frac{R}{R+r_C}\right)\left[\frac{1}{C} - \frac{r_C}{L}\left(r_L + r_{on}\right)\right]i_L(t) - \left(\frac{R}{R+r_C}\right)\left(\frac{r_C}{L} + \frac{1}{RC}\right)V_o(t) - \frac{r_C R}{\left(R+r_C\right)L}V_F \tag{4}$$

The state-space model equation of the on-mode can be achieved by (1) and (2) as below,

$$\begin{bmatrix}\dot{i}_L(t)\\ \dot{V}_o(t)\end{bmatrix} = \begin{bmatrix} -\frac{1}{L}\left(r_L + r_{on}\right) & -\frac{1}{L} \\ \frac{R}{R+r_C}\left[\frac{1}{C} - \frac{r_C}{L}\left(r_L + r_{on}\right)\right] & -\frac{R}{R+r_C}\left[\frac{r_C}{L} + \frac{1}{RC}\right]\end{bmatrix}\begin{bmatrix}i_L(t)\\ V_o(t)\end{bmatrix} + \begin{bmatrix}\frac{1}{L} & -\frac{1}{L}\\ \frac{R}{R+r_C}\frac{r_C}{L} & -\frac{R}{R+r_C}\frac{r_C}{L}\end{bmatrix}\begin{bmatrix}V_i(t)\\ V_F\end{bmatrix} \tag{5}$$

The state-space model equation of the off-mode can be achieved by (3) and (4) as below,

$$\begin{bmatrix}\dot{i}_L(t)\\ \dot{V}_o(t)\end{bmatrix} = \begin{bmatrix} -\frac{1}{L}\left(r_L + r_{on}\right) & -\frac{1}{L} \\ \frac{R}{R+r_C}\left[\frac{1}{C} - \frac{r_C}{L}\left(r_L + r_{on}\right)\right] & -\frac{R}{R+r_C}\left(\frac{r_C}{L} + \frac{1}{RC}\right)\end{bmatrix}\begin{bmatrix}i_L(t)\\ V_o(t)\end{bmatrix} + \begin{bmatrix}0 & -\frac{1}{L}\\ 0 & -\frac{R}{R+r_C}\frac{r_C}{L}\end{bmatrix}\begin{bmatrix}V_i(t)\\ V_F\end{bmatrix} \tag{6}$$

The above dynamic analysis is done for an input voltage during the positive half-wave. If a similar dynamic analysis is performed for the negative half-wave, the same state-space equations as given in (5) and (6) are obtained. So, this means that the state-space equations (5) and (6) are valid for both positive and negative half-wave input cases.

Thus, the small signal transfer function between the output voltage and PWM duty ratio can be obtained by (5) and (6) as follows.

$$G_{buck}(s) = \frac{\hat{V}_o(s)}{d(s)} = \frac{gs + \left(ag + cf\right)}{s^2 + \left(a+e\right)s + \left(ae - bc\right)} \tag{7}$$

The coefficients used in (7) are described as follows.

$$a = \frac{\left(r_L + r_{on}\right)}{L} \tag{8}$$

$$b = -\frac{1}{L} \tag{9}$$

$$c = \frac{R}{R + r_C}\left[\frac{1}{C} - \frac{r_C}{L}\left(r_L + r_{on}\right)\right] \tag{10}$$

$$e = \frac{R}{R + r_C}\left[\frac{r_C}{L} + \frac{1}{RC}\right] \tag{11}$$

$$f = \frac{\bar{V}_i}{L} \tag{12}$$

$$g = \frac{r_C R}{\left(R + r_C\right)L}\bar{V}_i \tag{13}$$

In (12)-(13), $\bar{V}_i$ represents the input voltage at the operating point.

3. THE PROPOSED HYBRID CONTROL METHOD

The proposed hybrid control method for controlling the proposed AC-AC regulator is presented in this section. The general control diagram of the proposed regulator is shown in Figure 6.

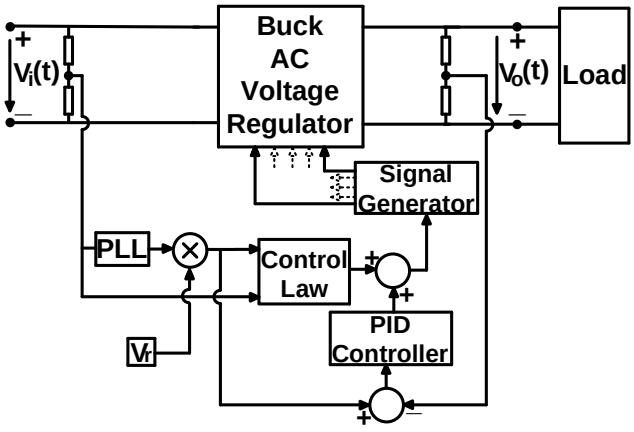

Figure 6 The general control diagram of the proposed regulator

The frequency of the input AC voltage is determined by the PLL, and the magnitude of the reference output AC voltage is described by V_r in Figure 6. Thus, the requested sine-wave reference output voltage can be defined as follows,

$$V_{ref}(wt) = V_r \sin wt \ . \tag{14}$$

The proposed hybrid controller is structured by two main units as seen in Figure 6. One of these units is the traditional closed-loop PID controller. The PID controller eliminates the error between the real output voltage and the reference output voltage, while satisfying the response performance according to the design criteria. The new developed feedforward controller, referred to as "control law (CL)" in Figure 6, is the other component of the hybrid controller. The CL has an open-loop controller structure and produces a PWM duty ratio according to the topology parameters as follows.

$$d_{CL}(wt) = \sqrt{\frac{2L\left|V_r \sin wt\right|\left(\left|V_r \sin wt\right| + V_F\right)}{\left|V_i(wt)\right|\left(\left|V_i(wt)\right| - \left|V_r \sin wt\right| - V_F\right)T_S R}} \tag{15}$$

In (15), T_S defines the PWM switching period. The PWM duty ratio produced by the CL as in (15) cannot directly provide the desired PWM duty ratio for achieving the reference output voltage. However, it will generate a duty ratio that is close to the actual one. As shown in (15), the duty ratio generated by the CL has a static structure which can be produced in a fast manner. Thus, the PID controller is supported by the CL to achieve the desired operating duty ratio with an improved response performance. Thus, the proposed hybrid control method ensures efficient and accurate active tracking of the reference output voltage to achieve sine-wave output voltage as close as possible and with low THD. Consequently, the desired operating PWM duty ratio is achieved by the PID controller and the CL which are part of the hybrid control method as follows.

$$d(wt) = d_{PID}(wt) + d_{CL}(wt) \tag{16}$$

In this paper, discrete-time control is selected for the control of the regulator operation. Thus, the regulator's control block diagram based on the proposed hybrid control method can be demonstrated in Figure 7.

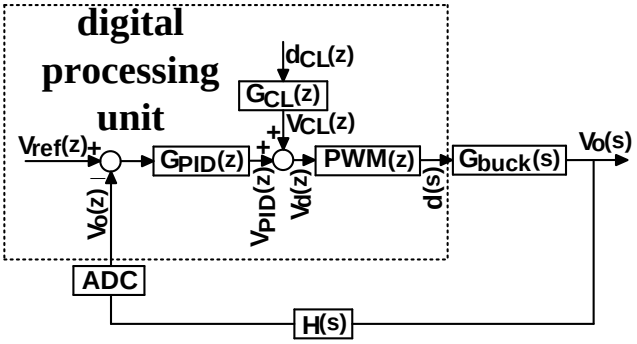

Figure 7 The discrete-time control block diagram based on the proposed hybrid control technique for the buck-type regulator

The relations between the control signals and the transfer functions of the discrete time control block diagram can be derived from Figure 7 as follow.

$$G_{CL}(z) = \frac{1}{PWM(z)} \tag{17}$$

$$V_d(z) = V_{CL}(z) + V_{PID}(z) \tag{18}$$

$$d(z) = V_d(z).PWM(z) \tag{19}$$

The transfer function of the discrete PID controller is defined in this paper as below,

$$G_{PID}(z) = K_P + K_I \frac{z}{z-1} + K_D \frac{z-1}{z} \tag{20}$$

4. THE RESULTS OF THE STUDY

In this section, the design steps, the simulation test results and the experimental test results of the proposed regulator study are presented.

4.1. The Design Parameters of the Regulator Circuit and the Control Method

A laboratory set-up is built for the proposed regulator's real-time experimental application. The set-up is designed for 0-200 Vp input voltage (50 Hz), 0-100 Vp output voltage, and 0.6 kW output power. IXFK98N50P3 type n-channel, high-speed, low on-resistance MOSFETs (V_{DSS}=500 V, r_{on}=50 mΩ, I_D=98 A, V_F=1.5 V) are selected for the active switches in the set-up topology. The values of the switching frequency, the inductor and the capacitor for the regulator circuit are determined as given in Table 2.

Table 2 The selected values of the capacitor, inductor and switching frequency

Switching Frequency f_s (kHz)	Capacitor		Inductor	
	C (μF)	r_C (mΩ)	L (μH)	r_L (mΩ)
50	3.3	180	47	130

The determined operating point parameters which are used for the design of the discrete time PID controller are shown in Table 3.

Table 3 The determined operating point parameters of the regulator operation

$\bar{V}_i$ (V)	$\bar{D}$	$\bar{V}_o$ (V)	R (Ω)
70	0.5	35	50

The parameters of the PID controller defined in (20) are achieved through the design and performance criteria as follows.

$$K_P = -0.124, \quad K_I = 0.052, \quad K_D = 0.0086 \tag{21}$$

4.2. The Simulation Studies

In order to validate the theoretical proposals of the study, simulation tests are applied to the proposed converter with the proposed hybrid control method.

Three different simulation test cases given in Table 4 are applied to the regulator system in MATLAB Simulink. The wave form test results obtained from simulation studies are given in Figures 8-10. The detailed numerical results of the simulation tests for the output are also presented in Table 5. In Table 5, THD_V and THD_I determine the THD values for voltage and current, respectively.

As seen from Figures 8-10 and Table 5, the proposed buck-type single-phase AC-AC regulator can provide the desired reference AC sine-wave voltages as close as possible and with low THD levels under 5% even in the case that the input AC voltages have harmonic components. Thus, both the wave form results in Figures 8-10 and the numerical results in Table 5

prove the accuracy and efficiency of the proposed hybrid control method for the active tracking of the reference output voltages.

Table 4 Test cases for the simulation tests

Test Cases No	Vi	Output Load Z	Desired output fundamental sine-wave voltage V_o (V)
1	120V sine + LOH (f=50Hz)	Resistive R=10Ω	100
2	100V sine + HOH (f=50Hz)	Inductive R=5Ω, L=47mH	80
3	80V sine + fluct. (f=50Hz)	Capacitive R=10Ω, C=1mF	50
fluct.: fluctuations, HOH: high order harmonics, LOH: low order harmonics			

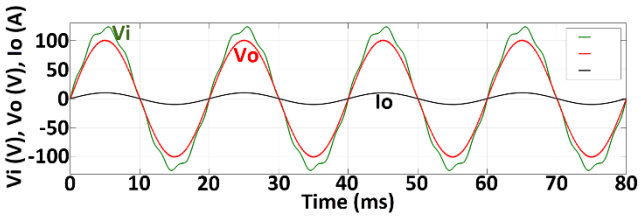

Figure 8 The simulation results for test case-1

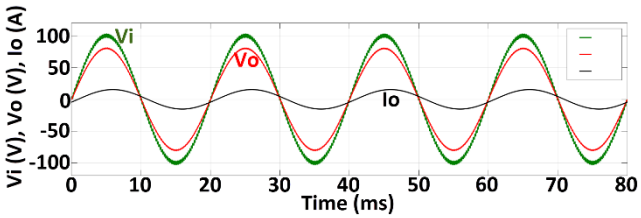

Figure 9 The simulation results for test case-2

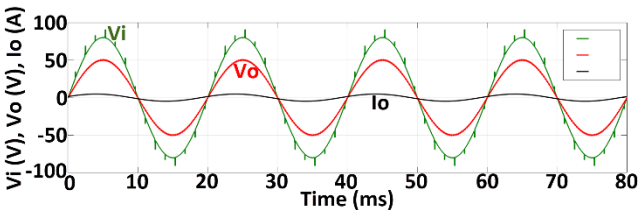

Figure 10 The simulation results for test case-3

Table 5 The obtained numerical simulation results of the test cases

Test Case No	Obtained Fundamental V_o (V)	THD_V (%)	THD_I (%)
1	100.3	2.01	2.01
2	80.2	1.97	1.91
3	50.1	1.99	2.11

4.3. The Experimental Studies

In order to validate the real-time practical application of the study, experimental tests are applied to the proposed AC/AC buck converter with the proposed hybrid control method. The experimental set-up of the regulator system is given in Figure 11.

Figure 11 The built experimental laboratory set-up of the regulator system

Three different experimental test cases given in Table 6 are applied to the experimental set-up of the regulator system. The wave form test results obtained from experimental studies are given in Figures 12-14. The detailed numerical results of the experimental tests for the output are also presented in Table 7.

As seen from Figures 12-14 and Table 7, the proposed buck-type single-phase AC-AC regulator can provide the desired reference AC sine-wave voltages experimentally as close as possible with low THD levels under 5%. Thus, both the wave form results in Figures 12-14 and the numerical results in Table 7 prove the accuracy and efficiency of the proposed hybrid control method for the active tracking of the reference output voltages in experiment.

Table 6 Test cases for the experimental tests

Test Cases No	V_i	Output Load-Z	Desired output fundamental sine-wave voltage-V_o (V)
1	100V sine (f=50Hz)	Resistive R=15Ω	70
2	70V sine (f=50Hz)	Inductive R=25Ω, L=10mH	55
3	85V sine (f=50Hz)	Capacitive R=20Ω, C=0.33mF	40

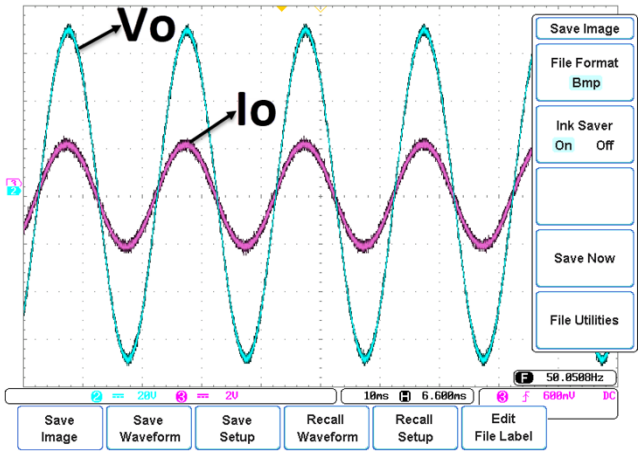

Figure 12 The experimental results for test case-1 (V/div=A/div for I_o)

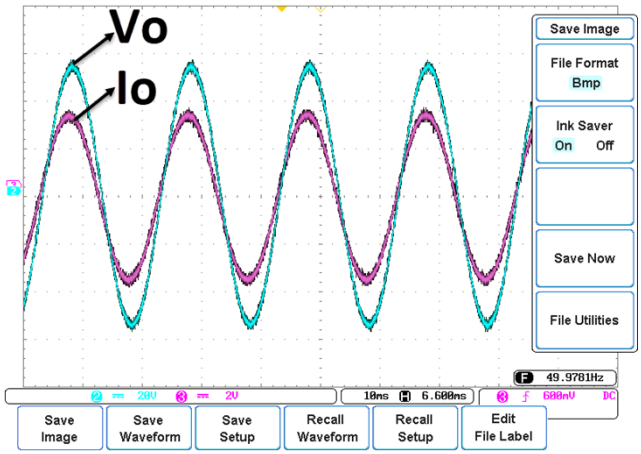

Figure 13 The experimental results for test case-2 (V/div=A/div for I_o)

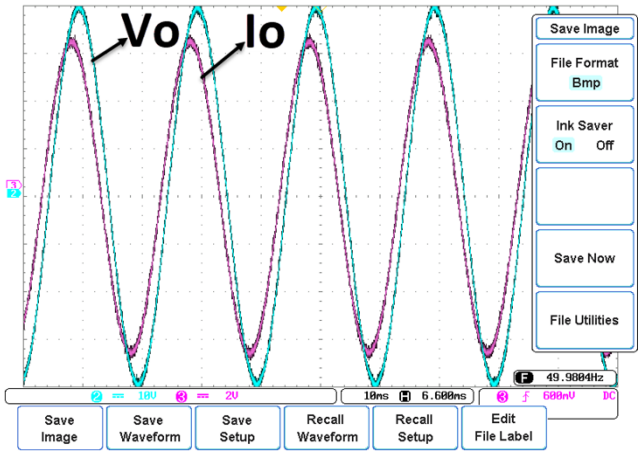

Figure 14 The experimental results for test case-3 (V/div=A/div for I_o)

Table 7 The obtained numerical experimental results of the test cases

Test Case No	Obtained Fundamental V_o (V)	THD_V (%)	THD_I (%)
1	69.8	2.19	2.15
2	55.2	2.14	2.06
3	40.1	2.08	2.21

In order to prove the efficiency of the proposed hybrid control technique for active tracking of the reference output voltage, a comparative test study is performed. In this comparative test study, the proposed hybrid control technique and the standalone PID control are applied to the proposed regulator separately for the experimental test case-2. The achieved output voltage waveforms for the mentioned two separate applications are shown together in Figure 15. The comparative numerical output THD results of the mentioned test cases are also given in Table 8.

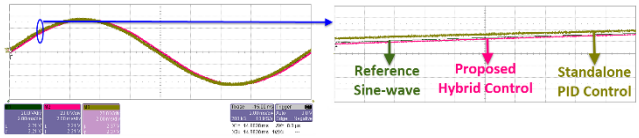

Figure 15 Comparative output voltage V_o wave form of the proposed hybrid control and the standalone PID control for test case-2 (20V/div, 2ms/div)

As can be seen from Figure 15, active tracking of the reference output sine-wave voltage is provided by the proposed hybrid control technique better than with the traditional PID control. So, this proves that the developed CL supports the PID controller and improves the active tracking capability. The results of the output THD are given in Table 8 also shows the capability of the proposed hybrid control technique to achieve a better sine-wave output voltage with high quality and low THD values lower than 5%.

Table 8 Comparative THD results for the proposed hybrid control and the standalone traditional PID control in the experimental test cases

Test Case No	THD (%) results of the proposed hybrid control method		THD (%) results of the traditional standalone PID control	
	THD_V	THD_I	THD_V	THD_I
1	2.19	2.15	2.31	2.30
2	2.14	2.06	2.27	2.22
3	2.08	2.21	2.22	2.38

The efficiency of the proposed buck-type single-phase regulator is achieved for different output power rates regarding the power rate, which is determined by the design criteria. The regulator's efficiency curve is shown in Figure 16. The proposed regulator provides good enough

efficiency with an average 95%, where the regulator is loaded with above half output loading.

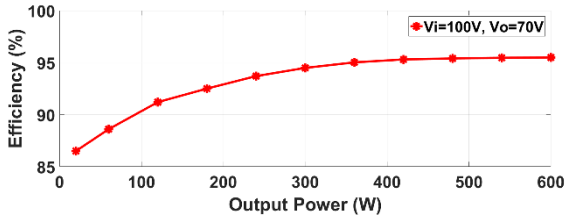

Figure 16 Regulator efficiency curve for different output power rates

5. CONCLUSION

This paper presents a single-phase switch-mode buck-type AC-AC voltage regulator using reduced numbers of elements in the regulator topology. A new hybrid control method composed of a closed-loop PID controller and an enhanced feedforward controller is used for the regulator control, in order to improve the active tracking ability of the reference output voltage to obtain an output voltage as close to the sine-wave with high quality in the case either the input AC voltage is an ideal sine wave or it includes harmonic components. Both simulation and experimental test results prove the ability of the presented switch-mode buck-type regulator to obtain the desired output voltage as close to the ideal sine waveform for different operating conditions with lower than 5% THD.

Acknowledgments

The topology and control theory of the proposed AC regulator in this study are patented by the co-author at the Austrian Patent Office as “Aktive Netzfilter” (patent no: AT 505460 B1, filed 10.07.2007, applied 15.06.2012).

Funding

The authors received no financial support for research and publication of this article.

The Declaration of Conflict of Interest/ Common Interest

No conflict of interest or common interest has been declared by the authors.

Authors' Contribution

The authors contributed equally to the study.

The Declaration of Ethics Committee Approval

The authors declare that this document does not require an ethics committee approval or any special permission.

The Declaration of Research and Publication Ethics

The authors of the paper declare that they comply with the scie The authors of the paper declare that they comply with the scientific, ethical and quotation rules of SAUJS in all processes and declare that Sakarya University Journal of Science and its editorial board have no responsibility for any ethical violations that may be encountered, and that this study has not been evaluated in any academic publication environment other than Sakarya University Journal of Science.

REFERENCES

[1] D. M. Lee, T. G. Habetler, R. G. Harley, T. L. Keister, and J. R. Rostron, “A voltage sag supporter utilizing a PWM-switched autotransformer,” IEEE Transactions on Power Electronics, vol. 22, no. 2, pp. 626–635, 2007.

[2] S. Subramanian and M. K. Mishra, “Interphase AC-AC topology for voltage sag supporter,” IEEE Transactions on Power Electronics, vol. 25, no. 2, pp. 514–518, 2010.

[3] A. Moghassemi and S. Padmanaban, “Dynamic voltage restorer (DVR): a comprehensive review of topologies, power converters, control methods, and modified configurations,” Energies, vol. 13, no. 16, article number: 4152, 2020.

[4] A. AbuHussein and M. A. H. Sadi, “Fault ride-through capability improvement of grid connected PV system using dynamic

voltage restorer," Electric Power Components and Systems, vol. 48, no. 12-13, pp. 1296–1307, 2020.

[5] J. Kaniewski, P. Szczesniak, M. Jarnut, and G. Benysek, "Hybrid voltage sag/swell compensators a review of hybrid AC/AC converters," IEEE Industrial Electronics Magazine, vol. 9, no. 4, pp. 37–48, 2015.

[6] M. K. Nguyen, Y. C. Lim, and J. H. Choi, "Single-phase z-source-based voltage sag/swell compensator," 2013 Twenty-Eighth Annual IEEE Applied Power Electronics Conference and Exposition, pp. 3138–3142, 2013.

[7] H. Hafezi and R. Faranda, "Dynamic voltage conditioner: a new concept for smart low-voltage distribution systems," IEEE Transactions on Power Electronics, vol. 33, no. 9, pp. 7582–7590, 2018.

[8] R. Faranda, A. Bahrami, and H. Hafezi, "Fault current limiting investigation for a single-phase dynamic voltage conditioner," 2019 IEEE Milan Powertech, 2019.

[9] R. Gupta and A. Kumar, "Control of multi-cell AC/DC and cascaded H-bridge DC/AC-based AC/DC/AC converter," IETE Journal of Research, early access, 2020.

[10] P. D. Singh and S. Gao, "Fuzzy based AC-DC-AC converter controlled micro hydro renewable power generation using parallel asynchronous generators for remote areas," International Journal of Renewable Energy Research, vol. 10, no. 1, pp. 260–273, 2020.

[11] K. Venkatesha, H. A. Vidya, R. Sinha, and G. Jayachitra, "Experimental analysis of symmetrical & asymmetrical PWM based single phase AC chopper for power quality improvement using FPGA real time controller," 2017 International Conference On Smart Grids, Power and Advanced Control Engineering, pp. 267–272, 2017.

[12] Y. B. Wang, P. Wang, G. W. Cai, C. Liu, D. B. Guo, H. W. Zhang, and B. D. Zhu, "An improved bipolar-type AC-AC converter topology based on nondifferential dual-buck PWM AC choppers," IEEE Transactions on Power Electronics, vol. 36, no. 4, pp. 4052–4065, 2021.

[13] S. Kim, D. Jang, H. G. Kim, and H. Cha, "Cascaded dual-buck AC-AC converter using coupled inductors," 2018 International Power Electronics Conference, pp. 2619–2624, 2018.

[14] A. A. Khan, H. Cha, J. W. Baek, J. Kim, and J. Cho, "Cascaded dual-buck AC-AC converter with reduced number of inductors," IEEE Transactions on Power Electronics, vol. 32, no. 10, pp. 7509–7520, 2017.

[15] A. Chakraborty, A. Chakrabarti, and P. K. Sadhu, "Analysis of a full-bridge direct AC-AC boost converter based domestic induction heater," Revue Roumaine Des Sciences Techniques - Serie Electrotechnique Et Energetique, vol. 64, no. 3, pp. 223–228, 2019.

[16] H. Sarnago, O. Lucia, A. Mediano, and J. M. Burdio, "Direct AC-AC resonant boost converter for efficient domestic induction heating applications," IEEE Transactions on Power Electronics, vol. 29, no. 3, pp. 1128–1139, 2014.

[17] H. F. Ahmed, H. Cha, A. A. Khan, and H. G. Kim, "A novel buck-boost AC-AC converter with both inverting and noninverting operations and without commutation problem," IEEE Transactions on Power Electronics, vol. 31, no. 6, pp. 4241–4251, 2016.

[18] A. A. Khan and H. Y. Cha, "A novel highly reliable three-phase buck-boost AC-AC converter," 2016 IEEE Energy Conversion Congress and Exposition, 2016.

[19] F. Yalcin, U. Arifoglu, and I. Yazici, "A new single phase inverter based on buck

converter," Sakarya University Journal of Science, vol. 24, no. 3, pp. 480–486, 2020.

[20] F. Himmelstoss, "Aktive Netzfilter," Austrian Patent, patent no: AT 505460 B1, filed 10 July 2007, applied 15 January 2012.

SAKARYA ÜNİVERSİTESİ
FEN BİLİMLERİ ENSTİTÜSÜ DERGİSİ

Sakarya University Journal of Science
SAUJS

ISSN 1301-4048 | e-ISSN 2147-835X | Period Bimonthly | Founded: 1997 | Publisher Sakarya University | http://www.saujs.sakarya.edu.tr/

Title: Phytochemical and Bioactivity Analysis of Several Methanolic Extracts of Nine Bryophytes Species

Authors: Ebru KOCADAĞ KOCAZORBAZ, Kerem TOK, Hichem MOULAHOUM, Rabia Nur ÜN

Recieved: 2021-01-26 20:17:34

Accepted: 2021-06-17 18:58:30

Article Type: Research Article

Volume: 25
Issue: 4
Month: August
Year: 2021
Pages: 938-949

How to cite
Ebru KOCADAĞ KOCAZORBAZ, Kerem TOK, Hichem MOULAHOUM, Rabia Nur ÜN; (2021), Phytochemical and Bioactivity Analysis of Several Methanolic Extracts of Nine Bryophytes Species. Sakarya University Journal of Science, 25(4), 938-949, DOI: 10.16984/saufenbilder.868944
Access link
http://www.saujs.sakarya.edu.tr/en/pub/issue/64755/868944

Sakarya University Journal of Science 25(4), 938-949, 2021

Phytochemical and Bioactivity Analysis of Several Methanolic Extracts of Nine Bryophytes Species

Ebru KOCADAĞ KOCAZORBAZ[1], Kerem TOK*[1], Hichem MOULAHOUM[1], Rabia Nur ÜN[1]

Abstract

Bryophytes are a class of organisms found all over the globe except the sea. They can grow on different surfaces and are known for their fragrant aromas and strongly hot and bitter taste. Bryophytes have been used in traditional Chinese medicine for the treatment of many pathological conditions. In the current study, we describe the bioactivities present in methanolic extracts obtained from 9 species of bryophytes. Plant samples were dried and extracted in a water/methanol solution which was explored for flavonoid and phenolic content. Afterward, the extracts were analyzed for their potential bioactivities including DPP4 inhibition, metal chelation, antioxidant, and antiglycation activities. Results indicate that the methanolic extracts of each species showed high effectiveness for different bioactivities. The current findings suggest these bryophytes as a promising source of therapeutics against oxidative stress, hypertension, and diabetes.

Keywords: Bryophytes, bioactive molecules, diabetes, antiglycation, DPP-4

1. INTRODUCTION

Bryophytes can be defined as an irregular group that includes three kinds of non-vascular land plants such as the hornworts, liverworts, and mosses. This division contains 1036 genera and about 18,409 species. The most important factor for these plants is the humid environment needed to live. Bryophytes are sometimes completely buried underwater, found on wet floors, humid environments, on soil and rocks, and tree trunks. The antioxidant activity of mosses has been reported to be higher than that of many vegetables. In research, the high antioxidant effect of moss has shown great importance in the preparation of drugs and cosmetic products. On the other hand, moss species have been widely used to treat some diseases owing to their high phenolic content [1]. Bryophytes have been used to treat various diseases such as anti-leukemic activity, wound healing, heart disease, nervous prostration, diarrhea, cold and fever, microbial infectious, angina [2-4]. They are still using for antimicrobial agents, source of antibiotics, used for infections and swellings, growth of hairs, skin ailments, antipyretic, antidote, urinary difficulties [5-7].

Diabetes mellitus (DM) is a multifactorial chronic metabolic disorder that is characterized by deteriorated carbohydrate metabolism. In addition to the metabolic problems of diabetes, long-term exposure to deteriorated metabolites leads to the

* Corresponding author: keremtok_95@hotmail.com.
[1] Ege University Faculty Of Science, Bornova, Izmir, Turkey.
E-Mail: ebru.kocadag.kocazorbaz@ege.edu.tr, hic_moul@hotmail.com, rabia.nur.un@ege.edu.tr.
ORCID: https://orcid.org/0000-0001-5611-5235; https://orcid.org/0000-0002-7244-3949; https://orcid.org/0000-0003-3934-6415; https://orcid.org/0000-0001-7903-9167.

development of microvascular and macrovascular complications including nephropathy, neuropathy, retinopathy, and atherosclerosis. There are two types of diabetes. These are type 1 (insulin-dependent, IDDM) and type 2 (non-insulin-dependent, NIDDM) diabetes mellitus [8]. According to the International Diabetes Federation, there are 463 million diabetics in the world, and it is believed that this number will increase to 700 million in 2045. The number of people exposed to this disease is increasing daily, which makes prevention approaches and new treatment development a necessity. One of the diabetes outcomes is the formation of advanced glycation end products (AGEs) under hyperglycemic conditions. Non-enzymatic glycation occurs between glucose and the amine terminal side of proteins which results in Schiff-base intermediates and eventually forms more stable Amadori compounds that later form AGEs. Accumulation of AGEs causes functional changes in tissue proteins [9]. These AGEs can cause various important diabetic complications such as rheumatoid arthritis, neurodegenerative diseases, cataract, Alzheimer's disease, etc. [10]. For this reason, preventive approaches against AGE formation are of high interest. Hypertension is amongst the most widespread chronic diseases and is a risk factor for coronary heart diseases, congestive heart failure, stroke, and kidney diseases. Hypertension and diabetes are often associated and are risk factors for each other. Hypertension can be treated with antihypertensive medicines and changes in lifestyle [11].

α-glucosidase and α-amylase are enzymes responsible for the hydrolysis of disaccharides, trisaccharides, oligosaccharides, and starch. These enzymes are important for the regulation of blood glucose levels in diabetic patients. Inhibition of these enzymes decreases carbohydrate digestion and delays glucose absorption. The strategy of inhibiting these target enzymes is a key point in obesity and type 2 diabetes treatments [12].

There are approved various reactive oxygen species (ROS) such as superoxide radicals, hydrogen peroxide, etc., and free radicals in our body [13]. These factors affect serious diseases and systems such as the inflammatory and cardiovascular system, diabetes, stroke, and cancer diseases [14]. Currently, there are many useable synthetic molecules demonstrating important antioxidant activities. Yet, the problem in using these molecules has been linked with some levels of harm to the body [15]. Hence, the investigation of natural antioxidative molecules from living sources has been important.

In this study, methanolic extracts of 9 types of mosses (*T. barbuloides, B. stricta, L. sciuroides, F. antipyretica, M. polymorpha, A. californica, C. conicum, B. pomiformis, G. lisae)* were evaluated for selected bioactivities such as α-glucosidase and Dipeptidyl peptidase 4 (DPP-4) inhibitory activities, anti-glycation activity, antioxidant and metal-chelating abilities. This study aims to propose these bryophytes as a source of natural bioactive compounds and their potential in medical approaches.

2. MATERIAL AND METHODS

2.1. Extraction of phenolics and flavonoids

The plant samples were identified by Prof. Dr. Adnan ERDAG, and the voucher numbers were defined [16]. All plant samples have been dried and pulverized. *A. californica* (1.13 g), *B. pomiformis* (7.45 g), *B. stricta* (7.28 g), *C. conicum* (4.98 g), *F. antipyretica var. gracilis* (4.29 g), *G. lisae* (2.80 g), *L. sciuroides* (4.90 g), *M. polymorpha* (10.29 g), and *T. barbuloides* (2.06 g) were boiled with methanol/water (1:1) in soxhlet for 4-6 hours. The aqueous extract was filtered and evaporated at 45°C using Heidolph Laborota 4000. The samples were lyophilized and stored at 4°C for the upcoming tests.

Table 1 Type, localization, and identification year of the various bryophytes used in the current work

Plants name	**Localization**	**Identification Year**
Antitrichia californica Sull. (Leucodontaceae)	Aydın, Turkey	03.02.1998
Bartramia pomiformis Hedw. (Bartramiaceae)	Aydın, Turkey	10.03.1998
Bartramia stricta Brid. (Bartramiaceae)	Cine, Aydın, Turkey	14.04.2000

Conocephalum conicum (L.) Underw. (Conocephalaceae)	Bozdogan, Aydın, Turkey	04.11.1999
Fontinalis antipyretica Hedw. var. *gracilis* (Lindb.) Schimp. (Fontinalaceae)	Besparmak dagı, Cavdar koyu, Aydın, Turkey	05.03.1999
Grimmia lisae De Not. (Grimmiaceae)	Cavdar koyu, Aydın, Turkey	27.01.1998
Leucodon sciuroides (Hedw.) Schwägr. (Leucodontaceae)	Cine, Aydın, Turkey	09.04.2000
Marchantia polymorpha L. (Marchantiaceae)	Cine, Aydın, Turkey	14.04.2000
Timmiella barbuloides (Brid.) Mönk. (Pottiaceae)	Cine, Aydın, Turkey	14.04.2000

2.2. Total phenolic content of extracts

The total phenolic content of samples was analyzed by the Folin-Ciocaltaue method with slight modifications [17]. Standards (Gallic acid, range between 0.05-0.5 mg/mL) and plant extracts were prepared in methanol. Test tubes containing 0.5 mL sample with different dilutions, 2.5 mL Folin reagent (10% in water), and sodium carbonate (20% in water) were vigorously mixed and kept in dark for an hour. The color change was measured at 750 nm and results were given as gallic acid equivalent (µg/mL GAE).

2.3. Total flavonoid content

The total flavonoid content of the extracts was analyzed according to Arvouet-Grand et al. method [18]. Standards (Quercetin, 5.0-100 µg/mL) and extracts were prepared in methanol. A reaction mixture consisting of a 1.0 mL sample of different dilutions and 1 mL $AlCl_3$ (2.0% in water). The tubes were incubated at 25°C for 10 min. The absorbance was read at 405 nm and results were given as quercetin equivalent (µg/mL QE).

2.4. Antioxidant activity

The evaluation of the anti-oxidant effects of the different plant extracts was determined by the CUPRAC method [19]. A mixture of $CuCl_2$ (25 µL, 10 mM), 7.5 mM neocuproine (prepared in EtOH), ammonium acetate buffer (1.0 M, pH 7.0) is deposited into a 96-well plate. 50 µL of the sample was added to the reaction mixture and incubated for 30 min at 37°C. The same procedure was applied for the standard curve using ascorbic acid (20-100 µmol/mL). The color changes were estimated at 450 nm and the antioxidant activity was calculated as mM ascorbic acid equivalent (AAE)/ µg phenolics.

2.5. Metal chelation efficiency

The samples were evaluated for their metal chelation efficiency via the Cu^{+2} chelation method [20]. The copper solution includes 10 mM hydroxylamine hydrochloride buffer (pH 5.0, 10 mM KCl). The reaction consisted in mixing 50 µL of different sample dilutions, 50 µL of copper solution (0.25 mM), and 25 µL of murexide (1.0 mM). The formed color was read separately at 462 and 530 nm after 3 min incubation at 25°C. EDTA was also evaluated as a control molecule. Metal chelation efficiency was calculated according to the following formula: Metal chelation efficiency (%) = $[1 - ((A_{sample} - A_{blank})/A_{control})] \times 100$.

2.6. DPP4 inhibition activity

The DPP4 inhibition activity of extracts was analyzed via the method described before [21]. Briefly, equal volumes (10 µL) of the enzyme and the plant extracts were pre-incubated in a 96-well plate at 37°C for 15 minutes. Then, 90 µL of 0.1 M Tris-HCl (pH 8.0) and 100 µL of the substrate (Gly-Pro-pNA, 2.0 mM) were added into the wells and incubated at the same conditions. Diprotin A was used as a positive reference control for DPP4 inhibition. The vivid yellow color of the end-product was analyzed at 405 nm and the results were given as inhibition percentage/µg phenolics. The inhibition percentage of samples was calculated with the following equation: % Inhibition = $[(A_{control} - A_{sample})/A_{control}] \times 100$.

2.7. α-Glucosidase Inhibition activity

The evaluation of α-glucosidase inhibition of plant extracts was determined according to Matsui et al. [22] with slight modifications. The first part of the reaction mixture contained 100 µL of 50 mM sodium phosphate buffer (pH 6.8), 50 µL of the enzyme (prepared from yeast), and 25 µL of plant samples or control drug, and pre-incubated for 15 min at 37°C. 75 µL of 4-Nitrophenyl α-D-glucopyranoside (4-NPGP, 2.0 mM) was added to start the reaction and the change in absorbance was followed at 405 nm with a thermo-scientific microplate reader. Acarbose was used as a positive control for α-Glucosidase inhibition. Results were presented as inhibition percentage/µg phenolics. The inhibition percentage of samples was calculated according to the following equation: % Inhibition = $[(A_{control} - A_{sample})/A_{control}] \times 100$.

2.8. Antiglycation activity

The in vitro antiglycation model system was established with BSA (10 mg/mL in sodium phosphate buffer, pH 7.4) and 500 mM D-glucose (in the same buffer) [23]. Briefly, reaction tubes containing BSA (1.0 mL), D-glucose solution (1.0 mL), 0.9 mL buffer, and 100 µL sample (dissolved in ddH_2O), and tubes were incubated at 60°C for 2 hours. Fluorescence of the advanced glycation end products (AGEs) was measured with an excitation wavelength of 370 nm and an emission wavelength of 440 nm. Aminoguanidine was also evaluated as a control molecule and. Antiglycation activity was calculated with the following formula: %inhibition = $[(A_{control} - A_{sample})/A_{control})] \times 100$.

2.9. Statistics

Bioactivity analyses were performed in triplicates and results are presented as mean ± SD. Statistical analysis was performed using Student's *t* test (GraphPad Software, San Diego, CA). $p<0.05$ was considered as statistically significant.

3. RESULTS AND DISCUSSION

Natural and plant-based remedies have seen a great interest in the recent years with the introduction of functional food stuff. They are very abundant and cheap to procure. However, several plant sources have not been explored for biomedical potential. Indeed, the phytochemistry data of bryophytes in the literature show a large number of bioactive compounds such as aromatic polyphenols, organic acids, acetogenins, phenylquinones, and terpenoids in their content that exhibit valuable potential bioactivities. However, scientific reports about these materials have been sporadic and scarce. For this reason, we aimed to explore a group of 9 bryophytes for their flavonoid and polyphenol content as well as measuring various disease-related activities in order to demonstrate the biomedical and therapeutic potential of these species.

3.1. Flavonoid and phenolic contents

Bryophytes are often associated with a distinctive smell that suggests the presence of aromatic molecules in their constitution such as phenolic compounds. One of the strategies to prevent or treat modern diseases is the use of flavonoids. Flavonoids are a major constituent of plant secondary metabolites with thousands of known structures that is both important to the physiology of plants but also possess a large medicinal application. They are found in vascular plants as well as bryophytes [24]. However, vascular plants have been receiving a great focus on their potential as flavonoid resources leading to bryophytes being less studied and only some sporadic reports can be found [25]. The lack of studies is mainly accredited to their small size which makes it is hard to collect in large enough amounts for chemical experiments such as flavonoids and phenolic compounds research [26]. Total flavonoid values provide insights on active substances with higher inhibitory activities present in plants. In the literature, the amount of flavonoids in plants has been reported between 95 µg/g to 25 mg/g for spermatophyte species while it is higher than 50 mg/g for pteridophytes [27-30]. Our results demonstrated total flavonoid content closer to spermatophytes values which

concur with previous studies on other bryophytes describing the same range of amounts [25].

Table 2 Total flavonoid and phenol amounts determined in different bryophytes species

Types of Bryophytes	Flavonoid content (µg QE/g plant)	Phenolic content (µg GAE/g plant)
T. barbuloides	34.8 ± 1.2	92.7 ± 1
B. stricta	28.6 ± 0.7	88.7 ± 1.6
L. sciuroides	19.1 ± 1.3	274 ± 5.7
F. antipyretica	41.1 ± 1.4	543 ± 6.2
M. polymorpha	37.8 ± 0.8	189 ± 3.3
A. californica	46.7 ± 1.1	223.7 ± 1.9
C. conicum	121.8 ± 3.9	222.7 ± 2.1
B. pomiformis	106.8 ± 2.8	223 ± 2.7
G. lisae	11.6 ± 0.5	96.4 ± 0.9

Total phenolic content was explored to determine the active substances found in the different bryophytes methanolic extracts. The results were calculated and given as µg gallic acid equivalent/g plant (Table 2). The maximum values were seen in *F. antipyretica*, *L. sciuroides*, *A. californica*, *C. conicum*, and *B. pomiformis* reaching 543 ± 6.2, 274 ± 5.7, 223.7 ± 1.9, 222.7 ± 2.1, and 223 ± 2.7 µg GAE/g plant, respectively. Aslanbaba et al. [31] investigated the phenolic properties of plants belonging to the bryophytes family obtained from methanolic extraction. According to the results, the phenolic contents were found in *T. tamariscinum* 1075.15 µg gallic acid equivalent/g plant, *P. riparioides* 784.25 µg gallic acid equivalent/g plant. It has been shown in a recent study that phenolic extracts from *T. tamariscinum* and *P. riparioides* were associated with antioxidant activity providing a basis for potential application in medicine, cosmetics, and the food industry [31]. The results provide great evidence that *F. antipyretica*, *L. sciuroides*, *A. californica*, *C. conicum*, and *B. pomiformis* extracts have potential antioxidative activity. Phenolic molecules in these species consider providing significant antioxidant activity.

3.2. Metal chelating activity

Metal chelating activity is very important for determining the antioxidant capacity which holds metals that cause lipid peroxidation. For this reason, chelating compounds bind transition metals in the organism resulting in preventing radical formation. Thus, one of their function is preventing the damage caused by free radicals [32]. In this study, metal chelating capacity was evaluated using the CUPRAC method. Metal chelating properties of extracts were compared according to the quantities of their phenol compounds. According to the results of the study, the metal chelating activity of nine bryophytes was given in Table 3 The highest metal-chelating effect was observed in *T. barbuloides*, *B. stricta*, *L. sciuroides*, *M. polymorpha* compared to the reference molecule EDTA (2.19 %/µg phenolic), while *C. conicum*, and *A. californica* were less effective than the reference molecule. Molecules in the organism can be affected by reactive oxygen species which increases during metal abundance. Metal chelating properties of phenolic compounds are able to prevent some various damages related to these metals. Moreover, phenolics with metal chelating ability facilitate mineral bioavailability.

Table 3 Biological activities of the different bryophytes extracts

Types of bryophytes	DPP-4 inhibitory (%/µg phenol)	Anti-glycation (%/µg phenol)	Metal chelating (%/µg phenol)	Antioxidant activity (mM AAE/ µg phenol)	α-Glucosidase inhibitory (IC_{50}:µg /mL phenol)
T. barbuloides	0.44 ± 2x10^{-2} ^{c}	N.D.	7.94 ± 0.9 ^{c}	27.70 ± 2.2	N.D.
B. stricta	0.68 ± 6x10^{-2} ^{c}	0.22 ± 1x10^{-3} ^{c}	3.95 ± 0.3 ^{c}	18.8 ± 0.8	114.1 ± 5.7 ^{c}
L. sciuroides	0.15 ± 3x10^{-3} ^{c}	N.D.	3.76 ± 0.4 ^{c}	25.56 ± 1.6	713.3 ± 3.9 ^{c}
F. antipyretica	0.04 ± 1x10^{-3} ^{c}	0.74 ± 0.1 ^{c}	0.29 ± 3x10^{-3} ^{c}	7.76 ± 0.4	N.D.
M. polymorpha	1.0 ± 1x10^{-2} ^{c}	N.D.	3.44 ± 0.2 ^{c}	11.08 ± 1	63.5 ± 2.8 ^{c}
A. californica	1.21 ± 7x10^{-2} ^{c}	0.84 ± 4x10^{-2} ^{c}	1.96 ± 0.3 ^{ns}	8.11 ± 0.3	161.3 ± 3.1 ^{c}
C. conicum	0.06 ± 2x10^{-2} ^{c}	0.07 ± 2x10^{-2} ^{c}	2.08 ± 0.2 ^{ns}	12.7 ± 0.7	62.66 ± 2.4 ^{c}
B. pomiformis	0.09 ± 3x10^{-2} ^{c}	N.D.	0.55 ± 0.1 ^{c}	1.26 ± 0.2	N.D.
G. lisae	N.D.	N.D.	1.51 ± 0.1 ^{b}	8.09 ± 0.6	123.8 ± 3.9 ^{c}

N.D.: Not determined.
ns: non-significant, [b]p<0.01, and [c]p<0.001 vs. different control molecules. Diprotin A was used as a control for DPP-4 inhibitory activity; aminoguanidine for antiglycation activity; EDTA for metal chelating activity; Ascorbic acid for antioxidant activity; and acarbose for α-Glucosidase inhibitory activity.

3.3. DPP-4 inhibitory activity

DPP-4 is a serine protease that cleaves N-terminal dipeptides from polypeptides. Its inhibitors not only stimulate insulin pancreatic β-cells but also helps in the regeneration and differentiation of β-cells. Incretin hormones such as GLP-1 and GIP are releasing in response to meal ingestion. The problem is both these hormones have a short half-life due to their rapid degradation by DPP-4. Inhibition of DPP-4 is necessary to maintain the endogenous inactive form of GLP-1 and its longer half-life.

Most synthetic inhibitors are well tolerated, adverse side effects are known such as mild infections and headaches [33, 34]. Therefore, studies have been focused on discovering the natural DPP-4 inhibitors as alternative treatments for NIDDM [35]. Mosses are rich in phenolic compounds [36]. Many studies have shown the presence of DPP-4 inhibitory activity in many phenolic-rich extracts [37-40]. Also, medicinal plants with DPP-4 inhibitory activity such as *O. europaea* [41], *C. australis* [42], *V. unguiculata, U. lobata, S. china, F. cretica, C. quinoa* [43] play an important role in the management of NIDDM by delaying the development of disease, complications and correcting metabolic abnormalities.

The phenolic extracts of different bryophytes were analyzed for their DPP4 inhibition activity. Results were evaluated according to the positive control molecule Diprotin A. The highest DPP-4 inhibitory activity was observed for *M. polymorpha* and *A. californica extracts* with $1 \pm 1\times10^{-2}$ %/µg phenol and $1{,}21 \pm 7\times10^{-2}$ %/µg phenol compared to 3.60%/µg phenol demonstrated by the control molecule (Table 3). The IC_{50} value of *M. polymorpha* was found as 42,7 µg/mL and 93,25 µg/mL for *A. californica* extracts (Figure 1). Studies on anti-diabetic activity from bryophytes are very limited [36]. This is the first report on the DPP-4 inhibitory activity of the *M. polymorpha* and *A. californica*. In this experiment, the results showed that the M. polymorpha and A. californica contained potential inhibitors for this enzyme. Our results indicate that the phenolic content of bryophytes has an impact on DPP-4 inhibition. Hence, finding a novel and natural molecule that plays a role in DPP-4 inhibition would cure or lower the risks of diabetes mellitus.

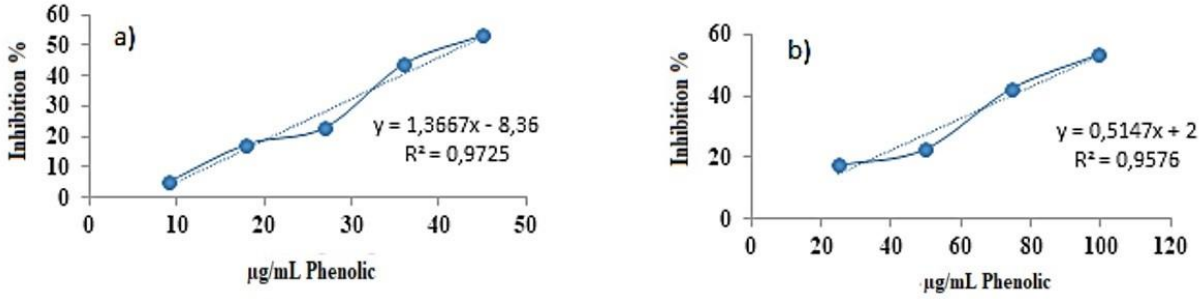

Figure 1 IC_{50} for DPP4 inhibitory activity of a) *M. polymorpha* and b) *A. californica*

3.4. Glucosidase inhibitory activity

The inhibition of polysaccharide hydrolysis enzymes such as α-glucosidase and α-amylase in the digestive system delays glucose absorption [44]. Due to the storage conditions and side effects of synthetic original inhibitors, interest has been increased in the search for finding new and natural antidiabetic drugs or other alternatives. Therefore, there is growing interest in α-glucosidase inhibition to develop novel pharmacological agents [45]. The effect of nine different bryophytes extracts on α-glucosidase activity was investigated. As shown in Table 3, *M. polymorpha* (IC_{50} = 63.5 µg/mL phenol) and *C. conicum* (IC_{50} = 62.66 µg/mL phenol) plants have

shown (Figure 2) the most effective α-glucosidase inhibitory activity compared to reference molecule acarbose (IC_{50} = 1.39 ± 0.23 mg/mL). Tran et al. investigated α-glucosidase inhibitory activity of n-hexane, chloroform, ethyl acetate, and ethanol extracts of the liverwort. They have found the ethyl acetate, ethanol, and n-hexane fractions of IC_{50} values 84.25, 361.40, and 11.89 µg/mL, respectively [46]. Our results show that extract of *M. polymorpha* and *C. conicum* has better α-glucosidase inhibitory activity compared to others. Pant et al. have shown that miscellaneous medicinal plants and related species belonging to bryophytes (*Asterella*, *Marchantia*), pteridophytes (*Adiantum*, *Oleandra*, and *Tectaria*), and flowering plants (*Hedychium*, *Rhus*, *Rubus*, *Smilax*, and *Sonchus*). The highest percentage inhibition of α - glucosidase found (81.13 ± 1.36) was showed from *R. chinensis* extracts [47]. This study suggests that *M. polymorpha* and *C. conicum* are promising sources of active compounds that can prevent the development of type 2 diabetes.

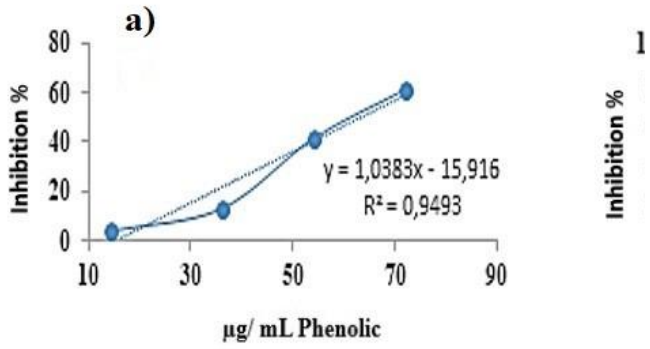

Figure 2 IC_{50} for α-glucosidase inhibitory activity of a) *M. polymorpha* and b) *C. conicum*

3.5. Antiglycation activity

Advanced glycation end products (AGEs) are formed non-enzymatically under long-term chronic hyperglycemic conditions and affect protein structures and functions. Diabetic complications, age-dependent diseases, Alzheimer's disease, rheumatoid arthritis, cancer, neurodegenerative diseases, cataract, and many others are associated with aggregates formed by AGEs [48]. Thus, the prevention of these aggregate formations is of great importance. It is very considerable to select a target for inhibiting glycation at distinctive stages such as Schiff base, advanced glycation end-products (AGE), and protein aggregation. It has been shown that liverworts (bryophytes) possess antidiabetic activities through the study of three species (*P. striatus, P. epiphylla, and B. oshimensis*) collected from Eastern Himalaya [49]. Brown algae extracts were shown to possess antiglycation effects in bovine serum albumin glycation models with fructose, glyoxal, and methylglyoxal. The antiglycative effect was associated with the presence of phenolic compounds in the extract (dieckol, phlorofucofuroeckol-A, and quercetin) [50]. Our results show that the *F. antipyretica* (0.74 ± 0.1%/µg phenol) and *A. californica* ($0.84 \pm 4x10^{-2}$ %/µg phenol) were very effective on antiglycation activity compared to control molecule Aminoguanidine (0.27 %/µg phenolic), and the *B. stricta* was similar to that of the control molecule. *C. conicum* antiglycation activity was insufficient.

4. CONCLUSION

In this study, different pharmacological activities (antiglycation, α-glucosidase and DPP-4 inhibition, antioxidant, and metal chelating ability) associated with diabetes were investigated in nine types of bryophytes methanolic extracts. To the best of our knowledge, this is the first report describing the bioactivity of these nine bryophytes and their potential as antidiabetics, antioxidants, and phenolic reservoirs. Bryophytes are poorly investigated compared to vascular plants which are exploited commercially. The production of active compounds obtained from bryophyte species can have a tremendous impact on commercial and medical applications especially in the fields of food, medicine, and pharmacy.

Declarations

Author's Contributions

1st Author performed the experiment and results analysis.

1st, 2nd, and 3rd Authors drafted and wrote the manuscript.

2nd and 3rd Author assisted in the analytical analysis, supervised the experiment's progress, results interpretation, and helped in manuscript preparation.

4th Author assisted in preparing the samples.

Funding

This work received no funding

Ethics

There are no ethical issues after the publication of this manuscript.

Consent for publication

All authors read and approved the current version for publication

Conflict of interest

There is no conflict of interest to be declared.

Acknowledgments

The authors thank Prof. Adnan ERDAG for providing the bryophyte samples. This research did not receive any specific grant from funding agencies in the public, commercial, or not-for-profit sectors.

REFERENCES

[1] E. L. Decker and R. Reski, "Mosses in biotechnology," *Curr Opin Biotechnol*, vol. 61, pp. 21-27, Feb 2020, doi: 10.1016/j.copbio.2019.09.021.

[2] A. Alam, "Some Indian bryophytes known for their biologically active compounds," *International Journal of Applied Biology and Pharmceutical Technology*, vol. 3, no. 2, pp. 239-246, 2012.

[3] Y. Asakawa, "Biologically active compounds from bryophytes," (in English), *Pure and Applied Chemistry*, vol. 79, no. 4, pp. 557-580, Apr 2007, doi: 10.1351/pac200779040557.

[4] A. S. Lubaina, D. P. Pradeep, J. M. Aswathy, Remya Krishnan M. K. V., and Murgan K., "Traditional knowledge of medicinal bryophytes by the kani tribes of Agasthiyarmalai biosphere reserve, southern western ghats," *Indo American Journal of Pharmaceutical Research,* vol. 4, pp. 2116-2121, 2014.

[5] A. G. Azuelo, L. G. Sariana, and M. P. Pabualan, "Some Medicinal Bryophytes: their Ethnobotanical Uses and Morphology," *Asian Journal of Biodiversity*, vol. 2, no. 1, 2011/12/01 2011, doi: 10.7828/ajob.v2i1.92.

[6] J. M. Glime, "Economic and ethnic uses of bryophytes," *Flora of North America,* vol. 27, pp. 14-41, 2007.

[7] A. Gulabani, "Bryophytes as economic plants," *Botanica,* 1974.

[8] J. M. Forbes and A. K. Fotheringham, "Vascular complications in diabetes: old messages, new thoughts," *Diabetologia*, vol. 60, no. 11, pp. 2129-2138, Nov 2017, doi: 10.1007/s00125-017-4360-x.

[9] J. Chaudhuri *et al.*, "The Role of Advanced Glycation End Products in Aging and Metabolic Diseases: Bridging Association and Causality," *Cell Metab*, vol. 28, no. 3, pp. 337-352, Sep 4 2018, doi: 10.1016/j.cmet.2018.08.014.

[10] R. Singh, H. K. Rao, and T. G. Singh, "Advanced glycated end products (ages) in diabetes and its complications: an insight," *Plant Archives,* vol. 20, no. 1, pp. 3838-3841, 2020.

[11] C. A. Emdin, S. G. Anderson, M. Woodward, and K. Rahimi, "Usual Blood Pressure and Risk of New-Onset Diabetes: Evidence From 4.1 Million Adults and a Meta-Analysis of Prospective Studies," *J Am Coll Cardiol*, vol. 66, no. 14, pp. 1552-

1562, Oct 6 2015, doi: 10.1016/j.jacc.2015.07.059.

[12] D. Kajaria, Ranjana, J. Tripathi, Y. B. Tripathi, and S. Tiwari, "In-vitro alpha amylase and glycosidase inhibitory effect of ethanolic extract of antiasthmatic drug - Shirishadi," (in eng), *J Adv Pharm Technol Res*, vol. 4, no. 4, pp. 206-9, Oct 2013, doi: 10.4103/2231-4040.121415.

[13] N. Xu, S. Jiang, P. B. Persson, E. A. G. Persson, E. Y. Lai, and A. Patzak, "Reactive oxygen species in renal vascular function," *Acta Physiol (Oxf)*, https://doi.org/10.1111/apha.13477 vol. 229, no. 4, p. e13477, Aug 2020, doi: 10.1111/apha.13477.

[14] T. Senoner and W. Dichtl, "Oxidative Stress in Cardiovascular Diseases: Still a Therapeutic Target?," *Nutrients*, vol. 11, no. 9, Sep 4 2019, doi: 10.3390/nu11092090.

[15] C. L. Curl, M. Spivak, R. Phinney, and L. Montrose, "Synthetic Pesticides and Health in Vulnerable Populations: Agricultural Workers," *Curr Environ Health Rep*, vol. 7, no. 1, pp. 13-29, Mar 2020, doi: 10.1007/s40572-020-00266-5.

[16] E. K. Kocazorbaz, R. N. Un, A. Erdag, and F. Zihnioglu, "Inhibitory Effects of Some Bryophytes on Glutathione-S - Transferase," *Current Enzyme Inhibition*, vol. 13, no. 1, pp. 34-40, 2017/02/02 2017, doi: 10.2174/1573408012666160628081431.

[17] V. L. Singleton, R. Orthofer, and R. M. Lamuela-Raventós, "[14] Analysis of total phenols and other oxidation substrates and antioxidants by means of folin-ciocalteu reagent," in *Oxidants and Antioxidants Part A*, ed: Elsevier, 1999, pp. 152-178.

[18] A. Arvouet-Grand, B. Vennat, A. Pourrat, and P. Legret, "[Standardization of propolis extract and identification of principal constituents]," (in fre), *Journal de pharmacie de Belgique*, vol. 49, no. 6, pp. 462-8, Nov-Dec 1994. [Online]. Available: https://www.ncbi.nlm.nih.gov/pubmed/7884635. Standardisation d'un extrait de propolis et identification des principaux constituants.

[19] R. Apak, K. Guclu, M. Ozyurek, S. E. Karademir, and M. Altun, "Total antioxidant capacity assay of human serum using copper(II)-neocuproine as chromogenic oxidant: the CUPRAC method," *Free Radic Res*, vol. 39, no. 9, pp. 949-61, Sep 2005, doi: 10.1080/10715760500210145.

[20] X. Li, X. Wang, D. Chen, and S. Chen, "Antioxidant Activity and Mechanism of Protocatechuic Acid in vitro," *Functional Foods in Health and Disease*, vol. 1, no. 7, p. 232, 2011/07/31 2011, doi: 10.31989/ffhd.v1i7.127.

[21] A. Zeytunluoglu and F. Zihnioglu, "Evaluation of some plants for potential dipeptidyl peptidase IV inhibitory effects in vitro," (in English), *Turkish Journal of Biochemistry-Turk Biyokimya Dergisi*, vol. 40, no. 3, pp. 217-223, 2015/01/01 2015, doi: 10.1515/tjb.2015.0004.

[22] T. Matsui, C. Yoshimoto, K. Osajima, T. Oki, and Y. Osajima, "In vitro survey of alpha-glucosidase inhibitory food components," *Biosci Biotechnol Biochem*, vol. 60, no. 12, pp. 2019-22, Dec 1996, doi: 10.1271/bbb.60.2019.

[23] H. K. Kani, E. K. Kocazorbaz, and F. Zihnioglu, "Investigation and isolation of peptide based antiglycating agents from various sources," (in English), *Turkish Journal of Biochemistry-Turk Biyokimya Dergisi*, vol. 44, no. 5, pp. 699-705, Oct 2019, doi: 10.1515/tjb-2018-0294.

[24] C. F. Xie and H. X. Lou, "Secondary metabolites in bryophytes: an ecological aspect," *Chem Biodivers*, vol. 6, no. 3, pp. 303-12, Mar 2009, doi: 10.1002/cbdv.200700450.

[25] X. Wang, J. Cao, X. Dai, J. Xiao, Y. Wu, and Q. Wang, "Total flavonoid concentrations of bryophytes from Tianmu Mountain, Zhejiang Province (China): Phylogeny and ecological factors," (in eng), *PLoS One*, vol. 12, no. 3, p. e0173003, 2017, doi: 10.1371/journal.pone.0173003.

[26] Y. H. Wu, H. Y. Yang, H. Luo, and Q. Gao, "Resources of medicinal bryophytes in north--eastern China and their exploitation," *Chinese Journal of Ecology*, vol. 23, no. 5, pp. 218-223, 2004.

[27] M. Atanassova, S. Georgieva, and K. Ivancheva, "Total phenolic and total flavonoid contents, antioxidant capacity and biological contaminants in medicinal herbs," *Journal of the University of Chemical Technology Metallurgy*, vol. 46, no. 1, 2011.

[28] J. G. Cao, Y. X. Zheng, X. Xia, Q. X. Wang, and J. B. Xiao, "Total flavonoid contents, antioxidant potential and acetylcholinesterase inhibition activity of the extracts from 15 ferns in China," (in English), *Industrial Crops and Products*, vol. 75, pp. 135-140, Nov 30 2015, doi: 10.1016/j.indcrop.2015.04.064.

[29] N. Saeed, M. R. Khan, and M. Shabbir, "Antioxidant activity, total phenolic and total flavonoid contents of whole plant extracts Torilis leptophylla L," (in eng), *BMC Complement Altern Med*, vol. 12, p. 221, Nov 16 2012, doi: 10.1186/1472-6882-12-221.

[30] X. Xia, J. G. Cao, Y. X. Zheng, Q. X. Wang, and J. B. Xiao, "Flavonoid concentrations and bioactivity of flavonoid extracts from 19 species of ferns from China," (in English), *Industrial Crops and Products*, vol. 58, pp. 91-98, Jul 2014, doi: 10.1016/j.indcrop.2014.04.005.

[31] B. Aslanbaba, S. Yilmaz, Ö. TonguÇ YayintaŞ, D. ÖZyurt, and B. DemİRata ÖZtÜRk, "Total Phenol Content and Antioxidant Activity of Mosses from Yenice Forest (Ida Mountain)," *Journal of Scientific Perspectives*, vol. 1, no. 1, pp. 1-12, 2017/09/01 2017, doi: 10.26900/jsp.2017.0.

[32] S. Sethi, A. Joshi, B. Arora, A. Bhowmik, R. R. Sharma, and P. Kumar, "Significance of FRAP, DPPH, and CUPRAC assays for antioxidant activity determination in apple fruit extracts," (in English), *European Food Research and Technology*, vol. 246, no. 3, pp. 591-598, Mar 2020, doi: 10.1007/s00217-020-03432-z.

[33] S. R. Lin *et al.*, "The perceptions of natural compounds against dipeptidyl peptidase 4 in diabetes: from in silico to in vivo," (in eng), *Ther Adv Chronic Dis*, vol. 10, p. 2040622319875305, 2019, doi: 10.1177/2040622319875305.

[34] D. Sharma, S. Kumar, S. Kumar, and D. Kumar, "DPP-IV Inhibitors from natural sources: An alternative approach for treatment and management of diabetes," (in English), *Indian Journal of Natural Products and Resources*, vol. 10, no. 4, pp. 227-237, Dec 2019. [Online]. Available: <Go to ISI>://WOS:000573214800001.

[35] K. G. P. Wasana, A. P. Attanayake, K. A. P. W. Jayatilaka, and T. P. Weerarathna, "Natural drug leads as novel DPP-IV inhibitors targeting the management of type 2 diabetes mellitus," (in English), *Journal of Complementary Medicine Research*, vol. 11, no. 1, pp. 43-53, 2020, doi: 10.5455/jcmr.2020.11.01.06.

[36] T. M. Lunic *et al.*, "Extracts Characterization and In Vitro Evaluation of Potential Immunomodulatory Activities of the Moss Hypnum cupressiforme Hedw," (in eng), *Molecules*, vol. 25, no. 15, p. 3343, Jul 23 2020, doi: 10.3390/molecules25153343.

[37] J. Fan, M. H. Johnson, M. A. Lila, G. Yousef, and E. G. de Mejia, "Berry and Citrus Phenolic Compounds Inhibit Dipeptidyl Peptidase IV: Implications in

Diabetes Management," (in eng), *Evid Based Complement Alternat Med*, vol. 2013, p. 479505, 2013, doi: 10.1155/2013/479505.

[38] P. Kalhotra, V. Chittepu, G. Osorio-Revilla, and T. Gallardo-Velazquez, "Phytochemicals in Garlic Extract Inhibit Therapeutic Enzyme DPP-4 and Induce Skeletal Muscle Cell Proliferation: A Possible Mechanism of Action to Benefit the Treatment of Diabetes Mellitus," (in eng), *Biomolecules*, vol. 10, no. 2, p. 305, Feb 14 2020, doi: 10.3390/biom10020305.

[39] C. H. Peng, Y. S. Yang, K. C. Chan, C. J. Wang, M. L. Chen, and C. N. Huang, "Hibiscus sabdariffa polyphenols alleviate insulin resistance and renal epithelial to mesenchymal transition: a novel action mechanism mediated by type 4 dipeptidyl peptidase," *J Agric Food Chem*, vol. 62, no. 40, pp. 9736-43, Oct 8 2014, doi: 10.1021/jf5024092.

[40] M. Zaklos-Szyda, A. Kowalska-Baron, N. Pietrzyk, A. Drzazga, and A. Podsedek, "Evaluation of Viburnum opulus L. Fruit Phenolics Cytoprotective Potential on Insulinoma MIN6 Cells Relevant for Diabetes Mellitus and Obesity," (in eng), *Antioxidants (Basel)*, vol. 9, no. 5, p. 433, May 16 2020, doi: 10.3390/antiox9050433.

[41] L. A. Malik, G. M. Aziz, and A. H. Ad'hiah, "The Potential of some Plant Extracts as Radical Scavengers and Dipeptidyl Peptidase-4 Inhibitors," (in English), *Baghdad Science Journal*, vol. 16, no. 1, pp. 162-168, 2019/03/17 2019, doi: 10.21123/bsj.2019.16.1(Suppl.).0162.

[42] B. A. R. Sukma, D. Indarto, and Y. H. Suselo, "Inhibition effect of Cuscuta australis ethanol extract containing actinodaphnine on dipeptidyl peptidase-4 enzyme activity in the MCF-7 cell line," presented at the AIP Conference Proceedings 2021, 030003, 2018. [Online]. Available: http://dx.doi.org/10.1063/1.5062727.

[43] G. Turdu, H. Gao, Y. Jiang, and M. Kabas, "Plant dipeptidyl peptidase-IV inhibitors as antidiabetic agents: a brief review," *Future Med Chem*, vol. 10, no. 10, pp. 1229-1239, May 1 2018, doi: 10.4155/fmc-2017-0235.

[44] P. McCue, Y. I. Kwon, and K. Shetty, "Anti-diabetic and anti-hypertensive potential of sprouted and solid-state bioprocessed soybean," (in eng), *Asia Pacific journal of clinical nutrition*, vol. 14, no. 2, pp. 145-52, 2005. [Online]. Available: https://www.ncbi.nlm.nih.gov/pubmed/15927931.

[45] F. Rahim *et al.*, "Synthesis, in vitro alpha-glucosidase inhibitory potential of benzimidazole bearing bis-Schiff bases and their molecular docking study," *Bioorg Chem*, vol. 94, p. 103394, Jan 2020, doi: 10.1016/j.bioorg.2019.103394.

[46] T. Q. Tran, H. N. Phan, A. L. Bui, and P. D. D. Quach, "Biological activities of in vitro liverwort Marchantia polymorpha L. extracts," (in English), *Notulae Botanicae Horti Agrobotanici Cluj-Napoca*, vol. 48, no. 2, pp. 826-838, Apr-Jun 2020, doi: 10.15835/nbha48211884.

[47] D. Pant, B. Aryal, D. Pun, S. Sharma, and G. P. Joshi, "Inhibition of a-amylase and a-glucosidase activities in vitro by extracts of selected medicinal plants," *Biodiversitas Journal of Biological Diversity*, vol. 22, no. 3, 2021/02/11 2021, doi: 10.13057/biodiv/d220314.

[48] N. A. Ansari and Z. Rasheed, "Non-enzymatic glycation of proteins: From diabetes to cancer," *Biochemistry (Moscow) Supplement Series B: Biomedical Chemistry*, vol. 3, no. 4, pp. 335-342, 2009/11/17 2009, doi: 10.1134/s1990750809040027.

[49] S. Mukhia, P. Mandal, D. K. Singh, and D. Singh, "Evaluation of anti-diabetic, antioxidant activity and phytochemical constituents of liverworts of eastern

himalaya," *Journal of Chemical and Pharmaceutical Research,* vol. 7, pp. 890-900, 01/01 2015.

[50] J. J. Park and W. Y. Lee, "Anti-glycation effects of brown algae extracts and its phenolic compounds," *Food Bioscience,* vol. 41, p. 101042, 2021/06 2021, doi: 10.1016/j.fbio.2021.101042.

SAKARYA ÜNİVERSİTESİ
FEN BİLİMLERİ ENSTİTÜSÜ DERGİSİ

Sakarya University Journal of Science
SAUJS

e-ISSN: 2147-835X | Founded: 1997 | Period: Bimonthly | Publisher: Sakarya University
http://www.saujs.sakarya.edu.tr/en/

Title: Spatial Appraisal of Seasonal Water Yield of the Sokoto-Rima Basin

Authors: Saheed Adekunle RAJI, Shakirudeen ODUNUGA, Mayowa FASONA

Recieved: 2020-09-25 21:05:23

Accepted: 2021-06-21 14:51:17

Article Type: Research Article

Volume: 25
Issue: 4
Month: August
Year: 2021
Pages: 950-968

How to cite
Saheed Adekunle RAJI, Shakirudeen ODUNUGA, Mayowa FASONA; (2021), Spatial Appraisal of Seasonal Water Yield of the Sokoto-Rima Basin. Sakarya University Journal of Science, 25(4), 950-968, DOI: https://doi.org/10.16984/saufenbilder.800302
Access link
http://www.saujs.sakarya.edu.tr/en/pub/issue/64755/800302

Sakarya University Journal of Science 25(4), 950-968, 2021

Spatial Appraisal of Seasonal Water Yield of the Sokoto-Rima Basin

Saheed Adekunle RAJI*[1], Shakirudeen ODUNUGA[2], Mayowa FASONA[3]

Abstract

Understanding the dynamics of water yield related to water balance is vital for the functioning of ecosystems and model-based computation of their respective ecosystem services. This is important for valuable water resource planning and management in dryland regions, such as the Sokoto-Rima basin. In this study, we assess the spatiotemporal dynamics of quickflow (QF), local recharge (LR), and baseflow (B) between 1992 and 2015 with the use of the Seasonal Water Yield (SWY) model of InVEST (Integrated Valuation of Ecosystem Service and Tradeoffs) software. Pre-classified landcover, rainfall, satellite-derived evapotranspiration, digital surface topography, and HYSOGs 250m soil datasets were used as software input. The result of the study showed that QF, LR, and B depict similar spatial distribution with peak values generated within water-bearing landcover areas, particularly water bodies and wetlands. QF was highest in 2002 (1,293.6 mm), and the subsequent years – 2012 and 2015 had reductions. Similar patterns were observed in LR and B with much lower values. The temporal trend for the 23-year period of the study showed that QF had an increasing rate of 85.331 mm while decreasing rates of 56.131 mm and 27.597 mm were detected for LR and B, respectively. Three essential parameters – alpha (α), beta (β), and gamma (γ) showed evidence of sensitivity to changes in seasonal water yield values. These water balance transactions provided an opportunity to review the impact of the sensitivity of the landcover, climate, and hydrogeological factors on water resources management, mainly freshwater accounting in the Sokoto-Rima basin of the northwestern part of Nigeria.

Keywords: Quickflow, local recharge, baseflow, InVEST, ecosystem services.

1. INTRODUCTION

Ecosystem services are, in many ways more than one, connected to freshwater systems and, by extension, convolutedly linked to socioeconomic development and human welfare [1-3]. This is because of the inevitability of water for food, medicine, and other human consumptive purposes, industrial heating and cooling, irrigation and other agrarian purposes, habitat for different species, support wetland functioning, and assessment of environmental dynamics [1-5].

*Corresponding author: E-mail: raji.saheed@fupre.edu.ng
[1] Federal University of Petroleum Resources Effurun, Department of Environmental Management and Toxicology, Effurun, Nigeria.
ORCID: https://orcid.org/0000-0002-5890-5414.
[2] University of Lagos, Department of Geography, Akoka-Yaba, Lagos, Nigeria.
E-mail: sodunuga@unilag.edu.ng
ORCID: https://orcid.org/0000-0003-4307-9428.
3 University of Lagos, Department of Geography, Akoka-Yaba, Lagos, Nigeria.
E-mail: mfasona@unilag.edu.ng
ORCID: https://orcid.org/0000-0002-7876-7397.

One of the natural attributes that can be used to define freshwater ecosystem services is water yield [6-8]. Water yield defines the amount of water available in a particular area regarding provisioning and regulatory functions; consequently, it is correlated with land use dynamics [6-7]. This is why the quantitative assessment of water yield is a valuable tool for expressing the nexus between populace and water. In addition, quantitative assessment of water yield can help in effective surveillance and management of water resources, particularly in a well-defined hydrological basin, by tracking changes and ensuring sustainability [4,5-8]. Key environmental factors such as precipitation, evapotranspiration, soil-water interrelations, terrain configuration and geology, vegetation and land use dynamics are measured [6-8].

Combining these factors to estimate water yield can be laborious, especially in data-scarce jurisdictions where data on environmental monitoring and hydrologic changes are unavailable, and inconsistent collection approaches were accessible [6]. Models are often used to resolve these challenges in which the environmental factors formed the foundational model inputs [7]. However, the paucity of suitable data typologies and formats can render the anticipated assessment sought by the model implausible. Reliance on satellite data sources and those generated using spatial statistics have been utilised to provide spatial visualisations of water yield.

Since models are a systematic replica of the natural world, the uncertainty of parameters measured from their outputs is vital [6, 7]. As regards freshwater ecosystem services, model estimates are often defined based on water inputs and output pathways in consideration of localised environmental conditions. Analysis of these uncertainties of these parameters via sensitivity to changes will help measure place-specific quantification assessments to identify controlling factors and influence on water yield. Also, this performance assessment will provide a good rank of parameters connected to local processes and controls on water yield. Literature on the application of these measures within the semi-arid ecosystem of West Africa remains a rarity. Existing measures are often based on non-spatial hydrological assessments such as [8-10].

Even though Nigeria is moderately water rich with per capita annual water availability value of 1,158 m^3 [11], this is spatially restricted to the south with a high all-year-round water density. İn the north, including the Sokoto-Rima basin, optimal functioning of freshwater ecosystem service complexes remains seasonal hence the heavy reliance on dams and irrigation projects to supply urban and agrarian purposes. However, researches on water yield have often concentrated on annual water yield [8-10, 12-13], while a few, such as [6-7], considered the import of seasonal water yield. These studies have shown that seasonal water yield is sufficient to capture the value of seasonal differences in water resource management, particularly for irrigation management, water requirements for crops, and urban water supplies in arid zones. However, these latter studies showcased the essence of seasonal water yield for dryland hydrological settings such as the Sokoto-Rima basin, existing studies such as [8, 10] focussed on a fraction of the issue. Questions on the dynamics and influence of seasonal water fluctuations remain largely unanswered. Knowing this will help address localised water scarcity issues as seasonal water deficit within the semi-arid is largely place-based.

In this research, the InVEST (Integrated Valuation of Ecosystem Services and Tradeoffs) seasonal water yield (SWY) model was employed in the Sokoto-Rima basin of the northwestern axis of Nigeria. Three water yield outputs, namely quickflow, baseflow and local recharge, were computed spatiotemporally. Notably, the SWY model was created by the Natural Capital Project (www.naturalcapitalproject.stanford.edu) based on the water-balance concept [19]. Also, the sensitivity of the vital parameters was assessed. The study results are expected to apply to other semi-arid areas in northern Nigeria and West Africa at large.

2. MATERIAL AND METHODS

2.1. The Study Area

The Sokoto-Rima basin is a transnational hydrological basin of West Africa that covers Nigeria, Benin and Niger. Nevertheless, this section of the study falls within the Nigeria section, which swaths within Latitudes 10˚32'35" N to 13˚32'55" N and Longitudes 3˚30'30" E to 8˚1'15" E with a total land area of 94,026.50 km^2 (Figure 1). Based on climate, the mesoscale convective processes associated with the tropical savanna climate of West Africa [14] directly influenced the research area. Two highly distinguished climatic seasons - wet and dry subsists with clearly defined rainfall and temperature variations. Mean annual rainfall ranges from 350 mm to 895 mm from north to south, increasing the spatial index. Mean temperature annually averages 30 ^{0}C with substantial variability where the value increases during the wet and post-dry seasons and low during the dry season [15].

Rivers and streams that flow under the influence of relief and elevation characterized freshwater systems of the Sokoto-Rima basin. The critical river systems are the Sokoto and Rima, where the basin derives its name. It flows from westwards with a series of confluences with Rivers Zamfara, Ka, Bunsuru, Maradi, Gagere, Konni and others. The relief rises from the eastern basement complex rocks with an elevation of 802 m above sea level and reduced to the lowest around the Niger plain south of the study area. The surrounding wetlands and plains have been subjected to extensive cultivation defining the agrarian nature of the Sokoto-Rima basin. Water-sensitive crops such as rice, millet, sorghum, maize have been cultivated with cattle, ram, sheep and goat domestically reared.

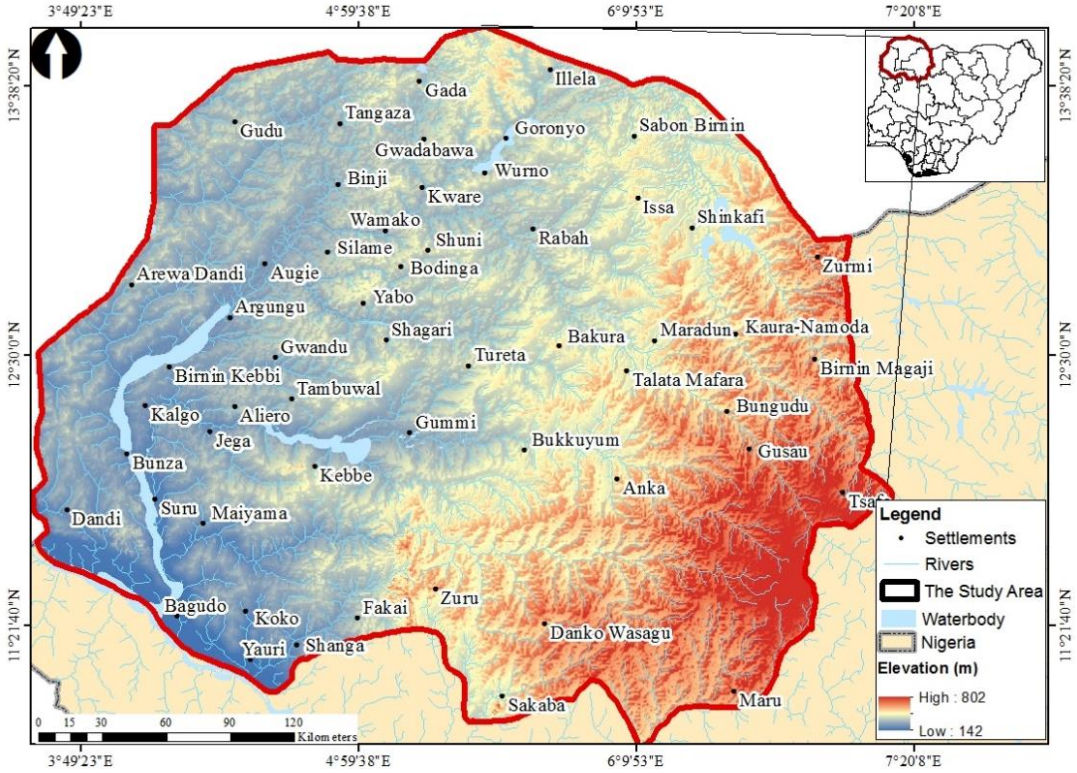

Figure 1 Location of the Sokoto-Rima basin in context of northern Nigeria with relief and the network of rivers and streams defining the basin

2.2. Data Sources and Characteristics

Multi-sourced spatial data with unique characteristics were used in this study. As shown in Table 1, we sourced these datasets from various archives and existed as texts, tables, raster and vector data files. So, to avoid computational incompatibilities, all the datasets were converted

using Geographical Information Systems (GIS) software to raster datasets, re-sampled to 100 metres spatial resolution and projected to Universal Transverse Mercator Zone 31 North (UTM Zone 31 N), where the study area is located. The associated data sources and other details are concisely presented in Table 1.

Table 1 Data characteristics and sources used in this study

s/N	Data	Resolution	Year	Data Source
1	CCI-LC Climate Change Initiative Landcover	300 metres	1992 2002 2012 2015	European Space Agency (ESA) Climate Change Initiative (CCI) Data Viewer at http://maps.elie.ucl.ac.be/CCI/viewer/profiles.php
2	Evapotranspiration (Eta version 4) v4 data	250 metres	1992 2002 2012 2015	USGS Famine Early Warning System (FEWS) Data for West Africa https://earlywarning.usgs.gov/fews/product/451
3	TAMSAT	0.0375° (~ 4 km)	1983-2019	Tropical Applications of Meteorology using Satellite data and ground-based observations https://www.tamsat.org.uk
4	Shuttle Radar Topography Mission (SRTM) 4.1	90 metres; vertical accuracy of 16 metres	2014	CGIAR Consortium for Spatial Information https://srtm.csi.cgiar.org/
5	HYSOG Soil Group	250 metres	2015	United States Oak Ridge National Library Distributed Active Archive Centre (ORNL DAAC) https://daac.ornl.gov/cgi-bin/dsviewer.pl?ds_id=1566
6	eMODIS NDVI Data	250 metres	2002 2012 2015	USGS Famine Early Warning System (FEWS) Data for West Africa https://earlywarning.usgs.gov/fews/product/451
7	Curve number (CN)	Dimensionless with range (0-100)	2007	Handbook of the United States Department of Agriculture (USDA) accessed online at https://directives.sc.egov.usda.gov/OpenNonWebContent.aspx?content=22526.wba
8	Crop/vegetation coefficient (Kc)	Dimensionless with range (0.114–0.689)	1998	Monthly crop factor values generated from the archives of the Food and Agriculture Organization of the United Nations (FAO) available online at the webportal: http://www.fao.org/3/x0490e/x0490e00.htm

The pre-classified and pre-processed Climate Change Initiative (CCI) landcover data of the European Space Agency (ESA) was used as the central data spine of the study. It has a spatial resolution of 300 meters and a 32-bit quantisation level sufficient to detect homogenous landcover classes. Its pre-processed nature ensures that edge-matching errors constraining large-scale utility have been eliminated. The period 1992, 2002, 2012 and 2015 were acquired based on data available from the data download portal http://maps.elie.ucl.ac.be/CCI/viewer/profiles.php.

Satellite-derived actual evapotranspiration (ETa) data for the periods 1992, 2002, 2012 and 2015 were sourced from the portal of the United States Geological Survey (USGS) Famine Early Warning Systems Network (FEWSNET) and produced using the Moderate Resolution Imaging Spectroradiometer (MODIS). The datasets were generated through the operational simplified surface energy balance (SSEBop) model advanced by [16] with a spatial resolution of 250 metres.

Also, rainfall datasets were generated from the Tropical Applications of Meteorology using Satellite data and ground-based observations (TAMSAT) specifically for Africa. The data was sourced from https://www.tamsat.org.uk/. It has a medium resolution of 0.0375° (roughly 4 km), suitable for defining long-term tropical climatology, particularly from a monsoon region. The acquired data was presented in netCDF format, which is suitable for GIS-based

application. Further details of satellite characterisation and ex-situ processing of TAMSAT data are available in [17].

Digital surface topography data was sourced from the Shuttle Radar Topography Mission (SRTM), having 90-metre (3-arc-second) spatial resolution. The data was acquired from the CGIAR Consortium for Spatial Information (CGIAR-CSI). It has a minimum vertical accuracy of 16 m which is suitable for the study.

Global Hydrologic Soil Groups (HYSOGs250m) data sourced from NASA's Distributed Active Archive Centre for Biogeochemical Analysis (DAAC) data employed in the study was via https://daac.ornl.gov/SOILS/guides/Global_Hydrologic_Soil_Group.html. İt has a spatial resolution of 0.002083° (250 m). The data is vital for ecohydrological modelling at a regional scale [18].

Other datasets acquired for the study include landcover sensitive CN (curve number), a pragmatic variable used to estimate direct hydrologic runoff or infiltration from excess precipitation. The values used in this study were extracted from the handbook of the United States Department of Agriculture (USDA). The monthly crop/vegetation coefficient (Kc) values for different landcover typologies within a cultivated semi-arid zone of the tropics were referenced from the archives of the Food and Agriculture Organization Food and Agriculture Organization of the United Nations (FAO).

2.3. Description of the InVEST Seasonal Water Yield (SWY) Model

Spatially explicit models are essential for estimating hydrological patterns, particularly in areas characterised by low and inconsistent data availability. These models are often used to augment data gaps for spatial planning of water ecosystem services and related resource management. This study adopted the InVEST SWY model because of its low data requirements, inherent spatially explicit nature of depicting water routing, and adoption of a streamlined water balancing approach [19]. The latter, however, has some level of uncertainty whose influence on water appraisal ability must be determined.

A comprehensive description of the InVEST SWY model can be found in [19]. The main computational procedure and the essential variables thereof are presented in this study, as shown in Figure 1. Four segmentation levels can be identified in the model. First, it computes quickflow (QF) at the interannual (monthly) level per pixel of the multispectral space. This is based on the NRCS curve number method, which calculates approximately interannual direct runoff using monthly precipitation and the number of rain events per period [28]-[34]. This is defined as:

$$QF_{i,m} = n_m \left(\left(a_{i,m} - S_i\right) exp\left(-\frac{0.2S_i}{a_{i,m}}\right) + \frac{S_i^2}{a_{i,m}} exp\left(\frac{0.8S_i}{a_{i,m}}\right) E_1\left(\frac{S_i}{a_{i,m}}\right)\right) (25.4\left[\frac{mm}{in}\right]) \quad (1)$$

$$QF_i = \sum_{m=1}^{12} QF_{i,m} \quad (2)$$

where: S_i latent highest soil moisture holding sequel to water flow; C_{NI} is the curve number for pixel *i*; $a_{i,\,m}$ is the mean rain depth on a rainy day at pixel *i* on month *m*; E_1 is the change integral function; and *t* is study period.

Second, the model segregates monthly available water between local recharge and evapotranspiration. On a particular pixel, this division is affected by factors that influence the availability of subsurface water for evapotranspiration, namely by up-slope recharge and α, β and γ parameters. Thus, evapotranspiration is defined as:

$$AET_{i,m} = \min\left(PET_{i,m}; P_{i,m} - QF_{i,m} + \alpha_m \beta L_{sum.avail,i}\right) \quad (3)$$

where $L_{sum.avail,i}$ is the sum of upslope subsurface water that is hypothetically accessible at pixel *i*, β is a spatial accessibility parameter that ranges between 0–1 and influenced by local terrain characteristics, and α_m is the portion of the (annual) upslope water support that is accessible in a given month *m*. The γ parameter, though optional, is a defined as a function of recharge at

a given pixel level within the multispectral space that is accessible and not lost to pixels at the downslope level. Third, the model computes the local recharge (LR) on a given pixel, which denotes the probable subsidy to aggregate annual baseflow:

$$L_i = P_i - QF_i - AET_i \quad (4)$$

where: L_i is the index of LR P_i annual precipitation of pixel i, QF is the yearly quickflow, AET_i actual evapotranspiration aggregated from monthly levels. Finally, index of Baseflow (B), i.e. the amount of water that gets to the stream, is computed as:

$$B_i = B_{sum,i} * \frac{L_{avail,i}}{L_{sum,}} \quad (5)$$

given that: $L_{sum,i} = L_i + \sum_j^i L_{sum,j} * P_{ji}$ (6)

where B_i is baseflow of pixel i, $L_{sum,i}$ is cummulative upstream recharge of pixel i.

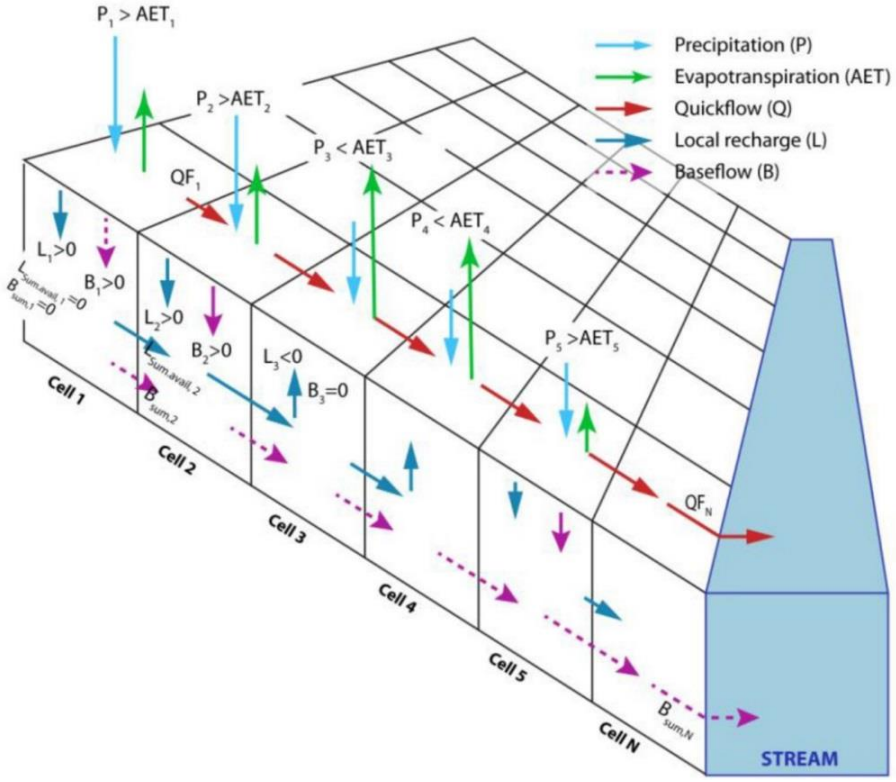

Figure 2 The InVEST Seasonal Water Yield model hydrologic channelling system depicting the pixel-based one-dimensional water flow path primed upon the simplified water balance approach (Source: [7])

2.4. Sensitivity Analysis of the InVEST SWY Model

The sensitivity of the critical variables of the SWY model was tested singularly as a measure of model performance and robustness. This analysis also provides an opportunity for testing the flexibility of the vital model-defining parameters per pixel within the multispectral space. The tested parameters were coefficients embedded in the model as provided by [19]. Notably, the variation of α showcases the import of interannual precipitation changes coupled with the possible unchanged local regime for a semi-arid area where water recharge is essential for different uses. Also, β is influenced by terrain characteristics, specifically soil typology and geology; hence, it is often less dynamic. Storage capacity, up-slope subsidy, and up-slope area are essential considerations when setting the numerical influence of β within the model. g parameter is also terrain influenced as observed with β but more on edaphic controls such that level of permeability often affects seasonally available water within a region. Due to the large-scale uniformity of soil-water context, the g parameter is often unchanged over the landscape. V parameter is the number of up-slope pixels that

contribute to a stream's definition in a given pixel. As a result, V is a function of SRTM data, and improvement in resolution characteristics could influence the expression of stream pixels within the multispectral space. V, α, β, and g parameters were adjusted by ±50% due to the possible nature of water fluctuation in a typical semi-arid region where there is established interannual water fluctuation. Expressly, V was varied from the default value of 1,000 to 500 and 1,500. The α parameter was also adjusted from the default value of 1/12 (indicating annual fluctuation) to 1/6 (biannual) and 1/24 (biennial). At the same time, both β and g were varied from the default value of 1 to ½ and 1½ each.

3. RESULT AND DISCUSSION

3.1. Spatiotemporal Dynamics of Quickflow in the Sokoto-Rima basin

The spatial distribution of quickflow, which is the hydrological response to direct water input from rainfall leading to increase river runoff within short intervals, is depicted in Figure 3. At the same time, the status levels were presented in Table 2. Five status levels were detected throughout the study periods, with fluctuating maximum and minimum values. This is not uncommon as quickflow characterisation is never highly dynamic [29]. However, the quickflow of the Sokoto-Rima basin is dominated by low flow levels with very low and low statuses. For instance, in 1992, the very low flow status occupied 38.15% (35,868.32 km^2) by the year 2015, it falls to 28.17% (26,490.24 km^2), while very high flow status improved from 9.07% (8,529.15 km^2) to 11.65% (10,950.54 km^2) suggesting that more areas received post-rainfall flow within 23 years. Also, the pattern of the shift in the amount of quickflow though disproportionate, shows increases over the years. Specifically, 38.5% increase in the low flow and a 19.63% upsurge in the magnitude of high flow. The associated temporal trend as displayed in Figure 6 portrays an increasing magnitude of quickflow with increasing rate of 85.331 mm per pixel with a pixel-based mean of 858.128 mm within the study period.

These intermittently high values of quickflow were spatially restricted to the headwaters located in the eastern part of the Sokoto-Rima basin (Figure 3). From these headwaters, quickflow was distributed spatially to other parts of the Sokoto-Rima basin. High quickflow values were also detected at the wetlands areas of the southern axis. The high quickflow observed within the downstream is partly due to its inherent landcover as mainly extensive wetlands of the Niger plain. As shown in Figure 3, the spatial pattern of quickflow distribution showed diverse values for each study period (a function of rainfall and other environmental factors). As shown in Figure 3, there is a south-north decreasing pattern of quickflow with exceptions in water-bearing landcover themes such as rivers, streams, lakes and dams in locations such as Sokoto, Goronyo, Talata-Mafara, Yauri, Maradi Argungu and Gusau, amongst others.

Table 2 Quickflow dynamics and relations in the Sokoto-Rima basin

1992			2002			2012			2015		
Status/ Modelled QF (mm)	**Land area (km^2)**	**%**	**Status/ Modelled QF**	**Land area (km^2)**	**%**	**Status/ Modelled QF**	**Land area (km^2)**	**%**	**Status/ Modelled QF**	**Land area (km^2)**	**%**
Very low (0-98.97)	35,868.32	38.15	Very low (0-151.11)	26,338.26	28.01	Very low (0-130.86)	30,607.87	32.55	Very low (0-137.07)	26,490.24	28.17
Low (98.98-267.06)	20,182.86	21.47	Low (151.12-411.23)	28,229.01	30.02	Low (130.87-363.79)	24,471.20	26.03	Low (137.08-385.93)	29,565.14	31.44
Moderate (267.07-453.42)	16,589.86	17.64	Moderate (411.24-671.35)	15,372.18	16.35	Moderate (363.80-596.72)	16,716.83	17.78	Moderate (385.93-617.32)	13,462.24	14.32
High	12,856.32	13.67	High	15,370.37	16.35	High	14,177.96	15.08	High	13,558.34	14.42

(453.43-643.43)			(671.35-905.97)			(596.73-805.89)			(617.32-796.32)		
Very high (643.44-924.8)	8,529.15	9.07	Very high (905.98-1293.6)	8,716.68	9.27	Very high (805.90-1205.2)	8,052.64	8.56	Very high (796.33-1106.3)	10,950.54	11.65
Total	**94,026.5**	**100**	**Total**	**94,026.5**	**100**	**Total**	**94,026.5**	**100**	**Total**	**94,026.5**	**100**

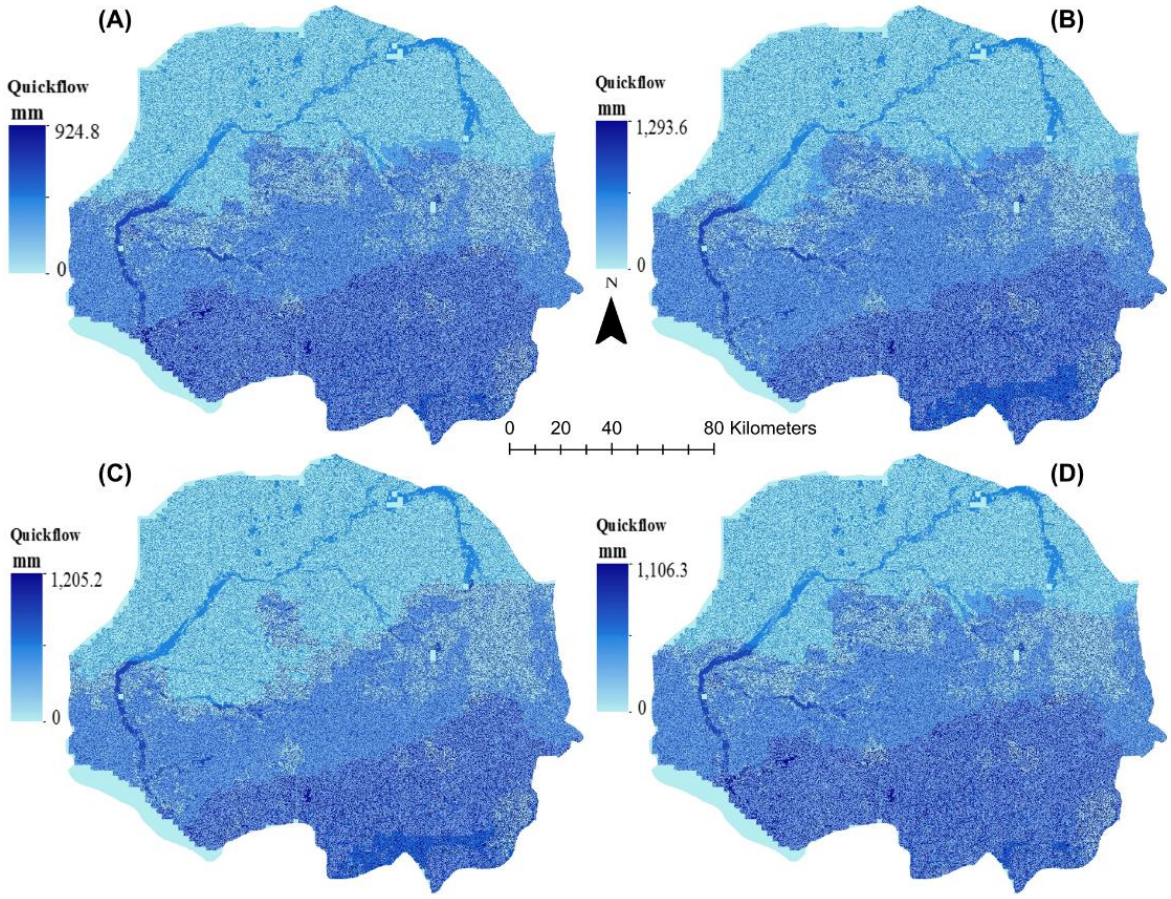

Figure 3 Spatial dynamics of quickflow of the Sokoto Rima basin for the year 1992 (A), 2002 (B), 2012 (C) and 2015 (D)

The spatial perspective of quickflow of the Sokoto-Rima basin for the study typified specifics that affirm the geography of post-floodwater distribution in the area. as displayed in Figure 4, the period 1992–2002 placed the marker for north-south change such that increases were detected in most parts of the south while decrease in quickflow was seen in the north. However, some areas of the west returned unchanged. The pattern changed significantly for the period 2002-2012: sustained increases were detected in some parts of the north that previously recorded decreases; similar patterns were also detected along the Sokoto River, particularly in parts of Kebbi; and a mosaic of decrease and unchanged patterns was detected in other parts of the study area. The period 2012-2015 showed the expansion of unchanged pattern, the dominance of declines in the east and increases in the west. On the whole, quickflow decreased northwards for the entire period of study, with local exceptions in some areas with specific socio-environmental influences.

These observations are not unexpected in dryland where rainfall drives hydrological response such that ephemeral streams become active and flash floods occur [9, 14-15]. Several factors have alluded to this. For instance, [8] asserted that water yield is a function of a consistent increase

in the amount of rainfall received per time in the Sokoto-Rima basin. [29] stated that apart from precipitation dynamics, landcover, change in vegetation could affect water yield, out of which quickflow is significant. [29] further affirmed that quickflow in low rainfall grassland area of Tibet contributes roughly 5% to water yield.

The contribution of quickflow in the expression of water yield remains critical, especially for semi-arid zones and for data-sparse regions where water availability data remain a daunting challenge [33, 31-33]. Quickflow is directly proportional to the amount of rainfall and landcover typologies. As a result, quickflow is a crucial factor in defining hydrological ecosystem services of the Sokoto-Rima basin. Quickflow is a vital index that aids water management for food security by boosting agriculture and ensuring energy security [33]. Therefore, consistent assessment of quickflow as a component of water yield is inevitable for the sustenance livelihoods and ecosystem services of the Sokoto-Rima basin.

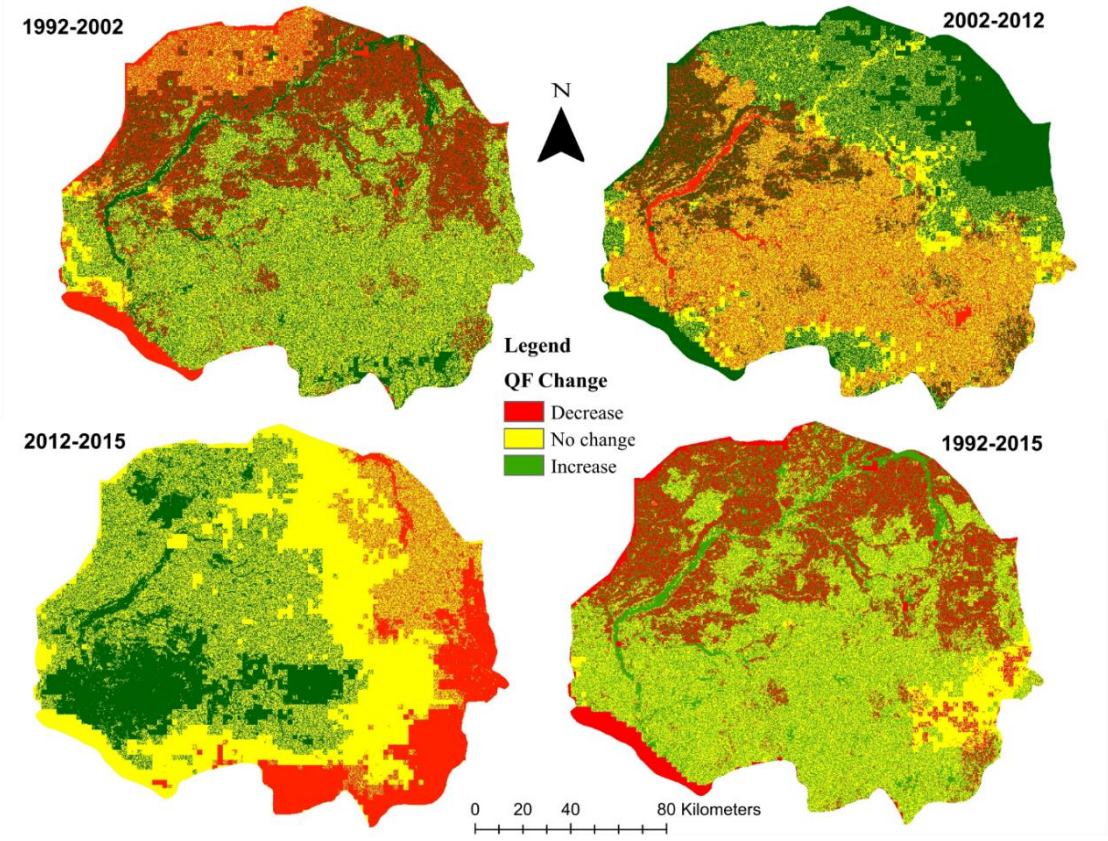

Figure 4 Pattern of spatiotemporal change in quickflow (QF) in the Sokoto Rima basin for the period 1992 to 2015

3.2. Spatial Variation of Local Recharge

As conceptualised in this study, variations in local recharge explain the pattern of changes in the potential contribution of rainfall (per pixel) in the basin to baseflow as influenced by the regional water balance. This shows that local recharge is directly proportional to excess rainfall feeding the groundwater and a significant factor in groundwater flow and characterisation. The spatiotemporal distribution of local recharge of the Sokoto-Rima basin for the study period is depicted in Figure 5, while the range of detected status is presented in Table 3. The concomitant temporal trend 6 portrays a decreasing magnitude of local recharge with rate of 56,131 mm per pixel with a pixel-based mean of 210,198 mm from 1992 to 2015 (Figure 6).

As shown in Table 3, local recharge is substantially low, averaging 46% very low status throughout the study. The very high grade recorded a meagre average of 0.025%, indicating a consistently low proportion and area extent. Overall, 71% of the low status were recorded

through strengthening the fact that the Sokoto-Rima basin is characterised by the low amount of water available per pixel. As depicted in Figure 5, the spatial equivalence of this shows that the south-north increasing index detected for the quickflow also subsists, though with periodic differentiations. Precisely, areas with a high amount of local recharge correlate directly with the extensive Niger plains. At the same time, moderate values were spatially delimited to some wetland areas while some of the permanent rivers and streams recorded the least importance. This scenario was detected in the baseline year (1992). By 2002, some wetlands in parts of the Sokoto-Shuni axis of the north recorded high values ranging from 311 to 931 mm, indicating an increase over time. This further expanded in 2012 to some parts of the headwaters of the northeast and the floodplains of the south. The trend persists till 2015, where roughly 13% of the landscape recorded a low amount of local recharge. The cumulative impact of the spatial distribution high amount of local recharge will lead to hydrological enrichment of the Sokoto-Rima basin, particularly wetlands and floodplains.

Table 3 Dynamics of Local Recharge characterisation in the Sokoto-Rima basin

1992			**2002**			**2012**			**2015**		
Status/ Modelled LR (mm)	**Land area (km^2)**	**%**	**Status/ Modelled LR (mm)**	**Land area (km^2)**	**%**	**Status/ Modelled LR (mm)**	**Land area (km^2)**	**%**	**Status/ Modelled LR (mm)**	**Land area (km^2)**	**%**
Very low (0-12.98)	45,611.11	48.51	Very low (0-61.29)	41,825.41	44.48	Very low (0-39.04)	41,883.66	44.54	Very low (0-44.74)	41,867.93	44.53
Low (12.99-82.54)	27,339.87	29.08	Low (61.3-180.02)	20,726.95	22.04	Low (39.05-141.66)	20,887.66	22.21	Low (44.75-143.96)	15,632.56	16.63
Moderate (82.55-169.48)	17,703.36	18.83	Moderate (180.03-311.94)	24,723.36	26.29	Moderate (141.67-257.11)	23,453.13	24.94	Moderate (143.97-243.18)	25,166.36	26.77
High (169.49-604.19)	3,347.04	3.56	High (311.95-931.98)	6,730.91	7.16	High (257.12-872.84)	7,781.82	8.28	High (243.19-725.11)	11,329.21	12.05
Very high (604.20-2273.5)	25.12	0.03	Very high (931.99-2620.6)	19.87	0.02	Very high (872.85-2527.6)	20.22	0.02	Very high (725.12-2567.8)	30.44	0.03
Total	**94,026.5**	**100**	**Total**	**94,026.5**	**100**	**Total**	**94,026.5**	**100**	**Total**	**94,026.5**	**100**

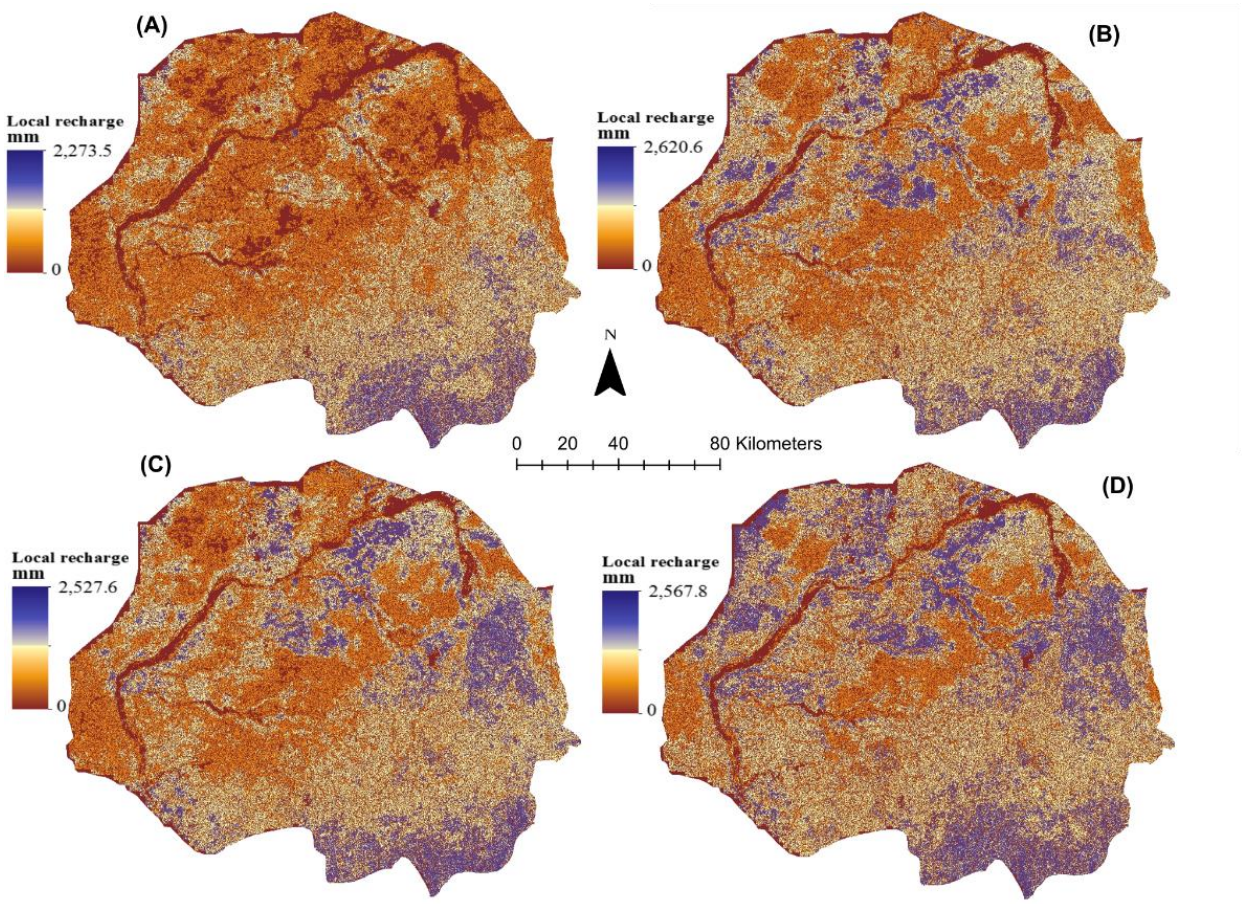

Figure 5 Spatial dynamics of local recharge of the Sokoto Rima basin for the years 1992 (A), 2002 (B), 2012 (C) and 2015 (D)

Relative to water balance, the amount of local recharge represents 2.5%, 5.1%, 2.6 and 2.3% of rainfall for 1992, 2002, 2012 and 2015, respectively. These are in concordance with [22], which computed that recharge rates for the Sokoto-Rima basin range between 2-7% of annual precipitation. It should be noted that hydrogeological factors influence the local recharge of a tropical basin such as the Sokoto-Rima. [23] affirmed that spatial distribution of artesian aquifers in locations such as Gundumi, Rima and Gwandu with varying depths influence available recharge. This is also to a great extent, geological age and associated constituents such as lithology, nature of deposits, and age range from the Cretaceous to Eocene. However, these aquifers are extensively confined apart from the open water bodies whose storage capacities with apparent seasonal climatic variations.

Marked distinctions exist within the spatial variations in local recharge of the Sokoto-Rima basin, as shown in Figure 7. This is obviously an accumulated characterisation of the observed spatiotemporal dynamics in local recharge relations and factors of change. The period 1992-2002 showed that wetland areas abutting the major rivers and streams recorded mixed increase and no change patterns throughout the study area. Decreases, however, were recorded in major rivers such as Sokoto, Rima, Ka, Maradi, and Zamfara. However, these observations flipped by the decade 2002-2012, where the increase was detected along with the water bodies, indicating ceteris paribus substantial water input. Minute instances of unchanged local recharge amounts were also detected all over the Sokoto-Rima basin. The period 2012-2015 witnessed few decreases and increase with no change dimension. For the entire study period, the magnitude of local recharge remained largely a mosaic of decrease interspersed with no change.

As shown in this study, local recharge (the proportion of local water balance that potentially feeds the baseflow) is a function of landcover,

precipitation and terrain characteristics. The result of the study also tallies with those of semi-arid areas of Ethiopia, particularly the Wabe Catchment of East Africa, with a similar spatiotemporal trend [32].

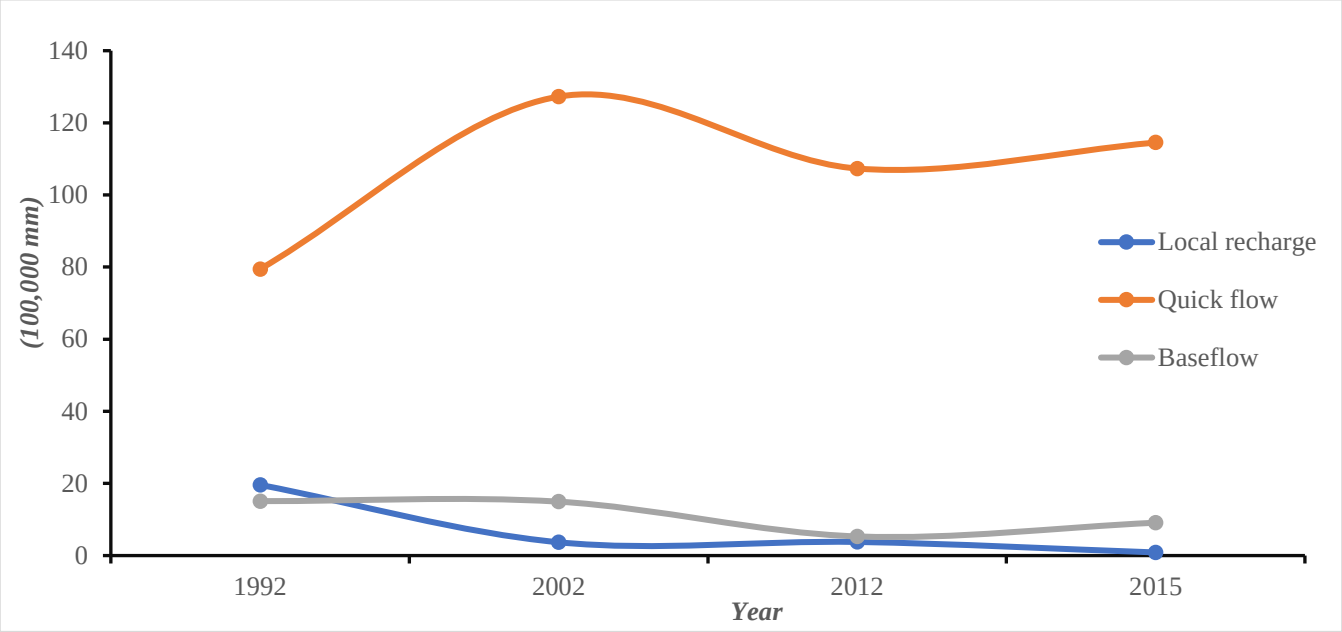

Figure 6 Temporal trend of quick flow, local recharge, and baseflow of the Sokoto-Rima basin for the period 1992, 2002, 2012 and 2015.

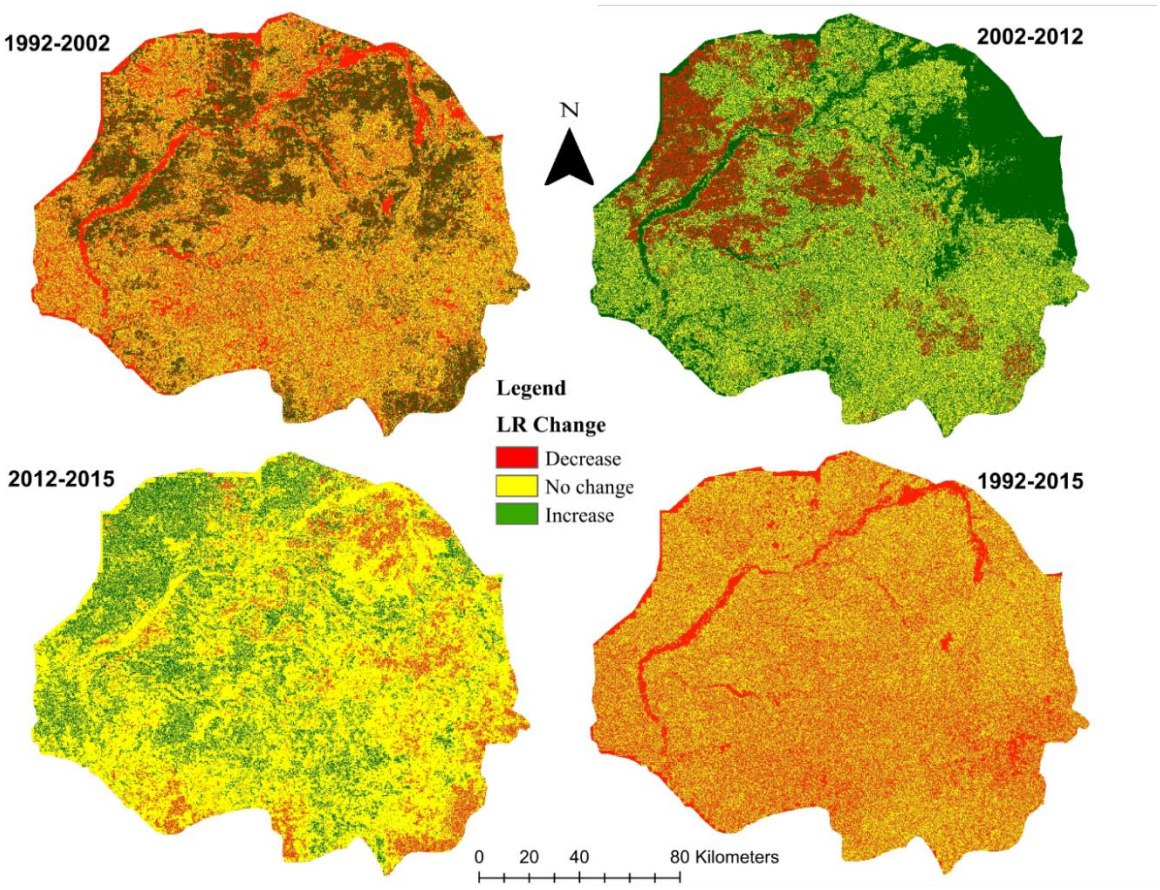

Figure 7 Pattern of spatiotemporal change in local recharge (LR) in the Sokoto Rima basin for the period 1992 to 2015

3.3. Baseflow Characteristics in the Sokoto-Rima

As developed in this study, Pixel-based baseflow is the actual contribution of a defined location in multispectral space to the amount of water that reaches a stream or a river [7, 19]. This shows that the equation of seasonal water yield is incomplete without the quantitative expression of baseflow. Spatial dynamics of baseflow in the Sokoto-Rima basin within the study period are presented in Table 4 and illustrated in Figure 8. Approximately 50% of the land area returned low baseflow status throughout the study period, while the proportion of high flow is <5% apart from 2002, which returned 5.4%. However, the proportion of moderate status has progressively increased from 18.27% (17,276.06 km^2) in 1991 to 26.28% (24,710.46 km^2) in 2015.

The associated spatial details revealed that the maximum baseflow level in 1992 was 4,723.43 mm; by 2002, it increased to 7.127.96 mm by a proportion of 50.91%. As shown in Figure 8, this change is primarily noticeable around water bodies and wetlands with substantial proportionate increases. The pattern observed in 2012 and 2015, as observed in Figure 8C and Figure 8D, showed a maximum of 6,771.24 mm and 5,888.58 mm, respectively depicting a gradual reduction by 5% and 17.39% from 2002 levels. Thus, the peak baseflow level of 7,127.96 mm was recorded in 2002. Decadal differences from 2002 to 2012 with reductions in the amount of baseflow, however, set regional delineations as decreases were recorded in the western part compared to increases in the west of and some parts of the northern section Sokoto-Rima basin. The temporal trend of baseflow in the Sokoto-Rima basin is shown in Figure 6 with decreasing pattern. Specifically, the trend showed a decreasing rate of 27.597 mm with an average yearly value of 180.189 mm within the period of study.

This correlates with the observation of quickflow and local recharge dynamics, particularly in locations where increases were detected. The further reductions noted in 2015 compared to 2012 mainly were detected in a few places in the east, while most of the study witnessed averagely unchanged values. The aggregate changes from 1992 to 2015 returned meagre changes over most of the Sokoto-Rima basin, while reductions in baseflow were observed in the north while wetlands of the central area had a tiny increase.

Table 4 Dynamics of Baseflow characterisation in the Sokoto-Rima basin

1992			**2002**			**2012**			**2015**		
Status/ Modelled B (mm)	**Land area (km^2)**	**%**	**Status/ Modelled B (mm)**	**Land area (km^2)**	**%**	**Status/ Modelled B (mm)**	**Land area (km^2)**	**%**	**Status/ Modelled B (mm)**	**Land area (km^2)**	**%**
Very low (0-98.97)	49,925.61	53.10	Very low (0-151.11)	39,967.39	42.51	Very low (0-130.86)	42,568.89	45.27	Very low (0-137.07)	39,495.79	42.00
Low (98.98-267.06)	24,475.97	26.03	Low (151.12-411.23)	28,242.14	30.04	Low (130.87-363.79)	28,100.93	29.89	Low (137.08-385.93)	25,342.58	26.95
Moderate (267.07-453.42)	17,276.06	18.37	Moderate (411.24-671.35)	20,067.47	21.34	Moderate (363.80-596.72)	19,684.30	20.93	Moderate (385.93-617.32)	24,710.46	26.28
High (453.43-643.43)	2,330.84	2.48	High (671.35-905.97)	5,074.19	5.40	High (596.73-805.89)	3,654.51	3.89	High (617.32-796.32)	4,396.64	4.68
Very high (643.44-924.8)	18.02	0.02	Very high (905.98-1293.6)	675.30	0.72	Very high (805.90-1205.2)	17.88	0.02	Very high (796.33-1106.3)	81.03	0.09
Total	**94,026.5**	**100**	**Total**	**94,026.5**	**100**	**Total**	**94,026.5**	**100**	**Total**	**94,026.5**	**100**

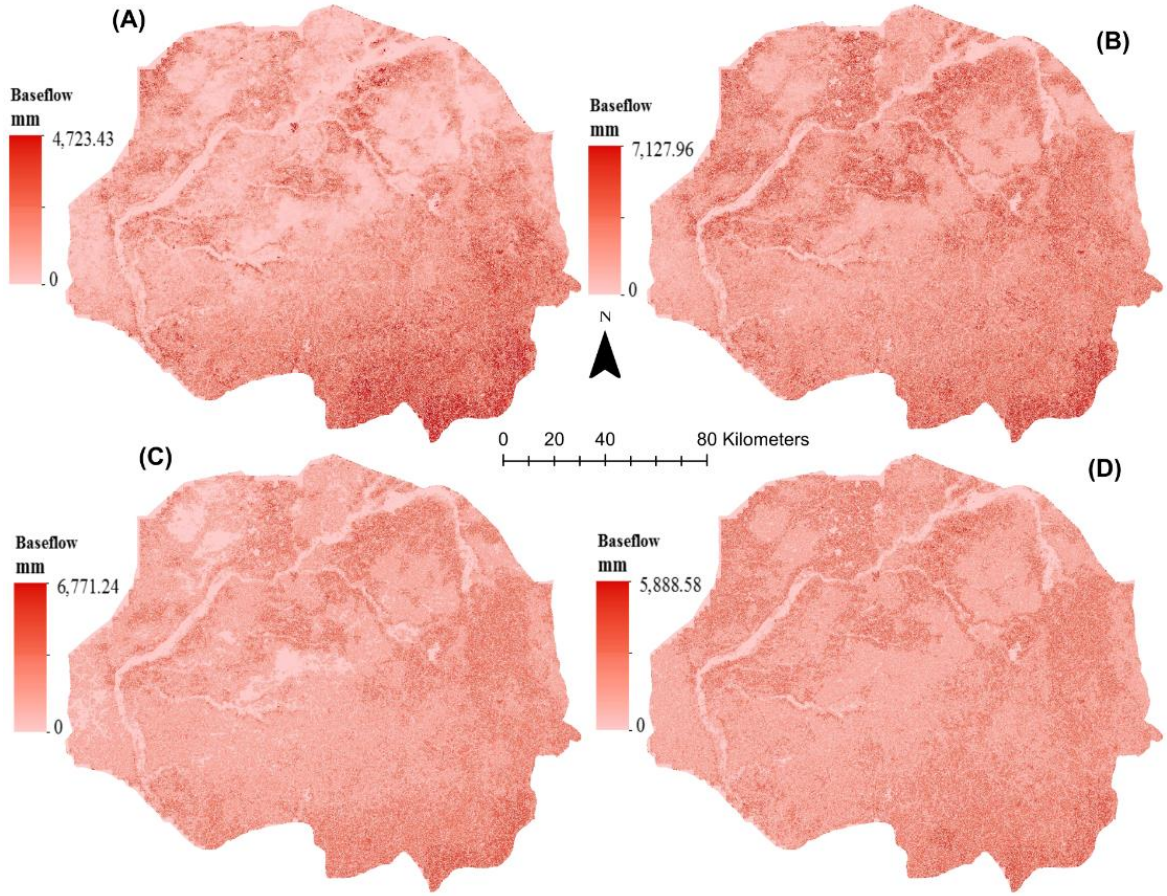

Figure 8 Dynamics of baseflow of the Sokoto Rima basin for the years 1992 (A), 2002 (B), 2012 (C) and 2015 (D)

There is some degree of spatial disparities in the pattern of baseflow of the Sokoto-Rima basin across this study. These observed variations are mapped and displayed in Figure 9, indicating non-linear dynamics in change patterns. The decade 1992-2002 showed that most of the study area recorded a mixed bag of dwindling and no-change pattern. There are exceptions of increase in wetland areas adjoining the major water bodies and woodlands where edaphic storage was detected to range between increase and zero variation. A completely different pattern was detected in the subsequent decade 2002-2012. An upsurge was noticed, obviously driven by cumulative precipitation input, with few exceptions in some of the north-western locations. The period 2012–2015 had minute decrease variations in some parts of the east and north while water bodies and floodplain of the Niger recorded no change. The aggregated spatial variation showed that a decrease in baseflow was detected in water bodies while the contiguous wetlands increased the quantum of baseflow.

Previous studies in the semi-arid areas of northern Nigeria, the nature and dynamics of groundwater characterization. [24] stated that the groundwater of the semi-arid northern Nigeria is generally available in small quantities, which to a considerable degree is the major source of potable water for its population. LR falls within the shallow groundwater, which is the main water point for the agricultural population of the Sokoto-Rima basin. Further, [24] opined that recharge from aquifer sources in the Sokoto-Rima basin is strongly influenced by geology. The Basement complex formation contributes an average of 40 mm/year, while others are affected by seasonal rainfall and proximity to water bodies ranged from 1 to 34 mm/year. However, it is anticipated that increasing demand for diverse water sources, majorly from municipal, agrarian, aquaculture and livestock coupled with climate change, sustainability of the current supply stock is vital. Thus projected that reliance on freshwater supplies from groundwater will increase by almost four-fold by 2030 [24-25].

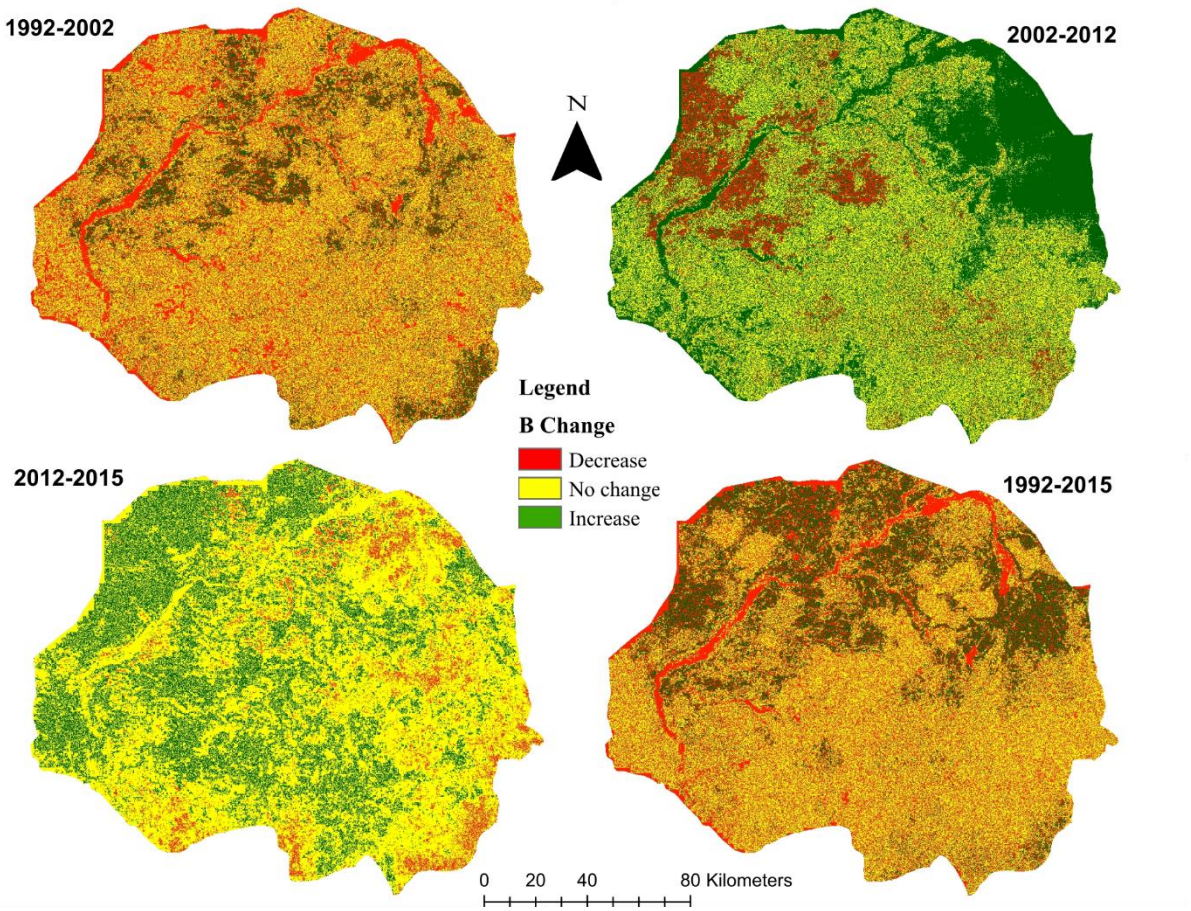

Figure 9 Pattern of spatiotemporal change in baseflow (B) in the Sokoto Rima basin for the period 1992 to 2015

3.4. Sensitivity Analysis of the SWY Model in the Sokoto-Rima basin

The set of equations used to typify the InVEST SWY model in terms of quickflow, local recharge, and baseflow are linear. Some of the associated variables nevertheless present a high possibility of sensitivity to changes in computational values. For instance, Figure 10 shows that a proportionate ±50% change in the critical parameters of θ, α, β, and γ can alter the amount of baseflow available per pixel within the multispectral space of the Sokoto-Rima basin. The least sensitive of the parameters assessed is f. Although this is analogous to the spatial resolution, it shows that threshold accumulation has a limited influence on baseflow. Thus, upslope relations and downslope reception exert limited influence on stream development. This is primarily related to the nature of the terrain as the Sokoto-Rima basin is geomorphologically a plain with exceptions along the eastern end where most of the rivers originate. The γ parameter returns some slight sensitivity with an average ±5.7% response to the proportionate adjustment. This sensitivity is a reflection of possible soil-water contexts under the influence of relief. This shows that soil-water relations are a local relief factor for baseflow availability annually. In addition, the soil characterisation contributes significantly to this extent of changes within the aquifer and groundwater traits possible within the semi-arid zone of Nigeria. The α and β parameters obviously influence baseflow as shown in Figure 10 with ±19% and ±15.7% response to adjustments, respectively. These are anticipated to drive increases and decreases in line with other covariates of water balance in the Sokoto-Rima basin and other similar semi-arid areas of West Africa. The shape and pattern of the response of these are also influenced to some degrees by landcover. For instance, [24] stated that baseflow characterisation is influenced by land characteristics, seasons and hydrogeological factors. α and β are direct correlates of these

factors integrated into the water balance computations enshrined into the InVEST SWY model. Local peculiarities are therefore critical in weighing the spatial performance of the InVEST SWY model.

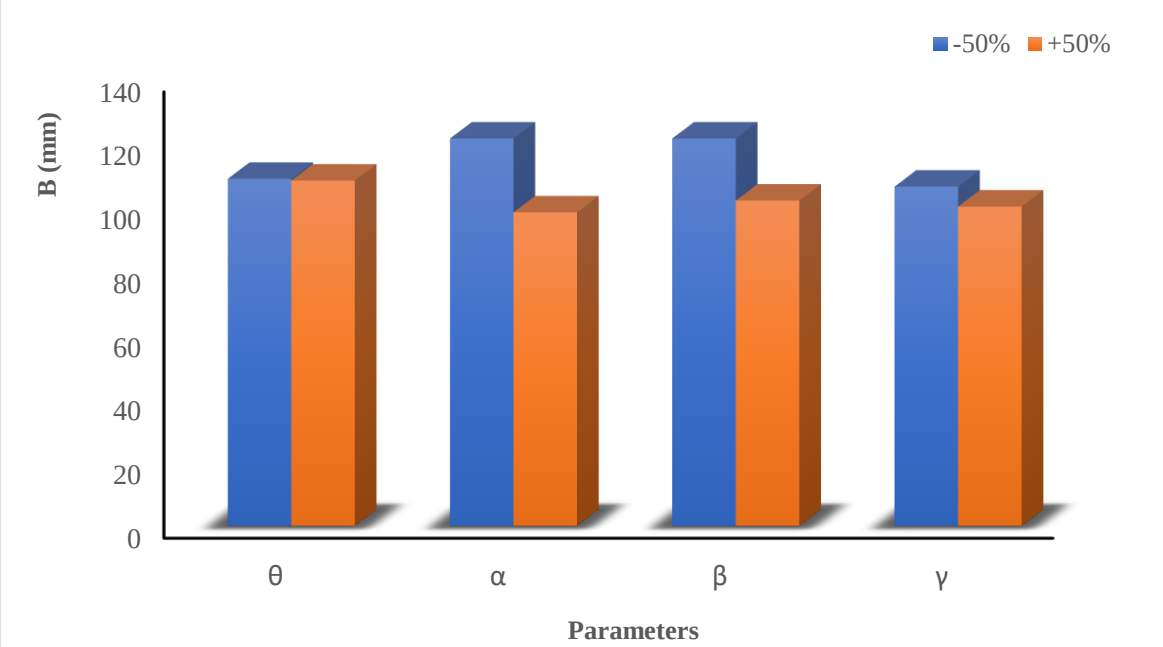

Figure 10 Pixel-based sensitivity test of the baseflow component of the SWY model as expressed by by f (Threshold accumulation), α (alpha parameter), β (beta parameter) and γ (gamma parameter)

3.5. Conclusion

Model-based computation of water yield using the tools of geographical information system is a burgeoning enterprise. In this research, we employed the SWY model in computing the quickflow, local recharge and baseflow using the InVEST software package for the semi-arid ecosystem of the northwestern part of Nigeria. The outcome mirrors some existing studies, particularly in terms of hydrogeological characteristics, seasonality and climate change on the computation of local recharge and baseflow, which are groundwater components of the study. This study becomes essential for the rational and deductive management of scarce water resources of the grasslands and savanna regions of the world where the Sokoto-Rima basin lies [26-27]. This will help policymakers use outputs of hydrological science as the basis for freshwater planning and management.

In addition, covariates of the adopted model require place-based sensitivity assessment to reflect data validation and model review areas. This has been tested for in the study, and the results showed that important covariates of baseflow exert significant influence on the aggregate quantity of SWY in the basin. Studies on landcover based scenarios on seasonal water yield on drylands such as the Sokoto-Rima basin help unveil context-specific factors influencing seasonal water yield and, to a large extent, the water balance relations.

4. REFERENCES

[1] Millennium Ecosystem Assessment, “Ecosystem and human well-being: biodiversity synthesis,” 2005. Island Press, Washington DC.

[2] H. Saarikoski, E. Primmer, S. Saarela, P. Antunes, R. Aszalos, F. Baro, P. Berry, G. G. Blanko, E. Gomez-Baggethun, L. Carvalho, J. Dick, R. Dunford, M. Hanzu, P. A. Harrison, Z. Izakovicova, M. Kertész, L. Kopperoinen, B. Köhler, ... and J. Young, “Institutional challenges in putting ecosystem service knowledge in practice,”

Ecosystem Services, vol. 29, no. 3, pp. 579–598, 2018.

[3] J. Yang, Y. C. E. Yang, H. F. Khan, H. Xie, C. Ringler, A. Ogilvie, O. Seidou, A. G. Djibo, F. van Weert, and R. Therme, "Quantifying the sustainability of water availability for the water-food-energy-ecosystem nexus in the Niger River Basin," Earth's Future, vol 6, pp. 1292–1310, 2018.

[4] J. A. Aznar-Sánchez, J. F. Velasco-Muñoz, L. J. Belmonte-Ureña, and F. Manzano-Agugliaro, "The worldwide research trends on water ecosystem services," Ecological Indicators, vol. 99, pp. 310–323, 2019.

[5] C. Guo, and H. Xu, "Use of functional distinctness of periphytic ciliates for monitoring water quality in coastal ecosystems," Ecological Indicators, vol. 96, pp. 213–218, 2019.

[6] F. Scordo, T. Lavender, C. Seitz, V. Perillo, J. Rusak, M. Piccolo, and G. Perillo, "Modeling water yield: assessing the role of site and region-specific attributes in determining model performance of the InVEST seasonal water yield model", Water, vol. 10, pp. 1496, 2019.

[7] P. Hamel, J. Valencia, R. Schmitt, M. Shrestha, T. Piman, R. P. Sharp, W. Francesconi, and A. J. Gusawa, "Modeling seasonal water yield for landscape management: Applications in Peru and Myanmar. Journal of Environmental Management," Journal of Environmental Management, vol. 270, pp. 110792, 2020.

[8] I. J. Ekpoh, and E. Nsa, "The effects of recent climatic variations on water yield in the Sokoto region of northern Nigeria," International Journal of Business and Social Science, vol. 2, no. 7, pp. 251–256, 2011.

[9] S. A. Abdullahi, M. M. Muhammad, B. K. Adeogun, and I. U. Mohammed, "Assessment of water availability in the Sokoto Rima River Basin," Resources and Environment, vol. 4, no. 5, pp. 220–233, 2014.

[10] H. Hamidu, M. L. Garba, Y. I. Abubakar, U. Muhammad, and D. Mohammed, "Groundwater resource appraisals of Bodinga and environs, Sokoto Basin north western Nigeria," Nigerian Journal of Basic and Applied Science, vol. 24, no. 2, pp. 92–101, 2016.

[11] Food and Agriculture Organization of the United Nations, "FAO AQUASTAT: Country profile Nigeria," 2016. Available: http://www.fao.org/3/i9807en/I9807EN.pdf

[12] C. Albert, C. Galler, J. Hermes, F. Neuendorf, C. Von Haaren, A. Lovett, "Applying ecosystem services indicators in landscape planning and management: The ES-in-Planning framework," Ecological Indicators, vol. 61, pp., 100–113, 2016.

[13] J. C. Clanet and A. Ogilvie, "Basin focal project Niger," CPWF Project Report series, Challenge Program on Water and Food, Colombo, Sri Lanka, p 124.

[14] P. G. Oguntunde, B. J. Abiodun, and G. Lischeid, "Rainfall trends in Nigeria, 1901-2000", Journal of Hydrology, vol. 411, pp. 207–218, 2011.

[15] I. B. Abaje, O. F. Ati, and E. O. Iguisi, "Recent trends and fluctuations of annual rainfall in the sudano-sahelian ecological zone of Nigeria: Risks and opportunities," Journal of Sustainable Society, vol. 1, no. 2, pp. 44–51, 2012.

[16] G. B. Senay, S. Bohms, R. K. Singh, P. H. Gowda, N. M. Velpuri, H. Alemu, J. P. Verdin, "Operational evapotranspiration mapping using remote sensing and weather datasets: A new parameterization for the SSEB approach," Journal of American Water Resources Association, vol. 49, no. 3, pp. 577–591, 2013.

[17] R. I. Maidment, D. Grimes, E. Black, E. Tarnavsky, M. Young, H. Greatrex, R. P. Allan et al., "A new, long-term daily satellite-based rainfall dataset for operational monitoring in Africa," Nature Scientific Data, vol. 4, no. 170063, 2017. DOI:10.1038/sdata.2017.63.

[18] C. W. Ross, L. Prihodko, J. Anchang, S. Kumar, W. Ji, and N. P. Hanan, "HYSOGs250m, global gridded hydrologic soil groups for curve-number-based runoff modeling," Scientific Data, vol. 5, no. 180091. https://doi.org/10.1038/sdata.2018.91

[19] R. S. Sharp, H. T. Tallis, T. Ricketts, A. D. Guerry, S. A. Wood, E. Nelson, D. Ennaanay, S. Wolny, et al., "InVEST 3.7 User's Guide," 2019. Available: http://releases.naturalcapitalproject.org/invest-userguide/latest/

[20] S. U. Wali, K. J. Umar, S. D. Abubakar, I. P. Ifabiyi, I. M. Dankani, I. M. Shera, S. G. Yauri, "Hydrochemical characterization of shallow and deep groundwater in Basement Complex areas of southern Kebbi State, Sokoto Basin, Nigeria," Applied Water Science, vol. 9, no 169, 2019. https://doi.org/10.1007/s13201-019-1042-5

[21] Japan International Cooperation Agency, "The project for review and update of Nigeria national water resources master plan: Volume 5 Supporting report", Federal Ministry of Water Resources, Nigeria, 2014.

[22] S. M. A. Adelana, P. I. Olasehinde, and P. Vrbka, "Groundwater recharge in the cretaceous and tertiary sediment aquifers of northwestern Nigeria, using hydrochemical and isotopic techniques," Groundwater and Human Development, E. Bocanegra, D. Martínez, H. Massone, H (Eds.), pp. 907–915, 2002.

[23] S. M. A. Adelana, P. I. Olasehinde, R. B. Bale, P. Vrbka, A. G. Edet and I. B. Goni, "An overview of the geology and hydrogeology of Nigeria", in Applied groundwater studies in Africa, S. M. A. Adelana and A. M. McDonald, Eds. Leiden, Netherlands: CRC Press/Balkema, vol 13, pp. 171–198, 2008.

[24] S. M. A. Adelana, P. I. Olasehinde, and P. Vrbka, "A quantitative analysis of groundwater recharge in part of the Sokoto basin, Nigeria," Journal of Environmental Hydrology, vol. 14, no. 5, pp. 1–16, 2016.

[25] A. L. Vogl, J. H. Goldstein, G. C. Daily, B. Vira, L. L. Bremer, R. I. McDonald, D. Shemie, B. Tellman and J. Cassin, "Mainstreaming investments in watershed services to enhance water security: barriers and opportunities," Environmental Science and Policy, vol. 75, pp. 19–27, 2017. https://doi.org/10.1016/j.envsci.2017.05.007

[26] K. A. Brauman, "Hydrologic ecosystem services: linking ecohydrologic processes to human well-being in water research and watershed management." Wiley Interdiscip. Rev. Water, vol. 2, pp. 345–358, 2015. https://doi.org/10.1002/wat2.1081.

[27] C. E. R. Lehmann, "Savannas need protection". Science, vol. 327, pp. 642–643, 2010.

[28] A. J Guswa, P. Hamel, K. Meyer, "Curve number approach to estimate monthly and annual direct runoff," Journal of Hydrological Engineering, 23, 2018. https://doi.org/10.1061/(ASCE)HE.1943-5584.0001606.

[29] H. Lu, Y. Yan, J. Zhu, T. Jin, G. Liu, G. Wu, L. C. Stringer, M. Dallimer, "Spatiotemporal water yield variations and influencing factors in the Lhasa River Basin, Tibetan Plateau," Water, 12, 1498, 2020. doi:10.3390/w12051498

[30] S.Minga-León, M. A. Gómez-Albores, K. M. Bâ, L. Balcázar, L. R. Manzano-Solís, A. P. Cuervo-Robayo, C. A. Mastachi-Loza, "Estimation of water yield in the

hydrographic basins of southern Ecuador," Hydrology and Earth System Sciences, https://doi.org/10.5194/hess-2018-529

[31] K. Sang-Wook, and J. Yoon-Young, "Application of the InVEST model to quantify the water yield of North Korean forests," Forests, 11, 804, 2020. DOI:10.3390/f11080804.

[32] M. Sahle, O. Saito, C. Fürst, K. Yeshitela, "Quantifying and mapping of water-related ecosystem services for enhancing the security of the food-water-energy nexus in tropical data–sparse catchment," Science of The Total Environment, Vol 646, 573–586, 2019.

[33] X. Yang, R. Chen, M. E. Meadows, G. Ji, J. Xu, "Modelling water yield with the InVEST model in a data scarce region of northwest China," Water Supply. doi:10.2166/ws.2020.026

[34] United States Department of Agriculture (USDA) – Natural Resources Conservation Service (NRCS), Chapter 10: estimation of direct runoff from storm rainfall. In Part 630: Hydrology: NRCS National Engineering Handbook, USDA National Resources Conservation Service, 2004. https://directives.sc.egov.usda.gov/OpenNonWebContent.aspx?content=17752.wba

SAKARYA ÜNİVERSİTESİ
FEN BİLİMLERİ ENSTİTÜSÜ DERGİSİ

Sakarya University Journal of Science
SAUJS

e-ISSN: 2147-835X | Founded: 1997 | Period: Bimonthly | Publisher: Sakarya University
http://www.saujs.sakarya.edu.tr/en/

Title: A New Approach to k–Jacobsthal Lucas Sequences

Authors: Hakan AKKUŞ, Rabia Nagehan ÜREGEN, Engin ÖZKAN

Recieved: 2021-03-01 14:00:08

Accepted: 2021-06-24 10:20:51

Article Type: Research Article

Volume: 25
Issue: 4
Month: August
Year: 2021
Pages: 969-973

How to cite
Hakan AKKUŞ, Rabia ÜREGEN, Engin ÖZKAN; (2021), A New Approach to k–Jacobsthal Lucas Sequences. Sakarya University Journal of Science, 25(4), 969-973, DOI: https://doi.org/10.16984/saufenbilder.842489
Access link
http://www.saujs.sakarya.edu.tr/en/pub/issue/64755/842489

Sakarya University Journal of Science 25(4), 969-973, 2021

A New Approach to k–Jacobsthal Lucas Sequences

Hakan AKKUŞ[1], Rabia Nagehan ÜREGEN*[1], Engin ÖZKAN[1]

Abstract

In this study, Catalan transformation $CS_{k,n}$ of k–Jacobsthal-Lucas sequences $S_{k,n}$ is defined. In addition, the transformation of $CS_{k,n}$ is written as the product of the Catalan matrix C which is the lower triangular matrix and the S_k matrix of type $n\ x\ 1$, and the Hankel transformations of some k–Jacobsthal-Lucas numbers is found.

Keywords: k–Pell sequences, k–Lucas sequence, k–Fibonacci sequence, Catalan Transform, Hankel Transform

1. INTRODUCTION

For any integer n, it is called a generalized Fibonacci-type sequence in the following form $G(n+1)=aG(n)+bG(n-1)$, $G(0)=m, G(1)=t$,where m,t,a and b are any complex numbers. There is an extensive work in the literature concerning Fibonacci-type sequences and their applications in modern science (see e.g.[1-8]). The known Jacobstahal-Lucas numbers have some applications in many branches of mathematics such as group theory, calculus, applied mathematics, linear algebra, etc. [9-12]. There exist generalizations of the Jacobsthal-Lucas numbers. This study is an extension of the papers [13-15].

In this paper, we put in for Catalan transform to the k–Jacobsthal-Lucas sequence and present application of the Catalan transform of the k–Jacobsthal-Lucas sequence. In section 2, we introduce some fundamental definitions of k–Jacobsthal-Lucas sequences and some basic theorems. In Theorem 2.1, we obtain Binet's formula of k–Jacobsthal-Lucas sequences and in Theorem 2.2, we give the relationship between positive and negative terms of k–Jacobsthal-Lucas numbers. In Theorem 2.3, we get Cassini identity for this sequence. In section 3, Catalan transform of k–Jacobsthal-Lucas sequence is given. Hankel transform of Catalan transformation of k–Jacobsthal-Lucas sequence is obtained in section 4.

2. k–JACOBSTHAL-LUCAS SEQUENCES

Let k be any positive real number. Then the k-Jacobsthal-Lucas sequences is defined

$S_{k,n+1} = S_{k,n} + 2k.S_{k,n-1}$ for $n \geq 1$ with the initial values $S_{k,0} = 2$ and $S_{k,1} = 1$.

* Corresponding author: rabia.uregen@erzincan.edu.tr
[1] Erzincan Binali Yildirim University, Institute Of Natural And Applied Sciences, Center, Turkey.
E-Mail: hakanakkus024@gmail.com; eozkan@erzincan.edu.tr
ORCID: https://orcid.org/0000-0001-9716-9424; https://orcid.org/0000-0002-6824-4752; https://orcid.org/ 0000-0002-4188-7248

When k=1, the known Jacobsthal-Lucas sequences is obtained. Characteristic equation of the sequence is

$r^2-r-2k=0$.

Its characteristic roots are

$r_1 = \frac{1+\sqrt{1+8k}}{2}$

and

$r_2 = \frac{1-\sqrt{1+8k}}{2}$

Characteristic roots verify the properties

$r_1 + r_2 = 1, \qquad r_1.r_2 = -2k$

$r_1 - r_2 = \sqrt{1+8k}$

Binet's formula for $S_{k,n}$ is

$S_{k,n} = r_1^n + r_2^n$.

k−Jacobsthal-Lucas sequences as numbered;

$S_{k,n+1} = S_{k,n} + 2k.S_{k,n-1}$

$S_{k,0} = 2$

$S_{k,1} = 1$

$S_{k,2} = S_{k,1} + 2k.S_{k,0} = 4k+1$

$S_{k,3} = S_{k,2} + 2k.S_{k,1}$

$= 4k+1+2k.1$

$= 6k+1.$

$S_{k,4} = S_{k,3} + 2k.S_{k,2}$

$= 6k+1+2k.(4k+1)$

$= 8k^2 + 8k+1.$

$S_{k,5} = S_{k,4} + 2k.S_{k,3}$

$= 8k^2 + 8k + 1 + 2k.(6k+1)$

$= 20k^2 + 10k + 1.$

$S_{k,6} = S_{k,5} + 2k.S_{k,4}$

$= (20k^2 + 10k + 1) + 2k.(8k^2 + 8k+1)$

$= 16k^3 + 36k^2 + 12k + 1.$

$S_{k,7} = S_{k,6} + 2kS_{k,5}$

$= 16k^3 + 36k^2 + 12k + 1 + 2k.(20k^2 + 10k + 1)$

$= 56k^3 + 56k^2 + 14k + 1.$

Theorem 2.1. Binet's formula of k−Jacobsthal-Lucas sequences are obtained from the relations.

$S_{k,n} = r_1^n + r_2^n$

Proof.

The solutions of the characteristic equation are

$r^2 - r - 2k = 0$,

$r_1 = \frac{1+\sqrt{1+8k}}{2}$ and $r_2 = \frac{1-\sqrt{1+8k}}{2}$.

$S_{k,n} = c.r_1^n + d.r_2^n$

for n = 0, it is $S_{k,0}$= 2 and for n=1, it is $S_{k,1} = 1$. Thus c = 1 and d =1 are obtained. So, the proof is completed.

Theorem 2.2. For the k−Jacobsthal-Lucas numbers, the following identity holds for:

$$S_{k,n} = (-2k)^n.S_{k,-n} .$$

Proof. By virtue of Binet's formula, we find that

$S_{k,-n} = r_1^{-n} + r_2^{-n}$

$= \frac{1}{r_1^n} + \frac{1}{r_2^n}$

$= \frac{r_1^n + r_2^n}{(r_1.r_2)^n}$ $\quad ((r_1.r_2)^n = (-2k)^n)$

$= \frac{S_{k,n}}{(-2k)^n}$.

$S_{k,n} = (-2k)^n.S_{k,-n}$.

Theorem 2.3. (Cassini identity) For the k−Jacobsthal-Lucas numbers, the following equailty holds:

$$S_{k,n+1}.S_{k,n-1}- S_{k,n}^2= (-2k)^{n-1}.(8k+1)$$

Proof. By using the Binet's formula, we have $S_{k,n+1}.S_{k,n-1}-S_{k,n}^2=$

$(a^{n+1} + b^{n+1}).(a^{n-1} + b^{n-1})- (a^n + b^n)^2$

$= a^{2n} + a^{n+1}.b^{n-1} + a^{n-1}.b^{n+1} + b^{2n} - a^{2n} - 2a^n b^n - b^{2n}$

$= (ab)^n \frac{a}{b} + (ab)^n \frac{b}{a}$ -2.$(ab)^n$

$= (ab)^n[\frac{a}{b} + \frac{b}{a} - 2]$

$= (-2k)^n(\frac{4k+1}{-2k} - 2)$

$= (-2k)^{n-1}.(8k + 1).$

3. CATALAN NUMBERS

For n ≥0, the n^{th} Catalan number [13] is defined as follows

$C_n = \frac{1}{n+1}$(2n,n) or $C_n = \frac{(2n)!}{(n+1)!n!}$

Its generating function is given by

C(x) = $\frac{1-\sqrt{1-4x}}{2x}$.

The first Catalan numbers are {1,1,2,5,14,132,429,1430,4862, …}.

3.1. Catalan Transform of the k−Jacobsthal-Lucas sequences

We define the Catalan transform of the k−Jacobsthal-Lucas sequences { $S_{k,n}$} as

C$S_{k,n}$= $\sum_{i=0}^{n} \frac{i}{2n-i}\binom{2n-i}{n-i} S_{k,i}$, $n \geq 1$ with

C$S_{k,0}$ = 0.

We can give the first few of Catalan transform of the first k−Jacobsthal-Lucas numbers. These are the polynomials in k:

$$CS_{k,1} = \sum_{i=0}^{1} \frac{i}{2-i}\binom{2-i}{1-i} S_{k,i}$$

$=1.S_{k,1} = 1,$

$$CS_{k,2} = \sum_{i=0}^{2} \frac{i}{4-i}\binom{4-i}{2-i} S_{k,i}$$

$= \frac{1}{3}\binom{3}{1} S_{k,1} + \binom{2}{0} S_{k,2}$

$= 4k +2.$

$$CS_{k,3} = \sum_{i=0}^{3} \frac{i}{6-i}\binom{6-i}{3-i} S_{k,i}$$

$= \frac{1}{5}\binom{5}{2} S_{k,1} + \frac{2}{4}\binom{4}{1} S_{k,2} + \frac{3}{3}\binom{3}{0} S_{k,3}$

$= \frac{1}{5} .10.1 + \frac{2}{4}.4.(4k + 1) + \frac{3}{3}.1.(6k + 1)$

$= 14k + 5.$

$$CS_{k,4} = \sum_{i=0}^{4} \frac{i}{8-i}\binom{8-i}{4-i} S_{k,i}$$

$= \frac{1}{7}\binom{7}{3} S_{k,1} + \frac{2}{6}\binom{6}{2} S_{k,2} + \frac{3}{5}\binom{5}{3} S_{k,3} + \frac{4}{4}\binom{4}{0} S_{k,4}$

$= \frac{1}{7}.35.1 + \frac{2}{6} .15 .(4k + 1) + \frac{3}{5} .5.(6k + 1) + \frac{4}{4}.1.(8k^2 + 8k + 1)$

$= 8k^2 + 46k + 14.$

$$CS_{k,5} = \sum_{i=0}^{5} \frac{i}{10-i}\binom{10-i}{5-i} S_{k,i}$$

$= \frac{1}{9}\binom{9}{4} S_{k,1} + \frac{2}{8}\binom{8}{3} S_{k,2} + \frac{3}{7}\binom{7}{2} S_{k,3} + \frac{4}{6}\binom{6}{1} S_{k,4} + \frac{5}{5}\binom{5}{0} S_{k,5}$

$= \frac{1}{9}.126.1 + \frac{2}{8}.56.(4k + 1) + \frac{3}{7}.21.(6k+1) + \frac{4}{6} .6.(8k^2 + 8k + 1) + \frac{5}{5}.1.(20k^2 + 10k + 1)$

$=52k^2+152k+42.$

$$CS_{k,6}=\sum_{i=0}^{6}\frac{i}{12-i}\binom{12-i}{6-i}S_{k,i}$$

$$=\frac{1}{11}\binom{11}{5}S_{k,1}+\frac{2}{10}\binom{10}{4}S_{k,2}+\frac{3}{9}\binom{9}{3}S_{k,3}+\frac{4}{8}\binom{8}{2}S_{k,4}+\frac{5}{7}\binom{7}{1}S_{k,5}+\frac{6}{6}\binom{6}{0}S_{k,6}$$

$=\frac{1}{11}.462.1+\frac{2}{10}.210.(4k+1)+\frac{3}{9}.84.(6k+1)+\frac{4}{8}.28.(8k^2+8k+1)+\frac{5}{7}.7.(20k^2+10k+1)+\frac{6}{6}.1.(16k^3+56k^2+14k+1)$

$=16k^3+268k^2+512k+132.$

We can show $\{S_{k,n}\}$ as the *n* x 1 matrix S_k and the product of the lower triangular matrix C as

$$\begin{bmatrix}CS_{k,1}\\CS_{k,2}\\CS_{k,3}\\CS_{k,4}\\\vdots\end{bmatrix}=\begin{bmatrix}1 & & & & \cdots\\1 & 1 & & & \cdots\\2 & 2 & 1 & & \cdots\\5 & 5 & 3 & 1 & \cdots\\\vdots & \vdots & \vdots & \vdots & \ddots\end{bmatrix}\begin{bmatrix}S_{k,1}\\S_{k,2}\\S_{k,3}\\S_{k,4}\\\vdots\end{bmatrix}$$

So, we have

$$\begin{bmatrix}1\\4k+2\\14k+5\\8k^2+46k+14\\\vdots\end{bmatrix}$$

$$=\begin{bmatrix}1 & & & & \cdots\\1 & 1 & & & \cdots\\2 & 2 & 1 & & \cdots\\5 & 5 & 3 & 1 & \cdots\\\vdots & \vdots & \vdots & \vdots & \ddots\end{bmatrix}\begin{bmatrix}1\\4k+1\\6k+1\\8k^2+8k+1\\\vdots\end{bmatrix}.$$

4. HANKEL DETERMINANT OF THE CATALAN k−JACOBSTHAL-LUCAS SEQUENCES

The Hankel matrix H of the integer sequence $A=\{a_0,a_1,a_2\ldots\}$ is the infinite matrix

$$H_n=\begin{vmatrix}a_0 & a_1 & a_2 & a_3 & \ldots\\a_1 & a_2 & a_3 & a_4 & \ldots\\a_2 & a_3 & a_4 & a_5 & \ldots\\a_3 & a_4 & a_5 & a_6 & \cdots\\\vdots & \vdots & \vdots & \vdots & \ddots\end{vmatrix}$$

with elements $h_{i,j}=a_{i+j-1}$. The Hankel matrix H_n of order *n* of A is the upper-left nxn submatrix of H, and h_n, the Hankel determinant of order n of A, is the determinant of the corresponding Hankel matrix of order *n*, h_n = det (H_n) [14,15].

In addition, by applying Hankel determinant return to the CS_k polynomials we obtain;

$HCS_1=Det[1]=1$

$$HCS_2=\begin{vmatrix}1 & 4k+2\\4k+2 & 6k+1\end{vmatrix}$$

$=6k+1-(16k^2+16k+4)$

$=-16k^2-10k-3.$

$$HCS_3=\begin{vmatrix}1 & 4k+2 & 14k+5\\4k+2 & 14k+5 & 8k^2+16k+14\\14k+5 & 8k^2+16k+14 & 52k^2+152k+42\end{vmatrix}$$

$=-384k^4-3232k^3+2024k^2+2282k-255.$

5. CONCLUSION

We introduced Catalan transformation of k−Jacobsthal-Lucas sequences and Hankel determinant of the Catalan k−Jacobsthal-Lucas sequences.

Acknowledgments

We would like to thank the editor referees for their valuable comments and remarks that led to a great improvement of the article.

REFERENCES

[1] A. F. Horadam, ‘’A generalized Fibonacci sequence’’. Amer. Math. Monthly, vol. 68, no. 5, pp. 455–459, 1961.

[2] N. Anuradha, ‘’Number of points on certain hyperelliptic curves defined over finite

fields'' Finite Fields and Their Applications, vol. 14, pp. 314-328, 2008.

[3] H. Bruhn, L. Gellert, and J. Günther, ''Jacobsthal numbers in generalized Petersen graphs'' Electronic Notes in Discrete Mathematics, vol. 49, pp. 465-472, 2015.

[4] E. Özkan, İ. Altun, A. Göçer, "On Relationship Among A New Family of k−Fibonacci, k−Lucas Numbers, Fibonacci And Lucas Numbers", Chiang Mai Journal of Scıence, vol. 44, pp. 1744-1750, 2017.

[5] E. Özkan, M. Taştan, A. Aydoğdu, ''3-Fibonacci Polynomials in The Family of Fibonacci Numbers'', Erzincan University Journal of the Institute of Science and Technology, vol. 12, no. 2, pp. 926-933, 2019.

[6] S. Falc´on and A. Plaza,2007. ''On the Fibonacci k−numbers'', Chaos Solitons Fractals, vol. 32, no. 5, pp. 1615–1624, 2007.

[7] C. Kizilates, "On the Quadra Lucas-Jacobsthal Numbers", Karaelmas Science and Engineering Journal, vol. 7, no. 2, pp. 619-621, 2017.

[8] C. Kizilates, N. Tuğlu, and B. Çekim, Binomial Transforms Of Quadrapell Sequences And Quadrapell Matrix Sequences, Journal of Arts and Scince, vol. 1, no. 38, pp. 69-80, 2017.

[9] T. Koshy,''Fibonacci and Lucas Numbers with Applications''. New York, NY: Wiley-Interscience Publication. 2001.

[10] M. Taştan, and E. Özkan, ''Catalan Transform of The k−Jacobsthal Sequence'', Electronic Journal of Mathematical Analysis and Applications, vol. 8, no. 2, pp. 70-74, 2020.

[11] A. Boussayoud, M. Kerada, M. and N. Harrouche, ''On the k -Lucas Numbers and Lucas Polynomials'', Turkish Journal of Analysis and Number Theory, vol. 5, no. 4, pp. 121-125, 2017.

[12] P. Barry, ''A Catalan transform and related transformations on integer sequences''. J.Integer Seq., vol. 8, no. 4, pp. 1-24, 2005.

[13] Falcon, S. (2013). ''Catalan Transform of the k−Fibonacci sequence''. Commun. Korean Math. Soc., vol. 28, no. 4, pp. 827–832, 2013.

[14] J. W. Layman, ''The Hankel transform and some of its properties''. J. Integer Seq., vol. 4, no. 1, pp. 1-11, 2001.

[15] P. M. Rajkovi´c, M. D. Petkovi´c,. and P. Barry, ''The Hankel transform of the sum of consecutive generalized Catalan numbers", Integral Transforms Spec. Funct., vol. 18, no. 4, pp. 285–296, 2007.

SAKARYA ÜNİVERSİTESİ
FEN BİLİMLERİ ENSTİTÜSÜ DERGİSİ

Sakarya University Journal of Science
SAUJS

ISSN 1301-4048 | e-ISSN 2147-835X | Period Bimonthly | Founded: 1997 | Publisher Sakarya University | http://www.saujs.sakarya.edu.tr/

Title: Investigation of Origami Inspired Sub-6 GHz Accordion Monopole Antenna for 5G Applications

Authors: Duygu Nazan GENÇOĞLAN, Şule ÇOLAK

Recieved: 2020-12-24 23:43:12

Accepted: 2021-06-27 12:34:38

Article Type: Research Article

Volume: 25
Issue: 4
Month: August
Year: 2021
Pages: 974-983

How to cite
Duygu Nazan GENÇOĞLAN, Şule ÇOLAK; (2021), Investigation of Origami Inspired Sub-6 GHz Accordion Monopole Antenna for 5G Applications. Sakarya University Journal of Science, 25(4), 974-983, DOI: 10.16984/saufenbilder.845515 Access link http://www.saujs.sakarya.edu.tr/en/pub/issue/64755/845515

Sakarya University Journal of Science 25(4), 974-983, 2021

Investigation of Origami Inspired Sub-6 GHz Accordion Monopole Antenna for 5G Applications

Duygu Nazan GENÇOĞLAN[1], Şule ÇOLAK*[1]

Abstract

This study presents an origami inspired sub-6 GHz accordion monopole antenna for 5G applications. Parametric study is performed by varying monopole height, fold width and bevel angle to examine the antenna performance in the 1 GHz - 6 GHz frequency range. The proposed antenna is designed with the values that yield the best performance in accordance with the results of parametric study. Antenna behavior is then evaluated in terms of Return Loss, gain and radiation pattern. The proposed antenna operates in 1.22 GHz - 6 GHz frequency range which covers almost the entire sub-6 GHz range with an approximate impedance bandwidth of 132%. Hence, the designed antenna structure has a good performance in the sub-6 GHz and it is a promising design for 5G applications.

Keywords: Accordion monopole antenna, communication systems, origami, sub-6GHz, 5G

1. INTRODUCTION

The millimeter-wave (mm-Wave) bands provide large bandwidths which contribute higher data transmission rate via Fifth Generation (5G) applications. Therefore, new challenges and demands have emerged by up to date applications [1-16]. The main purpose of 5G communication systems is to assure people's interaction, device interconnection, and connection of people to devices [17-19].

5G services are generally categorized as enhanced mobile broadband, mission-critical control, and massive Internet of Things (IoT) [3]. The IoT phenomena are generally associated with smart devices such as wireless communication systems, sensors and RFID systems [20]. Wireless communication systems with 5G applications consist of several components including batteries, sensors, actuators, interconnections and antennas [3-10, 14, 20]. Due to the compactness of IoT structure and high-speed data rate for wireless communication, antennas should be miniaturized with improved performance. Ramos et al. designed multilayer Yagi with compactness for IoT sensors whose operating frequency is 24 GHz. The proposed structure has been compared with the conventional planar type of Yagi-Uda version. The results showed that the prototype provided higher gain and larger bandwidth as compared to the conventional planar type [3]. Sanam et al. proposed a basic SRR loaded, dual-band UWB MIMO antenna for IoT applications with miniaturized antenna size. Additionally, SRR has been performed as a decoupling element

* Corresponding author: sulecolak@gmail.com
[1] Adana Alparslan Türkeş University of Science and Technology, Sarıçam, Adana, Turkey.
E-Mail: dngencoglan@atu.edu.tr
ORCID: https://orcid.org/0000-0002-9529-4544; https://orcid.org/0000-0001-5014-9514

for creating notch band feature between C-band and X-band range. The simulation and experimental results were compatible with each other [4]. Hassan et al. proposed dual band-notched structure with large bandwidth and compact size for IoT applications [5]. Similarly, there are many such studies on antenna design for 5G/IoT applications in the literature [6-15].

Origami is a kind of art which provides to fold the paper to obtain a shape corresponding to an object. This popular folding technique has recently been getting attention by the scientists and mathematicians [21-27]. This miracle work of art has also provided insight into electromagnetic system designers for a variety of applications as antennas [28-43] and absorbers [44], in the last few years.

Recently, implementation of smart devices such as electro-textiles and wearable antennas with IoT kits has been getting attention due to the advantages as small dimensions, lightweight, and flexibility [45-54]. Telecommunication operators generally prefer to employ their base station sites at the 3.5 GHz frequency band in order to employ 5G technology easily. Hence, the sub-6 GHz band by using the frequency of 3.5 GHz has been allocated as a candidate band for communication technology of 5G since 2018 [55-59].

In this study, an accordion monopole antenna is presented and analyzed in the sub-6 GHz frequency range for 5G applications. Section 2 depicts the design of the antenna by using Antenna Magus [60] and CST Microwave Studio Programs [61]. Additionally, parametric study is carried out by means of monopole height, fold width and bevel angle to obtain the best performance in the related frequency range. Then, in Section 3, proposed antenna is designed with selected values in accordance with the results of parametric study. Antenna performance with these specified dimensions is evaluated in terms of Return Loss, gain and radiation pattern in the 1 GHz - 6 GHz range. Finally, concluding remarks are discussed in the last part.

2. ANTENNA DESIGN

The accordion monopole antenna is analyzed by using Antenna Magus [60] and CST Microwave Studio Program [61]. Initially, broadband characteristic is considered for selecting the antenna structure via extensive database of Antenna Magus so to speed up the design [60]. Antenna physical dimensions are calculated considering the frequency range of sub-6GHz [60]. Then, the obtained antenna structure with its parameters is exported to CST MWS to determine the best antenna parameters. The proposed structure is obtained by folding a beveled metal plate into accordion shape, and placing it vertically on metal ground plane. The geometry of the designed structure is shown in Fig. 1. The proposed antenna is fed by 50 Ω coaxial cable. Copper is selected as the conducting material. Dimensions of antenna parameters are tabulated in Table-1.

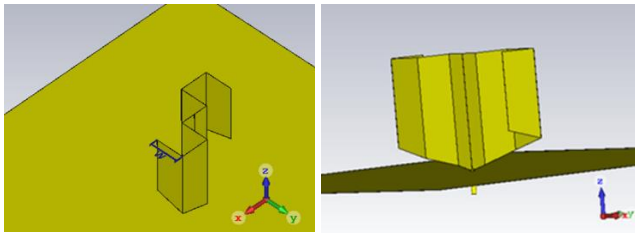

(a)

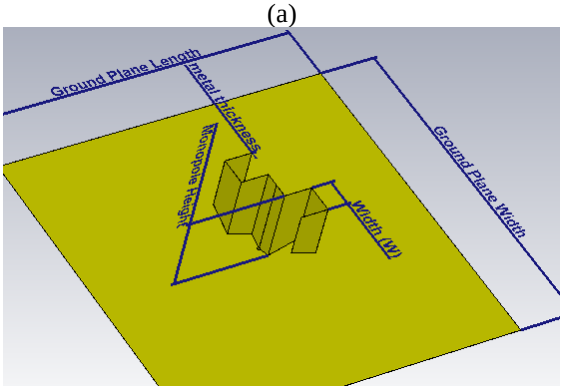

(b)

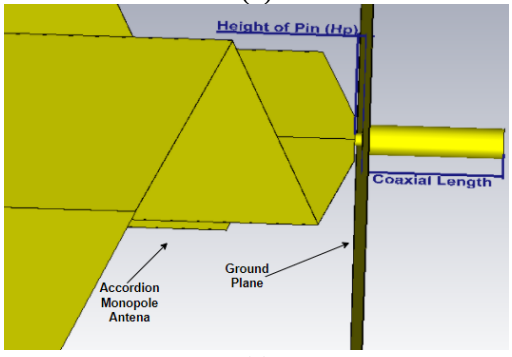

(c)

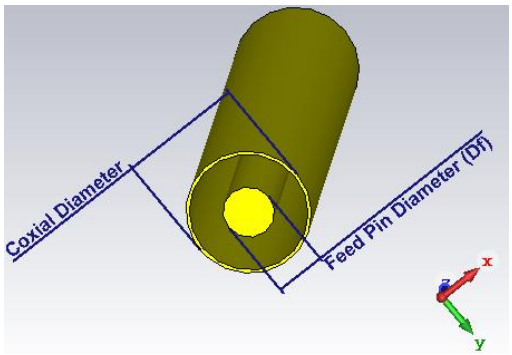

(d)

Figure 1 Geometry of origami inspired accordion monopole antenna with different views

Table 1 Physical Dimension Parameters of the Antenna

Parameters	Dimension and Units
Monopole fold width(W)	16 mm to 20 mm
Height of pin (Hp)	0.5 mm
Monopole height (Hm)	25 mm to 65 mm
Metal thickness	50 µm
Ground plane width	194.8 mm
Ground plane length	194.8 mm
Feed width	1 mm
Feed pin diameter (Df)	0.8 mm
Coaxial length	9 mm
Coaxial diameter	1.84 mm
Bevel angle (θ)	5° to 28°
Base width	4 mm

2.1. The Effect of Monopole Height on Antenna Performance

Due to the origami inspired structure, the designed antenna may show different performances with different monopole heights. That's why, the monopole height effect on the antenna characteristics is examined by using parameter sweep tool in CST MWS program. Parametric analysis of Return Loss for different heights are illustrated in Fig. 2. It is apparent from Fig.2 that the monopole height is changed, the resonance frequencies are shifted.

In Fig. 2a, when the monopole height is 25 mm, the bandwidth covers only a fraction of the sub 6 GHz range. As the monopole height is increased to 35 mm, the bandwidth increases slightly too. However, it still covers some part of the range. However, when monopole height is increased to 45 mm, the bandwidth is improved significantly and it covers almost the entire sub-6GHz band. In fact, the bandwidth in this case is 4.77 GHz, ranging from 1.22 GHz to 6 GHz.

In Fig. 2b, bandwidth increases slightly when the monopole height is increased gradually from 45 mm to 65 mm. The minimum Return Loss is achieved when monopole height is 65 mm. On the other hand, with 65 mm monopole height, the antenna has a larger size, which is a disadvantage for applications that require compact structures. Therefore, it is a trade-off that should be considered when designing the antennas. In other words, to achieve larger bandwidth, monopole height needs to be increased. Likewise, with a more compact antenna, the bandwidth is reduced. Considering this trade-off, monopole height is selected as 45 mm to obtain wideband characteristic and more compact size in the study.

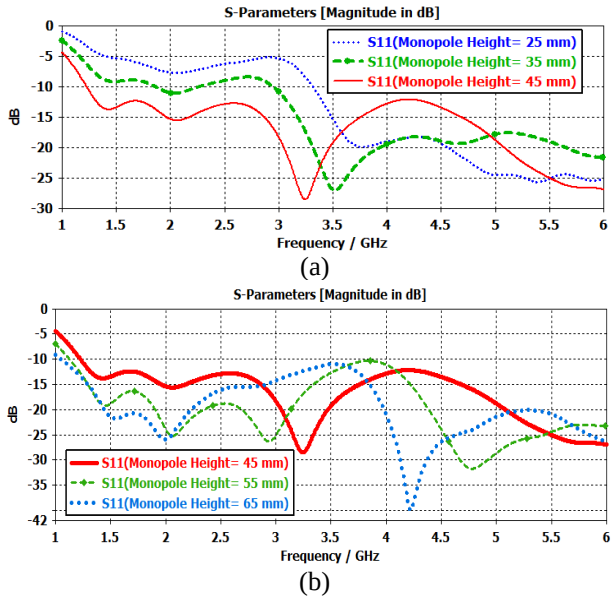

Figure 2 Return Loss plots for monopole heights of a) 25 mm, 35 mm, 45 mm, b) 45 mm, 55 mm, 65 mm

2.2. The Impact of Monopole Fold Width (W) on Antenna Characteristic

In this section, the fold width (W) impact on the proposed structure is examined by means of parametric study in CST MWS. Return Loss plots for different widths are illustrated in Fig. 3. In these figures, although there are slight differences in the bandwidths, 16 mm fold width yields better bandwidth with more compact size. Therefore, this value is selected for the proposed antenna.

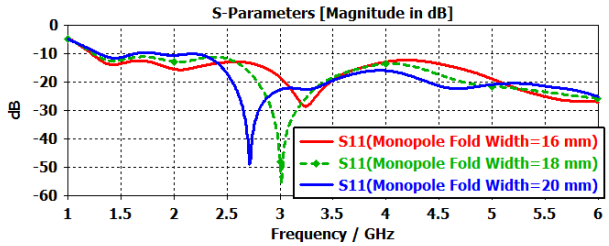

Figure 3 Antenna Return Loss plots for W= 16 mm, 18 mm, 20 mm

2.3. The Effect of Bevel Angle on Antenna Performance

Fig. 4 illustrates Return Loss graphs for six different bevel angles. According to the figures, the antenna with 15° and 20° bevel angles accomplish the -10 dB Bandwidth characteristics. However, the best Return Loss characteristic is achieved by the bevel angle of 20°. Therefore, bevel angle is selected as 20° for the proposed antenna.

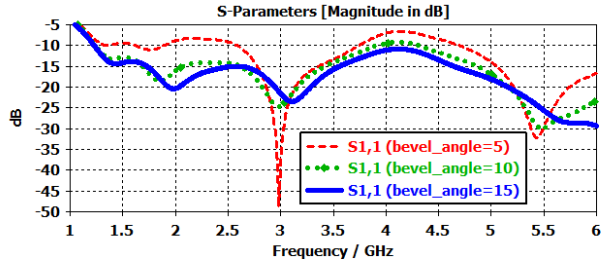

(a)

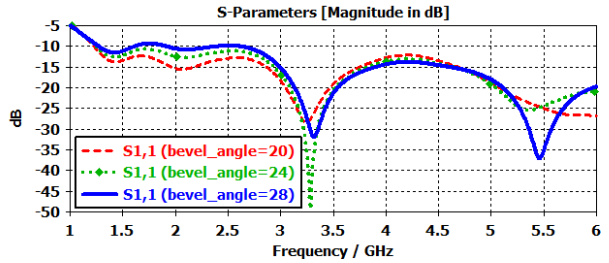

(b)

Figure 4 Antenna Return Loss plots for bevel angles of a) ——— 5°, ------ 10°, ····· 15°, b) ——— 20°, ------ 24°, ····· 28°

3. CHARACTERISTICS OF DESIGNED ANTENNA WITH PROPOSED DIMENSIONS

According to the results of parametric study, proposed antenna is designed with selected values, that is, monopole height of 45 mm, fold width of 16 mm and bevel angle of 20°. The Return Loss plot of the proposed structure, simulated by CST MWS is illustrated in Fig. 5. It is apparent from this figure that the bandwidth is 4.78 GHz ranging from 1.22 GHz to 6 GHz. Hence, it covers almost the entire sub-6 GHz band with an impedance bandwidth of 132%. The minimum Return Loss value is -28.20 dB, which occurs at the resonance frequency of 3.25 GHz.

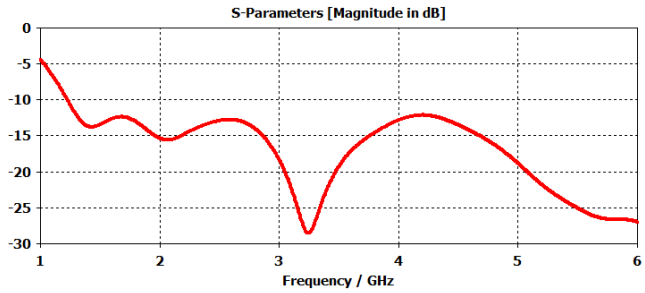

Figure 5 The Return Loss performance analysis of the proposed structure with determined dimensions

Radiation pattern characteristics of the proposed structure are depicted at different frequencies including the resonance frequency of 3.25 GHz, the lower frequency (1.22 GHz), and 6 GHz. Fig. 6 illustrates the far field 2D polar pattern and Fig. 7 shows 3D Gain of the antenna. It is seen from the figures that at lower frequencies, the antenna has omnidirectional radiation pattern. However, this characteristic tends to deteriorate with increasing frequency.

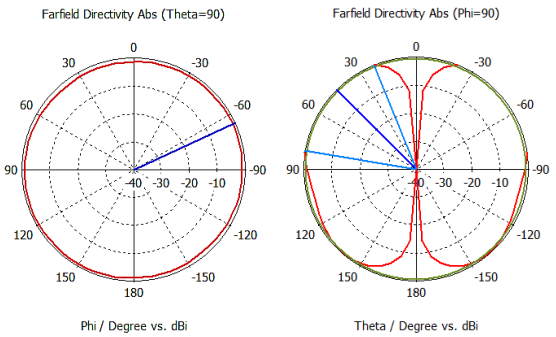

a) f = 1.22 GHz

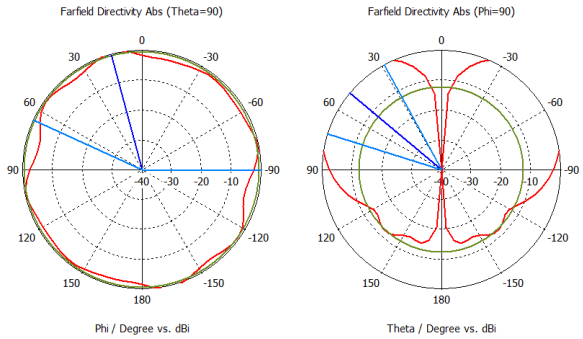

b) f= 3.25 GHz

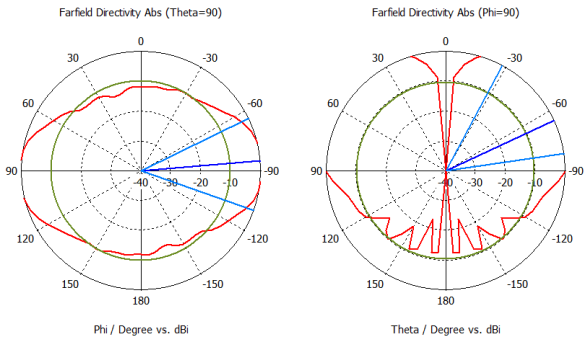

c) 6 GHz

Figure 6 2D Polar Pattern of the designed antenna at a) 1.22 GHz b) 3.25 GHz and c) 6 GHz

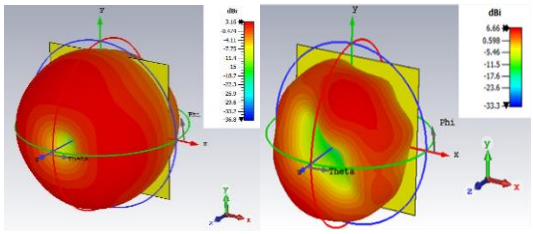

a) 1.22 GHz b) 3.25 GHz

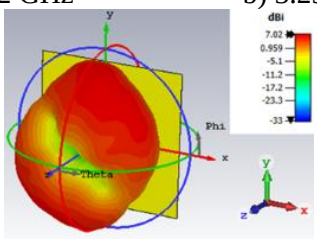

c) 6 GHz

Figure 7 3D Gain of the designed antenna at a) 1.22 GHz, b) 3.25 GHz, and c) 6 GHz

Fig.8 depicts the gain (dBi) and 3-dB beamwidth plots of the proposed antenna structure over the frequency range from 1.2 GHz to 6 GHz. It is deduced from the graphs that the gain increases while the 3 dB-Beamwidth decreases with increasing frequency.

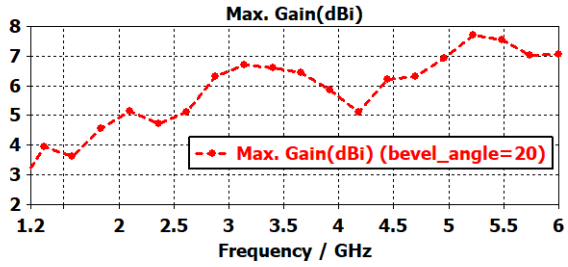

a)

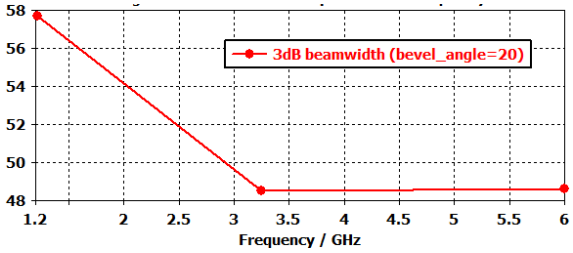

b)

Figure 8 a) Max Gain and b) 3 dB width of the proposed antenna versus frequency

This proposed antenna structure is compared with other origami based antenna structures in terms of operating frequency, bandwidth, and gain parameters as tabulated in Table 2. It is apparent from Table 2 that the proposed structure has broader bandwidth and higher gain. It is worth noting that the proposed design has promising performance as compared to the literature. Additionally, it has also acceptable characteristic for sub-6 GHz 5G communication systems.

Table 2 Origami Based Antenna Structures

Ref.	Origami Based Structures	Operating Frequency	Bandwidth	Max Gain
[28]	Bi-Directional Loop Antenna	1.29 -1.54 GHz 1.31 -1.45 GHz 1.32 -1.48 GHz	250 MHz 140 MHz 160 MHz	2.91 dBi 5.14 dBi 5.91 dBi
[29]	Quasi-Yagi Monopole Antenna	1.65-2.05 GHz	400 MHz	7.3 dBi
[42]	UWB Planar Monopole Antenna	689 - 3460 MHz	2.77 GHz	NA
[43]	Metal-Plate Monopole Antenna	2.18 - 6.59 GHz	4.41 GHz	<3 dB
This Work	Accordion Monopole Antenna	1.23 -6 GHz	4.77 GHz	7.72 dBi

4. CONCLUSIONS

In this research, an origami inspired accordion monopole antenna is examined in the sub-6 GHz range for 5G applications. A parametric study is performed by means of monopole height, fold width and bevel angle to achieve the best antenna performance in the related frequency range. According to simulation results, as the monopole height increases, bandwidth also increases.

However, since antenna size increases with height, it becomes a disadvantage for applications requiring compact structures. On the other hand, the bandwidth is slightly reduced with a more compact antenna. Therefore, there is a trade-off in terms of antenna size and bandwidth. Accordingly, the antenna with monopole height of 45 mm is proposed in this study that achieves a wider bandwidth and more compact size for 5G applications. Then, the effect of fold width of the monopole is examined on antenna characteristics. According to obtained results, bandwidth is decreased as the fold width is increased, and a better bandwidth is achieved with 16 mm fold width. Lastly, antenna behavior is examined by varying the bevel angle and it is seen that 20^0 bevel angle gives the best Return Loss characteristics. Finally, the performance of the proposed antenna with these specified dimensions is evaluated in terms of Return Loss, gain, and radiation pattern in the 1 GHz - 6 GHz range by using CST MWS Program. According to obtained result, the designed antenna covers almost the entire sub-6GHz band from 1.22 GHz to 6 GHz with an impedance bandwidth of 132%, and it has a good performance in the sub-6GHz range for 5G applications.

Funding

The authors have not received any financial support for the research, authorship or publication of this study.

The Declaration of Conflict of Interest/ Common Interest

No conflict of interest or common interest has been declared by the authors.

Authors' Contribution

The authors contributed equally to the study.

The Declaration of Ethics Committee Approval

The authors declare that this study does not require ethics committee permission or any special permission.

The Declaration of Research and Publication Ethics

The authors of the paper declare that they comply with the scientific, ethical and quotation rules of SAUJS in all processes of the paper and that they do not make any falsification on the data collected. In addition, they declare that Sakarya University Journal of Science and its editorial board have no responsibility for any ethical violations that may be encountered, and that this study has not been evaluated in any academic publication environment other than Sakarya University Journal of Science.

REFERENCES

[1] C. Di Paola, S. Zhang, K. Zhao, Z. Ying, T. Bolin, and G.F. Pedersen, "Wideband Beam-Switchable 28 GHz Quasi-Yagi Array for Mobile Devices," IEEE Transactions on Antennas and Propagation, 67(11), 6870-6882, 2019.

[2] J. Zhang, X. Ge, Q. Li, M. Guizani, and Y. Zhang, "5G millimeter-wave antenna array: Design and challenges," IEEE Wireless Communications, 24(2), 106-112, 2016.

[3] A. Ramos, T. Varum, and J. N. Natos, "Compact Multilayer Yagi-Uda Based Antenna for IoT/5G Sensors," Sensors 2018, 18(9), 2914, 2018.

[4] N. Sanam, B. T. P. Madhav, M. V. Rao, V. S. K. Nekkanti, V. K. Pulicherla, T. Chintapalli, and A. P. A. Yadlavalli, "Flag-like MIMO Antenna Design for Wireless and IoT Applications," International Journal of Recent Technology and Engineering, 8(1), 2019.

[5] S. A. Hassan, M. Samsuzzaman, M. J. Hossain, M. Akhtaruzzaman, and T. Islam, "Compact planar UWB antenna with 3.5/5.8 GHz dual band-notched characteristics for IoT applications," IEEE International Conference on Telecommunications and Photonics (ICTP), 195-199, 2017.

[6] S. V. Das, and T. Shanmuganantham, "Design of multiband microstrip patch antenna for IoT applications," IEEE International Conference on Circuits and Systems (ICCS), 87-92, 2017.

[7] V. K. Allam, B. T. P. Madhav, T. Anilkumar, and S. Maloji, "Novel Reconfigurable Bandpass Filtering Antenna for IoT Communication Applications," Progress In Electromagnetics Research, 96, 13-26, 2019.

[8] A. Satheesh, R. Chandrababu, I.S. Rao, "A compact antenna for IoT applications," International Conference on Innovations in Information, Embedded and Communication Systems (ICIIECS), 1-4,2017.

[9] I.Aggarwal, M.R. Tripathy, S. Pandey, "Metamaterial inspired multiband slotted antenna for application in IoT band," Online International Conference on Green Engineering and Technologies (IC-GET), 1-4, 2016.

[10] H. K. Raad, "An UWB Antenna Array for Flexible IoT Wireless Systems," Progress In Electromagnetics Research, 162, 109-121,2018.

[11] M. Hanaoui and M. Rifi, "Elliptical Slot Rectangular Patch Antenna Array with Dual Band Behaviour for Future 5G Wireless Communication Networks," 7th Mediterranean Congress of Telecommunications (CMT), pp.1-4,2019.

[12] M. I. Khattak, A. Sohail, U. Khan, Z. Barki, and, G. Witjaksono, "Elliptical slot circular patch antenna array with dual band behavior for future 5G mobile communication networks," Progress In Electromagnetics Research, 89, 133-147,2019.

[13] A. S. Kumar, R. Cheriyan, K. A. Ansal, D. S. Jose,"Metamaterial Inspired CPW Fed Multiband Antenna for IOT Applications," Journal of Remote Sensing GIS & Technology, 5(3), 2019.

[14] S. J. Yang, Y. M. Pan, Y. Zhang, Y. Gao and X. Y. Zhang, "Low-Profile Dual-Polarized Filtering Magneto-Electric Dipole Antenna for 5G Applications," in IEEE Transactions on Antennas and Propagation, vol. 67, no. 10, pp. 6235-6243, 2019.

[15] J. Yin, Q. Wu, C. Yu, H. Wang and W. Hong, "Broadband Symmetrical E-Shaped Patch Antenna with Multimode Resonance for 5G Millimeter-Wave Applications," in IEEE Transactions on Antennas and Propagation, vol. 67, no. 7, pp. 4474-4483, July 2019.

[16] J. G. Andrews, S. Buzzi, W. Choi, S. V. Hanly, A. Lozano, A.C. K. Soong, and J. C. Zhang, "What Will 5G Be?" in IEEE Journal on Selected Areas in Communications, vol. 32, no. 6, pp. 1065-1082, June 2014, doi: 10.1109/JSAC.2014.2328098.

[17] T. S. Rappaport, S.Sun, R. Mayzus, H. Zhao, Y. Azar, K. Wang, and F. Gutierrez, "Millimeter Wave Mobile Communications for 5G Cellular: It Will Work!," IEEE Access, 11, pp.335-349, 2013.

[18] C. X. Wang, F. Haider, X. Gao, X. H. You, Y. Yang, D. Yuan,and E. Hepsaydir,"Cellular architecture and key technologies for 5G wireless communication networks," in IEEE Communications Magazine,52(2),pp.122-130,2014.

[19] C. Loss, R. Gonçalves, C. Lopes, P. Pinho,and R. Salvado, "Smartcoat with a fully-embedded textile antenna for IoT applications,"Sensors, 16(6), 938,2016.

[20] K. Kuribayashi-Shigetomi, H. Onoe, S. Takeuchi, "Cell origami: self-folding of three-dimensional cell-laden microstructures driven by cell traction force". PloS one, 7(12), 2012.

[21] S. Kamrava,D Mousanezhad, H. Ebrahimi, R. Ghosh ,and A. Vaziri, A. "Origami-based cellular metamaterial with auxetic, bistable, and self-locking properties," Scientific reports, 7(1), 1-9, 2017.

[22] J. T. Overvelde, T. A. De Jong,Y. Shevchenko, S. A. Becerra, G. M. Whitesides, J. C. Weaver, and K Bertoldi, "A three-dimensional actuated origami-inspired transformable metamaterial with multiple degrees of freedom,"Nature communications, 7(1), 1-8,2016.

[23] R. Veneziano, T. J. Moyer, M. B. Stone, T. R. Shepherd, W. R. Schief, D.J. Irvine, and M. Bathe, "Role of nanoscale antigen organization on B-cell activation probed using DNA origami," Nat. Nanotechnology, 15, 716-723, 2020.

[24] A. L. Wickeler, H. E. Naguib,"Novel origami-inspired metamaterials:Design, mechanical, testing and finite element modelling,"Materials&Design",186,2020.

[25] Q. Lu, A. B. Clark, M. Shen and N. Rojas, "An Origami-Inspired Variable Friction Surface for Increasing the Dexterity of Robotic Grippers," in IEEE Robotics and Automation Letters, vol. 5, no. 2, pp. 2538-2545, April 2020,

[26] A. A. Deleo, J. O'Neil, H. Yasuda, M. Salviato, and J. Yang," Origami-based deployable structures made of carbon fiber reinforced polymer composites," Composites Science and Technology, 108060, 2020.

[27] S. Chaudhari, "Design and Development of Reconfigurable Origami Antennas Based on E-textile Embroidery, (Doctoral dissertation, The Ohio State University), 2018.

[28] Ying,Xu, Yeonju Kim, Manos M. Tentzeris, and Sungjoon Lim. "Bi-Directional Loop Antenna Array Using Magic Cube Origami," Sensors,19(18), 2019.

[29] S. I. H. Shah, M.M. Tentzeris, S. Lim, "A deployable quasi-Yagi monopole antenna using three origami magic spiral cubes," IEEE Antennas and Wireless Propagation Letters, 18(1), 147-151,2018.

[30] Shah, Syed Imran Hussain, and Sungjoon Lim, "Bioinspired DNA Origami Quasi-Yagi Helical Antenna with Beam Direction and Beam width Switching Capability," Scientific Reports,1-9,2019.

[31] M. Utayo, W.Sangthongngam, C. Kittiyanpunya, M. Krairiksh,"Pattern and frequency reconfigurable meander line Yagi-Uda antenna," International Conference on Advanced Technologies for Communications (ATC), 56-58, 2015.

[32] S.V. Georgakopoulos," Reconfigurable Origami Antennas," International Applied Computational Electromagnetics Society Symposium (ACES),1-2, 2019.

[33] N.E.Russo, C. L. Zekios, S. V. Georgakopoulos,"Capacity Reconfigurable Origami Enabled MIMO Antenna," United States National Committee of URSI National Radio Science Meeting (USNC-URSI NRSM), 1-2,2019.

[34] L. C. Wang. W. L. Song, Y. J. Zhang, M. J. Qu, Z. Zhao, M. Chen, and D. Fang," Active Reconfigurable Tristable Square-Twist Origami," Advanced Functional Materials, 1909087, 2020.

[35] C G. P.arrara, , N. E. Russo, C. L Zekios, S. V. Georgakopoulos,"A Deployable and Reconfigurable Origami Antenna for Extended Mobile Range," IEEE International Symposium on Antennas and Propagation and USNC-URSI Radio Science Meeting, 453-454, 2019.

[36] M. R. Khan, C. L. Zekios, S. Bhardwaj and S. V. Georgakopoulos, "Origami-Enabled Frequency Reconfigurable Dipole Antenna," 2019 IEEE International Symposium on Antennas and Propagation

and USNC-URSI Radio Science Meeting, pp. 901-902,2019.

[37] M. R. Khan, C. L. Zekios, S. V Georgakopoulos,and S.Bhardwaj, "Automated CAD and Modeling of Origami Structures for Reconfigurable Antenna Applications,"International Applied Computational Electromagnetics Society Symposium (ACES) 1-2, 2019.

[38] C. L. Zekios, X. Liu, M. Moshtaghzadeh, E. Izadpanahi, H. R. Radnezhad,P. Mardanpour, and S. V. Georgakopoulos, "Electromagnetic and mechanical analysis of an origami helical antenna encapsulated by fabric",ASME International Design Engineering Technical Conferences and Computers and Information in Engineering Conference, 2019.

[39] Y. Xu, Y. Kim, M. M. Tentzeris, S. Lim, "Bi-Directional Loop Antenna Array Using Magic Cube Origami". Sensors, 19(18), 3911, 2019.

[40] Renato Cicchetti, Emanuela Miozzi, and Orlandino Testa,"Wideband and UWB Antennas for Wireless Applications: A Comprehensive Review,"International Journal of Antennas and Propagation, vol. 2017, Article ID 2390808, 45 pages, 2017. https://doi.org/10.1155/2017/2390808

[41] D. Valderas, J. Legarda, I. Gutiérrez,and J. I. Sancho,"Design of UWB folded-plate monopole antennas based on TLM," IEEE Transactions on Antennas and Propagation, 54(6), 1676-1687, 2006.

[42] M. B. Perotoni, J. Costa, R. Enjiu," UWB (Ultra-wide band) accordion shaped planar monopole antenna," SBMO/IEEE MTT-S International Microwave and Optoelectronics Conference (IMOC) 1-4, 2015.

[43] K. L. Wong, S. W. Su, and C. L. Tang, "Broadband omnidirectional metal-plate monopole antenna". IEEE Transactions on Antennas and Propagation, *53*(1), 581-583,2005.

[44] Y.Shen, Y. Pang, J. Wang, H. Ma, Z. Pei and Q. Shaobo, "Origami-inspired metamaterial absorbers for improving the larger-incident angle absorption," Journal of Physics D: Applied Physics, 48(44), 445008, 2015.

[45] M. Mustaqim, B. A. Khawaja, H. T Chattha, K Shafique, M. J. Zafar, M. Jamil"Ultra-wideband antenna for wearable Internet of Things devices and wireless body area network applications," International Journal of Numerical Modelling: Electronic Networks, Devices and Fields, 32(6), e2590, 2019.

[46] P. K Goswami, G. Goswami, "Truncated T parasite staircase fractal U-slot antenna for multiple advance internet of things applications," Microwave and Optical Technology Letters, 62(2), 830-838, 2020.

[47] X. Lin, Y. Chen, Z. Gong, B. C. Seet, L. Huang,andY. Lu, "Ultra-Wideband Textile Antenna for Wearable Microwave Medical Imaging Applications," IEEE Transactions on Antennas and Propagation, 68(6), 2020.

[48] C. Loss, R. Gonçalves, P. Pinho, and P., R. Salvado," A Review of Methods for the Electromagnetic Characterization of Textile Materials for the Development of Wearable Antennas,"Wireless Power Transmission for Sustainable Electronics, 27-56, 2020.

[49] B. Muneer, F. K. Shaikh, and Z. Zhu, "Antennas for IoT Application: An RF and Microwave Aspect of IoT. In IoT Architectures, Models, and Platforms for Smart City Applications" 180-192, 2020.

[50] M.Ameena Banu, R.Tamilselvi, M. Rajalakshmi, M. Pooja Lakshmi, "IoT-based Wearable Micro-Strip Patch Antenna with Electromagnetic Band Gap Structure for Gain Enhancement," Inventive Communication and Computational

Technologies, Lecture Notes in Networks and Systems, 89, 2020.

[51] Y. Jiang, “Combination of wearable sensors and internet of things and its application in sports rehabilitation,” Computer Communications, 150, 167-176, 2020.

[52] A. Y. Ashyap, S. H. B. Dahlan, Z. Z.Abidin, M. I. Abbasi, M. R. Kamarudin, H. A. Majid, A.Alomainy, "An Overview of Electromagnetic Band-Gap Integrated Wearable Antennas," in IEEE Access, 8, pp. 7641-7658, 2020.

[53] L. Corchia, G. Monti, E. De Benedetto,A. Cataldo, L.Angrisani, P. Arpaia, L.Tarricone, “Fully-Textile, Wearable Chipless Tags for Identification and Tracking Applications,” Sensors,20(2),429,2020.

[54] N. Kumar, and R. Khanna, “A compact multi-band multi-input multi-output antenna for 4G/5G and IoT devices using theory of characteristic modes,” International Journal of RF and Microwave Computer-Aided Engineering, 30(1), e22012, 2020.

[55] B. A. Esmail,H. B.Majid,S. H Dahlan, Z. Z Abidin,M. K. Rahim,and M. Jusoh,”Planar antenna beam deflection using low-loss metamaterial for future 5G applications,” International Journal of RF and Microwave Computer-Aided Engineering, 29(10), e21867, 2019.

[56] S. Saxena, B.K. Kanaujia, S. Dwari, S. Kumar,R. Tiwari,”MIMO antenna with built-in circular shaped isolator for sub-6 GHz 5G applications,” Electronics letters, 54(8), 478-480, 2018.

[57] I. P. Belikaidis,A .Georgakopoulos, E. Kosmatos, V. Frascolla,and P.Demestichas, “Management of 3.5-GHz spectrum in 5G dense networks: A hierarchical radio resource management scheme,” IEEE Vehicular Technology Magazine, 13(2), 57-64, 2018.

[58] R. M. Vaghefi, R. C. Palat, G. Marzin, K. Basavaraju, Y. Feng and M. Banu, "Achieving Phase Coherency and Gain Stability in Active Antenna Arrays for Sub-6 GHz FDD and TDD FD-MIMO: Challenges and Solutions," in IEEE Access,8,pp. 152680-152696, 2020.

[59] Q. Amjad, A. Kamran, F. Tariq and R. Karim, "Design and Characterization of a Slot based Patch Antenna for Sub-6 GHz 5G Applications," 2019 Second International Conference on Latest trends in Electrical Engineering and Computing Technologies (INTELLECT), 2019.

[60] Antenna Magus. Available: http://www.antennamagus.com

[61] CST MWS (Computer Simulation Technology Microwave Studio Suite^{TM}).

SAKARYA ÜNİVERSİTESİ
FEN BİLİMLERİ ENSTİTÜSÜ DERGİSİ

Sakarya University Journal of Science
SAUJS

ISSN 1301-4048 | e-ISSN 2147-835X | Period Bimonthly | Founded: 1997 | Publisher Sakarya University | http://www.saujs.sakarya.edu.tr/

Title: Investigation of The Effects of Diaminopyridine and o-Vanillin Derivative Schiff Base Complexes of Mn(II), Mn(III), Co(II) and Zn(II) Metals on The Oxidative Bleaching Performance of H_2O_2

Authors: Murat TUNA, Tuğba UĞUR

Recieved: 2021-06-06 18:30:00

Accepted: 2021-06-28 21:51:16

Article Type: Research Article

Volume: 25
Issue: 4
Month: August
Year: 2021
Pages: 984-994

How to cite
Murat TUNA, Tuğba UĞUR; (2021), Investigation of The Effects of Diaminopyridine and o-Vanillin Derivative Schiff Base Complexes of Mn(II), Mn(III), Co(II) and Zn(II) Metals on The Oxidative Bleaching Performance of H_2O_2. Sakarya University Journal of Science, 25(4), 984-994, DOI: 10.16984/saufenbilder.948657 Access link http://www.saujs.sakarya.edu.tr/en/pub/issue/64755/948657

Sakarya University Journal of Science 25(4), 984-994, 2021

Investigation of The Effects of Diaminopyridine and o-Vanillin Derivative Schiff Base Complexes of Mn(II), Mn(III), Co(II) and Zn(II) Metals on The Oxidative Bleaching Performance of H_2O_2

Murat TUNA*[1], Tuğba UĞUR[1]

Abstract

Catalytic applications are widely used in industrial and individual applications today due to their many advantages, especially the energy and time they provide. For this purpose, many coordination compounds have been synthesized, and their catalytic performances have been investigated in recent years. In this study, the Schiff base ligand, (N,N'-bis(2-hydroxy-3-methoxyphenylmethylidene)-2,6-pyridinediamine, BHMP), was synthesized with 2,6-diaminopyridine with o-vanillin. Mn(II), Mn(III), Co(II), Zn(II) complexes were obtained with the synthesized ligand. Spectroscopic methods such as FT-IR, ^{1}H-NMR, UV-*vis*, Mass, and melting point determination methods were used for the structure elucidation of the synthesized compounds. The performances of the obtained complexes as bleach catalysts, which are an important application area of Schiff base complexes, were investigated. According to the bleaching measurement results, the highest catalytic effect on the bleaching performance of H_2O_2 in pH 10.5 buffer at 25 °C under homogeneous conditions was obtained with Co(II) complex. It was understood that this complex was followed by Mn(II), Mn(III), and Zn(II) complexes, respectively.

Keywords: Schiff base, o-vanillin, metal complexes, bleach catalyst

1. INTRODUCTION

The literature in which some metal complexes of Schiff bases are used as catalysts is expressed in thousands of publications in the last five years. These complex molecules are used as catalysts in many of these publications and have started to gain importance in industrial applications [1-6]. In addition to these application areas, these complexes have an important place in biological activities such as antibacterial, antifungal, and antitumor, analytical chemistry, paints, polymer industries, applications of vitamins and enzymes [7-12].

Mainly, manganese and iron Schiff base complexes used as oxidation catalysts have found a wide area of use in industrial and domestic laundry due to their catalytic effect, being harmless to the environment, and effective use on the bleaching potential of hydrogen peroxide. These complexes have played an important role in textile applications by preventing damage to the washed fabric while ensuring the bleaching of

* Corresponding author: tuna@sakarya.edu.tr
[1] Sakarya Univercity, Faculty of Arts and Sciences, Department of Chemistry, Turkey
E-Mail: tugba.ugur.3@hotmail.com
ORCID: https://orcid.org/ 0000-0002-8554-903X; https://orcid.org/ 0000-0003-2684-9902

stains, especially at low temperatures [13-14]. With this advancing technology, besides the ability to wash at low temperatures in washing machines, methods that can bleach using less water and include short-term washing programs are being developed [15-16]. Bleaching or whitening is defined as the de-coloration reaction by degrading the molecules that give color as a dye or paint-like by oxidation reaction [15-18]. For the bleachers containing hydrogen peroxide, the effective use temperature was reduced from 90 °C to less than 40 °C by using 1-5% of these molecules as activators in a washing period [15-16]. Due to the use of activators, both time and energy savings have been achieved. With the efforts to develop transition metal complexes as activators to replace the metal salts - due to the difficulty of use in alkaline conditions and its adverse effects on the fabric - proposed in the 1980s, the catalysts compatible with laundry and dishwashing detergents have been developed for the last decade [19-20]. Metal ions in most metal-containing catalysts as coordination compounds have partially empty orbitals in the d orbitals. These somewhat empty orbitals can be used in the resulting oxidation mechanisms. The ions of transition elements, such as especially manganese, iron, cobalt, nickel, palladium, platinum, tungsten, silver, and copper, have frequently been used in different oxidation numbers in obtaining these catalysts [21-27].

In this study, the Schiff base ligand, N,N'-bis(2-hydroxy-3-methoxyphenylmethylidene)-2,6-pyridinediamine, BHMP), was synthesized with 2,6-diaminopyridine with o-vanillin. Mn(II), Mn(III), Co(II), Zn(II) complexes were obtained with the synthesized ligand. Spectroscopic methods such as FT-IR, ^{1}H-NMR, ^{13}C-NMR, UV-*vis*, Mass, AAS, and melting point determination methods were used for the structure elucidation of the synthesized compounds. The performances of the obtained complexes as bleach catalysts, an important application area of Schiff base complexes, were investigated.

2. EXPERIMENTAL STUDIES

2.1. Materials and Devices

The materials used in this study were obtained from companies such as Merck, Fluka, and Aldrich. During chemical experiments; 2,6-Diaminopyridine, o-vanillin, Ethanol (EtOH), Methanol (MeOH), Dichloromethane (DCM), Acetone, Sodium carbonate (Na_2CO_3), Sodium bicarbonate ($NaHCO_3$), Dimethylformamide (DMF), Tetrahydrofuran (THF), Hexane, Nitric acid (HNO_3), Hydrochloric acid (HCI), Chloroform ($CHCl_3$), Deuterochloroform ($CDCl_3$), Hexadeutero-dimethyl sulfoxide (d_6-DMSO), Manganese(II) chloride hexahydrate ($MnCl_2.6H_2O$), Cobalt(II) chloride hexahydrate ($CoCl_2.6H_2O$), Zinc chloride ($ZnCl_2$), Sodium hydroxide (NaOH), Oxygen (O_2), Silica gel, Morine, Hydrogen peroxide (H_2O_2) and purified water are used.

For spectroscopic characterization of synthesized substances; Infrared Spectrometer ((Perkin Elmer Spectrum Two (PerkinElmer UATR Two diamond ATR)), ^{1}H-NMR Spectrometer, (Varian Mercury Plus 300 MHz Spectrometer), Bruker Microflex LT MALDI-TOF-MS Spectrometer (Gebze Technical University), UV-*vis* Spectrophotometer (Hitachi UV-2900 Spectrophotometer) and Melting Point Tester (Stuart SMP-10) were used.

2.2. Synthesis Studies

According to the literature data, the synthesis of the Schiff base ligand was carried out first [28-30]. Complexes were synthesized after it was understood that the structural characterization data of the obtained ligand molecule were compatible with the literature data. The synthesis plan is given in Scheme 1.

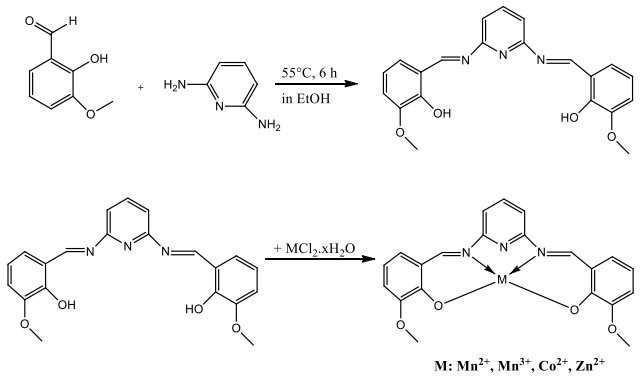

Scheme 1 The synthesis plan of Schiff base complexes

2.2.1. Synthesis of BHMP as a ligand

The Schiff base ligand, N,N'-bis(2-hydroxy-3-methoxyphenylmethylidene)-2,6-pyridinediamine, was prepared according to the references [28-30].

2.2.2. Synthesis of metal complexes

2.2.2.1. Synthesis of the Schiff base Manganese(II) complex

0.5 mmol (0.189 g) Schiff base ligand was dissolved in 20 mL THF. The temperature was fixed at 55 °C, and 0.5 mmol (0.063 g) $MnCl_2$ was added dropwise. The reaction mixture was cooled to room temperature after three hours, and the solvent was removed by a rotary evaporator. Afterward, chloroform washing, the solid product was obtained by centrifugation and kept waiting in a vacuum oven overnight. Yield: 0.127 g (58.79%), m.p. > 300 °C. FT-IR (PIKE MIRacleTM ATR) ν_{max}, cm^{-1}: 3063 (Ar, C–H), 2975 (aliph., C–H), 1630 (C=N), 1549 (C=C), 1442 (C–N), 1065 (C–O). MALDI-TOF-MS, (m/z): Calculated: 430.34; found: 430.11 [M^+].

2.2.2.2. Synthesis of the Schiff base Manganese(III) complex

1 mmol (0.378 g) Schiff base ligand was dissolved in 20 mL ethanol. 1 mmol (0.126 g) $MnCl_2$ solution in 20 ml ethanol was added. After starting the reaction at room temperature for 10-15 minutes, a solution of 0.002 mol (0.08 g) NaOH in a small amount of pure water was added to the mixture. The reaction mixture was continued the stirring at 80 °C for 2 hours. Then, O_2 gas was passed into the reaction medium with the help of a pump, and the reaction was continued for three hours. The resulting mixture was filtered, and the crude product was washed with hot ethanol. The precipitate was left to dry in the vacuum oven overnight. Yield: 0.31 g (71.59%), m.p. > 300 °C. FT-IR (PIKE MIRacleTM ATR) ν_{max}, cm^{-1}: 3079 (Ar, C–H), 2935 (aliph., C–H), 1605 (C=N), 1549 (C=C), 1436 (C–N), 1065 (C–O). MALDI-TOF-MS, (m/z): Calculated: 430.34; found: 429.98 [M^+].

2.2.2.3. Synthesis of the Schiff base Cobalt(II) complex

0.5 mmol (0.189 g) of Schiff base ligand was dissolved in 40 mL of methanol. After the temperature was fixed at 55 °C, a 0.5 mmol (0.065 g) $CoCl_2$ solution in 10 mL of methanol was added dropwise. After the reaction was continued for three hours, vacuum distillation was carried out, and after washing with chloroform, filtration was carried out to obtain a solid product. The precipitate was left in a vacuum oven overnight. Yield: 0.152g (69.72%), m.p. > 300 °C. FT-IR (PIKE MIRacleTM ATR) ν_{max}, cm^{-1}: 3060 (Ar, C–H), 2935 (aliph., C–H), 1630 (C=N), 1477 (C=C), 1436 (C–N), 1062 (C–O). MALDI-TOF-MS, (m/z): Calculated: 434.31; found: 466.09 [M^++CH_3OH+2].

2.2.2.4. Synthesis of the Schiff base Zinc(II) complex

0.5 mmol (0.189 g) Schiff base ligand was dissolved in 50 mL ethanol. After the temperature was fixed at 55 °C, a solution of 0.5 mmol (0.068 g) $ZnCl_2$ metal salt in 10 mL of ethanol was added dropwise. After the reaction was continued for three hours, vacuum distillation was carried out, and after washing with chloroform, filtration was carried out to obtain a solid product. The precipitate was left in a vacuum oven overnight. Yield: 0.121 g (54.75%), m.p. > 300 °C. FT-IR (PIKE MIRacleTM ATR) ν_{max}, cm^{-1}: 3050 (Ar, C–H), 2972 (aliph., C–H), 1599 (C=N), 1480 (C=C), 1436 (C–N), 1068 (C–O). MALDI-TOF-

MS, (m/z): Calculated: 439.05; found: 531.21 [M^++2C_2H_5OH].

2.3. Measuring the Effects of Molecules on Bleaching Performance

Bleaching activities for Morin dye of synthesized Schiff base metal complexes as oxidative bleach catalyst were tested to determine using UV-*vis* Spectroscopy. Morin is a dye in which the bleaching effects of the substances whose oxidative catalyst effect can be examined can be seen easily. Hydrogen peroxide (H_2O_2) was used as a bleacher in the kinetic analysis. The bleaching effect of hydrogen peroxide; is based on its decomposition, mainly depending on the pH value and hydrogen and perhydroxyl ion (HOO^-). This perhydroxyl ion then reacts with a hydrogen peroxide molecule to form the superoxide radical anion. Since hydrogen peroxide is a stable compound under acidic conditions, the perhydroxyl ion formation starts with the addition of alkali necessary for the initiation of decomposition. Perhydroxyl ion ($HO_2\bullet$) behaves like weak dibasic acid in an aqueous solution, and degradation continues [31]. The bleaching rate and the changes in absorbance versus time obtained as a result of the process that proceeds in this direction were graphed and it was investigated whether the complexes showed catalytic effects. It was provided to monitor the spectral changes and determine the bleaching rate of the dye as a percentage.

In order to carry out the analysis, 10 mg of the synthesized products were taken and completed with 10 mL of DMF. $NaHCO_3$ / Na_2CO_3 (pH: 10.5) was used and the buffer solution was prepared and placed in a quartz cuvette. Pure water was added to the reaction vessel on the heater and its temperature was kept at 25 °C. A magnetic stirrer was placed in the reaction vessel to ensure continuous mixing. After removing the baseline of the device, the initial absorbance of the Morine in the buffer solution was measured before the catalyst and hydrogen peroxide were added. Then 900 µL of Morine (in two parts), the calculated amount of catalyst for each complex and 480 µL H_2O_2 were added respectively. A peristaltic pump was used to transfer the reaction solution to the quartz cuvette in the UV-vis Spectrophotometer. In the spectrophotometer, 11 spectral values were recorded at 5-minute intervals with the kinetic-scanning program. The obtained values were converted into graphics for kinetic interpretation.

Morine bleaching was then followed as reductions in 411 nm absorbance, and the percentage of bleaching was calculated using the following equation depending on the change in absorbance values obtained [32].

$$Bleaching\ (\%) = \frac{(A_0 - A_t)}{A_0} x100$$

in the formula, A_0 = absorbance at zero time; A_t = absorbance at specific time.

3. RESULTS AND DISCUSSIONS

3.1. Structural Characterization

Common spectroscopic methods such as FT-IR, ^{1}H-NMR, UV-*vis*, and MS were used for the characterization of the synthesized compounds, and the results confirmed the expected results for the structures.

In the structural characterization of the synthesized BHMP ligand and its some metal complexes, FT-IR, ^{1}H-NMR, and MS methods were primarily used. In this context, since the ligand molecule was synthesized before, FT-IR, NMR, and mass analysis were carried out to compare with the literature data. It was seen that the data obtained from the measured spectra are in complete agreement with the literature data.

It has been observed that the wavenumber values of the peaks of OH, aromatic C=C, C=N, O-CH_3 functional groups seen in the FT-IR spectra are compatible with the literature data. In addition, NMR spectroscopy was used to characterize the ligand molecule, and the shifts in the NMR spectra obtained supported the FT-IR data and were observed to be compatible with the literature. Structural characterization of the ligand molecule was completed by mass spectroscopy, and it was observed that [M^+] = 379.47 m/z peaks

in the mass spectra (Fig. 3). In addition, the peaks seen in 395.30 m/z and 411.56 m/z in the mass spectra were interpreted as belonging to $[H_2L+H_2O^+]$ and $[H_2L+2H_2O^+]$ molecules, respectively. This situation is also supported by the spring peak seen at 3484 cm^{-1} in the FT-IR spectra, and this situation arising from the structural properties of the synthesized Schiff base ligand has also been demonstrated in the literature data (Fig. 2) [28].

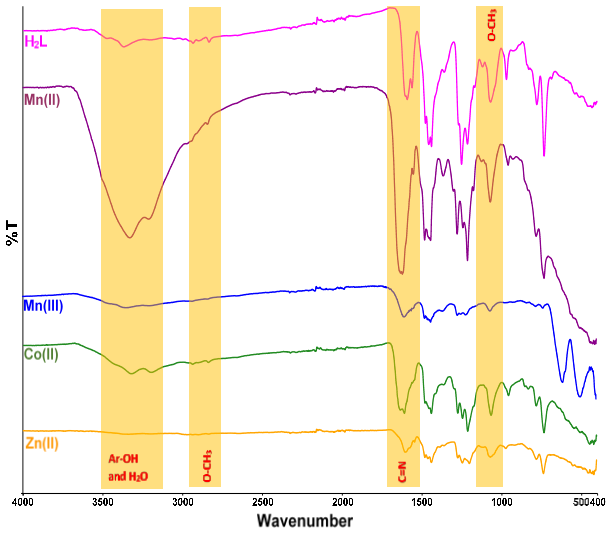

Figure 1 FT-IR spectra of synthesized ligands and complexes

The most basic functional group sought in the FTIR analysis of Schiff base ligands and their complexes is the peak of the C = N group seen in the range of approximately 1600-1700 cm^{-1}. While the peak in the FTIR spectrum of the ligand was observed at 1602 cm^{-1}, in the FTIR spectra of the metal complexes of the ligand, this peak was observed in the range of 1599-1630 cm^{-1} and the shift was interpreted that was due to metal-ligand bonding. On the other hand, a similar situation has been observed in the ligand molecule, which belongs to the C = N bond in pyridine, and the C = N stretching peak seen at 1561 cm^{-1} is in the range of 1542-1558 cm^{-1}. The decrease in the % transmittance values of these peaks was interpreted as the N atom coordinated with the metal atoms (Fig. 1) [28, 33, 34].

Peaks for phenolic hydroxyl groups, one of the most specific functional groups for the synthesized ligand molecule, were observed in the range of 3463-3194 cm^{-1} as expected, while the % transmittance changes seen in the FTIR spectra of the relevant metal complexes were interpreted as due to the hydroxyl group coordinated with the metal atoms. However, bound water in molecules in the synthesized complex molecules can be seen in FTIR spectra and mass spectra (Fig. 1) [28, 33, 34].

Another functional group-specific for the synthesized ligand molecule is the methoxy group. The O-C peak, one of the two critical peaks of this group, was observed in the range of 1062-1065 cm^{-1}. The other significant peak is the aliphatic C-H peak of the CH_3 group, and this peak was observed at approximately 2850 cm^{-1} in accordance with the literature data (Fig. 1) [35].

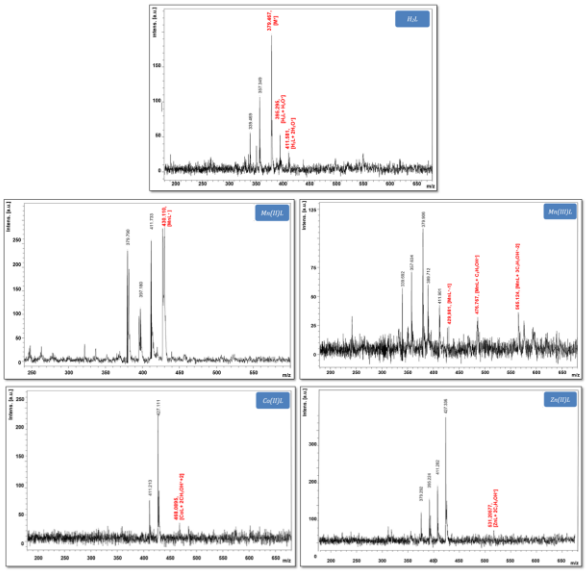

Figure 2 MS spectra of synthesized ligands and complexes

Mass spectra of synthesized Schiff base ligand and its metal complexes were taken in MALDI-TOF spectrometer and the presence of DMSO solvent. In the mass spectra, molecular ion peaks were observed at 379.467 and 430.110 m/z values for the ligand molecule and Mn(II) complex, respectively. On the other hand, for the Mn(III) complex, instead of the molecular ion peak, the peak ($[MnL]^+$-1) was observed at 429.981 m/z in the mass spectrum. In the mass spectra of the Co(II) and Zn(II) complexes; molecular ion peaks were not observed, and it was concluded that these complexes interacted with solvent molecules and, as a result, peaks with values of 468.0895 and 531.20577 m/z, respectively, were

the peaks of $[CoL+2CH_3OH+2]^+$ and $[ZnL+C_2H_5OH]^+$ molecules (Fig. 2) [36,37].

^{1}H-NMR spectra of the ligand molecule were taken in the presence of DMSO solvent. In the proton NMR spectrum were obtained signals, in consistent with the literature, 2.48 (6H), 3.82 (6H), 6.89 (2H), 7.08 (2H), 7.21 (2H), 7.41 (2H), 8.28 (H), 9.31 (2H), and 10.25 (2H) ppm, respectively [28].

As can be seen from Fig. 3, the Schiff base attached to the benzene ring showed a broad and strong absorption peak at 434 nm due to the n-p* transition with the unbounded electron pair electrons located on the nitrogen atom in the C=N group. In addition, a second peak was observed at 374 nm belonging to the ligand molecule and was thought to originate from the methoxy group attached to the benzene ring. Because the said peak was observed exactly in the complex molecules and it did not undergo any change, which strengthened this prediction. The peak Mn(II) Co(II) complexes of the azomethine group observed at a wavelength of 434 nm showed a blue shift at the wavelengths of 408 nm and 406 nm, respectively. It was observed that the said shift shifted more specifically at 382 nm in the Mn(III) complex.

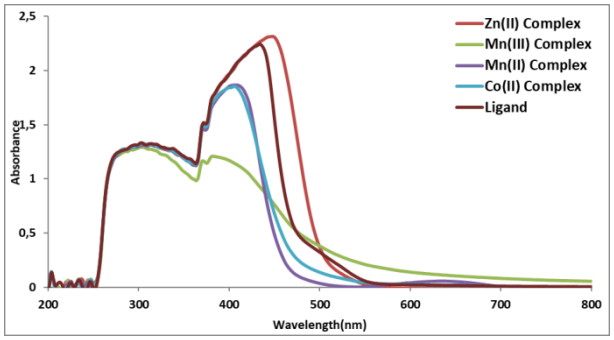

Figure 3 UV-*vis* spectra of synthesized ligands and complexes

On the other hand, in the Zn(II) complex, the azomethine peak in question is red-shifted and observed at a wavelength of 450 nm. The red shift was observed in Zn(II) complexes with fully occupied d orbitals, where the d orbitals in metal atoms depend on the presence of electrons, while the most prominent blue shift was observed in the Mn(III) complex with the poorest d orbital electrons. The weak peaks observed in the spectra of the ligands and their complexes in the range of about 270-360 nm are attributed to the p–π conjugation and n–π* transition between the lone pair electrons of the phenolic hydroxyl oxygen atom and the benzene ring, and the π-π* transition of the large conjugated bond in the benzene ring [28,38].

3.2. Bleaching Performances of The Complexes

Bleaching processes have been one of the main processes in today's industrial applications, especially in textiles, in all sectors where there is a need to eliminate the adverse effects of chromophores. For these processes, hydrogen peroxide, etc., bleaching agents are used. These agents act through a mechanism that provides the degradation of chromophore molecules with an oxidative effect. However, the improvement of the conditions of use has been the subject of research for a long time since the effects of these agents are shown depending on the need for a long time and high temperature. For this purpose, tetraacetylethynediamine (TAED) and nonanoxybenzene were synthesized as the first bleaching agent activator and started to be used in laundry detergents. In this way, it is ensured that the oxidation agents, which are effective above 60 °C, show the same performance below 40 °C. According to these results, the energy savings achieved have drawn attention to the importance of bleach activators. It has been tried as a complex molecular bleaching catalyst synthesized with many transition metal complexes. The main goal in these studies is to provide oxidation of chromophore groups in a shorter time and at low temperatures (preferably at room temperature) [39].

It is seen that very different complexes have been synthesized, especially in activator researches on hydrogen peroxide activators. However, when these studies are examined, it is seen that phthalocyanine complexes and Schiff base complexes show remarkable results [40,41]. For these reasons, in this study, the bleaching performance of the complexes obtained with the synthesized ligand molecule was investigated

against Morin dye. Morin dye was chosen here because of the polyphenolic chromophore properties of flavonoids as model markers for wine stains. In order to determine the decomposition rate of Morin dye at 25 °C, the complexes were prepared with carbonate buffer, and pH value of 10.5 was followed over the absorption values of Morin dye at 411 nm under homogeneous catalysis conditions with hydrogen peroxide. The measurements were made by measuring absorption every five minutes for 50 minutes.

The obtained spectral results are given graphically in Fig. 4. In the figure, it is seen that all complex molecules have an effect on the bleaching rate of hydrogen peroxide and a positive effect on the decomposition rate of Morin. However, the said effect did not occur at the same rate in the complex molecules, and it was observed that the Zn(II) complex, especially with the d^{10} electron structure, showed a relatively lower catalytic effect (Fig. 4.-IV). Similarly, it has been determined that the Mn(III) complex also functions as a lower activator compared to other complexes. It has been interpreted that the reason for this is that the catalytic effect is weakened, contrary to what is expected, with the effect of electrons coming from the helper ions bound into the molecular structure and the ligands to the empty d orbitals on the Mn(III) atom (Fig. 4.-II). Co(II) and Mn(II) complexes showed an effective catalytic effect in the degradation of Morin dye and it was observed that it caused an effective degradation in the first 5 minutes (Fig 4.-I and III). When the % bleaching performance of all complexes is examined, it is seen that the Co(II) and Mn(II) complexes reach a degradation rate of over 75% within the first 10 minutes.

Although the maximum effect was reached in the 15th minute for both complexes, it is seen that the Co(II) complex has a faster catalytic effect than the Mn(II) complex (Fig. 4.-V). When the final bleaching performances obtained as a result of the application were examined, it was observed that the highest performance as of 50 minutes belonged to the Co(II) complex with 87.44%. This is followed by Mn(II) with 85.23%, Mn(III) with 71.95% and Zn(II) with 53.98%, respectively.

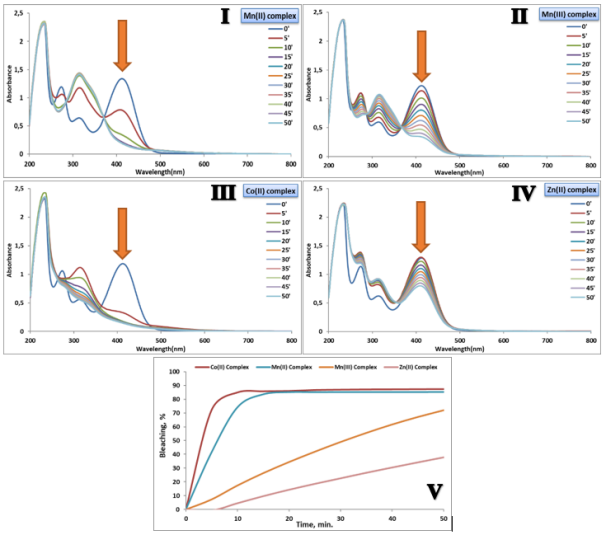

Figure 4 UV-*vis* spectral changes of Morin dye for bleaching experiments; (**I**) Mn(II) complex, (**II**) Mn(III) complex, (**III**) Co(II) complex, (**IV**) Zn(II) complex, and (**V**) under homogeneous conditions % bleaching performance

Table 2 The effects of complexes used as activators on % bleaching performance

Activator	**% Bleaching**	
(Catalyst) complex	**25. min**	**50. min**
Mn(II)	85.09	85.23
Mn(III)	41.87	71.95
Co(II)	86.76	87.44
Zn(II)	18.57	37.84

In addition, it was observed that the same performance values had the same order at 25 minutes of the measurements (Table 2). When the literature data is examined, the % bleaching performance remained at the level of 3.2% in 20 minutes and 5.26% in 45 minutes when the catalyst is not used (only H_2O_2 is used) under the same conditions, revealing the catalytic effects of the synthesized complexes. On the other hand, when the commercially used TAED molecule is compared with the bleaching performance in the literature, similar results are seen. The bleaching applications with TAED show a performance of 19.21% in 20 minutes and 42.68% in 45 minutes [39].

4. CONCLUSION

According to the results obtained from this study; the synthesis of transition metal complexes with the catalytic activity that can be considered effective in homogeneous conditions was carried out, and it was observed that especially Co(II) and Mn(II) complexes caused the bleaching performance of H_2O_2 to be realized at a very high rate in a concise time. In addition, according to other results obtained during the study; It is understood that it does not show the expected catalytic effect due to the occupied d orbitals in the Zn(II) complex and the side groups coordinated to the cavities in the Mn(III) complex.

One of the most important results obtained here is that the catalytic properties of Schiff base complexes are greatly affected by the interaction between ligand molecules and metal atoms. It was observed that especially the side groups coordinated with the molecule greatly affected this effect. According to all the activation results obtained, Co(II) complex was the catalyst with the highest activation. It has been clearly seen that the results obtained from this application show a highly effective catalytic effect when compared with commercially used TAED and only H_2O_2; thus, it will save both time and energy due to the application temperature.

Acknowledgments

We would like to thank Prof. Dr. Salih Zeki YILDIZ, one of the faculty members of Sakarya University Faculty of Arts and Sciences, Department of Chemistry, for sharing information in the realization of this study. In addition, we would like to thank the referees and editors for their support to the quality of the publication during the publication phase of the study.

Funding

"We did not receive any financial support for the research, authorship, or publication of this work." statement should be written. On the other hand, Tuğba Uğur worked with 100/2000 YÖK doctoral scholarships in this study.

The Declaration of Conflict of Interest/ Common Interest

No conflict of interest or common interest has been declared by the authors.

Authors' Contribution

Tuğba Uğur contributed to the design of the experiments and conducted experiments; Murat TUNA designed the experiments, analyzed and interpreted the data, revised the article. All authors discussed the results and contributed to the final manuscript.

The Declaration of Ethics Committee Approval

The authors declare that this document does not require an ethics committee approval or any special permission

The Declaration of Research and Publication Ethics

The authors of the paper declare that they comply with the scientific, ethical, and quotation rules of SAUJS in all processes of the paper and that they do not make any falsification on the data collected. In addition, they declare that Sakarya University Journal of Science and its editorial board have no responsibility for any ethical violations that may be encountered and that this study has not been evaluated in any academic publication environment other than Sakarya University Journal of Science.

REFERENCES

[1] A. Sakthivel, K. Jeyasubramanian, B. Thangagiri and J. Dhaveethu, “Recent advances in Schiff base metal complexes derived from 4-aminoantipyrine derivatives and their potential applications” Journal of Molecular Structure, vol. 1222, 128885, 2020.

[2] B. Naureen, G.A.Miana, K. Shahid, M. Asghar, S. Tanveer and A. Sarwar, “Iron (III) and zinc (II) monodentate Schiff base

metal complexes: Synthesis, characterization and biological activities" Journal of Molecular Structure, vol. 1231, 129946, 2021.

[3] N. Beyazit, D. Çakmak and C. Demetgül, "Chromone-based Schiff base metal complexes as catalysts for catechol oxidation: Synthesis, kinetics and electrochemical studies" Tetrahedron, vol. 73, no. 19, pp 2774-2779, 2017

[4] S. Sengupta, S. Khan, B. N. Mongal, W. Lewis, M. Fleck, S. K. Chattopadhyay and S. Naskar, "Electrocatalytic hydrogen production and carbon dioxide conversion by earth abundant transition metal complexes of the Schiff base ligand: (E)-1-((2-dimethylamino)-propylimino) methyl)naphthalene-2-ol" Polyhedron, vol. 191, Article ID 114798, 2020.

[5] A. A. Alshaheri, M. I. M. Tahir, M. B. A. Rahman, T. B. S. A. Ravoof and T. A. Saleh, "Catalytic oxidation of cyclohexane using transition metal complexes of dithiocarbazate Schiff base" Chemical Engineering Journal, vol. 327, pp. 423-430, 2017.

[6] B. Tamami and S. Ghasemi, "Catalytic activity of Schiff-base transition metal complexes supported on crosslinked polyacrylamides for hydrogen peroxide decomposition" Journal of Organometallic Chemistry, vol. 794, pp. 311-317, 2015.

[7] S. Annapoorani and C. Krishnan, "Synthesis and spectroscopic studies of trinuclear N4 Schiff base complexes" International Journal of Chem Tech Research, vol. 5, no. 6, pp.180–185, 2013.

[8] H. I. Ugras, I. Basaran, T. Kilic and U. Cakir, "Synthesis, complexation and antifungal, antibacterial activity studies of a new macrocyclic Schiff base" Journal of Heterocyclic Chemistry, vol. 43, no. 6. pp.1679-1684, 2006.

[9] L. Shi, H-M. Ge, Shu-H. Tan, H-Q. Li, Yong-C. Song and H-L. Zhu, "Synthesis and antimicrobial activities of Schiff bases derived from 5-chloro-salicylaldehyde" European Journal of Medicinal Chemistry, vol. 42, no. 4, pp. 558-564, 2007.

[10] A. A. Osowole, A. C. Ekennia and B. O. Achugbu, "Synthesis, Spectroscopic Characterization and Antibacterial Properties of some Metal (II) Complexes of 2-(6-methoxybenzothiazol-2-ylimino) methyl)-4-nitrophenol" Research and Reviews: Journal of Pharmaceutical Analysis, vol. 2, no. 2, pp. 1-5, 2013.

[11] S. M. Morgan, A. Z. El-Sonbati and H. R. Eissa, "Geometrical structures, thermal properties and spectroscopic studies of Schiff base complexes: Correlation between ionic radius of metal complexes and DNA binding" Journal of Molecular Liquids, vol. 240, pp. 752-776, 2017.

[12] T. Mangamamba, M. C. Ganorkar and G. Swarnabala, "Characterization of Complexes Synthesized Using Schiff Base Ligands and Their Screening for Toxicity Two Fungal and One Bacterial Species on Rice Pathogens" International Journal of Inorganic Chemistry, Article ID 736538, 2014.

[13] T. Wieprecht, M. Hazenkamp, H. Rohwer, G. Schlingloff and J. Xia, 2007. "Design and application of transition metal catalysts for laundry bleach" Comptes Rendus Chimie, vol. 10, no.4-5, pp. 326-340, 2007.

[14] R. Hage, J. W. de Boer, F. Gaulard and K. Maaijen, "Chapter There-Manganese and ıron bleaching and oxidation catalysts", Advances in Inorganic Chemistry, vol. 65, pp. 85-116, 2013.

[15] W. Woods, "Bleaching compositions and methods" U.S. Patent, no. 3532634, 1970.

[16] T. D. Finch and R. J. Wilde, "Oxygen bleaching systems in domestic laundry" European Patent, no. 141470, 1984.

[17] H. A. H. Alshamsi and A. K. A. H. Shdood, "Uv-ClO_2 Assisted decolorization of methylene blue", Journal of Chemical and Pharmaceutical Research, vol. 7, no. 9, pp. 36- 44, 2015.

[18] L. Simandi, "Catalysis by metal complexes" Kluwer Academic, Dordrecht, pp. 13, 1992.

[19] H. Korpi, P. Lahtinen, V. Sippola, O. Krause, M. Leskela, and T. Rep, "An efficient method to investigate metal-ligand combinations for oxygen bleaching" Applied Catalysis A. General vol. 268, pp. 199-206, 2004.

[20] P. Sen, D. Kara Simsek and S. Z. Yildiz, "Functional zinc(II) phthalocyanines bearing Schiff base complexes as oxidation catalysts for bleaching systems" Applied Organometalllic Chemistry, vol. 29, no. 8, pp. 509–516, 2015.

[21] H. Sakallıoğlu, "Manyetik Nanopartiküller Üzerine Desteklenmiş Schiff Bazı Türevi Metal Komplekslerinin Sentezleri ve Katalitik Etkinliklerinin İncelenmesi" Çukurova University, Institute of Science, Department of Chemistry, Master Thesis, 2013.

[22] K. C. Gupta and A. K. Sutar, "Catalytic activities of Schiff base transition metal complexes" Coordination Chemistry Reviews vol. 252, no. pp. 1420-1450, 2008.

[23] P. Sen, E. Yildirim and S. Z. Yildiz, "New alkaline media-soluble functional zinc(II) phthalocyanines bearing poly (hydroxylmethyl)iminomethane Schiff base complexes in catalytic bleaching" Synthetic Metals, vol. 215, pp. 41-49, 2016.

[24] K. C. Gupta, A. K. Sutar and C-C. Lin, "Polymer-supported Schiff base complexes in oxidation reactions" Coordination Chemistry Reviews, vol. 253, no. 13–14, pp. 1926-1946, 2009.

[25] A. M. Abu-Dief and I. M. A. Mohamed, "A review on versatile applications of transition metal complexes incorporating Schiff bases" Beni-Suef University Journal of Basic and Applied Sciences, vol. 4, no.2, pp. 119-133, 2015.

[26] S. J. McNeil, M. R. Sunderland and S. J. Leighs, "The utilisation of wool as a catalyst and as a support for catalysts" Applied Catalysis A: General, vol. 541, pp. 120-140, 2017.

[27] W. T. Eckenhoff, "Molecular catalysts of Co, Ni, Fe, and Mo for hydrogen generation in artificial photosynthetic systems" Coordination Chemistry Reviews, vol. 373, pp. 295-316, 2018.

[28] X. Li, C-H. Li, J-H. Jiang, et al. "Synthesis and microcalorimetric determination of the bioactivities of a new Schiff base and its bismuth(III) complex derived from o-vanillin and 2,6-pyridinediamine" Journal of Thermal Analysis and Calorimetry vol. 127, pp. 1767–1776, 2017.

[29] N. Galic´, Z. Cimerman, V. Tomisic, "Spectrometric study of tautomeric and protonation equilibria of o-vanillin Schiff base derivatives and their complexes with Cu(II)" Spectrochim Acta, Part A.,vol. 71, pp.1274–80, 2008.

[30] X. Li, J-H. Jiang, Q. Chen, at al. "Synthesis of nordihydroguaiaretic acid derivatives and their bioactivities on *S. pombe* and *K562* cell lines" European Journal of

Medicinal Chemistry, vol. 62, pp. 605-613, 2013.

[31] R. Hage and A. Lienke, "Applications of transition-metal catalysts to textile and wood-pulp bleaching" Angewandte Chemie Int. Ed., vol. 45, no. 2, pp. 206–222, 2005.

[32] P. Sen, S. Z. Yildiz, N. Dege, M. Atakay, B. Salih, "Functional Substituted Phthalocyanines Bearing Ter-pyridine Complexes as Macromolecular Oxidation Catalysts for Bleaching Systems" ChemistrySelect, vol.2, no. 9, pp. 2643 - 2650, 2017.

[33] P. Sen, D. Akagunduz, A. S. Aghdam, F. Ç. Cebeci, T. Nyokong and T. Catal, "Synthesis of Novel Schiff Base Cobalt (II) and Iron (III) Complexes as Cathode Catalysts for Microbial Fuel Cell Applications" Journal of Inorganic and Organometallic Polymers and Materials, vol. 30, pp.1110–1120, 2020.

[34] İ. Gönül, E. Fakı, B. Ay, M. Köse and S. Serin, "Cobalt(II), nickel(II) and copper(II) complexes of a Schiff base ligand: synthesis, structural characterization and luminescence properties" Transition Metal Chemistry, vol. 43, pp. 73–81, 2018.

[35] I. A. Gegen, "Detection of Methoxyl Group by Infrared Spectrocopy" Applied Spectrocopy, vol. 22, no. 3, pp. 164166, 1968.

[36] R. K. Shan, K. S. Abou-Melha, F. A. Saad, et al., "Elaborated studies on nano-sized homo-binuclear Mn(II), Fe(III), Co(II), Ni(II), and Cu(II) complexes derived from N2O2 Schiff base, thermal, molecular modeling, drug-likeness, and spectral" Journal of Thermal Analysis and Calorimetry, vol. 123, pp. 731–743, 2016.

[37] N. K. Ngan, K. M. Lo and C. S. R. Wong, "Synthesis, structure studies and electrochemistry of molybdenum(VI) Schiff base complexes in the presence of different donor solvent molecules" Polyhedron, vol 30, pp. 2922-2932, 2011.

[38] R. N. Egekenze, Y. Gultneh and R. Butcher, "Mn(III) and Mn(II) complexes of tridentate Schiff base ligands; synthesis, characterization, structure, electrochemistry and catalytic activity" Inorganica Chimica Acta, vol. 478, pp. 232–242, 2018.

[39] P. Sen, S. Z. Yildiz, "The investigation of oxidative bleaching performance of peripherally Schiff base substituted tri-nuclear cobalt-phthalocyanine complexes" Inorganica Chimica Acta, vol. 462, pp. 30-39, 2017.

[40] P. Sen, N. Dege and S.Z. Yildiz, "Tri-nuclear phthalocyanine complexes carrying N/O donor ligands as hydrogen peroxide catalysts, and their bleaching activity measurements by an online spectrophotometric method" Journal of Coordination Chemistry, vol. 70, no.16, pp. 2751-2770, 2017.

[41] P. Sen and S. Z. Yildiz, "Substituted manganese phthalocyanines as bleach catalysts: synthesis, characterization and the investigation of de-aggregation behavior with LiCl in solutions" Research on Chemical Intermediates, vol. 45, pp. 687–707, 2019.

SAKARYA ÜNİVERSİTESİ
FEN BİLİMLERİ ENSTİTÜSÜ DERGİSİ

Sakarya University Journal of Science
SAUJS

e-ISSN: 2147-835X | Founded: 1997 | Period: Bimonthly | Publisher: Sakarya University
http://www.saujs.sakarya.edu.tr/en/

Title: Treatability of Synthetic Wastewater Containing Reactive Yellow 145 Dyestuff by Ozonation Process

Authors: Pınar Nazire TANATTI

Recieved: 2021-02-08 17:49:39

Accepted: 2021-07-05 11:18:05

Article Type: Research Article

Volume: 25
Issue: 4
Month: August
Year: 2021
Pages: 995-1002

How to cite
Pınar Nazire TANATTI; (2021), Treatability of Synthetic Wastewater Containing Reactive Yellow 145 Dyestuff by Ozonation Process. Sakarya University Journal of Science, 25(4), 995-1002, DOI: https://doi.org/10.16984/saufenbilder.876926
Access link
http://www.saujs.sakarya.edu.tr/en/pub/issue/64755/876926

Sakarya University Journal of Science 25(4), 995-1002, 2021

Treatability of Synthetic Wastewater Containing Reactive Yellow 145 Dyestuff by Ozonation Process

Pınar Nazire TANATTI*[1]

Abstract

When the textile industry wastewater volume and considering the composition appears to be one of the most environmentally hazardous industries. Due to textile dyeing industry wastewater's basic properties, additional precautions are required besides conventional wastewater treatment to remove color. The most basic approach is to remove the wastewater colour and break down the chromophores and double bonds that make up the color by oxidative means. In this study, the treatability of wastewater containing Reactive Yellow 145 (RY 145) dyestuff by ozonation process has been investigated. The initial concentration of the wastewater containing RY 145 is 50 mg / L. In the study, pH, O_3 dose and reaction time parameters have been studied in RY 145 dye removal. The most appropriate removal of RY 145 from wastewater have occurred at pH 5, 0.05 g / L.h O_3 dose and 10 minutes reaction time. The removal efficiency of RY 145 has obtained as 99.07% under optimum conditions.

Keywords: Reactive Yellow 145, ozone, ozonation, advanced oxidation process

1. INTRODUCTION

Industrial growth and urbanization cause complexity in the structure of the wastewater discharged into the environment and an increase in its volume [1]. Today one of the most critical global challenges have water pollution from dyes [2]. These dyes and pigments are widely used as colorants in textiles, paints and cosmetics [3]. A large amount of wastewater is generated at the end of the production process in which dyes and chemicals, most of which are auxiliary chemicals and surfactants, are used in the textile industries [4]. The resulting wastewater is dangerous and toxic because it contains compounds known to be carcinogenic, such as various chemicals and large amounts of dyes, usually organic compounds of complex structures [5,6]. Dyestuffs used in the textile industry are classified depending on the chemical structure and dyeing properties [7]. In the chemical structures of dyestuffs, nitro (-NO_2), nitroso (-N = O), azo (-N = N-), carbonyl (-C = O), ethenyl (-C = C-) and thiocarbonyl (-CH = S) contain groups [8].

These dyes used in the textile industry cause significant environmental effects. If water rich in dyestuffs is discharged without treatment, this waters will have negative effects on the receiving environment. Dyeing wastes given to the receiving environment from the textile industry cause the receiving water to change colour and become dyed. Depending on the dye used, they have a toxic effect on plant and animal life,

* Corresponding author: ptanatti@subu.edu.tr
[1] Sakarya Vocational School, Environmental Protection Technologies Department, Turkey.
ORCID: https://orcid.org/0000-0002-2904-7334

prevent the river's self-purification capacity (assimilation capacity), cause the receiving water to color, reduce the light transmittance of the water, and decrease the photosynthesis rate of the aquatic flora. Therefore, in terms of ecology color removal processes enter into an important role in the treatment of wastewater containing high amounts of dyestuffs. Membrane [9], adsorption [10], electrochemical oxidation [11], coagulation [12], flocculation [13] and oxidation [14] methods were applied in the treatment of dye containing wastewater.

In the treatment of wastewater containing azo dyes, advanced Oxidation processes (AOPs) change the chemical structure of the azo dye and even break it down completely [15]. Ozonation, one of the AOPs, has high purification efficiencies in dye removal. Ozone is a strong oxidizer (redox potential 2.07 V) and reacts rapidly with organic and inorganic substances in aqueous solutions with its special dipole structure [16]. Ozone reacts with organic materials in two ways, directly in aqueous solutions and indirectly through hydroxyl radicals formed by its decomposition. Hydroxyl radicals have higher oxidisation compared to ozone (redox potential 2.33 V) and oxidize pollutants in water to the mineralization stage without any discrimination [17-19]. The ozone molecule selectively reacts with compounds containing C = C bonds, some functional groups (OH, CH_3, OCH_3) and anions (N, P, O, S) [20] but $OH\cdot$ oxidation is not selective [21]. As a result of the electrophilic nature of ozone, it generally reacts with aromatic rings by electrophilic substitution or 1,3-dipolar organic replacement reactions [22]. Many pollutants such as textile wastewater [23], water containing dyestuffs [24], water containing diethyl phthalate [25], water containing organic micropollutants [26], biodiesel wastewater [27], water containing Bisphenol A [28] and pharmaceutical wastewater [29] are treated from wastewater with the ozonation process.

In this study, dye removal has been investigated by using the ozonation method in waters containing RY 145. Dye is one of the most important problems processes from textile industry processes. Especially, there is a very dense dye material from the dying tank. It has been aimed to determine the optimum conditions by examining the pH, ozone (O_3) dose and reaction time parameters in the water with an initial RY 145 concentration of 50 mg / L. By using the ozone process, dye removal was achieved with less chemicals and shorter reaction time.

2. MATERIAL AND METHODS

2.1. RY 145 Sample Preparation and Measurement Method

Commercially available RY 145 ($C_{28}H_{20}ClN_9O_{16}S_5\ Na_4$) [30] dye has been used in the experiments. The molecular structure of RY 145 is shown in Fig. 1 [31]. 1 L stock solution containing 1000 mg/L RY 145 was prepared. By using the prepared stock solution, synthetic water with a total volume of 3 L and a concentration of 50 mg/L was obtained. Then, experiments have been conducted with solution containing an initial concentration of 50 mg / L RY 145 dye. All experiments have been performed on a synthetic water sample containing RY 145. In order to measure the values of RY 145 solution before and after treatment, the λ_{max} value of the dye has determined by spectrum scanning. The λ_{max} value of RY 145 has been found to be 413 nm after spectrum scanning.

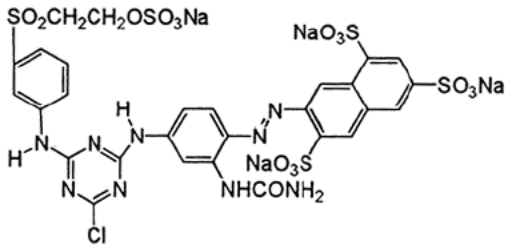

Figure 1 Molecular structure of RY 145

The calibration curve was prepared by taking measurements of the solutions prepared between 0.1 mg / L and 50 mg / L at 413 nm for the measurement of the dye with λ_{max} value during treatment. The regression coefficient (R^2) of the calibration curve obtained has found to be 0.9936. The line equation obtained from the calibration curve is given in Equation (1).

$$\text{RY 145 (mg/L)} = \frac{\text{ABS}}{0{,}0135} \quad (1)$$

2.2. Experimental reactor desing

Ozone is a very strong oxidant (E ° = + 2.07 V). Organic pollutants are oxidized by direct reaction (pH ≤ 2) with molecular ozone or indirect reactions (pH ≥ 7) from $OH^{\cdot}$ resulting from ozone decomposition under alkaline conditions [32,33].

The reactor used for RY 145 removal is given in Figure 2. SABO brand ozone generator with a capacity of 15 g / L.h has been used in the experiments. Experiments have carried out using a 250 mL glass reactor as the reactor.

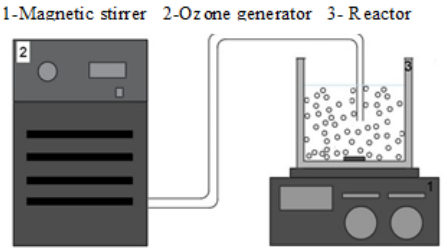

Figure 2 Ozonation reactor

3. RESULTS AND DISCUSSION

3.1. Effect of initial pH

The direct ozone reaction occurs at acidic pHs and in the presence of inhibitory scavengers that cause ozone degradation. $OH^{\cdot}$ has a high-speed and non-selective nature. Therefore, the indirect reaction occurs predominantly under radical type chain reaction or alkaline conditions and in the presence of solvents that trigger $OH^{\cdot}$ formation [21,34]. In addition, at low ozone dosages, due to radical scavengers such as carbonate and bicarbonate in wastewater, oxidation with molecular ozone occurs as a more dominant mechanism [35]. The direct and indirect reactions of ozone are given in the equations below [36].

Direct reactions:

$$O_3 + R \rightarrow \text{Products} \quad (2)$$

Indirect reactions: (total reaction)

$$3O_3 + H_2O \rightarrow 2OH^{\cdot} + 4O_2 \quad (3)$$

In order to investigate the effect of pH on dye removal efficiencies in wastewater with an initial concentration of 50 mg / L RY 145, a dose of 0.025 g / L.h O_3 and pH 3,5,7,9 and 11 at a reaction time of 5 minutes have been studied. RY 145 removal efficiencies are given in Figure 3. RY 145 removal efficiencies at pH 3, pH 5, pH 7, pH 9 and pH 11 have been found to be 49.93%, 69.66%, 57.90%, 55.02% and 66.62%, respectively, under the specified experimental conditions. The lowest removal efficiency has obtained at pH 3 in the ozone method. RY 145 removal efficiencies are high at pH 5 and pH 9. However, the highest removal efficiency is obtained at pH 5. In addition, considering that the initial pH of the solution is 6.86 and the highest RY 145 removal efficiency was obtained at pH 5, the most suitable pH was determined as 5.

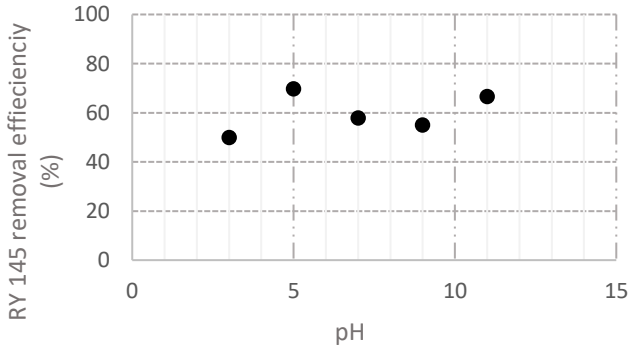

Figure 3 The effect of pH on RY 145 removal efficiency (O_3 dose: 0.025 g / L.h; Reaction time: 5 min)

The treatability of wastewater containing 500 mg / L RY 145 has investigated by ultraviolet-enhanced ozonation process and then pH 8 was determined as the optimum pH. In addition, RY 145 removal efficiency is around 80% in 150 minutes reaction time [37]. In addition, the optimum pH of RY 145 was obtained in the treatment of H_2O_2 / UV AOP. The removal efficiency of RY 145 in 1 hour reaction time was found to be 99% [30]. It is clear that there is RY 145 removal in both ozonation and H_2O_2 / UV process. However, in this study, both the removal

efficiencies are high in RY 145 removal by ozonation, and the reaction time is short. In addition, the optimum pH value found in the treatment of RY 145 by ozonation is the value that should not be spent too much chemical for its adjustment, considering the initial pH of the water.

3.2. Effect of O_3 dose

In order to examine the removal efficiency of wastewater containing RY 145 dye, O_3 dose has been studied between 0.0125 g / L.h and 0.125 g / L.h. Ozone solubility levels was measured in water and the concentration depending on the flow rate is given in the Table 1.

Table 1 The ozone concentration in water depending on the flow rate

Flow rate (g/L.h)	0.0125	0.05	0.075	0.1	0.15	0.3
Ozone concentration (mg/L)	0,19	0.64	1.08	1.3	1.8	2.6

While investigating the effect of O_3 dose on removal efficiencies by ozonation method, studies have been conducted at pH 5 and 5 min reaction time. Figure 3 shows The effect of O_3 dose on RY 145 removal efficiency. In the beginning, while the removal efficiency of RY 145 increases with the increase of O_3 dose, Figure 4 is shown that there is a slow increase in removal efficiency after 0.05 g / L.h O_3 dose. RY 145 removal efficiency has obtained 26.25% at a dose of 0.0125 g / L.h O_3, while RY 145 removal efficiency at a dose of 0.125 g / L.h O_3 has achieved 96.93%. At the ozone dose of 0.05 g / L.h, a rapid decrease in the removal efficiency after RY 145 removal has been determined. RY 145 removal efficiencies have been found 95.36%, 96.79% and 96.93% at 0.05 g / L.h, 0.1 g / L.h and 0.125 g / L.h O_3 doses. Although the ozone dose concentration increases from the ozone dose of 0.05 g / L.h, the increase in removal efficiency is approximately 1.5%. For this reason, the most suitable ozone dose has been determined as 0.05 g / L.h on the most suitable RY 145 removal efficiency.

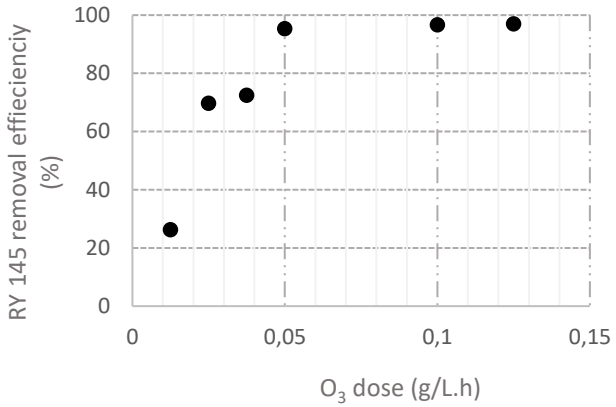

Figure 4 The effect of O_3 dose on RY 145 removal efficiency (pH 5; Reaction time: 5 min)

Even if there is an increase in the ozone dose, the amount of ozone dissolved in the wastewater may have reached saturation, so the increase in removal efficiency is gradually [38].

3.3. Effect of reaction time

The effect of reaction time on RY 145 removal efficiency has been investigated at pH 5 and 0.05 g / L.h O_3 dose. Removal efficiencies for RY 145 are given in Figure 5.

As seen from Figure 5, dye removal efficiencies increase as the reaction time increases. RY 145 removal efficiencies have been studied at reaction times of 1 min to 15 min. Ozone acts to break down compounds with high electron density, such as C = C bonds, activated aromatic systems, and protonated amines [39]. RY 145 removal efficiency has been found 41.59% at 1st min and 99.23% at 15th min. Also, RY 145 removal efficiency has been obtained as 99.07% at 10th min. Depending on the reaction time of RY 145, removal efficiencies increase rapidly until the 6th minute. Increases in removal efficiency after the 6th minute are slow. The removal efficiency has been determined 97.45% in the 6th minute. However, while the RY 145 concentration at the 6th minute was 1.274 mg / L, the RY 145 concentration at the 10th minute was 0.467 mg / L. In addition, the RY 145 concentration at the 15th minute is 0.385 mg / L. Considering the RY 145

concentrations, 10 min has been determined as the optimum reaction time.

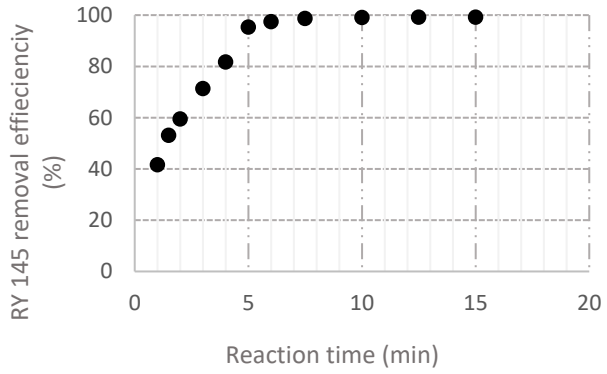

Figure 5 The effect of reaction time on RY 145 removal efficiency (pH 5; O_3 dose: 0.05 g / L.h)

Reaction times vary according to the AOPs used in dye removal. In UV treatment with Ni_3O_4-Co_3O_4 / Al_2O_3 catalyst, RY 145 could be removed in 60 minutes reaction time [40]. In addition, Reactive Golden treatment was studied by electrooxidation from AOPs. In the oxidation using RuO_2 / Ti electrode, only 96.4% efficiency was obtained in 6 hours reaction time [41].

4. RESULT

In the study, ozonation method has been used for the treatment of wastewater containing RY 145 dyestuff prepared synthetically. Optimum conditions in the treatment of RY 145 containing wastewater were found as pH 5, 0.05 g / L.h O_3 dose and 10 minutes reaction time. Optimum conditions in the treatment of RY 145 containing wastewater have been found as pH 5, 0.05 g / L.h O_3 dose and 10 minutes reaction time. Dye removal efficiency was found to be 99.07% under optimum conditions. It has been established that the ozonation method is a suitable process in waters containing RY 145 dyestuff. However, ozonation processes are methods that can be used in different combinations. Under favour this study, it can be predicted that RY 145 studies can be carried out with a more economical and environmentally friendly process by using different ozonation systems.

Ethical Approval and Consent to Participate

The manuscript has not been submitted to more than one journal for simultaneous consideration. The submitted work has been original and has not been published elsewhere in any form or language unless the new work concerns an expansion of previous work. A single study has not been split up into several parts to increase the quantity of submissions and not submitted to various journals or to one journal over time. Results have been presented clearly, honestly data manipulation. I have adhered to discipline-specific rules for acquiring, selecting and processing data. The manuscript does not report on or involve the use of any animal or human data or tissue; hence Ethics and Consent Participate is not applicable" in this paper.

Consent for publication

The manuscript does not contain data from any individual person hence "consent to publish" is not applicable.

Funding

There is no funding for the study.

Authors' contributions

NPT has done all the experiments of the study. All parts of the writing belong to NPT.

Competing Interests

There are no competing interests.

Availability of data and materials

The study is an experimental study. All results obtained in the study have been added to the publication. The manuscript does not contain any data, hence "Availability of data and materials" is not applicable.

REFERENCES

[1] V. Vijayakumar, R. Saravanathamizhan, and N. Balasubramanian, "Electro oxidation of dye effluent in a tubular electrochemical reactor using TiO_2/RuO_2 anode," Journal of Water Process Engineering, vol 9, pp. 155–160, 2016.

[2] J. Wu, Q. Li, W. Li, Y. Li, G. Wang, A. Li, and H. Li, "Efficient removal of acid dyes using permanent magnetic resin and its preliminary investigation for advanced treatment of dyeing effluents," Journal of Cleaner Production, vol. 251, 119694, 2020.

[3] E. Pagalan Jr, M. Sebron, S. Gomez, S. J. Salva, R. Ampustaa, A. J. Macarayoa, C. Joynoa, A. Idoa, and R. Arazoa, "Activated carbon from spent coffee grounds as an adsorbent for treatment of water contaminated by aniline yellow dye," Industrial Crops & Products, vol. 145, 111953, 2020.

[4] M. İlter, "Tekstil üretimi ve yardımcı kimyasallar," TMMOB Kimya Mühendisleri Odası, İzmir, 2015.

[5] E. GilPavas, I. Dobrosz-Gómez, and M. Á. Gómez-Garcíac, "Optimization of sequential chemical coagulation - electro-oxidation processfor the treatment of an industrial textile wastewater," Journal of Water Process Engineering, vol. 22, pp. 73-79, 2018.

[6] S. Marimutha, A. J. Antonisamy, S. Malayandi, K. Rajendran, P. C. Tsai, A. Pugazhendhi, and V. K. Ponnusamy, "Silver nanoparticles in dye effluent treatment: A review on synthesis, treatment methods, mechanisms, photocatalytic degradation, toxic effects and mitigation of toxicity," Journal of Photochemistry & Photobiology, B: Biology, vol. 205, 111823, 2020.

[7] A. K. Verma, R. R. Dash, and P. Bhunia, "A review on chemical coagulation/flocculation technologies for removal of colour from textile wastewaters," Journal of Environmental Management, vol. 93, pp. 154-168, 2012.

[8] G. Lofrano, S. Meriç, G. E. Zengin, and D. Orhon, "Chemical and biological treatment technologies for leather tannery chemicals and wastewaters: a review," Science of Total Environment, vol. 461-462, pp. 265-281, 2013.

[9] U. Habiba, J. J. L. Lee, T. C. Joo, B. C. Ang, and A. M. Afifi, "Degradation of methyl orange and congo red by using chitosan/polyvinyl alcohol/TiO_2 electrospun nanofibrous membrane," International Journal of Biological Macromolecules, vol. 131, pp. 821–827, 2019.

[10] N. Fahmi Khairol, N. Sapawe, and M. Danish, "Excellent performance integrated both adsorption and photocatalytic reaction toward degradation of congo red by CuO/Eggshell," Materials Today: Proceeding, vol. 19, pp. 1340–1345, 2019.

[11] N. P. Shetti, S. J. Malode, R. S. Malladi, S. L. Nargund, S. S. Shukla, and T. M. Aminabhavi, "Electrochemical detection and degradation of textile dye Congo red at graphene oxide modified electrode," Microchemistry Journal, vol. 146, pp. 387–392, 2019.

[12] M. Sillanpää, M. C. Ncibi, A. Matilainen, and M. Vepsäläinen, "Removal of natural organic matter in drinking water treatment by coagulation: a comprehensive review," Chemosphere, vol. 190, pp. 54–71, 2018.

[13] Q. Du, H. Wei, A. Li, and H. Yang, "Evaluation of the starch-based flocculants on flocculation of hairwork wastewater," Science Total Environment, vol. 601–602, pp. 1628–1637, 2017.

[14] P. Tan, Q. Bi, Y. Hu, Z. Fang, Y. Chen, and J. Cheng, "Effect of the degree of oxidation and defects of graphene oxide on adsorption of Cu^{2+} from aqueous solution," Appleid Surface Science, vol. 423, pp. 1141–1151, 2017.

[15] B. L. Alderete, J. Silva, R. Godoi, F. R. Silva, S. R. Taffarel, L. P. Silva, A. L. H. Garcia, H. M. Júnior, H. L. N. Amorim, and J. N. Picad, "Evaluation of toxicity and mutagenicity of a synthetic effluent containing azo dye after Advanced Oxidation Process treatment," Chemosphere, vol. 263, 128291, 2021.

[16] X. Li, W. Chen, L. Ma, H. Wang, and J. Fan, "Industrial wastewater advanced treatment via catalytic ozonation with an Fe-based catalyst," Chemosphere, vol. 195, pp. 336-343, 2018.

[17] R. Rosal, A. Rodríguez, J. A. Perdigon-Melon, A. Petre, and E. García-Calvo, "Oxidati on of dissolved organic matter in the effluent of a sewage treatment plant using ozone combined with hydrogen peroxide (O_3/H_2O_2)," Chemical Engineering Journal, vol. 149, pp. 311-318, 2009.

[18] F. Pan, Y. Luo, J. J. Fan, D. C. Liu, and J. Fu, "Degradation of disperse blue E-4R in aqueous solution by zero-valent iron/ozone," Clean Soil, Air, Water, vol. 40, pp. 422-427, 2012.

[19] Z. Xiong, Y. Yuan, B. Lai, P. Yang, and Y. Zhou, "Mineralization of ammunition wastewater by a micron-size Fe^0/O_3process (mFe^0/O_3)," RSC Advances, vol. 6, pp. 55726-55735, 2016.

[20] A.B. Alvares, C. Diaper, and S. A. Parsons, "Partial oxidation by ozone to remove recalcitrance from wastewaters – a review," Environmental Technology, vol. 22, pp. 409–427, 2001.

[21] B. Ning, N. Graham, Y. Zhang, M. Nakonechnyc, and M. G. El-Din, "Degradation of endocrine disrupting chemicals by ozone/AOPs," Ozone Science & Engineering, vol. 29, pp. 153–176, 2007.

[22] E. Mvula and C. Sonntag, "Ozonolysis of phenols in aqueous solution," Organic & Biomolecular Chemistry, vol 1, pp. 1749-1756, 2003.

[23] L. Bilińska, K. Blus, M. Gmurek, S. Ledakowicz, "Coupling of electro - coagulation and ozone treatment for textile wastewater reuse," Chemical Engineering Journal, vol. 358, pp. 992−100, 2019.

[24] J.B. Parsa, S.H. Negahdar, "Treatment of wastewater containing Acid Blue 92 dye by advanced ozone-based oxidation methods," Separation and Purification Technology, vol 98, pp. 315-320, 2012.

[25] L. Mansouri, C. Tizaoui, S.U. Geissen, L. Bousselmi, "A comparative study on ozone, hydrogen peroxide and UV based advanced oxidation processes for efficient removal of diethyl phthalate in water," Journal of Hazardous Materials, vol. 363, pp. 401‑411, 2019.

[26] M. Ekblad, P. Falås, H. El-taliawy, F. Nilsson, K. Bester, M. Hagman, M. Cimbritz," Is dissolved COD a suitable design parameter for ozone oxidation of organic micropollutants in wastewater?," Science of the Total Environment, vol. 658, pp. 449–456, 2019.

[27] N.P.Tanatti, M. Mehmetbaşoğlu, İ.A. Şengil, H. Aksu, E. Emin, "Kinetics and thermodynamics of biodiesel wastewater treatment by using ozonation process," Desalination and Water Treatment, vol. 161, pp. 108–115, 2019.

[28] N.P.Tanatti, E. Balkaya, İ.A. Şengil,"Kinetic and statistical analysis of Bisphenol A in wastewaters by ozonation and electrooxidation – ozonation processes," Desalination and Water Treatment, vol. 204, pp. 429–437, 2020.

[29] J. Zhan, Z. Li, G. Yu, X. Pan, J. Wang, W. Zhu, X. Han, Y. Wang, "Enhanced treatment of pharmaceutical wastewater by combining threedimensional electrochemical process with ozonation to in situ regenerate granular activated carbon particle electrodes,"

Separation and Purification Technology, vol. 208, pp. 12‑18, 2019.

[30] T. H. Bokharı, M. Kashıf, I. A. Bhattı, M. Zubaır, S. Adeel, M. Yousaf, M. Ahmad, M. Iqbal, M. Usman, M. Zuber, and A. Mansha, **"**Degradation study of C.I. Reactive Yellow 145 by advanced oxidation process," Asian Journal of Chemistry, vol. 25, pp. 8668-8672, 2013.

[31] Z. Gündüz, "Decolorization of dye solution containing Reactive Jakofiz Yellow by Electrocoagulation process: Investigation of some electrochemical variables," Omer Halisdemir University Journal of Engineering Sciences, vol. 8, pp. 665-674, 2019.

[32] E.V. Rokhina, J. Virkutyte, R. S. Varma, and V. Jegatheesan, "Treatment of Micropollutants in Water and Wastewater," Integrated Environmental Technology Series, IWA Publishing, London, pp. 360–424, 2010.

[33] R. Broséus, S. Vincent, K. Aboulfad, A. Daneshvar, S. Sauvé, B. Barbeau, and M. Prévost, "Ozone oxidation of pharmaceuticals, endocrine disruptors and pesticides during drinking water treatment," Water Resource, vol. 43, pp. 4707–4717, 2009.

[34] S. Irmak, O. Erbatur, and A. Akgerman, "Degradation of 17[beta]-estradiol and bisphenol A in aqueous medium by using ozone and ozone/UV techniques," Journal of Hazardous Material, vol. 126, pp. 54–62, 2005.

[35] N. Nakada, H. Shinohara, A. Murata, K. Kiri, S. Managaki, N. Sato, and H. Takada, "Removal of selected pharmaceuticals and personal care products (PPCPs) and endocrine-disrupting chemicals (EDCs) during sand filtration and ozonation at a municipal sewage treatment plant," Water Resource, vol. 41, pp. 4373–4382, 2007.

[36] R. H. Waldemer, P. G. C. Gottschalk, J. A. Libra, and A. Saupe, "Ozonation of Water and Waste Water, A Practical Guide to Understanding Ozone and its Applications," 2nd Ed, Wiley-VCH, Germany, 2010.

[37] S. Song, X. Xu, L. Xu, Z. He, H. Ying, J. Chen, and B. Yan, "Mineralization of CI Reactive Yellow 145 in Aqueous Solution by Ultraviolet – Enhanced Ozonation," Industrial & Engineering Chemistry Research, vol. 47, 5, pp. 1386–1391, 2008.

[38] H. Deng, "Ozonation mechanism of carbamazepine and ketoprofen in RO concentrate from municipal wastewater treatment: Kinetic regimes, removal efficiency and matrix effect," Science of Total Environment, vol. 717, pp. 137150, 2020.

[39] M. Deborde, S. Rabouan, J. P. Duguet, and B. Legube, "Kinetics of aqueous ozoneinduced oxidation of some endocrine disruptors," Environmental Science and Technology, vol. 39, pp. 6086–6092, 2005.

[40] E. J. Mohammad, A.J. Lafta, and S. H. Kahdim, "Photocatalytic removal of reactive yellow 145 dye from simulated textile wastewaters over supported (Co, $Ni)_3O_4/Al_2O_3$ co-catalyst," Polish Journal of Chemical Technology, vol. 18, pp. 1-9, 2016.

[41] D. S. Ibrahim, A. P. Anand, A. Muthukrishnaraj, R. Thilakavathi, and N. Balasubramanian, "In situ electro-catalytic treatment of a Reactive Golden Yellow HER synthetic dye effluent," Journal of Environmental Chemical Engineering, vol. 1, pp. 2‑8, 2013.

SAKARYA ÜNİVERSİTESİ
FEN BİLİMLERİ ENSTİTÜSÜ DERGİSİ

Sakarya University Journal of Science
SAUJS

ISSN 1301-4048 | e-ISSN 2147-835X | Period Bimonthly | Founded: 1997 | Publisher Sakarya University | http://www.saujs.sakarya.edu.tr/

Title: Morphological and Structural Observation on the Rectum of Bolua turkiyae Ünal, 1999 (Orthoptera, Tettigoniidae)

Authors: Damla AMUTKAN MUTLU, Irmak POLAT, Zekiye SULUDERE

Recieved: 2021-04-05 23:27:09

Accepted: 2021-07-05 20:47:16

Article Type: Research Article

Volume: 25
Issue: 4
Month: August
Year: 2021
Pages: 1003-1008

How to cite
Damla AMUTKAN MUTLU, Irmak POLAT, Zekiye SULUDERE; (2021), Morphological and Structural Observation on the Rectum of Bolua turkiyae Ünal, 1999 (Orthoptera, Tettigoniidae). Sakarya University Journal of Science, 25(4), 1003-1008, DOI: 10.16984/saufenbilder.910328
Access link
http://www.saujs.sakarya.edu.tr/en/pub/issue/64755/910328

Sakarya University Journal of Science 25(4), 1003-1008, 2021

Morphological and Structural Observation on the Rectum of *Bolua turkiyae* Ünal, 1999 (Orthoptera, Tettigoniidae)

Damla AMUTKAN MUTLU*[1], Irmak POLAT[1], Zekiye SULUDERE[1]

Abstract

This study presents the morphology and structure of the rectum in *Bolua turkiyae* Ünal, 1999 (Orthoptera, Tettigoniidae) using light and scanning electron microscopy. The digestive system in insects is split up three parts as the foregut, the midgut and the hindgut. The rectum is last part of the hindgut. The results show that the rectum of *B. turkiyae* consists of 6 rectal pads, in similar to rectal pads found in others Orthopteran species. The rectum contains the muscle tissue with connective tissue, epithelial layer with columnar cells, and the cuticular intima from the outside to inside. There is microvillus on the apical side of the columnar cells that serves in water and ion reabsorption.

Keywords: Rectal pads, hindgut, histology, electron microscope

1. INTRODUCTION

The Orthoptera order is split up two suborders as Caelifera in which the species have small antenna and Ensifera in which the species have long antenna [1, 2]. Orthopterans have an incomplete metamorphosis [3]. Most species lay their eggs in the ground or on the parts of plants. The eggs hatch and the young nymphs occur. The young nymphs become the adult individuals after almost 5 moulting stages [3].

Many species in Orthoptera order are considered pests of crops, which these species are known for wiping fields out in a day [3]. Many adult and nymph individuals can cause major agricultural damage by virtue of feeding on weeds, grasses or crops [3, 4]. Therefore, the ortopteran species have pretty economic importance. Knowing the biology of these species is of great importance for the steps to be taken in the pest management.

Bolua turkiyae Ünal, 1999 is a species which belongs to Tettigoniidae family in Orthoptera order in Ensifera suborder. This species is an endemic species to Turkey [5]. Since this species was found in Bolu province for the first time, Ünal 1999 gave the name of this city to it. Type locality of the species is expressed as Bolu, Kastamonu, Balıkesir [5-7].

Many studies have been conducted on the phylogeny, taxonomy and systematics of this species [5-7]. According to our research, no studies on the biology of *B. turkiyae* have been found. Therefore, in the present study, we focused on to find out the morphology and histology of the

* Corresponding author: damlamutkan@gazi.edu.tr
[1] Gazi University, Faculty of Science, Biology, Turkey
E-Mail: irmakyilmaz@gazi.edu.tr, zekiyesuludere@gmail.com.
ORCID: https://orcid.org/0000-0002-4780-8520; https://orcid.org/0000-0001-7230-4589; https://orcid.org/0000-0002-1207-5814

rectum region located in the last part of the digestive canal. Major function of the rectum in especially terrestrial insects is the removal of water from the faeces and provides an absorptive role.

2. MATERIALS AND METHODS

2.1. Insect Collecting and Rearing

Approximately 10 live male and 10 live female adult species of *B. turkiyae* were captured in Hamidiye Village, Bolu Province in Turkey. After being caught, they were put in plastic containers as live.

2.2. Light Microscopy

Live individuals were anesthetized with ethyl acetate fume and the digestive system was dissected out in phosphate buffered saline under a stereomicroscope (Leica EZ4). After taking general photograph of the digestive system, the rectum was removed from the digestive system and prepared for light (LM) and scanning electron microscopy (SEM) studies.

The samples were fixed in Formaldehyde solution. Afterwards, the dehydration was performed in rising series of the alcohol and the samples were embedded in paraffin. the sections which were taken almost 6-7 micron thick were stained with Hematoxylin-Eosin (H&E) and Mallory trichrome staining. Finally, The stained sections were turned into permanent slides with entellan and observed using an Olympus BX51 light microscope (Japan) mounted with a digital camera Olympus E330 (Japan) and the photographs were taken.

2.3. Scanning Electron Microscopy

Dissected rectums were fixed in glutaraldehyde in phosphate-buffered saline. The fixed specimens were dehydrated through a rising ethanol series. Then the drying process was performed with a Polaron CPD 7501 Critical Point Dryer. The coated samples with gold (Polaron SC 502) were investigated with a JEOL JSM 6060 LV SEM at an accelerating voltage of 10 kV and the photographs were taken.

3. RESULTS

The digestive system of adult *B. turkiyae* mainly consists of three distinct regions. These are the foregut, the midgut, and the hindgut. The hindgut is split up regions as the ileum, the colon and the rectum. The rectum which is the subject of the study is the last part of the hindgut in *B. turkiyae.* The rectum is an organ which has ovoid form (Figures 1, 2).

The rectum of *B. turkiyae* has different layers from outside to inside. The outer surface of this organ is covered with the muscle tissue and connective tissue with prominent tracheal network (Figures 2-4). It is observed that it has 6 rectal pads in the cross sections of light microscope (Figure 3). The epithelial layer shows a monolayer sequence (Figures 3-7). The nucleus of each columnar cell is located in the center of the cell and has ovoid shape (Figures 4, 6). The apical side of the cells has a large amount of microvillus which plays the reabsorption function (Figures 5, 7). The epithelium has a cuticular intima layer that separates the lumen content with epithelial layer. This cuticular intima surrounds the epithelium on the luminal side (Figures 3-7).

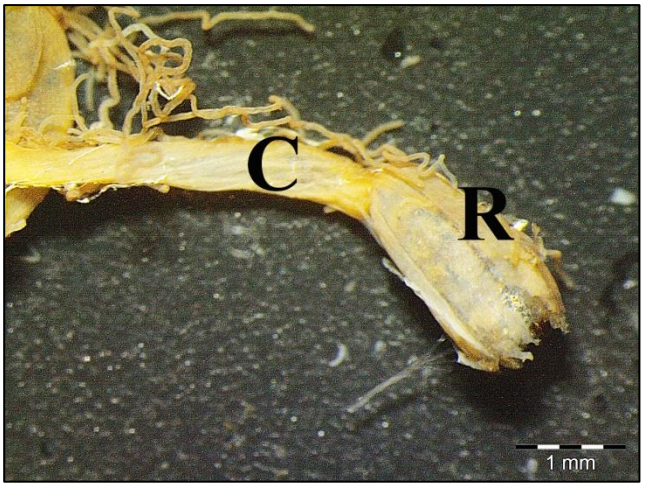

Figure 1 Stereomicroscope images of the hindgut of *B. turkiyae*. C: Colon, R: Rectum

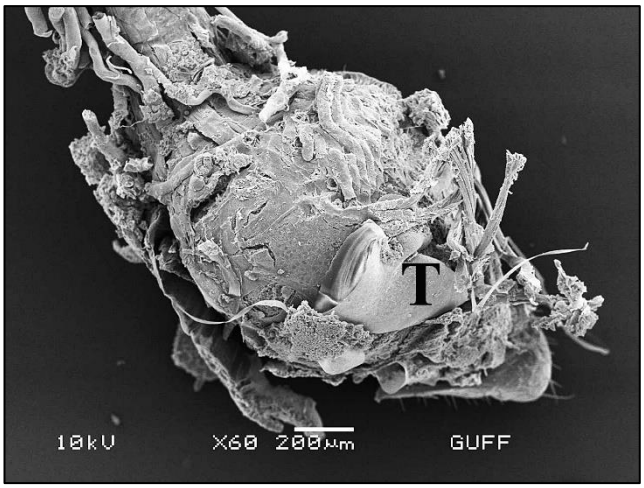

Figure 2 SEM micrograph of the general structure of the rectum of *B. turkiyae*. T: Trachea

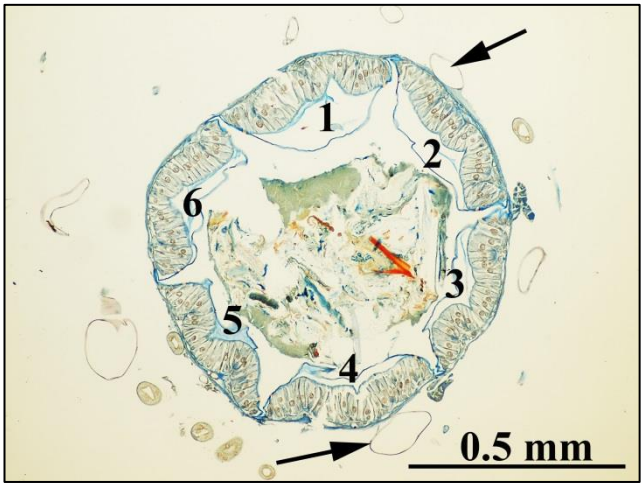

Figure 3 Light micrograph of the cross section of the rectum. →: Trachea (Mallory's trichrome staining)

Figure 4 Light micrograph of the cross section of the rectum. →: Trachea, E: Epithelial layer (H&E staining)

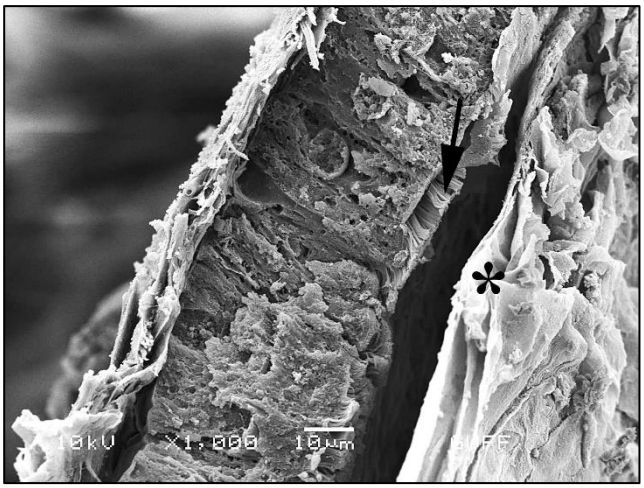

Figure 5 SEM micrograph of the cross section of the rectum. →: Microvillus, *: Cuticular intima layer

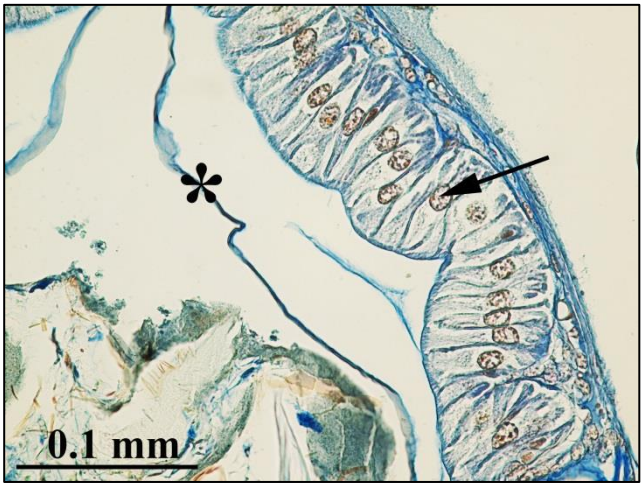

Figure 6 Light micrograph of the cross section of the rectum. →: Nucleus, *: Cuticular intima layer (Mallory's trichrome staining)

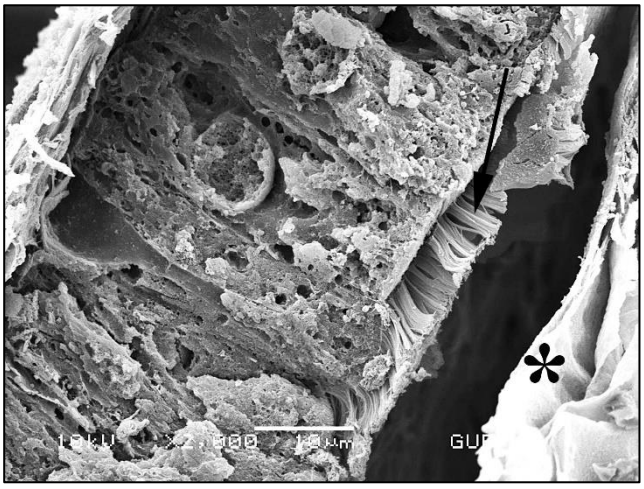

Figure 7 SEM micrograph of the cross section of the rectum. →: Microvillus, *: Cuticular intima layer

4. DISCUSSION

The rectal pads that are founded in some insect species are specialized structures of the rectum. These structures are appertaining to ion uptake and water removal to continue the body homeostasis [8, 9]. There is no rectal pad in rectum in some insect species such as *Pylaemenes mitratus* (Phasmid: Basillidae) [10] and *Karenia caelatata* (Hemiptera: Cicadidae) [11]. On the contrary, there is found the rectal pad in the rectum of *Streltzoviella insularis* (Lepidoptera: Cossidae) [12], *Cryptotermes brevis* (Blattodea, Kalotermitidae), *Cryptotermes cavifrons* (Blattodea, Kalotermitidae), *Coptotermes formosanus* (Blattodea, Rhinotermitidae), *Neotermes jouteli* (Blattodea, Kalotermitidae) [13], *Gryllus pennsylvanicus* (Orthoptera, Gryllidae) [14], and *Poecilimon cervus* (Orthoptera, Tettigoniidae) [15] similar to the rectum of *B. turkiyae*. The presence or not of rectal pads may be related to the insect's diet.

The rectal pads number can vary among the insect species. Although the number of the rectal pads is 6 in *G. pennsylvanicus* (Orthoptera, Gryllidae) [14], *Blattella germanica* (Orthoptera, Blattellidae) [16], and *Aedes aegypti* (Diptera, Culicidae) [17], this number is 4 in *Chrysoperla externa* (Neuroptera, Chrysopidae) [18]. The rectum of *B. turkiyae* has 6 rectal pads.

The epithelial cells have microvillus on the apical side of it. These microvilli help to reabsorption of the water, on the other hand it was indicated that the epithelial cells in the rectum of *Rhynchophorus phoenicis* (Coleoptera, Curculionidae) [19] and *P. cervus* (Orthoptera, Tettigoniidae) [15] do not have microvilli. It was remarked that the cells have either apical membrane infoldings or epithelial foldings. Contrary, in *Calliphora erythrocephala* (Diptera, Calliphoridae) [20] and *Melanoplus femurrubrum* (Orthoptera, Acrididae) [21] they have well developed microvilli in rectal cells.

In this paper, we focused to determine the morphology and structure of the rectum. Although the data we have obtained reveal some differences, they are mostly similar to the rectum structure of other insect species.

Acknowledgments

The author expresses thanks to Prof. Dr. Mustafa ÜNAL (Bolu Abant Izzet Baysal University, Faculty of Arts and Sciences, Biology Department) for his help diagnose the species.

The Declaration of Conflict of Interest

No conflict of interest has been declared by the authors.

Authors' Contribution

The authors contributed equally to the study.

The Declaration of Ethics Committee Approval

This study does not require ethics committee permission or any special permission.

The Declaration of Research and Publication Ethics

The authors of the paper declare that they comply with the scientific, ethical and quotation rules of SAUJS in all processes of the paper and that they do not make any falsification on the data collected. In addition, they declare that Sakarya University Journal of Science and its editorial board have no responsibility for any ethical violations that may be encountered, and that this study has not been evaluated in any academic publication environment other than Sakarya University Journal of Science.

REFERENCES

[1] D. T. Gwynne, “Phylogeny of the Ensifera (Orthoptera): a hypothesis supporting multiple origins of acoustical signalling, complex spermatophores and maternal care in crickets, katydids, and weta”, Journal of Orthoptera Research, vol. 4, no. 4, pp. 203-218, 1995. doi:10.2307/3503478. JSTOR 3503478.

[2] P. K. Flook and C. H. F. Rowell, "The Phylogeny of the Caelifera (Insecta, Orthoptera) as Deduced from mtrRNA Gene Sequences", Molecular Phylogenetics and Evolution, vol. 8, no. 1, pp. 89-103, 1997. doi:10.1006/mpev.1997.0412. PMID 9242597.

[3] H. V. Hoell, J. T. Doyen, and A. H. Purcell, "Introduction to insect biology and diversity", 2nd ed. Oxford University Press, pp. 392-394, 1998. ISBN 978-0-19-510033-4.

[4] F. P. Biagio, F. K. Tamaki, W. R. Terra, and A. F. Ribeiro, "Digestive morphophysiology of *Gryllodes sigillatus* (Orthoptera: Gryllidae)", Journal of Insect Physiology, vol. 55, pp. 1125-1133, 2009.

[5] A. Mol, M. S. Taylan, E. Demir, and D. Şirin, "Contribution to the knowledge of Ensifera (Insecta: Orthoptera) fauna of Turkey", Journal of the Entomological Research Society, vol. 18, no. 1, pp. 75-98, 2016.

[6] M. Ünal, "Notes on Orthoptera of western Turkey, with description of a new genus and four new species", Journal of Orthoptera Research, vol. 8, pp. 243-255, 1999.

[7] B. Çiplak, "Distribution of Tettigoniinae (Orthoptera, Tettigoniidae) bush-crickets in Turkey: the importance of the Anatolian Taurus Mountains in biodiversity and implications for conservation", Biodiversity & Conservation, vol. 12, no. 1, pp. 47-64, 2003.

[8] L. Liu and B. Z. Hua, "Ultrastructure of the rectum of the soil-spraying larva in *Bittacus cirratus* (Mecoptera: Bittacidae)", Protoplasma, vol. 256, no. 6, pp. 1487-1494, 2019.

[9] R. F. Chapman, "The insects: structure and function", 5th ed. Cambridge University Press, Cambridge (UK), pp. 546-584, 2013.

[10] M. H. Nasır and S. Azman, "Gross anatomy and histology of alimentary system of stick insect, *Pylaemenes mitratus* (Phasmid: Basillidae)", Serangga, vol. 24, no. 1, pp. 151-158, 2019.

[11] H. Zhong, Y. Zhang, and C. Wei, "Morphology, histology and ultrastructure of the alimentary canal of the adult mute cicada, *Karenia caelatata* (Hemiptera: Cicadidae)", Acta Entomologica Sinica, vol. 63, no. 4, pp. 421-432, 2020.

[12] X. Wang, H. Lu, Y. Shao, and S. Zong, "Morphological and ultrastructural characterization of the alimentary canal in larvae of *Streltzoviella insularis* (Staudinger) (Lepidoptera: Cossidae)", Entomological Research, vol. 48, no. 4, pp. 288-299, 2018.

[13] J. Zukowski and N. Y. Su, "A comparison of morphology among four termite species with different moisture requirements", Insects, vol. 11, no. 5, pp. 1-10, 2020.

[14] L. E. Des Marteaux, J. R. Stinziano, and B. J. Sinclair, "Effects of cold acclimation on rectal macromorphology, ultrastructure, and cytoskeletal stability in *Gryllus pennsylvanicus* crickets", Journal of Insect Physiology, vol. 104, pp. 15-24, 2018.

[15] I. Polat, "The Ultrastructural Features of the Digestive, Excretory, Female and Male Reproductive Systems of *Poecilimon cervus* Karabag, 1950", Gazi University, Graduate School of Natural and Applied Sciences, PhD Thesis, 2016. (in Turkish).

[16] S. Ishii and Y. Kuwahara, "An aggregation pheromone of the German cockroach *Blattella germanica* L. (Orthoptera: Blattellidae): I. Site of the pheromone production", Applied Entomology and Zoology, vol. 2, no. 4, pp. 203-217, 1967.

[17] A. Lajevardi and J. P. V. Paluzzi, "Receptor characterization and functional activity of pyrokinins on the hindgut in the adult mosquito, *Aedes aegypti*", Frontiers in Physiology, vol. 11, pp. 1-16, 2020.

[18] P. C. Dantas, J. E. Serrão, H. C. P. Santos, and G. A. Carvalho, "Anatomy and histology of the alimentary canal of larvae and adults of *Chrysoperla externa* (Hagen, 1861) (Neuroptera: Chrysopidae)", Arthropod Structure & Development, vol. 60, pp. 1-7, 2021.

[19] O. O. Temitope, "A study of the morphology and histology of the alimentary tract of the adult palm weevil", International Journal of Histology and Cytology, vol. 2, no. 3, pp. 125-129, 2015.

[20] B. L. Gupta and M. J. Berridge, "A coat of repeating subunits on the cytoplasmic surface of the plasma membrane in the rectal papillae of the blowfly, *Calliphora erythrocephala* (Meig.), studied in situ by electron microscopy", Journal of Cell Biology, vol. 29, pp. 376-382, 1966.

[21] W. S. Marshall, "The rectal sac of the red-legged grasshopper, *Melanoplus femur-rubrum* DeGeer", Annals of Entomological Society of America, vol. 38, pp. 461-471, 1945.

SAKARYA ÜNİVERSİTESİ
FEN BİLİMLERİ ENSTİTÜSÜ DERGİSİ

Sakarya University Journal of Science
SAUJS

e-ISSN: 2147-835X | Founded: 1997 | Period: Bimonthly | Publisher: Sakarya University
http://www.saujs.sakarya.edu.tr/en/

Title: Effect of The Filler Type and Particle Distribution Changes on Polyester Matrix Composites

Authors: Şevki EREN, Serkan SUBAŞI

Recieved: 2020-08-16 19:31:54

Accepted: 2021-07-07 11:48:00

Article Type: Research Article

Volume: 25
Issue: 4
Month: August
Year: 2021
Pages: 1009-1019

How to cite
Şevki EREN EREN, Serkan SUBAŞI; (2021), Effect of The Filler Type and Particle Distribution Changes on Polyester Matrix Composites. Sakarya University Journal of Science, 25(4), 1009-1019, DOI: https://doi.org/10.16984/saufenbilder.781256
Access link
http://www.saujs.sakarya.edu.tr/en/pub/issue/64755/781256

Sakarya University Journal of Science 25(4), 1009-1019, 2021

Effect of The Filler Type and Particle Distribution Changes on Polyester Matrix Composites

Şevki EREN*[1], Serkan SUBAŞI[2]

Abstract

In this study, the effect of the usage of additives at different initiator ratios as well as the usage of fillers of different types and different grain distributions on resin consumption and compressive strength of polyester matrix composites were investigated. Orthophthalic unsaturated polyester resin (UP) was used as a matrix. The initiator (methyl ethyl ketone peroxide) at the ratio of 1.0%, 1.5%, and 2.0% and the accelerator (cobalt octoate) at the ratio of 1.0% by weight was used to start the polymerization. Silica, basalt, and quartz sand were used as the filler type. All fillings used in the study were prepared in the grain size distribution of the American Foundry Society (AFS 40-45) and the grain size distribution determined by reference to the Fuller equation (F 1.0). Resin consumption and compressive strength of produced composites were determined, and SEM analyses were carried out. As a result of the study, in all filled composites, the minimum resin consumption was achieved at a starting rate of 1.0%. The highest compressive strength was determined as 130.43 MPa in the basalt filled composite and in the AFS40-45 grain distribution.

Keywords: Polyester matrix composites, filler grain distribution, resin consumption, fuller equation, American foundry society

1. INTRODUCTION

The mechanical properties of the composite are affected by the size, shape, aspect ratio, and distribution of the reinforcing particles [1-3]. It has been reported that the increase of the specific surface area and the contents of the fillers enhance the mechanical and impact properties of the composites. However, when the size of the fillers becomes smaller and the content of the fillers becomes higher, the viscosity of the composite resin will be too high to process. In that case, the interfacial strength will be a more important factor due to the increased surface area of the fillers [4]. Fuller and Thompson [5], emphasized the important effect of aggregate grading on the properties of concrete. The problem of the best possible proportioning of aggregates and their contribution to optimal proportioning for the concrete mixture has been the subject of many experimental and theoretical investigations. One early example is presented by Fuller and Thompson 1907 in a series of curves which are

* Corresponding author: seren@ahievran.edu.tr
[1] Ahi Evran University, Vocational School of Technical Sciences, Kırşehir, Turkey.
ORCID: https://orcid.org/0000-0003-0773-4034
[2] Düzce University, Engineering Faculty, Düzce, Turkey.
E-Mail: serkansubasi@duzce.edu.tr
ORCID: https://orcid.org/0000-0001-7826-1348

currently used for the optimization of concrete and asphalt aggregates [5].

Most foundries in the United States use the AFS grain fineness number as a general indication of sand fineness [6]. This number is calculated from the size distribution, which is determined by standard ASTM sieves. Each fraction is multiplied with a weighting factor, the results are added together and divided by 100. AFS number gets bigger as the average size decreases. The AFS number is considered to be proportional to the number of grains per unit weight [7]. In the industry, AFS 35 (390μm), 40 (340 μm), 45 (300 μm), 50 (280 μm), 55 (240 μm), 60 (220 μm), 65 (210 μm), 70 (195 μm), 80 (170 μm), 90 (150 μm), etc. different AFS grain fineness numbers are used [6].

The primary purpose of fillers is to restrict the movement of the polymer chain, thereby increasing hardness, abrasion resistance, stiffness, and strength but reducing ductility. [1, 8-11]. They can also be used to reduce the cost of the product, control the shrinkage of the product, or increase the formatting of the material [9, 10]. Several analyses have been carried out to study the effects of particulates on the mechanical properties of polymeric composites;

Haddad and Kobaisi [12] determined the pressure strength of the polymer concrete produced by using coarse-grained basalt aggregate, sand, and fly ash with UP resin as 190 MPa. Ateş and Aztekin [13] conducted a study on the densities and mechanical properties of quartz sand filler reinforced (5% -45%) and UP matrix composites and obtained the highest compressive strength value as 131.009 MPa in 10% quartz sand volume ratio. Mahdi et al. [14], studied PET that consisting styrene and obtained from waste bottles using methyl ethyl ketone peroxide (MEKP) as a free radical initiator and cobalt naphthenate (CoNp) as the catalyst, then mixed with inorganic aggregate (10% w/w aggregate/resin). The maximum compressive strength was determined as 42.2 MPa that is higher (28.5 MPa) than the compressive strength of the neat polymer composites. Ateş and Barnes [15], prepared polymer concrete composite specimens by using polyester and quartz as binder and filler material, in different aggregate diagrams and binder ratio. The highest compression strength was obtained at 95.8 MPa. Ateş [16], examined the change of the compressive strength properties of the polyester and epoxy resin-based composite material having quartz sand as a filler which has different grain distributions and produced by using binder material at different ratios. The highest compressive strength value was obtained as 62.8 MPa in a mixture of 18% resin + 82% quartz filler. Akıncı [17], in his study, reported that the content of basalt filler added to the raw resin affected the structural integrity and mechanical properties of the composite. Moloney et al. [18], studied the effects of several parameters on the mechanical properties of particulate composites. The results showed that the tensile strength, tensile modulus, flexural strength, flexural modulus, compressive yield strength, and fracture toughness improved with an increasing volume fraction of silica particulates.

The main objectives of this study are to investigate the usage of additives at different initiator ratios and how particle size distribution and type of filler influence the resin consumption and compressive strength of polyester matrix composites.

This study was supported by TUBITAK (The Scientific and Technological Research Council of Turkey), University-Industry Cooperation Project (Project Number: 5140058) in Turkey.

2. MATERIALS and METHODS

2.1. Matrix Materials

Unsaturated orthophthalic polyester resin (Polipol 3562-SR) was used as a matrix structure. The initiator (methyl ethyl ketone peroxide; MEKP; Akperox ER 59) at the ratio of 1.0%, 1.5%, and 2.0% and the accelerator (Cobalt Octoate; Akkobalt RC88) at the ratio of 1.0% by weight were used to start the polymerization. Resins and additives used in the study are given in Figure 1 and the mechanical properties of raw polyester resin types are given in Table 1. Some physical

properties of polyester resin mixtures used in different initiator ratios are given in Table 2.

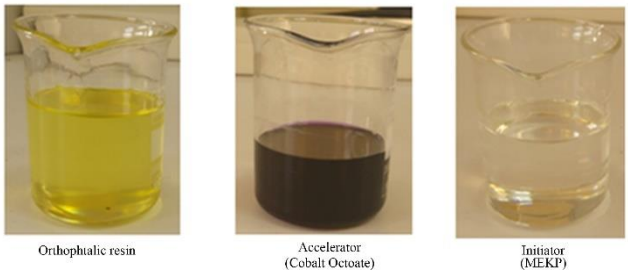

Figure 1 Visual of raw resin, initiator and accelerator

Table 1 Mechanical properties of orthophtalic resin

Property	**Orthophtalic Resin**
Tensile modülüs (MPa)	3550
Tensile strength (MPa)	74
Flexural strength (MPa)	125
Flexural modülüs (MPa)	3800
Elongation at break (tensile) (%)	3.15

Table 2 Some physical properties of polyester resin mixtures used in different initiator ratios

Initiator ratio (%)	Orthophtalic Resin		
	Gelling time (min)	Gelling temperature (0C)	Peak exotherm temperature (0C)
1.0	15	28.5	189.8
1.5	13	29	177
2.0	10	32.8	182.6

2.2. Filling Materials

Three types of fillers were used in the study: silica sand, basalt sand, and quartz sand, in the range of 0-1000 μm, with different grain distributions. A picture of the filling materials used is shown in Figure 2. The chemical and physical analyses of the filling materials used are given in Table 3 and Table 4 respectively.

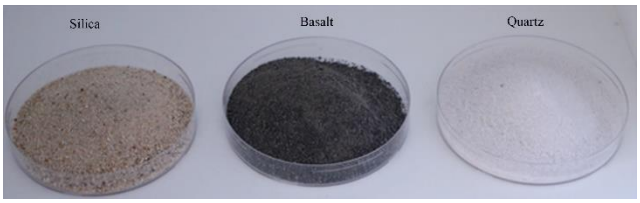

Figure 2 Filling materials

Table 3 Chemical compositions of filling materials

Chemical Composition	Filling materials (%)		
	Quartz Sand	Silica Sand	Basalt Sand
SiO2	99.18	98.94	61.21
Al2O3	0	0.08	13.61
Fe2O3	0.02	0.1	5.72
MgO	0	0	3.90
CaO	0.16	0.12	6.20
Na2O	0	0	2.63
K2O	0.03	0.05	2.83
TiO2	0.04	0.12	0.76
MnO	-	-	0.13
SO2	0.02	0.3	-
P2O5	0.01	0.01	-
Cr2O3	0.004	0.053	-
Mn2O3	0.0017	0.0035	-

Table 4 Physical properties of filling materials

Physical parameters	Filling materials		
	Quartz Sand	Silica Sand	Basalt Sand
Moisture content (%)	0.002	0.6	0.5
Relative density (g/cm^3)	2.55	2.74	2.57
Loose unit weight (g/cm^3)	1.616	1.537	1.541
Compact unit weight (g/cm^3)	1.791	1.723	1.764
Water absorption ratio (%)	2.03	2.73	2.29
Specific surface area (m^2/kg)	12.07	11.3	10.42
The average grain size (μ)	237	245	254

2.3. Mixture Design of Filled Composites

The polymerization reaction was carried out at room temperature. Firstly, the orthophtalic resin, methyl ethyl ketone peroxide, and cobalt octoate were added to the beher, and immediately after, the former mixture stirred 2 min at 400 rpm in the magnetic stirrer. Before the curing, the former prepared solution was transferred to ultrasonic homogenizer (Bandelin, RK 100 H, Germany) and sonicated for 1 min at 35 kHz to improve the homogeneity. Then the obtained mixture was transferred and the fillers that prepared according

to predetermined particle distributions were added and mixed at 1000 rpm for 1 min in the ultraturrex disperser (Heidolph, Hei TORQUE 100, Germany) before the resin reached the gelling time. Finally, the obtained suspension poured for molding to a steel cylinder (35mm * 70mm) with controlled leveling and kept at room temperature for 1 h and afterward was transferred to an oven (Utest, UTD 1035, Turkey) in order to keep at 80 °C for 24h. Pre-mold, release agent (Poliya, Polivaks SV-6, Turkey) were applied to the molds to remove easily after curing. The preparation process of filled composites is shown in Figure 3.

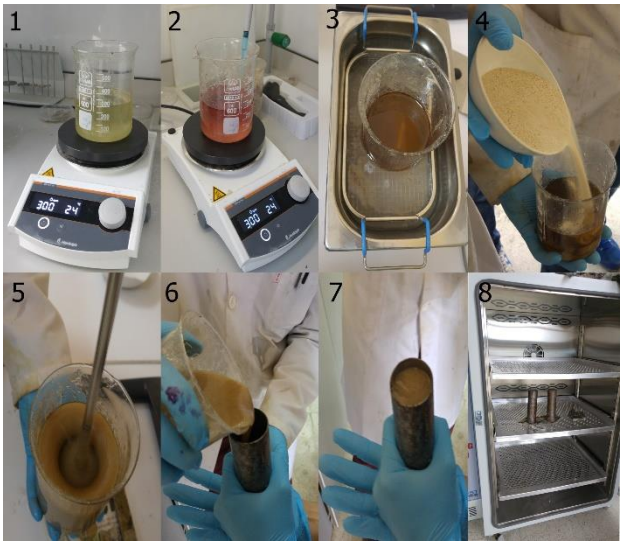

Figure 3 The preparation process of filled composites

Filling grain distributions have been prepared by referencing the Fuller equation. The reference Fuller equation is given Eq. (1) [5].

$$P = 100 \text{ x } (\frac{d}{D})^n \quad (1)$$

In the referenced Fuller equation, n coefficient value was chosen as 1.0 and after determining the amount of material required to be taken between each sieve, these materials were mixed to form a blend and made ready for mixing with resins.

F 1.0: The grain distribution generated by taking n=1.0 in the Fuller equation

P is the total percent of particles passing through (or finer than) sieve, %

D is the maximum size of aggregate, mm

d is the diameter of the current sieve (1000µ), mm

n is the exponent of the equation

Also, fillings used in the study were prepared in the grain size distribution of the AFS 40-45. AFS 40-45 and Fuller 1.0 grain distribution curves used in the production of filled samples are given in Figure 4.

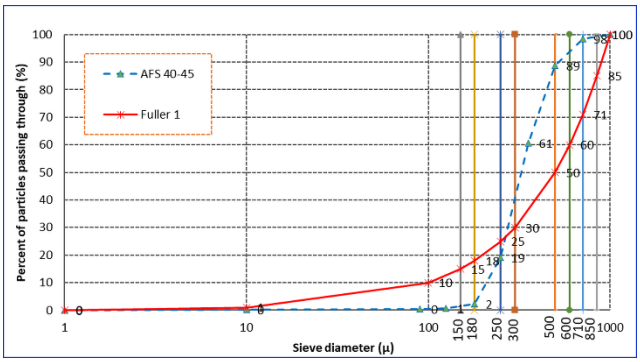

Figure 4 AFS 40-45 and Fuller 1.0 grain distribution curves

2.4. Compressive Strength Test

The compressive strength was performed according to the ASTM C 579-01 [19] standard. The loading speed is 41 MPa/min. For the pressure test, 3 samples were produced from each mixture. A visual representation of the cylindrical specimens extracted from the mold and the cutting operations of these samples is given in Figure 5, a visual representation of the cut cylinder samples for pressure testing is given in Figure 6 and a visual representation of the pressure test is given in Figure 7.

Figure 5 Cylinder samples and cutting process

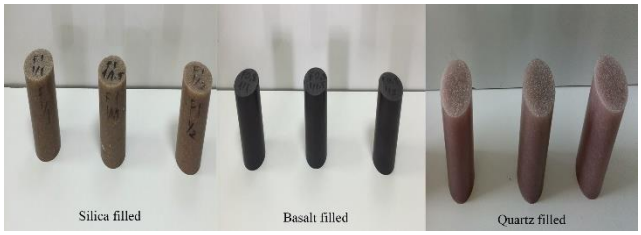

Figure 6 The pressure testing samples

Figure 7 The pressure test of the filled composites

2.5. Resin Consumption

The weights of the cut samples were weighed to determine the resin consumption quantities of the filled resin mixtures. After the samples were placed in the ash furnace, the temperature of the ash furnace was set to approximately 650 ^{0}C in order to completely blow out the polyester and the samples were kept for 2 hours at this temperature. After the samples removed from the ash furnace were kept until they reached the ambient temperature, their weights were weighed, and their resin consumption was determined. A visual representation of cut samples to determine the resin consumption is shown in Figure 8 and a visual representation of resin consumption testing of filled composites is shown in Figure 9.

Figure 8 The resin consumption samples

Figure 9 Resin consumption testing of filled composites

2.6. SEM Analysis

For SEM analysis, cross-section images were taken of the samples at 20 kV acceleration voltage (FEI, Quanta 250, Netherland). The specimens were mounted with tweezers onto a substrate with carbon tape and coated with a thin layer of gold/palladium mixture.

3. RESULTS and DISCUSSION

3.1. Compressive Strength Test Results and Evaluation

The combined representation of the average compressive strength of the filled resin mixtures in different grain distributions due to the change in the initiator ratio is given in Table 5.

Table 5 The average compressive strength values of the filled resin mixtures

Initiator ratio (%)	Compressive strength values (MPa)					
	AFS 40-45			FULLER 1.0		
	Silica sand	Basalt sand	Quartz sand	Silica sand	Basalt sand	Quartz sand
1.0	116	130	130	128	129	117
1.5	118	124	112	122	124	121
2.0	124	116	115	112	121	122

Changes in the average compressive strength of silica, basalt, and quartz-filled resin mixtures with a grain distribution of AFS40-45 and F1.0 due to the change in the initiator ratio are given in Figure 10, Figure 11, Figure 12, Figure 13 and Figure 14 respectively. The graph showing the compressive strength in the first three rows among all filled composites is shown in Figure 15.

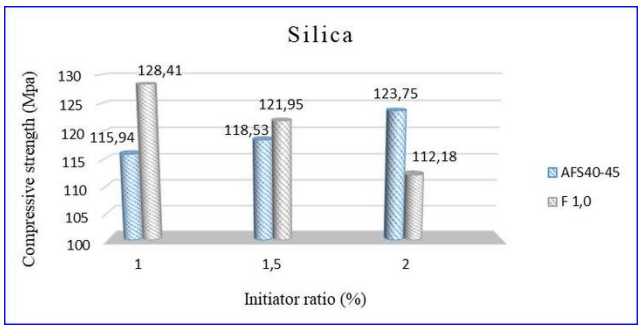

Figure 10 Compressive strengths in silica filled composites

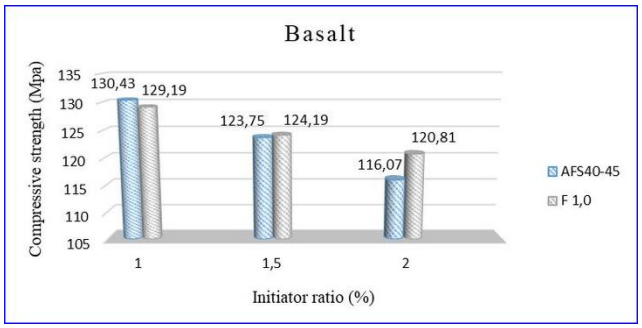

Figure 11 Compressive strengths in basalt filled composites

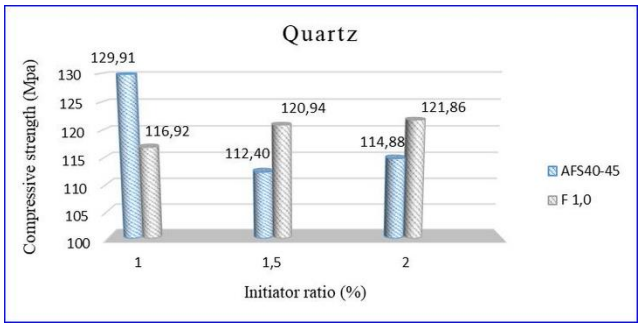

Figure 12 Compressive strengths in quartz filled composites

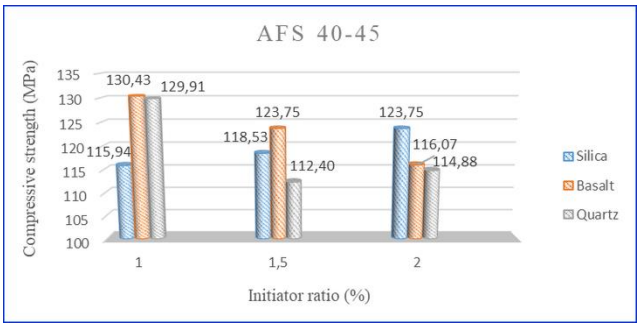

Figure 13 Compressive strengths of AFS 40-45 grain distributed fillers

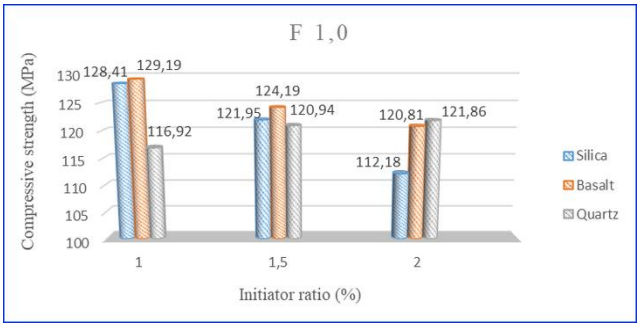

Figure 14 Compressive strengths of F 1,0 grain distributed fillers

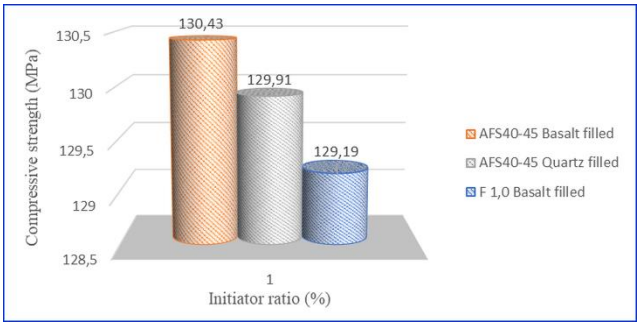

Figure 15 Compressive strengths in the first three rows

Pressure tests on silica-filled resin mixtures with AFS 40-45 grain distribution showed that their compressive strength increased as the initiator rate increased. The lowest compressive strength value was obtained at a 1.0% initiator rate and this value was determined as 115.94 MPa. The compressive strength increased to 118.37 MPa in a 1.5% initiator ratio and reached the maximum compressive strength value of 123.75 MPa in a 2.0% initiator ratio. The percentage of increases was 2.09% and 6.73% respectively. However, it is thought that by increasing the rate of initiator, the strength will decrease as the heat value of the mixture will increase.

The highest compressive strength value of silica-filled resin mixtures in F 1.0 grain distributed was determined as 128.41 MPa at the rate of 1.0% initiator. However, by increasing the rate of initiator, compressive strength also decreased. As a result, the highest compressive strength of all silica-filled resin mixtures was obtained in the F 1.0 grain distribution and the initiator ratio of 1.0%, and this strength value was obtained as 10.75% higher than the silica-filled composite in the AFS 40-45 grain distribution. When these results were evaluated together, AFS 40-45 grain distribution has uniform grain distribution, while F 1.0 grain distribution has a better-rated grain distribution, so it was observed that strength values increased only with the improvement made in grain distribution.

In basalt-filled resin mixtures, the highest compressive strength values for each different grain class were obtained at the initiator ratio of 1.0%. As the initiator ratio increased, the compressive strength values of all grain distributed mixtures decreased. The highest compressive strength value was determined as 130.43 MPa in the "AFS40-45" grain distributed mixture. The second highest strength was determined as 129.19 MPa in the F 1.0 grain distributed mixture.

The highest compressive strength value in quartz filled resin mixtures was obtained as 129.91 MPa in AFS 40-45 grain distribution and 1.0% initiator ratio. As the initiator ratio increased, the compressive strength values of AFS 40-45 grain distributed mixtures decreased, while F 1.0 grain distributed mixtures increased.

In AFS 40-45 grain distributed filled resin mixtures, the highest compressive strength was obtained in basalt and quartz fillings and a 1.0% initiator ratio. The strength value of basalt-filled composites with a 1.0 % initiator ratio was determined as 12.49% higher than silica-filled composites, while the strength value of quartz-filled composites was determined as 12.05% higher than silica-filled composites. When these results were evaluated together, it was observed that in composites with grain distribution of AFS 40-45 the filler type had a significant effect on compressive strength, and higher strengths were obtained when basalt and quartz fillings were used.

In F 1.0 grain distributed filled resin mixtures, the highest compressive strength was obtained in basalt and silica fillings and a 1.0% initiator ratio. In quartz-filled composites with the same initiator ratio, a lower strength value was obtained. The strength value of basalt and silica-filled composites with a 1% initiator ratio was determined as 10.26% and 9.4% higher than quartz-filled composites with the same initiator ratio, respectively. In addition, it was observed that the strength values of silica and basalt filled composites decreased with increasing initiator ratio, while quartz filled composites increased. When these results were evaluated together, it was observed that in composites with grain distribution of F 1.0, the filler type had a significant effect on compressive strength, and higher strengths were obtained when basalt and silica fillings were used.

- When the results of filled composites are evaluated;

Among all filled composites, the highest 3 compressive strengths were obtained as a 1.0% initiator ratio.

The highest compressive strength value was determined as 130.43 MPa in the AFS40-45 grain class basalt filled resin mixture. This strength value was found to be approximately 1.0% higher than basalt filled composites with F 1.0 grain distribution. The second highest strength value was determined as 129.91 MPa in AFS40-45 grain distributed quartz filled resin mixture. This strength value was determined as 0.55% higher than basalt filled composites with F 1.0 grain distributed.

The compressive strength value of polymer concrete, determined by Haddad and Kobaisi [12] as 190 MPa, was 45.67% higher than the maximum strength value determined in this study (130.43 MPa). When these data are evaluated, the strength values of the fillings in the composite increase as the grain diameter grows larger.

The highest compressive strength values determined in the scope of the study and the strength values determined by Ateş and Aztekin [13] on quartz-filled composites were close together.

Ateş [16] determined that the change in resin and filling ratios and grain distribution curves affected the compressive strength of polymer concrete. These results were found to support the results obtained in the study.

Akıncı [17], in his study, reported that the content of basalt filler added to the raw resin affected the structural integrity and mechanical properties of the composite.

3.2. Resin Consumption Amounts of Filled Resin Mixtures

Resin consumption amounts of filled resin mixtures in different grain distributions are given in Table 6.

Table 6 Resin consumption amounts of filled resin mixtures in different grain distributions

Initiator ratio (%)	Average resin consumption amounts (%)					
	Silica sand		Basalt sand		Quartz sand	
	AFS 40-45	F 1.0	AFS 40-45	F 1.0	AFS 40-45	F 1.0
1.0	52	49	53	51	59	53
1.5	51	50	51	51	55	55
2.0	54	52	52	52	55	55

Among all filled resin mixtures, the least resin consuming mixtures were obtained at the grain distribution of F 1.0 and the initiator rate of 1.0%. In these mixtures, the minimum resin consumption was obtained in silica-filled mixtures and this ratio was determined as 49%. In basalt filled mixtures, this ratio was 51% and in quartz filled mixtures it was 53%. Among all filled resin mixtures, the most resin consuming mixtures were obtained in composites with a grain distribution of AFS 40-45. In silica-filled composites, the amount of resin consumption obtained in F 1.0 grain distribution and 1.0% initiator ratio was 6.12% less than the amount of resin consumption in AFS 40-45 grain distribution with the same initiator ratio. In the same grain distribution comparison, 3.92% less resin consumption was achieved in basalt-filled composites, while 11.32% less resin consumption was achieved in quartz-filled composites. The reason for this is considered to be that composites in the grain class AFS 40-45 have uniform grain distribution, whereas composites in the grain class F1.0 have a better-graded distribution. It is believed that good grading of the particles allows the composite to have a less porous structure, thereby causing the composite to consume less resin.

3.3. SEM Images and Morphological Analysis of Filled Resin Mixtures

SEM images of filled composites with the highest 3 compressive strengths are shown in Figure 16, Figure 17, and Figure 18 respectively.

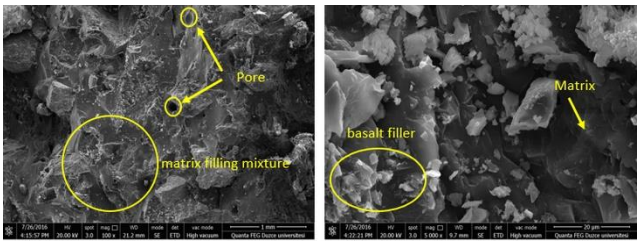

Figure 16 SEM image of AFS 40-45 distributed basalt filled composite

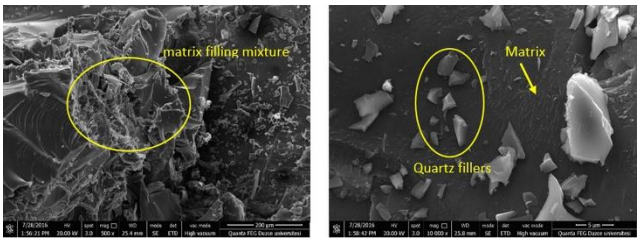

Figure 17 SEM image of AFS 40-45 distributed quartz filled composite

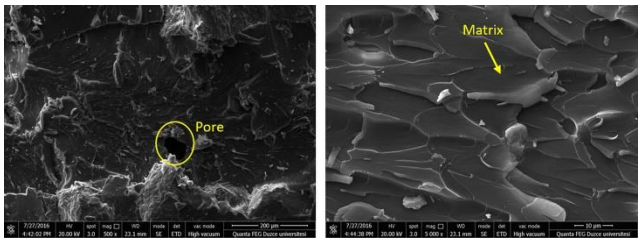

Figure 18 SEM image of F 1.0 distributed basalt filled composite

When the SEM images of the AFS40-45 and F 1.0 grain distributed basalt filled composites were examined, it was seen that the basalt fillings were homogeneously distributed, the matrix structure completely wetted the filling material and the adherence of the resin and fillings was very good. It is thought that the failure is not due to the loss of adherence because of the adhesion between the filling material and the matrix interface is very good.

When the SEM images of quartz-filled composites in the AFS 40-45 grain distribution were examined, it was observed that the quartz fillers in the polyester matrix were largely uniformly distributed within the matrix structure and that the matrix structure completely wetted the filling material.

4. CONCLUSION

Among all filled composites, the highest 3 compressive strengths were obtained as a 1.0% initiator ratio.

Among all filled resin mixtures, the three highest compressive strength was determined as 130.43 MPa in basalt filled resin mixture in AFS 40-45 grain distribution, 129.91 MPa in quartz filled resin mixture in AFS 40-45 grain distribution and 129.19 MPa in basalt filled resin mixture in F 1.0 grain distribution.

Among all filled resin mixtures, the least resin consuming mixtures were obtained at the grain distribution of F 1.0 and the initiator rate of 1.0%. Composites produced in F 1.0 grain distribution and 1.0% initiator ratio consumed less resin than composites in AFS 40-45 grain distribution. In silica-filled composites, the amount of resin consumption obtained in F 1.0 grain distribution and 1.0% initiator ratio was 6.12% less than the amount of resin consumption in AFS 40-45 grain distribution with the same initiator ratio. In the same grain distribution comparison, 3.92% less resin consumption was achieved in basalt-filled composites, while 11.32% less resin consumption was achieved in quartz-filled composites. The reason for this is considered to be that composites in the grain class AFS 40-45 have uniform grain distribution, whereas composites in the grain class F1.0 have a better-graded distribution. It is believed that good grading of the particles allows the composite to have a less porous structure, thereby causing the composite to consume less resin.

As a result of the study, it was concluded that the filler type and grain distribution used affected the mechanical properties and resin consumption of the composites.

Acknowledgments

This study is supported by the Scientific and Technological Research Council of Turkey (TUBITAK). Project Number: 5140058

Research and Publication Ethics

This paper has been prepared within the scope of international research and publication ethics.

Ethics Committee Approval

This paper does not require any ethics committee permission or special permission.

Conflict of Interests

The author declared no potential conflicts of interest concerning the research, authorship, and/or publication of this paper.

REFERENCES

[1] S. Ahmed and F.R. Jones, “A review of particulate reinforcement theories for polymer composites,” Journal of Materials

Science, vol. 25, no. 12, pp. 4933-4942, 1990.

[2] S. Kang, S. I. Hong, C. R. Choe, M. Park, S. Rim, and J. Kim, "Preparation and characterization of epoxy composites filled with functionalized nano-silica particles obtained via sol-gel process," Polymer, vol. 42, no. 3, pp. 879–887, 2001.

[3] S.S. Ray and M. Okamoto, "Polymer/layered silicate nanocomposites: a review from preparation to processing," Progress in Polymer Science, vol. 28, no. 11, pp.1539–1641, 2003.

[4] P. Singh, A. Kaushik, and Kirandeep, "Mechanical and transport properties of colloidal silica-unsaturated polyester composites," Journal of Reinforced Plastics and Composites, vol. 25, no. 2, pp. 119-140, 2006.

[5] W.B. Fuller and S.E. Thompson, "The laws of proportioning concrete," Trans. Amer. Soc. Civ. Engrs. Bd., vol. 59, no.67, 1907.

[6] A.Turkeli, http://mimoza.marmara.edu.tr/~altan.turkeli/files/cpt-2-sand_sand.pdf, (accessed 24/06/2019).

[7] MOLDING SAND, particle sizing for the foundry industry, https://www.retsch-technology.com/applications/technical-basics/molding-sand/(accessed24.12.2019).

[8] J. Jacobs and T. Kilduff, "Engineering materials technology: structures, processing, properties, and selection," 2nd ed., Prentice-Hall, pp. 263-299, 1994.

[9] L. Horath, "Fundamentals of materials science for technologists: properties, testing and laboratory exercises," 2nd ed., Prentice-Hall, pp. 100-133, 2001.

[10] S.H. Mansour and S.L. Abd-El-Messiah, "Electrical and mechanical properties of some polymeric composites," Journal of Applied Polymer Science, vol. 83, no. 6, pp. 1167–1180, 2002.

[11] B.D. Agarwal, L.T. Broutman, and K. Chandrashekhara, "Analysis and performance of fibre composites," 3rd ed., John Wiley, New York, 2006.

[12] H. Haddad and M. Al Kobaisi, "Influence of moisture content on the thermal and mechanical properties and curing behavior of polymeric matrix and polymer concrete composite," Materials & Design, vol. 49, pp. 850-856, 2013.

[13] E. Ateş, and K. Aztekin, "Parçacık ve fiber takviyeli polimer kompozilerin yoğunluk ve basma dayanımı özellikleri," Journal of the Faculty of Engineering & Architecture of Gazi University, vol. 26, no. 2, pp. 479–486, 2011.

[14] F. Mahdi, H. Abbas, and A.A. Khan, "Strength characteristics of polymer mortar and concrete using different compositions of resins derived from post-consumer PET bottles," Construction and Building Materials, vol. 24, no. 1, pp. 25-36, 2010.

[15] E. Ateş and S. Barnes, "The effect of elevated temperature curing treatment on the compression strength of composites with polyester resin matrix and quartz filler," Materials & Design, vol. 34, pp. 435-443, 2012.

[16] E. Ateş, "Optimization of compression strength by granulometry and change of binder rates in epoxy and polyester resin concrete," Journal of Reinforced Plastics and Composites, vol. 28, no. 2, pp. 235-246, 2008.

[17] A. Akıncı, "Mechanical and morphological properties of basalt filled polymer matrix composites," Archives of Materials Science and Engineering, vol. 35, no. 1, pp. 29-32, 2009.

[18] A.C. Moloney, H.H. Kausch, T. Kaiser, and H.R. Beer, "Parameters determining the strength and toughness of particulate filled epoxide resins," Journal of Materials Science, vol. 22, no. 2, pp. 381-393, 1987.

[19] ASTM (2012) C579 – 01: Standard test methods for compressive strength of chemical-resistant mortars, grouts, monolithic surfacings, and polymer concretes. ASTM International, USA.

SAKARYA ÜNİVERSİTESİ
FEN BİLİMLERİ ENSTİTÜSÜ DERGİSİ

Sakarya University Journal of Science
SAUJS

e-ISSN: 2147-835X | Founded: 1997 | Period: Bimonthly | Publisher: Sakarya University
http://www.saujs.sakarya.edu.tr/en/

Title: Suggestions for Designing Test Specimens and Testing Procedures to Impregnate Wood Material by Pre-vacuumed Immersion Method Realized Using a Special Device

Authors: İlker USTA

Recieved: 2020-06-08 16:26:09

Accepted: 2021-07-07 12:09:14

Article Type: Research Article

Volume: 25
Issue: 4
Month: August
Year: 2021
Pages: 1020-1030

How to cite
İlker USTA; (2021), Suggestions for Designing Test Specimens and Testing Procedures to Impregnate Wood Material by Pre-vacuumed Immersion Method Realized Using a Special Device. Sakarya University Journal of Science, 25(4), 1020-1030,
DOI: https://doi.org/10.16984/saufenbilder.749447
Access link
http://www.saujs.sakarya.edu.tr/en/pub/issue/64755/749447

Sakarya University Journal of Science 25(4), 1020-1030, 2021

Suggestions for Designing Test Specimens and Testing Procedures to Impregnate Wood Material by Pre-vacuumed Immersion Method Realized Using a Special Device

İlker USTA*[1]

Abstract

This study, which promised remarkable contributions for designing of experimental samples and trial device to treat wood by pre-vacuumed immersion method, was conducted to test the impregnability of wood material according to the pre-vacuumed immersion process and to reveal the usability of plug (cylindrical) samples in impregnation experiments in addition to the cuboid (rectangular prism) samples. In this perspective, samples to be subjected to immersion test were initially dried to an average moisture content of 12% and than prepared for the flow pathways to determine the possible preservative uptake as the percentage of void volume filled and net dry salt retention in radial and longitudinal flow pathways, and in triplex [i.e. three flow pathways including tangential flow] and than impregnated using with 3% concentration of boron compound by normal and pre-vacuumed immersion method based on the immersion of 120 minutes, and pre-vacuum process of 30 minutes at –0.84 bar (640 mmHg). According to the experimental evidences that have been provided, it was observed that the preparation techniques for cuboids and plugs were suitable with each other in terms of the preservative uptake in either flow pathway, while the preparation process and the period of the data collection were shorter in plugs than that for cuboids. And samples impregnated by pre-vacuumed immersion method were determined to have a slightly higher preservative uptake than those impregnated with normal immersion method. At this point, it was also observed that in both experimental arrangements, the level of preservative uptake was minimal in radial samples compared to longitudinal samples. Therefore, based on the outcomes of this study, some remarks and recommendations for future work can be deduced on the use of plugs and cuboids, and also pre-vacuumed immersion process in the context of permeability examinations of any wood material.

Keywords: Wood, impregnation, immersion method, test device, cuboid and plug samples

1. INTRODUCTION

This study has been carried out with an innovative perspective in terms of its depth, and it contains original constructions aiming to test the impregnability of wood material with a new methodological arrangement within the scope of the immersion method. Although impregnation of wood material is based on experience gained through trial and error learning, it is in fact a very

* Corresponding author: iusta@hacettepe.edu.tr
[1] Hacettepe University, Vocational Technology School, Ankara, Turkey.
ORCID: https://orcid.org/0000-0002-0470-5839

special subject developed based on the numerous findings obtained through long-term scientific research involving extensive tests. Therefore, this experimental study, which includes a methodological innovation, is expected to make a significant contribution to the field of wood science and technology, primarily in the wood protection area.

As mentioned by Usta [1], wood, the most valuable and functional material on earth derived from trees grown with the practices of sustainable forestry, has been widely used for various purposes in everyday life since the beginning of human history. Wood, however, is a natural material that needs to be protected against biotic and abiotic pests exposed by the conditions beyond its natural endurance limit. In this respect, the protection of wood, which is a naive material with its fibrous and porous structure, against these pests is at the focus of the impregnation applications realized by the many different methods with the presence of various preservatives. However, amenability to preservative treatment of wood is a very real problem with some of the refractory tree species in terms of the flow rate of liquid which can be synonymously described with permeability. Therefore, the subject of impregnation of wood with the theme of permeability has been extensively investigated in many studies in wood science and technology literature.

As we all know that submerging wood samples in a liquid until a set of time and then comparing with either the weight gained due to fluid uptake or in relation to an absolute quantity of liquid within volume, is the most simple and reliable technique to determine permeability. At this point, the most convenient way of measurement for permeability which can be synonymously described with flow rate of liquid [2], the most effective method of sample preparation for the impregnation test as either cubic or cuboid (i.e. longer in the axial direction) [3, 4], the most suitable practice for sealing all but one of the surfaces of the experimental sample to restrict penetration to one direction either parallel to grain (i.e. longitudinally) or perpendicular to grain (i.e. either tangentially or radially) [5], and the most usable manner to prepare test sample from bark to pith using a borer to give a cylindrical core [6] have been explained and exemplified in detail. In addition, various wood protection methods and many preservatives have been developed in order to protect wood material and to extend its service life against any damages and pests that destroy wood. Accordingly, the immersion method, one of the oldest known methods of wood preservation, is one of the methods developed for the impregnation of wood throughout human history, and it is widely used today with several different operational arrangements to effectively protect wood [7]. In this context, as we can easily see the protective fluids manufactured in a wide range of products for use in the operational arrangements of the immersion method designed in different constructions and point of views, this study was carried out as a new methodological approach to impregnation of wood by pre-vacuumed immersion method using cuboid and plug samples.

This study was therefore conducted following the pioneering comparative works of Usta on the impregnation of wood material by pre-vacuumed method [7] and special preparation of the experimental samples as cuboid and plug samples [8]. Thus, in this study, the impregnation of wood material based on the trial species Bornmullerian fir (*Abies bornmulleriana* Mattf.) by pre-vacuumed immersion method and the special preparation of the experimental samples as the plugs and cuboids were demonstrated in terms of both the preparative period of time and the amenability to fluid uptake. In this context, this experimental study was carried out on the basis of the studies conducted by Usta [7, 8]. Also, the data assembly regarding the experimental processing was made according to the exemplification by Usta and Hale [9] and Usta [10] for the determination of the physical properties of wood material including kiln drying and preservative treatment.

2. MATERIALS AND METHODS

Within the scope of the study, the issues that form the basis of the realization of the research were explained under the following headings: wood

species, impregnation solution, preparation of experimental samples, wood preservation, data assembly and experimental processing.

2.1. Wood Species

The wooden test samples used in this study were selected from Bornmullerian fir (*Abies bornmulleriana* Mattf.), i.e. also known as Uludağ Göknarı in Turkish [11], which is a major softwood species indigenous to Turkey [12]. This tree species was particularly selected for this study, because it is being representative of the most important commercial plantation fir species within the country.

At this point, according to data related to Turkey's forest assets described in 2015, in the forests in Turkey where a spreading area up to 2.62% of fir taxa [13], Bornmullerian fir has the most extensive distribution, and spreads almost as much as the sum of the spreading areas of all other fir taxa in the forests [14].

Bornmullerian fir is a different type of tree species with its unique nature and this situation is reflected in wood material derived from it. For instance, wood material that is obtained from Bornmullerian fir is used in many fields, especially in joinery, and has the potential to provide long-term service when used after impregnation. However, because of its difficult impregnability due to its anatomical structure, Bormullerian fir is tried to be protected by impregnation with various techniques and preservatives, at least with a required amount of preservative [7].

2.2. Impregnation Solution

In our study, although there are many different types of preservatives for wood impregnation in terms of immersion method, Wolmanit-CB was used particularly. In this regard, Wolmanit-CB, which is a CCB based preservative prepared from copper-chromium-boron mixture from the water-soluble salts in the form of mixture of potassium dichromate ($K_2Cr_2O_7$) and copper sulfate ($CuSO_4$ $5H_2O$) and boric acid (H_3BO_3) as a dry mixture in certain proportions [15], is one of the most effective preservatives for protecting wood from deterioration caused by fungi and insects, and also from degradation by fire [16].

Therefore, since it is a widely used preservative in the framework of wood protection applications in the priority of immersion method, Wolmanit-CB (containing approximately 48% $K_2Cr_2O_7$, 28% $CuSO_4$ $5H_2O$, and 24% H_3BO_3) was preferred as an experimental impregnation solution and used at a concentration of 3%.

2.3. Preparation of Experimental Samples

As it can be seen in Figure 1, for preparation of the specimens, a disk of 35 cm in diameter and 40 cm in length was cut into halves from the pith and flattened to form an internal edge as a large part. Then the experimental samples were produced as the plugs and the cuboids from the sapwood zone of Bornmullerian fir (*Abies bornmulleriana* Mattf.) according to the descriptions of Usta [8]. In this respect, based on the operational workflow as shown in Figure 2, after the workbench-based preparation of the disc, which was the source of the experimental samples, the cuboid (rectangular prism) samples were produced as 30 mm in length, 20 mm in width, and 20 mm in thickness using band saw, plane, thickener, and circular saw machines respectively, whereas the plug (cylindrical) samples were prepared with a diameter of 15 mm and a length of 30 mm by core forming drill using band saw, top drill, and circular saw machines.

A schematic overview of the sample preparation for the experimental wood preservation by both cuboid and plug samples can be seen in Figure 1, where the anatomical sections of wood and the flow pathways were also illustrated. The test pieces, which were prepared in this way, were dried up to 12% of the air dry moisture content and were subjected to the surface preparation process according to the fluid permeability directions determined in the experimental design and prepared for impregnation by normal or pre-vacuumed immersion method. In this case, the diagrammatic representation for the process of coating and leaving open of the sample surfaces

for the examination of fluid uptake was demonstrated in Figure 3.

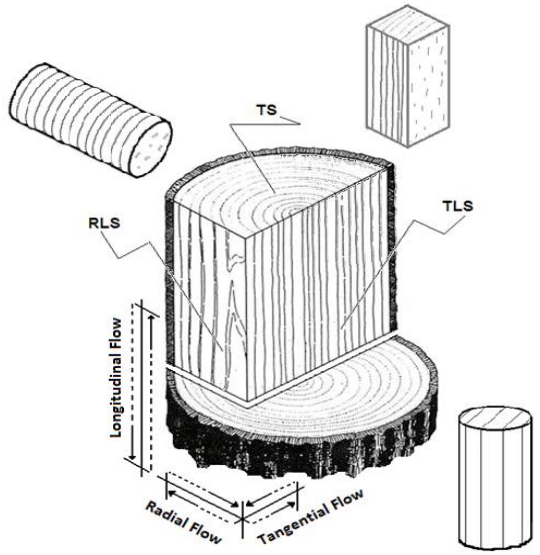

Figure 1 Schematic overview of the sample preparation for the experimental wood preservation by the cuboid and plug samples (i.e. the anatomical sections and flow pathways were also illustrated)

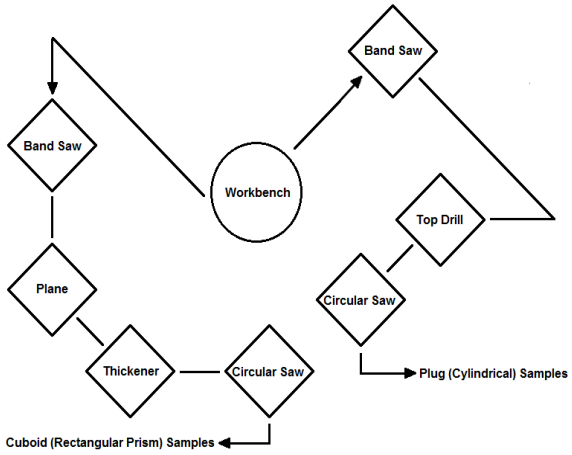

Figure 2 Operational workflow for collecting samples

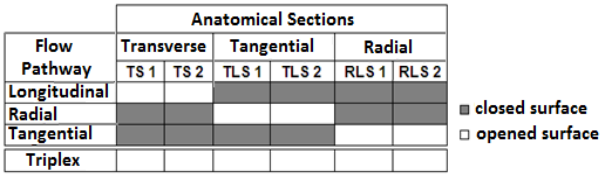

Figure 3 The diagrammatic representation for the process of coating and leaving open of the sample surfaces for the examination of fluid uptake [10]

In this study, as shown in Figure 3, longitudinal and radial flow pathways and also triplex were prepared to determine preservative uptake, apart from the tangential flow pathway. In this setup, which was based on the primary preparation of significant flow differences, the radial and longitudinal flow directions were specially prepared for the purpose of conducting a comparative fluid uptake both radially and longitudinally, while the triplex (three flow pathways including tangential flow) was prepared for control purposes. In this context, although tangential flow was not included in a review in this study, triplex flow was considered as a composite of flow in all three directions.

The experimental design, in terms of the criteria to provide information regarding exemplary subjects about the differences between the preparation and application methods, was shown in Table 1, in which the number of trial combinations was represented for either impregnation method to determine the possible fluid uptake in both radial and longitudinal flow pathways (i.e. while in this process, one surface of the related pathway can be closed or left opened if necessary, one surface was left opened for radial and longitudinal directions and no surfaces of the triplex samples were covered in our study). At this point, the sealant, which was adhering well to wood material and be strong and elastic enough coating to withstand wetting and lateral swelling, was used for sealing the surfaces of the experimental samples. Also, as the number of replicates in a comparison the experimental findings should be at least three to allow a minimal statistical analysis, the number of the test samples for determination the fluid uptake was made five in each examination.

Table 1 The experimental design based on the period of time (v: vacuum, i: immersion)

Method		**Flow Pathway**	**Period of Time (minutes)**	
Sample	**Immersion**		**v**	**i**
Cuboid	Normal	Radial	---	120
		Longitudinal	---	120
		Triplex	---	120
	Pre-Vacuumed	Radial	30	120
		Longitudinal	30	120
		Triplex	30	120
Plug	Normal	Radial	---	120
		Longitudinal	---	120
		Triplex	---	120
	Pre-Vacuumed	Radial	30	120
		Longitudinal	30	120
		Triplex	30	120

2.4. Wood Preservation

In this study, which was carried out in order to make a theoretical contribution by looking at wood preservation applications with a new perspective, it has been investigated how pre-vacuum application affects the absorption of the protective liquid in the longitudinal and radial directions (and also the combinations of all flow pathways including the tangential with the triplex samples) in wood protection performed by the immersion method using cuboid and plug samples with boron compound for the Bornmullerian fir (*Abies bornmulleriana* Mattf.) which is one of the refractory tree species. In this context, after the samples were dried to an air dry state of 12% moisture content, they were prepared by the surface preparation process according to the experimental design shown in Table 1 and were equally distributed according to the fluid flow direction group and were impregnated using boron compound with 3% concentration by normal and pre-vacuumed immersion method. Meanwhile, the immersion time was applied 120 minutes for all samples, and pre-vacuum process was performed for the test pieces subjected to pre-vacuumed immersion for 30 minutes at –0.84 bar (640 mmHg) as described by Usta [7].

The impregnation of the test samples was carried out in the test device shown in Figure 4. In terms of its importance in the realization of this study, this device, which has been designed by Usta [7] for the purpose of improving the protective liquid absorption by applying pre-vacuum in the immersion method and is an innovative idea in the field of wood protection, is an experimental design named as wood impregnation media combined with the holding container, is equipped with a mechanism that allows vacuuming to be carried out, as well as equipment that allows the intake of the protective liquid and to be discharged at the end of the process, and hence it provides pre-vacuum treatment in the immersion method. Accordingly, the control samples were placed in the holding container shown in Figure 4, and covered with lid, and then they were impregnated in normal immersion process for 120 minutes in the preservative liquid filled into the impregnation media, whereas in the pre-vacuumed immersion process, all of the trial samples were impregnated for a period of 120 minutes in the preservative liquid filled into the impregnation media after pre-vacuum application of –0.84 bar (640 mmHg) for 30 minutes.

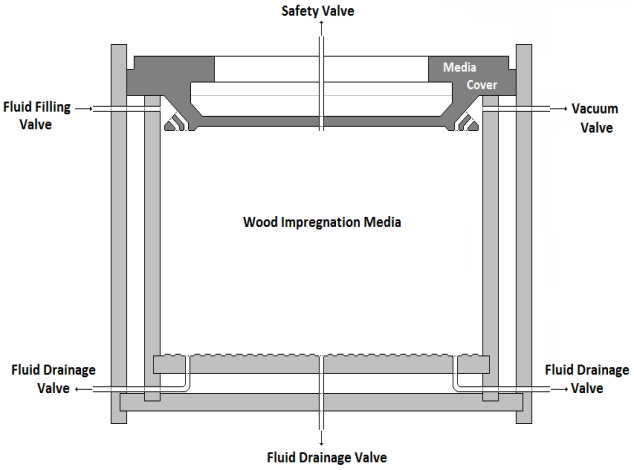

Figure 4 Illustration of experimental device designed for pre-vacuum process in wood preservation by immersion method [7]

2.5. Data Assembly and Experimental Processing

Since studies of the physical properties of wood are normally made on representative samples, in addition to the preparation of the samples to be impregnated, twelve cuboid samples with a length of 20 mm were also prepared and used to determine the following physical properties of wood material subjected to impregnation testing according to the instructions in Figure 5, which was designed by Usta and Hale [9], i.e. Do (g cm^{-3}) oven-dry wood density; Volumetric Shrinkage (%) based on the directions T tangential (the way to the growth ring cycle), R radial (the way to the radial tissue), L longitudinal (the way to the axial tissue); Volumetric Swelling depending on the volumetric shrinkage; FSP (%) fibre saturation point; MC (max) (%) maximum amount of moisture that wood material can reach. Each of these physical properties has different details in themselves [17, 18], it is important to emphasized, however, that numerous research data in relation with determination of properties under the scope of wood physics revealed that these properties were interrelated with one another directly or indirectly [19-23]. Possible effects of these

factors reflect as quantitative to accomplishment potential aimed at wood material impregnation and make causality remarkable [24]. In this respect, the determination of these properties before impregnation is an important issue since they all have reflections on the evaluation of wood preservation process. According to this, because the interaction between moisture content and wood density and porosity directly affects the level of preservative liquid [25], the physical properties that must be known prior to the impregnation process for the experimental wood samples are the amount of moisture available in wood material and the density value and porosity ratio at this moisture level [26-27]. On the other hand, as described by Usta [7], fibre saturation point (FSP) ranging from 25% to 35% at all tree species, which is a function of the oven-dry density and the percentage of volumetric swelling values of wood material, stands out as an important factor for the possible absorption of protective liquid. Accordingly, the high FSP value of the experimental wood material subjected to impregnation can be considered to contribute to the relative increase in the amount of preservative bonding to the cell wall as it will affect the inclusion of the protective fluid in the intercellular spaces in the cell wall in addition to the lumen. In addition or alternatively, some modifications to the present impregnation process, re-arrangement of the permeability of the protective liquid, and some special preparation of wood material may be required for this to be carried out effectively.

Inasmuch as the fact that the physical properties studied within wood physics have direct or indirect effects on wood protection, when it is described and interpreted consistently as to how they inter-direct each other, level of absorption of protective liquid by wood material becomes meaningful and may convert to an effective qualification in terms of all implementations [9, 28]. Because of this, after completion of the impregnation process according to normal or pre-vacuumed immersion method, DMC (wood density at respective moisture content as gram per cubic centimetre) and P (porosity, i.e. percentage of void volume of wood material in terms of the amount of moisture available) were determined primarily for the examination of the values of VVF (percentage of void volume filled by preservative solution depending on the percentage of available moisture content of wood material which was being questioning) and NDS (net dry salt absorbed after impregnation as kilogram per cubic metre) according to the directive in Figure 5, which was prepared in detail by Usta and Hale [9]. It is, in fact, that this experimental process, which appears to be complex in content, involves successive data compilations. In this perspective, in accordance with the data collection guide shown in Figure 5, the basic physical properties of the experimental material were determined by the oven drying process, while the test samples were impregnated with the immersion treatment process after they had reached a moisture content of 12 percent by the kiln drying process and after preparing the surfaces of the test samples in accordance with the flow directions.

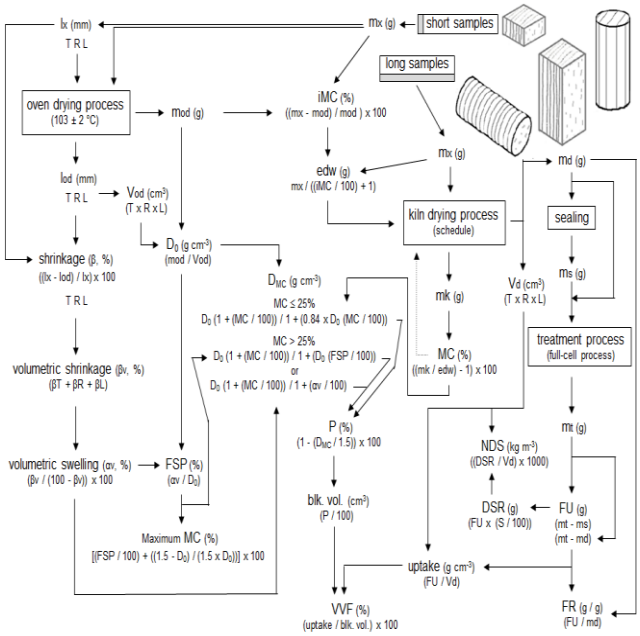

Figure 5 A schematic representation of data assembly and the experimental processing [9]

Citations of abbreviations and definitions used in this guide that were shown in Figure 5 sequentially on the base of the process can be defined as follows: mx (g), the green mass; lx (mm), length at green condition in either of the 3 directions (T, tangential; R, radial; L, longitudinal); lod (mm), length after oven drying; Vod (cm^3), block volume after oven drying; mod (g), oven-dried mass; D_0 (g cm^{-3}), oven-dry wood density; D_{MC} (g cm^{-3}), wood

density at respective moisture contents (MC ≤ 25%, equal to-and/or-below 25 percent moisture content; MC > 25%, above 25 percent moisture content); P (%), porosity; blk. vol. (cm^3), the amount of space available in a given block volume; FSP (%), fibre saturation point; iMC (%), initial moisture content; edw (g), estimated dry weight after kiln drying; mk (g), mass of the sample for control the current MC at regular intervals; MC (%), current moisture content at regular intervals during drying; Vd (cm^3), block volume after kiln drying; md (g), mass after kiln drying (before treatment); ms (g), sealed mass; mt (g), mass after treatment process; FU (g), fluid uptake (the gross preservative solution absorption), FR (g/g), fluid retention (preservative retention on a whole-block basis); NDS (kg m^{-3}), net dry salt absorbed after impregnation; DSR (g), dry salt retention on the base of its strength; S (%), strength of solution; uptake (g cm^{-3}), dry salt loadings based on weight per volume; VVF (%), void volume filled by preservative solution.

3. RESULTS AND DISCUSSIONS

The results were explained and evaluated under the following headings, according to the purpose of the study: collection of samples, physical properties of wood material, preservative uptake.

3.1. Collection of Samples

When we look at the comparison of the preparation processes of the different sample types in terms of cuboid (rectangular prism) samples and plug (cylindrical) samples, which is one of the main objectives of this study, it was seen that the sample preparation process was different due to the production of the existing sample types by using the necessary machines within different works and processes. In this perspective, regarding the preparation of samples required for the study, the cuboids (20 mm in width and 20 mm in thickness and 30 mm in length) were produced using band saw, planer, thickness and circular saw machines, while the plugs (15 mm in diameter and 30 mm in length) were produced using band saw, top drill and circular saw machines. Accordingly, while the band saw centered work was in the preparation of cuboid samples, the top drill machine came to the fore in the production of plug samples. In this context, it was seen that according to the period of time for collection of the experimental samples both the cuboid (rectangular prism) samples and the plug (cylindrical) samples, the preparation of the plugs were completed in almost half the time of the preparation of the cuboids.

3.2. Physical Properties of Wood Material

The physical properties of wood material experimented in this study were given in Table 2 as a basic indicator of the oven-dry wood density and fibre saturation point. Because the effects of these properties of wood on fluid uptake in the impregnation process cannot be ignored, the shrinkage and swelling, which closely concerns both of these properties, were also shown in this table, i.e. the shrinkage was shown for all three directions and volumetrically, while the swelling was only shown volumetrically.

Table 2 Physical properties of wood material (Bornmullerian fir) tested in this study

D_o	Shrinkage (%)				α_v (%)	FSP (%)
	T	R	L	β_v		
0.425	8.4	3.7	0.6	12.7	14.5	34.1

Abbreviations shown in Table 2 regarding the physical properties of experimental wood material can be defined as follows: D_o: oven-dry density (g cm^{-3}), T: tangential direction (the way to the growth ring cycle), R: radial direction (the way to the radial tissue), L: longitudinal direction (the way to the axial tissue), β_v: volometric shrinkage, α_v: volumetric swelling, FSP: fibre saturation point (%).

In addition to the data shown in Table 2, the other physical properties of Bornmullerian fir regarding the permeability were found to be as follows: the maximum amount of moisture that wood material can reach (MC max) was 202.6%; percentage of available moisture content of test samples (MC) was 12.0%; wood density (D_{MC}) of test samples at respective moisture content was 0.457 g cm^{-3}; porosity (void volume of wood material in terms of the amount of moisture available) (P) was 69.5%.

When Table 2 was evaluated, it was alson seen that the moisture of Bornmullerian fir at the fibre saturation point was high when compared to other coniferous species described by Tsoumis [29], and Bozkurt and Göker [30] as a reflection of the volumetric swelling value. In this context, as explained by Forest Products Laboratory [31], high fibre saturation point is considered to be an important indicator that contributes to the realization of high level of liquid absorption since it is a factor to increase the maximum moisture content. This findings were compatible with the results obtained by Usta [7] and it was seen that the experimental samples typically exemplified the trial tree species in terms of their physical characteristics.

3.3. Preservative Uptake

The preservative fluid absorption performance due to absolute void volume and flow directions of impregnated wood material according to normal and pre-vacuumed immersion method was shown in Table 3 as a fundamental indicator of wood density at respective moisture content and the porosity (void volume) of wood material in terms of the amount of moisture available in this moisture level. Table 3 herein illustrates the findings of the percentage of void volume filled by preservative or in other words, it shows preservative fluid absorption performance of experimental wood material due to void volume and flow directions of impregnated samples according to normal and pre-vacuumed immersion method. The results given in Table 3 for the impregnation of the test samples of the Bornmullerian fir with normal and pre-vacuumed immersion applications showed that the preparation of the experimental samples as either cuboid or plug has no effect on the fluid uptake in either flow direction (radially and longitudinally, and also in triplex that was standing for the combinations of all flow pathways including the tangential direction). Furthermore, it was found that the amount of preservative liquid absorption in the samples treated with the pre-vacuumed immersion process was a slightly higher in comparison with normal immersion process when all the test samples subjected to impregnation were compared in terms of the amount of preservative solution contained by the existing cell cavities of wood. These results coincide with the results obtained by Usta [7] for the experimental samples impregnated in accordance with the normal and pre-vacuumed immersion method based on the same amount of moisture. This was also the case in the amount of dry salt, which means that the impregnation solution loaded into the impregnated specimens to be settled in wood in the form of a residue after the solvent water has evaporated completely. In this respect, it was found that the net dry salt retention (the quantity of preservative solution absorbed by the experimental wood specimens) showed a similar distribution with void volume filled by preservative solution as a result of all samples impregnated with normal and pre-vacuumed immersion method. Of course, although the impregnability of the experimental wood material was evaluated based on the percentage of void volume filled by preservative solution and net dry salt absorbed after the impregnation process without indication of depth penetration, this was supported by the outcomes of this study.

On the other hand, as an important determination, the amount of void volume filled by preservative fluid were found to be greater than 10% but less than 30% when all experimental samples were evaluated, since the immersion process was performed with samples having air dry moisture of 12%. To take a closer look at this result, the percentage of void volume filled with preservative solution for all types of test specimens varies between 10.2% and 25.9% in normal immersion, and 12.5% and 28.0% in pre-vacuum immersion. At this point, when a comparison was made according to the trial pattern, it was seen that the least uniform alignment of the preservative fluid uptake according to the flow pathways was revealed in the form of Radial < Longitudinal < Triplex, regardless of the type of the sample preparation and the way of impregnation either normal or pre-vacuumed immersion.

Table 3 The absorption performance of wood material in terms of flow directions according to normal and pre-vacuumed immersion method

Method		Flow Pathway	Absorption	
Sample	Immersion		VVF	NDS
Cuboid	Normal	Radial	10.2	2.1
		Longitudinal	18.1	3.7
		Triplex	25.9	5.3
	Pre-Vacuumed	Radial	12.5	2.6
		Longitudinal	22.0	4.5
		Triplex	27.6	5.7
Plug	Normal	Radial	10.4	2.1
		Longitudinal	18.2	3.8
		Triplex	25.8	5.3
	Pre-Vacuumed	Radial	12.7	2.6
		Longitudinal	22.3	4.6
		Triplex	28.0	5.8

Abbreviations in Table 3 for the preservative fluid absorption were as follows: VVF: percentage of void volume filled by preservative solution, NDS: net dry salt absorbed after the impregnation process (kg m^{-3}).

4. CONCLUSIONS

This study, which aims to determine the effect of pre-vacuum process according to the flow directions in the protection of wood material by the immersion method in 12% moisture content, which is a common use condition, is a clear example in terms of impregnation of the dried wood material by immersion method. Considering that this study was carried out with the samples having air dry moisture content at 12% level, the preservative fluid uptake of the test samples was found to be relatively low compared to impregnation by the immersion method using samples with high moisture content. However, the feasibility of the immersion method with a pre-vacuumed process has been proven experimentally once again and it may be useful to examine this subject in detail through extensive research in the field of wood preservation. In addition, if a general evaluation is made in the context of the impregnation results obtained by this study, it has been observed that the plug samples (15 mm in diameter and 30 mm in length) can be used for the same purposes as well as the cuboids (20 mm in width and 20 mm in thickness and 30 mm in length) in the experimental wood impregnation applications. It is obvious that this would also provide significant savings in terms of sample preparation and detection cycle, because in this study, the period of the data collection were shorter in plugs than that for cuboids.

In light of these findings, it can be stated that this study is meant to be a reference for interested implementers to examine wood material to expand its capability in impregnation by immersion method. It is therefore obvious that this study will shed light on future studies involved in the same topic by comparing the experimental samples to be prepared in different moisture contents and the tests to be carried out with different immersion times.

When we compare the usage areas of wood, which is widely used as a versatile and functional material, it is obvious that the impregnation of wood material is a great necessity when viewed in terms of its use in wet interiors (due to direct splash) and outdoors (because of direct rain or sprinkler). In this study, which was carried out with a special test device, it was determined that performing the immersion method in the pre-vacuum priority increased protective fluid uptake and contained relatively more impregnation material (as the amount of net dry salt) in the fibrous and porous structure of wood material. Therefore, it can be said that moving the results of this study to an industrial dimension "within the framework of wood preservation by pre-vacuumed immersion method" will have an important place in the preservation of wood material by immersion method using boron compounds. Because of the fact that wood is in the life with appropriate protection processes and makes a great contribution to the protection of nature and environment, the design and development of wood preservation applications with different propositions is necessary for the existence of wood. Thus, the diversification the immersion method, as exemplified in this study with reference to the pre-vacuumed process, can be considered as an effort involving originality and innovation in terms of impregnating wood material with a woodlover approach.

Overall, the outcomes of this study showed a comprehensive understanding and methodological view of wood science and technology, and thereby enlarging our experience for looking for the new challenges and opportunities for wood preservation.

Acknowledgments

This study, which is carried out to devise ways to examine wood protection in terms of the collection and preparation of the experimental samples, and also the application of vacuum process in immersion method, is an improved version of the preliminary study entitled "Suggestive remarks for designing of experimental samples and trial devices to treat wood by pre-vacuumed immersion method" that was presented in summary on the IRG (International Wood Protection Research Group) website in 2019, (available via https://www.irg-wp.com/search-irg-docs.html) (access date; 21 December 2019), and hence, the author would like to express his sincere thanks and gratitude to the IRG.

REFERENCES

[1] İ. Usta, "Ahşap koruma," Yapı Dünyası, vol. 258-259, pp. 8-17, 2017.

[2] A. J. McQuire, "Radial permeability of timber,", PhD thesis, University of Leeds, 1970.

[3] Z. Koran, "Air permeability and creosote retention of Douglas-fir," Forest Products Journal, vol. 14, no. 4, pp. 159–166, 1964.

[4] R. D. Graham, "Sink-float test to determine treatability of Douglas-fir," Forest Product Journal, vol. 14, no. 11, pp. 516, 1964.

[5] Hayashi, S., K. Nishimoto, and T. Kishima, "Study on the liquid permeability of softwoods," Wood Research, vol. 36, pp. 47–57, 1967.

[6] R. Wheeler, "Equipment suitable for measuring angle of grain and for obtaining small timber samples from living trees," Commonwealth Forestry Review, vol. 43, no. 4, pp. 314–319, 1964.

[7] İ. Usta, "Batırma yöntemi ile ahşap korumada ön vakum uygulamasının borlu emprenye maddesi absorpsiyonuna etkisi," 2. Ulusal Bor Çalıştayı, pp. 275–288, 2008.

[8] I. Usta, "Comparison of cubic and plug samples for preparation and data assembly in permeability study," International Research Group on Wood Preservation, Document No: IRG/WP 00–20197, 2000.

[9] I. Usta, and M. D. Hale, "A novel guide for the determination of the physical properties of wood including kiln drying and full-cell preservative treatment," The International Research Group on Wood Preservation, Document No: IRG/WP: 04–20298, 2004.

[10] İ. Usta, "Ağaç malzeme fiziksel özelliklerinin tespitinde ve ahşap koruma performans değerlendirmesinde örnek bir kılavuz olarak Şematik Rehber kullanımı," Selçuk Üniversitesi Teknik Online Dergisi, vol. Özel Sayı (UMK-2015), pp. 407–420, 2015.

[11] G. Eliçin, "Sözlük (Bitki Adları)," İstanbul: İstanbul Üniversitesi Orman Fakültesi Yayınları, Yayın No: 2633/273, 1980.

[12] M. Konukçu, "Statistical Profile of Turkish Forestry," Ankara: Devlet Planlama Teşkilatı, 1998.

[13] "Türkiye Orman Varlığı Kitabı: 2015," https://www.ogm.gov.tr/ekutuphane/Yayinlar/T%C3%BCrkiye%20Orman%20Varl%C4%B1%C4%9F%C4%B1-2016-2017.pdf accessed 09 June 2018.

[14] Y. Tayanç, B. Çengel, G. Kandemir, and E. Velioğlu, "Türkiye'de yayılış gösteren göknar (*Abies spp*.) popülasyonlarının genetik çeşitliliği ve filogenetik sınıflandırılması," Orman Genel Müdürlüğü Orman Ağaçları ve Tohumları Islah Araştırma Enstitüsü, Teknik Bülten No: 33, Yayın No: 47, 2012.

[15] Wolman GmbH, "Wolmanit-CB," Technical Leaflet 501–65, 1965.

[16] R. İlhan, "Göknar tel direklerinin Wolmanit-CB ve Tanalith-C ile emprenye edilmesine dair araştırmalar" Ormancılık Araştırma Enstitüsü Teknik Bülteni 26, 1968.

[17] F. F. P. Kollmann, and W. A. Cote, Principles of Wood Science and Technology, 1: Solid Wood, Berlin: Springer–Verlag, 1968.

[18] J. M. Dinwoodie, "Timber: Its Structure, Properties and Utilisation," London: MacMillan Press Ltd., 1981.

[19] W. B. Banks, "Some factors affecting the permeability of Scots pine and Norway spruce,", Journal of the Institute of Wood Science, vol. 5 no. 1, pp. 10–17, 1970.

[20] Nicholas, D. D. and J. F. Siau, "Factors influencing treatability of wood," In: Wood Deterioration and Its Prevention by Preservative Treatments, 2: Preservatives and Preservative Systems, pp. 299–343, New York: Syracuse University Press, 1973.

[21] A. J. McQuire, "Effect of wood density on preservative retention in fence posts," New Zealand Journal of Forestry Science, vol. 5, pp. 105–109, 1975.

[22] A. Y. Bozkurt, "Ağaç Teknolojisi," İstanbul: İstanbul Üniversitesi Orman Fakültesi Yayınları, Yayın No: 3403/380, 1986.

[23] K. A. Flynn, "A review of the permeability, fluid flow, and anatomy of spruce (Picea spp.)," Wood and Fiber Science, vol. 27, no. 3, pp. 278–284, 1995.

[24] J. F. Siau, "Flow in Wood," New York: Syracuse University Press, 1971.

[25] A. Y. Bozkurt, Y. Göker, and N. Erdin, "Emprenye Tekniği," İstanbul: İstanbul Üniversitesi Orman Fakültesi Yayınları, Yayın No: 3779/425, 1993.

[26] R. B. Hoadley, "Understanding Wood: A Craftman`s Guide to Wood Technology," London: The Taunton Press, Inc., 1980.

[27] R. A. Eaton, and M. D. C. Hale, "Wood: Decay, Pests and Protection," London: Chapman and Hall Ltd., 1993.

[28] J. F. Siau, "Transport Processes in Wood," Berlin: Springer–Verlag, 1984.

[29] G. Tsoumis, "Science and Technology of Wood: Structure, Properties and Utilisation," New York: Van Nostrand Reinhold, 1991.

[30] A. Y. Bozkurt, and Y. Göker, "Fiziksel ve Mekanik Ağaç Teknolojisi," İstanbul: İstanbul Üniversitesi Orman Fakültesi Yayınları, Yayın No: 3445/388, 1987.

[31] Forest Products Laboratory (FPL), "Wood Handbook: 72," Madison: United States Department of Agriculture, Forest Service, 1987.

SAKARYA ÜNİVERSİTESİ
FEN BİLİMLERİ ENSTİTÜSÜ DERGİSİ

Sakarya University Journal of Science
SAUJS

ISSN 1301-4048 | e-ISSN 2147-835X | Period Bimonthly | Founded: 1997 | Publisher Sakarya University | http://www.saujs.sakarya.edu.tr/

Title: Photoluminescence Investigation of Tb Doped Yb_2O_3 Phosphors Produced by Precipitation Method

Authors: Fatma UNAL

Recieved: 2021-03-11 21:51:02

Accepted: 2021-07-07 16:18:29

Article Type: Research Article

Volume: 25
Issue: 4
Month: August
Year: 2021
Pages: 1031-1036

How to cite
Fatma UNAL; (2021), Photoluminescence Investigation of Tb Doped Yb_2O_3 Phosphors Produced by Precipitation Method. Sakarya University Journal of Science, 25(4), 1031-1036, DOI: 10.16984/saufenbilder.895402
Access link
http://www.saujs.sakarya.edu.tr/en/pub/issue/64755/895402

Sakarya University Journal of Science 25(4), 1031-1036, 2021

Photoluminescence Investigation of Tb Doped Yb_2O_3 Phosphors Produced by Precipitation Method

Fatma UNAL*[1]

Abstract

In this study, un-doped and Tb doped ytterbium oxide (Yb_2O_3:Tb^{3+}) particles with different dopant rates (2, 4, 6 and 8 at. %) were produced by precipitation method, followed by subsequent calcination at 1000 °C for 2 h. The crystal structure of all particles was cubic Yb_2O_3 structure. The presence of Tb ion in Yb_2O_3 host structure was proved from the XRD peak shift results. The crystal structure expanded compared to un-doped Yb_2O_3 particles with doping, confirming calculated lattice parameter (LP) values. The LP, crystallite size (CS) and dislocation density values were in the range of 1.0428 – 1.0596 nm, 16 – 25 nm and 0.00189 – 0.00391 nm^{-2}, respectively. Only one sharp emission peak was observed at 506 nm corresponding to $^5D_4 – {}^7F_6$ transition (green emission) from photoluminescence (PL) spectra of the phosphor particles. The PL emission intensities were found to be strongly dependent on both CS and dopant rate. There was a positive correlation between increasing CS, decreasing lattice strain/dislocation density and PL intensity. Crystal defects decreased and PL intensity increased up to 6 at. % dopant rate.

Keywords: Terbium doped ytterbium oxide phosphors, photoluminescence emission, precipitation method, Williamson-Hall analysis

1. INTRODUCTION

Lanthanide oxides have unique and versatile physical and chemical properties such as high melting point, corrosion resistance, excellent thermal stability, high dielectric constant, mechanical strength, good protective behavior, luminescence, etc. [1-3]. Among the lanthanide oxides, ytterbium oxide (Yb_2O_3) particles exhibit extraordinary properties [4]. Correspondingly, they have many application areas such as high-temperature superconducting materials, colored glasses, technical ceramic, varistors, catalyst, electro-catalysis, solid-state laser, phosphor, stabilizer, optical fiber, solid oxide fuel cell, medical echo probe, imaging, scintillator and NIR photovoltaic up-converters [1-3, 5-13]. However, since its commercialized use in electronic devices is limited due to the high band gap (~5 eV) of Yb_2O_3, lanthanide dopant elements (such as La, Ho, Gd, Er, Eu etc.) were integrated into the Yb_2O_3 host structure [1, 2, 9-11, 13]. They can be synthesized by many methods such as electrospinning, sol-gel, hydrothermal method, spray pyrolysis, precipitation [2, 3, 5-8]. While there are limited number of publications on the production of lanthanide doped Yb_2O_3 particles [1, 9-11, 13], there is no comprehensive study on

* Corresponding author: fatmaunal@hitit.edu.tr
[1] Hitit University, Corum, Turkey.
ORCID: https://orcid.org/ 0000-0003-4476-2544

the synthesis and photoluminescence (PL) properties of Yb_2O_3:Tb^{3+} particles. Herein, the first study on the effects of dopant rate and crystallite size (CS) values on the PL properties of Yb_2O_3:Tb^{3+} particles was reported.

2. EXPERIMENTAL STUDY

Un-doped and Tb doped ytterbium oxide (Yb_2O_3:Tb^{3+}) particles with different dopant rates (2, 4, 6 and 8 at. %) were produced by precipitation method using analytical grade, 99.99% purity, ytterbium (III) nitrate hydrate ($Yb(NO_3)_3 \cdot xH_2O$) and terbium-nitrate-hydrate ($Tb(NO_3)_3 \cdot xH_2O$). For example, 300 ml of 0.1 M solution was prepared for each sample. 10.56 gr of Yb-nitrate and 0.207 g of Tb-nitrate salts were used in order to produce 2 at. % Tb doped Yb_2O_3 particles. After dissolving appropriate amounts of nitrate salts in ultrapure water, they were mixed for 15 min in ambient conditions. Afterwards, 1 M ammonium carbonate ($(NH_4)_2CO_3$) solution was slowly added to each solution till precipitation was completed. The solutions were stirred in a magnetic stirrer for 3 h. They were centrifuged at 5000 rpm for 5 min to collect precipitate, which were further washed several times with distilled water and once with ethanol. Dried particles at 80°C for 24 hours were subjected to calcination at 1000 °C for 2 hours in a furnace. Sample codes are shown in Table 1.

Table 1 Sample codes of all the particles

Sample code	Temperature (°C) / Time (h)	Dopant rate (at. %)
Yb_2O_3	1000 / 2	0
02Tb:Yb_2O_3		2
04Tb:Yb_2O_3		4
06Tb:Yb_2O_3		6
08Tb:Yb_2O_3		8

All particles were investigated by X-ray diffraction technique (XRD) in order to find out phase structure. Using the XRD broadening data, lattice parameter (LP) and crystallite size (CS) values were computed with Williamson–Hall (W–H) and Cohen-Wagner (C–W) methods, respectively [5, 14]. To characterize the microstructural parameter (lattice strain, dislocation density), average CS values were computed with W–H analysis integrated with uniform deformation model. The diffraction peak's broadenings were measured by Eq. 1.

$$\beta_{hkl} = [(\beta_{hkl})^2_{measured} - \beta^2_{(instrumental)}]^{1/2} \quad (1)$$

The CS values of particles were computed with W–H by Eq. 2,

$$\beta_{hkl} cos\theta = \frac{k\lambda}{D} + (4\varepsilon sin\theta) \quad (2)$$

where β_{hkl} is calculated correct broadening of the XRD diffraction peak, k is a constant (0.89), θ is diffraction angle, λ is X-ray Cu-K_α wavelength (1.5406 Å), D and ε are denoted by crystallite size and lattice strain, respectively. The dislocation density was calculated by Williamson-Smallman formalism [14] (Eq. 3):

$$\delta = \frac{1}{D^2} \quad (3)$$

where δ is dislocation density and D is crystallite size. Photoluminescence (PL) emission spectra of Tb doped particles were taken between 300 nm and 800 nm under 254 nm excitation at room temperature.

3. RESULTS AND DISCUSSION

3.1. Structural Analysis

XRD patterns of un-doped and Tb doped Yb_2O_3 particles are given in Fig 1. It was determined that all the produced particles had body centered cubic Yb_2O_3 crystalline phase with space group *Ia*-3 (JCPDS card no: 00-43-1037) and no impurity phase was detected in the particles.

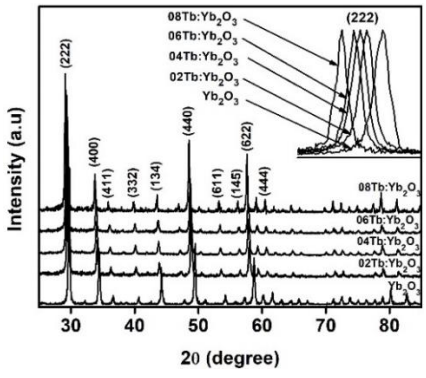

Figure 1 XRD patterns of all the particles

All diffraction peaks had strong intensity and narrow width indicating superior crystalline quality. Shifts in the XRD peaks occurred compared to the peak of the un-doped Yb_2O_3 sample depending on dopant rate. When Tb dopant element entered the Yb_2O_3, the peaks shifted to lower diffraction angles (inset Fig 1.) and Yb_2O_3 host expanded. Because Tb^{3+} ionic radius (0.0923 nm) is larger than that of Yb^{3+} (0.0858 nm) [15, 16]. This expansion in the structure was confirmed by the calculated lattice parameter values.

For the C-W and W-H calculations, the plots of (a) versus $f(\theta^{hkl})$ and ($\beta_{hkl}\cos\theta$) versus ($4\sin\theta$) for them are given in Fig 2.

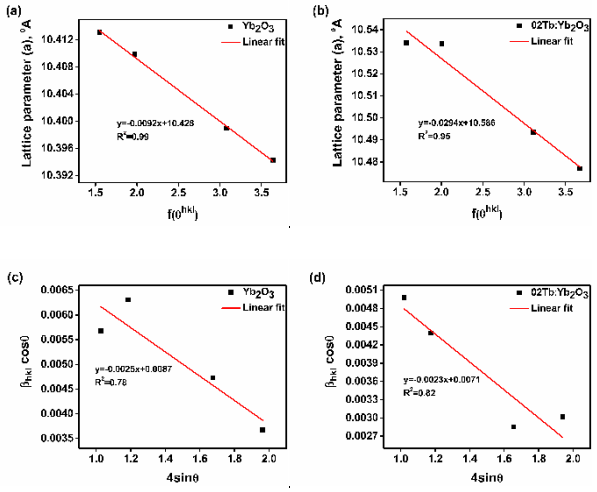

Figure 2 (a,b) C-W plots and (c,d) W-H plots of Yb_2O_3 and 02Tb:Yb_2O_3 samples

For example, according to the C–W plots of Yb_2O_3 and 02Tb:Yb_2O_3 samples the lattice parameters were 10.428 Å (R^2=99) and 10.586 Å (R^2=95), respectively. According to the W-H plots of Yb_2O_3 and 02Tb:Yb_2O_3 samples the CS values were 16 nm (R^2=78) and 19 nm (R^2=82), respectively. LP and CS values of all the particles are given in Table 2.

Table 2 Microstructural parameters of all particles.

Sample code	Lattice parameter (a/nm)	Crystallite size (nm)	Lattice strain (Ɛ)	Dislocation density (δ/nm^{-2})
Yb_2O_3	1.0428	16	-0.0025	0.00391
02Tb:Yb_2O_3	1.0586	19	-0.0023	0.00277
04Tb:Yb_2O_3	1.0590	21	-0.0016	0.00227
06Tb:Yb_2O_3	1.0593	25	-0.0011	0.00160
08Tb:Yb_2O_3	1.0596	23	-0.0014	0.00189

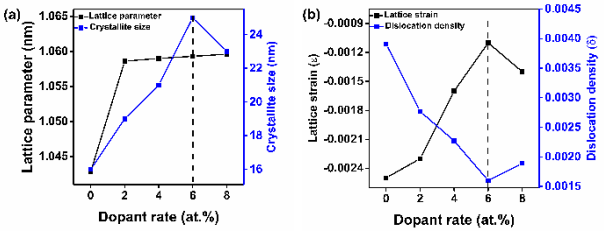

Figure 3 (a) Crystallite size and lattice parameter and (b) lattice strain and dislocation density as a function of dopant rate.

It was determined that the dopant rate enlarged the crystallites up to 6 at.%, which indicates a positive correlation between crystallite size and lattice parameter (Fig 3a). According to the dislocation density and lattice strain values, there was an improvement in crystallinity due to the reduction of crystal defects with doping. The 06Tb:Yb_2O_3 sample exhibited minimum lattice strain and dislocation density values.

3.2. Photoluminescence Analysis

The excitation spectra (Fig.4) showed the maximum excitation peak was centred at 254 nm which is belonging to 4f – 5d transition of Tb^{3+}. Thus, Un-doped and Tb doped Yb_2O_3 phosphor particles were excited by 254 nm source (inset in Fig. 4) and resulting PL emission spectra were recorded ranging from 300 nm to 800 nm. While the un-doped Yb_2O_3 particles exhibited no emission in the visible region, the Tb doped particles exhibited green emission. In addition, the PL intensity increased with the increase in the dopant rate up to 6 at. % due to the abundance of luminescence centres. Since increasing crystallite size and decreasing dislocation density improved the crystallinity, an increase in the PL emission intensity was accordingly observed. Above this dopant rate value, it was observed that the crystal defects / dislocation density values increased and the PL intensity decreased which indicates the concentration quenching of the luminescence. In the literature, Tb doped oxide particles exhibited multiple number of emission peaks. Additionally, the strongest emission peak reported to be at around 545 nm, accompanied by a low intensity emission at around 500 nm [17-22]. Contrary to the literature, the emission spectra of all the

Yb_2O_3:Tb particles were located at 506 nm associated to $^5D_4 - {}^7F_6$ transition (green emission).

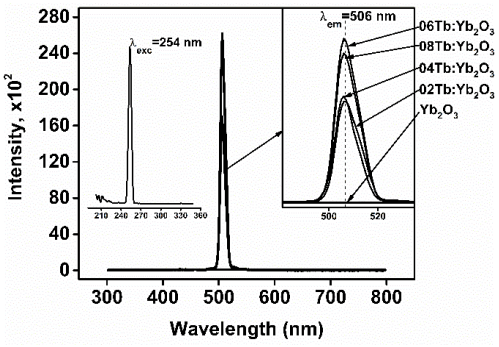

Figure 4 Excitation and emission spectra of all the particles

The PL intensity at 506 nm in emission spectra gradually increased with increasing CS and dopant rate, as shown in Fig. 4a and 4b, indicating the strong effect of the CS and the dopant rate. It was shown that the PL intensity of the Tb doped particles had a linear relationship with the CS values, indicating the improving in crystallinity (Fig. 4a). It was observed that 02Tb:Yb_2O_3 sample had the lowest PL emission intensity whereas 06Tb:Yb_2O_3 sample exhibited the highest PL emission intensity. The emission intensity value decreased for 08Tb:Yb_2O_3 sample. These results clearly show that the optimum Tb ion rate is 6 at.% for the highest PL emission intensity (Fig. 4b).. Additionally, the dopant rate had a greater significance on the PL intensity than crystallite size.

4. CONCLUSIONS

In this study, Yb_2O_3:Tb^{3+} particles having bixbyite-type cubic structure were successfully synthesized by precipitation method.

LP and CS values were in the range of 10.428 – 10.596 Å and 16 – 25 nm, respectively. Doping Tb into the Yb_2O_3 crystal increased both LP and CS values which in return decreased the dislocation density up to 6 at. % dopant rate. Further doping, started to increase lattice imperfections.

PL emission peak of all phosphor particles were centred at 506 nm corresponding to $^5D_4 - {}^7F_6$ transition (green emission). It was found that the optimum Tb dopant rate was 6 at.% due to both increasing luminescence centres and improved crystallinity, resulting in the highest PL emission intensity. However, a decrease was also observed in PL intensity above 6 at. % due to the concentration quenching.

The CS and dopant rate affected the PL intensity but, the dopant rate was more significance.

The Declaration of Conflict of Interest/ Common Interest

No conflict of interest or common interest has been declared by the author.

REFERENCES

[1] Kumar, S., Chaudhary, S., Chaudhary, G.R. 2020. Modulating physicochemical properties in Gd^{3+}@Yb_2O_3 nanospheres for efficient electrochemical monitoring of H_2O_2. *Materials Science and Engineering C*, 114, 111059.

[2] Yang, J., Shen, J., Huang, Q., Guan, Y., Miao, J. 2018. Hydrothermal synthesis and photoluminescence of host sensitized Yb_2O_3: Ho^{3+} nanorods. *Materials Research Express*, 6, 1.

[3] Henriques, M.S., Ferreiraac, A.C., Cruza, A., Ferreiraa, L.M., Brancoa, J.B., Brazdab, P., Jurekb, K., Storad, T., Gonçalvesa, A.P. 2015. Preparation of Yb_2O_3 submicron and nano materials via electrospinning. *Ceramics International*, 41, 10795–10802.

[4] Sohn, Y. 2018. Yb_2O_3 nanowires, nanorods and nano-square plates. *Ceramics International*, 44, 3341–3347.

[5] Unal, F., Kaya, F. 2020. Modelling of relation between synthesis parameters and average crystallite size of Yb_2O_3 nanoparticles using Box-Behnken design. *Ceramics International*, 46, 26800–26808.

[6] Suo, H., Guo, C., Li, L. 2015. Host sensitized spherical up-conversion

phosphor $Yb_2O_3:Er^{3+}$. *Ceramics International*, 41, 7017–7020.

[7] Zheng, Y., Lü, Q., Wang, J., Zhang, G., Gao, Y., Liu, Z. 2014. Emission behaviors of Yb_2O_3 nanoparticles pumped by 980 nm laser at different power densities. *Optics & Laser Technology*, 63, 39–44.

[8] Titov, A.A., Sokolova, N.P., Vorob'eva, M.V., Opolchenova, N.L., Eremenko, Z.V., Stepareva, N.N. 2009. Synthesis and microstructure of nanocrystalline Yb_2O_3 powders. *Inorganic Materials*, 45, 884–888.

[9] Wang, X., Li, Y., Zhou, Y., He, Y. 2019. Application of a novel endocrine disruptor bisphenol A electrochemical sensor based on analogous heterostructure characteristics of La-doped Yb_2O_3 nanomaterials. *Analytical Methods*, 11, 5613–5622.

[10] Liu, Z., Li, Z., Liu, J., Gu, S., Yuan, Q., Ren, J., Qu, X. 2012. Long-circulating Er^{3+}-doped Yb_2O_3 up-conversion nanoparticle as an in vivo X-Ray CT imaging contrast agent. *Biomaterials*, 33, 6748–6757.

[11] Qian, C., Zeng, T., Liu, H. 2013. Synthesis and downconversion emission property of Yb_2O_3: Eu^{3+} nanosheets and nanotubes. *Advances in Condensed Matter Physics*, 519869.

[12] Yuan, F., Wang, J., Miao, H., Guo, C., Wang, W.G. 2012. Investigation of the crystal structure and ionic conductivity in the ternary system $(Yb_2O_3)_x$–$(Sc_2O_3)_{(0.11-x)}$–$(ZrO_2)_{0.89}$ (x=0–0.11). *Journal of Alloys and Compounds*, 549, 200–205.

[13] Chaudhary, S., Kumar, S., Chaudhary, G.R. 2019. Tuning of structural, optical and toxicological properties of Gd^{3+} doped Yb_2O_3 nanoparticles. *Ceramics International*, 45, 19307–19315.

[14] Emil, E., Gürmen, S. 2020. A straightforward approach for the synthesis of nanostructured Y_2O_3 particles: Synthesis, morphology, microstructure and crystal imperfection. *Physica E: Low-dimensional Systems and Nanostructures*, 115, 113668.

[15] Li, X., Yang, Z., Guan, L., Guo, J., Wang, Y., Guo, Q. 2009. Synthesis and luminescent properties of $CaMoO_4:Tb^{3+}$, R+ (Li+, Na+, K^+). *Journal of Alloys and Compounds*, 478, 684–686.

[16] Tsuboi, T., Kaczmarek, S.M., Boulon, G. 2004. Spectral properties of Yb^{3+} ions in $LiNbO_3$ single crystals: Influences of other rare-earth ions, OH^- ions, and γ-irradiation. *Journal of Alloys and Compounds*, 380, 196–200.

[17] Kumamoto, N., Nakauchi, D., Kato, T., Okada, G., Kawaguchi, N., Yanagida, T. 2017. Photoluminescence, scintillation and thermally-stimulated luminescence properties of Tb-doped $12CaO{\cdot}7Al_2O_3$ single crystals grown by FZ method. *Journal of Rare Earths*, 35, 957–963.

[18] Sotiriou, G.A., Franco, D., Poulikakos, D., Ferrari, A. 2012. Optically Stable Biocompatible Flame-Made SiO_2-Coated $Y_2O_3:Tb^{3+}$ Nanophosphors for Cell Imaging. *ACS Nano*, 6, 3888–3897.

[19] Gupta, A., Brahme, N., Bisen, D.P. 2014. Electroluminescence and photoluminescence of rare earth (Eu , Tb) doped Y_2O_3 nanophosphor. *Journal of Luminescence*, 155, 112–118.

[20] An, T., Benalloul, P., Barthou, C., Giang, L.T., Vu, N., Minh, L. 2007. Luminescence, energy transfer, and upconversion mechanisms of Y_2O_3 nanomaterials doped with Eu^{3+}, Tb^{3+}, Tm^{3+}, Er^{3+}, and Yb^{3+} ions. *Journal of Nanomaterials*, 48247.

[21] Muenchausen, R.E., Jacobsohn, L.G., Bennett, B.L., McKigney, E.A., Smith, J.F., Valdez, J.A., Cooke, D.W. 2007. Effects of Tb doping on the photoluminescence of Y_2O_3:Tb nanophosphors. *Journal of Luminescence*, 126, 838–842.

[22] Tu, D., Liang, Y., Liu, R., Li, D. 2011. Eu/Tb ions co-doped white light luminescence Y_2O_3 phosphors. *Journal of Luminescence*, 131, 2569–2573.

SAKARYA ÜNİVERSİTESİ
FEN BİLİMLERİ ENSTİTÜSÜ DERGİSİ

Sakarya University Journal of Science
SAUJS

e-ISSN: 2147-835X | Founded: 1997 | Period: Bimonthly | Publisher: Sakarya University
http://www.saujs.sakarya.edu.tr/en/

Title: Antivirus Mask Selection Under Spherical Fuzzy Information

Authors: Serhat AYDIN, Emrah KÖKSALMIŞ

Recieved: 2021-03-23 22:28:18

Accepted: 2021-07-09 17:21:09

Article Type: Research Article

Volume: 25
Issue: 4
Month: August
Year: 2021
Pages: 1037-1048

How to cite
Serhat AYDIN, Emrah KÖKSALMIŞ; (2021), Antivirus Mask Selection Under Spherical Fuzzy Information. Sakarya University Journal of Science, 25(4), 1037-1048, DOI: https://doi.org/10.16984/saufenbilder.902048
Access link
http://www.saujs.sakarya.edu.tr/en/pub/issue/64755/902048

Sakarya University Journal of Science 25(4), 1037-1048, 2021

Antivirus Mask Selection Under Spherical Fuzzy Information

Serhat AYDIN*[1], Emrah KÖKSALMIŞ[1]

Abstract

Many individuals are facing antivirus mask scarcity with the exponential spread of COVID-19. A functional antivirus mask needs to be selected and made usable for everyone. Selection mask problem contains qualitative criteria, therefore utilizing fuzzy logic for this problem is a useful approach. To optimize the efficiency of choosing antivirus masks, we propose using one of the new types of ordinary fuzzy sets, named Spherical fuzzy sets. For this purpose, we determine 4 different alternatives and 6 criteria. Then, we gather the data under spherical information and applied the Spherical fuzzy AHP method to the problem. Then, we propose an entropy based Spherical fuzzy AHP method. We compare the results of Spherical fuzzy AHP method, and an entropy based Spherical fuzzy AHP method. Moreover, we present a sensitivity analysis to explain how our model is influenced by changes in different weights of criteria. Finally, the best antivirus mask is determined for public use and we present the advantages of the proposed method in results section.

Keywords: Mask selection, spherical fuzzy sets, spherical AHP, COVID-19

1. INTRODUCTION

The Coronavirus Disease 2019 (COVID-19) epidemic occurred in the city of Wuhan, Hubei province in December 2019. The World Health Organisation announced the coronavirus (COVID-19) a pandemic on March 11, 2020 [1]. The infection spread to 330,000 persons within 2 weeks, resulting in 13,700 deaths [2]. The common signs of COVID-19 infection can be summarized as follows: cough, symptoms of respiration, shortness of breath, and fever. In more serious cases, influenza, severe acute respiratory syndrome, renal failure and even death may result from infection [3].

Being well educated on the COVID-19 virus, the illness it causes, and how it progresses, is the safest way to deter and slow down transmission. By washing your hands or using an alcohol-free rub regularly and not rubbing your skin, shield yourself and others from infection. The COVID-19 infection spreads basically through beads of spit or release from the nose when a contaminated individual hacks or wheezes, so it is important to take preventive measures [4].

Under the COVID-19 outbreak, masks have become important items for work and travel for hospital stays and ordinary citizens. Also, the use of masks to avoid droplet dissemination is advised by the authorities [5-7], so wearing a mask is one of the most significant prevention steps.

* Corresponding author: saydin3@hho.edu.tr
[1] Air Force Academy, İstanbul, Turkey.
E-Mail: ekoksalmis@hho.edu.tr
ORCID: https://orcid.org/0000-0003-0861-8297; https://orcid.org/0000-0003-4922-2125.

MacIntyre et al. [8] found that mask conformity greatly decreases the risk of infection with influenza. Brienen et al. found that the use of face masks across the population may play an important role in delaying an influenza pandemic [9]. The worldwide market for masks and other personal safety devices are now 150 times that of the average amount, and the price is too much that of regular times in this pandemic. Perhaps, this mask scarcity problem will be further compounded by people's inadequate and wasteful usage of personal protection equipment to make it persist for a long period. Therefore, the powerful basic step to cope with the mask scarcity and the COVID-19 dissemination is to customize the usage of antivirus masks according to diverse individuals.

It is everybody's basic duty and responsibility to resist the COVID-19 without unnecessary security, particularly in the situation of the COVID-19 spreading and a mask shortage. Therefore, the rational collection and use of masks have a vital functional meaning for various classes of individuals. Masks of the same quality as those used by front-line medical personnel are not required for most persons. When selecting a mask to maximize the distribution of medical services, several factors must be considered. However, the limited knowledge and ambiguity of the COVID-19 extension increase the difficulties and challenges of choosing a suitable antivirus mask for decision-making. Therefore, considering qualitative factors in choosing mask is essential.

There are many different methods to make a consistent decision. On the other hand, when it comes to evaluating quantitative factors, fuzzy logic, suggested by Zadeh [10], is a very useful mathematical means to consider the qualitative factors. Also, fuzzy logic is an effective theory for modeling uncertainty. This is a mathematical means of expressing complexity and confusion in matters of decision-making. The theory of fuzzy sets has been the basis for the development of the linguistic approach and its corresponding fuzzy logic. In this approach any variable is treated as a linguistic variable, i.e., it can assume linguistic values. A linguistic value is composed of its syntactic value or label, a sentence belonging to a term set, and its semantic value, the membership distribution of a fuzzy set defined on a universe of discourse. Fuzzy logic is a logic whose truth-values are linguistic [11]. More information about linguistic fuzzy sets can be seen with the related references such as [12- 17].

Fuzzy logic theory has also been used as a logical tool in many MCDM methods. Fuzzy sets are a grouping of objects with a membership rating continuum. Each fuzzy set is aligned with a membership function, which assigns each object a membership score. The membership grades are normally set at [0,1]. FSs define the membership value $\mu_{(x)}$ and $0 \leq \mu_{(x)} \leq 1$. In the last 50 years, new types of fuzzy sets have been introduced to define the uncertainty more accurately. Therefore, a few extensions of fuzzy sets have been developed such as Intuitionistic fuzzy sets (IFSs) [18] Pythagorean fuzzy sets (PFSs) [19] q-rung orthopair fuzzy sets (q-ROFs) [20].

Spherical fuzzy sets (SFSs) are suggested by Kutlu Gündoğdu and Kahraman [21]. SFSs are based on the spherical fuzzy distances and satisfy the condition as follows $0 \leq {\mu_{(x)}}^2 + {v_{(x)}}^2 + {\pi_{(x)}}^2 \leq 1$. The hesitancy degree is represented by $\pi_{(x)}$ and hesitancy degree can be determined in the spherical representation based on the given membership and non-membership values. So, a decision maker's hesitancy may be specified independently of membership degrees and non-membership degrees.

Multi criteria decision making (MCDM) is a collection of strategies that form a decision science sub-branch and combine numerous approaches. The approach of modeling and assessing the decision process according to the criteria in such a way that the expert's benefit is maximized after the process is based on MCDM. Many researchers developed different MCDM methods as follows: AHP [22], ANP [23], TOPSIS [24], ELECTRE [25], etc.

Analytic Hierarchy Process (AHP) is a systematic method that can easily solve the problems that contain several alternatives and several criteria. It is based on the creation and identification of the

priority vector of the synthesized pairwise comparison matrix. AHP uses integer numbers to calculate the importance of alternatives, but real-world challenges require considerable vagueness and ambiguity, also require the use of fuzzy numbers. AHP and fuzzy logic have since been merged and transformed into an interactive paradigm called fuzzy AHP.

In the literature there some studies about the COVID-19 mask using and selection problem as follows: Yang et al. [26] proposed a decision support algorithm for selecting an antivirus mask over the COVID-19 with fuzzy sets. They evaluated 6 different alternatives according to the 4 different criteria. They proposed some aggregation spherical fuzzy operators to handle the problem. Shahzadi and Akram [27] developed an MCDM method to assess an antivirus mask with Fermatean fuzzy sets. Moreover, they developed some aggregation operators and gave some properties of proposed operators. Wang et al. [28] realized a laboratory study to Selection of homemade mask materials for preventing transmission of the COVID -19. They demonstrated that the risk of contamination can be reduced to the fullest degree by homemade masks using available materials. Lam et al. [29] suggested some precautions and replied frequently asked questions on mask selection problem. Fen et al. [30] discussed about the rational use of face masks in the COVID-19 pandemic. They compared the recommendations for using a mask by different health authorities. Zheng et al. [31] suggested some recommendations to overcome the pandemic. They discussed many issues in their paper such as Medical masks selection, hand-hygiene items, gloves, etc. They collected and summarized the expertise obtained from delivering pharmacy services during the COVID-19 epidemic in Chinese community pharmacies. Bartoszko et al. [32] compared the different types of masks for healthcare workers. They conducted an observational study and concluded that medical masks and N95 respirators provide similar protection against the pandemic. There are few studies on the COVID-19 mask selection problem, most of the research use empirical data to solve the mask selection problem. Therefore, there is a gap in the literature to use an MCDM method to evaluate the mask used during the COVID-19 pandemic.

In this study, we used a hybrid model including SFSs and AHP method. The method, named Spherical Fuzzy AHP, is utilized to solve the mask selection decision making problem. The criteria are determined to evaluate the mask selection problem, and steps of the algorithm are applied to the problem. Moreover, we present an entropy based Spherical fuzzy AHP method, and we implement the proposed method to the mask selection problem. Also, a sensitivity analysis is applied. In application section, the proposed method is applied to an important subject: COVID 19 mask selection problem. The World Health Organization (WHO) advises the use of masks as part of a comprehensive package of prevention and control measures to limit the spread of SARS-CoV-2, the virus that causes COVID-19. Therefore, using a suitable mask is important to prevent the spread of virus. The proposed method is utilized to select the best mask during pandemic for this aim. The originality of the paper is that it proposes a hybrid method including the entropy theory and spherical fuzzy AHP method to solve the mask selection problem for the first time in the literature.

The remainder of the paper's composition is as follows: The preliminaries of SFSs and the steps of the Spherical fuzzy AHP method are introduced in Section 2. An example is given with Spherical fuzzy AHP method in Section 3. Section 4 clarifies the proposed method and clarifies the calculation steps of the proposed method to the mask selection problem. A sensitivity analysis is performed in Section 5. Finally, the conclusion is given in Section 6.

2. MATERIAL AND METHOD

First, we represent the preliminaries of spherical fuzzy sets in this section. Then, we discuss the spherical AHP method.

2.1. Preliminaries of Spherical Fuzzy Sets

Definition 1: A spherical fuzzy set $\tilde{A}_S$ of the universe of discourse U is given by

$$\tilde{A}_S = \{\langle u, (\mu_{\tilde{A}_S}(u), v_{\tilde{A}_S}(u), \pi_{\tilde{A}_S}(u))\rangle | u \in U\} \quad (1)$$

Where,

$$\mu_{\tilde{A}_S}: U \to [0,1], v_{\tilde{A}_S}(u): U \to [0,1], \pi_{\tilde{A}_S}: U \to [0,1]$$

and

$$0 \leq \mu^2_{\tilde{A}_S}(u) + v^2_{\tilde{A}_S}(u) + \pi^2_{\tilde{A}_S}(u) \leq 1 \forall u \in U \quad (2)$$

For each u, the numbers $\mu_{\tilde{A}_S}(u), v_{\tilde{A}_S}(u)$ and $\pi_{\tilde{A}_S}(u)$ are the degree of membership, non-membership and hesitancy of $u$to $\tilde{A}_S$, respectively.

Definition 2: Basic Operators

$$\tilde{A}_S \cup \tilde{B}_S = \Big\{ max\{\mu_{\tilde{A}_S}, \mu_{\tilde{B}_S}\}, min\{v_{\tilde{A}_S}, v_{\tilde{B}_S}\}, min\Big\{\Big(1 - \Big((max\{\mu_{\tilde{A}_S}, \mu_{\tilde{B}_S}\})^2 + (min\{v_{\tilde{A}_S}, v_{\tilde{B}_S}\})^2\Big)\Big)^{1/2}, max\{\pi_{\tilde{A}_S}, \pi_{\tilde{B}_S}\}\Big\}\Big\} \quad (3)$$

$$\tilde{A}_S \cap \tilde{B}_S = \Big\{ min\{\mu_{\tilde{A}_S}, \mu_{\tilde{B}_S}\}, max\{v_{\tilde{A}_S}, v_{\tilde{B}_S}\}, max\Big\{\Big(1 - \Big((min\{\mu_{\tilde{A}_S}, \mu_{\tilde{B}_S}\})^2 + (max\{v_{\tilde{A}_S}, v_{\tilde{B}_S}\})^2\Big)\Big)^{1/2}, min\{\pi_{\tilde{A}_S}, \pi_{\tilde{B}_S}\}\Big\}\Big\} \quad (4)$$

$$\tilde{A}_S \oplus \tilde{B}_S = \Big\{\big(\mu^2_{\tilde{A}_S} + \mu^2_{\tilde{B}_S} - \mu^2_{\tilde{A}_S}\mu^2_{\tilde{B}_S}\big)^{1/2}, v_{\tilde{A}_S}v_{\tilde{B}_S}, \Big(\big(1-\mu^2_{\tilde{B}_S}\big)\pi^2_{\tilde{A}_S} + \big(1-\mu^2_{\tilde{A}_S}\big)\pi^2_{\tilde{B}_S} - \pi^2_{\tilde{A}_S}\pi^2_{\tilde{B}_S}\Big)^{1/2}\Big\} \quad (5)$$

$$\tilde{A}_S \otimes \tilde{B}_S = \Big\{\mu_{\tilde{A}_S}\mu_{\tilde{B}_S}, \big(v^2_{\tilde{A}_S} + v^2_{\tilde{B}_S} - v^2_{\tilde{A}_S}v^2_{\tilde{B}_S}\big)^{1/2}, \Big(\big(1-v^2_{\tilde{B}_S}\big)\pi^2_{\tilde{A}_S} + \big(1-v^2_{\tilde{A}_S}\big)\pi^2_{\tilde{B}_S} - \pi^2_{\tilde{A}_S}\pi^2_{\tilde{B}_S}\Big)^{1/2}\Big\} \quad (6)$$

$$\lambda \cdot \tilde{A}_S = \Big\{\Big(1 - \big(1-\mu^2_{\tilde{A}_S}\big)^{\lambda}\Big)^{1/2}, v^{\lambda}_{\tilde{A}_S}, \Big(\big(1-\mu^2_{\tilde{A}_S}\big)^{\lambda} - \big(1-\mu^2_{\tilde{A}_S}-\pi^2_{\tilde{A}_S}\big)^{\lambda}\Big)^{1/2}\Big\} \quad (7)$$

$$\tilde{A}^{\lambda}_S = \Big\{\mu^{\lambda}_{\tilde{A}_S}, \Big(1 - \big(1-v^2_{\tilde{A}_S}\big)^{\lambda}\Big)^{1/2}, \Big(\big(1-v^2_{\tilde{A}_S}\big)^{\lambda} - \big(1-v^2_{\tilde{A}_S}-\pi^2_{\tilde{A}_S}\big)^{\lambda}\Big)^{1/2}\Big\} \; \lambda > 0 \quad (8)$$

Definition 3: For these SFS $\tilde{A}_S = (\mu_{\tilde{A}_S}, v_{\tilde{A}_S}, \pi_{\tilde{A}_S})$ and$\tilde{B}_S = (\mu_{\tilde{B}_S}, v_{\tilde{B}_S}, \pi_{\tilde{B}_S})$, the followings are valid under the condition$\lambda, \lambda_1, \lambda_2 > 0$.

$$\tilde{A}_S \oplus \tilde{B}_S = \tilde{B}_S \oplus \tilde{A}_S \quad (9)$$

$$\tilde{A}_S \otimes \tilde{B}_S = \tilde{B}_S \otimes \tilde{A}_S \quad (10)$$

$$\lambda(\tilde{A}_S \oplus \tilde{B}_S) = \lambda\tilde{A}_S \oplus \lambda\tilde{B}_S \quad (11)$$

$$\lambda_1\tilde{A}_S \oplus \lambda_2\tilde{A}_S = (\lambda_1 + \lambda_2)\tilde{A}_S \quad (12)$$

$$(\tilde{A}_S \otimes \tilde{B}_S)^{\lambda} = \tilde{A}^{\lambda}_S \otimes \tilde{B}^{\lambda}_S \quad (13)$$

$$\tilde{A}^{\lambda_1}_S \otimes \tilde{A}^{\lambda_2}_S = \tilde{A}_S{}^{\lambda_1+\lambda_2} \quad (14)$$

Definition 4: Spherical Weighted Arithmetic Mean (SWAM) with respect to $w = (w_1, w_2 \ldots\ldots, w_n); w_i \in [0,1]; \sum_{i=1}^{n} w_i = 1$, SWAM is defined as;

$$SWAM_w(A_{S1}, \ldots\ldots, A_{Sn}) = w_1A_{S1} + w_2A_{S2} + \ldots\ldots + w_nA_{Sn}$$

$$= \Big\{\Big[1 - \prod_{i=1}^{n}(1-\mu^2_{A_{Si}})^{w_i}\Big]^{1/2}, \prod_{i=1}^{n} v^{w_i}_{A_{Si}}, \Big[\prod_{i=1}^{n}(1-\mu^2_{A_{Si}})^{w_i} - \prod_{i=1}^{n}(1-\mu^2_{A_{Si}}-\pi^2_{A_{Si}})^{w_i}\Big]^{1/2}\Big\} \quad (15)$$

Definition 5: Spherical Weighted Geometric Mean (SWGM) with respect to $w = (w_1, w_2 \ldots\ldots, w_n); w_i \in [0,1]; \sum_{i=1}^{n} w_i = 1$, SWGM is defined as;

$$SWGM_w(A_1, \ldots\ldots, A_n) = A_{S1}{}^{w_1} + A_{S2}{}^{w_2} + \ldots\ldots + A_{Sn}{}^{w_n}$$

$$= \Big\{\prod_{i=1}^{n}\mu^{w_i}_{A_{Si}}, \Big[1 - \prod_{i=1}^{n}(1-v^2_{A_{Si}})^{w_i}\Big]^{1/2}, \Big[\prod_{i=1}^{n}(1-v^2_{A_{Si}})^{w_i} - \prod_{i=1}^{n}(1-v^2_{A_{Si}}-\pi^2_{A_{Si}})^{w_i}\Big]^{1/2}\Big\} \quad (16)$$

2.2. Spherical Fuzzy AHP

This section covers the steps of the Spherical fuzzy AHP method. Figure 1 represents the steps of the method.

Step 1. Build the hierarchical structure

Step 1 includes establishing a hierarchical structure. The hierarchical structure includes at least 3 levels; aim, which is at the top, attributes identified in the middle and alternatives at the bottom.

Step 2. Establish pairwise comparisons using spherical fuzzy judgment matrices. Table 1 represents the linguistic terms with spherical numbers. After establishing the pairwise comparisons matrices, matrices need to be checked for consistency. For this purpose, linguistic terms are converted to their corresponding score indices, as seen in Table 1. After constructing pairwise comparison matrices, consistency formula, developed by Saaty [22], is applied.

Step 3. Compute the criteria and alternatives' local weights including spherical information.

In this step, Equation (17) is utilized to get local weight of each alternative.

$$SWAM_w(A_{S1},\ldots\ldots,A_{Sn}) = w_1A_{S1} + w_2A_{S2}+\ldots\ldots+w_nA_{Sn} =$$

$$\left\langle [1-\prod_{i=1}^{n}(1-\mu_{A_{Si}}^2)^{w_i}]^{1/2}, \prod_{i=1}^{n} v_{A_{Si}}^{w_i}, [\prod_{i=1}^{n}(1-\mu_{A_{Si}}^2)^{w_i} - \prod_{i=1}^{n}(1-\mu_{A_{Si}}^2-\pi_{A_{Si}}^2)^{w_i}]^{1/2}\right\rangle \quad (17)$$

where $w = 1/n$.

Step 4. Calculate the spherical global weights.

In this step, Equation (18) is utilized to get Spherical fuzzy global weights.

$$\prod_{j=1}^{n}\tilde{A}_{S_{ij}} = \tilde{A}_{S_{i1}} \otimes \tilde{A}_{S_{i2}}\ldots\otimes \tilde{A}_{S_{in}}\ \forall i$$

$$i.e.\ \tilde{A}_{S_{11}} \otimes \tilde{A}_{S_{12}} = \left\langle \mu_{\tilde{A}_{S_{11}}}\mu_{\tilde{A}_{S_{12}}}, \left(v_{\tilde{A}_{S_{11}}}^2 + v_{\tilde{A}_{S_{12}}}^2 - v_{\tilde{A}_{S_{11}}}^2 v_{\tilde{A}_{S_{12}}}^2\right)^{1/2}, \left(\left(1-v_{\tilde{A}_{S_{12}}}^2\right)\pi_{\tilde{A}_{S_{11}}}^2 + \left(1-v_{\tilde{A}_{S_{11}}}^2\right)\pi_{\tilde{A}_{S_{12}}}^2 - \pi_{\tilde{A}_{S_{11}}}^2\pi_{\tilde{A}_{S_{12}}}^2\right)^{1/2}\right\rangle \quad (18)$$

Then, the final score of each alternative is determined via Equation (19).

$$\tilde{F} = \sum_{j=1}^{n}\tilde{A}_{S_{ij}} = \tilde{A}_{S_{i1}} \oplus \tilde{A}_{S_{i2}}\ldots\oplus \tilde{A}_{S_{in}}\forall i$$

$$i.e.\ \tilde{A}_{S_{11}} \oplus \tilde{A}_{S_{12}} = \left\langle \left(\mu_{\tilde{A}_{S_{11}}}^2 + \mu_{\tilde{A}_{S_{12}}}^2 - \mu_{\tilde{A}_{S_{11}}}^2\mu_{\tilde{A}_{S_{12}}}^2\right)^{1/2}, v_{\tilde{A}_{S_{11}}}v_{\tilde{A}_{S_{12}}}, \left(\left(1-\mu_{\tilde{A}_{S_{12}}}^2\right)\pi_{\tilde{A}_{S_{11}}}^2 + \left(1-\mu_{\tilde{A}_{S_{11}}}^2\right)\pi_{\tilde{A}_{S_{12}}}^2 - \pi_{\tilde{A}_{S_{11}}}^2\pi_{\tilde{A}_{S_{12}}}^2\right)^{1/2}\right\rangle \quad (19)$$

Table 1 Linguistic Scale

Linguistic Expression	(μ, v, π)	**Score Index (SI)**
Extremely preferred (ExP)	(0.9,0.1,0.0)	9
Very strongly preferred (VSP)	(0.8,0.2,0.1)	7
Strongly preferred (SP)	(0.7,0.3,0.2)	5
Moderately preferred (MP)	(0.6,0.4,0.3)	3
Equally preferred (EP)	(0.5,0.4,0.4)	1
Moderately low preferred (MLP)	(0.4,0.6,0.3)	1/3
Low preferred (LP)	(0.3,0.7,0.2)	1/5
Very low preferred (VLP)	(0.2,0.8,0.1)	1/7
Extremely low preferred (ELP)	(0.1,0.9,0.0)	1/9

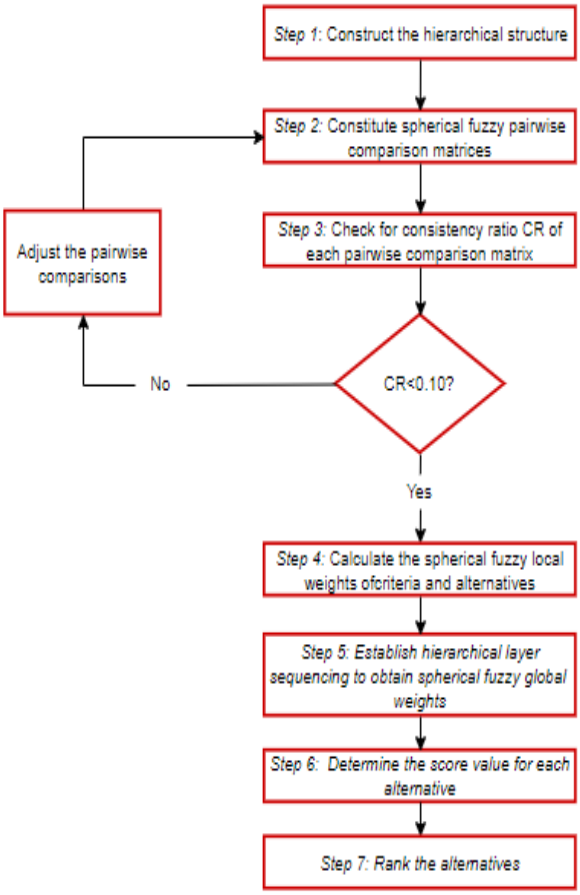

Figure 1 The steps of the Spherical fuzzy AHP [33]

Step 5. The final score of each alternative is defuzzified by using the score function by Equation (20).

$$S(\tilde{w}_j^s) = \sqrt{\left|100 * \left[\left(3\mu_{\tilde{A}_s} - \frac{\pi_{\tilde{A}_s}}{2}\right)^2 - \left(\pi_{\tilde{A}_s} - \frac{v_{\tilde{A}_s}}{2}\right)^2\right]\right|} \quad (20)$$

Step 6. At the last step, the alternatives are ordered according to their defuzzified final scores in descending order.

3. THE RESEARCH FINDINGS AND DISCUSSION

In this part of the paper, the mask selection problem is handled by spherical AHP method. As the determined criteria contains both tangible and intangible data, we use Spherical data in mask selection problem. Moreover, the mask selection problem is handled with hierarchical structure. Therefore, using Spherical AHP method is useful to overcome the mask selection problem.

First, the masks are determined for public consumption. The determined four different alternatives are as follows; A_1: N95 mask, A_2: Cloth mask, A_3: FFP1 mask, A_4: Surgical mask. After a literature review, six criteria have been determined. Criteria are Fluid Resistance (C_1), Breathability (C_2), Reusability (C_3), and Ergonomic design (C_4), Bacterial filtration (C_5), Particulate filtration (C_6). Pairwise comparison matrices are fulfilled by us after gathering data from different mask users' experience.

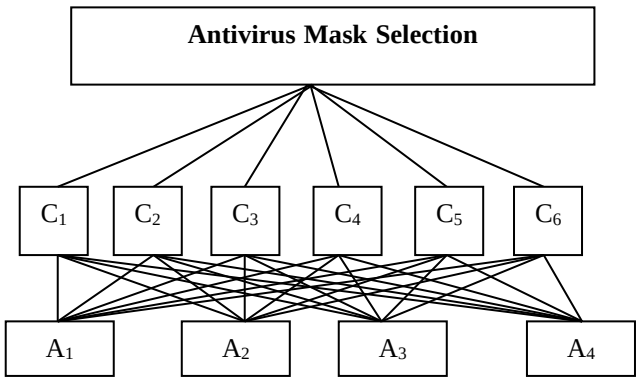

Figure 2 The hierarchical structure

Step 1. The hierarchical structure is established as seen in Figure 2.

Step 2. Pairwise comparisons are established as seen in Tables 2-8. Tables 2-8 also includes spherical weights ($\tilde{w}^s$) and crisp weights ($\bar{w}^s$), and consistency ratios (CR).

Table 2 Pairwise comparison of criteria

Criteria	**C_1**	**C_2**	**C_3**
C_1	EP	MP	VSP
C_2	MLP	EP	MP
C_3	VLP	MLP	EP
C_4	MLP	EI	VSP
C_5	EP	MP	VSP
C_6	MLP	MP	SP
Criteria	**C_4**	**C_5**	**C_6**
C_1	MP	EP	MP
C_2	EP	MLP	MLP
C_3	VLP	VLP	LP
C_4	EP	MLP	MLP
C_5	MP	EP	MP
C_6	MP	MLP	EP
	$\widetilde{w}^s$	**$\bar{w}^s$**	**CR**
C_1	(0.36, 0.72, 0.26)	0.207	0.055
C_2	(0.27, 0.79, 0.25)	0.147	
C_3	(0.18, 0.87, 0.17)	0.080	
C_4	(0.32, 0.76, 0.24)	0.182	
C_5	(0.35, 0.71, 0.28)	0.204	
C_6	(0.31, 0.76, 0.25)	0.179	

Table 3 Pairwise comparison of alternatives according to C_1

C_1	**A_1**	**A_2**	**A_3**	**A_4**
A_1	EP	VSP	SP	SP
A_2	VLP	EP	MLP	MLP
A_3	LP	MP	EP	LP
A_4	LP	MP	SP	EP
	$\widetilde{w}^s$		**$\bar{w}^s$**	**CR**
A_1	(0.70, 0.29, 0.22)		0.345	0.027
A_2	(0.39, 0.58, 0.30)		0.180	
A_3	(0.45, 0.53, 0.30)		0.212	
A_4	(0.59, 0.40, 0.26)		0.288	

Table 4 Pairwise comparison of alternatives according to C_2

C_2	**A_1**	**A_2**	**A_3**	**A_4**
A_1	EP	MP	ExP	VSP
A_2	MLP	EP	MP	SP
A_3	ELP	MLP	EP	MLP
A_4	VLP	LP	MP	EP
	$\widetilde{w}^s$		**$\bar{w}^s$**	**CR**
A_1	(0.76, 0.24, 0.206)		0.379	0.096
A_2	(0.57, 0.41, 0.30)		0.273	
A_3	(0.39, 0.60, 0.31)		0.176	
A_4	(0.44, 0.55, 0.29)		0.206	

Table 5 Pairwise comparison of alternatives according to C_3

C_3	**A_1**	**A_2**	**A_3**	**A_4**
A_1	EP	MP	LP	MLP
A_2	MLP	EP	VLP	LP
A_3	SP	VSP	EP	MP
A_4	MP	SP	MLP	EP
	$\widetilde{w}^s$		**$\bar{w}^s$**	**CR**
A_1	(0.47, 0.51, 0.31)		0.219	0.043
A_2	(0.37, 0.61, 0.28)		0.170	
A_3	(0.67, 0.31, 0.25)		0.331	
A_4	(0.57, 0.41, 0.30)		0.273	

Table 6 Pairwise comparison of alternatives according to C_4

C_4	**A_1**	**A_2**	**A_3**	**A_4**
A_1	EP	SP	VSP	MP
A_2	LP	EP	MP	LP
A_3	VLP	MLP	EP	LP
A_4	MLP	SP	SP	EP
	$\widetilde{w}^s$		**$\bar{w}^s$**	**CR**
A_1	(0.67, 0.31, 0.25)		0.331	0.086
A_2	(0.45, 0.53, 0.30)		0.212	
A_3	(0.37, 0.61, 0.28)		0.170	
A_4	(0.60, 0.38, 0.27)		0.292	

Table 7 Pairwise comparison of alternatives according to C_5

C_5	**A_1**	**A_2**	**A_3**	**A_4**
A_1	EP	SP	VSP	SP
A_2	LP	EP	MLP	MLP
A_3	VLP	MP	EP	EP
A_4	VLP	MP	EP	EP
	$\widetilde{w}^s$		**$\bar{w}^s$**	**CR**
A_1	(0.70, 0.29, 0.23)		0.345	0.081
A_2	(0.41, 0.56, 0.31)		0.187	
A_3	(0.48, 0.48, 0.33)		0.223	
A_4	(0.49, 0.46, 0.34)		0.228	

Table 8 Pairwise comparison of alternatives according to C_6

C_6	**A_1**	**A_2**	**A_3**	**A_4**
A_1	EP	EP	SP	MP
A_2	EP	EP	MLP	MLP
A_3	VLI	SMI	EP	MLP
A_4	MLP	MP	MP	EP
	$\widetilde{w}^s$		**$\bar{w}^s$**	**CR**
A_1	(0.59, 0.37, 0.32)		0.279	0.047
A_2	(0.45, 0.49, 0.35)		0.206	
A_3	(0.47, 0.51, 0.31)		0.219	
A_4	(0.54, 0.44, 0.32)		0.252	

Step 3. Spherical fuzzy local weights of alternatives are calculated as seen Table 9.

Table 9 Spherical fuzzy weighted matrix

Alternatives	**C1**	**C2**
A1	(0.25, 0.75, 0.29)	(0.20, 0.80, 0.27)
A2	(0.14, 0.83, 0.29)	(0.15, 0.83, 0.29)
A3	(0.16, 0.81, 0.30)	(0.10, 0.87, 0.27)
A4	(0.21, 0.77, 0.30)	(0.12, 0.86, 0.27)
	C3	**C4**
A1	(0.08, 0.91, 0.21)	(0.21, 0.79, 0.28)
A2	(0.07, 0.92, 0.19)	(0.14, 0.83, 0.27)
A3	(0.12, 0.89, 0.20)	(0.12, 0.86, 0.26)
A4	(0.10, 0.90, 0.21)	(0.19, 0.80, 0.28)
	C5	**C6**
A1	(0.25, 0.74, 0.31)	(0.18, 0.80, 0.31)
A2	(0.14, 0.81, 0.31)	(0.14, 0.82, 0.31)
A3	(0.17, 0.79, 0.33)	(0.15, 0.83, 0.29)
A4	(0.17, 0.78, 0.33)	(0.17, 0.81, 0.30)

Step 4 and Step 5. Spherical fuzzy global preference weights and defuzzified values of final scores of each alternative can be seen in Table 10.

Table 10 Defuzzified final score values and ranking of alternatives

	Total	**Total**	**Ranking**
A1	(0.48, 0.25, 0.72)	7.379	1
A2	(0.32, 0.35, 0.47)	3.965	3
A3	(0.33, 0.35, 0.47)	4.159	4
A4	(0.39, 0.30, 0.46)	5.498	2

Step 6. Alternatives are ranked in descending order according to the defuzzified final scores

Alternative 1 > Alternative 4 > Alternative 3 > Alternative 2

Alternative 1 is chosen the best according to the ranking scores.

4. ENTROPY BASED SPHERICAL FUZZY AHP

In this section of the paper, we insert the entropy theory into the Spherical fuzzy AHP method. In decision-making problems, entropy theory is used to determine how much useful information the existing data have. We used a combination of fuzzy logic and entropy theory to determine the value of information in a spherical fuzzy environment in this article. We propose to use entropy theory to find criteria weight. Therefore, we proposed the entropy formula and weighting formula.

$$E(A_i) = \frac{1}{n}\sum_{i=1}^{n} \frac{\pi^2_{\tilde{A}_S}(u_i)+1-\left|\mu^2_{\tilde{A}_S}(u_i)-v^2_{\tilde{A}_S}(u_i)\right|}{\pi^2_{\tilde{A}_S}(u_i)+1+\left|\mu^2_{\tilde{A}_S}(u_i)-v^2_{\tilde{A}_S}(u_i)\right|}, \forall_i \quad (21)$$

$$d_i = 1 - E(A_i), \forall_i \quad (22)$$

$$w_i = \frac{d_i}{\sum_{i=1}^{n} d_i}, \forall_i \quad (23)$$

The suggested spherical AHP's steps are as follows.

Step 1 and Step 2. The computation algorithm of these steps is similar with Spherical fuzzy AHP.

Step 3 The criteria's weights are determined using Eq. (23). Alternatives' local weights are computed by using Eq. (17).

Step 4. The spherical global weights are computed by using Eq. (24).

$$\tilde{A}_{S_{ij}} = \bar{w}_j \cdot \tilde{A}_{S_i} = \left\langle \left(1-\left(1-\mu^2_{\tilde{A}_S}\right)^{\bar{w}_j}\right)^{1/2}, v^{\bar{w}_j}_{\tilde{A}_S}, \left((1-\mu^2_{\tilde{A}_S}\right)^{\bar{w}_j} - \left(1-\mu^2_{\tilde{A}_S}-\pi^2_{\tilde{A}_S}\right)^{\bar{w}_j}\right)^{1/2} \right\rangle \forall i \quad (24)$$

Step 5. The final spherical fuzzy AHP scores are obtained by carrying out the spherical fuzzy arithmetic addition by using Eq. (19).

Step 6 and Step 7. The computation algorithm of these steps is similar with Spherical fuzzy AHP.

The calculation steps of the proposed method are clarified as follows.

Step 1 and Step 2. The hierarchical structure is established as seen in Figure 2 and the pairwise comparisons are established as seen in Tables 2-8.

Step 3. The weights of the criteria are computed by using Eq. (23) below. Table 11 represent the Spherical fuzzy weighted matrix of alternatives.

$w_{C1} = 0.129$ $w_{C2} = 0.118$ $w_{C3} = 0.300$
$w_{C4} = 0.154$ $w_{C5} = 0.144$ $w_{C6} = 0.152$

Table 11 Spherical fuzzy weighted matrix

Alternatives	C_1	C_2
A_1	(0.29, 0.85, 0.11)	(0.31, 0.84, 0.11)
A_2	(0.15, 0.93, 0.12)	(0.21, 0.90, 0.13)
A_3	(0.17, 0.92, 0.12)	(0.14, 0.94, 0.12)
A_4	(0.23, 0.89, 0.12)	(0.16, 0.93, 0.11)
	C_3	C_4
A_1	(0.27, 0.82, 0.19)	(0.30, 0.84, 0.13)
A_2	(0.21, 0.86, 0.17)	(0.19, 0.91, 0.13)
A_3	(0.41, 0.71, 0.18)	(0.15, 0.93, 0.12)
A_4	(0.33, 0.77, 0.20)	(0.26, 0.86, 0.14)
	C5	C6
A_1	(0.30, 0.84, 0.12)	(0.25, 0.86, 0.16)
A_2	(0.16, 0.92, 0.13)	(0.19, 0.90, 0.16)
A_3	(0.19, 0.90, 0.15)	(0.19, 0.90, 0.14)
A_4	(0.20, 0.89, 0.15)	(0.22, 0.88, 0.15)

Step 4 and Step 5. Spherical fuzzy global preference weights and defuzzified values of final scores of each alternative can be seen in Table 12.

Table 12 Defuzzified final score values and ranking of alternatives

	Total	Total	Ranking
A_1	(0.64, 0.49, 0.14)	11.213	1
A_2	(0.44, 0.65, 0.22)	5.317	4
A_3	(0.53, 0.57, 0.21)	8.363	3
A_4	(0.55, 0.55, 0.20)	8.954	2

Step 6. Alternatives are ranked in descending order according to the defuzzified final scores

Alternative 1 > Alternative 4 > Alternative 3 > Alternative 2

Alternative 1 is chosen the best according to the ranking scores. As seen in step 6, the ranking of Alternative 3 and Alternative 2 is different in Spherical fuzzy AHP and an entropy based spherical Fuzzy AHP method. We discuss the reason of this situation in Section 6.

5. SENSITIVITY ANALYSIS

We applied sensitivity analysis in this section to illustrate how our model is susceptible to changes in criteria weights. We assign different weights to the criteria and observe the changes in ranking results of alternatives. The various crisp weights of parameters as seen in Table 13 and Figure 3 illustrates the results of the sensitivity analysis.

Table 13 Cases with different criteria weights

Cases	Criteria weights
Case 1	(0.40, 0.15, 0.15, 0.10, 0.10, 0.10)
Case 2	(0.10, 0.40, 0.10, 0.15, 0.10, 0.15)
Case 3	(0.10, 0.10, 0.50, 0.15, 0.05, 0.10)
Case 4	(0.05, 0.05, 0.30, 0.40, 0.10, 0.10)
Case 5	(0.10, 0.10, 0.60, 0.05, 0.05, 0.10)
Case 6	(0.10, 0.05, 0.35, 0.30, 0.10, 0.10)

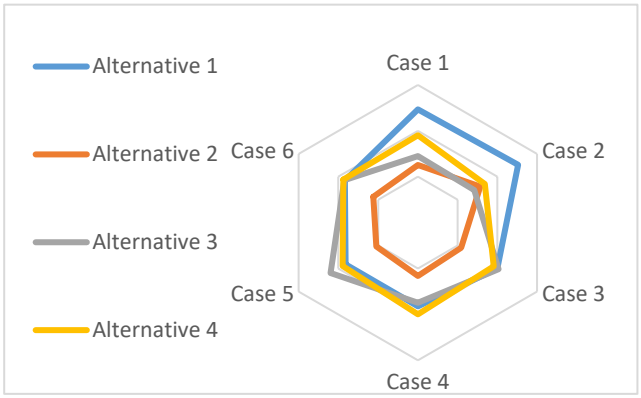

Figure 3 Sensitivity analysis

We get different outcomes for different situations in the sensitivity study. For example, in Case 3, if the third parameter is given the maximum weight, Alternative 3 is ranked first among alternatives, while it is ranked third in Case 1. In Case 4, if the fourth parameter is given the maximum weight, Alternative 4 is ranked first among alternatives, while it is ranked second in Case 1. As seen sensitivity analysis, third and fourth criteria have big impact on ranking alternatives. When we assign large weights to them, Alternative 3 and Alternative 4 can get the first rank. We can infer that the model is susceptible to changes based on the findings of the sensitivity analysis.

6. RESULTS

The COVID-19 is much more contagious, despite sharing common properties with other deadly coronaviruses, and has been the greatest threat to healthcare systems in many nations, including the developed ones with the most modern healthcare facilities. Infection prevention is the key to

reducing the harm done by the COVID-19 before vaccines and/or specific medications are available [29]. This can be achieved by isolation, supportive treatment, and self-protection. In this manner, using anti-virus masks plays a major role in protecting against the COVID-19.

The sector in which the person using the mask works is important for the mask selection. Moreover, the mask selection problem not only contains quantitative factors and but also contains qualitative factors. In this paper, we deal with the mask selection problem with qualitative factors. To do this aim, we determined 4 different alternatives and 6 conflicting criteria. We gathered the data under spherical information; therefore, we implemented the Spherical fuzzy AHP method to the problem. Finally, alternatives are ranked according to their final scores and the N95 masks get the first rank according to the criteria. Surgical masks get the second rank, FFP1 masks get the third rank and Cloth masks get the fourth rank.

In this paper, we also proposed an entropy based Spherical fuzzy AHP method to overcome the mask selection problem. First, we utilized entropy theory to get the criteria weights. Then we calculate the final scores of alternatives and rank them. We observe that the proposed method gives same ranking results with Spherical AHP method. However, the proposed method gives more sensitive results by comparison the Spherical AHP method. The reason of this, the entropy theory calculates how much valuable knowledge the current data provide. Therefore, the proposed model more sensitive than the Spherical fuzzy AHP method.

Ultimately, we can summarize the practical benefits of the proposed method as follows i) if the data is gathered under spherical environment ii) if the demonstration of the problem can be structured as a hierarchy iii) if the decision maker needs to calculate the how much valuable knowledge the current data provide, then using the proposed method gives effective and efficient results.

In future studies, new criteria can be determined for the problem, and the Spherical AHP method can be applied by more criteria. Also, new types of fuzzy extensions can be applied to the problem such as neutrosophic fuzzy sets, q-rung orthopair fuzzy, picture fuzzy sets, etc.

Funding

The authors have not received any financial support for the research, authorship or publication of this study.

The Declaration of Conflict of Interest/ Common Interest

No conflict of interest or common interest has been declared by the authors

Authors' Contribution

The authors contributed equally to the study.

The Declaration of Ethics Committee Approval

This study does not require ethics committee permission or any special permission.

The Declaration of Research and Publication Ethics

The authors of the paper declare that they comply with the scientific, ethical and quotation rules of SAUJS in all processes of the paper and that they do not make any falsification on the data collected. In addition, they declare that Sakarya University Journal of Science and its editorial board have no responsibility for any ethical violations that may be encountered, and that this study has not been evaluated in any academic publication environment other than Sakarya University Journal of Science.

REFERENCES

[1] D. Cucinotta, and M. Vanelli, "WHO declares COVID-19 a pandemic", Acta Biomed, vol. 91 no.1, pp 57-160, 2020.

[2] https://www.bbc.com/news/world-51235105. Access date: 31.01.2021.

[3] B. W. Schuller, D. M. Schuller, K. Qian, J. Liu, H. Zheng, X. Li, "Covid-19 and computer audition: An overview on what speech and sound analysis could contribute in the sars-Cov-2 corona crisis", ArXiv preprint arXiv:2003.11117, 2020.

[4] https://www.who.int/health topics/coronavirus. Access date: 31.01.2021.

[5] General Secretariat for National Defence "National plan for the prevention and control of influenza pandemic", General Secretariat for National Defence Report Plan, Paris, pp.1-78, 2007.

[6] The Department of Health and Ageing, "Australian health management plan for pandemic influenza: important information for all Australians", Canberra: Department of Health and Ageing, Australian Health Management Plan, Australia, pp. 1-232, 2006.

[7] United States Department of Health and Human Services, "Department of health and human services", HHS pandemic influenza plan. Washington, pp.1-396, 2005.

[8] C.R. MacIntyre, S. Cauchemez, D.E. Dwyer, H. Seale, P. Cheung, G. Browne, M. Fasher, J. Wood, Z. Gao, R. Booy, N. Ferguson, "Face mask use and control of respiratory virus transmission in households", Emerging Infectious Diseases, vol. 15, no.2, pp. 233–41, 2009.

[9] N.C.J. Brienen, A. Timen, J. Wallinga, J.E. Van Steenbergen, P.F.M. Teunis, "The effect of mask use on the spread of influenza during a pandemic", Risk Anal, vol. 30 no. 8, pp. 1210–8, 2009.

[10] L.A. Zadeh, "Fuzzy sets", In Fuzzy sets, Fuzzy logic, and Fuzzy systems, vol. 6, pp. 394-432, 1996.

[11] P. P. Bonissone, "A fuzzy sets based linguistic approach: theory and applications", Institute of Electrical and Electronics Engineers (IEEE), pp. 99-111,1980.

[12] S. Zeng, M. Qiyas, M. Arif, T. Mahmood, "Extended version of linguistic picture fuzzy TOPSIS method and its applications in enterprise resource planning systems", Mathematical Problems in Engineering, vol. 2019, Article ID 8594938, 2019.

[13] A. A. Khan, M. Qiyas, S. Abdullah, J. Luo, M. Bano, "Analysis of Robot Selection Based on 2-Tuple Picture Fuzzy Linguistic Aggregation Operators", Mathematics vol.7, no. 10 pp.1000-1019, 2019.

[14] M. Qiyas, S. Abdullah, S. Ashraf, L. Abdullah, "Linguistic picture fuzzy Dombi aggregation operators and their application in multiple attribute group decision making problem", Mathematics, vol. 7, no.8, pp.764-786, 2019.

[15] M. Qiyas, S. Abdullah, S. Ashraf, M. Aslam, "Utilizing linguistic picture fuzzy aggregation operators for multiple-attribute decision-making problems", International Journal of Fuzzy Systems, vol.22, no. 1, pp.310-320, 2020.

[16] M. Qiyas, S. Abdullah, S. Ashraf, S. Khan, A. Khan, "Triangular picture fuzzy linguistic induced ordered weighted aggregation operators and its application on decision making problems", Mathematical Foundations of Computing, vol. 2, no. 3, pp.183-201, 2019.

[17] S. Ashraf, S. Abdullah, S. Khan, "Fuzzy decision support modeling for internet finance soft power evaluation based on sine trigonometric Pythagorean fuzzy information" Journal of Ambient Intelligence and Humanized Computing, vol. 12, no. 2, pp. 3101-3119, 2021.

[18] K. Atanassov, "Intuitionistic fuzzy sets", International Journal Bioautomation, vol. 20, no. 1, 2016.

[19] R.R. Yager, "Pythagorean fuzzy subsets". In 2013 Joint Ifsa World Congress and Nafips Annual Meeting, Edmonton, AB, Canada, pp. 57-61, 2013.

[20] R.R. Yager, "Generalized orthopair fuzzy sets", IEEE Transactions on Fuzzy Systems, vol. 25, no. 5, pp. 1222-1230, 2016.

[21] F. Kutlu Gündoğdu, C. Kahraman, "Spherical fuzzy sets and spherical fuzzy TOPSIS method", Journal of Intelligent and Fuzzy Systems, vol. 36, no.1, pp. 337-352, 2019.

[22] T.L. Saaty, The Analytic Hierarchy Process, McGraw- Hill, New York pp.78-99, 1980.

[23] T.L. Saaty, "Decision making with dependence and feedback: The analytic network process" (Vol. 4922). Pittsburgh: RWS publications, 1996.

[24] G.H. Tzeng, J.J. Huang, "Multiple Attribute Decision Making: Methods and Applications". Springer-Verlag Berlin Heidelberg, pp. 69-76, 2011.

[25] B. Roy, "Classement et choix en présence de points de vue multiples", Revue Française D'informatique et de Recherche Opérationnelle, vol.2, no. 8, pp. 57-75, 1968.

[26] Z. Yang, X. Li, H. Garg, M. Qi, "Decision support algorithm for selecting an antivirus mask over COVID-19 pandemic under spherical normal fuzzy environment", International Journal of Environmental Research and Public Health, vol. 17, no. 10, pp. 3407-3418, 2020.

[27] G. Shahzadi, M. Akram, "Group decision-making for the selection of an antivirus mask under fermatean fuzzy soft information", Journal of Intelligent and Fuzzy Systems, (Preprint), pp. 1-16, 2021.

[28] D. Wang, Y. You, X. Zhou, Z. Zong, H. Huang, H. Zhang, X. Yong, Y. Cheng, L. Yang, Q. Guo, Y. Long, Y. Liu, J. Huang, L. Du, "Selection of homemade mask materials for preventing transmission of COVID-19: A laboratory study", Plos One, vol. 15, no. 10, e0240285, 2020.

[29] D.S.C. Lam, R.L.M. Wong, K.H.W. Lai, C.N. Ko, H.Y. Leung, V.Y.W. Lee, J.Y.N.M. Lau, S.S. Huang, "COVID-19: special precautions in ophthalmic practice and FAQs on personal protection and mask selection", Asia-Pacific Journal of Ophthalmology, vol.9, no. 2, pp. 67-77 2020.

[30] S. Feng, C. Shen, N. Xia, W. Song, M. Fan, B.J. Cowling, "Rational use of face masks in the COVID-19 pandemic", The Lancet Respiratory Medicine, vol. 8, no.5, pp. 434-436, 2020.

[31] S. Q. Zheng, L.Yang, P.X. Zhou, H.B. Li, F. Liu, R.S. Zhao, "Recommendations and guidance for providing pharmaceutical care services during COVID-19 pandemic: A China perspective", Research in Social and Administrative Pharmacy, vol. 17, no. 1, pp. 1819–1824, 2020.

[32] J.J. Bartoszko, M.A.M. Farooqi, W. Alhazzani, M. Loeb, "Medical masks vs N95 respirators for preventing COVID-19 in healthcare workers: A systematic review and meta-analysis of randomized trials", Influenza and Other Respiratory Viruses, vol. 14, no. 4, pp. 365-373, 2020.

[33] F. K. Gündoğdu, C. Kahraman, "A novel spherical fuzzy analytic hierarchy process and its renewable energy application", Soft Computing, vol. 24, no. 6, pp. 4607-4621, 2020.

SAKARYA ÜNİVERSİTESİ
FEN BİLİMLERİ ENSTİTÜSÜ DERGİSİ

Sakarya University Journal of Science
SAUJS

e-ISSN: 2147-835X | Founded: 1997 | Period: Bimonthly | Publisher: Sakarya University
http://www.saujs.sakarya.edu.tr/en/

Title: Extended Back-EMF Based Industrial Sensorless Drive System for PMSMs

Authors: Burak GÖRDÜK, Murat YILMAZ

Recieved: 2021-01-25 01:29:47

Accepted: 2021-07-13 14:12:56

Article Type: Research Article

Volume: 25
Issue: 4
Month: August
Year: 2021
Pages: 1049-1060

How to cite
Burak GÖRDÜK, Murat YILMAZ; (2021), Extended Back-EMF Based Industrial Sensorless Drive System for PMSMs. Sakarya University Journal of Science, 25(4), 1049-1060, DOI: https://doi.org/10.16984/saufenbilder.867649
Access link
http://www.saujs.sakarya.edu.tr/en/pub/issue/64755/867649

Sakarya University Journal of Science 25(4), 1049-1060, 2021

Extended Back-EMF Based Industrial Sensorless Drive System for PMSMs

Burak GÖRDÜK*[1], Murat YILMAZ[1]

Abstract

Field Oriented Control (FOC) of Permanent Magnet Synchronous Motors (PMSM) is utilized in many industrial applications due to its high performance. Semiconductor manufacturers provide specialized solutions and tools for this technique. However, such solutions are protected with closed source codes. This reduces the flexibility and the performance of such systems. This paper presents the conducted studies of controller and embedded software design for FOC of a PMSM using extended back-Electromotive Force (EMF) observer. Observer is derived from motor analytical model. Accurate position and speed estimations are observed using the simulations. An inverter board is obtained from market and a controller board with microcontroller is designed. Extended back-EMF observer model is implemented in embedded software. The developed drive system is fully capable to replace the existing closed source solutions with the benefits of having a robust and flexible structure that can be fine-tuned according to the application. Performance in nominal speed range with no-load and full-load along with transient loading is tested with a 3000 rpm industrial fan motor. The developed drive system is capable to operate down to 200 rpm and maintain stability under load disturbances, compensating the 10% speed error during nominal load transitions in one second.

Keywords: Permanent magnet synchronous motor, field oriented control, sensorless, back-electromotive force, observer

1. INTRODUCTION

Electric motor driven systems became the backbone of the way of life we know today. Countless applications count on electric machines. It is estimated that half of the power generated globally is consumed by electric motors [1]. In many high-tech applications such as defense industry, aerospace, aviation and electric vehicles, nature of the application and sector requires using of the best performing technologies and components. For some other industries such as white and brown goods and industrial applications, domestic and global regulations provide requirements of using efficient and environment-friendly technologies [2]. This high-level specification on drive systems design is then followed as replacing old fashioned induction and DC motors with efficient motors.

Permanent Magnet Synchronous Motors (PMSM) count on permanent magnets placed on rotor for field flux generation. These motors should have a rotating stator field synchronous to rotor field. Thus, using of a driver is necessary with such

* Corresponding author: burakgorduk@gmail.com
[1] Istanbul Technical University, Department of Electrical Engineering, Istanbul, Turkey.
E-Mail: myilmaz@itu.edu.tr
ORCID: https://orcid.org/0000-0002-2333-0649; https://orcid.org/0000-0003-1584-1788.

motors. Objective of the driver is to apply three-phase voltages to stator, which generates a field vector that is perpendicular to rotor field vector in order to generate maximum torque and drive the motor in an efficient way. Nature of these drive systems require accurate rotor position information. This information can be obtained by utilizing sophisticated position sensors like Hall-effect sensors, encoders and resolvers. Although these sensors provide position information that is crucial for vector control, an undeniable burden comes with utilization of position sensors. Increased size, complexity and cost of motor production combined with the increased maintenance frequency due to position sensors, push designers and researches on developing methods of rotor position estimation without position sensors. In many products, especially home appliances, sensorless vector control is much appreciated and used.

Sensorless vector control made its way to literature in late 1980's especially emerging from T. Ohtani's studies [3]. In his proposed method, a rotor flux estimator with a lag circuit imposing the induced voltage of motor and command of the rotor flux, thus enabling calculation of rotor flux even at standstill. He also states his method as being less dependent to motor parameters than conventional vector control strategies. Systems utilizing Model Reference Adaptive Control (MRAC) were also developed for speed estimation from measured voltage and current values [4 - 6]. Estimated speed is then used as feedback of the vector control system. MRAC based systems contain pure integrators that are affected from resistance change due to thermal variations. Change of resistance due to temperature can be compensated using MRAC [7]. F.Z J. Holtz and J. Quan also used pure integrator for stator flux estimation [8]. With the help of a nonlinear inverter model, their model self-adjusted voltage distortions while drift components were compensated by offset identification. This method shown high dynamic performance even at very low speeds but unable to estimate speed at near standstill points.

An additional emphasis should be laid on position estimation schemes used in sensorless vector control. Various types of observers, state filters and controllers are proposed as position estimators. Luenberger type observers can be used in such schemes, providing observation of system state vector while identifying the system parameters [9]. Extended Luenberger observer can be utilized for a nonlinear dynamical system and it observes rotor flux while identifying rotor time constant simultaneously [10]. Luenberger observers are also utilized for back-electromotive force (EMF) and flux linkage estimation [11, 12]. Studies with rotor position estimation based on flux linkages are also presented [13, 14]. Flux linkages are obtained by the use of integrators. The problem with these schemes is that integration drift and offset may eventually degrade the estimator performance [15]. Using of an Extended Kalman Filter (EKF) is proposed to eliminate the errors caused by these drifts and offsets [16]. EKF is utilized for sensorless control of PMSM [17]. Though EKF performs well under nominal conditions, this method has issues at startup due to divergence of the EKF estimator. Moreover, computational complexity of EKF is also a burden to processing power in the digital controller side. Use of Sliding Mode Observers (SMO) is proposed for electric drives due to the benefits of order reducing, disturbance rejection and parameter insensitivity [18 - 20]. Robustness of the controller is supported by the use of adaptive methods in a Brushless DC Motor (BLDC) driver, which filled the gaps of unfavorable aspects of EKF [21]. SMO is further investigated in drive systems of PMSM for back-EMF estimation [22].

This paper presents the studies conducted for designing a sensorless vector control system for PMSMs. The study concentrated on the design of a controller board and requisite software for FOC of a PMSM. Sensorless position estimation is based on a Luenberger type extended back-EMF observer. Theory of the observer is explained in detail with motor mathematical model. Operation of the observer is verified by simulations. Position and speed estimation is found accurate and dynamic. Drive system is then verified by laboratory experiments. A controller board is designed in order to be used with an inverter board. Necessary embedded software is

developed for a 32-bit microcontroller on the controller board. Drive system is operated without position sensors for the whole working range. Loading conditions and transient response of the system is tested. Drive system responded fast and maintained stable operation under load disturbances. At the end of the study, a reusable and reconfigurable drive system is developed. This system can replace the industrial solutions with closed source codes. This provides flexibility and fine-tuning based on the application.

This paper presents the general background and the motivation of the study in Chapter 1. Theory of operation and modeling of PMSM is given in Chapter 2. Chapter 3 provides information on the position and speed estimation using extended back-EMF observer. Simulations of the position estimation scheme are presented in Chapter 4. Chapter 5 explains the hardware and embedded software design of the system. Experimental results are given in detail in Chapter 6.

2. FIELD ORIENTED CONTROL OF PMSM

2.1. Mathematical Model of PMSM

It is useful to analyze electric motors using their mathematical expressions. This is achieved by converting the electrical equivalent model of the motors into mathematical models. Three-phase PMSM can be mathematically modeled with the phase voltages expressed as in equation 1.

$$\begin{bmatrix} u_a \\ u_b \\ u_c \end{bmatrix} = R_S \cdot \begin{bmatrix} i_a \\ i_b \\ i_c \end{bmatrix} + \rho \begin{bmatrix} L_a & M_{ab} & M_{ac} \\ M_{ab} & L_b & M_{bc} \\ M_{ac} & M_{bc} & L_c \end{bmatrix} \cdot \begin{bmatrix} i_a \\ i_b \\ i_c \end{bmatrix} + \begin{bmatrix} L_a & M_{ab} & M_{ac} \\ M_{ab} & L_b & M_{bc} \\ M_{ac} & M_{bc} & L_c \end{bmatrix} \cdot \rho \begin{bmatrix} i_a \\ i_b \\ i_c \end{bmatrix} + \begin{bmatrix} e_a \\ e_b \\ e_c \end{bmatrix} \quad (1)$$

where, u_a, u_b and u_c are the three-phase voltages, i_a, i_b and i_c are the three-phase currents, R_s is the phase resistance, ρ is the derivative operator, Mab, M_{ac} and M_{bc} are the mutual inductances, L_a, L_b and L_c are the self-inductances, e_a, e_b and e_c are the three phase induced back-EMF voltages that are given in equation 2.

$$\begin{bmatrix} e_a \\ e_b \\ e_c \end{bmatrix} = \omega_e \cdot \psi_{PM} \cdot \rho \begin{bmatrix} \cos(\theta_e) \\ \cos(\theta_e - 2\pi/3) \\ \cos(\theta_e + 2\pi/3) \end{bmatrix} \quad (2)$$

where, ω_e is the electrical speed of rotor, Ψ_{PM} is the flux linkage of the permanent magnets and θ_e is the rotor electrical position. Maximum torque is generated when stator field vector is perpendicular to flux linkage of permanent magnets. Considering only the fundamental signals, generated torque on the machine air gap is expressed in equation 3.

$$T_e = \frac{i_a \cdot e_a}{\omega_e} + \frac{i_b \cdot e_b}{\omega_e} + \frac{i_c \cdot e_c}{\omega_e} \quad (3)$$

where, T_e is the electrical torque generated in air gap. In this expression, phase back-EMF waveforms are generated according to winding distributions on the stator and the generated flux according to magnetization technique used on permanent magnets. Stator windings of a PMSM are usually distributed in such a way to generate sinusoidal back-EMF voltage. For the torque equation, phase currents and back-EMFs should match. Otherwise, torque ripple can be generated on the output that is not desired. In order to maintain a smooth torque output, phase currents has to be generated sinusoidal. Electrical torque in the air gap can be coupled with mechanical characteristics of the machine in order to compute operating point of the machine as given in equation 4.

$$J_m \cdot \frac{d}{dt}\omega_e = T_e - T_L - B_m \cdot \omega_e \quad (4)$$

where, J_m is mechanical inertia, B_m is viscous friction coefficient, T_L is mechanical load applied on the shaft.

2.2. PMSM in Rotating Reference Frame

Stator voltage equation of the motor is obtained using Clarke and Park transformations on the fundamental model with the assumption of angle input of the Park transformation is rotor electrical angle. This way, obtained *d-q* axis variables are

defined in a synchronous rotating reference frame. Stator voltage equations are expressed as given in equation 5.

$$\begin{bmatrix} u_d \\ u_q \end{bmatrix} = \begin{bmatrix} R_S & -\omega_e L_q \\ \omega_e L_d & R_S \end{bmatrix} \cdot \begin{bmatrix} i_d \\ i_q \end{bmatrix} + \begin{bmatrix} L_d & 0 \\ 0 & L_q \end{bmatrix} \cdot \rho \begin{bmatrix} i_d \\ i_q \end{bmatrix} + \omega_e \cdot \psi_{PM} \cdot \begin{bmatrix} 0 \\ 1 \end{bmatrix} \quad (5)$$

where, u_d and u_q are the phase voltages, i_d and i_q are the phase currents, L_d and L_q are the inductances in direct and quadrature axis respectively. Electromagnetic torque can be obtained by a simple expression of flux linkages and currents as given in equation 6.

$$T_e = \frac{3}{2} \cdot 2p \cdot \left(\left(L_d - L_q \right) \cdot i_d \cdot i_q + \psi_{PM} \cdot i_q \right) \quad (6)$$

Electromagnetic torque consists of two components. The first term is reluctance torque whereas, the second term represents the synchronous torque. In a PMSM, most of the torque will be generated due to quadrature axis current. Thus, it is fair to assume quadrature-axis current i_q will represent and control the torque output of the machine itself. However, it should be noted that in a highly salient machine as per maximum torque per ampere approach, direct-axis current i_d has to be utilized to generate maximum torque. For most of the applications that use low saliency machines, i_d is kept zero in operations below nominal speed and torque is generated and measured solely by i_q.

FOC exploits the simple mathematical model of PMSM in *d-q* axis and utilizes speed and current controllers in *d-q* coordinate system. A generalized block scheme of FOC is given in Fig. 1. There are 3 PI controllers in this scheme. First PI controller controls the speed and generates i_q reference. Other two PI controllers control the current. Current controllers in synchronous frame outputs voltage references v_d and v_q. These reference values are then transformed into *α-β* coordinate system and applied to stator phases using space vector modulation. Phase currents are then sampled and converted into *d-q* coordinate system. It can be seen that there are two inner loops for current and one outer loop for speed control in a FOC system. Control frequency for the speed loop is generally determined based on the mechanical inertia of the system. Current control loops are related with time constant of the stator phases and usually a lot frequent than speed control loop.

3. EXTENDED BACK-EMF OBSERVER

Extended back-EMF model of the PMSM in *α-β* coordinate system is obtained from the model in *d-q* coordinate system. Phase voltage equation given in equation 5 is re-written with a symmetrical inductance matrix as given in equation 7.

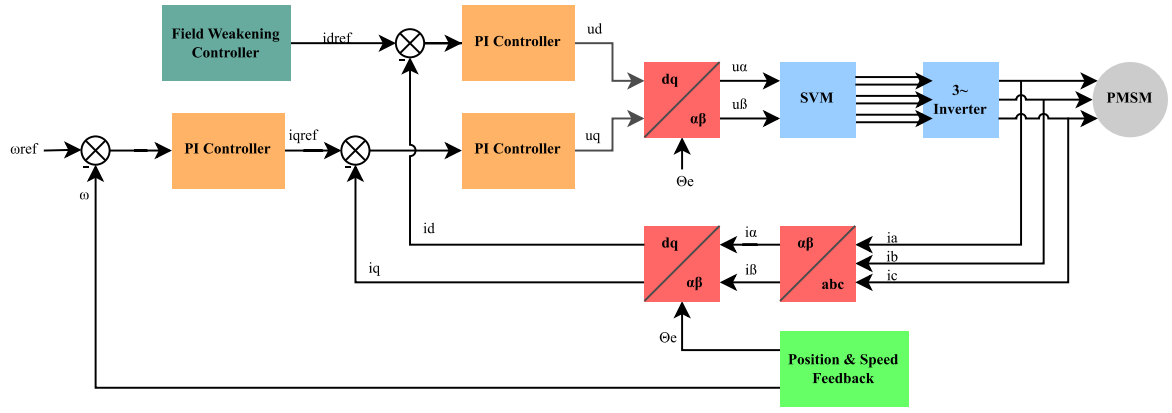

Figure 1 General block diagram of FOC

$$\begin{bmatrix} u_d \\ u_q \end{bmatrix} = \begin{bmatrix} R_S + \rho L_d & -\omega_e L_q \\ \omega_e L_q & R_S + \rho L_d \end{bmatrix} \cdot \begin{bmatrix} i_d \\ i_q \end{bmatrix} + \left(\left(L_d - L_q \right) \cdot \left(\omega_e \cdot i_d - \rho i_q \right) + \omega_e \cdot \psi_{PM} \right) \cdot \begin{bmatrix} 0 \\ 1 \end{bmatrix} \quad (7)$$

Equation 8 is obtained after applying inverse Park transformation.

$$\begin{bmatrix} u_\alpha \\ u_\beta \end{bmatrix} = \begin{bmatrix} R_S + \rho L_d & \omega_e \left(L_d - L_q \right) \\ -\omega_e \left(L_d - L_q \right) & R_S + \rho L_d \end{bmatrix} \cdot \begin{bmatrix} i_\alpha \\ i_\beta \end{bmatrix} + \left(\left(L_d - L_q \right) \cdot \left(\omega_e \cdot i_d - \rho i_q \right) + \omega_e \cdot \psi_{PM} \right) \cdot \begin{bmatrix} -\sin\left(\theta_e\right) \\ \cos\left(\theta_e\right) \end{bmatrix} \quad (8)$$

In this expression, rightmost term can be considered as the extended back-EMF part of the model as it contains crucial information of rotor electrical position.

Equation 8 is then re-arranged with back-EMF term is replaced with back-EMF matrix and the model is transformed into Laplace domain as given in equation 9.

$$\begin{bmatrix} u_\alpha \\ u_\beta \end{bmatrix} = \begin{bmatrix} R_S + sL_d & \omega_e \left(L_d - L_q \right) \\ -\omega_e \left(L_d - L_q \right) & R_S + sL_d \end{bmatrix} \cdot \begin{bmatrix} i_\alpha \\ i_\beta \end{bmatrix} + \begin{bmatrix} e_\alpha \\ e_\beta \end{bmatrix} \quad (9)$$

This relatively easy model to implement estimators and observers will only estimate the extended back-EMF part of the model. Using of a Luenberger observer is very typical for such application that requires state estimation with a feedback observer. In order to obtain rotor position information, two current observers are used in α and β axis. These observers are based on motor model given in equation 9 except the extended back-EMF part is removed from this model. Both observers utilize a compensator that corrects the error between estimated and measured currents. Assuming the observer is stable, current error in steady state will diverge to zero, making the compensators to output the back-EMF part of the model. Compensator outputs *L(α)* and *L(β)* correspond to ($-e_\alpha$) and ($-e_\beta$) respectively.

Control block diagram of the extended back-EMF observer is given in Fig. 2. In this block diagram, estimated state variables are shown as $\hat{\imath}_\alpha$, $\hat{\imath}_\beta$, $\hat{e}_\alpha$ and $\hat{e}_\beta$. They represent the estimation of α-β axis currents and extended back-EMF terms. The compensator block consists of a simple PI controller.

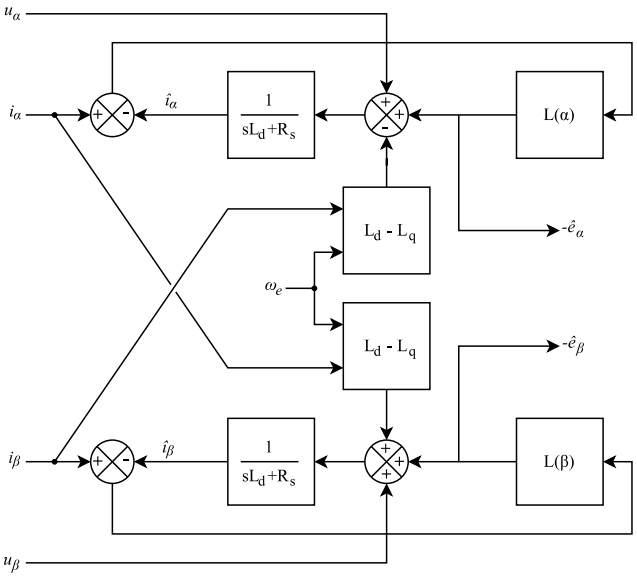

Figure 2 Extended back-EMF observer block diagram

3.1. Angle Tracking Observer

Estimated back-EMF signal obtained from the observer has to be decomposed and rotor position has to be extracted from the back-EMF signals. Many applications utilize an observer for this task. These observers are called as angle-tracking observers. A very simple angle-tracking observer can be implemented using the trigonometric subtraction formula of the sinus signal as given in equation 10.

$$\sin\left(\theta_e\right)\cos\left(\hat{\theta}_e\right) - \cos\left(\theta_e\right)\sin\left(\hat{\theta}_e\right) = \sin\left(\theta_e - \hat{\theta}_e\right) \quad (10)$$

This equation can be made if α and β components of estimated back-EMF signals are considered as sine and cosine values of θ_e. Right hand side of the equation is the sinus function of error between the position of back-EMF signal and estimated

position obtained from angle-tracking observer's output. If this error is small, then this equation can be approximated to position error of the observer as given in equation 11.

$$\sin\left(\theta_e - \hat{\theta}_e\right) \approx \theta_e - \hat{\theta}_e \tag{11}$$

Angle-tracking observer utilizes an integrator coupled with a PI controller for compensation. PI controller clears position error by outputting the estimated rotor electrical position while the integrator provides a filter to the input signal and improves ramp response. For a more practical approach, integrator and PI controller block places are switched. This provides rotor electrical speed as the output of PI controller and rotor electrical position as the output of the integrator. This arrangement is more convenient as it provides smooth information of speed and position simultaneously. Block diagram of the angle-tracking observer is given in Fig. 3.

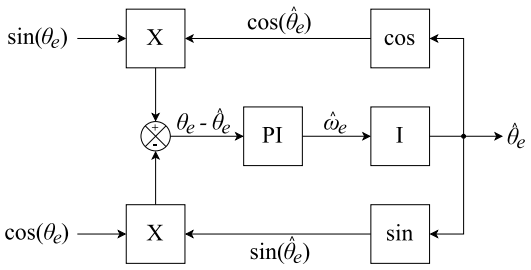

Figure 3 Angle tracking observer block diagram

4. SIMULATION OF THE SENSORLESS DRIVE SYSTEM

In order to verify position estimation schemes, a simulation model is created in MATLAB Simulink (MathWorks, Natick, MA, USA) environment. The motor parameters given in Table 1 are used for the motor model. These motor parameters belong to an actual motor that is used in industrial fan systems, which is then used in experimental work phase of the study. System is modeled and simulated as a continuous system. The simulation starts with no-load and 3000 rpm speed reference. Nominal torque of 0.2 Nm is applied at 0.75 s simulation time. Speed reference is generated by speed ramp generator block. Simulations are done with 6000 rpm/s selected as acceleration and deceleration ratio.

Table 1 Motor parameters

Parameter	Unit	Value
Nominal Voltage	[V]	24
Nominal Current	[A]	3.4
Nominal Power	[W]	62
Nominal Torque	[Nm]	0.2
Peak Torque	[Nm]	0.6
Nominal Speed	[rpm]	3000
Pole Pairs	-	2
Back-EMF Constant	[V.sec/rad]	0.0023
R_S	[Ω]	0.437
L_d	[mH]	0.536
L_q	[mH]	0.548

Speed controller minimizes the error between desired and estimated speed using a PI controller that outputs the i_q reference. Two PI controllers for motor currents are used for compensation that output *d-q* axis voltage references. They are then transformed into three-phase voltages and applied to the stator phases. Output of the extended back-EMF observer are the back-EMF terms. The angle-tracking observer extracts estimated rotor electrical position and speed. Fig. 4 shows the speed estimation performance. Extended back-EMF observer model is given in Fig. 5.

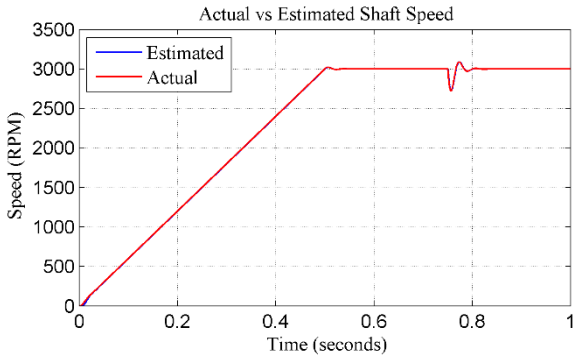

Figure 4 Speed estimation performance

Fig. 6 shows the extended back-EMF estimation with zoomed-in view. Fig. 7 shows the position estimation performance of extended back-EMF observer method.

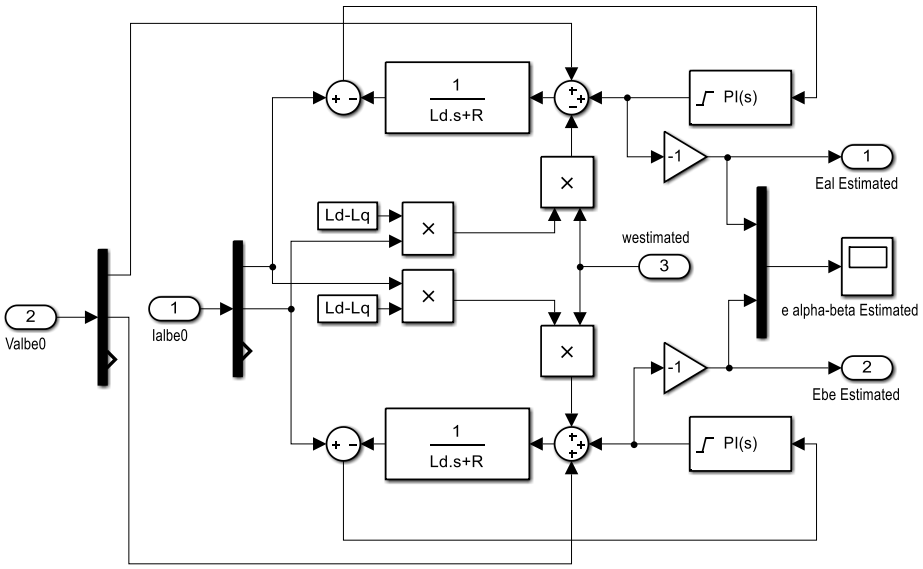

Figure 5 Simulink model of extended back-EMF observer

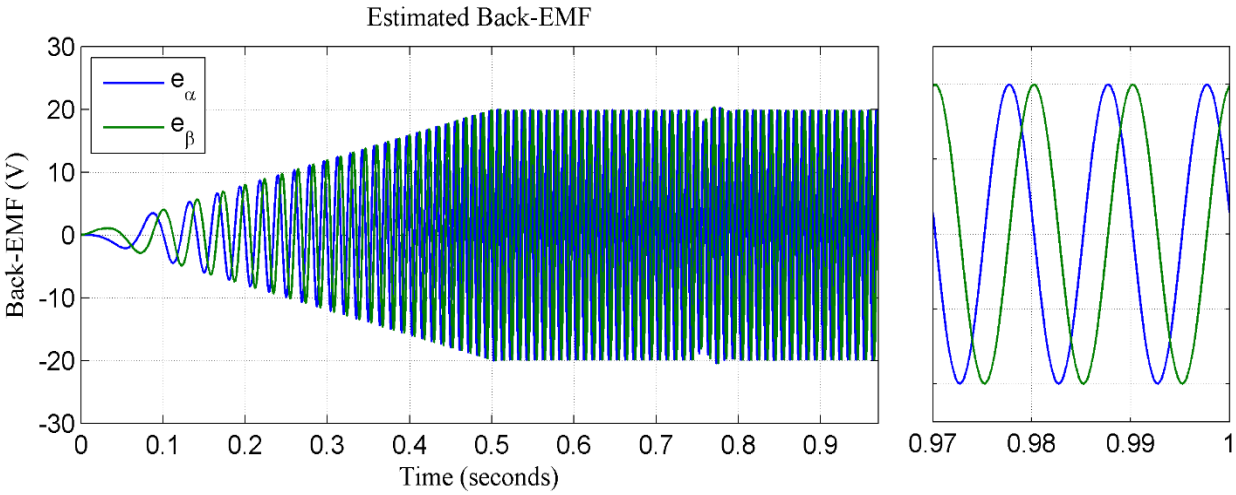

Figure 6 Back-EMF estimation with zoomed-in view

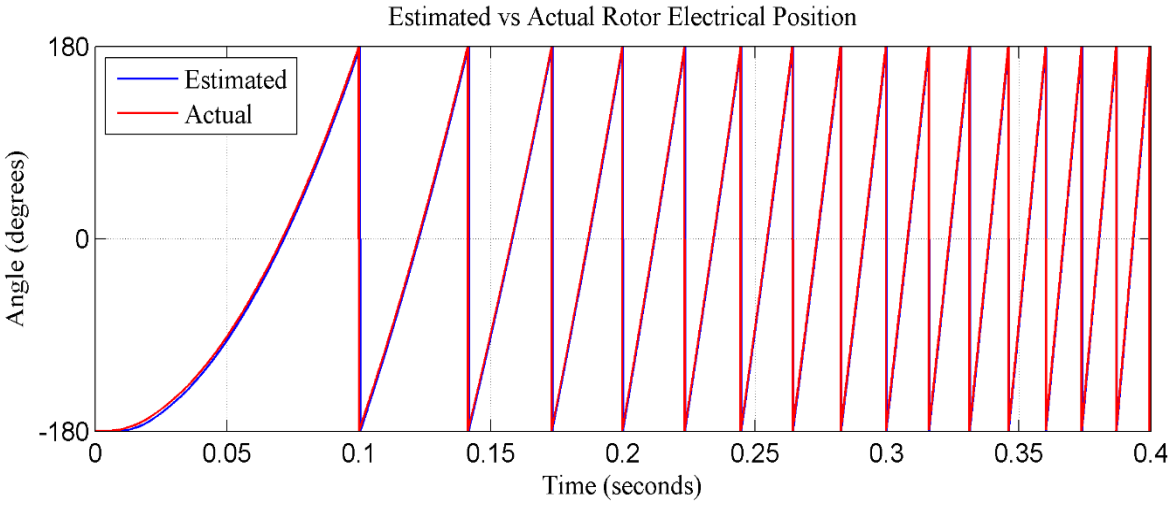

Figure 7 Position estimation performance

It can be said that position estimation is accurate and has a very high dynamic performance. Since the startup is done as open loop, position estimation error from standstill to 200 rpm has no effect on the performance of the control.

Low pass filter used in the angle-tracking observer provides a smooth speed estimation output with no significant delay present. The simulation verifies transient and steady state operation of the extended back-EMF observer with angle-tracking observer.

5. DESIGN OF A SENSORLESS FOC DRIVE

This study concentrates on the design of a controller board and requisite software development for FOC of a PMSM. For the three-phase inverter hardware a ready-to-use development board is selected.

Schematic design of the controller board is made according to the signals that are used in the development board. Two headers are used in order to connect the controller board to the inverter board. Printed circuit board design is done as a two-layer board. Placement of the components is made according to the layout of the inverter board in order to prevent any collisions. Headers are placed according to the headers on the inverter boar so that two boards connect easily. Total size of the controller board is 60 x 96.52 mm. Connection of the controller board with the inverter board is done easily as intended. Inverter board has a switching regulator that generates 5V output from the DC supply voltage and this 5V supply is sent to controller board. A linear regulator is used on controller board in order to generate 3.3V logic power supply that provides power for the microcontroller, operational amplifiers and comparators. Fig. 8 shows the designed drive system. DC input power is supplied to the system via a two-contact screw terminal. Three-phase motor output is connected to a three-contact screw terminal.

Embedded software for FOC is developed. The general structure of the software has multiple Finite State Machine (FSM) structures.

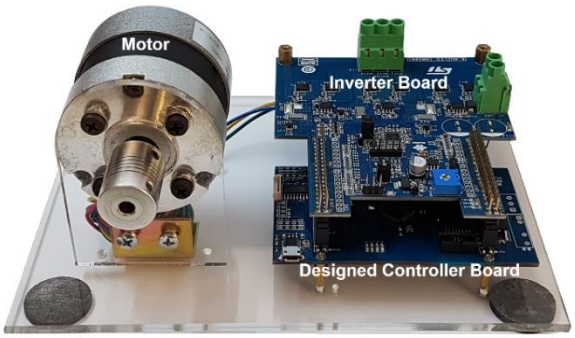

Figure 8 Complete drive system

Main state machine consists of the states “Init”, “Ready”, “Run” and “Fault” as shown in Fig. 9 along with the state transitions.

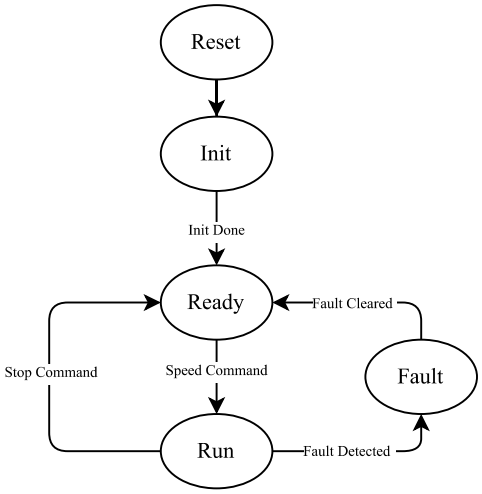

Figure 9 Main state machine diagram

Microcontroller automatically goes through a Power-On Reset (POR) after it is powered up. After the reset microcontroller goes into initialize state. This state defines the functions necessary for initializing requisite microcontroller peripherals such as clock generation, general-purpose timers, pulse width modulation and analog to digital converter. State is automatically changed to ready after initializing is done. When microcontroller is in ready state, speed command is expected as a user input. If a non-zero speed reference is set, then the state transition from ready state to run state is executed.

6. EXPERIMENTAL RESULTS

Experimental verification of the driver system is done by conducted laboratory experiments. The

PMSM with the parameters given in Table 1 is driven with the designed drive system. In order to test dynamic behavior of the system, a test bench that is capable of loading the motor is set up. The test bench consists of a 400V rated PMSM coupled to the driven motor's shaft, which acts as a generator. Output of the generator is rectified using a three-phase rectifier. Obtained DC voltage is then fed into a variable resistor. Setup used for obtaining experimental results is given in Fig. 10.

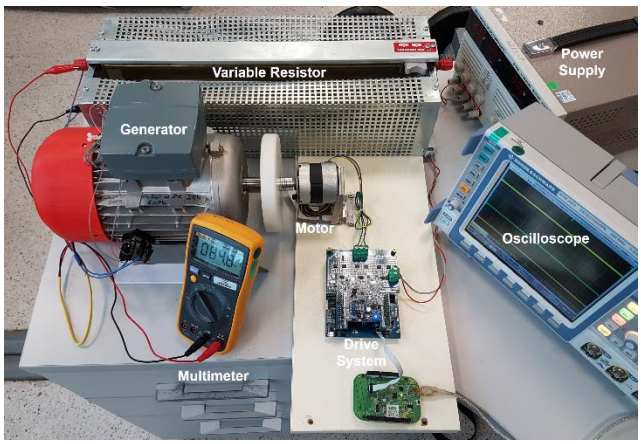

Figure 10 Experimental test setup

Real time control and data acquisition of the drive system is done using a debugging tool. This tool is capable of sampling and modifying software variables along with a recorder functionality that provide time plots of the signals. Performance of the extended back-EMF observer can be obtained from these graphs. The detailed waveforms of the position estimation scheme in nominal speed are given in Fig. 11.

Performance of the drive system is evaluated by two different tests. No load performance of the system is tested first.

a)

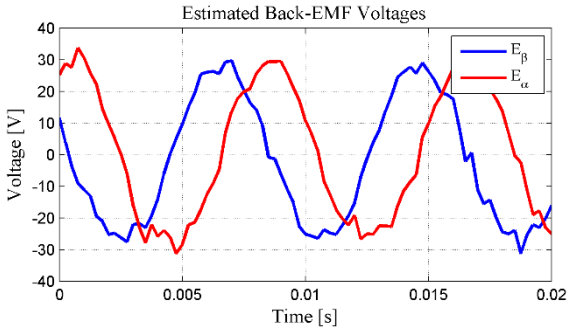

b)

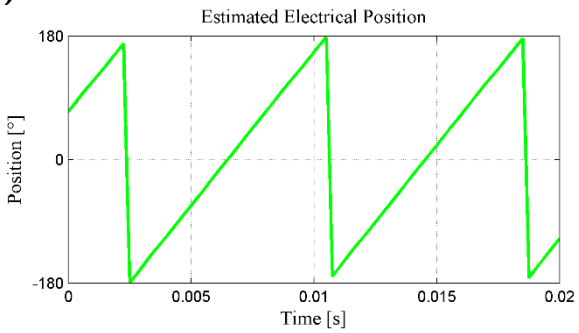

Figure 11 (a) Estimated back-EMF voltages, (b) Estimated electrical position

Applying of nominal speed command with transient changes and speed reversal is tested. Fig. 12 shows the speed ramp and actual shaft speed. Acceleration is set to 2000 rpm/sec. It can be seen that the drive system is capable of following the speed ramp accurately.

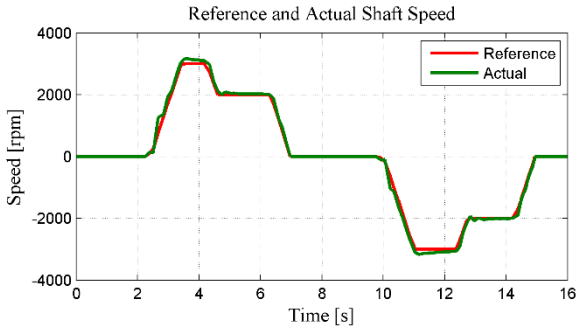

Figure 12 No-load speed control performance

Fig. 13 shows the applied voltages of alpha and beta.

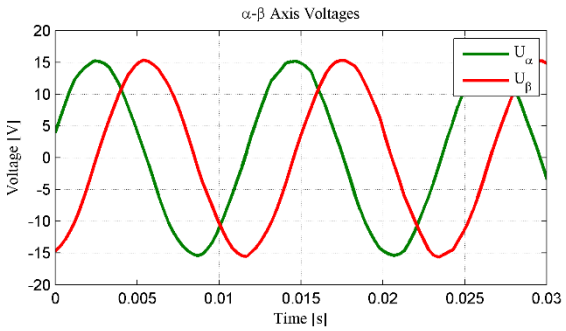

Figure 13 Applied stator voltages in α-β axis

Duty cycles at the output of the space vector modulation corresponding to reference voltages are given in Fig. 14.

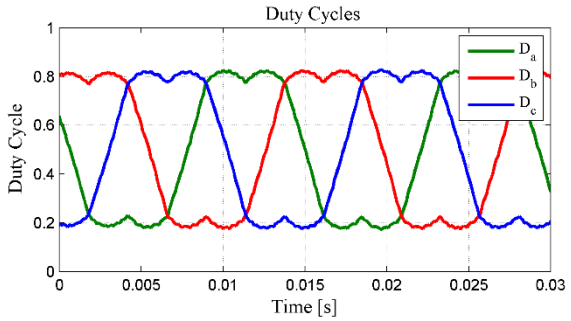

Figure 14 Three-phase duty cycle values

Waveforms of phase currents are shown in Fig. 15.

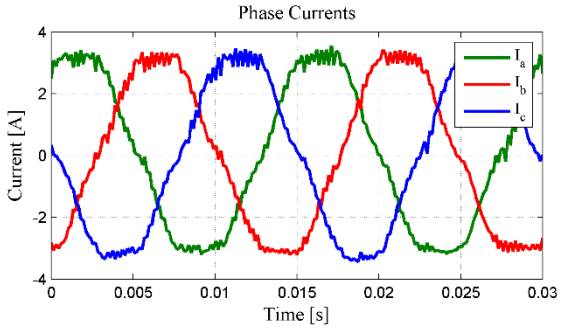

Figure 15 Three-phase currents

Fig. 16 shows the calculated *d-q* axis currents. It can be seen that the i_d is kept at zero while i_q is increased to nominal load current.

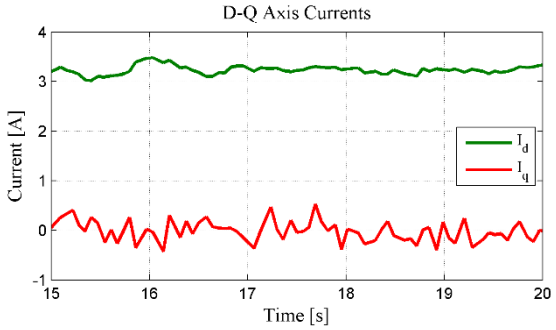

Figure 16 Phase currents in *d-q* axis

The second test for the validation of the drive system performance was the dynamic response of the system under transient changes on load. This transient load change is achieved by switching the variable resistor to a fixed point. Fig. 17 shows the system variables under transient changes. This graph starts with the machine loaded nominally, then when the time stamp shows 8s, connection to the load resistor is switched off. This sudden load change causes an overshoot of 10%. Speed overshoot is compensated within approximately 1 second. At time stamp of around 9.5s machine is again fully loaded. This transient loading cause machine shaft speed to decrease about 10%, which is then compensated in approximately 1 second. It is observed that the system remains stable under transient changes in load.

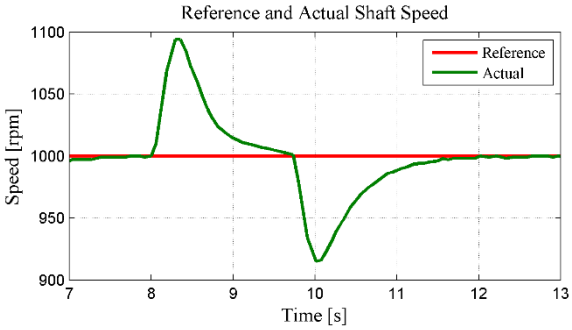

Figure 17 Dynamic performance of the system

7. CONCLUSION

In this study, an industrial-grade sensorless FOC drive system for PMSM using extended back-EMF observer is designed and implemented. Scope of this study covers design of the control stage along with the embedded software. For the sensorless position estimation extended back-EMF observer is analyzed in detail. This observer is a Luenberger type state observer that utilizes the system model inside the controller. State estimation is based on processing measured and known state variables into the system model. Verification of the sensorless position estimation is done using simulations. This is achieved by creating a FOC drive model simulation for extended back-EMF observer. Position estimation is compared with actual position and it is found out that estimation is accurate and dynamic. Sensorless drive system is also implemented in hardware and software. System verification is done by conducting laboratory experiments; 24 V, 62 W, 3000 rpm motor that is been used in industrial fan applications is driven. No-load and full-load performance of the system is tested along with the transient loadings. Transient and steady state response of the system is found stable and dynamic. Along with the succesful results of the experiments, an industrial-grade drive system that is re-configurable and flexible is obtained.

Such a system is capable of replacing existing conservative solutions and thus offer greater customization.

Funding

The author (s) has no received any financial support for the research, authorship or publication of this study.

The Declaration of Conflict of Interest/ Common Interest

No conflict of interest or common interest has been declared by the authors.

Authors' Contribution

The first author contributed 60%, the second author contributed 40% to the study.

The Declaration of Ethics Committee Approval

This study does not require ethics committee permission or any special permission.

The Declaration of Research and Publication Ethics

The authors of the paper declare that they comply with the scientific, ethical and quotation rules of SAUJS in all processes of the paper and that they do not make any falsification on the data collected. In addition, they declare that Sakarya University Journal of Science and its editorial board have no responsibility for any ethical violations that may be encountered, and that this study has not been evaluated in any academic publication environment other than Sakarya University Journal of Science.

REFERENCES

[1] D. Maheswaran, V. Rangaraj, K. K. J. Kailas and W. A. Kumar, "Energy efficiency in electrical systems," 2012 IEEE International Conference on Power Electronics, Drives and Energy Systems (PEDES), pp. 1-6, 2012.

[2] Directive 2009/125/EC of the European Parliament and of the Council of 21 October 2009 establishing a framework for the setting of ecodesign requirements for energy-related products, OJ L 285, pp. 10–35, 2009.

[3] T. Ohtani, N. Takada and K. Tanaka, "Vector control of induction motor without shaft encoder," IEEE Transactions on Industry Applications, vol. 28, no. 1, pp. 157-164, 1992.

[4] C. Schauder, "Adaptive speed identification for vector control of induction motors without rotational transducers," IEEE Transactions on Industry Applications, vol. 28, no. 5, pp. 1054-1061, 1992.

[5] L. Li, X. Guo, P. Zeng, Z. Li, K. Chen and J. Cao, "Sensorless Vector Control for Automotive Auxiliary Motors in the Full Speed Range," 2019 22nd International Conference on Electrical Machines and Systems (ICEMS), pp. 1-4, 2019.

[6] S. Padhy, R. M. Pindoriya, C. Subramanian and Z. Husain, "Encoder-less speed control of PMSM drive using adaptive observer," 2018 IEEMA Engineer Infinite Conference (eTechNxT), pp. 1-6, 2018.

[7] V. Medam, S. Basak, Y. T. Rao and C. Chakraborty, "An adaptive rotor resistance estimation technique for vector controlled induction motor drive suitable for electric vehicle application," IECON 2019 - 45th Annual Conference of the IEEE Industrial Electronics Society, pp. 2604-2609, 2019.

[8] J. Holtz and Juntao Quan, "Sensorless vector control of induction motors at very low speed using a nonlinear inverter model and parameter identification," IEEE Transactions on Industry Applications, vol. 38, no. 4, pp. 1087-1095, 2002.

[9] L. Yan and X. Song, "Design and Implementation of Luenberger Model-Based Predictive Torque Control of Induction Machine for Robustness Improvement," IEEE Transactions on Power Electronics, vol. 35, no. 3, pp. 2257-2262, 2020.

[10] T. Orlowska-Kowalska, "Application of extended Luenberger observer for flux and rotor time-constant estimation in induction motor drives," IEE Proceedings D - Control Theory and Applications, vol. 136, no. 6, pp. 324-330, 1989.

[11] J. Lai, C. Zhou, J. Su, M. Xie, J. Liu and T. Xie, "A Permanent Magnet Flux Linkage Estimation Method Based on Luenberger Observer for Permanent Magnet Synchronous Motor," 2019 22nd International Conference on Electrical Machines and Systems (ICEMS), pp. 1-6, 2019.

[12] F. P. Scalcon, C. J. Volpato, T. Lazzari, T. S. Gabbi, R. P. Vieira and H. A. Gründling, "Sensorless Control of a SynRM Drive Based on a Luenberger Observer with an Extended EMF Model," IECON 2019 - 45th Annual Conference of the IEEE Industrial Electronics Society, pp. 1333-1338, 2019.

[13] M. F. Moussa, Y. Gaber and M. El Attar, "Vector control drive of permanent magnet motor without a shaft encoder," 2008 12th International Middle-East Power System Conference, pp. 249-254, 2008.

[14] G. Chen, S. Yang and J. Chen, "Advantages of Flux-based Position Sensorless Drive for Surface Permanent Magnet Machine," IECON 2019 - 45th Annual Conference of the IEEE Industrial Electronics Society, pp. 899-903, 2019.

[15] G. Chen, J. Chen and S. Yang, "Implementation Issues of Flux Linkage Estimation on Permanent Magnet Machine Position Sensorless Drive at Low Speed," IEEE Access, vol. 7, pp. 164641-164649, 2019.

[16] G. Garcia Soto, E. Mendes and A. Razek, "Reduced-order observers for rotor flux, rotor resistance and speed estimation for vector controlled induction motor drives using the extended Kalman filter technique," IEE Proceedings - Electric Power Applications, vol. 146, no. 3, pp. 282-288, 1999.

[17] M. S. Termizi, J. M. Lazi, Z. Ibrahim, M. H. N. Talib, M. J. A. Aziz and S. M. Ayob, "Sensorless PMSM drives using Extended Kalman Filter (EKF)," 2017 IEEE Conference on Energy Conversion (CENCON), Kuala Lumpur, pp. 145-150, 2017.

[18] V. I. Utkin, "Sliding mode control design principles and applications to electric drives," in IEEE Transactions on Industrial Electronics, vol. 40, no. 1, pp. 23-36, Feb. 1993.

[19] J. Sun, G. Cao, S. Huang and Q. Qian, "A Sliding Mode Observer for Position Estimation of the Planar Switched Reluctance Motor," 2019 IEEE International Electric Machines & Drives Conference (IEMDC), San Diego, CA, USA, pp. 1342-1347, 2019.

SAKARYA ÜNİVERSİTESİ
FEN BİLİMLERİ ENSTİTÜSÜ DERGİSİ

Sakarya University Journal of Science
SAUJS

e-ISSN: 2147-835X | Founded: 1997 | Period: Bimonthly | Publisher: Sakarya University
http://www.saujs.sakarya.edu.tr/en/

Title: Investigation of Cyber-Attack Methods and Measures in Smart Grids

Authors: İsa AVCI

Recieved: 2021-06-22 12:29:25

Accepted: 2021-07-13 15:35:21

Article Type: Research Article

Volume: 25
Issue: 4
Month: August
Year: 2021
Pages: 1061-1074

How to cite
İsa AVCI; (2021), Investigation of Cyber-Attack Methods and Measures in Smart Grids. Sakarya University Journal of Science, 25(4), 1061-1074, DOI: https://doi.org/10.16984/saufenbilder.955914
Access link
http://www.saujs.sakarya.edu.tr/en/pub/issue/64755/955914

Sakarya University Journal of Science 25(4), 1061-1074, 2021

Investigation of Cyber-Attack Methods and Measures in Smart Grids

İsa AVCI*[1]

Abstract

Smart grids have been developing rapidly with the development of technologies in recent years. In the field of critical infrastructures such as natural gas, electricity, water, and energy systems, which are among the smart grids, its use has been increasing in Turkey and all over the world in recent years. With the increase in the use of smart grids, security problems have also gained importance. Cybersecurity attacks against these networks are increasing every year. In this research study, smart cities, smart networks, and the most common cybersecurity attack methods against these systems were investigated. The studies on security in smart grids in the last 10 years have been examined and presented in a table. As a result of these researches, cyber-attacks that are experienced and likely to occur in smart networks were determined. The 20 most used cyber-attack methods were analyzed. In addition, the measures that can be taken against cyber-attacks are analyzed in detail. In addition, in this article, studies on security problems in smart grids are examined and evaluated.

Keywords: Smart grid, smart grid security, cyber-security, security measures

1. INTRODUCTION

Emerging information and communication technologies, in addition to the increasing population in big cities, due to the increase in construction investments and megacities in energy demand, comes to the fore the need for intelligent networks. Optimum operation of the natural gas grid has been a major challenge, particularly in the energy sector, but the fact that this goal can be achieved with the smart grid concept underlines the need to invest in the smart grid concept.

Smart grids have become widespread in the last years with the developing technology, and with the developing technology, the risks and security vulnerabilities that may occur come to the fore. Smart grids especially cover electricity, water, and natural gas networks and their usage areas [1].

It is a fact that cyber-attacks already offer an opportunity in terms of anonymity and deniability. In addition, it is difficult to determine who and who are financed by these attacks and which countries are behind these attacks. Therefore, it is very difficult to determine the risks and threats in cyberspace and to take precautions against them. In such an environment, it is no longer mentioned about ensuring absolute cybersecurity but instead aims to make cybersecurity risks manageable and acceptable. It is recognized that being in an open and connected environment such as the Internet carries some risks associated with increased accessibility. It is

* Corresponding author: drisaavci@gmail.com
[1] Karabuk University, Faculty of Engineering, Karabuk, Turkey.
ORCID: https://orcid.org/0000-0001-7032-8018

imperative to be prepared for cyber incidents by managing these risks with a holistic approach involving all stakeholders and to ensure their continuity by eliminating these incidents with the least damage.

This study aims to assist studies that will conduct research, development, and design, especially on smart grids. First, the definitions of the smart grid and city concepts are made. Then, the most common cyber-attacks in smart networks are given. In addition, academic studies on security and cybersecurity in smart networks are examined and given as a table. Here, the main purpose is to present what studies are carried out on security issues in smart networks and which studies are required.

2. SMART CITY

Smart cities are based on the idea of restructuring the situations of cities in a way that provides maximum efficiency with a focus on people and nature. In addition, smart cities have a human-oriented, strategic, development, change, environment that creates and supports a management approach. Due to these reasons, these cities are city structures with improved service areas and living standards. These structures are based on creating new living spaces that are comfortable, healthy, people-oriented, self-sufficient, where resources are consumed efficiently and intelligently, respectful to nature, environmental problems are minimized by using innovative and sustainable methods.

Smart cities encompass energy infrastructure, traffic management, waste management, health, transportation, water supply, and other services. Thus, a smart city has a mutually beneficial interaction between service providers and citizens. Information and Communication Technologies (ICT) are used to increase the quality, efficiency, and consistency of urban services in smart cities. It also aims to reduce the costs of the smart city and reduce resource consumption and improve communication between citizens and the state. Research on smart cities started in the 2000s and there are many definitions of smart cities. For example, smart cities are defined as the combination of reliable infrastructure, data quality, and corporate infrastructure [2]. The main purpose of the development and dissemination of smart cities;

- Suitability of urban vehicles,
- The elegance of the city administration,
- Habitability of the living space,
- The intelligence of infrastructures,
- Long-term network security effectiveness.

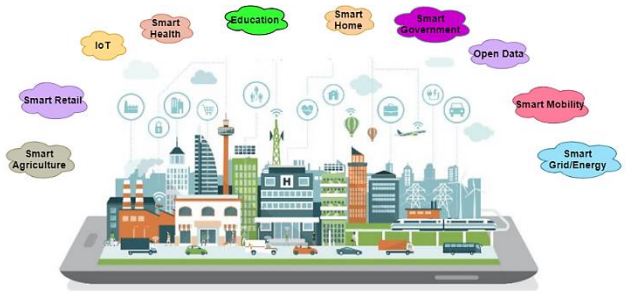

Figure 1 Smart cities overview [3].

The International Telecommunication Union (ITU) analyzed nearly 100 applications and used them to develop the following innovations. Smart, resilient metropolitan areas are modern cities that use ICT and other regulations to make urban operations, utilities, and competitiveness more vibrant and efficient [4].

3. SMART GRID

Infrastructure services are very important as an integral part of urban life. As the urban population continues to increase, control over these facilities becomes critical. Increasing population, Information Technology (IT) makes it impossible to use to manage applications and infrastructure.

The International Electrotechnical Commission (IEC) 61850 standard, which is the smart grid field communication protocol, is the standard protocol for all protection, calculation, testing, and monitoring functions. The fact that the products manufactured by many manufacturers are produced following this protocol protects in terms of security. Otherwise, many different manufacturers cannot use asynchronous or parallel interfaces and protocols. In the technical field, equipment standardization and

interoperability have long been practiced together [5].

Siemens reports on the development of the smart grid and the new energy era, where its goals are diverse, chaotic, and competitive. The smart grid will provide energy stability, flexibility, and efficiency, not overloads, reductions, and blackouts. Mechanization will increase significantly and substations will help reduce preparation and operating expenses and labor intensity. Ongoing comprehensive monitoring will improve the way equipment, plant, and network work [6]. In addition, ICT forms the vital link between energy generation, transmission, distribution, and consumption.

The key element that effectively validates the smart grid application is the performance and capacity to execute integrated, scalable, and interoperable responses linked to engineering science. This will track the energy consumption of the smarter in the world, using the mobile devices of the customers, using the internet or private home monitors, and at the same time, these services will be implemented through meter data management systems. The meter also detects power surges and interruptions, and services to be used as a sensor network can also be used to connect or disconnect from a remote connection [7].

Network security, the biggest challenge in smart grid deployment, is maintaining a consistent appearance across all applications. Independent interfaces must be protected by a comprehensive border service that provides multiple layers of protection to prevent attacks. In addition, validating running applications and network architecture with a power management tool called CISCO EnergyWise can improve energy efficiency and significantly reduce costs [8].

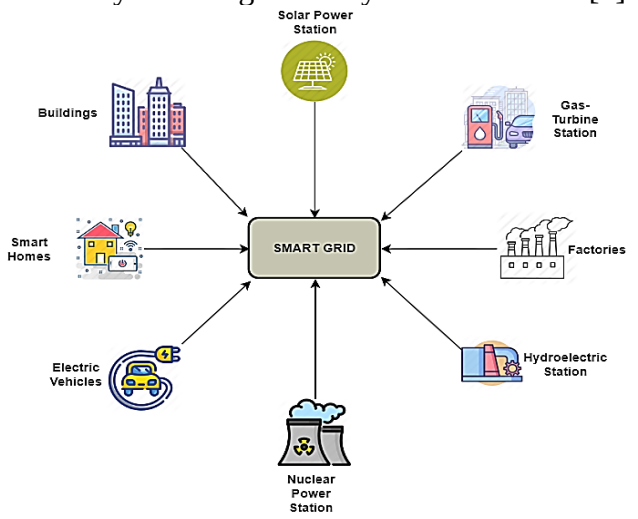

Figure 2 Smart grids overview [9].

A smart grid system should have the following features;

- Digitalization,
- Intelligence,
- Durability,
- Personalization,
- Flexibility.

Digitization means having a digital platform that makes the system fast and reliable. Intelligence means using smart technology. Durability means that the system should not be affected by any attack, Personalization means that the system should be customer-specific. Finally, flexibility means that the smart grid must be compatible, expandable, and adaptable [10].

Figure 3 below shows the ranking of the sectors most affected by cyberattacks in the world as of September 2017. According to the survey, 26% of respondents in the energy sector said that their companies have been exposed to cyber attacks in the last 12 months [11].

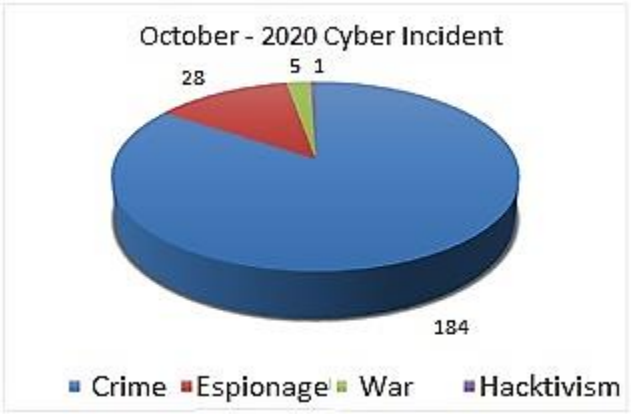

Figure 3 Cyber events that took place in October-2020 [11]

4. MOST FREQUENTLY USED CYBER ATTACK METHODS

Cybersecurity contains much more comprehensive and vital components than viruses infecting personal computers, antivirus programs that need to be updated, blocking of advertisements to e-mails, or the capture of personal information [12]. These and similar situations are of course important, but when it comes to cybersecurity, smart cities and networks should be one of the first things to consider. Because when evaluated in terms of national security; In case of service loss or disruption of services that may occur in smart networks, it may cause large-scale economic damage, loss of life, or national security weaknesses [13]. Therefore, these critical systems are the most important assets to be protected within the scope of cybersecurity. This study has tried to draw attention to this issue.

The most common cyber-attack methods are listed below [14-81];

- Distributed Denial of Service (DDoS)
- Logic Bomb
- Slave Computers (Botnet, Zombie)
- Zero-Day Exploits
- Advanced Persistent Threats (APT)
- Baiting - Phishing Attacks
- Rear Door (Back Door - Trap Door)
- Rootkit
- Spyware (Spyware - Adware)
- Attack Kits
- Ransomware
- Social Engineering
- Sending Unwanted Bulk Messages (Email) (Spam - Bulk - Junk Mail)
- Listening of Network Traffic (Sniffing - Monitoring)
- Use of Malware (Virus - Worm - Trojan horse etc.)
- Cryptographic Attacks
- IP Spoofing - Hiding (IP Spoofing)
- Digital Manipulation
- Open Microphone Listening
- Session Hijacking
- Listening of Network Traffic (Sniffing - Monitoring)
- Use of Malware (Virus - Worm - Trojan horse etc.)
- Cryptographic Attacks
- IP Spoofing - Hiding (IP Spoofing)
- Digital Manipulation
- Open Microphone Listening
- Session Hijacking
- Wire Tapping
- Internet Service Attacks
- Programs that Record Keyboard Operations (Keyloggers)
- SQL Injection

When all studies were examined, these attack types were determined. Especially the most common cybersecurity attacks have been tried to be given in this study.

5. INVESTIGATION OF SECURITY OF SMART GRIDS

Studies on cybersecurity in smart networks are given in chronological order. In recent years, intensive academic studies have been carried out on smart grids in the world and our country.

Dönmez explains the subject of integration, which is indispensable for the efficient operation of smart grids, discusses with practical examples given from structural and technical aspects [5]. Iyer et al. mentioned cyber threats and risks in smart grids in his cybersecurity for smart grid, cryptography, and privacy study [10]. Yan et al. summarize the requirements and potential vulnerabilities in smart grid cybersecurity

Examine the available communication and cybersecurity solutions for smart grid communication [12]. Goel et al. describe the main security threats and cybersecurity in smart grid technologies as well as information about the vulnerabilities of smart grid strategies to protect from security breaches, recommendations on methodologies, and technologies [13].

Kara and Çelikkol discuss the situation in Turkey in terms of the overall structure of the communication protocols of the SCADA system, as well as the precautions that need to be taken for the safe operation of the system in the SCADA transmission and distribution infrastructure of the electricity used [15]. Knap investigates attack vectors, management, and secure network for intelligent networks, SCADA, and other industrial control systems [16]. Burmester et al. provide a framework for modeling the security of cyber-physical systems. In this structure, the behavior of competitors, aspects of cyber-physical aspects is combined [17].

Rice et al. provide systems engineering applied to a cyber-attack scenario on cybersecurity issues and the implementation of an intelligent network system shows the various methods and concepts of the discipline [18]. Ashok et al. propose a game-theoretical formulation model of defense and attack by determining specific attack and defense scenarios of cyber-physical security in smart grids [19]. Anwar et al. provide cyber-attacks and solution methods in smart grid infrastructures are taken into consideration. Especially energy networks and SCADA systems are exemplified [20].

Liu et al. propose a model named ATSE that detects and predicts attacks by scanning and monitoring abnormal data traffic and bad data leaks in network traffic in smart grids [21]. Suleiman et al. propose for data to be safe and realistic in transmission lines and equipment in smart networks, as well as against attacks and leaks for a system security threat model (SSTM) [22]. Arabo explains cyber threats and precautions that may occur on critical infrastructure and smart devices used in smart home ecosystems are listed [23]. Knowles et al. provide the latest preparations and research for this risky and configuration. Implementation of special safety measures for industrial control systems, safety as a barrier to making this equipment [24].

Tawde et al. provide an overview of the structure of security mechanisms for communications SCADA at substation device Bump-in-Wire (BITW). It also provides a security solution that eliminates key management problems by integrating Protocol key distribution and management CDAC Sec-KeyD in IEC 62351 for the protection of the IEC 61850 protocol [25]. Drias et al. provide comprehensive cybersecurity issues for industrial control systems (ICS) are discussed. General SCADA structures and components are described [26]. Cherdyntseva et al. developed methods on cybersecurity risks in SCADA systems and precautions to be taken were investigated [27].

Wei et al. provide that the impact of smart grid data communication network-based attacks are caused examine the results of real-time and electricity. Moreover, the study and research of intelligent network security provide information on both field operations [28]. Mishra et al. present a new model for optimizing protection against burst attacks in smart networks. In addition, a rotation algorithm has been developed [29]. Young et al. offer a framework comprising of cyber insurance sector operating principles to measure risks. The framework for discussing critical infrastructure owners and operators of cybersecurity investments and optimization techniques to propose levels of insurance [30].

Şenol emphasizes that deterrence can be achieved with the cyber power gained by information and communication systems; information was given on the concepts of cyber power, deterrence, cyber attack, and cyber warfare; information technology, especially Internet's development and after the expansion in the world and some of the major events and consequences of cyber attacks experienced in Turkey revised; The content and results of the cyber attacks on Sony in 2014 were evaluated [31].

Stuart Borlase evaluations on infrastructures, technologies, and solutions used in smart networks are discussed [32]. Zhou et al. provide that cybersecurity standards, procedures, and best practices on SCADA are thoroughly reviewed. Thanks to these standards, defense theory in depth is recommended [33]. Do et al. explain that cyber-attacks and vulnerabilities made to the SCADA system were analyzed. In addition, SCADA architectures are given in detail. Measures and approaches to be taken against attacks have been analyzed [34]. Pour et al. provide that vulnerabilities of smart grid systems, possible intentional attacks, and precautions to be taken against these threats are discussed [35]. Antón et al. provide that the cyber-attacks your industry and infrastructure companies have been exposed to in the last 20 years are discussed. In addition, different attack types and their entry points are analyzed [36]. Kuzlu et al. provide that the standards used in intelligent networks and protocols are discussed in detail and explained [37].

Deng et al. explain that on the smart grid cyber-physical attacks and countermeasures (CCPA) are discussed. A vector measuring means for neutralizing the effect of physical attack vectors (PMI) can synthesize data injection attack vectors based on measurements carefully and thus recorded can prevent detecting invalid data before determining the CCP [38]. Shaileshwari et al. provide that the use of SDN network infrastructure against cyberattacks in smart networks and to provide a smart communication network is discussed [39]. Nazir et al. discuss SCADA tools and techniques for detecting security vulnerabilities in the system. A comprehensive summary of the chosen approach is provided, with an indication of feasibility [40].

Bretas et al. present a methodology for the cyber-physical security of smart grids and therefore discusses the possibility of diagnostics, identification, and verification [41]. Eder-Neuhauser et al. defense methods against common malicious software in smart networks are discussed [42]. At the same time, 19 malware types are compared. Baig et al. provide that by identifying specific threats smart cities and intelligent manner realistically with a view, looking around with a holistic view of the city [43]. Anwaar AlDairi et al. provide smart cities to discuss cybersecurity challenges and current solutions [44]. Otuoze et al. explain that cyberattacks can occur in smart networks and the classification of these attacks is discussed [45]. Maglaras et al. provide that security issues and solutions on Industrial Control Systems and IoT are covered [46].

Luo et al. provide that cyberattacks on smart city observers aim to aid detection and isolation. They propose a graph-based algorithm based on the theory of measurements [47]. Ding et al. explain that security control and attack detection approaches and mathematical models are examined. In addition, specific approaches are summarized in the study [48]. Saini et al. discuss how should a better cybersecurity level be in smart cities without too much modeling are discussed [49]. Kurt et al. propose a powerful online false data injection (FDI) and interference attack detection algorithm that provides online estimates and outcome predictions of unknown and time-varying attack parameters [50].

Pate-Cornell et al. cyber risk management and analysis models in smart grids and critical infrastructures are discussed. Especially Markov and Bayesian analysis models are shown. Measures to be taken against risks are discussed [51]. Kurt et al. explore online detection of deceptive attacks and the prevention of service attacks on an intelligent network. The system is modeled as a linear dynamic system with discrete time, and the state is estimated using the Kalman filter. Detectors for intrusion detection and recognition are proposed [52].

Tarıq et al. explain that away smart grid and service-oriented development methodologies such as global networking systems (CPS) offer [53]. Lopez et al. propose a new architecture divided into five subnets, which allows the integration of a cloud infrastructure responsible for executing predictive analytics to conform to the demand response by implementing a load balancing algorithm [54]. Farraj et al. propose an adaptive parametric feedback linearization (PFL) control scheme to achieve the temporal flexibility

of smart grids. In addition, data integrity and availability are verified for intelligent network attacks [55]. Che et al. provide that a cyber cascade monitoring system (CCS) is proposed to detect malfunctions triggered by potential data attacks [56].

Şimşek et al.the TPS3 security protocol is recommended to protect data privacy in smart cities [57]. Ni et al. based on reinforcement learning to determine the most appropriate order-based attack on certain targets propose a new solution for a multi-stage game between offensive and defensive [58]. Kim et al. explore the need for smart grids and explores industry initiatives to combat and respond to smart grid security threats [59]. Mrabet et al. reviews security requirements and provide descriptions of various serious cyberattacks and recommend a cybersecurity strategy for detecting and countering these attacks [60]. Kimani et al. examine the basic security IOT-based challenges and problems that prevent the growth of the smart grid [61].

Hossain et al. explore the next generation of the smart grid electricity grid (SG) in the network with the emergence of big data and machine learning applications was conducted as a comprehensive study [62]. Islam et al. explores the vulnerability and hazards associated with the components of the smart energy system and relevant communication standards, including devices with support for the Internet of Things, and explores the measures to be taken against cyber attacks [63].

Sakhnini et al. discuss the object of the Internet to the (IoT) based on bibliometric research articles about security aspects of smart grids provide an overview [64]. Kumar et al. provide that traditional energy networks and smart metering networks in this article provide a brief overview of the targets of cyber attacks in real-world events [65]. De Dutta et al. aim to provide an overview and history of some of the existing solutions for detecting and preventing cyber threats and security issues affecting machine-to-machine communication (M2M), applications in smart grid, M2M data in the smart grid [66]. Gusrialdi et al. is highlighting the close relationship between the physical communication network system, the system offers an overview of the cyber attacks on power systems from a theoretical perspective [67].

Khan et al. provide various critical aspects of Blockchain technology such as operating mode, possible improvement proposals using Proof-of-Stake, and other special options are analyzed in different ways [68]. Mollah et al. provide a comprehensive overview of the implementation of blockchain in a smart grid. So can be solved by the blockchain determines the basic security problem of the intelligent network scenario [69]. Gündüz M. Z. et al. provide a comprehensive overview of the implementation of blockchain in a smart grid. Thus, it detects the basic security problems of smart grid scenarios that can be solved with blockchain [70]. Mathas et al. examine smart grid threat environments, identifies threats specific to that infrastructure, assess the severity of each type of attack, lists features and methods that can be used to detect attacks and should be used to mitigate them [71].

Ferrag et al. base on available smart grid fog SCADA systems to provide a comprehensive overview of cybersecurity solutions [72]. Moghadam et al. the key to overcoming the security weaknesses of the mix at the right time to facilitate coordination and proposes a secure communication protocol based on the private key [73]. Zhang et al. production, transmission, distribution, and improved monitoring of all network components, including consumers, two-way communication to ensure the protection and optimization of digital technology, advanced detection offers examples of their computing infrastructure and software capabilities [74]. Hittini et al. explore a smart grid false data injection protocol to prevent distribution systems (FDIPP) have been proposed. The protocol hierarchy and distribution system is designed to work on many assets matching a new hierarchical network architecture [75].

Amin et al. discuss Naive Bayes offers a new algorithm based on belief propagation (BP), a higher rate of detection than the current machine learning classifiers, such as support vector machines to detect both random and hidden FDIA in intelligent networks [76]. Shrestha et al.

propose a methodology called "Classification of intelligent network security» (SGSC), which focuses on the characteristics of the expanded measurement systems infrastructure (AMI), designed for complex systems, such as intelligent networks [77]. Jeyaraj et al. suggest a deep learning algorithm for multi-dimensional analysis and classification of non-periodic electricity. It should be noted that aid in the detection of power theft consumer intermittent load curve [78].

Gandi et al. explain that renewable energy source (RES) with the increasing use of inertial damping system that affects the stability of the system and the stresses that can cause failure. The protection of these systems with the introduction of renewable energy sources and managing systems has become more complex. Therefore, to solve these problems in a wind energy system with a reliable energy storage system implementing an intelligent control technique is proposed [79]. Khan et al. purpose software-based key elliptic curve cryptography (PALKA) intelligent network unified structure design. Based on a random oracle model and informal security analysis, PALKA's official security review and Avispa simulation based on a formal security analysis of PALKA were tested to return PALKA against man-in-the-middle and duplications. PALKA's lower information and communication about the user compared to other related protocols in the same environment [80]. Tufail et al. discuss attacks by using artificial intelligence (FDIA), which can be very useful by methods such as the prevention and subsequent FDIA through encryption, multifactor authentication, and configuration intrusion detection system. In addition, timely updates and patches can minimize the possibility of invasion [81].

Table 1 Cybersecurity attacks and measures in smart grids

	Cyber-Attack Methods	**Cyber Security Attack Measures**		
		1	**2**	**3**
1	DDoS	Operation-Based Defensive Architecture[15]	IDS[41]	IPS[19]
2	Man in The Middle (MITM)	Operation-Based Defensive Architecture[56]	TARP: Ticket-Based Address Resolution Protocol	TARP: Ticket-Based Address Resolution Protocol
3	APT-Malware (Worm,Trojan,Rootkit, Virus)	IPS/IDS[34]	Signature-Based Prevention[51]	Signature-Based Prevention[67]
4	Replay Attack	Operation-Based Defensive Architecture[48]	Neural Network Based IDS[76]	Single Sign-On Protocol Based on Dynamic Double Password[81]
5	Spoofing(ARP,IP,GPS)	IDS[31]	MAC-IP Database Center[67]	Using AES and RSA Encryption
6	MODBUS/TCP Protocol Attack	IPS/IDS[33]	SSL VPN[66]	Explicitly define a set of allowed MODBUS commands, register values, and binary coils[51]
7	DNP3 Protocol Attack	Encapsulated within TLS[48]	Implement DNP3 Secure[44]	Block the DNP3 based traffic from corporate into control networks through IPS[44]
8	Malicious Command and Software Injection	Signature-Based Prevention[48]	Ensemble of Deep Belief Network (DBN)[45]	PIVOT Algorithm[69]
9	Buffer Overflow	Real-Time Operation System(RTOS)	Hardware/Software Address Protection (HSAP)	Fonksiyon İşaretleyici XOR (HSAP)[65]
10	Social Engineering	Empirical Database[58]	Mean Time-To-Compromise Metric[63]	X
11	Physical Attack (Sensor, Actuator, Camera)	IPS/IDS[22]	Detection Algorithms[60]	A fuzzy-logic-based approach for modeling[59]

12	SQL Injection	Cyber Threat Intelligence (OSINT, SOCMINT, HUMINT)[44]	Create static function calls for external commands[61]	Use library calls implementation technique in programming[55]
13	Zero-Day Attack	Signature detection technique used by intrusion detection and prevention Systems[17]	Anomaly detection based intrusion detection technique[31]	Attack Database[23]
14	Unauthorized Access Activities	Using secret keys, either in a peer-to-peer manner or via a trusted third party[19]	Signature-based intrusion detection technique[35]	Machine Learning-Based IDS[33]
15	Insider-Outsider Attacks	State-based IDS rules	X	X
16	Network Traffic Anomaly	SDN[16]	Automatic Intelligent Cyber Sensor[46]	Intrusion Detection Mechanism[27]
17	Back Doors	IPS/IDS[32]	Luenberger Observers (LOs) and Unknown Input Observers (UIOs)	Machine Learning-Based IDS[28]
18	Reconnaissance Attacks	Ensemble of Deep Belief Network[37]	Machine Learning-Based IDS[17]	State-based IDS rules[44]
19	Sniffing	IPS/IDS[34]	Signature-Based Prevention[48]	X
20	Cryptographic Attacks	State based IDS rules[59]	X	X

With the research and development of security technologies in the details given in the table, smart grid research has been rapid in this area. Especially with the increasing cyber attacks in recent years, we have presented in this article by investigating how experts and institutions in the sector can deal with these attacks and what precautions they should take. As a result of the research, it has been observed that there are more attacks on SCADA, especially in smart networks. For this reason, it should be aimed to take more intensive measures for security studies specific to SCADA, PLC, RTU, HMI and to protect smart grid systems by developing new safe models. In addition to smart grids, critical infrastructures, and industrial control systems (ICS), safe models and methods, must be protected. The methods given in the examinations made in this study are intended to provide convenience to researchers.

6. CONCLUSION

The development of smart grids all over the world and in our country has accelerated in recent years. The rapid increase in technological developments in smart grids makes security problems in this area important. Increasing cybersecurity attacks in recent years draw attention to the importance of these problems in terms of economy, sustainability, and security. In this study, national and international academic studies on the security problems of smart grids were examined. Particular attention was drawn to this issue by providing information about possible and experienced cyber-attacks. When the academic studies conducted in the last 10 years are examined, it has been evaluated that the attacks against SCADA and industrial control systems have increased and that these systems should be protected with more secure hardware and software. In addition, in this study, the most common and possible cyberattack methods in smart networks were examined and 20 attack methods were analyzed. The development of smart grids brings with it security problems. In this article, the importance of these problems and the precautions that can be taken against cyber attacks are researched and given in a table. In addition, in the light of the information obtained here, cyber attacks that may occur in smart networks and the measures that can be taken against them are given by researching. By giving

studies on this subject, academicians working on this subject and companies with smart grids were informed. This study aims to shed light on the researches and studies to be done on this subject.

Funding

The author (s) has no received any financial support for the research, authorship, or publication of this study.

The Declaration of Conflict of Interest/ Common Interest

No conflict of interest or common interest has been declared by the authors.

Authors' Contribution

The authors contributed equally to the study.

The Declaration of Ethics Committee Approval

This study does not require ethics committee permission or any special permission.

The Declaration of Research and Publication Ethics

The authors of the paper declare that they comply with the scientific, ethical, and quotation rules of SAUJS in all processes of the paper and that they do not make any falsification on the data collected. In addition, they declare that Sakarya University Journal of Science and its editorial board have no responsibility for any ethical violations that may be encountered and that this study has not been evaluated in any academic publication environment other than Sakarya University Journal of Science.

REFERENCES

[1] İ. Avcı, C. Özarpa, M. A. Aydın, A Survey of International Security Standards for Smart Grids, Industrial Control System and Critical Infrastructure, 12th International Exergy, Energy and Environment Symposium (IEEES-12), December 20-24, Doha, Qatar, 2020.

[2] A. Caragliu, C. Del Bo and P. Nijkamp, Smart cities in Europe (2009), In 3rd Central European Conference in Regional Science, 2009.

[3]Channelpostmea,http://www.channelpostmea.com/2017/03/02/dubai-wants-to-become-a-global-benchmark-for-smart-cities. Accessed Time: 02.03.2017.

[4] Z. Sang, Z. Luo, M. Mulquin, Standardization roadmap for smart sustainable cities. Technical report, International Telecommunication Union (ITU), 2015.

[5] M. Dönmez, Akıllı şebekeler ve entegrasyon (smart grids and integration), BTC Business Technology, 2013.

[6] Siemens Aktiengesellschaft, Smart grids and the new age of energy, http://www.energy.siemens.com/hq/de/stromuebertragung/transformatoren/assets/pdf/siemens-transformers-power-engineering-guide-7-1.pdf, 2014. Accessed Time:01.04.2021

[7] S. Borlase, Smart grids: infrastructure, technology, and solutions, CRC Press, 2016.

[8] Cisco Energy Optimization Service, http://www.cisco.com/web/strategy/docs/energy/energy_optimization_service_aag.pdf, retrieved from CISCO, 2021. Accessed Time:07.05.2021.

[9] F. Feroze, N. Javaid, Towards Enhancing Demand Side Management using Evolutionary Techniques in Smart Grid. 10.13140/RG.2.2.34456.49920, 2017.

[10] S. Iyer, Cyber Security for Smart Grid, Cryptography, and Privacy, International Journal of Digital Multimedia Broadcasting, USA, 2011.

[11]Hacmageddon,https://www.hackmageddon.com/2018/04/17/16-31-march-2018-

cyberattacks-timeline/. Accessed Time:: 21.03.2021.

[12] Y. Yan, et al., A Survey on Cyber Security for Smart Grid Communications, IEEE Communications Surveys & Tutorials, Vol. 14, No. 4, 2012.

[13] S. Goel, and A. Jindal, Evolving Cyber Security Challenges to the Smart Grid Landscape, International Journal of Advance Research, Ideas and Innovations in Technology, 2017.

[14] M. Yıldız, Siber Suçlar ve Kurum Güvenliği, Denizcilik Uzmanlık Tezi, T.C. Ulaştırma Denizcilik ve Haberleşme Bakanlığı, 2014.

[15] M. Kara, and S. Çelikkol, Kritik Altyapılar: Elektrik Üretim ve Dağıtım Sistemleri SCADA Güvenliği, 4. Ağ ve Bilgi Güvenliği Sempozyumu. Accessed Time:07.05.2021, 2011.

[16] E. Knapp, Industrial Network Security: Securing Critical Infrastructure Networks for Smart Grid, SCADA, and Other Industrial Control Systems, Elsevier Inc, 2011.

[17] M. Burmester and et al., Modeling security in cyber-physical systems, https://www.sciencedirect.com/science/journal/18745482, Pages 118-126, 2012.

[18] E. B. Rice, A. AlMajali, Mitigating the Risk of Cyber Attack On Smart Grid Systems, Science Direct, Elsevier, Procedia Computer Science 28, pp. 575 – 582, 2014.

[19] A. Ashok et al., Cyber-physical security of Wide-Area Monitoring, Protection and Control in a smart grid environment, Journal of Advanced Research, Cairo University, 2014.

[20] A. Anwar, A.N. Mahmood, Cybersecurity of smart grid infrastructure, The State of the Art in Intrusion Prevention and Detection, CRC Press, Taylor & Francis Group, USA, pp. 449-472, January 2014.

[21] T. Liu et al, Abnormal traffic-indexed state estimation: Acyber–physical fusion approach for Smart Grid attack detection, Elsevier, 2015.

[22] Suleiman, H. et al., Integrated smart grid systems security threat model, Elsevier, 2015.

[23] A. Arabo, Cyber Security Challenges within the Connected Home Ecosystem Futures, Procedia Computer Science, Volume 61, 2015, pp. 227-232, 2015.

[24] W. Knowles et al., 2015, A survey of cybersecurity management in industrial control systems, International Journal of Critical Infrastructure Protection Volume 9, p. 52-80, June 2015.

[25] R. Tawde et al., Cyber Security in Smart Grid SCADA Automation, IEEE Sponsored 2nd International Conference on Innovations in Information, Embedded, and Communication Systems (ICIIECS), 2015.

[26] Z. Drias et al., Analysis of Cyber Security for Industrial Control Systems, International Conference on Cyber Security of Smart Cities, Industrial Control System, and Communications (SSIC), 2015.

[27] Y. Cherdantseva et al., A review of cybersecurity risk assessment methods for SCADA systems, Computers & Security, Volume 56, February 2016, p.1-27, 2016.

[28] M. Wei, W. Wang, Data-centric threats and their impacts to real-time communications in smart grid, Computer Networks, Volume 104, p. 174-188, 2016.

[29] S. Mishra et al., Optimal packet scan against malicious attacks in smart grids, Theoretical Computer Science, Volume 609, Part 3, pp. 606-619, 2016.

[30] D. Young et al., A framework for incorporating insurance in critical

infrastructure cyber risk strategies, International Journal of Critical Infrastructure Protection Volume 14, p. 43-57, 2016.

[31] M. Şenol, Siber Güçle Caydırıcılık Ama Nasıl?, Uluslararası Bilgi Güvenliği Mühendisliği Dergisi, Cilt:2, No:2, Ankara, pp.10-17, 2016.

[32] S. Borlase, Smart grids: infrastructure, technology, and solutions, 2017.

[33] X. Zhou et al., What should we do? A structured review of SCADA system cyber security standards, Proceedings of 2017 4th International Conference on Control, Decision and Information Technologies (CoDIT'17) , Barcelona, Spain, 2017.

[34] V. L. Do et al., Security of SCADA Systems Against Cyber-Physical Attacks, IEEE A&E System Magazine, 2017.

[35] M. M. Pour et al., A Review on Cyber Security Issues and Mitigation Methods in Smart Grid Systems, IEEE, 2017.

[36] S. D. Antón et al., Two Decades of SCADA Exploitation: A Brief History, IEEE Conference on Application, Information and Network Security (AINS), 2017.

[37] M. Kuzlu et al., A Comprehensive Review of Smart Grid Related Standards and Protocols, ICSG Istanbul, 2017.

[38] R. Deng et al., CCPA: Coordinated Cyber-Physical Attacks and Countermeasures in Smart Grid, IEEE Transactions on Smart Grid, Vol. 8, No. 5, 2017.

[39] M. U. Shaileshwari et al., Software Defined Networking for Smart Grid Communications and Security Challenges, ISGW 2017: Compendium of Technical Papers, p. 103-112, 2017.

[40] S. Nazir et al., Assessing and augmenting SCADA cybersecurity: A survey of techniques, Computers & Security Volume 70, September 2017, pp. 436-454, 2017.

[41] A. S. Bretas et al., Smart grids cyber-physical security as a malicious data attack: An innovation approach, Electric Power Systems Research, Volume 149, pp. 210-219, 2017.

[42] P. Eder-Neuhauser et al., Cyber-attack models for smart grid environments, Sustainable Energy, Grids and Networks Volume 12, p. 10-29, 2017.

[43] Z. A. Baig et al., Future challenges for smart cities: Cyber-security and digital forensics, Digital Investigation Volume 22, pp. 3-13, 2017.

[44] A. AlDairi, L. Tawalbeh, Cyber Security Attacks on Smart Cities and Associated Mobile Technologies, The International Workshop on Smart Cities Systems Engineering, Elsevier, 2017.

[45] A.O. Otuoze et al., Smart grids security challenges: Classification by sources of threats, Journal of Electrical Systems and Information Technology, 2018.

[46] L. A. Maglaras et al., Cybersecurity of critical infrastructures, ICT Express, Volume 4, Issue 1, 2018.

[47] X. Luo et al., Observer-based cyber-attack detection and isolation in smart grids, International Journal of Electrical Power & Energy Systems Volume 101, p. 127-138, 2018.

[48] D. Ding et al., A survey on security control and attack detection for industrial cyber-physical systems, Neurocomputing Volume 275, p. 1674-1683, 2018.

[49] S. Saini et al., Modelling for Improved Cyber Security in Smart Distribution System, International Journal on Future Revolution in Computer Science & Communication Engineering, Volume: 4 Issue: 2, pp.56-59, 2018.

[50] M. N. Kurt et al., Real-Time Detection of Hybrid and Stealthy Cyber-Attacks in

Smart Grid, Cornell University Library, 2018.

[51] M-E. Pate-Cornell et al., Cyber Risk Management for Critical Infrastructure: A Risk Analysis Model And Three Case Studies, Risk Analysis, Vol. 38, No. 2, 2018.

[52] M. N. Kurt, et al., Distributed Quickest Detection of Cyber-Attacks in Smart Grid, IEEE Transactions on Information Forensics and Security, Vol. 13, Number: 8, 2018.

[53] M. U. Tarıq, and M. Wolf, Improving the Safety and Security of Wide-Area Cyber-Physical Systems Through a Resource-Aware, Service-Oriented Development Methodology, Proceedings of the IEEE | Vol. 106, No. 1, 2018.

[54] J. Lopez et al., A Resilient Architecture for the Smart Grid, IEEE Transactions on Industrial Informatics, 2018.

[55] A. Farraj et al., A Distributed Control Paradigm for Smart Grid to Address Attacks on Data Integrity and Availability, IEEE Transactions On Signal and Information Processing Over Networks, Vol. 4, No. 1, 2018.

[56] L. Che et al., Cyber Cascades Screening Considering the Impacts of False Data Injection Attacks, Transactions on Power Systems, IEEE, 2018.

[57] M. U. Şimşek et al., TPS3: A privacy-preserving data collection protocol for smart grids, Information Security Journal: A Global Perspective, p.102-118, 2018.

[58] Z. Ni and S. Paul, "A Multistage Game in Smart Grid Security: A Reinforcement Learning Solution," in IEEE Transactions on Neural Networks and Learning Systems, vol. 30, no. 9, pp. 2684-2695, Sept. 2019, DOI: 10.1109/TNNLS.2018.2885530.

[59] S.-K. Kim, J.-H. A. Huh, Study on the Improvement of Smart Grid Security Performance and Blockchain Smart Grid Perspective, Energies 2018, 2018.

[60] Z. El Mrabet, N. Kaabouch, H. El Ghazi, H. El Ghazi, Cyber-security in smart grid: Survey and challenges. Computers & Electrical Engineering, 67, pp. 469-482, 2018.

[61] K. K. Kimani, O. V. Vitalice, K. Langat, Cybersecurity challenges for IoT-based smart grid networks, International Journal of Critical Infrastructure Protection, Volume 25, Pages 36-49, 2019.

[62] E. Hossain, I. Khan, F. Un-Noor, S. S. Sikander, and M. S. H. Sunny, "Application of Big Data and Machine Learning in Smart Grid, and Associated Security Concerns: A Review," in IEEE Access, vol. 7, pp. 13960-13988, 2019.

[63] S. N. Islam, Z. Baig, S. Zeadally, Physical layer security for the smart grid: vulnerabilities, threats, and countermeasures. IEEE Transactions on Industrial Informatics, 15(12), 6522-6530, 2019.

[64] J. Sakhnini et al., Security aspects of Internet of Things aided smart grids: A bibliometric survey, Internet of Things, 100111, 2019.

[65] P. Kumar, Y. Lin, G. Bai, A. Paverd, J. S. Dong and A. Martin, "Smart Grid Metering Networks: A Survey on Security, Privacy and Open Research Issues," in IEEE Communications Surveys & Tutorials, vol. 21, no. 3, pp. 2886-2927, 2019.

[66] S. De Dutta, R. Prasad, Security for Smart Grid in 5G and Beyond Networks. Wireless Pers Commun 106, 261–273 2019. https://doi.org/10.1007/s11277-019-06274-5, 2019.

[67] A. Gusrialdi, Z. Qu, Smart Grid Security: Attacks and Defenses. In: Stroustrup J.,

Annaswamy A., Chakrabortty A., Qu Z. (eds) Smart Grid Control. Power Electronics and Power Systems. Springer, Cham. https://doi.org/10.1007/978-3-319-98310-3_13, 2019.

[68] F. A. Khan, M. Asif, A. Ahmad, M. Awais, H. A. Alharbi, Blockchain technology, improvement suggestions, security challenges on the smart grid and its application in healthcare for sustainable development, Sustainable Cities and Society, Volume 55, 102018, 2020.

[69] M. B. Mollah et al., "Blockchain for Future Smart Grid: A Comprehensive Survey," in IEEE Internet of Things Journal, DOI: 10.1109/JIOT.2020.2993601, 2020.

[70] M.Z. Gunduz, and R. Das, Cyber-security on the smart grid: Threats and potential solutions, Computer Networks, Volume 169, 107094, 2020.

[71] C.-M. Mathas et al., Threat landscape for smart grid systems. In Proceedings of the 15th International Conference on Availability, Reliability and Security (ARES '20). Association for Computing Machinery, New York, NY, USA, Article 111, 1–7. DOI: https://doi.org/10.1145/3407023.3409229, 2020.

[72] M. A. Ferrag et al., Cybersecurity for fog-based smart grid SCADA systems: Solutions and challenges, Journal of Information Security and Applications, Volume 52, 102500, 2020.

[73] M. F. Moghadam, M. Nikooghadam, A. H. Mohajerzadeh, B. Movali, A lightweight key management protocol for secure communication in smart grids, Electric Power Systems Research, Volume 178, 106024, 2020.

[74] Y. A. Zhang, H. Schwefel, H. Mohsenian-Rad, C. Wietfeld, C. Chen, and H. Gharavi, "Guest Editorial Special Issue on Communications and Data Analytics in Smart Grid," in IEEE Journal on Selected Areas in Communications, vol. 38, no. 1, pp. 1-4, 2020.

[75] H. Hittini, A. Abdrabou, L. Zhang, FDIPP: False Data Injection Prevention Protocol for Smart Grid Distribution Systems. Sensors 2020, 20, 679, 2020.

[76] B. R. Amin, S. Taghizadeh, S. Maric, M. J. Hossain, R. Abbas, Smart Grid Security Enhancement by Using Belief Propagation, IEEE Systems Journal, 2020.

[77] M. Shrestha, C. Johansen, J. Noll, D. Roverso, A Methodology for Security Classification applied to Smart Grid Infrastructures, International Journal of Critical Infrastructure Protection, 28, 100342, 2020.

[78] P. R. Jeyaraj, E. R. S. Nadar, A. Kathiresan, S. P. Asokan, Smart grid security enhancement by detection and classification of non-technical losses employing deep learning algorithm, International Transactions on Electrical Energy Systems, e12521, 2020.

[79] I. Gandhi, L. Ravi, V. Vijayakumar, V. Subramaniyaswamy, Improving Security for Wind Energy Systems in Smart Grid Applications using Digital Protection Technique, Sustainable Cities and Society, 102265, 2020.

[80] A. A. Khan, V. Kumar, M. Ahmad, S. Rana, D. Mishra, PALK: Password-based anonymous lightweight key agreement framework for smart grid, International Journal of Electrical Power & Energy Systems, Volume 121, 106121, ISSN 0142-0615,https://doi.org/10.1016/j.ijepes.2020.106121, 2020.

[81] S. Tufail, S. Batool, A. I. Sarwat, False Data Injection Impact Analysis In AI-Based Smart Grid, 10.13140/RG.2.2.32994.25282, 2021.

SAKARYA ÜNİVERSİTESİ
FEN BİLİMLERİ ENSTİTÜSÜ DERGİSİ

Sakarya University Journal of Science
SAUJS

e-ISSN: 2147-835X | Founded: 1997 | Period: Bimonthly | Publisher: Sakarya University
http://www.saujs.sakarya.edu.tr/en/

Title: Comparison of Maximum Power Point Tracking Methods Using Metaheuristic Optimization Algorithms for Photovoltaic Systems

Authors: Necati BİLGİN, İrfan YAZİCİ

Recieved: 2021-05-11 18:11:39

Accepted: 2021-07-14 15:46:41

Article Type: Research Article

Volume: 25
Issue: 4
Month: August
Year: 2021
Pages: 1075-1085

How to cite
Necati BİLGİN, İrfan YAZİCİ; (2021), Comparison of Maximum Power Point Tracking Methods Using Metaheuristic Optimization Algorithms for Photovoltaic Systems. Sakarya University Journal of Science, 25(4), 1075-1085, DOI: https://doi.org/10.16984/saufenbilder.936254
Access link
http://www.saujs.sakarya.edu.tr/en/pub/issue/64755/936254

Sakarya University Journal of Science 25(4), 1075-1085, 2021

Comparison of Maximum Power Point Tracking Methods Using Metaheuristic Optimization Algorithms for Photovoltaic Systems

Necati BİLGİN*[1], İrfan YAZİCİ[1]

Abstract

The maximum power value that can be obtained from photovoltaic systems can change continuously due to environmental conditions such as temperature, sunlight and partial shading. Direct current-direct current (DC-DC) converters and maximum power point tracking (MPPT) algorithms are required, especially in cases of partial shading, in order for the photovoltaic systems to operate at the maximum power point, that is, to draw the maximum possible power value from the system. In this study, simulation studies has been carried out for two different partially shaded scenarios using the boost-type DC-DC converter and MPPT algorithm in the PV array consisting of 3 panels connected in series. In the simulation studies, the output powers obtained by the application of particle swarm optimization, cuckoo optimization, bat optimization and firefly optimization techniques as MPPT algorithm has been compared. In the scenarios examined, the firefly optimization algorithm reached the maximum power point faster, and it has been observed that the firefly optimization method obtained the highest average power at the end of the simulation periods.

Keywords: Photovoltaic system, partially shaded condition, MPPT, optimization algorithms, DC-DC converter

1. INTRODUCTION

Today, due to the decrease in limited natural energy resources such as natural gas and oil and the huge damage to the environment, the tendency towards renewable energy sources such as sun, wind and geothermal has increased. Photovoltaic (PV) systems based on semiconductor elements have been developed in order to use the energy coming from the sun in electrical systems. As PV systems are considered as reliable and promising renewable energy sources, they are expected to play a key role among power generation systems in the future [1]. However, maximum power point tracking methods have to be used to keep the power that can be obtained from the PV system at the maximum level.

Various optimization algorithms such as Particle Swarm Optimization (PSO), Bat Optimization (BO), Firefly Optimization (FO), etc. have been proposed as MPPT techniques in the studies, depending on the application [2-6]. Dolara et al. compared the energies obtained from the PV module for 2 different solar irradiation conditions using classical MPPT techniques such as open voltage, short circuit, incremental conductance,

* Corresponding author: necatibilgin@hotmail.com
[1] Sakarya University, Faculty of Engineering, Department of Electrical and Electronics Engineering, Turkey.
E-Mail: iyazici@sakarya.edu.tr
ORCID: https://orcid.org/0000-0002-6309-5989; https://orcid.org/0000-0003-3603-7051

perturb and observe [7]. Miyatake M. et al. compared the results obtained from particle swarm optimization with Fibonacci search method, hill climb method and constant voltage methods [8]. Eltamaly A.M. et al. proposed a new method for maximum power point tracking (MPPT) based on the bat optimization [9]. Ding J. et al. proposed a new MPPT method created by combining particle swarm optimization and cuckoo search optimization [10]. Dhivya P. et al. compared the MPPT results obtained by perturb and observe method, particle swarm optimization and firefly optimization [11].

In this study, a simulation study has been carried out with a PV system consisting of a PV array, boost converter and MPPT controller. In order to see the performance of different optimization methods on MPPT, 4 different metaheuristic optimization techniques has been used and the PV system output powers obtained as a result of the simulation has been compared.

2. PHOTOVOLTAIC SYSTEM

PV systems convert the energy in sunlight directly into electrical energy. This transformation was first discovered by French scientist Alexandre Edmond Becquerel in 1839 [12]. Later, it was used in space research with the discovery of semiconductor materials such as silicon with PV property. Although it was not preferred in the past due to its application cost, its use has gained great momentum in the last 20 years.

The main applications of PV systems are stand-alone (water pumping, home and street lighting, electric vehicles, military and space applications) or grid-dependent configurations (hybrid systems, power plants) whose use has increased recently [13].

Basic elements of PV systems are cells formed with semiconductor diodes. Cells can be made of various semiconductor materials. When the cell absorbs photons from sunlight, electrons are freed from silicon atoms and are attracted by a grid of metal conductors, resulting in a direct current flow and electricity is produced [14].

One-diode or two-diode equivalent circuits are used to model the cell. In this study, the single diode circuit model given in Figure 1 is used.

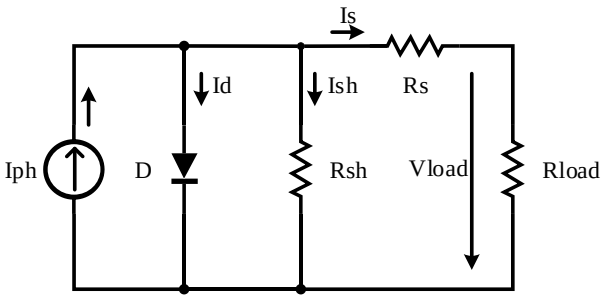

Figure 1 One-diode equivalent circuit

For one-diode model, the output current is obtained with Kirchoff's current law given in equation (1) [15].

$$I_s = I_{ph} - I_d - I_{sh} \tag{1}$$

Here, I_{ph} is the photocurrent generated, I_d is the saturation current, I_{sh} represents the current flowing through the parallel resistor. Mathematical expression of the cell given in equation (2) is obtained when the saturation current and the current flowing through the parallel resistance are reformed in the equation [15].

$$I_s = I_{ph} - I_0 \left\{ \exp\left\lfloor \frac{q(V + R_s I_s)}{nkT_k} \right\rfloor - 1 \right\} - \frac{V + R_s I_s}{R_{sh}} \tag{2}$$

Here, I_0 is the diode saturation current, I_s and V are the current and voltage of the PV cell, respectively, and R_{sh} and R_s are the parallel and series resistors, respectively. k represents Boltzmann constant with value $1.38x10^{-23} J/K$, q charge amount of an electron with value $1.602x10^{-19} C$, and T_k is cell temperature.

The cellular groups formed in the protective laminated surface are called modules in order to reduce the effects of cells from various environmental conditions and to obtain higher powers compared to cells. Cells are connected in parallel to increase the current and in series to increase the voltage, depending on the area of use.

The groups of modules obtained by connecting modules in series or in parallel in order to obtain higher powers compared to modules are called arrays. When constituting arrays, modules are connected in parallel to increase the current and in series to increase the voltage.

In PV systems, the output power varies depending on solar irradiation and temperature. As the solar irradiation increases, the current increases and so the output power also increases. On the other hand, as the temperature increases, the voltage decreases and so the output power decreases. Changes in current, voltage and output power according to solar irradiation and temperature are given in Figure 2 and Figure 3.

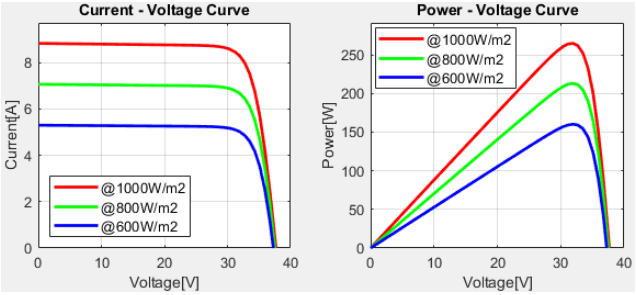

Figure 2 Effects of solar irradiation on I-V and P-V curves

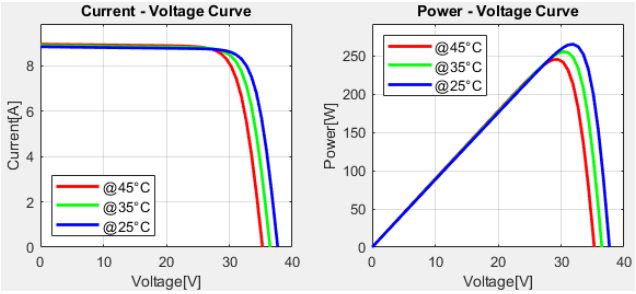

Figure 3 Effects of temperature on I-V and P-V curves

In a system built with PV arrays, some modules may generate less power than others due to partial shading caused by environmental causes such as buildings, trees, and clouds [16]. In such cases, the efficiency of the system decreases and less output power is obtained. In Figure 4, the power-voltage (P-V) curves of the changes in the output power of an array whose modules are subject to partial shading are given. As can be seen from the curves, when the modules on the system are exposed to equal sunlight, only one maximum power point (MPP) is formed in the P-V curve and this point is the global MPP. However, when the modules are exposed to different sunlight, more than one MPP is formed, the largest of these points is the global MPP and the others are the local MPP.

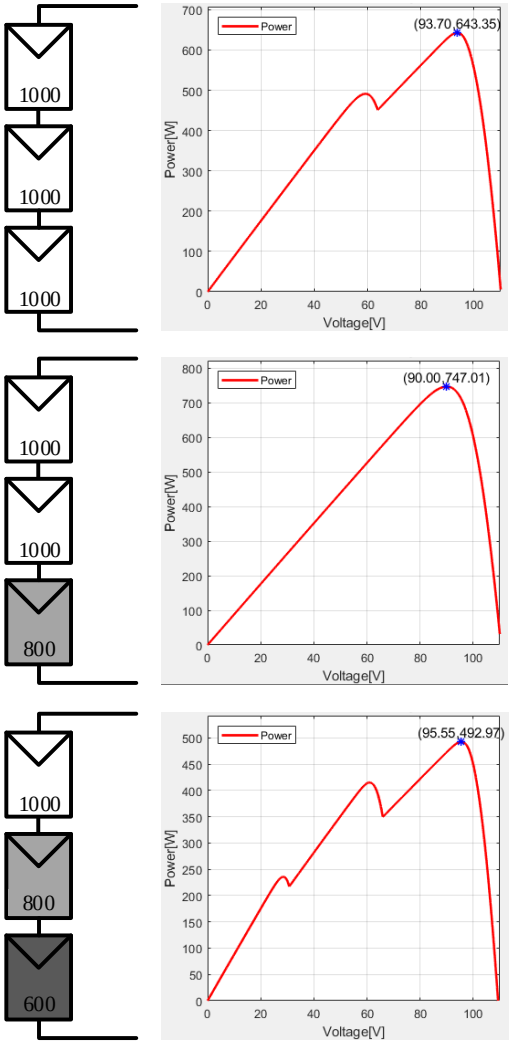

Figure 4 Effects of partially shaded condition on P-V curve

In this study, boost type DC-DC converter is used to adjust the power value drawn from the PV system. In Figure 5, MPPT block diagram consisting of PV system, MPPT controller and boost converter is given.

In the boost converter, when the S switch is ON, the D diode is reverse polarized, the V_{PV} input voltage is applied to the L inductor. The current increases from zero current in the inductor when operating in discontinuous mode or from a certain

starting current when operating in continuous mode to its peak value.

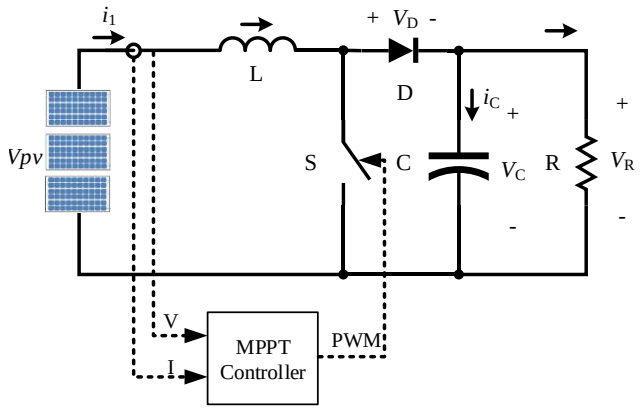

Figure 5 MPPT block diagram

When the S switch is turned OFF, the voltage on the inductor is reversed, causing the diode voltage to be above the input voltage. The diode V_{PV} transfers the energy of the inductor L to these elements, as well as the energy transferred to the capacitor C and the load R by the input voltage. In this way, V_R voltage is greater than V_{PV} voltage. In this study, equations (3), (4) and (5) has been used while calculating the boost converter parameters [17].

$$V_0 = \frac{V_{in}}{1-D} \tag{3}$$

$$L_{\min} = \frac{R(1-D)^2 D}{2 f_s} \tag{4}$$

$$C_{\min} = \frac{DV_0}{\Delta V_0 f_s R} \tag{5}$$

Here, V_0 is the output voltage of the converter, V_{in} is the PV array voltage, and D is the duty ratio of the PWM sign that determines the ON-OFF position of the switching element in the circuit. R is the load resistance, f_s is the sampling frequency, and ΔV_0 represents the ripple in the output voltage.

3. OPTIMIZATION ALGORITHMS

3.1. Particle Swarm Optimization (PSO)

PSO, developed by James Kennedy and Russell C. Eberhart in 1995, is an optimization algorithm based on socio-psychological theory [18]. The algorithm deals with the search for optimum values of individuals called particles in a population.

In each iteration performed in the PSO algorithm, the positions and velocities of each particle and the global optimum position are updated. The following equations (6) and (7) are used to update the position and velocity of the particles in the population [19].

$$v_i(k+1) = \omega \times v_i(k) + c_1 \times r_1 \times (P_{best_i} - x_i(k)) \quad (6)$$
$$+ c_2 \times r_2 \times (G_{best} - x_i(k))$$

$$x_i(k+1) = x_i(k) + v_i(k+1) \tag{7}$$

Here, $v_i(k)$ is velocity for the i 'th particle at the k 'th iteration, ω is the weight function constant, c_1 and c_2 positive constants in the range of [0, 2], r_1 and r_2 uniformly distributed random numbers in the range of [0, 1]. $x_i(k)$ is position for the i 'th particle at the k 'th iteration, P_{best_i} is the best position for the i 'th particle and G_{best} represents the best position so far. The flowchart used for MPPT based on PSO is given in Figure 6 [20].

3.2. Cuckoo Search Optimization (CSO)

CSO was developed by Xin-She Yang and Suash Deb in 2009 by transforming the parasitic life situation resulting from some cuckoo birds laying their eggs in their nests to other birds' nests into an optimization technique [21]. Some cuckoo species can mimic the shape and color of the nesting bird, which increases the likelihood of breeding. It is also known that cuckoo birds lay their eggs at a certain time, so that their eggs hatch some time before that of the nest-owning bird. After early hatching, cuckoo birds destroy the eggs of some nesting birds to increase their chicks' chances of getting more food. It is also

possible that nesting birds will notice the cuckoo's eggs and destroy them. Sometimes nesting birds leave their nest altogether and go elsewhere to build a new nest [22]. New nests in CSO are obtained by using the L´evy flight with the following equation (8) [23].

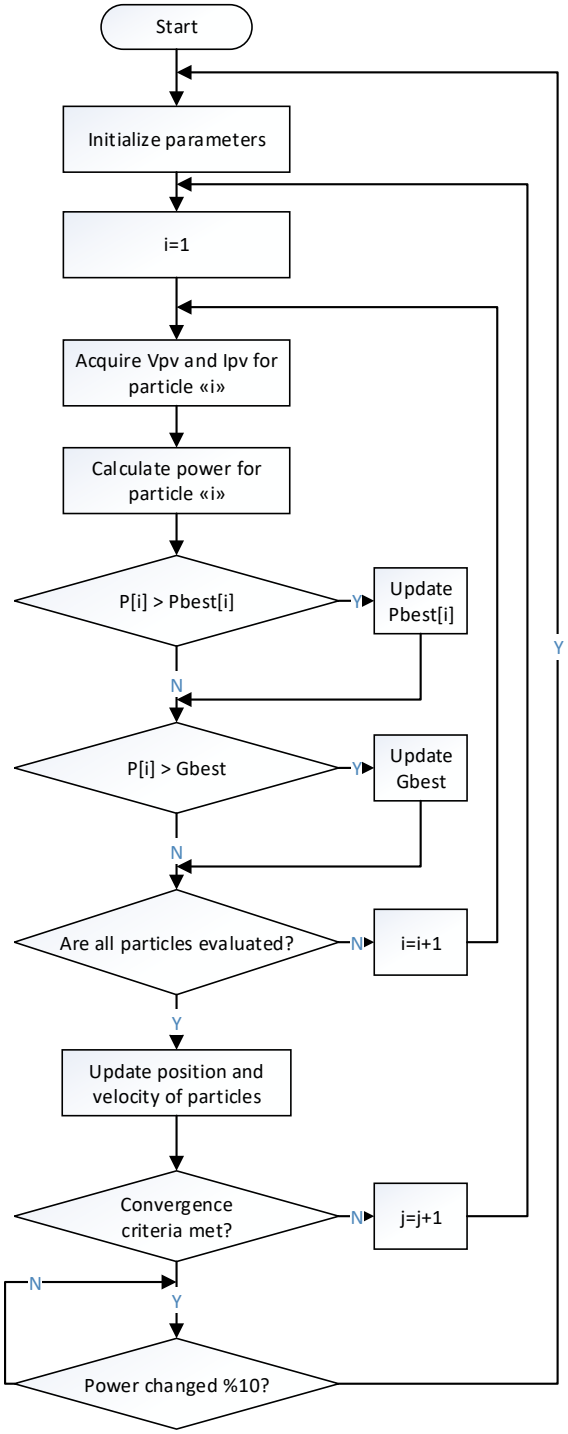

Figure 6 Flowchart of PSO algorithm

$$x_{ij}(k+1) = x_{ij}(k) + \alpha \oplus Le'vy(\lambda) \qquad (8)$$

Here, $x_{ij}(k)$ is the nest, $\alpha = a_0\left(x_{best} - x_i\right)$ and α_0 is the initial step interval, $\oplus$ and λ represents the entry-wise multiplication operation and the flight parameter of L´evy, respectively. The Lévy flight is a random walk in which the step lengths have a Lévy distribution, which is a probability distribution. The flow diagram used for MPPT based on CSO is given in Figure 7 [24].

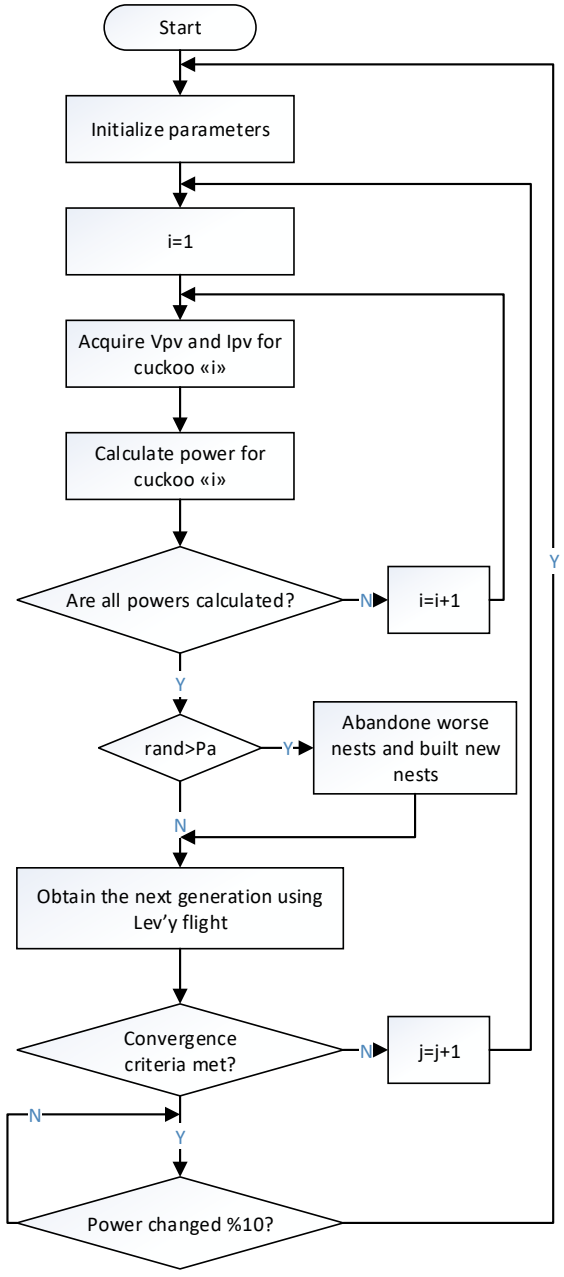

Figure 7 Flowchart of CSO algorithm

3.3. Bat Optimization (BAO)

BAO is one of the algorithms developed by taking inspiration from nature. The algorithm developed by Xin-She Yang in 2010 is based on sound echolocation of bats. Bats express their distance to prey or food by changing the frequencies of the sounds they make. In this way, it enables the population to obtain more solutions that are diverse.

For the bat algorithm, the following equations (9), (10) and (11) are basically used [25].

$$f_i = f_{\min} + \beta(f_{\max} - f_{\min}) \quad (9)$$

$$v_i^k = v_i^{k-1} + (x_i^{k-1} - x_{best})\, f_i \quad (10)$$

$$x_i^k = x_i^{k-1} + v_i^k \quad (11)$$

Here, $\beta \in [0,1]$ is a random number, x_{best} is the best position in bats, f_i is the frequency for i'th bat, $f_{\min}$ and $f_{\max}$ are the minimum and maximum frequency, respectively. Each bat initially has a randomly assigned frequency between $f_{\min}$ and $f_{\max}$. x_i^k and v_i^k represent the position and velocity of the i'th bat at the k'th iteration, respectively. The flowchart of the BAO algorithm is given in Figure 8 [18].

3.4. Firefly Optimization (FFO)

FFO is a meta-heuristic optimization technique based on swarm intelligence and inspired by the light emitted by fireflies, developed by Xin-She Yang in 2008 [26]. The two main functions of the light emitted by fireflies are to attract mating partners and potential prey.

The positions of fireflies in FFO are updated by equation (12) [27].

$$x_i^{k+1} = x_i^k + \beta(r) \times (x_i^k - x_j^k) + \alpha(rand - \frac{1}{2}) \quad (12)$$

Here, x_i^k and x_j^k are the position of i and j fireflies at the k'th iteration, respectively, $\beta(r)$ is the attraction function. Flowchart of FFO algorithm is given in Figure 9 [28].

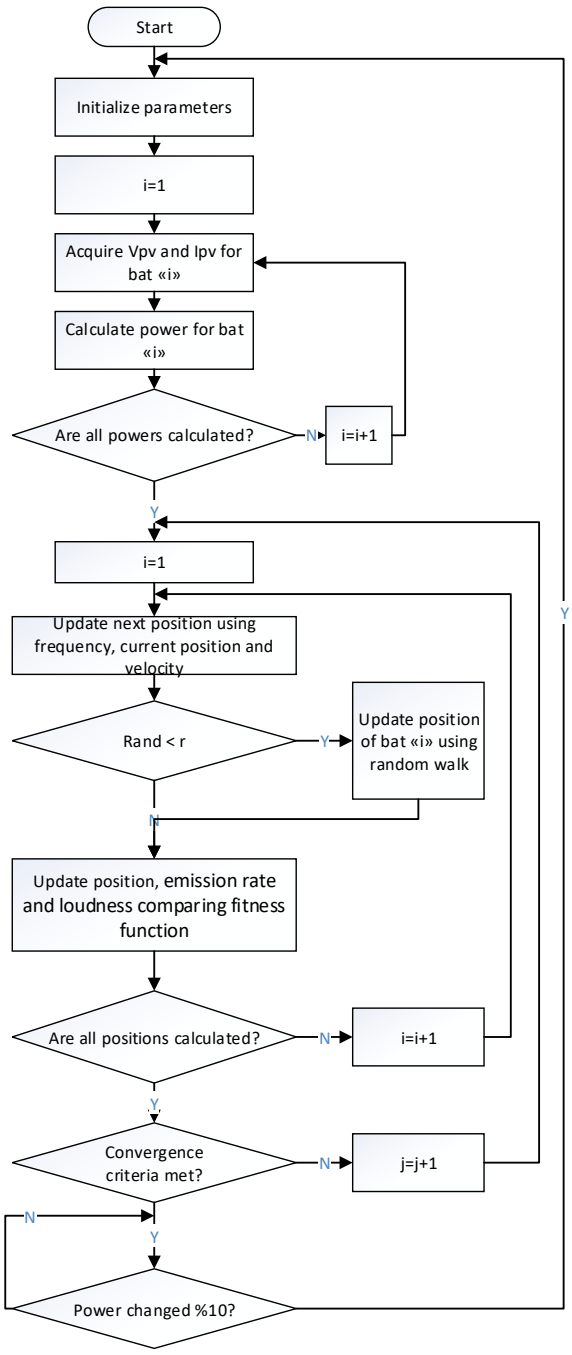

Figure 8 Flowchart of BAO algorithm

4. SIMULATION RESULTS

In order to compare the MPPT performance of the optimization algorithms given above, the system consisting of 3-PV modules connected in series has been examined for two scenarios involving partial shading. The simulation study has been

carried out with Matlab R2020b software. For the scenarios, the simulation time of 1.5 s is divided into 3 equal parts and a different partial shading conditions are discussed at every 0.5 s. Partially shaded conditions and scenarios created are given in Table 1 and Table 2.

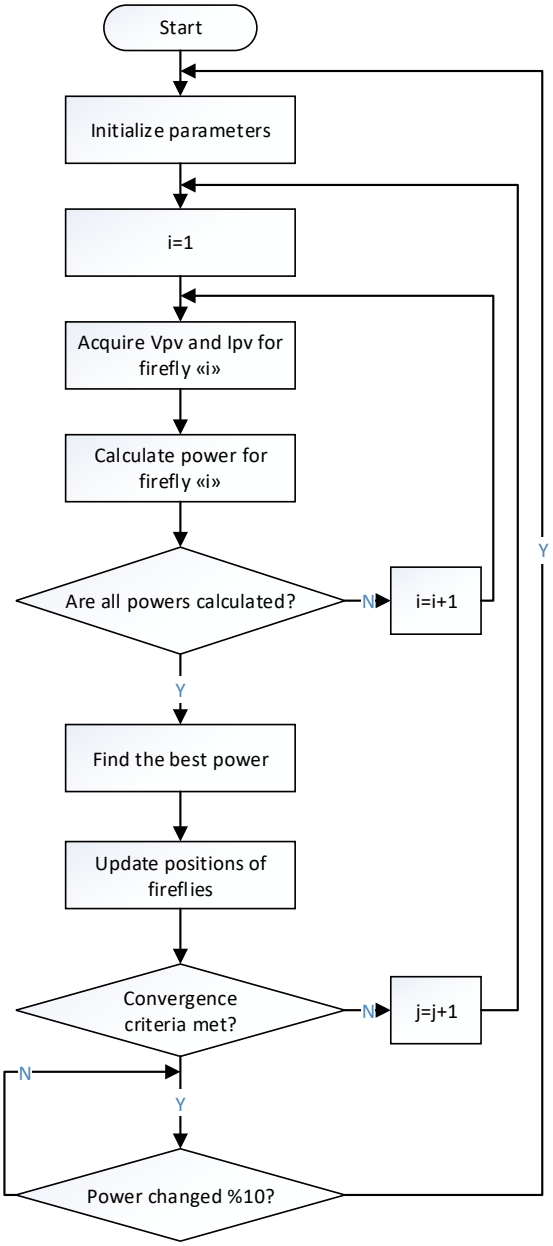

Figure 9 Flowchart of FFO algorithm

The system has constraint for maximum power at operating conditions due to nonlinear and inverse proportional relation between voltage and current as seen in Figure 2 and Figure 3. While the current varies 0 to short circuit current (I_{sc}), the voltage varies 0 to open circuit voltage (V_{oc}). When controlled current or voltage, the system can be operated at maximum power. In this study, voltage control mode has been selected and DC-DC boost converter has been used in order to control voltage. Voltage has been controlled by changing of the duty ratio of converter under limits of 0 to 1.

Table 1 Partially shaded conditions (PSC)

PSC	Module 1	Module 2	Module 3	Maximum Power(P_{max})
PSC-1	1000	1000	1000	747
PSC-2	760	888	401	391.4
PSC-3	994	977	598	496
PSC-4	943	426	984	472.1
PSC-5	553	278	436	229.4
PSC-6	329	864	540	286.4

Table 2 Simulated scenerios

Scenario	0 to 0.5 s	0.5 to 1.0 s	1.0 to 1.5 s
Scenario-1	PSC-1	PSC-5	PSC-3
Scenario-2	PSC-2	PSC-6	PSC-4

4.1. Power obtained from Scenario-1

In Scenario-1, all of the algorithms have reached MPP as seen in Figure 10. However, the times of algorithms to reach the global MPP has different, and the algorithm with the best value in terms of time has been FFO. In order to see the changes in the output power in more detail, the power between 0.5 and 0.8 s is shown in Figure 11 in a zoomed way. The MPP values reached by the algorithms are given in Table 3. According to Figure 10, Figure 11 and Table 3, even if FFO has the highest P_{avg}, PSO, CSO and BAO algorithms have the lowest power deviation at the MPP. As a result, if simulation period was be longer, PSO, CSO and BAO would obtain higher power depending on the PSC.

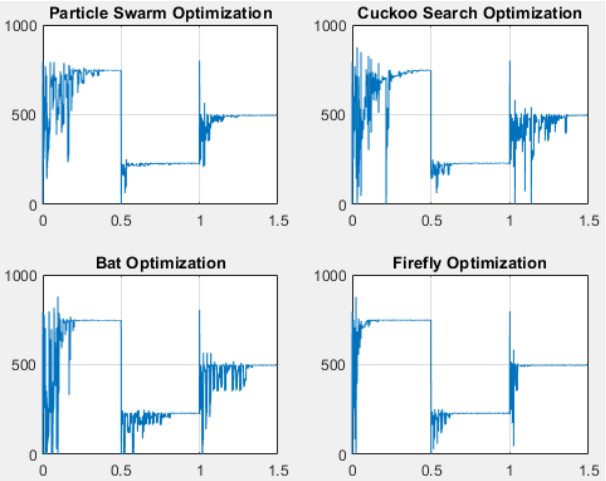

Figure 10 PV system output power for Scenario-1

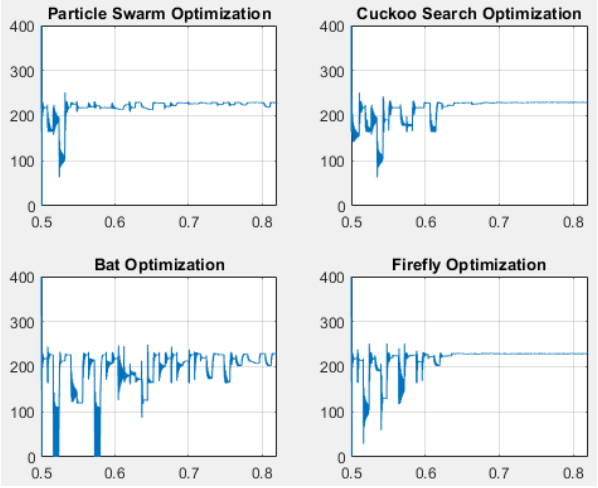

Figure 11 PV system output power between 0.5 and 0.8 s for Scenario-1

Table 3
Power values obtained with Scenario-1

Algorithm	P_{max1} (PSC-1)	P_{max2} (PSC-5)	P_{max3} (PSC-3)	P_{avg}
Theoric	747.00	229.4	496.00	-
PSO	**746.78**	228.58	495.93	500.99
CSO	744.16	**229.43**	496.05	482.09
BAO	746.07	229.05	**496.08**	491.47
FFO	746.77	229.03	495.93	**531.46**

4.2. Power obtained from Scenario-2

In Scenario-2, all of the algorithms have reached MPP as seen in Figure 12. However, since the individuals used in CSO cannot converge to each other, they create oscillations in the output power. In addition, the times of algorithms to reach the global MPP has differed, and the algorithm with the best value in terms of time has been ABO. The MPP values reached by the algorithms are given in Table 4. As shown in Figure 12 and Table 4, even if FFO has the highest P_{avg}, difference between theoric power and power obtained by algorithm has been lowest for PSO at each MPP. As a result, if the simulation period was longer, best algorithm would be PSO for scenario-2.

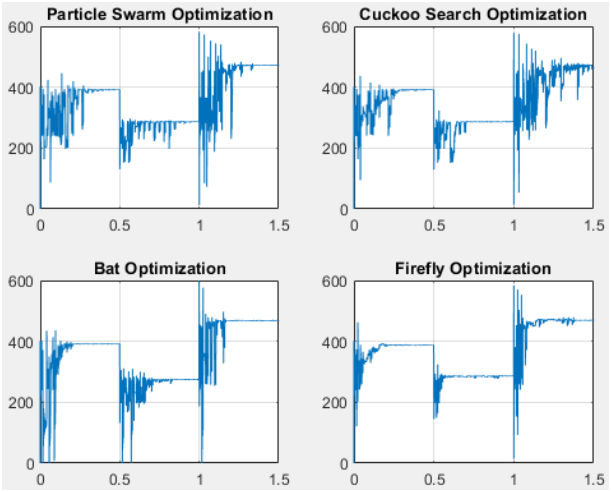

Figure 12 PV system output power for Scenario-2

Table 4 Power values obtained with Scenario-2

Algoritm	P_{max1} (PSC-2)	P_{max2} (PSC-6)	P_{max3} (PSC-4)	P_{avg}
Theoric	391.4	286.4	472.1	-
PSO	**391.22**	**286.40**	**471.63**	362.19
CSO	391.18	286.26	467.57	364.35
BAO	391.18	275.05	468.28	365.21
FFO	387.64	286.23	468.96	**377.63**

5. CONCLUSION

In this study, 4 different optimization techniques as MPPT method in PV systems have been examined comparatively in case of partial shading conditions. Among the optimization algorithms examined in the simulation studies, it has been shown that the FFO method provides better results in terms of the reaching time to the maximum power and value of the maximum power.

Funding

The author (s) has no received any financial support for the research, authorship or publication of this study.

The Declaration of Conflict of Interest/ Common Interest

The authors have declared no conflict of interest or common interest.

Authors' Contribution

N.B.: Literature review, writing codes of simulation, carrying out the simulation studies and writing the article

İ.Y.: Determining the method and scope of research and coordinating its writing

The Declaration of Ethics Committee Approval

This study does not require ethics committee permission or any special permission.

The Declaration of Research and Publication Ethics

The authors of the paper declare that they comply with the scientific, ethical and quotation rules of SAUJS in all processes of the paper and that they do not make any falsification on the data collected. In addition, they declare that Sakarya University Journal of Science and its editorial board have no responsibility for any ethical violations that may be encountered, and that this study has not been evaluated in any academic publication environment other than Sakarya University Journal of Science.

REFERENCES

[1] K. K. Tse, M. T. Ho, H. S. -H. Chung, and S. Y. Hui, "A novel maximum power point tracker for PV panels using switching frequency modulation," IEEE Transactions on Power Electronics, vol. 17, no. 6, pp. 980-989, 2002.

[2] O. Ezinwanne, F. Zhongwen, and L. Zhijun, "Energy performance and cost comparison of MPPT techniques for photovoltaics and other applications," Energy Procedia, vol. 107, pp. 297-303, 2017.

[3] S. E. Babaa, M. Armstrong, V. Pickert, "Overview of maximum power point tracking control methods for PV systems," Journal of Power and Energy Engineering, vol. 2, no. 8, pp. 59-72, 2014.

[4] F. D. Murdianto, M. Z. Efendi, R. E. Setiawan, and A. S. L. Hermawan, "Comparison method of MPSO, FPA, and GWO algorithm in MPPT SEPIC converter under dynamic partial shading condition," 2017 International Conference on Advanced Mechatronics, Intelligent Manufacture, and Industrial Automation (ICAMIMIA), Surabaya, pp. 315-320, 2017.

[5] N. Khanam, B. H. Khan, and T. Imtiaz, "Maximum power extraction of solar PV system using meta-heuristic MPPT techniques: A comparative study," 2019 International Conference on Electrical, Electronics and Computer Engineering (UPCON), Aligarh, pp. 1-6, 2019.

[6] M. A. Dirmawan, Suhariningsih, and R. Rakhmawati, "The comparison performance of MPPT perturb and observe, fuzzy logic controller, and flower pollination algorithm in normal and partial shading condition," 2020 International Electronics Symposium (IES), Surabaya, pp. 7-13, 2020.

[7] A. Dolara, R. Faranda, S. Leva, "Energy comparison of seven MPPT techniques for PV systems," Journal of Electromagnetic Analysis and Applications, vol. 1, no. 3, pp. 152-162, 2009.

[8] M. Miyatake, M. Veerachary, F. Toriumi, N. Fujii, and H. Ko, "Maximum power point tracking of multiple photovoltaic arrays: A PSO approach," IEEE Transactions on Aerospace and Electronic Systems, vol. 47, no. 1, pp. 367-380, 2011.

[9] A. M. Eltamaly, M. S. Al-Saud, and A. G. Abokhalil, "A novel bat algorithm strategy for maximum power point tracker of

photovoltaic energy systems under dynamic partial shading," IEEE Access, vol. 8, pp. 10048-10060, 2020.

[10] J. Ding, Q. Wang, Q. Zhang, Q. Ye, and Y. Ma, "A hybrid particle swarm optimization-cuckoo search algorithm and its engineering applications," Mathematical Problems in Engineering, vol. 2019, pp. 1-12, 2019.

[11] P. Dhivya, and K. R. Kumar, "MPPT based control of sepic converter using firefly algorithm for solar PV system under partial shaded conditions," 2017 International Conference on Innovations in Green Energy and Healthcare Technologies (IGEHT), Coimbatore, pp. 1-8, 2017.

[12] W. Xiao, "Photovoltaic power system modeling, design, and control," Chennai, Wiley, 2017.

[13] R. Faranda, and S. Leva, "Energy comparison of MPPT techniques for PV Systems," WSEAS Transactions on Power Systems, vol. 3, no. 6, pp. 446-455, 2008.

[14] M. R. Shaikh, S. Shaikh, S. Waghmare, S. Labade, and A. Tekale, "A review paper on electricity generation from solar energy," International Journal for Research in Applied Science and Engineering Technology, vol. 5, no. 9, pp. 1884-1889, 2017.

[15] R. Anand, S. D, and B. Kumar, "Global maximum power point tracking for PV array under partial shading using cuckoo search," 2020 IEEE 9th Power India International Conference (PIICON), Sonepat, pp. 1-6, 2020.

[16] R.-E. Precup, T. Kamal, and S. Z. Hassan, "Solar photovoltaic power plants - Advanced control and optimization techniques," Singapore, Springer, 2019.

[17] K. Aygül, "Butterfly optimization algorithm based maximum power point tracking of photovoltaic systems under partial shading condition," Adana, Cukurova University, 2019.

[18] M. V. Rocha, L. P. Sampaio, and S. A. Silva, "Comparative analysis of ABC, Bat, GWO and PSO algorithms for MPPT in PV systems," 8th International Conference on Renewable Energy Research and Applications, Brasov, pp. 347-352, 2019.

[19] G. Dilep, and S. Singh, "An improved particle swarm optimization based maximum power point tracking algorithm for PV system operating under partial shading conditions," Solar Energy, vol. 158, pp. 1006-1015, 2017.

[20] H. Chaieb, and A. Sakly, "Review and comparison of BAT and PSO MPPT's based algorithms for photovoltaic system," WSEAS Transactions on Power Systems, vol. 13, pp. 108-117, 2018.

[21] A. M. Kamoona, J. C. Patra and A. Stojcevski, "An enhanced cuckoo search algorithm for solving optimization problems," 2018 IEEE Congress on Evolutionary Computation (CEC), Rio de Janeiro, pp. 1-6, 2018.

[22] J. Ahmed, and Z. Salam, "A soft computing MPPT for PV system based on cuckoo search algorithm," 4th International Conference on Power Engineering, Energy and Electrical Drives, Istanbul, pp. 558-562, 2013.

[23] M. I. Mosaad, M. O. el-Raouf, M. A. Al-Ahmar, and F. A. Banakher, "Maximum power point tracking of PV system based cuckoo search algorithm; review and comparison," Energy Procedia, vol. 162, pp. 117-126, 2019.

[24] T. P. Dao, "Cuckoo search algorithm: Statistical-based optimization approach and engineering applications," Singapore, Springer, 2021.

[25] A. Brabazon, and S. McGarraghy, "Foraging-inspired optimisation algorithms," Dublin, Springer, 2018.

[26] K. Sundareswaran, S. Peddapati, and S. Palani, "MPPT of PV systems under partial shaded conditions through a colony of flashing fireflies," IEEE Transactions on Energy Conversion, vol. 29, no. 2, pp. 463-472, 2014.

[27] M. Mohanty, S. Selvakumar, C. Koodalsamy, and S. Simon, "Global maximum operating point tracking for PV system using fast convergence firefly algorithm," Turkish Journal of Electrical Engineering & Computer Sciences, vol. 27, pp. 4640-4658, 2019.

[28] L. N. Palupi, T. Winarno, A. Pracoyo, and L. Ardhenta, "Adaptive voltage control for MPPT-firefly algorithm output in PV system," IOP Conference Series: Materials Science and Engineering, East Java, vol. 732, pp. 1-9, 2020.

SAKARYA ÜNİVERSİTESİ
FEN BİLİMLERİ ENSTİTÜSÜ DERGİSİ

Sakarya University Journal of Science
SAUJS

ISSN 1301-4048 | e-ISSN 2147-835X | Period Bimonthly | Founded: 1997 | Publisher Sakarya University | http://www.saujs.sakarya.edu.tr/

Title: Response Surface Methodology-Based optimization of Inulinase Production from New Bacillus Isolates

Authors: Sercan ÖZBEK YAZICI, Selmihan ŞAHİN, Bahadır TÖRÜN, Hacı Halil BIYIK, İsmail ÖZMEN

Recieved: 2021-03-16 12:38:04

Accepted: 2021-07-23 15:42:40

Article Type: Research Article

Volume: 25
Issue: 4
Month: August
Year: 2021
Pages: 1086-1101

How to cite
Sercan ÖZBEK YAZICI, Selmihan ŞAHİN, Bahadır TÖRÜN, Hacı Halil BIYIK, İsmail ÖZMEN; (2021), Response Surface Methodology-Based optimization of Inulinase Production from New Bacillus Isolates. Sakarya University Journal of Science, 25(4), 1086-1101, DOI: 10.16984/saufenbilder.897660
Access link
http://www.saujs.sakarya.edu.tr/en/pub/issue/64755/897660

Sakarya University Journal of Science 25(4), 1086-1101, 2021

Response Surface Methodology-Based optimization of Inulinase Production from New *Bacillus* Isolates

Sercan ÖZBEK YAZICI*[1], Selmihan ŞAHİN[2], Bahadır TÖRÜN[3], Hacı Halil BIYIK[3], İsmail ÖZMEN[2]

Abstract

This study aimed to investigate new bacterial sources with the ability to produce inulinase and to optimize fermentation conditions for inulinase production. The inulinase production was carried out using newly isolated *Bacillus licheniformis* and *Bacillus velezensis* among identified sixteen bacterial strains. The four essential variables incubation time (1-3 days), temperature (25-40°C), pH (5-7), and Wheat Bran **(**WB**)** level (1-5%) determined by the Plackett–Burman design (PB) were selected for optimization studies with Box-Benhken Design (BBD). These parameters were found to be very effective on inulinase production**.** The maximum inulinase activities for *B. licheniformis* and *B. velezensis* were 401.18 EU/mL and 344.61 EU/mL. Both inulinases sustained 50% of their initial activity at 30°C for 9 days. The results point out that bacteria are an important source as inulinase producer. The new isolates can be used in production of inulinase for industrial processes.

Keywords: Bacteria inulinase, response-surface methodology, optimization, submerged fermentation

* Corresponding author: sozbekyazici@hotmail.com
ORCID: https://orcid.org/0000-0003-3406-4291
[1] Burdur Mehmet Akif Ersoy University,
[2] Suleyman Demirel University
E-Mail: selmihansahin@sdu.edu.tr, ismailozmen@sdu.edu.tr
ORCID: https://orcid.org/0000-0003-0486-3949; https://orcid.org/0000-0002-5457-8188
[3] Aydın Adnan Menderes University
E-Mail: bahadrtrn@gmail.com, hbiyik@adu.edu.tr
ORCID: https://orcid.org/ 0000-0001-5142-1882; https://orcid.org/ 0000-0003-0258-054X

1. INTRODUCTION

Inulin is present in many plants and is a fructose polymer consisted of fructose residues and a glucose moiety at the terminal end. It is an essential source in the production of fructose and fructooligosaccharides, which are used in industrial areas such as food, pharmaceutical, and medical applications [1]. Moreover, fructose is 1.5 times sweeter than sucrose and it is generally considered the preferred safe sweetener in several foods and beverages. In addition, fructose has advantages such as less production costs and increased flavor, color, and product stability [2]. Fructose can be obtained from inulin by acid hydrolysis. However, that process leads to fructose degradation and low yield production. Therefore, the use of inulinases is considered to be a desirable approach to obtain high fructose syrups from inulin because of 95% pure fructose yield in a single-stage process [3, 4].

Inulinases are industrially significant enzymes, but the production cost of the enzyme continues to be a major problem in its large-scale application. Using microorganisms as potential sources for inulinase production can result in high enzyme yield and stability, which reduces the cost [5]. Although fungi such as *Aspergillis*, *Penicillium*, *Kluyveromyces sp.* are the most common microorganisms to produce inulinase, bacteria and yeast also can produce inulinase. There are previous reports on the production of inulinase from bacteria such as *Bacillus* sp., *Streptomyces* sp., *Xanthomonas* sp., *Clostridium* sp. that can grow in environmental conditions such as high temperature, alkalinity, acidity, and salinity [1]. However, there is still a need to explore microorganisms for inulinase production with high yield and superior properties. Moreover, the synthesis of the enzyme by microorganisms is dependent on growth conditions, mainly the carbon source. The type of carbon source used in the medium affects growth, sporulation, and cell wall structure in microorganisms, which in turn can affect the secretion of the enzyme [1,6]. Inulinases have different catalytic properties depending on the microbial origin such as molecular mass, optimum pH, optimum temperature, thermal and pH stabilities [7]. Therefore, the appropriate carbon source and optimal fermentation conditions should be determined to increase enzyme production. Previously, the conventional "one-factor-at-a-time" approach or statistical approaches have been used to determine optimal conditions for enzyme production. Statistical optimization facilitates determining parameters effective in enzyme production and the interactions between these parameters with lesser experiments while conventional methods are both laborious and time-consuming. Factor design and response surface analysis, which are among the current statistical methods, are considered significant tools for optimization analysis. Especially, the statistical approach using PB design and response surface methodology (RSM) have a larger and wider application for optimization due to their advantages [8, 9]

Based on all these findings, this study aims to investigate new bacterial sources with the ability to produce inulinase with high activity. For this, the fermentation conditions of these microorganisms are optimized for the production of inulinase with a low-cost substrate using statistical methods and increase the yield of enzyme production. After that, the obtained inulinases from *B.licheniformis* and *B. velezensis* were characterized by determining their optimum pH, temperature, and thermal stability.

2. MATERİALS AND METHODS

2.1. Materials

Inulin from Alfa Aesar, Sucrose from Sigma, glucose from Sigma, fructose from Merck, and 3.5-dinitrosalicylic acid from Sigma were purchased. Other chemical reagents used in experiments were analytical grade.

2.2. Identification of bacterial strains

Materials and Methods

Soil samples were collected aseptically from Buharkent, Aydın geothermal sources and brought back to laboratory. Soil samples for isolation of microbes were obtained from the 15 to 20 cm layers below soil surface.

Nutrient agar was used for all experiments concerning screening, isolation and culture of microbes. Ten grams of each soil sample was added to 90 ml of autoclaved physiologic saline water (0.85%) and homogenized with shaker (150 rpm). Ten-fold dilutions were prepared from 10^{-1} to 10^{-7} and 100 µl of these dilutions were inoculated on growth media and incubated at 55°C for 24-48 hours. Each different colony were selected from the mixed culture and inoculated and incubated at 55°C for 24-48 hours until pure cultures were obtained [10]. Each isolate were stored in 20 % Skim milk solution at -20°C.

DNA isolation of the samples were made with GeneMark Bacterial Genomic DNA purification kit according to the manufacturers instructions. After isolations DNA concentration and purity was measured with nanodrop spectrometer (Thermo Scientific). 16S universal rDNA primers were used (27F: 5'-AGA GTT TGA TCM TGG CTC AG-3', 1492R: 5'-CGG TTA CCT TGT TAC GAC TT-3') [11]. PCR reactions were carried out at initial denaturation 95ºC 5 min, denaturation 94ºC 30 sec, annealing 58ºC 30 sec, extension 72ºC 45 sec with 35 cycles and final extension at 72ºC 10 mins. Reagents concentrations were 10X Taq Buffer, 0.5M dNTP mix, 10 pM from each primer, 7.5 mM MgCl2 and 1U Taq polymerase with the final volume of 25 µl. PCR products were sent to sequencing (Atlas Biotechnology, Turkey).

Evolutionary analysis and tree construction were made with MEGA X software. The evolutionary history was inferred using the Maximum Likelihood method [12, 13, 14].

2.3. Determination of bacterial strain producing inulinase

A rapid plate screening assay was used to screen for inulinase-producing bacterial strains [14, 15]. For this, nutrient agar (NA) plates containing 1% w / v inulin were used to grow the bacterial strains, incubating at 40°C for 2 days. Lugol's iodine solution (5 mL) was added to plates and incubated for 10 min at room temperature. Afterward, the plates were washed with distilled water. The hydrolytic zone around the colony obtained is evidence of extracellular inulinase.

2.4. Submerged fermentation medium and inoculum preparation

Before starting the study, the strains were grown on NA slants at 40°C for two days.

Table 1
The activity of enzyme obtained with basal mediums selected according to the previous literature

Medium	**Enzyme activity (EU/mL)**		**Reference**
	B.licheniformis	***B. elezensis***	
1%inulin, 0.3% K_2HPO_4, 0.1% KH_2PO_4, 0.3% yeast extract, 0.3% peptone	35.21 ± 0.01	45.77 ± 0.01	[17]
0.5 % inulin, 0.3% $NaNO_3$, 0.5% $CaCl_2$,0.3% yeast extract	47.32 ± 0.09	66.32 ± 0.2	[18]
2%inulin, , 0.5% $(NH_4)_2SO_4$, 0.5% yeast extract	11.49 ± 0.03	15.78 ± 0.06	[19]
0.02%inulin, 0.04% K_2HPO_4, 0.008%$MgSO_4$ 0.2%peptone, 0.2%yeast extract	24.11 ± 0.9	45.21 ± 0.11	[20]

1% inulin, 0.1% K_2HPO_4, 0.05% $MgSO_4$ $7H_2O$, 0.015%$CaCl_2.2H_2O$, 0.05% NaCl, 0.2% yeast extract, 0.3% peptone	64.012 ± 0.7	69.23 ± 0.14	[21]
1% inulin, 0.2%KH_2PO_4, 0.05% $MgSO_4$, 0.5% $NaNO_3$	101.45 ± 0.04	89.13 ± 0.07	[22]

In 250 ml Erlenmeyer flask, a loopful of bacteria was used to inoculate nutrient broth (NB, 100 ml).After that, the flasks were incubated at 37°C and 150 rpm for one day. The optical density of NB was measured at 600 nm until it reached at 1.0. 1 mL of NB was used for inoculation of the inulinase production medium [21, 23]

In SmF where the production of enzyme takes place, the media components were determined according to the literature research (Table 1). After 100 mL of medium was prepared in 250 mL Erlenmeyer flask, the pH was adjusted to 6.5. The media was incubated at 30 ºC, and 150 rpm for 2 days for enzyme production after the medium was autoclaved. Among those tested the medium which provided the highest activity was used as medium components in SmF for enzyme production.

2.5. Optimization of inulinase production from isolates

2.5.1. Determining carbon source and fermentation parameters by PB experimental design

PB design was used to test the effect of eleven variables (carbon sources in media and fermentation parameters). For this, the effect of fructose, glucose, maltose, sucrose, lactose, onion peel, wheat bran, oat bran concentrations as carbon sources on enzyme production were evaluated, ranging from low to high. Concentrations of 0.1% and 1% levels Fermentation parameters including incubation period (1-4 days), incubation temperature (25-45 °C), and initial pH (5-8) were also tested at 2 levels as high and low. For all tests, inulinase activity was taken as a response. The variables and their levels are presented in Supplementary Table S1.

2.5.2. Optimization of fermentation parameters by using BBD

The four variables obtained from PB Design were further analyzed for optimization of inulinase production using BBD. The variables determined were incubation time (24-72 hours), incubation temperature (25-40°C), initial pH (5-7), and WB concentration (1-5%) as carbon source. For BBD analyses, three levels as high (+1), medium (0) and, low (-1) were described (Table 2).

Table 2
Levels of the factors tested in Box-Behnken Design independent variables

Symbol	Variable	Units	Coded levels		
			-1	0	1
A	Initial pH		5	6.25	7.5
B	Incubation temperature	^{0}C	25	32.5	40
C	Wheat Bran (WB)	%	1	3	5
D	Incubation time	h	24	48	72

The experimental design method was carried out by 29 experiments in duplicates. The response function coefficients were identified by regression using the experimental data and Design-Expert V7 trial version. The model equation for 4 variable systems is as follows:

$$Y = \beta_0 + \beta_1 A + \beta_2 B + \beta_3 C + \beta_4 D + \beta_{11} A^2 + \beta_{22} B^2 + \beta_{33} C^2 + \beta_{44} D^2 + \beta_{12} AB + \beta_{13} AC + \beta_{14} AD + \beta_{23} BC + \beta_{24} BD + \beta_{34} CD \quad (1)$$

Where Y is the predictable response (inulinase activities of *B. licheniformis* and *B. velezensis*), β_0 is the model constant; independent variables are A, B, C, and D term; β_1, β_2, β_3, and β_4 are linear

coefficients, and β_{11}, β_{22}, $\beta 3_3$, and β_{44} are the quadratic coefficient.

2.6. Enzyme assay

Activity assays were performed based on the previous study [24]. The crude enzyme was used to analyze inulinase activity. One unit of inulinase activity was the amount of enzyme that catalyzes the release of 1 µmol of fructose per minute per mL.

2.7. Effect of pH and temperature on enzyme activity

To determine the effect of pH on inulinase activity, three buffer solutions including Na-acetate (0.1 M, pH 4.0-5.0), K-phosphate (0.1 M, pH 6.0-7.0), and Tris-HCl (0.1M, pH 8.0-9.0) were used in activity assay.

The effect of temperature on the inulinase activity was determined at different temperatures between 30-60 ºC. Also, the thermal stability of enzymes was evaluated at 60ºC by the standard assay procedure after 1h incubation at different temperatures between 30-60 ºC. Enzyme activities were determined as relative activities by taking 100% of the activity at the start of the experiment.

3. RESULTS AND DISCUSSION

3.1. Identification of bacterial strains

Sixteen bacteria were isolated and identified by molecular characterization (Supplementary Table S2). From 16 samples, 1 Genus and 4 different species were found.

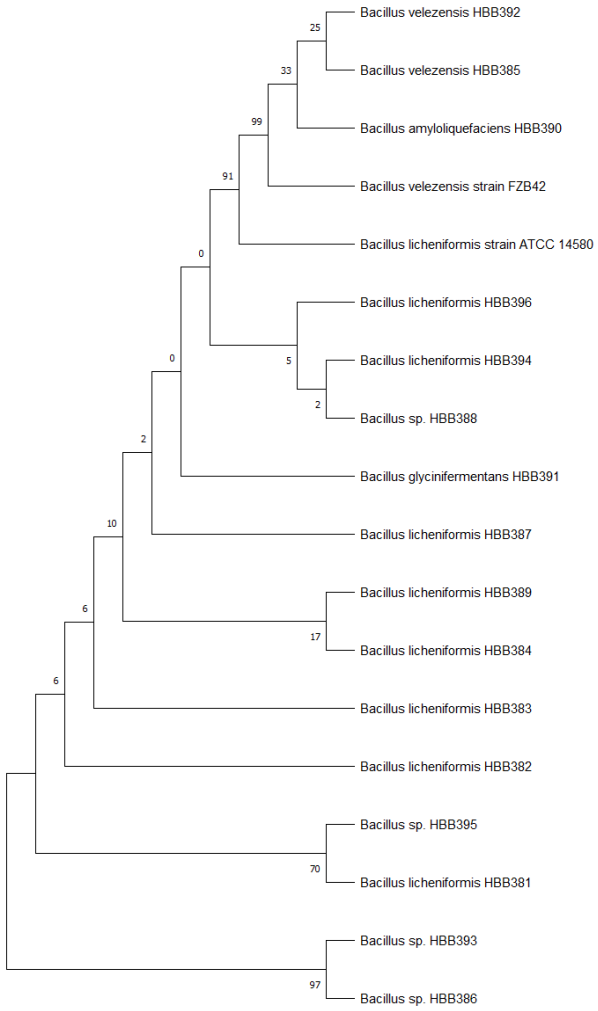

Figure 1 Phylogenetic relationships of *Bacillus* species

The evolutionary history was inferred by using the Maximum Likelihood method and Hasegawa-Kishino-Yano model (Fig. 1). The percentage of trees in which the associated taxa clustered together is shown next to the branches. Evolutionary analyses were conducted with MEGA X software.

All species isolate were *Bacillus* species. Different strains of *Bacillus licheniformis* were abundant in soil samples. This result is similar to the results of Llarch et al [25], Balsam et al [26].

3.2. Bacteria strains selection for inulinase production and identification

The microorganism and medium selection are significant factors in determining the outcome of

inulinase production. Extracellular hydrolytic enzymes are detected by plate screening assay [16]. In this work, bacteria were screened out based on the assay of plate screening. Among the sixteen molecularly identified microorganisms, *Bacillus licheniformis* strain SCRSW1 HBB387 and *Bacillus velezensis* strain KKLV HBB392 shown a clear zone indicating the presence of extracellular inulinase on their agar plates on agar plates (Supplementary Fig. S1). Hence, the bacteria strains were used to produce inulinase through the study.

3.3. Optimization of inulinase production

3.3.1. Determination of basal medium

Micronutrients are critical for enzyme production for making significant contribution to maintain the osmotic pressure of the environment. Moreover, suitable concentrations of trace elements are reported to be essential for the substrate usage of microorganisms [27]. In previous studies, a medium consisting of different components was used for inulinase production, and enzyme production was successfully performed. In this study, the media used in the previous studies given in Table 1 were tested to obtain maximum enzyme production. Maximum inulinase activity was observed as 101.45 ± 0.04 for *B.licheniformis* and 89.13 ± 0.07 U/mL for *B. velezensis* in medium containing 0.5% $NaNO_3$, 0.2% $MgSO_4$, 0.2% KH_2PO_4, 0.4% yeast extract, 1%inulin on a rotary shaker at 30°C, 150 rpm, pH 7.0 for two days [22]. Hence, this medium was selected as a basal medium for further experiment.

The complex nitrogen sources have been reported to be better than inorganic nitrogen sources. Jain et al. [28] found that yeast extract was the best nitrogen source to conjunct with dahlia extract for inulinase production, followed by the beef extract. The lowest inulinase activities from *B. licheniformis* and *B. velezensis* when $(NH_4)_2SO_4$ was used as a nitrogen source in the fermentation medium. It can be associated with acidic conditions caused by ammonium salts because highly acidic conditions may inhibit the synthesis of inulinase [29].

3.3.2. Determination of significant variables by PB design

Various bacterial sources as inulinase producers have been reported to exploit sucrose, starch inulin, and inulin-rich plant extracts to produce inulinase. Characteristically, inulinases syntheses require an inducer. Inulin takes a function as a carbon source as well as an inducer for inulinase production [1, 30]. However, catabolic suppression may occur due to a high inulin concentration, which reduces enzyme yield [31]. In this study, 1% raw inulin was used in the production medium.

Plackett Burman design was carried out to identify factors that can affect inulinase production from bacterial sources. All cultivations were performed at 30°C under agitation (150 rpm) in a rotary shaker. Eleven variables were screened for their influence on enzyme production, and the inulinase activities are illustrated in Table 3. The maximum activities for *B. licheniformis* and *B. velezensis* were observed at run number 12 for two bacteria, with 14.41 and 34.3 EU/mL, respectively.

In the PB design, the p values of the model by ANOVA analysis show that the model is significant ($p < 0.05$). Also, the productions of inulinase from both bacteria were found to be affected by WB, incubation temperature, initial pH, and incubation time ($p<0.05$) (Supplementary Table S3). Hence, other insignificant variables were neglected, and the optimum levels of these four variables were determined by the BBD design. The effects of variables are presented in Pareto charts (Supplementary Figures S2 and S3). One of the four significant variables that screened, WB concentration, exerted a positive effect. However, incubation temperature, initial pH, and incubation time exerted negative effects on enzyme production. In another study where 11 parameters were scanned affecting inulinase production from *Arthrobacter mysorens* strain no.1 by PB, pH and temperature were not significant [32]. It has been reported that the cost of enzyme production is reduced by the use of low-cost complex substrates as a carbon source [33]. This study indicates that WB was more effective than other carbon sources. In previous studies in which inulinase production was

optimized, the effects of different carbon sources were evaluated.

Table 3
Real values of the variables in PB experimental design with values of inulinase activity

Run order	Fruktoz	Sucrose	Glucose	Maltose	Lactose	Onion peel	Oat bran	Wheat bran	Temperature	pH	Time	Experimental value for	Experimental value for *B.*
	%	%	%	%	%	%	%	%	ºC		Day	EU/mL	EU/mL
1	1.00	1.00	1.00	0.10	0.10	1.00	3.00	1.00	45.00	8.00	1.00	0.39	0.61
2	1.00	0.10	0.10	0.10	1.00	1.00	3.00	3.00	25.00	8.00	4.00	2.1	15.1
3	0.10	0.10	0.10	1.00	0.10	3.00	3.00	1.00	45.00	8.00	4.00	0.18	2.66
4	1.00	1.00	0.10	1.00	1.00	3.00	1.00	1.00	25.00	8.00	1.00	3.52	15.1
5	1.00	1.00	0.10	0.10	0.10	3.00	1.00	3.00	45.00	5.00	4.00	5.64	13.99
6	0.10	0.10	1.00	0.10	1.00	3.00	1.00	3.00	45.00	8.00	1.00	5.65	10.8
7	0.10	1.00	1.00	0.10	1.00	3.00	3.00	1.00	25.00	5.00	4.00	5.05	15.9
8	0.10	1.00	0.10	1.00	1.00	1.00	3.00	3.00	45.00	5.00	1.00	8.32	18.09
9	0.10	1.00	1.00	1.00	0.10	1.00	1.00	3.00	25.00	8.00	4.00	5.75	15.4
10	0.10	0.10	0.10	0.10	0.10	1.00	1.00	1.00	25.00	5.00	1.00	8.34	25.64
11	1.00	0.10	1.00	1.00	1.00	1.00	1.00	1.00	45.00	5.00	4.00	0.81	7.3
12	1.00	0.10	1.00	1.00	0.10	3.00	3.00	3.00	25.00	5.00	1.00	14.41	34.3

Rawat et al. [33] obtained maximum inulinase activity in medium with the dahlia extract. In another study, *Tithonia rotundifolia* was reported to be effective in inulinase production [34]**.** Trivedi et al. [35] obtained maximum inulinase production using chicory root powder (21.9 EU/mL). However, glucose, fructose, and sugarcane bagasse were reported to be poor inducers for inulinase production, 5.8 EU/mL, 5.1 EU/mL, and 4.7 EU/mL, respectively. The highest inulinase activity from *X. campestris* pv. *Phaseoli* KM 24 mutant was observed in sucrose (5.19 EU/mL) [36]. The maximal activities of *B. polymyxa* 722, *B. subtilis* 68, and *B. polymyxa* 29 were observed in the presence of sucrose, starch/molasses, and starch, respectively [37]. There are previous studies in parallel with our study, which support that WB is an important source of carbon to increases production of inulinase [31, 38]. WB contains 1–4% inulin and has a high nutritional value for microorganisms [35]. Apart from this, WB is a cheap and available substrate. All these features make them an essential resource for large scale fermentation.

3.3.3. BBD for optimization of fermentation medium

The relation between the significant variables (initial pH, incubation temperature, incubation time, and WB concentration) obtained by PB experiment was developed using BBD to produce maximum enzyme [34]. The enzyme productions from both bacteria were carried out by experimental designs and the results are shown in Table 4.

ANOVA analysis showed the significant of the model ($p < 0.0001$) (Supplementary Table S4).

The regression equations for inulinase activity responses (Y) were obtained, and these equations are given below:

$Y_{\text{Inulase activity for } B.licheniformis}$=+374.18 -22.54 *A-25.14 *B -88.56*C+26.15 *D-4.46 *A*B+ 9.08 *A *C -5.36*A*D+32.87 *B*C-16.23 *B*D-17.23*C*D-145.54 *A^2-112.43*B^2-111.8 *C^2-123.31*D^2 (2)

$Y_{\text{Inulase activity for } B.\ velezensis}$=+328.65+82.42 *A +34.98 *B+34.10 *C+15.27 *D+17.18*A*B+ 11.70*A*C+48*A*D-5.80*B*C+ 15.63 *B*D +32.58*C*D-108.8*A^2-102.57*B^2-94.23 *C^2-82.11 *D^2 (3)

The coefficients of determination (R^2) for inulinase activities of *B. licheniformis* and *B. velezensis* were calculated as 0.99.

Table 4
Experimental design-based BBD for the optimization of inulinase production

Run order	Initial pH	Incubation Temperature (^{0}C)	Incubation time (h)	WB (%)	*B.licheniformis* Inulinase activity(EU/mL)	*B. velezensis* Inulinase activity(EU/mL)
1	7.5	25.00	48.00	3.00	105.54	147.4
2	6.25	32.50	72.00	1.00	40.09	132.22
3	6.25	32.50	48.00	3.00	375.18	325.25
4	5	32.50	72.00	3.00	39.1	74.66
5	6.25	40.00	48.00	5.00	121.3	221.74
6	6.25	32.50	48.00	3.00	385.11	315.25
7	6.25	40.00	48.00	1.00	108.36	159.74
8	6.25	32.50	48.00	3.00	371.27	335.25
9	6.25	25.00	24.00	3.00	315.57	33.51
10	7.5	32.50	48.00	1.00	73.24	205.85
11	6.25	25.00	72.00	3.00	59.24	168.14
12	5	32.50	24.00	3.00	236.3	14.85
13	6.25	25.00	48.00	1.00	123.03	102.25
14	7.5	32.50	24.00	3.00	176.34	158
15	5	40.00	48.00	3.00	123.88	55.33
16	7.5	32.50	72.00	3.00	15.45	264.6
17	6.25	32.50	72.00	5.00	64.42	233.29
18	6.25	25.00	48.00	5.00	200.9	101.74
19	6.25	40.00	72.00	3.00	62.12	151.25
20	5	25.00	48.00	3.00	155.79	23.25
21	5	32.50	48.00	5.00	160.18	61.33
22	6.25	40.00	24.00	3.00	186.96	159.81
23	6.25	32.50	24.00	1.00	167.34	139.04
24	7.5	32.50	48.00	5.00	115.21	231.77
25	6.25	32.50	48.00	3.00	371.11	335.25
26	5	32.50	48.00	1.00	96.76	37.33
27	6.25	32.50	48.00	3.00	368.24	332.25
28	6.25	32.50	24.00	5.00	260.57	109.79
29	7.5	40.00	48.00	3.00	55.78	248.22

* Experimental results

The “Predicted R-Square” of 0.97 and 0.98 was in reasonable agreement with the “Adjusted R-Square” of 0.99 and 0.97 for *B. licheniformis* and *B. velezensis*, respectively. This model can be used in navigating the design space.

These variables have been shown by statistical analysis to significantly affect inulinase activity. In this case, the model F-value of 206.27 and 185.51, for *B. licheniformis* and *B. velezensis*, respectively, imply that the model is significant. There is only a 0.01% chance that a "Model F-Value" this large could occur due to noise. Values

of "Prob > F" less than 0.05 indicate model terms are significant. In this case, for *B. licheniformis*; the linear, square, and interaction coefficients for all parameters were statistically significant for all parameters, except for the interaction of pH and incubation temperature, time, and WB concentration (AB, AC, and AD). When analyzed for *B. velezensis*, significant model terms are statistically significant for all parameters, except for the interaction of pH and WB concentration (AD). The "Lack of Fit" of 0.1029 and 0.3210 for *B. licheniformis* and *B. velezensis*, respectively, implie the Lack of Fit is not significant relative to the pure error. Non-significant lack of fit is good for the model fitness (Table 5).

All parameters had the same effective impacts on enzyme production (based on the p-value). The interactions between parameters are analyzed with contour graphics. The two-dimensional contours (2D) were drawn by using BBD.

Table 5
ANOVA analyses for models obtained from the BBD

Factor	**df**	**Inulinase activity of *B.licheniformis***		**Inulinase activity of *B. velezensis***	
		Coefficient Estimate	**Prob > F**	**Coefficient Estimate**	**Prob > F**
β_0	14	374.18	< 0.0001*****	328.65	< 0.0001*****
B_1	1	-22.54	< 0.0001*****	82.42	< 0.0001*****
B_2	1	-25.14	< 0.0001*****	34.98	< 0.0001*****
B_3	1	-88.56	< 0.0001*****	34.10	< 0.0001*****
B_4	1	26.15	< 0.0001*****	15.27	0.0002*****
B_{12}	1	-4.46	0.4498	17.18	0.0054*****
B_{13}	1	9.08	0.1361	11.70	0.0420*****
B_{14}	1	-5.36	0.3660	0.48	0.9281
B_{23}	1	32.87	< 0.0001*****	-35.80	< 0.0001*****
B_{24}	1	-16.23	0.0134	15.63	0.0097*****
B_{34}	1	-17.23	0.0095	32.58	< 0.0001*****
B_{11}	1	-145.54	< 0.0001*****	-108.80	< 0.0001*****
B_{22}	1	-112.43	< 0.0001*****	-102.57	< 0.0001*****
B_{33}	1	-123.31	< 0.0001*****	-94.23	< 0.0001*****
B_{44}	1	-111.80	< 0.0001*****	-82.11	< 0.0001*****
Lack of Fit	14		0.1029		0.3210

*****Significantly different at $p < 0.05$. β_0: intercept; β_1, β_2, β_3, and β_4: linear regression coefficients for pH, temperature, time, and WB; β_{12}, β_{13}, β_{14}, β_{23}, β_{24}, and β_{34}: regression coefficients for interaction between pH and temperature, pH and time, pH and WB concentration, temperature and time, temperature and WB concentration; Time and WB concentration; β_{11}, β_{22}, β_{33} and β_{44}: quadratic regression coefficients for pH x pH, temperature x temperature, time x time, WB concentration x WB concentration.

2D contour plots enable visualizing the relationship between responses and each variable as well as the type of interactions between two test variables. The circular contour plots show the insignificant interactions between the correspondent variables; whereas an elliptical

contour plots show important interactions [32]. Therefore, the relationships between parameters for optimization of fermentation conditions are analyzed based on the results obtained through experiments and their interpretation is made based on diagrams. It was determined that enzyme productions were remarkably affected by all parameters in the model ($p < 0.05$).

The inulinase activity from *B. licheniformis* increased evidently at first as pH increase as well as incubation temperature and time also increased. However, these values decreased when the two variables ascended continually (Fig. 2).

The linear effect of the initial pH (**A**) was significant ($p< 0.0001$), and its quadratic ($\mathbf{A}^2$) had a significant **(**$p<0.05$), which is the negative effect on the enzyme activity of *B. licheniformis*. Moreover, the negative and insignificant effects of pH and incubation time, pH and incubation temperature and pH and WB concentration on inulinase activity ($p>0.05$) could be seen from Fig. 2a, c, e for the presence of circular contour, which was consistent with results of coefficients of the regression equation in Table 5. The maximum activity was obtained at pH 6.25 (385.11 EU/mL). However, Fig. 2b, c, and d demonstrate that inulinase activity was maximum at 32.5°C. Inulinase activity remarkably decreased up 36°C. It is seen that high temperature and long incubation time negatively affect enzyme production. Differently, the singular effect of WB concentration on enzyme activity was positive for its plus coefficient. The activity of inulinase was maximum between 3% and 4% WB concentrations (Fig. 2d, e, and f). Fig 2d and f graphed the effects of incubation temperature and incubation time with WB concentration on enzyme activity and their interactions. However, interactions of WB concentration with incubation temperature and incubation time had a negative effect on enzyme activity (Table 5).

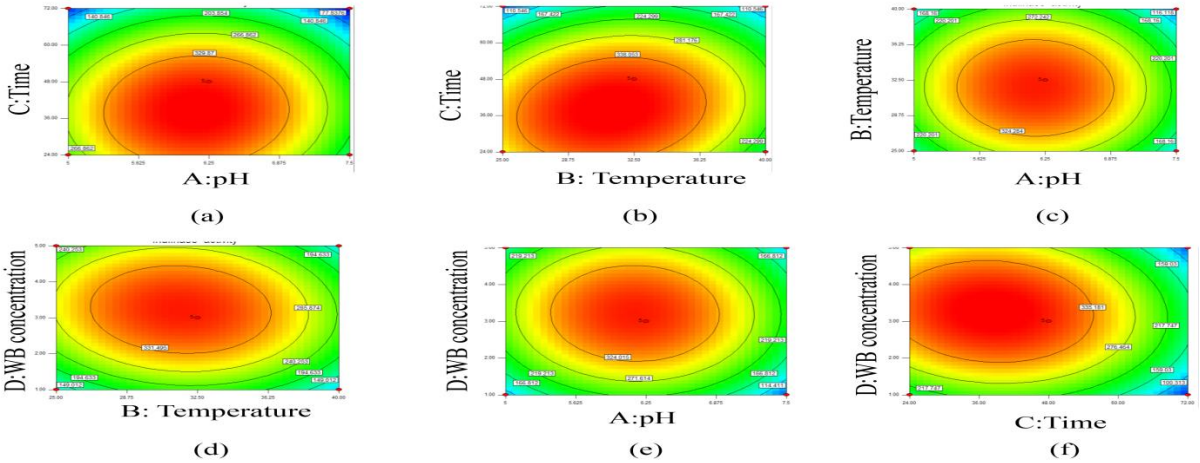

Figure 2 2-D plots of the combined effect of two variables on the inulinase activity from *B.licheniformis*

The enzyme activity was the maximum at 3% WB concentration at 32.5°C and 36h, and then exhibited a decreasing trend.

In the study, all parameters affected the enzyme production from *B. velezensis* ($p < 0.05$). However, the interaction between WB concentration and pH (AD) was insignificant ($p > 0.05$) (Table 5). Inulinase activity from *B. velezensis* was constant, almost in the range of pH 6.25-6.8. The highest activity was found at pH 6.25, like inulinase activity from *B. licheniformis* (see in Fig. 3a, c, and e). Also, Fig. 3b, c, and d illustrate that the highest inulinase activity from *B. velezensis* is obtained at ranged of 32.5°C (335.25 EU/mL). The relationship between temperature and time was negative; it could be seen that it retained its activity for a longer time at low temperatures as seen in Fig. 3b. However, the inulinase activity from *B. velezensis* decreased significantly after 60h of incubation. Furthermore, inulinase productions of both bacterial decreased significantly at higher temperatures than 36°C.

The result shows that the increase in temperature may have caused the denaturation of enzymes.

The pH and temperature of the fermentation medium in inulinase production are the most significant variables. Generally, bacterial inulinases are produced in fermentation media with pH between 4.8 and 7.0, and a temperature of 35-37°C is optimal for bacterial growth and enzyme production [30]. Zherebtsov et al. [37] suggested that *Bacillus* sp. viz. *B. polymyxa* 29, *B. polymyxa* 722, and *B. subtilis* 68 were obtained inulinase in the optimal parameters for the growth to be pH 7.0 and 33-35°C. In addition, optimal culture conditions for inulinase production from *Marinimicrobium* sp. LS-A18, were pH 7.5, 37°C, and 96 h with inulinase activity of 14.6 EU/mL [39]. According to experimental results, the maximum inulinase activities were obtained in the midpoint of the response plot as 385.11 EU/mL for *B. licheniformis*, and 335.25 EU/mL for *B. velezensis*. The findings were acquired at 48h of incubation time, 32.5°C of incubation temperature, initial pH of 6.25, and 3% (v/v) WB (Table 4).

By employing the software of Design-Expert, the optimum values of the independent variables tested for *B. licheniformis* were predicted as 6.1 of initial pH, 30.5°C of incubation temperature, 35.05h of incubation time, and 3.1% of WB concentration with 396.504 EU/mL of inulinase activity. For *B. velezensis*, the optimum values were predicted as 6.7 of pH, 33.9°C, 55.7h, and 3.59% WB concentration with 350.171 EU/mL of inulinase activity. These predictions were validated by experiments in which 401.18 EU/mL of inulinase activity for *B .licheniformis* and 344.61 EU/mL of inulinase activity for *B. velezensis.* Experimental activity results were close to the activity predictions for both bacteria. The statistical model made a strong prediction of the experimental results.

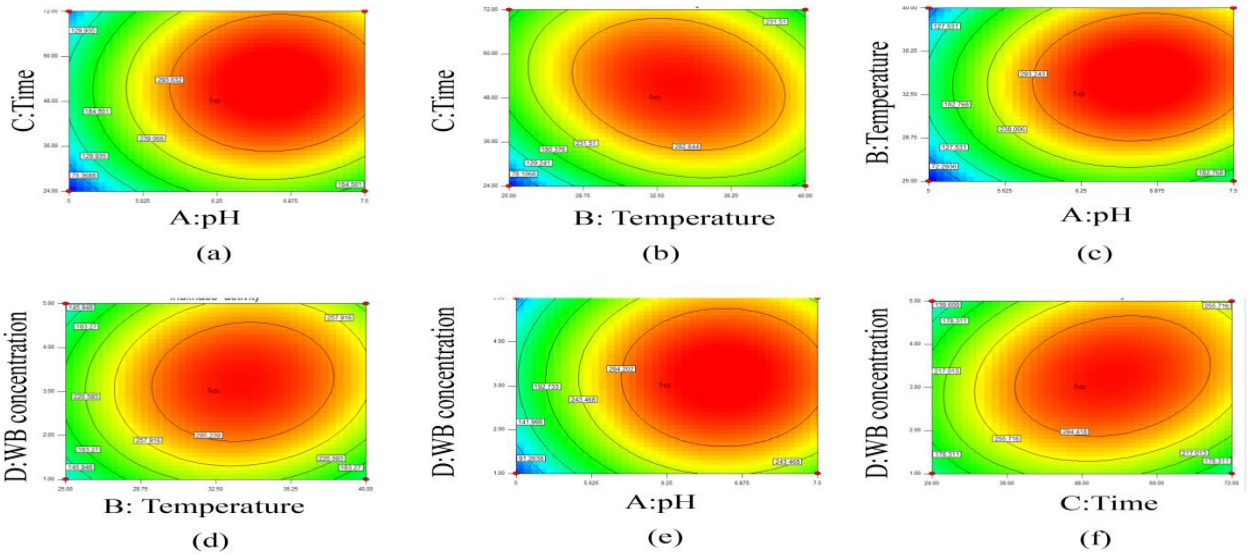

Figure 3 2-D plots of the combined effect of two variables on the inulinase-specific activity *B. velezensis*

In another study, the highest level of inulinase production (9.24 EU/mL) was observed at 35-40, pH 7.0, and medium with 3% sucrose [36]. Kamble et al. [32] tested *Tithonia rotundifolia* as a substrate for inulinase production from *Arthrobacter mysorens* and obtained the maximum inulinase activity with 1669.45 EU/mL 30^0C in the rotary shaker at 120 rpm after 48 h.

3.4. Effect of pH and temperature on enzyme activity

To date, all microbial inulinases have generally been shown to have optimum pH ranging from

3.5 to 7.0 and temperature stability in the range 10-80°C [1, 39]. As seen in Fig. 4a, the inulinase from *B. licheniformis* showed optimum activity at pH 5.0, while optimum activity at pH 6.0 was observed for inulinase from *B. velezensis*. Bacteria inulinase generally exhibit optimal activity in the pH range of 6.0-7.0, while the optimal pH ranges of 3.0-6.0 for fungal inulinases [39]. The Inulinase enzyme from *Bacillus* sp. demonstrated optimum activity at 55 °C and pH 6.5. [22] while inulinase from *Acetobacter diazotropicus* SRT4 exhibit optimal activity at pH 5.5 [40].

In order to determine the optimum temperatures of the enzymes obtained in this study, enzyme activities were tested at 30ºC-60ºC. The activities of inulinase from both bacteria were preserved at 30ºC for 120 minutes (Figure 4b).

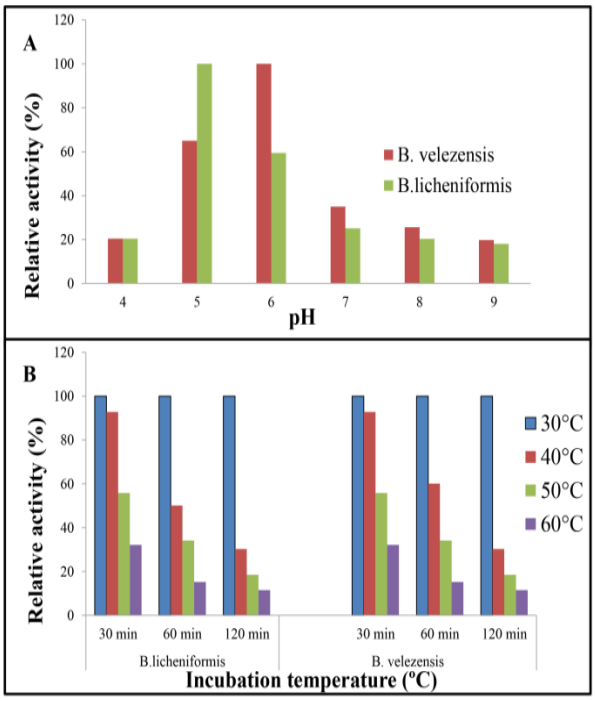

Figure 4 Effect of pH and temperature on inulinases activity from *B.licheniformis* and *B. velezensis*

Similarly, Kwon et al. [41] found the optimum temperature for the inulinase obtained from *B. polymyxa* MGL21 as 35ºC. In the study, enzyme thermostability was investigated by incubating both inulinases at 30ºC for 11 days and the remaining activity was determined. The enzymes retained 50% of their activities until 9 days, indicating that they were quite stable at 30ºC (Fig. 5). After 11 days, the inulinase from *B.licheniformis* and *B. velezensis* sustained 28% and 33% of its initial activity, respectively. This study found that both inulinases have remarkable thermostability.

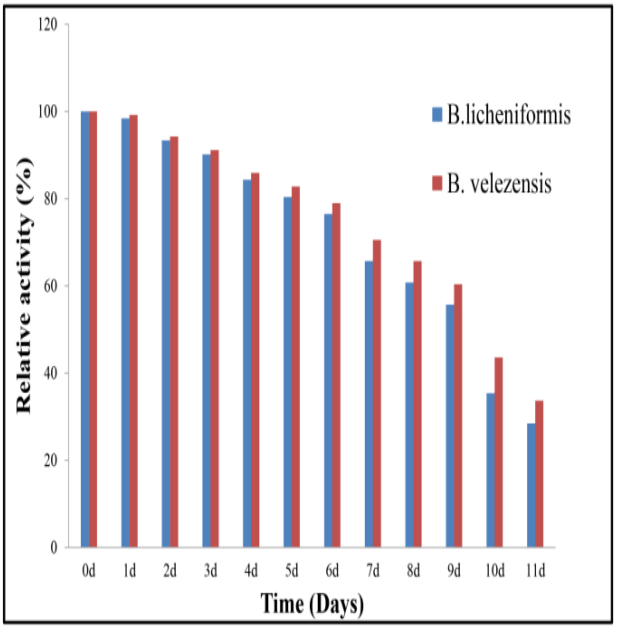

Figure 5 Thermalstability of inulinases from *B.licheniformis* and *B. velezensis* at 30°C

4. CONCLUSION

In this study, sixteen bacteria were isolated from soil samples, and molecular identifications were made. All species isolated were *Bacillus*. Among the tested microorganisms for inulinase activity, *B. licheniformis* strain SCRSW1 and *B. velezensis* strain KKLV showed a clear zone on agar plate containing 1% w/v inulin. The bacteria strains were selected to produce inulinase. Fermentation parameters and different substrates were evaluated to find the fermentation conditions supporting maximum enzyme productions by PB. WB and the fermentation parameters (pH, temperature, and time) were found to be very effective on inulinase production**.** Also, fermentation conditions were optimized by using BBD for the maximum value of inulinase for both bacteria. The maximum inulinase activities for *B. licheniformis* and *B. velezensis* were 401.18 EU/mL and 344.61

EU/mL under predicted optimum conditions by the software of Design-Expert. The obtained inulinases were found to be quite stable at 30ºC.

Moreover, optimizations were achieved successfully with high enzyme activities. The results point out that the bacteria are significant source as inulinase producers. The new isolates *B. licheniformis* and *B. velezensis* can be used to produce inulinase for industrial processes. Moreover, the highest inulinase production was obtained with WB, which is an inexpensive carbon source. It means that industrial use of WB is possible.

The Declaration of Conflict of Interest/ Common Interest

No conflict of interest or common interest has been declared by the authors.

The Declaration of Ethics Committee Approval

Ethics Committee Approval is not required.

The Declaration of Research and Publicatıon Ethics

The authors of the paper declare that they comply with the scientific, ethical and quotation rules of SAUJS in all processes of the paper and that they do not make any falsification on the data collected. In addition, they declare that Sakarya University Journal of Science and its editorial board have no responsibility for any ethical violations that may be encountered, and that this study has not been evaluated in any academic publication environment other than Sakarya University Journal of Science.

REFERENCES

[1] R. S. Singh, K. Chauhan, and J. F. A Kennedy, "Panorama of bacterial inulinases: production, purification, characterization and industrial applications," International Journal of Biological Macromolecules, vol. 96, pp. 312-322, 2017.

[2] F. Gong, T. Zhang, Z. Chi, J. Sheng, J. Li, and X. Wang, "Purification and characterization of extracellular inulinase from marine yeast *Pichia guilliermondii* and inulin hydrolysis by the purified inulinase," Biotechnology and Bioprocess Engineering, vol. 34, pp. 179-185, 2008.

[3] P. K. Gill, R. K. Manhas, and P. Singh, "Purification and properties of a heat-stable exoinulinase isoform from *Aspergillus fumigatus*," Bioresource Technology, vol. 97, no. 7, pp. 894-902, 2006.

[4] M. Germec and I. Turhan, "Partial purification and characterization of *Aspergillus niger* inulinase produced from sugar-beet molasses in the shaking incubator and stirred-tank bioreactors," International Journal of Biological Macromolecules, vol. 64, pp. 3789-3799, 2020.

[5] D. Das, M. R. Bhat, and R. Selvaraj, "Review of inulinase production using solid-state fermentation," Annals of Microbiology, vol. 69, pp. 201–209, 2019.

[6] R. A. Pessoni, M. R. Braga, and R. D. C. L. Figueiredo-Ribeiro, "Purification and properties of exo-inulinases from *Penicillium janczewskii* growing on distinct carbon sources," Mycologia, vol. 994, pp. 493-503, 2007.

[7] M. Beran, J. Pinkrová, M. Urban, and J. Drahoras, "Immobilisation of endoinulinase on polyhydroxybutyrate microfibers," Czech Journal of Food Sciences, vol. 34, pp. 541-546, 2016.

[8] S. M. Basheer, S. Chellappan, P. S. Beena, R. K. Sukumaran, K. K. Elyas, and M. Chandrasekaran, "Lipase from marine *Aspergillus awamori* BTMFW032: Production, partial purification and application in oil effluent treatment," New Biotechnology, vol. 286, pp. 627-638, 2011.

[9] Y. Zhang, X. Zhang, W. Qi, J. Xu, Z. Yuan, and Z. Wang, "Ann and Rsm Based Optimization of Cellulase Production by *Hypocrea sp* Z28 by Submerged Fermentation," Cellulose Chemistry and

Technology**,** vol. 523, no. 4, pp. 259-264, 2018.

[10] Y. Zhang, W.P. Wu, D.M. Hu, Y.Y. Su, L. Ca, "A new thermophilic species of *Myceliophthora* from China, Mycological Progress, vol. 13(1), pp.165–170, 2014.

[11] H. Jiang, H. Dong, G. Zhang, B. Yu, L.R. Chapman, M.W. Fields, "Microbial Diversity in Water and Sediment of Lake Chaka, an Athalassohaline Lake in Northwestern China," Applied and Environmental Microbiology, vol. 72(6), pp.3832-3845, 2006.

[12] M. Hasegawa, H. Kishino, and T. Yano, "Dating the human-ape split by a molecular clock of mitochondrial DNA," Journal of Molecular Evolution, vol. 22, pp. 160-174, 1985.

[13] J. Felsenstein, "Confidence limits on phylogenies, an approach using the bootstrap," Evolution, vol. 39, pp. 783-791, 1985.

[14] S. Kumar, G. Stecher, M. Li, C. Knyaz, and K. Tamura, "MEGA X: Molecular Evolutionary Genetics Analysis across computing platforms," Molecular Biology and Evolution, vol. 35, pp. 1547-1549, 2018.

[15] J. J Allais, S. Kammoun, P. Blanc, C. Girard, and J. C. Baratti, "Isolation and characterization of bacterial strains with inulinase activity," Applied and Environmental Microbiology, vol. 52, pp. 1086-1090, 1986.

[16] X. Li, L. Z. Guo, Q. Fu, and W. D. Lu, "A simple and rapid plate assay for screening of inulin degrading microorganisms using Lugol's iodine solution," African Journal of. Biotechnology, vol. 1046, pp. 9518-9521, 2011.

[17] K. Keto, T. Araki, T. Kitamura, N. Morita, M. Moori, and Y. Suzuki, "Purification and Properties of a Thermostable Inulinase β-D-Fructan Fructohydrolase from *Bacillus stearothermophilus* KP1289," Starch-Stärke, vol. 517, pp. 253-258, 1999.

[18] E. Y. Tohamy, "Purification and characterization of exoinulinase enzyme from *Sterptomyces grisenus*," Pakistan Journal of Biological Sciences, vol. 95, pp. 911-916, 2006.

[19] W. Gao, Y. Bao, Y. Liu, X. Zhang, J. Wang, and L. An, "Characterization of thermo-stable endoinulinase from a new strain *Bacillus smithii* T7," Applied Biochemistry and Biotechnology, vol. 1573, pp. 498-506, 2009.

[20] S. Gavrailov and V. Ivanova, "Effects of nitrogen and carbon sources on the production of inulinase from strain *Bacillus sp.* SG113," Acta Scientifica Naturalis, vol. 31, pp. 69-74, 2016.

[21] S. Jeza, S. B. Maseko and J. Lin, "Purification and characterization of exo-inulinase from *Paenibacillus sp*. d9 strain," Protein Journal, vol. 37, no. 1, pp. 70-81, 2018.

[22] R. Ramapriya, A. Thirumurugan, T. Sathishkumar, and D. R. Manimaran, "Partial purification and characterization of exoinulinase produced from *Bacillus sp*.," Journal of Genetic Engineering and Biotechnology, vol. 162, pp. 363-367, 2018.

[23] Y. Suberu, I. Akande, T. Samuel, A. Lawal, and A. Olaniran, "Optimization of protease production in indigenous *Bacillus* species isolated from soil samples in Lagos, Nigeria using response surface methodology," Biocatalysis and Agricultural Biotechnology, vol. 18, 101011, 2019, https://doi.org/10.1016/j.bcab.2019.01.049.

[24] M. Ilgın, M. Germec, and I. Turhan, "Inulinase production and mathematical modeling from carob extract by using

Aspergillus niger," Biotechnology Progress, vol. 36, p. e2919, 2019.

[25] À. Llarch, N. A. Logan, J. Castellví, M. J. Prieto, and J. Guinea, "Isolation and Characterization of Thermophilic *Bacillus* spp. from Geothermal Environments on Deception Island, South Shetland Archipelago," Microbial Ecology, vol. 34(1), pp. 58-65, 1997.

[26] B. T. Mohammad, H. I. Al Daghistani, A. Jaouani, S. Abdel-Latif, and C. Kennes, "Isolation and Characterization of Thermophilic Bacteria from Jordanian Hot Springs: *Bacillus licheniformis* and *Thermomonas hydrothermalis* Isolates as Potential Producers of Thermostable Enzymes," International Journal of Microbiology, vol. 2017, pp.1-12, 2017.

[27] H. Sattar, Z. Bibi, A. Kamran, A. Aman, and S. A. U. Qader, "Degradation of complex casein polymer: Production and optimization of a novel serine metalloprotease from *Aspergillus niger* KIBGE-IB36," Biocatalysis and Agricultural Biotechnology, vol. 21, p. 101256, 2019, https://doi.org/10.1016/j.bcab.2019.101256

[28] S. Jain, P. Jain, and N. Kango, "Production of inulinase from *Kluyvermyces marxianus* using dahlia tubers extract," Brazilian Journal of Microbiology, vol. 43, no. 1, pp. 62-69, 2012.

[29] S. N. Muslim, A. M. Ali, I. A. Salman, I. M. A. L. Kadmy, and S. N. Muslim, "Detection of the optimal conditions for inulinase productivity and activity by *Acinetobacter baumannii* isolated from agricultural *rhizosphere* soil," Biological Sciences, vol. 21, pp. 1-7, 2015.

[30] R. Singh and R. Singh, "Inulinases. Current Developments in Biotechnology and Bioengineering Current Developments in Biotechnology and Bioengineering: Production, Isolation and Purification of Industrial Products," Elsevier, pp. 423-446, 2017, http://dx.doi.org/10.1016/B978-0-444-63662-1.00018-X.

[31] C. Xiong, W. Jinhua, and L. Dongsheng, "Optimization of solid-state medium for the production of inulinase by *Kluyveromyces* S120 using response surface methodology," Biochemical Engineering Journal, vol. 342, pp. 179-184, 2007.

[32] P. P. Kamble, M. V. Kore, S. A. Patil, J. P. Jadhav, and Y. C. Attar, "Statistical optimization of process parameters for inulinase production from *Tithonia* weed by *Arthrobacter mysorens* strain no.1," Journal of Microbiological Methods, vol. 149, pp. 55-66, 2018.

[33] H. K. Rawat, S. Chand Jain, and N. Kango, Production and properties of inulinase from *Penicillium sp.* NFCC 2768 grown on inulin-rich vegetal infusions," Biocatalysis and Biotransformation, vol. 331, pp. 61-68, 2015.

[34] P. P. Kamble, S. S. Suryawanshi, J. P. Jadhav, and Y.C. Attar, "Enhanced inulinase production by *Fusarium solani* JALPK from invasive weed using response surface methodology," Journal of Microbiological Methods, vol. 159, pp. 99-111, 2019.

[35] S. Trivedi, J. Divecha, and A. Shah, "Optimization of inulinase production by newly isolated *Aspergillus tubingensis* CR16 using low cost substrates," Carbohydrate Polymers, vol. 901, pp. 483-490, 2012.

[36] K. Naidoo, M. Ayyachamy, K. Permaul, and S. Singh, "Enhanced fructooligosaccharides and inulinase production by a *Xanthomonas campestris* pv.phaseoli KM 24 mutant," Bioprocess and Biosystems Engineering, vol. 325, pp. 689-695, 2009.

[37] N. A. Zherebtsov, S. A. Shelamova, and I. N. Abramova, "Biosynthesis of inulinases

by *Bacillus* bacteria," Applied Biochemistry and Microbiology, vol. 386, pp. 544-548, 2002.

[38] A. A. Onilude, I. F. Fadaunsi, and E. O. Garuba, "Inulinase production by *Saccharomyces sp.* in solid state fermentation using wheat bran as substrate," Annals Microbiology, vol. 622, pp. 843-848, 2012.

[39] X. Li, L. Z. Guo, and W. D. Lu, "Alkaline inulinase production by a newly isolated bacterium *Marinimicrobium sp.* LS–A18 and inulin hydrolysis by the enzyme," World Journal of Microbiology and Biotechnology, vol. 281, pp. 81-89, 2012.

[40] Y. Tambara, J. V. Hormaza, C. Perez, A. Leon, J. Arrieta, and L. Hernandez, "Structural analysis and optimized production of fructo-olgiosaccharides by levansucrase from *Acetobacter diazotrophicus* SRT4," Biotechnology Letter, vol. 21, pp. 117–121, 1999.

[41] H. J. Kwon, S. J. Jeon, D. J. You, K. H. Kim, Y. K. Jeong, Y. H. Kim, Y. M. Kim, and B. W. Kim, "Cloning and characterization of an exoinulinase from *Bacillus polymyxa,"* Biotechnology Letter, vol. 25, pp. 155-159, 2003.